

WL-TR-96-2102



**AN EXPERIMENTAL INVESTIGATION
OF TRANSVERSE INJECTION FROM
CIRCULAR AND ELLIPTICAL NOZZLES
INTO A SUPERSONIC CROSSFLOW**

**MARK R. GRUBER
ABDOLLAH S. NEJAD
J. CRAIG DUTTON**

JAN 1996

FINAL REPORT FOR 01/01/93 TO 01/01/96

APPROVED FOR PUBLIC RELEASE; DISTRIBUTION IS UNLIMITED

19961104 102

**AERO PROPULSION AND POWER DIRECTORATE
WRIGHT LABORATORY
AIR FORCE MATERIEL COMMAND
WRIGHT-PATTERSON AFB OH 45433-7251**

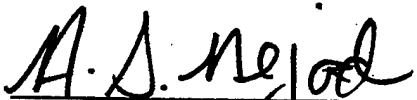
WRIGHT LABORATORY

NOTICE

When Government drawings, specifications, or other data are used for any purpose other than in connection with a definitely Government-related procurement, the United States Government incurs no responsibility or any obligation whatsoever. The fact that the government may have formulated or in any way supplied the said drawings, specifications, or other data, is not to be regarded by implication, or otherwise in any manner construed, as licensing the holder, or any other person or corporation; or as conveying any rights or permission to manufacture, use, or sell any patented invention that may in any way be related thereto.

This report is releasable to the National Technical Information Service (NTIS). At NTIS, it will be available to the general public, including foreign nations.

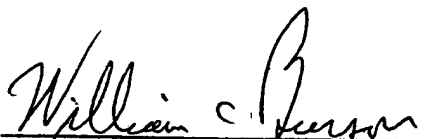
This technical report has been reviewed and is approved for publication.



ABDOLLAH S. NEJAD, PhD
Project Manager, WL/POPT
Experimental Research Branch
Advanced Propulsion Division



ABDOLLAH S. NEJAD, PhD
Acting Chief
Experimental Research Branch
Advanced Propulsion Division



WILLIAM C. BURSON, PhD
Acting Chief
Advanced Propulsion Division

If your address has changed, if you wish to be removed from our mailing list, or if the addressee is no longer employed by your organization please notify WL/POPT, WPAFB, OH 45433-7251 to help us maintain a current mailing list.

Copies of this report should not be returned unless return is required by security considerations, contractual obligations, or notice on a specific document.

REPORT DOCUMENTATION PAGE			Form Approved OMB No. 0704-0188	
Public reporting burden for this collection of information is estimated to average 1 hour per response, including the time for reviewing instructions, searching existing data sources, gathering and maintaining the data needed, and completing and reviewing the collection of information. Send comments regarding this burden estimate or any other aspect of this collection of information, including suggestions for reducing this burden, to Washington Headquarters Services, Directorate for Information Operations and Reports, 1215 Jefferson Davis Highway, Suite 1204, Arlington, VA 22202-4302, and to the Office of Management and Budget, Paperwork Reduction Project (0704-0188), Washington, DC 20503.				
1. AGENCY USE ONLY (Leave blank)		2. REPORT DATE January 1996	3. REPORT TYPE AND DATES COVERED Final, January 1993 - January 1996	
4. TITLE AND SUBTITLE An Experimental Investigation of Transverse Injection from Circular and Elliptical Nozzles into a Supersonic Crossflow			5. FUNDING NUMBERS PE 61102F PR 2308 TA S1 WU 01	
6. AUTHOR(S) Dr. Mark R. Gruber Dr. Abdollah S. Nejad Prof. J. Craig Dutton				
7. PERFORMING ORGANIZATION NAME(S) AND ADDRESS(ES) Experimental Research Branch Advanced Propulsion Division 1950 Fifth Street Wright-Patterson AFB OH 45433-7251			8. PERFORMING ORGANIZATION REPORT NUMBER	
9. SPONSORING/MONITORING AGENCY NAME(S) AND ADDRESS(ES) Aero Propulsion and Power Directorate Wright Laboratory Air Force Materiel Command Wright-Patterson AFB OH 45433-7251 POC: Dr. Gruber, WL/POPT, (937) 255-4141			10. SPONSORING/MONITORING AGENCY REPORT NUMBER WL-TR-96-2102	
11. SUPPLEMENTARY NOTES				
12a. DISTRIBUTION /AVAILABILITY STATEMENT Approved for public release; distribution is unlimited.			12b. DISTRIBUTION CODE	
13. ABSTRACT (Maximum 200 words) Transverse injection of helium and air through circular and elliptical nozzles into a supersonic crossflow was investigated using optical diagnostics and probe-based measurement techniques. Shadowgraph visualizations documented the global characteristics of the jet/freestream interaction. Rayleigh/Mie scattering allowed ensembles of digital images from several measurement planes in each case to be collected. Pitot and concentration probes were used in the helium injection cases. The images provide mean and standard deviation statistics, spreading and penetration characteristics, large-scale mixing and convective velocity information, bow and separation shock features, and two-dimensional spatial correlation fields. Results indicate that the elliptical nozzle produces jets with greater lateral spread and suppressed transverse penetration compared to the jets from the circular nozzle. Injectant molecular weight does not strongly affect the jet's penetration, although it leads to substantial compressibility differences that dramatically influence the characteristics of the large-scale shear layer structures and the entrainment and mixing occurring between the injectant and crossflow. Probe measurements provide quantitative comparisons of total pressure losses and mixing characteristics. Results suggest better near field mixing and lower total pressure losses in the elliptical injection flowfield.				
14. SUBJECT TERMS Transverse injection, supersonic flow, laser diagnostics, turbulent flow, compressible flow.			15. NUMBER OF PAGES 311	
			16. PRICE CODE	
17. SECURITY CLASSIFICATION OF REPORT UNCLASSIFIED	18. SECURITY CLASSIFICATION OF THIS PAGE UNCLASSIFIED	19. SECURITY CLASSIFICATION OF ABSTRACT UNCLASSIFIED	20. LIMITATION OF ABSTRACT SAR	

TABLE OF CONTENTS

	Page
LIST OF TABLES.....	vi
LIST OF FIGURES.....	vii
NOMENCLATURE	xix
1. INTRODUCTION.....	1
2. LITERATURE REVIEW.....	5
2.1 Jet Penetration	5
2.2 Injection Flowfield Structure	9
2.3 Injectant/Freestream Mixing.....	13
2.4 Time-Averaged Computations	17
2.5 Summary.....	19
3. EXPERIMENTAL APPARATUS.....	21
3.1 Air Supply and Control System.....	21
3.2 Wind Tunnel.....	22
3.2.1 Inlet Section	22
3.2.2 Settling Chamber.....	23
3.2.3 Supersonic Nozzle and Test Section	24
3.2.4 Diffuser Section.....	26
3.3 Flow Quality Measurements.....	27
4. EXPERIMENTAL METHODS.....	29
4.1 General Data Acquisition.....	29
4.2 Shadowgraph Photography.....	30
4.3 Planar Rayleigh/Mie Scattering	31
4.3.1 Theory and Implementation.....	32
4.3.2 Particle Response.....	35
4.3.3 Particle Seeding Technique.....	36

	Page
4.3.4 Noise Considerations.....	38
4.4 Probe-Based Measurements	39
4.4.1 Pitot Pressure Probe.....	39
4.4.2 Concentration Probe	40
4.4.3 Data Reduction for Injectant Concentration.....	44
5. RESULTS AND DISCUSSION.....	46
5.1 Experimental Conditions	46
5.2 Shadowgraph Flow Visualizations.....	48
5.3 Planar Rayleigh/Mie Scattering Images	50
5.3.1 End View Images.....	53
5.3.1.1 Instantaneous Images	54
5.3.1.2 Ensemble-Averaged Results	58
5.3.1.3 Standard Deviation Results	65
5.3.2 Single-Shot Side View Images	78
5.3.2.1 Instantaneous Images	79
5.3.2.2 Ensemble-Averaged Results	83
5.3.2.3 Standard Deviation Results	88
5.3.2.4 Spatial Correlation Results.....	94
5.3.3 Bow Shock/Jet Boundary Interaction Images.....	100
5.3.3.1 Instantaneous Images	101
5.3.3.2 Ensemble-Averaged and Standard Deviation Results ...	106
5.3.4 Double-Pulsed Side View Images.....	108
5.3.4.1 Instantaneous Image Pairs.....	110
5.3.4.2 Large-Scale Convection Velocity Measurements	111
5.4 Pitot and Concentration Probe Measurements.....	115
5.4.1 Pitot Probe Results.....	115

	Page
5.4.2 Concentration Probe Results.....	120
5.5 Discussion.....	125
5.5.1 Shock Structure.....	125
5.5.2 Transverse Penetration and Lateral Spread	127
5.5.3 Large-Scale Structures.....	129
5.5.4 Entrainment and Mixing Issues	132
6. CONCLUSIONS AND RECOMMENDATIONS.....	135
6.1 Summary of Major Results and Conclusions.....	137
6.2 Recommendations for Future Work.....	143
TABLES.....	147
FIGURES.....	155
APPENDIX: ESTIMATION OF COMPRESSIBILITY LEVELS	283
REFERENCES	292

LIST OF TABLES

	Page
Table 2.1 Incompressible Transverse Injection Penetration Correlations and Conclusions	147
Table 2.2 Compressible Transverse Injection Penetration Correlations and Conclusions	148
Table 3.1 Injector Geometries	149
Table 5.1 Experimental Conditions	150
Table 5.2 Interrogation Planes.....	151
Table 5.3 Ensemble-Averaged Two-Dimensional Spatial Correlation Results	151
Table 5.4 Area-Averaged Total Pressure Values	152
Table 5.5 Area-Averaged Concentration Values.....	152
Table 5.6 Contributions of Present Work.....	153

LIST OF FIGURES

	Page
Figure 1.1 Transverse Injection Flowfield Schematic	155
Figure 1.2 Perspective View of Transverse Injection Flowfield.....	155
Figure 2.1 Comparison of Transverse Jet Penetration Correlations.....	156
Figure 2.2 Smoke-Wire Visualization of Low Speed Jet in Crossflow Showing Shear Layer Vortices ($J = 4$) [from Fric and Roshko ⁴⁹]	156
Figure 2.3 Smoke-Wire Visualization of Low Speed Jet in Crossflow-Wide View Showing Shear Layer Vortices ($J = 4$) [from Fric and Roshko ⁵³]	157
Figure 2.4 Dye Injection Visualization of Low Speed Jet in Crossflow Showing Shear Layer Vortices ($J = 4.8$) [from Perry, et al. ⁵²].....	157
Figure 2.5 Smoke-Wire Visualization of Low Speed Jet in Crossflow Showing Wake Vortices ($J = 4.8$) [from Fric and Roshko ⁵³].....	157
Figure 3.1 Air Supply System Schematic	158
Figure 3.2 Schematic of Supersonic Combustion Tunnel.....	158
Figure 3.3 Photograph of Supersonic Combustion Tunnel	159
Figure 3.4 Schematic of Settling Chamber.....	159
Figure 3.5 Photograph of Transition Section with One Piece Installed.....	160
Figure 3.6 Photograph of Completed Transition Section.....	160
Figure 3.7 Nozzle Section/Test Section Schematic.....	161
Figure 3.8 Illustration of Injector Configurations	161
Figure 3.9 Photograph of Injectors	162
Figure 3.10 Jet Gas Supply Schematic.....	162
Figure 3.11 Photograph of Pitot Pressure Rake	163
Figure 3.12 Photograph of Boundary Layer Rake.....	163

	Page
Figure 3.13 Streamwise and Spanwise Mach Number Distributions at Transverse Centerline	164
Figure 3.14 Transverse and Spanwise Mach Number Distributions at $x = 111$ mm	164
Figure 3.15 Transverse and Spanwise Mach Number Distributions at $x = 283$ mm	165
Figure 3.16 Pressure Ratio Profiles from Nozzle Sidewalls at $p_o = 317$ kPa	165
Figure 3.17 Contours of Rake Total Pressure Normalized by Freestream Total Pressure ...	166
Figure 4.1 Schematic of General Data Acquisition System	167
Figure 4.2 Schematic of Pulsed Shadowgraph System.....	167
Figure 4.3 Photograph of Pulsed Shadowgraph System.....	168
Figure 4.4 Schematic of End View Rayleigh/Mie Scattering Optical Arrangement.....	168
Figure 4.5 Photograph of End View Rayleigh/Mie Scattering Optical Arrangement.....	169
Figure 4.6 Schematic of Side View Rayleigh/Mie Scattering Optical Arrangement	169
Figure 4.7 Photograph of Side View Rayleigh/Mie Scattering Optical Arrangement	170
Figure 4.8 Schematic of Double Pulsed Rayleigh/Mie Scattering Optical Arrangement	170
Figure 4.9 Photograph of Double Pulsed Rayleigh/Mie Scattering Optical Arrangement ..	171
Figure 4.10 Delay System Electrical Schematic.....	171
Figure 4.11 Silane Seeding System Schematic.....	172
Figure 4.12 Photograph of Silane Seeding System.....	172
Figure 4.13 Illustration of Mean Flow Probe Designs (Side View)	173
Figure 4.14 Schematic of Probe Installation.....	173
Figure 4.15 Photograph Showing Probe Drive Hardware.....	174
Figure 4.16 Model of Concentration Probe.....	174
Figure 4.17 Schematic of Sampling Vessel.....	175
Figure 4.18 Concentration Probe Calibration Profiles	175
Figure 5.1 Shadowgraph of Circular Injection Using Air (Case C1A)	176
Figure 5.2 Shadowgraph of Circular Injection Using Helium (Case C2H).....	176

Figure 5.3	Shadowgraph of Elliptical Injection Using Air (Case E1A).....	177
Figure 5.4	Shadowgraph of Elliptical Injection Using Helium (Case E2H)	177
Figure 5.5	Standard Deviation Intensity Traces from Case C1A at $x/d_{eff} = 4$ a) Transverse Data Trace from $z/d_{eff} = 0$ and b) Spanwise Data Trace from $y/d_{eff} = 1.8$	178
Figure 5.6	Instantaneous End View Images of Circular Injection Using Air (Case C1A) at $x/d_{eff} = 0$	179
Figure 5.7	Instantaneous End View Images of Circular Injection Using Air (Case C1A) at $x/d_{eff} = 4$	180
Figure 5.8	Instantaneous End View Images of Circular Injection Using Air (Case C1A) at $x/d_{eff} = 8$	181
Figure 5.9	Instantaneous End View Images of Circular Injection Using Air (Case C1A) at $x/d_{eff} = 10$	182
Figure 5.10	Instantaneous End View Images of Circular Injection Using Helium (Case C2H) at $x/d_{eff} = 0$	183
Figure 5.11	Instantaneous End View Images of Circular Injection Using Helium (Case C2H) at $x/d_{eff} = 4$	184
Figure 5.12	Instantaneous End View Images of Circular Injection Using Helium (Case C2H) at $x/d_{eff} = 8$	185
Figure 5.13	Instantaneous End View Images of Circular Injection Using Helium (Case C2H) at $x/d_{eff} = 10$	186
Figure 5.14	Instantaneous End View Images of Elliptical Injection Using Air (Case E1A) at $x/d_{eff} = 0$	187
Figure 5.15	Instantaneous End View Images of Elliptical Injection Using Air (Case E1A) at $x/d_{eff} = 4$	188

	Page
Figure 5.16 Instantaneous End View Images of Elliptical Injection Using Air (Case E1A) at $x/d_{eff} = 8$	189
Figure 5.17 Instantaneous End View Images of Elliptical Injection Using Air (Case E1A) at $x/d_{eff} = 10$	190
Figure 5.18 Instantaneous End View Images of Elliptical Injection Using Helium (Case E2H) at $x/d_{eff} = 0$	191
Figure 5.19 Instantaneous End View Images of Elliptical Injection Using Helium (Case E2H) at $x/d_{eff} = 4$	192
Figure 5.20 Instantaneous End View Images of Elliptical Injection Using Helium (Case E2H) at $x/d_{eff} = 8$	193
Figure 5.21 Instantaneous End View Images of Elliptical Injection Using Helium (Case E2H) at $x/d_{eff} = 10$	194
Figure 5.22 Normalized Ensemble-Averaged End View Images of Circular Injection Using Air (Case C1A) a) $x/d_{eff} = 0$, b) $x/d_{eff} = 4$, c) $x/d_{eff} = 8$, and d) $x/d_{eff} = 10$	195
Figure 5.23 End View Penetration Contours for Case C1A a) $x/d_{eff} = 0$, b) $x/d_{eff} = 4$, c) $x/d_{eff} = 8$, and d) $x/d_{eff} = 10$	196
Figure 5.24 Normalized Ensemble-Averaged End View Images of Circular Injection Using Helium (Case C2H) a) $x/d_{eff} = 0$, b) $x/d_{eff} = 4$, c) $x/d_{eff} = 8$, and d) $x/d_{eff} = 10$	197
Figure 5.25 End View Penetration Contours for Case C2H a) $x/d_{eff} = 0$, b) $x/d_{eff} = 4$, c) $x/d_{eff} = 8$, and d) $x/d_{eff} = 10$	198
Figure 5.26 Normalized Ensemble-Averaged End View Images of Elliptical Injection Using Air (Case E1A) a) $x/d_{eff} = 0$, b) $x/d_{eff} = 4$, c) $x/d_{eff} = 8$, and d) $x/d_{eff} = 10$	199

	Page
Figure 5.27 End View Penetration Contours for Case E1A a) $x/d_{eff} = 0$, b) $x/d_{eff} = 4$, c) $x/d_{eff} = 8$, and d) $x/d_{eff} = 10$	200
Figure 5.28 Normalized Ensemble-Averaged End View Images of Elliptical Injection Using Helium (Case E2H) a) $x/d_{eff} = 0$, b) $x/d_{eff} = 4$, c) $x/d_{eff} = 8$, and d) $x/d_{eff} = 10$	201
Figure 5.29 End View Penetration Contours for Case E2H a) $x/d_{eff} = 0$, b) $x/d_{eff} = 4$, c) $x/d_{eff} = 8$, and d) $x/d_{eff} = 10$	202
Figure 5.30 Transverse Penetration Profiles from Ensemble-Averaged End View Images..	203
Figure 5.31 Lateral Spread Profiles from Ensemble-Averaged End View Images Using d_{eff} to Normalize the Spanwise Axis	203
Figure 5.32 Lateral Spread Profiles from Ensemble-Averaged End View Images Using Physical Spanwise Nozzle Exit Dimension to Normalize the Spanwise Axis ..	204
Figure 5.33 Relative Spreading in the Spanwise and Transverse Planes	204
Figure 5.34 Area Ratios Determined Using Areas Enclosed Inside 90% Contours from Ensemble-Averaged End View Images.....	205
Figure 5.35 Normalized Standard Deviation End View Images of Circular Injection Using Air (Case C1A) a) $x/d_{eff} = 0$, b) $x/d_{eff} = 4$, c) $x/d_{eff} = 8$, and d) $x/d_{eff} = 10$...	206
Figure 5.36 Spanwise Profiles of Normalized Standard Deviation for Case C1A a) $x/d_{eff} = 0$, $y/d_{eff} = 1.3$, b) $x/d_{eff} = 4$, $y/d_{eff} = 1.8$, c) $x/d_{eff} = 8$, $y/d_{eff} = 1.8$, and d) $x/d_{eff} = 10$, $y/d_{eff} = 1.8$	207
Figure 5.37 Transverse Profiles of Normalized Standard Deviation for Case C1A a) $x/d_{eff} = 0$, $z/d_{eff} = 0$, b) $x/d_{eff} = 4$, $z/d_{eff} = 0$, c) $x/d_{eff} = 8$, $z/d_{eff} = 0$, and d) $x/d_{eff} = 10$, $z/d_{eff} = 0$	208
Figure 5.38 Normalized Standard Deviation End View Images of Circular Injection Using Helium (Case C2H) a) $x/d_{eff} = 0$, b) $x/d_{eff} = 4$, c) $x/d_{eff} = 8$, and d) $x/d_{eff} = 10$	209

	Page
Figure 5.39 Spanwise Profiles of Normalized Standard Deviation for Case C2H a) $x/d_{eff} = 0$, $y/d_{eff} = 1.3$, b) $x/d_{eff} = 4$, $y/d_{eff} = 1.8$, c) $x/d_{eff} = 8$, $y/d_{eff} = 1.8$, and d) $x/d_{eff} = 10$, $y/d_{eff} = 1.8$	210
Figure 5.40 Transverse Profiles of Normalized Standard Deviation for Case C2H a) $x/d_{eff} = 0$, $z/d_{eff} = 0$, b) $x/d_{eff} = 4$, $z/d_{eff} = 0$, c) $x/d_{eff} = 8$, $z/d_{eff} = 0$, and d) $x/d_{eff} = 10$, $z/d_{eff} = 0$	211
Figure 5.41 Normalized Standard Deviation End View Images of Elliptical Injection Using Air (Case E1A) a) $x/d_{eff} = 0$, b) $x/d_{eff} = 4$, c) $x/d_{eff} = 8$, and d) $x/d_{eff} = 10$...	212
Figure 5.42 Spanwise Profiles of Normalized Standard Deviation for Case E1A a) $x/d_{eff} = 0$, $y/d_{eff} = 1.3$, b) $x/d_{eff} = 4$, $y/d_{eff} = 1.8$, c) $x/d_{eff} = 8$, $y/d_{eff} = 1.8$, and d) $x/d_{eff} = 10$, $y/d_{eff} = 1.8$	213
Figure 5.43 Transverse Profiles of Normalized Standard Deviation for Case E1A a) $x/d_{eff} = 0$, $z/d_{eff} = 0$, b) $x/d_{eff} = 4$, $z/d_{eff} = 0$, c) $x/d_{eff} = 8$, $z/d_{eff} = 0$, and d) $x/d_{eff} = 10$, $z/d_{eff} = 0$	214
Figure 5.44 Normalized Standard Deviation End View Images of Elliptical Injection Using Helium (Case E2H) a) $x/d_{eff} = 0$, b) $x/d_{eff} = 4$, c) $x/d_{eff} = 8$, and d) $x/d_{eff} = 10$	215
Figure 5.45 Spanwise Profiles of Normalized Standard Deviation for Case E2H a) $x/d_{eff} = 0$, $y/d_{eff} = 1.3$, b) $x/d_{eff} = 4$, $y/d_{eff} = 1.8$, c) $x/d_{eff} = 8$, $y/d_{eff} = 1.8$, and d) $x/d_{eff} = 10$, $y/d_{eff} = 1.8$	216
Figure 5.46 Transverse Profiles of Normalized Standard Deviation for Case E2H a) $x/d_{eff} = 0$, $z/d_{eff} = 0$, b) $x/d_{eff} = 4$, $z/d_{eff} = 0$, c) $x/d_{eff} = 8$, $z/d_{eff} = 0$, and d) $x/d_{eff} = 10$, $z/d_{eff} = 0$	217
Figure 5.47 End View Mixing Zone Contours for Case C1A a) $x/d_{eff} = 0$, b) $x/d_{eff} = 4$, c) $x/d_{eff} = 8$, and d) $x/d_{eff} = 10$	218

	Page
Figure 5.48 End View Mixing Zone Contours for Case C2H a) $x/d_{eff} = 0$, b) $x/d_{eff} = 4$, c) $x/d_{eff} = 8$, and d) $x/d_{eff} = 10$	219
Figure 5.49 End View Mixing Zone Contours for Case E1A a) $x/d_{eff} = 0$, b) $x/d_{eff} = 4$, c) $x/d_{eff} = 8$, and d) $x/d_{eff} = 10$	220
Figure 5.50 End View Mixing Zone Contours for Case E2H a) $x/d_{eff} = 0$, b) $x/d_{eff} = 4$, c) $x/d_{eff} = 8$, and d) $x/d_{eff} = 10$	221
Figure 5.51 Area Ratios Determined from End View Standard Deviation Contours	222
Figure 5.52 Shape Factors Determined from End View Standard Deviation Contours	222
Figure 5.53 Instantaneous Side View Images of Circular Injection Using Air (Case C1A) .	223
Figure 5.54 Instantaneous Side View Images of Circular Injection Using Helium (Case C2H)	225
Figure 5.55 Instantaneous Side View Images of Elliptical Injection Using Air (Case E1A).	227
Figure 5.56 Instantaneous Side View Images of Elliptical Injection Using Helium (Case E2H)	229
Figure 5.57 Normalized Ensemble-Averaged Side View Images of Circular Injection Using Air (Case C1A).....	231
Figure 5.58 Transverse Profiles of Normalized Mean Intensity for Case C1A	231
Figure 5.59 Normalized Ensemble-Averaged Side View Images of Circular Injection Using Helium (Case C2H).....	232
Figure 5.60 Transverse Profiles of Normalized Mean Intensity for Case C2H	232
Figure 5.61 Normalized Ensemble-Averaged Side View Images of Elliptical Injection Using Air (Case E1A)	233
Figure 5.62 Transverse Profiles of Normalized Mean Intensity for Case E1A.....	233
Figure 5.63 Normalized Ensemble-Averaged Side View Images of Elliptical Injection Using Helium (Case E2H).....	234
Figure 5.64 Transverse Profiles of Normalized Mean Intensity for Case E2H	234

	Page
Figure 5.65 Transverse Penetration Profiles from Ensemble-Averaged Side View Images a) Circular Injection, b) Elliptical Injection, and c) Circular and Elliptical Injection Correlations.....	235
Figure 5.66 Normalized Standard Deviation Side View Images of Circular Injection Using Air (Case C1A)	237
Figure 5.67 Transverse Profiles of Normalized Standard Deviation for Case C1A	237
Figure 5.68 Normalized Standard Deviation Side View Images of Circular Injection Using Helium (Case C2H).....	238
Figure 5.69 Transverse Profiles of Normalized Standard Deviation for Case C2H	238
Figure 5.70 Normalized Standard Deviation Side View Images of Elliptical Injection Using Air (Case E1A)	239
Figure 5.71 Transverse Profiles of Normalized Standard Deviation for Case E1A.....	239
Figure 5.72 Normalized Standard Deviation Side View Images of Elliptical Injection Using Helium (Case E2H).....	240
Figure 5.73 Transverse Profiles of Normalized Standard Deviation for Case E2H	240
Figure 5.74 Two-Dimensional Spatial Correlation Fields from Upstream Instantaneous Side View Images of Circular Injection Using Air (Case C1A)	241
Figure 5.75 Two-Dimensional Spatial Correlation Fields from Downstream Instantaneous Side View Images of Circular Injection Using Air (Case C1A)	243
Figure 5.76 Two-Dimensional Spatial Correlation Fields from Upstream Instantaneous Side View Images of Circular Injection Using Helium (Case C2H).....	245
Figure 5.77 Two-Dimensional Spatial Correlation Fields from Downstream Instantaneous Side View Images of Circular Injection Using Helium (Case C2H).....	247
Figure 5.78 Two-Dimensional Spatial Correlation Fields from Upstream Instantaneous Side View Images of Elliptical Injection Using Air (Case E1A).....	249

	Page
Figure 5.79 Two-Dimensional Spatial Correlation Fields from Downstream Instantaneous Side View Images of Elliptical Injection Using Air (Case E1A).....	251
Figure 5.80 Two-Dimensional Spatial Correlation Fields from Upstream Instantaneous Side View Images of Elliptical Injection Using Helium (Case E2H)	253
Figure 5.81 Two-Dimensional Spatial Correlation Fields from Downstream Instantaneous Side View Images of Elliptical Injection Using Helium (Case E2H)	255
Figure 5.82 Ensemble-Averaged Two-Dimensional Spatial Correlation Fields from Side View Images of Circular Injection Using Air (Case C1A) a) Upstream Image and b) Downstream Image	257
Figure 5.83 Ensemble-Averaged Two-Dimensional Spatial Correlation Fields from Side View Images of Circular Injection Using Helium (Case C2H) a) Upstream Image and b) Downstream Image.....	258
Figure 5.84 Ensemble-Averaged Two-Dimensional Spatial Correlation Fields from Side View Images of Elliptical Injection Using Air (Case E1A) a) Upstream Image and b) Downstream Image	259
Figure 5.85 Ensemble-Averaged Two-Dimensional Spatial Correlation Fields from Side View Images of Elliptical Injection Using Helium (Case E2H) a) Upstream Image and b) Downstream Image.....	260
Figure 5.86 Instantaneous Images of Bow Shock/Jet Boundary Interaction Upstream of Circular Injector Using Air (Case C1A).....	261
Figure 5.87 Instantaneous Images of Bow Shock/Jet Boundary Interaction Upstream of Elliptical Injector Using Air (Case E1A)	263
Figure 5.88 Ensemble-Averaged Image of Bow Shock/Jet Boundary Interaction Upstream of Circular Injector Using Air (Case C1A).....	265
Figure 5.89 Ensemble-Averaged Image of Bow Shock/Jet Boundary Interaction Upstream of Elliptical Injector Using Air (Case E1A)	265

	Page
Figure 5.90 Intensity Profiles from Ensemble-Averaged Bow Shock/Jet Boundary Interaction Images of Cases C1A and E1A at $x/d_{\text{eff}} = 0$	266
Figure 5.91 Standard Deviation Image of Bow Shock/Jet Boundary Interaction Upstream of Circular Injector Using Air (Case C1A).....	266
Figure 5.92 Standard Deviation Image of Bow Shock/Jet Boundary Interaction Upstream of Elliptical Injector Using Air (Case E1A)	267
Figure 5.93 Intensity Profiles from Standard Deviation Bow Shock/Jet Boundary Interaction Images of Cases C1A and E1A at $x/d_{\text{eff}} = 0$	267
Figure 5.94 Large-Scale Convection Velocity and Structure Convection Angle Determination	268
Figure 5.95 Instantaneous Double-Pulsed Image Pair from Circular Injection Using Air (Case C1A) with Laser Pulse Delay of $\Delta t = 2 \mu\text{s}$	269
Figure 5.96 Instantaneous Double-Pulsed Image Pair from Circular Injection Using Helium (Case C2H) with Laser Pulse Delay of $\Delta t = 1 \mu\text{s}$	269
Figure 5.97 Instantaneous Double-Pulsed Image Pair from Elliptical Injection Using Air (Case E1A) with Laser Pulse Delay of $\Delta t = 2 \mu\text{s}$	270
Figure 5.98 Instantaneous Double-Pulsed Image Pair from Elliptical Injection Using Helium (Case E2H) with Laser Pulse Delay of $\Delta t = 1.2 \mu\text{s}$	270
Figure 5.99 Large-Scale Convection Velocity as a Function of Streamwise Position for Circular Injection Using Air (Case C1A).....	271
Figure 5.100 Structure Convection Angle as a Function of Streamwise Position for Circular Injection Using Air (Case C1A).....	271
Figure 5.101 Large-Scale Convection Velocity as a Function of Streamwise Position for Circular Injection Using Helium (Case C2H)	272
Figure 5.102 Structure Convection Angle as a Function of Streamwise Position for Circular Injection Using Helium (Case C2H).....	272

	Page
Figure 5.103 Large-Scale Convection Velocity as a Function of Streamwise Position for Elliptical Injection Using Air (Case E1A)	273
Figure 5.104 Structure Convection Angle as a Function of Streamwise Position for Elliptical Injection Using Air (Case E1A)	273
Figure 5.105 Large-Scale Convection Velocity as a Function of Streamwise Position for Elliptical Injection Using Helium (Case E2H).....	274
Figure 5.106 Structure Convection Angle as a Function of Streamwise Position for Elliptical Injection Using Helium (Case E2H).....	274
Figure 5.107 Measurement Locations for Probe-Based Studies a) $x/d_{eff} = 4$ and b) $x/d_{eff} = 10$	275
Figure 5.108 Contours of Normalized Pitot Pressure ($\Pi_{2,\infty}$) from Circular Injection Using Helium (Case C2H) a) $x/d_{eff} = 4$ and b) $x/d_{eff} = 10$	276
Figure 5.109 Contours of Normalized Pitot Pressure ($\Pi_{2,\infty}$) from Elliptical Injection Using Helium (Case E2H) a) $x/d_{eff} = 4$ and b) $x/d_{eff} = 10$	277
Figure 5.110 Contour Plots Showing Measured Pitot Pressure Ratio Π_{ce} a) $x/d_{eff} = 4$ and b) $x/d_{eff} = 10$	278
Figure 5.111 Helium Mole Fraction Contours from Circular Injection Using Helium (Case C2H) a) $x/d_{eff} = 4$ and b) $x/d_{eff} = 10$	279
Figure 5.112 Helium Mole Fraction Contours from Elliptical Injection Using Helium (Case E2H) a) $x/d_{eff} = 4$ and b) $x/d_{eff} = 10$	280
Figure 5.113 Helium Mass Fraction Contours from Circular Injection Using Helium (Case C2H) a) $x/d_{eff} = 4$ and b) $x/d_{eff} = 10$	281
Figure 5.114 Helium Mass Fraction Contours from Elliptical Injection Using Helium (Case E2H) a) $x/d_{eff} = 4$ and b) $x/d_{eff} = 10$	282
Figure A.1 Schematic of Region of Interest for Convective Mach Number Calculation	289
Figure A.2 Schematic of Mixing Layer Convective Frame of Reference	289

NOMENCLATURE

a	semi-major axis of an ellipse, speed of sound, constant
A	area
A^*	critical area
A_c, A_3	concentration probe sensor plane area
A_1	concentration probe inlet area
A_4	concentration probe choked exit area
A_{90}	area enclosed by the 90% contour taken from ensemble-averaged end view images
A_{xs}	cross-sectional area
b	semi-minor axis of an ellipse
B	background light in an image
Background	a background image
C	constant
$C(\Delta x, \Delta y)$	spatial correlation
C^*	critical flow function
d	diameter
d_{eff}	effective diameter
d_f	hot-film diameter
d_p	particle diameter
D	binary diffusion coefficient
$f()$	functional dependence
FP	fixed-pattern intensity level associated with a detector
I	intensity
\bar{I}	average intensity
I_f	hot-film current

I_0	input light intensity
I_{scatter}	scattered light intensity
I_1	maximum scattering intensity in seeded fluid
I_2	minimum scattering intensity in unseeded fluid
I^s	scattered light intensity from a uniform distribution of scattering particles
I'	intensity fluctuation = $I - \bar{I}$
J	jet-to-freestream momentum flux ratio
k	constant value, turbulent kinetic energy, thermal conductivity
Kn	Knudsen number (ratio of mean free path to particle diameter)
ℓ	mean free path
l	active sensor length
L	characteristic length scale
\dot{m}	mass flow rate
M	Mach number, mixedness parameter
M_c	convective Mach number
M_x	local Mach number
\mathcal{M}_{Air}	air molecular weight
\mathcal{M}_{He}	helium molecular weight
n	numerical index
n_p	number of particles
N	number of images
Nu	Nusselt number
p	static pressure
p_{eb}	effective back pressure
p_0	total pressure
p_{tp}	total pressure parameter

$\overline{p_{o_a}}$	area-averaged total pressure definition
$\overline{p_{o_b}}$	area-averaged total pressure definition
$\overline{p_{o_c}}$	area-averaged total pressure definition
P	perimeter
\dot{Q}_f	heat transfer rate from hot-film to surrounding fluid
r_o	effective radius = $(A_G / \pi)^{1/2}$
r_p	particle radius
R	gas constant, detector response
Re, Re_x	local Reynolds number = UL / ν
R_f	hot-film resistance
R_s	anemometer series bridge resistance
R_G	area ratio = A_G / A_{90}
R_{90}	area ratio = A_{90} / A_{xs}
Response	a response image
S	scalar value, large-scale shape parameter = $P / 2\pi r_o$
S_1	perpendicular polarization component
S_2	parallel polarization component
Sc	Schmidt number = ν / D
Scalar	scalar distribution
Signal	a signal image
S/N	signal-to-noise ratio
t_p	particle response time
t_{δ_ω}	large-eddy rollover time
T	static temperature
T_f	hot-film temperature
T_o	total temperature

u	velocity, streamwise mean velocity
U	characteristic velocity
U_c	convection velocity
U_1	velocity of high speed stream
U_2	velocity of low speed stream
v	transverse mean velocity
V	anemometer response voltage
w	spanwise mean velocity
x	streamwise coordinate
x_{He}	helium mole fraction
$\overline{x_{He}}$	area-averaged helium mole fraction
y	transverse coordinate
y_{He}	helium mass fraction
$\overline{y_{He}}$	area-averaged helium mass fraction
z	spanwise coordinate

Greek

α	empirical constant in Nusselt number-Reynolds number relation, structure inclination angle
β	empirical constant in Nusselt number-Reynolds number relation
δ	boundary layer thickness
δ_ω	shear layer vorticity thickness
δ_x^*	local turbulent boundary layer displacement thickness
Δr	structural displacement from image #1 to image #2
Δt	laser sheet time separation
ΔU	velocity difference = $U_1 - U_2$
Δx	pixel resolution in streamwise direction, lag parameter

Δy	pixel resolution in transverse direction, lag parameter
Δz	pixel resolution in spanwise direction
ε	eccentricity, dissipation
γ	specific heat ratio
λ	wavelength
λ_K	Kolmogorov scale
λ_B	Batchelor scale (diffusion scale)
ϕ	direction of structure convection
μ	dynamic viscosity
ν	kinematic viscosity
$\bar{\nu}$	mean kinematic viscosity
Π	pressure ratio
ρ	density
σ	standard deviation
σ_{fd}	standard deviation from fluid dynamic turbulence
σ_{norm}	normalized standard deviation
$\bar{\sigma}_\infty$	average freestream standard deviation
θ	injection angle, injector inclination angle, scatter direction
θ_M	Mach angle
ω	vorticity

Superscripts

+	upper bound
-	lower bound

Subscripts

act	actual
analytical	value resulting from theoretical analysis
bottom	bottom of injectant plume
c	circular injector, concentration probe sensor plane
cl	injector centerline
C	cold
e	exit, elliptical injector
experimental	value resulting from analysis of experimental data
f, ∞	freestream
H	hot
i	pixel x-location
j	jet, pixel y-location
max	maximum value
meas	measured value
mid	centerline of Mach disk, centerline of injectant plume
p	particle
top	deepest penetration of Mach disk, top of injectant plume
x	streamwise coordinate
xs	cross section
σ	standard deviation
1	manifold condition, concentration probe inlet station, station upstream of normal shock, first image, high speed stream
2	settling chamber condition, station downstream of normal shock, second image, low speed stream
3	concentration probe station
4	concentration probe exit station

1. INTRODUCTION

The flowfield created by the introduction of a gaseous fuel stream into a supersonic flow is of both fundamental and practical interest to the hypersonic propulsion community, as well as to those interested in the study of reaction control systems on high speed vehicles. In the propulsion engineering sector, an understanding of the mechanisms that govern the fuel dispersion and fuel/air mixing in this compressible shear flow is crucial for the successful development of an air-breathing supersonic combustion engine. As the name implies, the mixing and combustion processes must take place in a supersonic stream due to the undesirable effects associated with decelerating a supersonic flow ($M > 6$) to appropriate speeds for subsonic combustion. Residence times within such combustors will necessarily be short; thus, the mixing and combustion must occur rapidly to avoid the prohibitive weight penalty of a long combustion chamber.

From a practical standpoint, transverse injection into a supersonic air stream represents one of several fuel injection concepts for these engines. A second basic injection concept under consideration involves parallel injection. Each configuration presents distinct advantages and difficulties. In parallel injection, the compressible free shear layer formed between the oxidizer and fuel streams suffers from a severely reduced growth rate compared to an incompressible shear layer of the same velocity and density ratios.^{1,2} Also, mixing between the two streams in this configuration is relatively slow. However, parallel injection produces the maximum thrust due to injection since the fuel stream is aligned with the combustor axis. Wall injection concepts, on the other hand, provide significant fuel penetration, which is vital for near-field mixing. However, transverse injection creates a strong disturbance in the freestream and requires that freestream momentum be used to turn the jet. Thus, gains due to near-field mixing are tempered by freestream momentum losses. Other injection concepts include the use of ramps or struts to promote flameholding regions and additional sources of vorticity generation designed to enhance the mixing between the fuel and air. These more complex geometries all utilize some variation of either parallel or transverse injection through which the fuel stream is introduced into the

supersonic crossflow. Thus, a fundamental understanding of the basic injection concepts will enhance the ability to incorporate them into more complicated configurations, ultimately leading to more intelligent and efficient combustor designs. The present investigation focuses on transverse injection flowfields.

Schematics of the flowfield created by the transverse injection of an underexpanded gas stream into a supersonic flow appear in Figs. 1.1 and 1.2. Figure 1.1 illustrates the qualitative features of the flowfield in a plane through the spanwise jet centerline. A three-dimensional bow shock forms ahead of the injectant stream and interacts with the approaching turbulent boundary layer resulting in separation. A barrel shock also occurs as the underexpanded jet accelerates into the crossflow. Acceleration of the jet core flow continues until a normal shock, or Mach disk, forms. Directly downstream of the jet plume, another separated zone develops in the region between the jet exit and the boundary layer reattachment point. Figure 1.2 is a perspective view of the three-dimensional flowfield. This schematic shows the pair of counter-rotating vortices generated within the jet fluid as it flows out of the orifice. It also illustrates how the three-dimensional bow shock interacts with the separation shock as they sweep around the injector. A horseshoe vortex region forms near the jet exit and wraps around the injector as illustrated in the schematic. Finally, the Cartesian coordinate system established for the present investigation appears in Fig. 1.2 with the origin placed at the center of the injector exit. In this system, x , y , and z denote the streamwise, transverse, and spanwise directions. Both schematics depict time-averaged, rather than instantaneous, flowfields.

The complex interaction between the injectant fluid and the freestream is investigated in the present study through the use of several experimental techniques in order to provide useful information regarding the flowfield. Shadowgraph photography using a pulsed light source offers instantaneous visualizations of the spatially-averaged compressible flowfield. Planar Rayleigh/Mie scattering images obtained from particles seeded into the freestream reveal more detailed information concerning the structural organization and large-scale mixing characteristics of the interaction, while probe-based measurement techniques document the important quantities of total

pressure and time-averaged injectant concentration. The laser-based Rayleigh/Mie scattering technique used here is nonintrusive and provides good spatial resolution, while the probe measurements are intrusive to the flow.

The primary objective of the present research is to gain a better understanding of the dominant features that govern the near-field mixing and structural characteristics in flowfields created by transverse injection into supersonic streams. Two specific injector configurations, namely jets with circular and elliptical orifice geometries, have been examined here and each injector was operated at one condition (governed by the jet-to-freestream momentum flux ratio) with two injectant gases. Thus, four distinct cases have been studied. Rayleigh/Mie scattering was performed for all cases while the probe-based measurements were conducted in one case for each injector. The scattering results obtained from the end view planes provide information regarding the growth and orientation of the counter-rotating vortex pair that develops in the injectant fluid. Additionally, these images show the development of the shear layer vortices around the periphery of the jet interface. The disintegration of the jet core region is also apparent, and averaged transverse and lateral jet penetration data are obtained. Temporally correlated side view images provide measurements of the convection velocity of the large-scale structures present within the shear layer formed between the injectant and freestream fluids. Ensembles of individual images from this view allow for statistical examination of the large-scale shear layer eddies. They also provide transverse penetration data and permit examination of the separation zone upstream of the jet exit. The intrusive measurements result in planar contours of two important quantities for consideration in supersonic combustion ramjet (SCRAMJET) engines: the pitot pressure (or total pressure) loss and the mixture composition in either mole or mass fraction. As described above, transverse injection provides rapid fuel penetration in the near-injector region which improves the near-field mixing but produces larger freestream total pressure losses than parallel injection. Finding an injector geometry that enhances the fuel/air mixing in the near-field while reducing the freestream total pressure losses would represent an improvement in terms of a practical injector design. To this end, the elliptical and circular nozzle geometries are investigated for comparison.

The available literature concerning transverse jets in both supersonic and subsonic crossflows is summarized in Chapter 2. Also included throughout Chapter 2 is a review of the literature pertaining to elliptical jets. Chapter 3 contains a complete documentation of the experimental facility, while a discussion of the experimental techniques employed in the present investigation is given in Chapter 4. Results of the experiments are presented and discussed in Chapter 5, followed by conclusions and recommendations for future work in Chapter 6.

2. LITERATURE REVIEW

This chapter contains a review of the available work performed in several injection flowfields. Consideration is given to both basic and complex injection schemes. Additionally, attention is paid to the differences that arise between circular and noncircular injection flowfields. First, analytical and experimental studies of transverse jet penetration are discussed. Information is gathered from circular injection into both subsonic and supersonic crossflows. This is followed by a survey of investigations into the injection flowfield structure. Again, both subsonic and supersonic crossflows are considered. Studies attempting to quantify the mixing characteristics of the jet/freestream interaction are presented. This information is gathered from several studies of basic and complex geometries. Finally, a brief review of several numerical investigations into the problem of transverse injection into a supersonic stream is provided. Computational fluid mechanics can provide a strong tool for both fundamental and practical investigations into these important flows.

2.1 Jet Penetration

Early analytical models of the flowfield created by sonic transverse injection into a supersonic stream, developed by Zukoski and Spaid³ and Schetz and Billig,⁴ used control volume analyses of assumed jet/freestream interface geometries. Zukoski and Spaid³ neglected the freestream boundary layer and any mixing between the injectant and freestream near the orifice. A momentum balance applied to a prescribed plume geometry resulted in an expression for the penetration depth of the locus of maximum injectant concentrations. A similar model developed by Schetz and Billig⁴ suggested that the jet-to-freestream momentum flux ratio, given by

$$J = \frac{(\rho u^2)_{e,j}}{(\rho u^2)_{\infty}} = \frac{(\gamma p M^2)_{e,j}}{(\gamma p M^2)_{\infty}}, \quad (2.1)$$

is the principal parameter controlling the jet's penetration. Another important idea introduced in this study is the "effective back pressure" (p_{eb}) concept. This pressure, analogous to the back pressure in a flowfield formed by a jet issuing into a quiescent environment,⁵ is the average pressure in the near-field region surrounding the injector orifice. Schetz and Billig⁴ suggested that pressure-matched injection (i.e., $p_{e,j} = p_{eb}$) produced optimum penetration compared to simply operating the jet at underexpanded conditions. This is attributed to reduced shock losses within the jet fluid. Experimental results of Chrans and Collins⁶ verified these models concerning the penetration scaling³ and the role of the jet-to-freestream momentum flux ratio.⁴

When injected into a supersonic crossflow, the transverse jet experiences a highly varying pressure field due to the presence of the bow shock and separation regions both upstream and downstream of the injector orifice. As was mentioned above, knowledge of the near-field pressure distribution may hold the answer to the problem of accurately predicting the jet's transverse penetration characteristics. Several experimental^{3,7-10} and numerical¹¹⁻¹⁵ studies present wall static pressure data along the centerline of the jet extending both upstream and downstream of the injector orifice. However, since the circumferential variation of the pressure field is required to accurately determine the effective back pressure value, these centerline data do not shed much light on the issue of jet penetration. In a recent study, Everett, et al.¹⁶ experimentally determined the near-field wall static pressure distribution about a circular jet injected into a Mach 1.6 crossflow using pressure-sensitive paint. This technique afforded spatial resolution far superior to that obtained from conventional static pressure taps. The authors found a linear variation in the experimentally determined value of effective back pressure (obtained by circumferentially integrating the measured pressure field) with the jet-to-freestream momentum flux ratio, thus indicating that J is an appropriate parameter to use in correlating penetration results.

Another model derived by Billig, et al.¹⁷ relied on the concept of effective back pressure to predict the penetration of the center of the Mach disk and the jet centerline trajectory. This model showed that increases in jet Mach number produce slight increases in transverse jet penetration. It also predicted that for constant mass flux ratio injection, increases in jet total pressure would

produce little or no increase in penetration of the centerline profile, while increases in freestream Mach number reduced penetration. Data gathered by Cohen, et al.¹⁸ showed that this model performed quite well. Cohen, et al.¹⁸ also proposed a separate correlation of the form

$$\frac{y}{d} = \frac{k}{1 + \cos \theta} J^{0.5}, \quad \begin{cases} y = y_{top}, & k = 1.51 \\ y = y_{mid}, & k = 1.05 \end{cases} \quad (2.2)$$

where θ is the angle between the injector axis and the crossflow axis, d is the jet diameter, and y_{top} and y_{mid} describe the top and middle of the Mach disk position. This expression adequately reduced all of the Mach disk data collected by the authors.

Heister and Karagozian¹⁹ proposed a model based on the behavior of the counter-rotating vortex pair formed within a pressure-matched jet. The model accounted for changes in vortex strength along the jet trajectory and the effects of wave drag on the vortices. A force balance applied to the vortices, coupled with mass and momentum balances along the trajectory, closed the model. The computed results and trends observed for penetration, defined as the upper surface of the jet, compared quite well with experimental data taken at nearly pressure-matched conditions.²⁰

In addition to the analytical results presented above, empirical methods for quantifying the penetration of wall jets injected into crossflows are widely used. In their investigation of round turbulent jets issuing into low speed streams, Pratte and Baines²¹ examined the effects of J on penetration and found that the jet's trajectory was of the form

$$\frac{y}{d \cdot J^{0.5}} = f\left(\frac{x}{d \cdot J^{0.5}}\right). \quad (2.3)$$

Application of this expression to penetration profiles obtained from photographs of a smoke-filled air jet resulted in descriptions for the top, middle, and bottom jet trajectories. The authors tried the scaling of Keffer and Baines²² and found it unsatisfactory for describing the far-field penetration characteristics, though the performance of the inverse J scaling suggested in Ref. 22 proved encouraging in the near-field. The correlations of Pratte and Baines²¹ show promise for results

obtained by means other than smoke visualization (e.g., planar laser-induced fluorescence (PLIF)).^{23,24} Table 2.1 summarizes these and other incompressible data.²⁵⁻²⁸

The penetration of sonic or supersonic jets in supersonic crossflows has been the subject of several experimental studies;^{6,18,20,29-40} Table 2.2 presents their empirical correlations and conclusions. Techniques used to determine the extent of penetration vary widely and include schlieren photography, probe-based concentration measurements, and laser diagnostics. Papamoschou and Hubbard³⁸ used visual analysis of schlieren photos to identify the effects of such parameters as freestream and jet Mach numbers, jet-to-freestream density ratio, static pressure ratio, and momentum flux ratio on the extent of transverse jet penetration. Results showed that neither the density ratio nor the jet Mach number strongly affected the extent of penetration. A weak dependence on freestream Mach number was shown, but the jet-to-freestream momentum flux ratio was found to be the key parameter governing the jet's penetration. They also provided evidence for an optimum penetration at a certain static pressure ratio, thus supporting Schetz and Billig's effective back pressure idea.⁴ The effects of freestream and jet Mach numbers found by Papamoschou and Hubbard³⁸ conflicted with earlier results^{17,31} where isolated effects of M_∞ and M_j were not observed due to wide variations in J . It is noteworthy that Hersch, et al.⁴¹ cautioned against determination of the jet edge using visual analysis of schlieren photos. They used a visual technique and a densitometer to analyze schlieren photos and found that visual analysis often underestimated penetration of the jet by nearly 15%.

Rothstein³⁶ used PLIF to study a reacting transverse injection flowfield for a wide range of momentum flux ratios. The resulting penetration data correlated well with both the typical power law relation used by other authors (e.g., Rogers^{34,35}) and the modified log law of McDaniel and Graves²⁰ shown in Table 2.2. More recently, Gruber, et al.⁴⁰ used planar Mie scattering from condensed ice crystals to determine the extent of penetration of a sonic helium jet injected into a Mach 2 freestream. A pseudo-velocity thickness definition for the jet edge (i.e., 90% of the mean freestream intensity) produced near-field results that compared well with both the PLIF data of Rothstein³⁶ and the modified log law of McDaniel and Graves.²⁰ For the three values of J studied,

the data showed a high degree of collapse in the near-field using the scaling law suggested by Keffer and Baines.²² A plot illustrating the performance of several penetration correlations appears in Fig. 2.1. The equations from Table 2.2 were used to construct the curves shown for $J = 2.9$, $M_\infty = 2$, $M_j = 1$, and $\theta = 90^\circ$. As is evident from the equations in the table and the plots shown in Fig. 2.1, wide variations in the correlations occur. Both Torrence³² and McClinton⁴² suggested that different freestream boundary layer thicknesses helped cause these variations. Closer examination of the experiments conducted by Rogers^{34,35} shows that his boundary layer thickness-to-jet diameter ratio was 2.7, while in Gruber, et al.,⁴⁰ this value was approximately 1.0. With a thicker layer of low momentum fluid upstream of the injector, one would expect a jet with the same value of J to penetrate farther into the freestream before being swept downstream by the crossflow fluid. This observation explains, at least in part, the differences observed in Fig. 2.1. It should also be noted that the contours presented do not all use the same definition of the jet edge (see Table 2.2). However, the variation in the definitions is not very significant. In fact, the definition used by Torrence^{32,33} should actually produce a contour higher than the correlation of Rogers^{34,35} since Torrence^{32,33} uses the $\sim 0\%$ level to define the jet edge. Thus, it is expected that these correlation curves should comparably describe the penetration of a sonic jet ($J = 2.9$) injected transversely into a Mach 2 freestream.

2.2 Injection Flowfield Structure

Studies demonstrating the formation of large-scale structures in the flowfield created by a jet injected into a low speed stream are widely available.^{24,26,43-53} Fric and Roshko^{49,53} conducted an experimental study using the smoke-wire visualization technique in an attempt to compose a complete picture of the development of large-scale structures in this flowfield. Their photos illustrate the emergence of four types of vortical structures near the injector: the shear layer vortices, the counter-rotating pair, the horseshoe vortices in the near-wall region, and the vortex system formed in the wake region.

The shear layer vortices developed from vorticity contained in the jet boundary layer, and oriented themselves in such a way as to roll up into the freestream fluid. This indicates that the injectant fluid moved with a higher velocity tangent to the interface than the freestream fluid in the injector near-field. Figures 2.2-2.4 show selected photos from Fric and Roshko^{49,53} and Perry, et al.⁵² that illustrate the characteristics of these eddies in the near- and far-field regions of the transverse injection flowfield. The first two photos are from an interaction with $J = 4$ using smoke-wire visualization at the spanwise centerline of the flow (i.e., $z/d = 0$). In the first photo (Fig. 2.2), the periodic nature of the shear layer vortices situated at the interface clearly appears. Also apparent is the large-scale entrainment that occurs at the interface. The right edge of this photo is roughly four jet diameters downstream of the injector centerline. By this location, the vortices appear to lose their coherent structure and begin to break up. Figure 2.3 more clearly presents this occurrence. This photo distinctly shows the transition from highly organized structures near the jet orifice to much more disorganized eddies in the far-field (the right edge here is about nine diameters downstream). Significant intrusions of the freestream into the jet fluid occur as well. The use of a single stream of dye in the crossflow impinging on the issuing jet shows very similar behavior in the near-field (see Fig. 2.4). This photo of the flowfield created by a circular jet with a $J \approx 5$ again highlights the periodicity of the shear layer eddies and the large-scale mixing they cause.

The counter-rotating structures, which also formed from vorticity present in the jet boundary layer,^{46,49} appeared two-dimensional in nature and were oriented in the streamwise direction.⁴⁷ These vortices persisted far downstream, although their strengths were reduced due to viscous dissipation.⁴³ Other authors have presented evidence of the dominance of these counter-rotating vortices formed within the injectant.^{26,45} Horseshoe vortices formed in the near-wall region from vorticity within the crossflow boundary layer and vorticity generated due to the wall pressure gradient resulting from the jet/freestream interaction. These structures bent around the jet orifice before proceeding downstream. In a more recent study devoted to the examination of these vortices, Kelso and Smits⁵¹ found that the horseshoe vortex system can be steady, oscillating, or

coalescing, depending on the flow conditions. In the unsteady modes, the authors found that the motions within the wake intermittently became coupled to the horseshoe vortex motions.

The most interesting findings of Fric and Roshko^{49,53} were the vortices observed in the wake region downstream of the injector. McMahon, et al.⁴⁴ obtained vortex shedding measurements from the wake region thereby acknowledging the presence of such structures, but the dynamics of their formation and their characteristic motions were unknown. By tagging different regions with smoke, Fric and Roshko^{49,53} found that the jet's vorticity did not contribute to the formation of wake vortices; rather, these structures formed from vorticity present in the crossflow boundary layer. They also showed a dramatically different wake structure compared to that formed behind a solid protrusion placed in the crossflow. Figure 2.5 is a photograph taken from their work that documents these eddies. Here, smoke injected directly into the wake of a flowfield with $J = 100$ distinctly shows these string-like vortices that form in the wake and attach themselves to the bottom of the jet. Another recent study by Kelso, et al.⁵⁰ provides further support for these wake structures. These authors used a laser scanning system to obtain three-dimensional images of their water tunnel flow that readily show the structure in the wake region.

Fundamental investigations of the structure of wall injection into a supersonic flow are less common than for the low speed case. As discussed in the previous section, Heister and Karagozian¹⁹ proposed a model of the flow based on the dominant counter-rotating vortex pair formed within the jet. Other experimental^{32,40,54-62} and numerical^{7,12,63-67} studies of basic and complex injection flowfields consistently document the presence of these characteristic eddies. However, the shock structures within the freestream and the underexpanded jet, along with the time-averaged features of the flow, received more attention than the role of this important vortex pair in the near-field region. Recently, instantaneous images obtained using PLIF of nitric oxide^{68,69} and acetone⁷⁰ and Mie scattering^{37,40,70,71} have revealed large-scale vortices present within the shear layer at the jet/freestream interface. These vortices, similar to those observed by Fric and Roshko⁴⁹ in that their orientation suggests faster injectant fluid tangent to the interface near the injector, appeared to contribute significantly to the near-field entrainment. Surface flow

visualization studies^{7,32,70} clearly illustrate the region where horseshoe vortices wrap around the injector orifice. Both Gruber, et al.⁷¹ and VanLerberghe⁷⁰ have presented some evidence indicating that the wake vortices found in incompressible transverse injection flowfields are preserved in their compressible counterparts.

In addition to the vortex structure of the injection flowfield, recent studies of the velocity field also provide information concerning the structure of the jet/freestream interaction. In his study of a circular jet injected into a Mach 1.6 crossflow, Santiago⁷² used two-component laser Doppler velocimetry (LDV) to obtain extensive mean and fluctuating velocity information in the spanwise centerplane and two crossflow planes of the flowfield. The measured velocities clearly showed the shock structure within the jet/freestream interaction, including the barrel shock, Mach disk, and the bow shock. Also evident in these results are the upstream and downstream separation regions. The measured turbulence intensities provide indications of the locations of the shear layers on the upper and lower edges of the jet as it turns due to the momentum of the freestream. In an earlier investigation, Gaillard, et al.⁷³ used LDV to examine the development of the counter-rotating pair of vortices within the jet. By simultaneously measuring the streamwise, transverse, and spanwise components of velocity, the authors computed the component of vorticity oriented in the streamwise direction, i.e.,

$$\omega_x = \frac{\partial w}{\partial y} - \frac{\partial v}{\partial z}. \quad (2.4)$$

By plotting contours of constant streamwise vorticity, the authors illustrated the cores of the counter-rotating vortices that form within the jet fluid. These measurements were carried out at four streamwise planes and the authors documented the decay of the streamwise vorticity within the cores of these vortices. Their measurements also identified the vorticity within the horseshoe vortices found near the wall of this flowfield.

Circular and noncircular jets exhibit very different structural characteristics in the presence of both quiescent and co-flowing environments.⁷⁴⁻⁷⁸ Studies of a small aspect ratio elliptical jet showed that the boundary layer momentum thickness varied around the circumference of the jet

orifice.⁷⁴ Ho and Gutmark⁷⁵ found that the instability in the elliptic jet arose from the maximum vorticity associated with the smallest momentum thickness. This asymmetric instability led to the development of asymmetric vortices around the nozzle exit. An important result of this asymmetry was that the spreading characteristics in the major- and minor-axis planes became very different as the flow developed in the streamwise direction. At some point downstream, depending on the aspect ratio of the nozzle, the widths of the jet in the two planes were equal. However, downstream of this point an axis-switch occurred as the spreading of the minor-axis plane overtook that of the major-axis.^{76,77} Thus, the rate of spread in the minor-axis plane was larger than the rate of spread in the major-axis plane. This minor-axis spreading was significantly greater than the spread associated with a circular jet, where symmetric vortices form at the nozzle exit. The expansion ratio of the jet also affected the structure; underexpanded elliptical jets spread much faster than perfectly expanded or subsonic elliptical jets.⁷⁶ The shock structure within the underexpanded jet contributed strongly to this result through acoustic feedback between sound waves and the large structures of the shear layer.⁷⁹ Similar feedback effects occurred in circular underexpanded jets. However, these effects manifested themselves in mode changes within the jet structure and alterations of the near-field pressure fluctuations rather than in spreading enhancement.⁷⁸

2.3 Injectant/Freestream Mixing

Kamotani and Greber²⁶ examined the mixing in a heated subsonic jet injected into a subsonic crossflow using thermocouple measurements. They compared results obtained from a free jet to those from two crossflow injection cases and found that the maximum temperature decayed faster within the crossflow cases. The authors examined the near-field behavior closely and showed that the maximum temperature decayed faster for smaller jet-to-freestream momentum flux ratios. However, the far-field decay was independent of J . The two transverse injection cases exponentially approached the same maximum temperature level in the far-field. More recently, Smith, et al.²³ and Lozano, et al.²⁴ used PLIF of acetone to study injectant concentrations in an

incompressible transverse injection flowfield. The acetone vapor provided the molecular seed for the fluorescence measurements. The resulting images of Smith, et al.²³ produced a relative resolution of approximately 4.3 for their highest momentum ratio case far downstream (26 diameters). The relative resolution is defined as the ratio of the characteristic probe dimension to the diffusion scale of the flow given by Batchelor⁸⁰ as

$$\lambda_B \approx \frac{\delta_\omega}{Re^{3/4} \cdot Sc^{1/2}}, \quad (2.5)$$

where δ_ω is the vorticity thickness of the mixing layer, Re is the Reynolds number based on the mixing layer properties (i.e., the vorticity thickness, the mean kinematic viscosity, and the velocity difference), and Sc is the Schmidt number. Spanwise centerline concentration profiles obtained from the end views of the various cases demonstrated nearly Gaussian distributions. However, neither study provided any quantitative results for the maximum injectant concentration decay with downstream position.

Several studies of mixing in both basic and complex supersonic injection flowfields exist. Zukoski and Spaid³ used a concentration probe to study mixing in the flowfield created by a single circular injector issuing transversely into a supersonic crossflow. Their measurements showed relatively rapid reduction of the maximum injectant concentration downstream of the orifice. The authors also found the concentration profiles to be insensitive to the state of the approaching boundary layer. Torrence³² and Rogers³⁴ performed similar measurements in single circular transverse jet flows. Torrence³² showed that near-field mixing within the core of the jet decreased with increases in the jet-to-freestream momentum flux ratio. However, core concentration levels in the far-field approached the same values, with the higher J jets producing more lateral and transverse spreading. Rogers³⁴ showed transverse concentration profiles with Gaussian-type shapes that were independent of J above the point of maximum concentration. Other mixing studies of single transverse injector flowfields^{7,54} showed similar characteristics.

McDaniel, et al.^{20,55,56,58,61,62,81-87} conducted many investigations of complex supersonic flowfields including staged injection with and without a backstep, and swept and

unswept ramp injection. These studies include both experimental and numerical investigations into the time-averaged mixing characteristics associated with various combustor geometries. In staged injection flowfields without a backstep, the rate of near-field mixing appears to be critical.^{58,62} Since there are only two dominant types of vorticity that contribute to near-field mixing (i.e., shear layer and counter-rotating vortices), enhancing the growth of these structures directly leads to more rapid mixing between the injectant and freestream near the injector exit. Small-scale turbulent mixing dominates the far-field. Thus, an important method of achieving better mixing on the whole is to promote near-field vortex mixing. Enhancement of streamwise vorticity occurred in swept ramp flowfields^{61,86} where the vortices shed from the ramp interacted with the injectant fluid in the near-field. Results indicated slower mixing with increases in freestream Mach number due to concomitant increases in shear layer convective Mach number. Proposed by Bogdanoff,⁸⁸ this parameter is given by either

$$M_{c,1} = \frac{U_1 - U_c}{a_1} \text{ or } M_{c,2} = \frac{U_c - U_2}{a_2}, \quad (2.6)$$

and characterizes the structure's velocity (U_c) relative to either the velocity of the high speed stream (U_1) or the low speed stream (U_2). The convective Mach number plays an important role in the growth of compressible mixing layers^{1,2} as well as the mixing characteristics^{89,90} and stability^{91,92} of these shear flows.

Schetz, et al.⁹³⁻⁹⁹ studied many types of transverse and oblique injection flowfields using concentration probes. Mixing enhancement techniques included combined tangential and normal injection,⁹³ low angle injection,⁹⁴ unsteady shock impingement,⁹⁶ injector yaw,^{97,98} and multiple injectors.⁹⁹ A summary paper⁹⁵ presents the important results of many of these studies. Low angle injection studies showed increased downstream mixing with increased momentum flux ratio while near-field mixing decreased.⁹⁴ Combining low angle transverse injection with injector yaw produced no increase in the rate of maximum injectant concentration decay, but the mixing region became larger due to the larger frontal area of the injectant plume.^{97,98} Multiple injectors were used to create an "aerodynamic ramp" in an attempt to avoid losses associated with a physical ramp

injector.⁹⁹ Concentration decay results indicated that the array of injectors produced better mixing than simply low angle injection or ramp injection.

Another supersonic mixing enhancement concept studied by Waitz, et al.^{67,100} involved creation of streamwise vorticity through the generation of baroclinic torque. A contoured step injector mounted in a supersonic flow produced a compression wave that interacted with the injectant stream. The pressure gradient created by the wave and the density gradient within the injectant combined to produce vorticity that lifted the injectant plume away from the wall. The authors found that approximately 35% of the injectant mass flux was mixed below the stoichiometric limit by 30 step heights downstream.

In an attempt to quantify the mixing characteristics of parallel injection into the base region formed behind an extended strut in supersonic flow, Glawe, et al.¹⁰¹ computed statistics from planar Mie scattering images. These images showed the face-on view of the flowfield. Peak standard deviation contours provided both the cross-sectional area and the perimeter of the mixing zone. These quantities were combined to produce a shape factor that describes the mixing potential of the injection scheme. A novel mixedness parameter, M , defined as

$$M = 1 - \sqrt{\frac{\frac{1}{N-1} \sum (I - \bar{I})^2}{[(I_1 - \bar{I})(\bar{I} - I_2)]}} \quad (2.7)$$

was used to quantify the small-scale mixing behavior. In this definition, N is the number of images collected, I represents the light intensity collected at a given pixel location, I_1 is the maximum scattering intensity in the freestream, I_2 is the minimum scattering intensity in the jet, and \bar{I} is the mean intensity at a given pixel location. Results obtained using these techniques showed stark differences between various injection geometries and gave good indications concerning the best mixing configuration. The mixedness parameter defined by Eq. 2.7 is similar to the results of other studies, where the concepts of macromixing (large-scale mixing, engulfment), micromixing (molecular-scale diffusion), and mixedness are discussed.^{102,103}

In their studies of jets formed by elliptical nozzles, Schadow, et al.^{74,77,104} found that the mixing characteristics, like the structural characteristics, differed substantially from those associated with circular jets. In the first study,⁷⁴ thermocouples measured the mixing and combustion performance of circular and elliptical jets issuing into a co-flowing stream. Results of the centerline measurements showed that combustion temperatures achieved in a 3:1 aspect ratio elliptical jet flowfield were significantly higher than in the circular jet downstream of about two injector diameters, indicating better mixing by the elliptical jet. The development of asymmetric vortices in an elliptic jet also enhanced mixing in dump combustors,¹⁰⁴ where gas sampling provided concentration measurements. The final study⁷⁷ involved hot wire velocity measurements within circular and elliptical jets at various expansion ratios. Results showed faster amplification of the turbulence intensity in the core of the elliptical jet compared to the circular jet for all expansion ratios, leading to faster turbulent mixing.

2.4 Time-Averaged Computations

Injection of a secondary stream into a supersonic crossflow has also been the subject of several time-averaged numerical investigations. These simulations provide information regarding numerous fluid dynamic quantities of interest including injectant concentrations, static pressure distributions on the injector wall, velocity fields, and Mach number fields, among others.

Injectant concentrations have been predicted in several numerical investigations.^{7,63-65,85-87,105,106} Uenishi, et al.^{63,64} studied mixing and combustion in flowfields created by a single normal injector in a supersonic crossflow along with single and staged transverse jets injected downstream of a backstep into a supersonic crossflow. The authors used the three-dimensional Navier-Stokes equations and the algebraic eddy viscosity turbulence model of Baldwin and Lomax.¹⁰⁷ Their results showed significant asymmetries developing in the counter-rotating vortex pair. Comparisons of their injectant mass fraction data to the experimental results of McDaniel and Graves²⁰ showed good general agreement though the transverse penetration and lateral spread of the jet were usually overpredicted. In their simulation of an oblique jet issuing into a supersonic

crossflow, Riggins and McClinton¹⁰⁵ focused mainly on the downstream portions of the flowfield (i.e., $x/d > 20$) and the comparison between relatively high and low enthalpy freestreams. Injectant gases were either helium or hydrogen. The results show significant effects of freestream enthalpy on the time-averaged concentration profiles and the jet penetration, although it should be noted that the jet-to-freestream momentum flux ratios of the two cases were very different (case 1, $J = 0.56$; case 2, $J = 1.80$). As discussed in §2.1, the jet-to-freestream momentum flux ratio is the key parameter describing the penetration of a transverse jet into the crossflow; therefore, the comparisons made in the aforementioned investigation are biased by the differences in J . Computed mass fractions reported in Aso, et al.⁷ focus mainly on streamwise positions near the injector exit ($0 \leq x/d \leq 12$) of an injection flowfield with $J = 1.95$. Their results, obtained using the three-dimensional Navier-Stokes equations with the Baldwin-Lomax turbulence model, indicate the emergence of the counter-rotating vortex pair in the jet fluid and they show the development of the jet as it exits the nozzle and is swept downstream. However, none of the contours presented are labeled making interpretation of the results quite difficult.

Wall static pressure distributions are commonly reported results from numerical investigations into transverse injection flowfields. McDonough and Catton¹⁴ modeled a three-dimensional transverse injection flowfield using the full 3D Reynolds-averaged Navier-Stokes equations but were unable to accurately predict either the wall static pressure distribution at the spanwise centerline of the injector or the velocity field. The authors put forth several possibilities for the poor agreement of their results to those from experiments including poor resolution near the solid wall and insufficient shock-capturing capability of their numerical algorithm. Other authors have shown good agreement with experimental pressure data from both two- and three-dimensional injection configurations.^{7,11-13,15,85,106,108} In a recent study employing the time-averaged 2D Navier-Stokes equations coupled with the Baldwin-Lomax algebraic turbulence model,¹⁰⁸ better accuracy was found in the wall pressure distribution along with the downstream characteristics of the jet flow than shown in a similar study using a two-equation ($k-\epsilon$) turbulence model and a compressibility correction.¹⁵ Despite the popularity of the wall static pressure

prediction, Segal, et al.⁸⁵ noted that this quantity alone is not enough to validate the performance of the calculation. Their wall pressure predictions were in good agreement with experimental results but the injectant concentrations predicted in their simulation were unphysical in that increasing injectant concentration was observed with increasing streamwise positions. Only one of the aforementioned studies provides any information regarding the total pressure distribution found within the transverse injection flowfield, and this information is limited to a single streamwise plane located at 80 injector diameters downstream.¹⁰⁵ This quantity, as mentioned in Chapter 1, is very important in terms of the practical application of any injection strategy in a supersonic combustor due to the significant losses that can be incurred in the freestream which essentially diminish the potential for thrust production.

2.5 Summary

Clearly, substantial efforts have been made to understand the flowfield created by transverse injection into a supersonic stream. Early work included analytical and experimental investigations of basic injector flowfields. More recently, experimental and numerical efforts have been directed largely at more complex flowfields; these studies have produced mainly qualitative or time-averaged results that shed little light on the fundamental mechanisms that control near-field mixing. Conspicuously lacking are detailed descriptions of the vortex dynamics that govern the initial mixing region. Large-scale structure has been visualized but no attempts to quantify either the growth and orientation of the dominant streamwise vortex pair or the characteristics of the shear layer eddies at the jet/freestream interface have been made. Many studies have alluded to the importance of vortex mixing in the near-field of the jet/freestream interaction and have even attempted to enhance the generation of streamwise vorticity by using injector arrays or intrusive hardware components. However, the characteristics of these near-field vortices are not understood in the basic transverse injection flowfield.

The objective of this study is to add more detail to the understanding of the near-field vortex dynamics developing in simple transverse injection flowfields using shadowgraph

photography, planar Rayleigh/Mie scattering, and probe-based measurements. Of particular interest are the interfacial eddies formed in the mixing layers that develop at the windward edge of the jet fluid and the counter-rotating vortex pair generated within the injectant fluid. These two classes of vortices strongly influence the entrainment of freestream fluid into the jet. The influences of injectant molecular weight and compressibility on the structural and mixing characteristics found in the jet/crossflow interaction are also of significant interest. Potential fuels for these combustion concepts range from hydrogen to hydrocarbons making molecular weight and compressibility important issues. Also, geometric effects are of interest in that finding a passive means of increasing the mixing rate or reducing the total pressure losses associated with transverse injection would be advantageous.

The following chapter describes the experimental facility used in the present study of transverse injection into a supersonic crossflow. Descriptions of the facility hardware and control system are included along with a summary of flow quality measurements made with no injection.

3. EXPERIMENTAL APPARATUS

The experiments documented herein were conducted in a continuous flow supersonic facility designed to allow studies of the basic fluid dynamic mechanisms that govern the fuel-air mixing in supersonic combustors using conventional and state-of-the-art nonintrusive diagnostic techniques. This facility is located at Wright-Patterson Air Force Base, Ohio. Further descriptions of the supersonic tunnel may be found elsewhere.¹⁰⁹⁻¹¹¹

3.1 Air Supply and Control System

The wind tunnel used in these experiments requires several systems for operation. Various turbine and reciprocating compressors are available to produce approximately 15.4 kg/s of clean, compressed air at a maximum supply pressure of 5.27 MPa. All of this air can be heated to a maximum stagnation temperature of 922 K using a gas-fired heat exchanger. Two supply lines, one suited for high temperatures and one for ambient temperatures, transport the air to the test cells supported by the Advanced Propulsion Division. Remotely actuated routing valves isolate each test cell from this system. Each cell requires a separate air supply system to tap into the main lines, and a schematic of the existing system used by the supersonic research facility appears in Fig. 3.1. Once inside the test cell, the hot and cold lines merge in an insulated expansion loop that carries the resulting warm air through a supply manifold to the supersonic wind tunnel mounted inside a clean room with a controlled atmosphere. A pair of Masoneilan control valves (TVC-1902 and PVC-1903) provide the means for regulating the hot and cold air flow rates. The supply manifold has three active and two inactive exhaust branches, as shown in the schematic. One of the three active branches supplies the wind tunnel, while the other two provide atmospheric venting (during system idle through the vent valve VV-1905) and pressure relief capabilities, respectively. The two inactive branches allow for future facility expansion.

A Johnson-Yokogawa distributed control system allows the operation of the supersonic facility to be continually monitored and adjusted to maintain the desired stagnation conditions over

the entire duration of a run. This system has a variety of analog and digital input/output (I/O) boards used for monitoring such devices as the valve limit switches, electropneumatic transducers, pressure transmitters, and thermocouples. All of this information comes to the system operator and appears on a computer monitor for easy interpretation. Key measurements for proper system operation include the pressure and temperature in the supply manifold ($p_{o,1}$ and $T_{o,1}$ monitored during system start-up), and settling chamber pressure and temperature ($p_{o,2}$ and $T_{o,2}$ monitored during run-time). Typically, the system is allowed to idle until the desired conditions are achieved in the supply manifold. During this idle time, the air exhausts through the vent valve. Once the desired conditions have been obtained, the block valve (BV-1904) opens, initiating flow through the tunnel. At this time, the vent valve closes until the desired stagnation pressure results in the settling chamber. Small adjustments in valve positions may be made during the tunnel run to ensure nearly constant stagnation conditions. After setting the appropriate run conditions, the facility may be operated on a continuous basis.

3.2 Wind Tunnel

Five major components comprise the supersonic tunnel, including the inlet section, the settling chamber, the nozzle section, the test section, and the diffuser (schematic and photograph shown in Figs. 3.2 and 3.3, respectively). Descriptions of each component appear in corresponding order in the sections that follow.

3.2.1 Inlet Section

The inlet section transports the air from the supply manifold described above to the settling chamber. Four pieces make up this section, including the upper manifold, the lower manifold, the block valve, and the expansion section (see Fig. 3.2). Six stainless steel flexible hoses connect the upper and lower manifolds and allow for thermal growth in the upstream direction. The lower manifold, block valve, and expansion section mount onto support carts that roll on a pair of rails, which anchor to the bed plate of the test cell. These carts allow for roll-away maintenance and

additional thermal growth management. The 152 mm Masoneilan block valve prevents flow from entering the test section during system idle. Closing this valve and opening the vent valve allows a specific set of run conditions to be maintained while test section hardware modifications are made. A seed injection port found just downstream of the block valve provides a convenient location for the addition of seed media for laser sheet lighting diagnostics such as Mie scattering. This port can be fitted with numerous injection components to ensure a wide variety of potential seed types. Also, since injection occurs upstream of the settling chamber, the entire freestream flow may be seeded uniformly. Finally, the expansion section houses a rearward-facing perforated cone, Fig. 3.4, to provide a means of evenly distributing the flow as it exits the block valve and enters the 610 mm settling chamber.

3.2.2 Settling Chamber

The settling chamber conditions the air using an array of three mesh screens, one coarse (12 x 12 x 0.457 mm) and two fine (20 x 20 x 0.330 mm), and a 75 mm long section of honeycomb (6.35 mm cell size) to break up large-scale turbulence and straighten the flow before acceleration by the supersonic nozzle. This chamber withstands pressures up to 2.86 MPa at temperatures of 922 K. Additionally, the settling chamber size produces air velocities of approximately 15.2 m/s over the range of desired operating conditions for the combustion tunnel. Pressure and temperature sensors installed in the chamber provide feedback to the control system and documentation for the duration of a tunnel run. The entire chamber mounts to a support stand (fixed at the downstream end, rolling at the upstream end) which supports its weight and the force experienced due to the subatmospheric pressure of the exhaust system. This stand also anchors to the bed plate of the test cell. These features appear in Figs. 3.2 and 3.3. Also, a schematic of the settling chamber illustrating the flow conditioning devices appears in Fig. 3.4.

Due to the change in geometry from the axisymmetric settling chamber to the planar nozzle section, a transition region between the two is required to prevent vortex shedding from the sharp corners that would exist without one. This transition takes place using four precision machined

pieces, each made from one-quarter of a 152 mm diameter stainless steel rod. When assembled, these pieces form a section 76.2 mm deep with outer edge dimensions of roughly 305 mm square and inner edge dimensions of roughly 152 mm square. The assembly then fastens inside the flange that separates the nozzle from the settling chamber to provide the desired contour. Figure 3.4 includes a cross-sectional illustration of the nozzle flange, while Figs. 3.5 and 3.6 present further clarification of this part of the design. These figures are photographs of the transition with one piece and all four pieces installed (flow direction is into the page), respectively.

3.2.3 Supersonic Nozzle and Test Section

A planar two-dimensional nozzle, designed using a method of characteristics code developed by Carroll, et al.¹¹² produces the desired expansion to a Mach number of 2.0 at the entrance to the test section. This code computes the contour of a continuous slope converging-diverging nozzle yielding a uniform exit flow aligned with the nozzle axis. Boundary layer growth is not accounted for in this inviscid code. However, corrections for viscous effects are accomplished using boundary layer displacement thickness calculations resulting from Burke's equation,¹¹³ which relates the local turbulent boundary layer displacement thickness to the local Mach and Reynolds numbers as follows:

$$\frac{\delta_x^*}{x} = 0.0463 \frac{M_x^{1.311}}{\text{Re}_x^{0.276}}. \quad (3.1)$$

This correction procedure assumes that the displacement thickness is zero at the nozzle throat and is a linear function of the streamwise coordinate, x . Such a procedure introduces negligible errors into the correction.¹¹⁴ Applying the entire viscous correction to the upper and lower contoured walls of the nozzle preserves the parallel nature of the sidewalls and makes the final nozzle exit dimensions 131 mm high by 152 mm wide. Upstream of the nozzle throat is a contraction that provides a smooth transition between the exit of the nozzle flange discussed above and the throat. The sidewalls of the nozzle section are instrumented with a row of pressure taps on the transverse

centerline that permits documentation of the centerline wall pressure distribution from the entrance of the nozzle through the throat and to the exit. These taps appear in the schematic illustrated in Fig. 3.7.

The constant area test section, shown in Fig. 3.7, provides a large degree of optical access so that a wide variety of nonintrusive diagnostic techniques may be used to examine the flow. A pair of fused silica windows mounted in the side walls and a single fused silica window mounted in the top wall provide the necessary access. The side windows allow direct viewing of the entire transverse dimension of the test section and approximately 445 mm in the streamwise dimension. The top window provides the same optical access length in the streamwise dimension with approximately 76.2 mm across the spanwise dimension. Because each window has two orientations, i.e., one upstream and one downstream, a total viewing length of 787 mm results in the streamwise dimension. A fourth fused silica window, mounted in the diffuser section of the facility, yields direct optical access to the plane perpendicular to the flow direction and allows for visualization of the entire span of the tunnel (see Figs. 3.2 and 3.3).

An array of test inserts mounted in the bottom wall of the test section allows for a variety of injection configurations to be incorporated into the same hardware without the need for significant modifications. These inserts appear in Fig. 3.7. For the present injection experiments, two special inserts have been fabricated with nozzles having circular and elliptical exit geometries. Figure 3.8 contains schematics of these injectors; photos appear in Fig. 3.9. Each convergent injector contour was precision machined with a contraction region fit by a cubic polynomial. For appropriate comparison between the two geometries, each has the same cross-sectional area. Thus, each injector has the same effective diameter, d_{eff} , defined by

$$d_{eff} = 2\sqrt{A_{xs}/\pi}, \quad (3.2)$$

where A_{xs} is the cross-sectional area. Table 3.1 lists the pertinent geometrical features of the injectors used in this investigation, including the eccentricities (ϵ), defined as

$$\varepsilon = \sqrt{1 - \frac{b^2}{a^2}}, \quad (3.3)$$

and the semi-major (a) and semi-minor (b) axes of each orifice.

A special piping system was constructed to supply the injectors with the desired gas. Tube trailers containing large volumes of high pressure (13.9 MPa) air or helium were available outside the test cell. A high-pressure regulator fed a 50 mm supply line with gas from the trailer. This line led to a manifold in the test cell, where a 25 mm line provided gas to the injector. A dome regulator placed in this line controlled the injectant pressure. A small amount of gas from the supply line loaded the regulator dome allowing very repeatable pressure conditions to be set at the jet exit. A pair of solenoid valves placed between the dome supply line and the regulator dome itself conserved the injectant gas and allowed rapid loading and unloading. A full-port shut-off valve was placed upstream of the low pressure regulator, and a master solenoid was installed just upstream of the injector exit to allow fast on/off capability once appropriate supply conditions were set. Figure 3.10 illustrates the jet gas supply system and its components. A pressure transducer fed from a small pressure tap (1.59 mm diameter) placed near the jet exit and a thermocouple installed in the jet gas supply line provided the instrumentation for monitoring the injectant operating conditions.

3.2.4 Diffuser Section

The final component of the supersonic research facility is the diffuser. This device connects the exit of the test section to the exhaust line of the facility. The simple dump diffuser was designed to slow and cool the air flow to appropriate velocities and temperatures required by the air coolers of the air facility. Water spray injection cools the flow as required. In addition to its role in deceleration and cooling of the flow, the diffuser houses the end-viewing port that allows visual investigation of the test section cross-sectional plane. The diffuser hangs from an A-frame support allowing a large unobstructed area beneath the test section for placement of necessary optical diagnostic equipment (see Figs. 3.2 and 3.3).

3.3 Flow Quality Measurements

Prior to any injection experiments, a characterization of the new facility was required. Various conventional measurement techniques were used to characterize the facility. Pitot pressure rake studies examined the streamwise, transverse, and spanwise variations in the Mach number distribution within the test section. Wall static pressure measurements were obtained from the nozzle section to examine the symmetry of the flow through the nozzle. Finally, boundary layer rake profiles documented the boundary layer growth on the test section bottom wall.

The pitot pressure rake used for the calibration studies was incorporated into one of the removable test inserts of the test section bottom wall. This allowed movement of the rake along the streamwise direction to any of the five available locations. The rake could also be traversed in the transverse direction. The probes connected to a bank of Pressure Systems Incorporated (PSI) pressure transducers. Signals from this system traveled to a personal computer for storage and future reduction. Figure 3.11 shows a photograph of the rake. As described earlier, the nozzle sidewalls were equipped with pressure taps (Fig. 3.7) that allowed documentation of the centerline wall static pressure distribution from the contraction region entrance to the nozzle exit. The boundary layer rake, shown via photograph in Fig. 3.12, was mounted in place of the pitot rake on one of the test inserts and could be moved in the streamwise direction. Only the bottom wall profiles could be obtained (due to the existence of the top wall window). The flow in the test section is essentially symmetric about the transverse centerline; thus the bottom wall profiles are representative of the top wall also.

Results of the pitot pressure rake studies are illustrated in Figs. 3.13-3.15. These figures show Mach number distributions across the span of the test section at various streamwise and transverse positions. Figure 3.13 shows Mach number distributions at the transverse centerline for four streamwise positions. The Mach number distribution is uniform for each position, but slightly decreasing with downstream distance from about 1.98 at the nozzle exit to about 1.95 at the final station. Figures 3.14 and 3.15 show the Mach number distributions across the span and height of the test section at two streamwise measurement stations. The position closest to the

nozzle exit is documented in Fig. 3.14. The Mach number distributions are very uniform across the entire span with a value of $M = 1.98$. This plot shows the symmetry of the flow about the transverse and spanwise centerlines as it exits the nozzle. Figure 3.15 presents the same three distributions at an intermediate streamwise location. Evidence of probe blockage is apparent at the highest transverse location; the two traces that do not exhibit this effect are again symmetric about the spanwise centerline and uniform across about 102 mm of the test section.

Comparison of the two opposing nozzle sidewall pressure profiles gives some information concerning the symmetry of the nozzle flow about the spanwise centerline of the tunnel. Figure 3.16 illustrates the profiles obtained for a stagnation pressure of 317 kPa. In the plot, the profiles of both the north and south sidewalls are presented. Both sidewall profiles collapse on each other. Combining this with the symmetric test section Mach number profiles presented above, these data suggest spanwise symmetry through the nozzle.

Finally, the development of the bottom wall boundary layer is illustrated in Fig. 3.17. The boundary layer rake measured total pressures at enough transverse positions so that at least one measurement was made within the freestream, which yields the total pressure downstream of a normal shock at Mach 2. The plot in Fig. 3.17 shows transverse contours of measured total pressure normalized by the freestream measurement. The dashed lines show the individual streamwise measurement locations, and represent the locations where the pressure ratio takes a value of zero. Boundary layer development can be clearly observed. A pitot thickness definition describing the boundary layer thickness (i.e., δ is equal to the transverse position where the measured p_0 is ~98% of $p_{0,\infty}$) indicates that the boundary layer grows from about 5.20 mm thick at the first measurement station to roughly 11.7 mm thick at the last downstream station.

The following chapter describes the various diagnostic tools and experimental methods that were used in the present study of transverse injection into a supersonic crossflow. These techniques were used to gather the desired information regarding the near-field mixing and structural characteristics of the flowfield. They also helped to identify the global flowfield characteristics and to adjust hardware to provide a disturbance-free test section flow.

4. EXPERIMENTAL METHODS

This chapter presents descriptions of the various experimental tools used to examine the transverse injection flowfields studied in this investigation. The jet/freestream interactions were documented using shadowgraph visualizations, planar Rayleigh/Mie scattering images, and probe-based measurements. Additionally, a general data acquisition system recorded wind tunnel stagnation conditions, injectant stagnation temperature, and injectant exit pressure.

4.1 General Data Acquisition

Proper documentation of flow conditions is an important part of any experimental investigation. For the present study, two independent streams created the flowfield of interest. Thus, both the freestream and injectant flows required monitoring. This section presents a description of the instrumentation used for this purpose.

The settling chamber of the supersonic tunnel had four instrumentation ports: two for stagnation temperature and two for stagnation pressure. As discussed earlier, the control system used one of each to maintain run conditions as constant as possible. However, the control system did not record these values for experimental documentation. The other two instrumentation ports allowed for this. A separate thermocouple (Type K with an ice-point reference module) and pressure transducer (0-690 kPa) were calibrated and installed to record chamber temperature and pressure. Signals from these devices went to a pair of Preston 8300 XWB signal amplifiers. The outputs of these amplifiers then traveled to a National Instruments A/D board that was controlled and read by a personal computer. A data acquisition code allowed either visual inspection of the raw and corrected data on the monitor, or recording of the data on disk at a specified sample rate. The personal computer reduced the data to a usable form for further analysis on another machine.

A similar instrumentation scheme documented the operating conditions of the jet flow. A thermocouple (Type K with an ice-point reference module) placed in the jet supply line provided the injectant stagnation temperature, while a pressure transducer (0-690 kPa) connected to the

pressure tap at the exit of the jet nozzle measured the exit static pressure. Again, signals from these instruments went to a pair of Preston amplifiers and then to the A/D board. Figure 4.1 presents a schematic of the electronic configuration used for acquiring the pressure and temperature signals.

Thermocouple calibration was achieved using one of two methods. The injectant thermocouple, because of the relatively low temperatures being measured, was calibrated using a three-point method. An ice bath, room temperature, and a boiling bath provided the points used in the calibration. A least-squares curve fit was obtained and the coefficients were used to convert the digital output of the A/D board to engineering units (here, °F). The settling chamber thermocouple was calibrated using an Omega temperature calibrator (Model CL-801) due to the potentially high temperatures experienced. Eight points were used from room temperature through about 533 K (500 °F). Again, a least-squares fit was obtained and the raw data were converted using the coefficients. This calibration device quotes an accuracy of $\pm 0.1\%$ which translates to approximately ± 0.25 K at the high end of the present range.

A Druck DPI 500 Digital Pressure Indicator was used to calibrate the pressure transducers. This device, which has a highly accurate internal pressure transducer calibrated using a secondary pressure standard, used supply pressure from a nitrogen bottle and a vacuum pump for absolute reference. Each transducer had the same range (0-690 kPa) and thus they were calibrated together. Here, hysteresis effects were taken into account by calibrating both up and down the range of the transducers. This procedure resulted in a 21 point calibration. Once again, a least-squares fit was performed and the resulting coefficients converted the data into useful engineering units (psia).

4.2 Shadowgraph Photography

Shadowgraph photography, which is a very common technique for observing second order density gradients in compressible flowfields, provided qualitative flow visualizations of the injection cases examined in this study. The character of the freestream flow was also examined. Figure 4.2 shows a schematic of the pulsed shadowgraph system used in this investigation while a photograph of the physical arrangement appears in Fig. 4.3. Here, a Xenon nanopulser with a

pulse duration of approximately 10 ns produced the light needed to illuminate the test section. Positioning the lamp at the focal point of a 100 mm diameter 500 mm focal length lens resulted in a collimated beam of light. After passing through the test section, another 100 mm diameter lens collected the light and focused it onto the film plane of a large format (102 mm x 127 mm) Polaroid back plane camera. Photographs were then taken of the flowfield using Polaroid ASA 3000 film. A pair of optical rails held all the components except the two large lenses which were fixed to the optical table. This allowed for easy alignment of the various optical components.

4.3 Planar Rayleigh/Mie Scattering

The principal diagnostic tool used in this investigation to gather fluid dynamic information is a planar imaging technique that relies on the scattered laser light from particles suspended in the flowfield of interest. This technique is nonintrusive in nature since the probe used is simply a thin sheet of laser light. Planar imaging techniques have become quite popular due to the relative simplicity of their implementation. Requirements for such measurements include a pulsed laser, sheet forming optics, optical windows in the test apparatus (unnecessary if the flowfield is open to the environment), some form of recording medium that is sensitive to light intensity, and support equipment including optical benches, optical mounts, etc. Also required for these measurements is a scattering medium within the flowfield of interest. This medium may be naturally occurring (such as ice crystals formed by expanding moist air to supersonic velocities), or it may be introduced into the flow from an outside source (for example, ethanol that will condense in a cold supersonic freestream or silicone oil droplets injected into the freestream through an atomizer). In either case, issues concerning the ability of the particles to follow the turbulent fluctuations within the flowfield arise. The following sections discuss this issue along with the theory and implementation of the technique, the method used for seeding the crossflow, and inherent errors arising due to the finite number of scattering particles in the probe volume.

4.3.1 Theory and Implementation

A complete description of the theory of Mie scattering appears in van de Hulst's text.¹¹⁵ Briefly, light scattered from a particle has an angular dependence given by

$$\frac{I_{scatter}(\theta)}{I_o} = \frac{\lambda^2 (|S_1(\theta)|^2 + |S_2(\theta)|^2)}{8\pi^2 r_p^2} \quad (4.1)$$

where S_1 and S_2 are the perpendicular and parallel polarization components of the total scattered light, λ is the wavelength of incident and scattered light, and r_p is the radius of the scattering particle. Wickramasinghe¹¹⁶ gives the solution to these equations as an infinite series of Ricatti-Bessel functions. This solution converges quickly for particles that are small compared to the wavelength of the incident light (i.e., $d_p \ll \lambda$) yielding the Rayleigh scattering solution.

As alluded to above, experimental techniques based on Mie or Rayleigh scattering rely on the collection of light scattered by particles (and/or molecules in the case of Rayleigh scattering) suspended in the flowfield of interest. In the context of a typical experiment utilizing a planar scattering technique, a thin laser sheet illuminates the particle-laden flowfield. The pulse duration of the laser sheet is typically short (about 10 ns) so that the flow is effectively frozen in time. The pixel array of an intensified charge coupled device (ICCD) camera obtains a digital image of the flowfield by collecting the light scattered by the particles. The resulting image contains relative intensity information where high intensities correspond to particle-containing regions. This intensity information is directly related to seeded fluid concentration if the particles used for scattering are passive participants in the mixing. Nonpassive seeds can also produce concentration information if the local thermodynamic conditions are accurately modeled. However, in either case, the mixing information obtained is only spatially resolvable down to the scale of the imaging pixels. A finite amount of signal integration occurs in planar scattering techniques, as in conventional methods such as schlieren photography, since the light sheet has a finite thickness. The pixel array yields an averaged intensity over a pixel volume defined by the pixel area and the sheet thickness. When compared to the diffusion scale (i.e., the Batchelor scale defined in Eq.

2.5) of the high Reynolds number flowfields encountered in supersonic mixing investigations, the probe volume is quite large. This fluid dynamic length scale is critical in determining the molecular mixedness of compressible mixing flowfields. Since the probe volume attainable in the planar scattering technique is much larger than the diffusion scale, it is impossible to determine whether fluid is mixed on the molecularly scale or simply “stirred” at the macroscopic level. Thus, mixing interpretations are limited to those involving large-scale “stirring” of the fluids.^{117,118}

For the present experiments, three optical arrangements provide the means by which the flowfield is interrogated. Figures 4.4-4.7 present schematics and photographs of the configurations used for single-shot images while Figs. 4.8 and 4.9 illustrate the double-shot arrangement. For the single-shot experiments, a Spectra Physics Quanta-Ray DCR-4 Nd:YAG laser provided the laser beam. The output of the laser passed through a second harmonic generator to produce a beam of light at 532 nm (approximately 400 mJ/pulse). A turning prism directed this beam to the three-axis traversable optical table mounted beneath the test section where a combination of mirrors, prisms, and lenses (-150 mm cylindrical and 500 mm biconvex) produced the collimated laser sheet used for illuminating the transverse injection flowfield. For end view images, the sheet entered the test section through one side window (see Fig. 4.4), while in the side view images, the sheet entered through the top window (see Fig. 4.6). The laser sheet produced had a width of approximately 50 mm and a thickness (measured using a photodiode and an oscilloscope) of roughly 200 μm at the long focal waist.

In the single-shot experiments, a single Princeton Instruments ICCD camera (384 x 576 pixel array) and image acquisition system (controller model ST-130) obtained the flowfield images. The camera was water cooled and purged with nitrogen to reduce dark current noise. A Nikon UV-Nikkor 105 mm f/4.5 telephoto lens placed in front of the pixel array improved the resolution associated with the pixel area. A Princeton Instruments pulse generator (model PG-10) synchronized the laser flash lamp and the camera so that only a single laser pulse was imaged, and a 486-based computer running the CSMA image acquisition software collected the images. All of these pieces appear in the schematics of Figs. 4.4 and 4.6. The instantaneous images were stored

on the internal hard drive of the computer and were later moved to tape for archival and processing purposes. Further image analysis was done using the acquisition computer and a Power Macintosh.

For successful double-shot images, two single-shot systems were combined. Two Nd:YAG lasers (the DCR discussed above and a Spectra Physics GCR-170) produced two vertically polarized laser beams at 532 nm. This allowed both beams to be combined on a 50% beam splitter optic so that a single optical train could be used to produce the two coincident laser sheets required. Two independent camera systems, as described above, were placed on opposite sides of the test section. Careful adjustments of the cameras using a common transparent target led to identical imaging areas with identical resolutions. Each camera was gated around a single laser pulse so that two temporally correlated images could be obtained. The time delay between the arrival of the first and second laser sheets was set using a custom built delay controller coupled with a pulse generator. Figure 4.8 is a schematic of the optical components of the double-shot imaging experiments; a photograph appears in Fig. 4.9.

Two distinct hurdles arose in setting up the double-shot experiments. First, the two individual computer systems had to be synchronized with respect to each other. That is, they had to have a master/slave relationship. Operating this way ensured that each system started from the same temporal reference. This also allowed a single operator to run the imaging part of the experiment rather than having one person directing each camera system. A computer code written for the CSMA acquisition software gave the two computers the ability to communicate with each other through their printer ports. Once the master machine was cued up to begin acquiring data, it was instructed by the code to wait for a ready response from the slave machine. A monostable multivibrator chip (DM74121) provided an adjustable time delay (from 2 to 20 sec) for the two systems and their individual software programs to come to equilibrium. Having the two systems at the same starting point brings up the next hurdle: controlling the time delay between the laser sheets. Another DM74121 chip was used to open a window for firing the master laser. Since it was operated in a free-running mode, the master laser fired at 10 Hz during the time the window

was opened (between 1 and 5 sec). The first electronic pulse from the lamp of the master laser traveled through a DM74LS08 “and” gate to the master imaging system trigger and to the delay pulse generator (Systron Donner, Model 100C). This device was used to fire the slave laser and to set the desired delay between the two laser sheets. A LeCroy 9314L digital oscilloscope received signals from each camera system and a photodiode (placed behind the 50% beam splitter) allowing the temporal separation of the laser sheets to be monitored and proper gating of each camera to be achieved. The first laser pulse from the slave laser triggered the slave imaging system resulting in the collection of two temporally correlated images separated in time by the delay set on the pulse generator. The acquisition software was allowed to loop until the desired ensemble size had been completed. The two-camera delay system appears in Fig. 4.10.

4.3.2 Particle Response

Particle response characteristics in Rayleigh/Mie scattering experiments are very important. The seed particles must follow the fluctuations within the turbulent flowfield so that the collected images may be accurately interpreted. Samimy and Lele¹¹⁹ found that accurate particle response for Mie scattering images required a Stokes number, defined as the ratio of the particle response time scale to the characteristic fluid dynamic time scale, of less than about 0.5. The particle response time is modeled using a Stokesian drag law¹²⁰ given by

$$t_p = (1 + 2.76 \cdot Kn) \frac{\rho_p d_p^2}{18\mu}, \quad (4.2)$$

and the characteristic fluid dynamic time used is the large-eddy rollover time that takes the form

$$t_{\delta_\omega} = \frac{\delta_\omega}{\Delta U}, \quad (4.3)$$

where ΔU is the velocity difference across the shear layer. Thus, both particle size and specific gravity play major roles in the ability of a seed medium to adequately follow the turbulent fluctuations within compressible flowfields. Maxwell's relation, given by

$$\ell \cong 1.5 \frac{\mu}{\rho a}, \quad (4.4)$$

allows estimation of the mean free path and thus calculation of the Knudsen number, assuming a nominal particle diameter is available.

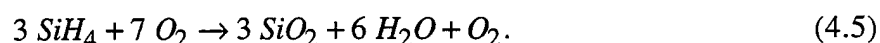
4.3.3 Particle Seeding Technique

As discussed above, the Rayleigh/Mie scattering technique requires some medium within the flow that scatters laser light. There are several options for introducing seed into the present facility. First, since the supply air contains water vapor, operating the freestream at a low enough stagnation temperature produces a uniform distribution of ice crystals within the test section. These ice crystals have been characterized by several authors in the past¹²¹⁻¹²⁴ and are roughly 0.02 μm in diameter. Such particles provide excellent response to the turbulent fluctuations in several flowfields encountered in this facility (Stokes numbers of approximately 0.003 for present conditions).^{40,101} However, since the existence of these particles is critically dependent on the thermodynamic conditions of the jet/freestream interaction, quantitative mixing interpretations are not well founded unless an effective model can be developed that describes the condensation/evaporation phenomena that occur. The present flowfield is far too complex from a thermodynamic standpoint to allow an accurate model to be developed, thus making images obtained using these particles somewhat qualitative.

Another option for seeding the flowfield involves the use of solid particles. Such particles can either be generated through chemical reaction or can be obtained commercially. Two viable candidates for chemical reactions include titanium tetrachloride and silane. Titanium tetrachloride (TiCl_4) reacts rapidly with water vapor to form solid titanium dioxide (TiO_2) and hydrochloric acid (HCl). Systems designed to regulate this reaction are currently in place at the present facility and this technique has been used extensively as a seeding method for laser Doppler velocimetry (LDV).^{125,126} Two disadvantages of this technique are the production of hydrochloric acid and the relatively high specific gravity of the particles ($\text{SG} \approx 4$). The hydrochloric acid is detrimental to

the stainless steel nozzles and test section. The specific gravity issue relates to the particle's ability to follow the turbulent fluctuations in the flow. The conditions expected in this investigation, assuming a nominal particle diameter of 0.4 μm , produce a Stokes number of approximately 0.6. This value lies slightly above the limit suggested by Samimy and Lele,¹¹⁹ thus removing this seeding method from consideration.

Silane (SiH_4) is a pyrophoric gas that, when exposed to oxygen, burns to form primarily solid silicone dioxide (SiO_2), water, and hydrogen. In their study of the silane/oxygen reaction, Hartman, et al.¹²⁷ found that the stoichiometry for reactions with less than 30% silane in oxygen took the form



Thus, unlike the reaction discussed above, the silane reaction produces no chemically detrimental byproducts. In another study, Rogers, et al.¹²⁸ used an electron microscope to characterize the silicone dioxide particle sizes. The authors found that a nominal particle diameter of 0.2 μm results from this reaction. This is approximately half the size of the titanium dioxide particles. Also, the specific gravity of silicone dioxide is roughly 2.2, making the Stokes number, found using the expected operating conditions, approximately 0.09. Though this Stokes number is not nearly as low as that resulting from ice crystals, these solid particles are small enough to allow accurate interpretation of the images. Additionally, the particles are truly passive participants in the fluid dynamic mixing processes encountered in the jet/freestream interaction. Therefore, large-scale mixing information may be directly obtained from the images. As discussed previously, molecular mixing information cannot be directly inferred from the images obtained here since the relative resolution of pixel size to diffusion scale of the flow is large due to the high Reynolds numbers encountered. For such measurements, a molecular tracer must be used. Clearly, the silane seeding technique allows for the most accurate images of the flowfield among the methods considered here.

During initial hot-flow experiments with this technique, acquired signal-to-background levels were found to be too low for acceptable data quality. Thus, the SiO_2 seeding technique was

supplemented by operating the facility at ambient temperatures so that the particles provided nucleation sites for condensation of naturally occurring water vapor in the freestream air. This technique provided adequate signal-to-background levels; however, the completely passive nature of the SiO_2 particles was sacrificed making reliable quantitative measurements of injectant concentration unlikely. A separate examination of particle size, accomplished by rotating the polarization of the incident light, indicated that the combined seeding technique produced particles that reside in the Rayleigh scattering regime. Since the incident wavelength in these experiments was 532 nm, an upper bound on the particle size resulting from the combined seeding technique is $\sim 0.5 \mu\text{m}$. Recomputing the Stokes number using this particle diameter yields a value of about 0.38 suggesting that even the particles with this upper bound diameter accurately follow the turbulent fluctuations in the flowfield and give planar images that produce accurate information.

The silane injection system appears via schematic and photograph in Figs. 4.11 and 4.12. The figures show key components of the system including check valves, regulators, shutoff valves, and remotely activated solenoid valves. Nitrogen provides the flush gas for the system. A regulator sets the outlet pressure of the nitrogen bottle and a solenoid valve opens while the silane is idle to allow flushing. A vacuum pump connects to another leg of the cross so that the entire system can be evacuated. Finally, the supply leg of the system consists of a shutoff valve followed by a regulator, a pair of check valves, and a solenoid valve. The check valves straddle the solenoid valve so that the silane reaction can be delayed until just prior to entering the tunnel.

4.3.4 Noise Considerations

The signals recorded in the scattering experiments have noise levels associated with the finite number of particles within the probe volume. Assuming that Poisson statistics describe this shot noise,¹²⁹ then the signal-to-noise ratio is defined as $S/N = (n_p)^{1/2}$ where n_p is the number of particles within the imaging probe volume. The effects of this shot noise arise in the measured experimental standard deviation. Rosenweig¹³⁰ found that the error induced due to random

fluctuations in the concentration field could be estimated using the measured standard deviation profile and the signal-to-noise ratio from

$$\sigma_{fd} \approx \sqrt{\sigma_{meas}^2 - \frac{1}{(S/N)^2}}, \quad (4.6)$$

where σ_{fd} is the standard deviation from fluid dynamic turbulence and σ_{meas} is the measured standard deviation. High values of the signal-to-noise ratio therefore lead to the conclusion that the measured standard deviations are representative of the fluid fluctuations as long as no other outside effects (e.g., evaporation of seed media) complicate the measurement.

4.4 Probe-Based Measurements

This phase of the present work involves the use of two traversable probes coupled simultaneously with the measurements made using the general data acquisition system outlined in section 4.1. The traversable devices include a pitot pressure probe and a concentration probe. Descriptions of each of these probes and the data collection and processing techniques follow below; schematics of the probes appear in Fig. 4.13.

4.4.1 Pitot Pressure Probe

The pitot pressure probe used in this investigation was made from 3.18 mm OD stainless steel tubing. The wall thickness of the pitot tube was 0.406 mm resulting in a 2.36 mm inner diameter and a capture area of 4.38 mm². The tube was manufactured with an elbow allowing it to be placed in close proximity to the bottom wall of the test section. The tube was secured to the test section side wall using a stainless steel diamond shaped strut. This fixture had a height of about 7.6 mm, a width of 25 mm, and a length of 203 mm. The probe slid into this strut and mounted to its end in a notched cradle using silver solder. This assembly fit directly into the test section side wall and was allowed to slide in the transverse direction using a dynamically sealing o-ring. Installation in this manner gave the probe freedom to move through the flowfield of interest along

the spanwise direction (the $\pm z$ -axis) as well as in the transverse direction (the $\pm y$ -axis). To adequately seal the probe mechanism, an aluminum canister fitted with an o-ring mounted to the side wall. This canister enclosed the strut when completely extracted from the tunnel. The open end of the canister contains nylon ferrules secured with stainless steel fittings that provide a dynamic seal for the probe tube's spanwise motion. Figure 4.14 illustrates the entire mechanism, which is common to all the traversable probes used herein. A programmable micrometer drive system and control unit (L.C. Smith Model TPP-02440) provided the means for the spanwise traversing capability of the probe while vertical traverses required the use of the optical table placed beneath the test section. Figure 4.15 is a photograph showing the hardware external to the test section. A pressure transducer (0-345 kPa) attached to the aft end of the pitot pressure probe. Signals from this device traveled to the data acquisition system. As with the pressure transducers used in the general data acquisition system, a Druck DPI 500 Digital Pressure Indicator provided the necessary calibration.

4.4.2 Concentration Probe

To measure the local steady-state gas concentration in the transverse jet flowfield using helium as the injectant, an aspirated probe based on previous designs was constructed. This probe analyzes a sample of the flowfield immediately after extraction, thereby reducing the time required for concentration data compared to probes that require post-collection analysis of a stored sample. The bases for the current probe's design are the works of Thomas and Schetz¹³¹ and Ninnemann and Ng;¹³² the details of the probe design appear below after a brief discussion of its operating principles.

The model used to design the existing probe involves a small inlet followed by a divergent section containing a normal shock. Downstream of the divergent section is a constant area region containing the sensor plane followed by a choked orifice. These regions appear in the sketch shown in Fig. 4.16. Mass continuity for this system may be expressed as

$$\rho u = p_o M \sqrt{\frac{\gamma}{RT_o}} \left[1 + \frac{\gamma-1}{2} M^2 \right]^{-(\gamma+1)/2(\gamma-1)} \quad (4.7)$$

or

$$(\rho u)^* = \frac{p_o C^*}{\sqrt{T_o}} \quad (4.8)$$

since the flow through the choked orifice is sonic ($M = 1$). In this expression C^* is the critical flow function defined by

$$C^* = \sqrt{\frac{\gamma}{R}} \left(\frac{2}{\gamma+1} \right)^{(\gamma+1)/2(\gamma-1)} \quad (4.9)$$

Since, for steady state conditions, the mass flow rate through the sensor plane must equal that through the choked orifice the sensor plane mass flux may be expressed as a function of only the total pressure, total temperature, area ratio, and gas composition:

$$\rho u = \frac{p_o C^*}{\sqrt{T_o}} \frac{A^*}{A_c}. \quad (4.10)$$

Recall that C^* is only a function of the gas properties (see Eq. 4.9).

The rate of heat transfer from a hot-film probe placed at the sensor plane to the surrounding fluid may be determined from the film resistance (R_f) and the film current supplied by the anemometer (I_f) as

$$\dot{Q}_f = I_f^2 R_f \quad (4.11)$$

For a constant temperature anemometer, the film current can be related to the anemometer response voltage by the following expression, where R_s is the series bridge resistance:

$$I_f = \frac{V}{R_f + R_s}. \quad (4.12)$$

Defining the Nusselt number in terms of the heat transfer rate from the hot-film and the temperature difference between the film and the fluid gives

$$Nu = \frac{\dot{Q}_f}{\pi k l (T_f - T_o)} \quad (4.13)$$

where k and l are the thermal conductivity of the gas mixture and the active sensing length of the film, respectively. Inserting the expressions for heat transfer rate and film current into the Nusselt number definition results in the following expression involving only system properties (R_s and l), gas properties (k and T_o), and constants (R_f and T_f):

$$Nu = \frac{R_f}{(R_f + R_s)^2} \frac{V^2}{\pi k l (T_f - T_o)}. \quad (4.14)$$

The Nusselt number is also related to the Reynolds number using empirical constants that depend on the helium concentration in the volume of fluid being sampled. The appropriate length scale for use in the Reynolds number is the diameter of the hot-film (d_f); thus the relationship takes the form

$$Nu = \alpha \left(\frac{\rho u d_f}{\mu} \right)^\beta. \quad (4.15)$$

Equating the expressions in Eqs. 4.14 and 4.15 and inserting the expression for the mass flux at the sensor plane given by Eq. 4.10 yields the following governing equation for the anemometer response voltage:

$$V^2 = \frac{(R_s + R_f)^2}{R_f} \pi k l \alpha \left(\frac{d_f}{\mu} \frac{p_o}{\sqrt{T_o}} \frac{A^*}{A_c} C^* \right)^\beta (T_f - T_o). \quad (4.16)$$

This expression contains several parameters; however, it is only a function of the sample gas total pressure, p_o , the total temperature, T_o , and the helium concentration, x_{He} . Therefore, for known values of the system parameters (i.e., R_s , R_f , l , d_f , and T_f) and the gas properties (i.e., k and μ), the helium concentration in the sample may be uniquely determined from the anemometer response voltage once the total pressure and total temperature of the sample gas are found.

Having outlined the principles behind the probe's operation, the details of the design are now addressed. In order for accurate measurements of stagnation pressure using a static port at the sensor location within the probe, the Mach number there must fall in the low subsonic range (i.e.,

$p = 0.999p_0$ for $M < 0.05$). Such a low value of the Mach number also ensures an accurate measurement of the stagnation temperature. Therefore, an appropriate area ratio A_3/A_1 must be specified to properly diffuse the incoming flow (see Fig. 4.16 for station references). A second consideration in choosing this area ratio is the shock location within the divergent section of the probe. A value of $A_3/A_1 = 15$ was selected based on these two requirements. Additionally, the area of the choked orifice must be specified to maintain both sonic conditions at the exit and reasonable pressures within the sensing region of the probe. To satisfy both of these conditions, a value of $A_4/A_1 = 1$ was chosen. The probe was made from stainless steel tubing with an outer diameter of 3.18 mm and an inner diameter of 2.36 mm. An inlet of 0.610 mm diameter is tapered over a length of 5.55 mm to the inner diameter of the tube. This gives the desired area ratio of 15. The sample extracted by this probe flows into the sampling vessel shown in Fig. 4.17. The vessel contains an inlet that accepts the sample from the flowfield, a sensor plane where the pressure, temperature, and hot-film measurements simultaneously occur, and a choked exit port that leads to an externally operated vacuum pump.

A National Instruments AT-MIO-16X multifunction input/output board handles all the data acquisition for the concentration probe measurements including signals from the hot-film, the pressure transducer, and the thermocouple. This board connects to a Zenith 286-AT personal computer that runs the necessary data acquisition program. The hot-film anemometry system consists of a Thermal Systems Incorporated (TSI) 1220-20 hot-film sensor and a Dantec Type-55M01 constant temperature anemometer fitted with a DISA Type-55M10 CTA standard resistance bridge. A low-pass filter (Frequency Devices Model 9002) conditions the anemometer signal by removing the fluctuating components and retaining the DC portion (cut-off frequency set to 50 Hz). This filtered signal then travels to the data acquisition board and into the computer. A digital oscilloscope monitors both filtered and unfiltered signals for visual signal verification. A calibrated pressure transducer (0-689 kPa) makes pressure measurements. Finally, a calibrated Type K thermocouple, referenced using an Omega Engineering Type K cold junction compensator, makes temperature measurements.

The calibration procedure for the concentration probe consists of two steps. First, Dalton's Law of Partial Pressures governs the filling of a small mixing tank containing the probe with a known molar concentration of helium in air. That is, the initially evacuated tank is filled to a specific pressure with air and then to a higher pressure with helium. The two gases are allowed to diffuse for a period of time resulting in a uniform mixture. The vacuum pump then begins to draw the pressure in the tank down allowing measurements of voltage and temperature to be made at different pressures for a given helium concentration. This procedure is then repeated for the range of helium concentrations expected in the experiment. The second step in the calibration process involves reducing the collected data to compute the empirical constants α and β in Eq. 4.16. Also, the calibration data reduction code produces theoretical curves (logarithmic curve fits relating anemometer voltage to the sample stagnation pressure) at various helium concentrations for visual reference and interpolation in the final data reduction process. The calibration curves obtained in the present investigation appear in Fig. 4.18. Anemometer voltage was recorded over a wide sampling pressure range for helium mole fractions from 0% to 99%. Each of the 11 curves appears in the figure; these curves are used in the data reduction to obtain a unique value of the sampled helium concentration for the measured values of pressure and voltage. After generating the calibration curves shown in Fig. 4.18, known concentrations were sampled again to examine the measurement error. Over the range of helium concentrations, the probe measurements were found to be accurate to within $\pm 2\%$ (i.e., $x_{\text{He, act}} = x_{\text{He, meas}} \pm 0.02$).

4.4.3 Data Reduction for Injectant Concentration

The data obtained from the concentration probe require a specific reduction procedure to arrive at the mass and mole fractions of the sampled gas. This procedure uses the measurements from the sampling vessel (hot-film voltage, total pressure, and total temperature) and the logarithmic curve fit results of the probe calibration in an iterative process whereby the known calibration constants (α and β) bound the computed voltage using Eq. 4.16 between two helium concentrations. That is, for the measured total pressure and temperature, two helium

concentrations are used to compute two values of the hot-film voltage that lie above (V^+) and below (V^-) the actual measured hot-film voltage value. Then, linear interpolation between these two voltages results in the determination of the measured helium mole fraction from

$$x_{He, meas} = \left(\frac{V_{meas} - V^-}{V^+ - V^-} \right) (x_{He}^+ - x_{He}^-) + x_{He}^- \quad (4.17)$$

The code also computes the helium mass fraction and produces both sets of data for presentation.

The following chapter presents the results of applying these experimental techniques to the flowfields created by injecting helium and air transversely through circular and elliptical nozzles into a nominally Mach 2 freestream.

5. RESULTS AND DISCUSSION

The sections that follow present the various results obtained in this investigation of circular and elliptical transverse injection into a supersonic crossflow. Operating conditions deduced from the pressure and temperature data collected appear first. Next, instantaneous shadowgraph photos of the four jet/crossflow interaction cases provide qualitative insight into the basic shock structure of the flowfields as well as the differences regarding injector geometry and injectant gas. Planar images obtained from two orthogonal flow planes produce a wealth of information about the jet's interaction with the freestream. Instantaneous images give indications of the highly intermittent jet interface and the three-dimensionality of the flow. These shots also illustrate the general features of the flowfields and how the large-scale structures affect those features. Statistical analyses of the image ensembles then produce more objective viewpoints for comparing the mixing characteristics of the four cases studied. Finally, mean flow measurements obtained using intrusive probes are presented and discussed. These results give quantitative measures of important practical quantities of interest and provide still more comparisons between the two injector geometries examined.

5.1 Experimental Conditions

The general data acquisition system described in §4.1 permitted monitoring of the flow conditions. For the six laser sheet interrogation planes examined for each case in this study, 1000 samples of pressure and temperature data were obtained from each of the four channels of interest (namely, $p_{0,\infty}$, $p_{e,j}$, $T_{0,\infty}$, and $T_{0,j}$). These samples (totaling 6000 for each of the four cases) were analyzed to produce mean flow conditions for the injection flowfields examined in this investigation. Table 5.1 documents the various quantities that were either measured directly or computed from the measured values. The four cases listed in the table are numbered as follows: air and helium injection through the circular nozzle are cases C1A and C2H, respectively, while air and helium injection through the elliptical nozzle are cases E1A and E2H. Dynamic viscosity

values were found one of two ways depending on the gas. Sutherland's law of viscosity for air, given as

$$\mu = \frac{1.458 \times 10^{-6} \cdot T^{1.5}}{110.4 + T} \quad (5.1)$$

where the units of T are Kelvin and μ are Pa-sec, was used for the freestream and injectant air. To arrive at viscosity values for helium (cases C2H and E2H), μ was assumed to be only a weak function of pressure allowing interpolation from a table of thermophysical gas properties at atmospheric pressure.¹³³ Due to the fact that the wind tunnel used in these experiments drew its air from the ambient, day-to-day temperature variations occurred and affected the experimental conditions mildly; however, the freestream conditions shown in the table were essentially constant over the course of the experiments. Variations in the jet flow conditions between the two injectant gases were implemented such that the jet-to-freestream momentum flux ratios were held nearly equal. As found in the data presented in the table, a mere 1% variation in J occurred between the air and helium injection cases. For all practical purposes, the four cases examined in this study operated at the same value of J and are therefore comparable in terms of the expected values of jet penetration into the crossflow. Also, since the disturbance to the freestream flow depends directly on the jet's presence, no drastic changes in the fluid mechanics associated with these injection schemes are expected to result from this small variation in J . It should be noted that very substantial differences exist between the jet exit velocities and densities found using helium and air. The values in the table indicate that the helium exit velocity is nearly three times that of air while its density is roughly 13% of the exiting air density.

The final rows of Table 5.1 include estimates of key mixing layer parameters for the circular injection cases including the Reynolds number, the Kolmogorov length scale given by

$$\lambda_K \approx \frac{\delta_\omega}{Re^{3/4}}, \quad (5.2)$$

and the convective Mach number (see Eq. 2.6). These properties were computed at a single point within the mixing layer where compressibility may have its largest effect (see the Appendix for

details concerning the convective Mach number calculation). Note that the Reynolds number appearing in the denominator of Eq. 5.2 is based on the mixing layer properties (i.e., the vorticity thickness, the mean kinematic viscosity, and the velocity difference). The Kolmogorov scale defines the size of the smallest turbulent scales that are produced in the turbulent cascade. This length scale is smaller than the Batchelor scale (shown in Eq. 2.5) for gaseous flows where the Schmidt number is generally of order one, while in liquid flows, λ_K is larger than the Batchelor scale due to the relatively large Schmidt numbers encountered. The results presented in the table indicate that mixing layer compressibility issues cannot be ignored when assessing the mixing performance and structural characteristics associated with injection of simulated fuels. That is, because of the drastically different properties of the two injectant gases used in this investigation, the convective Mach number of the helium mixing layer in the near-field of the injector exit is nearly three times that of the air mixing layer. As discussed in §2.3, compressibility plays an important role in the growth, mixing, and stability of two-stream shear layers. Thus, simulating hydrogen fuel with air will likely lead to incorrect interpretations of the fundamental behavior of the large-scale eddies that form in the mixing regions of these transverse injection flowfields due to compressibility effects.

Table 5.2 provides an overview of the flowfield planes examined in this study. All streamwise and spanwise locations are normalized by the effective jet exit diameter and are measured from the injector centerline (i.e., $x/d_{eff} = 0$ is at the streamwise centerline of the injector as shown in the flowfield schematic of Fig. 1.2). The information in the table includes interrogation location and diagnostic technique used for each case. Table 5.2 also includes the image ensemble sizes obtained in the single-shot end and side view experiments.

5.2 Shadowgraph Flow Visualizations

Instantaneous shadowgraph photos for each of the four cases appear in Figs. 5.1-5.4. The camera was focused at the spanwise centerline of the tunnel (i.e., $z/d_{eff} = 0$) though spatial integration effects occur across the entire span. The scale of the photographs is approximately

twice the actual scale of the injection flowfield. The freestream flows from left to right and the jet fluid enters vertically before being turned downstream. Clearly present in each photo is the freestream shock structure created by the presence of the jet. Both the bow shock and the separation shock formed ahead of the injector orifice are captured. It is interesting to note that the inclination of the bow shock changes with the injector geometry. Figures 5.1 and 5.2 illustrate the flowfield created by the circular jet (cases C1A and C2H). Compared to the bow shocks created in the elliptical cases (cases E1A and E2H in Figs. 5.3 and 5.4), those in the circular cases appear stronger, as judged by their inclinations to the freestream. The waves in the elliptical cases reach the tops of the photos at positions downstream of the waves generated in the circular cases. Also, comparing the behavior of the shock waves near the injector wall shows the circular cases having substantially larger regions of normal shock activity than cases E1A and E2H. Another feature in these photos worth some attention is the area beneath the separation shock ahead of the injector orifice. The shadowgraphs suggest that the elliptical injector produces a smaller region than the circular orifice, while each jet has the same effective diameter and operates at essentially the same jet-to-freestream momentum flux ratio. In both photos of the elliptical injection flowfields, the separation shocks formed upstream of the bow shocks appear at lower elevations and do not extend as far upstream as those revealed in Figs. 5.1 and 5.2 for the circular jet cases. This is presumably due to the tapered geometry of the elliptical orifice.

In addition to the freestream shock structure, the characteristics of the jet also appear in these photographs. In the cases where the injectant is air (Figs. 5.1 and 5.3), the jet shock structure is observed. The barrel shock created in case E1A appears to be oriented at a steeper angle above the bottom wall than that associated with the circular orifice (case C1A). Also apparent in each case is the Mach disk at the downstream end of the barrel shock. Beyond the shock structure in these two figures, the large-scale eddies formed at the interface between the jet and freestream fluids are also visible. These structures form immediately as the jet exits into the freestream. The shadowgraphs indicate that the structures roll into the freestream in the near-field region as observed in previous work.^{37,40,70}

The photos of the helium injection cases (Figs. 5.2 and 5.4) appear quite different in comparison. Here, the jet's shock structure is not apparent in the shadowgraphs. However, the interface between the jet and freestream is clarified somewhat due to the density difference between the underexpanded helium and crossflow air. As the injectant gas expands into the crossflow, its density drops. Conversely, the freestream fluid experiences an increase in density as it passes through the bow shock. The results of Santiago⁷² show the Mach number in the mixing layer at the upper edge of an air jet with $J = 1.7$ injected into a Mach 1.6 freestream to be roughly 1.5. For the present case, a larger value within the shear layer is more probable since the jet has a higher value of J . Assuming a value of $M = 2$ in the mixing layer permits calculations of the density ratio between the jet fluid and freestream fluid downstream of the bow shock. For various shock angles (90° to $\sim 30^\circ$ depending on the shock strength), the ratio ρ_j/ρ_∞ takes values between 1.06 to 2.78 when the injectant fluid is air. Similarly, the ratio falls between 0.16 to 0.43 for helium. Thus, the density difference between the freestream and injectant is much larger in the near-field (near 90° shock angle) for helium injection than for air resulting in a more visible interface. These density differences also explain the absence of the jet shock structure in the shadowgraphs of Figs. 5.2 and 5.4 for helium injection. Spatial integration effects of the line-of-sight shadowgraph technique hide these features. The structures that reside at the helium interface look rather amorphous compared to those that form in the air cases. Nonetheless, large-scale behavior is clearly visible. Other features in the helium photos that are absent from those taken with air injection are curved shock waves in the region above the jet. These waves are most probably shocklets generated by the large-scale eddies. Some of these waves are relatively strong as indicated by the curvature change induced in the bow shock at their point of intersection.

5.3 Planar Rayleigh/Mie Scattering Images

The results of the planar imaging experiments are presented in the following sections. Before presenting any of the specific imaging results, issues regarding the image ensemble size and the basic image processing are discussed. Results of the end view imaging studies appear first

with instantaneous images followed by statistical results. Both ensemble-averaged and standard deviation analyses are discussed in detail. Following this discussion, images from the side view are shown. Three separate experiments for this particular view resulted in single-shot images, images of the near-field interaction between the bow shock and the jet boundary, and double-pulsed image pairs. Instantaneous results appear for each of these three experiments along with mean and standard deviation statistics from the single-shot and bow shock/jet boundary experiments. Two-dimensional spatial correlations were computed from the single-shot experiments while the temporally correlated image pairs resulted in measurements of large-scale convection velocities.

Image ensemble size is an important issue that arises when examining the statistical properties computed within a given flowfield. For the present investigation, several factors required consideration before making the decision as to how many images were to be acquired. First, a large enough sample size (N) is desired for convergence of the mean and standard deviation computed from the images (on a pixel by pixel basis) using

$$\bar{I}_{i,j} = \frac{\sum_{n=1}^N I_{i,j}}{N} \quad (5.3)$$

and

$$\sigma_{i,j} = \sqrt{\frac{\sum_{n=1}^N (I_{i,j} - \bar{I}_{i,j})^2}{N-1}}. \quad (5.4)$$

However, each 14 bit image requires approximately 0.45 megabytes of disk space for storage. Also, consumption of silane used to seed the freestream flow and consumption of helium used as the injectant gas occur very rapidly in this flowfield. Therefore, large ensembles of images prove to be rather costly in terms of data storage and gas supplies. To make an appropriate compromise, the results of a sensitivity study guided the choice of ensemble size. Figure 5.5 presents these results, where an ensemble of 200 images from an end view of case C1A was obtained and analyzed for standard deviation. Typically, the first moment (i.e., the standard deviation about the

mean) should require a larger ensemble for statistical convergence than the ensemble-average. The curves shown in Fig. 5.5a are transverse data traces taken from the spanwise centerline of the jet at $x/d_{\text{eff}} = 4$. Here, the results of the standard deviation calculation using 25, 50, 100, and 200 images are presented. A clear trend toward convergence of the statistics follows as the number of images used in the calculation increases. The general shapes of the four traces are similar and they seem to converge rather well for sample sizes above 50. The spanwise data traces from this streamwise imaging plane (taken from a transverse position of $y/d_{\text{eff}} = 1.8$) appear in Fig. 5.5b and give similar trends involving statistical convergence and shape similarity. Therefore, the bulk of the single-shot experiments conducted in this study used 100 images as the ensemble size for statistical computations. However, the two imaging planes at $x/d_{\text{eff}} = 0$ and 8 from each case of end view results contained only 20 images due to the economic issues mentioned earlier.

The raw images collected in this investigation required that a correction procedure be used for removal of stray reflected light and nonuniformities in both the laser sheet and the detector response. Long¹³⁴ presents details of the correction method used herein. This method requires that three sets of images be taken at each location: signal images, background images, and response images, all of which are represented in Eqs. 5.5-5.7 below.

$$\text{Signal}_{i,j} = R_{i,j}(I_{i,j} + B_{i,j}) + FP_{i,j} \quad (5.5)$$

$$\text{Background}_{i,j} = R_{i,j}B_{i,j} + FP_{i,j} \quad (5.6)$$

$$\text{Response}_{i,j} = R_{i,j}(I_{i,j}^S + B_{i,j}) + FP_{i,j} \quad (5.7)$$

In these expressions, i and j are pixel locations, R represents the two-dimensional detector response function, B is the background light, FP is the fixed-pattern level associated with the detector, I is the actual intensity incident upon the detector, and I^S is the intensity incident upon the detector from a uniform (or known) concentration of scattering particles of value S . Then, the experimental scalar distribution can be determined by

$$Scalar_{i,j} = S \frac{Signal_{i,j} - Background_{i,j}}{Response_{i,j} - Background_{i,j}} = S \frac{I_{i,j}}{I_{i,j}^s}. \quad (5.8)$$

Note that this correction procedure assumes that the background intensity, camera response, and fixed-pattern noise remain constant throughout the various ensembles of collected images. In the present experiments, the value of S is unknown. However, the above correction technique results in images of the ratio

$$\frac{Scalar_{i,j}}{S} = \frac{I_{i,j}}{I_{i,j}^s} \quad (5.9)$$

which takes values from nearly zero where the actual signal is zero to ideally unity where the actual signal is equal to that of the purely seeded freestream. Thus, using a truly passive scalar seed medium should result in corrected images with intensity values that are proportional to the amount of injectant fluid present at any given pixel location. These images were then multiplied by a constant value that maximized the dynamic range for conversion from the CSMA format to the TIFF format, permitting further image processing using software running on a Power Macintosh.

5.3.1 End View Images

Visualizing the jet/freestream interaction from the end provides a cross-sectional look at the flow such as that illustrated in Fig. 1.2. Moving the image plane in the direction of the freestream flow makes it possible to develop an understanding of the entire flowfield's development. True end views obtained using the access window sketched in Fig. 3.2 proved unacceptable due to very poor spatial resolution. Placing the camera at a shallow angle oblique to the laser sheet (about 65° from the direction of laser sheet propagation) resulted in significantly enhanced pixel resolution, but the signal-to-noise ratio was relatively low ($S/N \approx 10-12$) due to the angular dependence of the scattered intensity. Spatial resolution in the transverse direction varied roughly ± 5 pixels across the 578 pixel span of the image due to the oblique camera placement. In the present arrangement, this translated to a variation of $\pm 455 \mu m$ from the left side of the image to the right side. Effects of non-unity pixel aspect ratio (i.e., $\Delta y/\Delta z \neq 1$) resulting from the camera's oblique angle with the

laser sheet were corrected simply by stretching the spanwise axis. This procedure resulted in images with pixel resolutions given by $(\Delta x, \Delta y, \Delta z) = (200 \mu\text{m}, 90.7 \mu\text{m}, 90.7 \mu\text{m})$. Each end view image displayed in this section covers approximately 6.4 effective diameters (40.6 mm) in the spanwise direction and 5.4 effective diameters (34.3 mm) in the transverse direction. The flow direction in all the images is out of the paper. Reversing the image gray scale yields images where pure seeded crossflow fluid appears black while pure unseeded jet fluid appears white. This procedure highlights the features at the jet/freestream interface. One final note regarding the experimental procedure involves the camera gain and laser power. These two parameters were set at the first measurement station in order to maximize the dynamic range of the initial image. As the image plane traversed downstream, no adjustments to these system parameters were made thus yielding similar freestream signal levels for all interrogation planes.

Instantaneous images provide a great deal of information regarding the structure of the flowfield and the characteristics of the jet. Ensemble-averaged images reveal transverse jet penetration and lateral jet spread. Finally, analyses of standard deviations provide substantial information concerning the fluctuations in this highly turbulent, three-dimensional flowfield. From these images it will be shown that descriptions of the flowfield in the time-mean sense are not sufficient to gain an understanding of where the large-scale mixing regions form and how enhancement of those regions can be accomplished.

5.3.1.1 Instantaneous Images

Instantaneous end view images of case C1A obtained from streamwise locations $x/d_{\text{eff}} = 0, 4, 8, \text{ and } 10$ appear in Figs. 5.6-5.9, respectively. The four images of Fig. 5.6 at the streamwise centerline of the jet clearly show the shape of the bow shock and illustrate the three-dimensional nature of the flow by showing the intersection of the bow shock with the separation shock at the right and left sides of the images. The curved bow shock suddenly changes shape at the outer edges of the upper right image where the separation shock has wrapped around the injector orifice. Notice also the change in signal level across the bow shock. This phenomenon arises due to the

increased density across the sharp discontinuity created by the shock wave. Greater changes in signal level from the level in the approaching freestream occur as the shock strength increases. Prominent features in the images from this location are the large-scale eddies that form in the interfacial region between the jet and freestream fluids. These structures appear to form at the earliest stages of the flowfield's development and intermittently influence the position of the bow shock. The larger eddies reside at the upper edge of the jet while the sides of the jet show predominantly small-scale structures.

As the image plane moves downstream, the vortical structure of the jet becomes quite dramatic. Figure 5.7 shows four select images from $x/d_{eff} = 4$ that give indications of the highly intermittent behavior found in this case. Large- and small-scale vortices appear regularly throughout these images although there appears to be no preferred pattern to their formation. Evidence of the counter-rotating vortex pair emerges now as the jet elevates entirely above the bottom wall of the test section. Large extrusions from the jet fluid into the freestream have been captured; these features increase the interfacial surface area and perimeter of the jet fluid thereby increasing the potential for diffusion of freestream fluid across the strained interface. Farther downstream, the jet becomes severely broken and highly convoluted. Increased intermediate gray levels observed at $x/d_{eff} = 8$ (Fig. 5.8) indicate that the jet and freestream fluids are mixing, although some areas of nearly pure jet fluid (white) remain near the core of the jet. Regions suggesting the presence of eddy shocklets appear (upper and lower right images of Fig. 5.8). Finally, by $x/d_{eff} = 10$ (Fig. 5.9), the gray levels dominate the mixing region and the jet's interface appears completely broken and inundated with small-scale structures that ride on the larger eddies.

The circular injector fueled with helium (case C2H) produces a flowfield with some interesting differences compared to the above discussion. Figures 5.10-5.13 present four instantaneous images for this case taken from each of the four streamwise image planes. Features found in Fig. 5.10 at $x/d_{eff} = 0$ compare well with those shown in Fig. 5.6 from case C1A and include the bow shock contour and its intersection with the separation shock. Also, the large-scale structures at the upper edge of the interaction remain prominent with smaller eddies located at the

sides of the jet. However, as the image plane moves downstream, the helium jet appears to retain more of its identity than the air jet. Figure 5.11 shows the images from the second streamwise position (i.e., $x/d_{eff} = 4$). Here, the counter-rotating vortex pair becomes clear as freestream fluid fills the void created between them. The jet interfacial structure in these images is less broken than in case C1A (Fig. 5.7) and small-scale eddies are more frequent than large-scale extrusions. Thus, the increased compressibility level of the helium jet seems to detrimentally affect its structural characteristics. Figure 5.12 shows images from $x/d_{eff} = 8$. These shots indicate an increase in lateral spread from those just upstream. However, the imaged region contains sharper gradients between the jet and freestream fluids than were found in case C1A (Fig. 5.8). The interface appears highly broken and populated with small-scale mushroom-shaped eddies. Continuing downstream to $x/d_{eff} = 10$, the images in Fig. 5.13 illustrate similar characteristics in that the intensity gradients between the jet and freestream fluids remain relatively sharp. These images continue to show the spatial development of the jet along with relative intensity decreases that are indicative of mixing between the two streams. The large-scale vortex pair within the jet fluid and small-scale interfacial eddies remain very prominent.

Injection through the elliptical nozzle results in several similar characteristics, although important differences also arise. Figures 5.14-5.17 show the instantaneous results from case E1A. Immediately visible in the images taken at $x/d_{eff} = 0$ (Fig. 5.14) is the lower transverse extent of the bow shock compared to either circular injection case. Measurements of the maximum vertical bow shock position in case C1A yield values between roughly 4.3 and 4.7 effective diameters above the bottom wall. Similar measurements from case E1A give values between 4.0 and 4.3 effective diameters. This reduction in transverse extent indicates that the shock generated in the elliptical flowfield is weaker than the shock in the circular flowfield. This result follows from the smaller frontal area of the elliptical injector along with a slightly reduced transverse penetration (discussed in a later section). Nonetheless, the weaker shock found in the elliptical injection flowfield translates into smaller total pressure losses across the mixing region. This is a desirable feature when considering injector candidates for SCRAMJET combustors where mixing

performance and total pressure losses are both crucial factors. In addition to the bow shock features, the images from the first measurement location show similar large-scale structure development but shallower transverse penetration than their circular counterparts. The images also reveal a lateral spread that compares closely to that observed in case C1A. Recall that the orifice dimension in the spanwise direction of the elliptical injector is approximately half that of the circular injector (see Table 3.1). As the image plane moves downstream, this enhanced lateral spreading trend continues. In fact, images shown in Fig. 5.15 for $x/d_{eff} = 4$ reveal lateral spreads that exceed those from case C1A indicating that the elliptical orifice leads to more rapid spreading in the spanwise direction than the circular geometry. Structurally, the images from case E1A contain similar large-scale eddies as those from case C1A. The counter-rotating vortex pair within the jet dominates the cross-sectional structure while several prominent interfacial eddies appear as well. Many of these interfacial structures appear mushroom-shaped and provide significant sites for freestream engulfment. Suppression of transverse penetration continues. By $x/d_{eff} = 8$ (Fig. 5.16), the jet interface seems highly broken and small-scale eddies become more prominent as they ride on the counter-rotating pair. Again, mixing of the two streams is suggested by the shallower intensity gradients from the jet region to the freestream. Finally, images from $x/d_{eff} = 10$ (Fig. 5.17) show the jet as completely broken with pockets of freestream fluid penetrating all the way into the core region. Lateral spread continues to be as large or larger than observed in case C1A.

Figures 5.18-5.21 show selected instantaneous images obtained from injecting helium through the elliptical nozzle (case E2H). These images show characteristics that are similar to those presented above in that the transverse penetration of the jet seems suppressed compared to the circular cases, the lateral spread associated with the elliptical nozzle is greater than or equal to that achieved using the circular orifice (whose orifice dimension in the spanwise direction is twice that of the elliptical nozzle), and the helium injectant seems to mix relatively poorly when compared to using air as indicated by the lack of intermediate gray levels and prominence of sharp intensity gradients found in the images. Figure 5.19 shows images from $x/d_{eff} = 4$ that exhibit this lack of intermediate scales very well. These images consistently show the jet region characterized by large

areas that indicate nearly pure injectant fluid. By contrast, the images from case E1A at $x/d_{eff} = 4$ (Fig. 5.15) show the jet region being broken up by intrusions of freestream fluid. Small-scale interfacial eddies form more frequently than the large-scale protrusions commonly observed in air injection (low compressibility) cases, while the counter-rotating vortex pair created within the jet fluid continues to be prominent in Figs. 5.20 and 5.21 at $x/d_{eff} = 8$ and 10, respectively. Finally, bow shock strength in this flowfield, inferred from the images at $x/d_{eff} = 0$ (Fig. 5.18), again appears weaker than the shocks created in the circular cases, although not to the degree that was observed in the elliptical injection flowfield using air. The mean jet exit static pressure computed from the data taken during the image collection at this streamwise imaging plane was slightly higher (by about 5%) than the mean exit pressure computed using all the data obtained from this injection case. This larger value of the jet exit pressure caused the jet-to-freestream momentum flux ratio to be approximately 3.0 for the ensemble of 20 images collected at $x/d_{eff} = 0$ for case E2H. This discrepancy created a relatively stronger bow shock compared to the one at $x/d_{eff} = 0$ in case E1A and resulted in the elevation of the bow shock at this image plane being higher. Further ramifications of this elevated pressure condition appear in the results that follow as well.

5.3.1.2 Ensemble-Averaged Results

Figures 5.22-5.29 present the normalized ensemble-averaged images and their respective penetration contours obtained from the four flowfields examined in this investigation. The ensemble sizes used for calculating these averages were either 20 or 100 images depending on the streamwise imaging plane (20 shots at $x/d_{eff} = 0$ and 8, 100 shots at $x/d_{eff} = 4$ and 10). The images presented are normalized by the average freestream intensity downstream of the bow shock (except for those from $x/d_{eff} = 0$, where an average from the freestream upstream of the bow shock is used due to the appreciable particle number density increase across the strong regions of the shock). This procedure results in normalized intensities decreasing from near unity in the undisturbed freestream (dark) to lower levels in the regions containing injectant fluid (light). Scales indicating the normalized mean intensity levels appear below each of the images. Each

penetration contour shown corresponds to a normalized intensity level of 90%. This arbitrary choice of an intensity threshold adequately describes the jet penetration in these flowfields.⁴⁰ Actually, the definition used to select the penetration contour resembles the velocity thickness definition employed in the description of the edges of a compressible mixing layer.¹³⁵ For the transverse injection flowfields, the 90% definition provides a boundary between essentially pure freestream fluid and mixed fluid at some intermediate mixture fraction. Thus, regions falling outside this contour contain either pure freestream fluid (values near 100%) or jet fluid mixed with the seeded freestream to a signal level above the 90% threshold. In contrast, fluid within the penetration contour can be either pure unseeded injectant (values near 0%) or injectant fluid mixed with the seeded freestream fluid to a level that brings the signal below the 90% threshold.

The ensemble-averaged image presented in Fig. 5.22a shows the uniform freestream above the curved cross section of the bow shock found in case C1A at $x/d_{eff} = 0$. The jet fluid appears light in the image and extends from approximately $z/d_{eff} = -1$ to 1. Some freestream entrainment is indicated at the upper edge of the jet region by the intermediate gray scales found there. This is the location where large-scale eddies first appear as illustrated by the instantaneous images presented earlier. The sharp gradients along the sides of the jet fluid suggest that the small-scale eddies formed there do not provide significant freestream entrainment as the jet exits the orifice and interacts with the crossflow. Moving downstream to $x/d_{eff} = 4$ (Fig. 5.22b), the counter-rotating vortex pair formed within the jet fluid appears. These two structures create a void region within the central core of the jet allowing engulfment of freestream fluid. Peripheral mixing between the two streams seems to have increased by this station as suggested by the marked increase in gray levels at the edges of the jet. Figures 5.22c and 5.22d show the two average images computed for $x/d_{eff} = 8$ and 10, respectively. These two images illustrate characteristics similar to those from Fig. 5.22b, although the effects of the small ensemble size at $x/d_{eff} = 8$ are apparent in the image in Fig. 5.22c. By the final image plane location, the amount of mixed fluid appears to have substantially increased over that shown in the image from $x/d_{eff} = 4$. Intermediate gray scales dominate the entire central area occupied by the jet.

The penetration contours derived from these four ensemble-averaged images are plotted in Fig. 5.23. These contours show the progressive spatial development of the jet boundary found using the 90% definition discussed above. The kidney-shaped cross section becomes very apparent by roughly four effective diameters downstream of the jet exit. This cross-sectional shape is indicative of the pair of counter-rotating vortices formed within the jet from the vorticity present in the boundary layer of the injector nozzle. Other notable features in these contours include rapid elevation of the jet off the bottom wall, increasing transverse penetration until about $x/d_{eff} = 8$, and rapid lateral spreading very near the injector exit followed by what appears to be contraction farther downstream. This contraction trend is consistent with previous data obtained farther upstream⁴⁰ and suggests large-scale entrainment whereby seeded freestream (and therefore higher signal levels) propagates into the jet fluid. No appreciable contraction in the transverse direction occurs since mixing and penetration result in opposing trends. Once the jet's transverse momentum has vanished, no mechanism remains for further transverse penetration. Downstream of this point, the contour will contract in the vertical direction as more freestream is entrained into the jet.

Globally, the averaged images from case C2H, shown in Fig. 5.24, present similar results to those just discussed from the air injection case. The uniform freestream and average bow shock contours appear clearly in Fig. 5.24a along with the areas where the bow shock and separation shock interact. The jet fluid behaves much like that shown in Fig. 5.22a where large-scale eddies contribute to freestream engulfment and to the intermediate gray levels found at the upper edge. Sharp gradients at the sides of the jet result from the small-scale eddies' inability to entrain such large quantities of freestream fluid. The ensemble-averaged images from farther downstream contain features similar to those for case C1A with the exceptions that larger areas of jet fluid occur and the normalized mean intensities are lower indicating less freestream fluid within the jet region. Thus, increased compressibility appears to result in substantially less entrainment of freestream fluid into the jet. Intermediate gray scales are common, but the core region of the jet remains very distinguishable at $x/d_{eff} = 4$ and 8. Figure 5.24d closely resembles its counterpart from air injection at $x/d_{eff} = 10$ except that the jet appears to occupy more area and purer injectant cores

persist within the jet region. Penetration contours obtained from these images, shown in Fig. 5.25, reveal that the lateral contraction phenomenon occurring in air injection is not as pronounced for case C2H. Figure 5.25 illustrates many of the same features as the contours from case C1A in that kidney-shaped profiles develop and transverse penetration increases until roughly $x/d_{eff} = 8$. The magnitude of transverse penetration appears slightly larger than for case C1A, but this can be explained by the slightly larger value of J for the helium injection case. One observation is clear though: the helium (high compressibility) and air (low compressibility) injection cases result in different entrainment characteristics as inferred from the relative levels of lateral contraction of the penetration contours.

Images displaying the ensemble-averaged flowfield from case E1A are presented in Fig. 5.26. The weaker bow shock generated in the elliptical injection flowfield at $x/d_{eff} = 0$ appears in Fig. 5.26a. The maximum transverse extent of the shock in this figure is about 4.0 effective diameters compared to approximately $4.5d_{eff}$ for case C1A. The jet is wider than the one created by the circular orifice but suffers from a suppressed transverse extent. This flatter appearance persists as the image plane moves to $x/d_{eff} = 4$ where the counter-rotating structure becomes noticeable. Also observed in this image are the relatively unmixed jet cores on either side of the spanwise centerline. Farther downstream, the jet region becomes dominated by gray scales except for two areas of nearly pure injectant in the cores of the counter-rotating vortices. Actually, in Fig. 5.26c, the jet nearly splits into two sides as the void region between the pair of streamwise-oriented vortices drives upward. The final image at $x/d_{eff} = 10$ (Fig. 5.26d) looks similar to Fig. 5.26c in that the cores persist while the rest of the region occupied by the jet suggests some intermediate level of mixing. Applying the 90% intensity definition to these ensemble-averaged images results in the contours presented in Fig. 5.27. Immediately apparent from these contours is the reduced transverse extent of the jet in this case compared to either of the two previously discussed. However, the contours from $x/d_{eff} = 0$ and $x/d_{eff} = 4$ show the significant lateral spread associated with the elliptical geometry. Kidney-shaped contours indicating the presence of the counter-rotating vortex pair develop as expected with deep freestream protrusions into the central

jet region occurring downstream of $x/d_{eff} = 4$. The penetration contours contract with increasing streamwise distance in a similar manner to those obtained from the ensemble-averaged images of case C1A.

Figure 5.28 shows the ensemble-averaged images obtained from the elliptical injection flowfield using helium, case E2H. As with the previous set of images from case E1A, these indicate slightly reduced transverse penetration values compared to circular injection of helium (Fig. 5.24). Other features in these images are similar to those presented above including the relatively slow lateral contraction found in case C2H. Persistent core regions similar to those of case E1A appear in Figs. 5.28c and 5.28d at $x/d_{eff} = 8$ and 10, respectively. Additionally, the jet region in these downstream positions contains slightly larger regions of nearly pure jet fluid than was found in the elliptical injection flowfield using air. Close examination of the penetration contours derived from these images shown in Fig. 5.29 confirms the observation that the rate of lateral contraction is smaller than that in case E1A. Figures 5.27 and 5.29 have several similarities including well-defined kidney-shaped contours downstream of $x/d_{eff} = 4$, rapid lateral spreading in the injector near-field, and suppression of transverse penetration compared to the respective circular injection cases.

The results of analyzing the 90% contours for transverse penetration and lateral spread appear in Figs. 5.30-5.33. The penetration results in Fig. 5.30 indicate that the jets reach their maximum extent into the crossflow by roughly $x/d_{eff} = 8$. In fact, downstream of $x/d_{eff} = 4$, only slight changes occur. Results from each injector geometry demonstrate comparable values providing more evidence that the jet-to-freestream momentum flux ratio is a valid correlating parameter for transverse jet penetration (helium injection produces slightly deeper transverse penetration consistent with its slightly larger value of J). Also, elliptical injection produces somewhat shallower penetration levels. This fact is most likely a manifestation of the momentum thickness instability that leads to axis-switching. One other item worth noting concerns the data presented at $x/d_{eff} = 0$ that indicate case E2H having a substantially higher transverse penetration than case E1A. As mentioned in the discussion of the instantaneous images from this streamwise

plane, the jet exit pressure for case E2H was about 5% higher than desired, resulting in a momentum flux ratio of approximately 3.0. This slightly elevated value of J produces the deeper penetration observed in Fig. 5.30 for case E2H at $x/d_{\text{eff}} = 0$.

Figures 5.31 and 5.32 present the lateral spreading results where the data are normalized by d_{eff} and the physical spanwise nozzle exit dimension (2b), respectively. All four cases shown in Fig. 5.31 start with about the same absolute spanwise spread at $x/d_{\text{eff}} = 0$ and 4 with the elliptical cases being consistently wider than the corresponding circular cases. From here, the spreading trends are not completely clear, though all cases eventually indicate some lateral contraction occurring. Helium cases contract at a slower rate on average than the air injection cases, implying that the two injectant gases mix with the freestream air differently. Presumably, contours obtained from farther downstream would show sharp contraction trends in the helium injection cases as well. This being the case, mixing in the helium injection flowfields could then be described as slower than the mixing of freestream and injectant in the air injection cases. The near-field mixing layer convective Mach numbers (see Table 5.1) suggest that compressibility issues may contribute to this observation; this issue will be discussed further after the rest of the data are presented. One observation from these data is clear though: the jets created using elliptical nozzles spread laterally into the crossflow up to 25% more than corresponding jets from circular nozzles operated at the same jet-to-freestream momentum flux ratio. By normalizing the lateral spread data with the spanwise nozzle exit dimension, the differences in lateral spreading rate become even more apparent. Figure 5.32 presents these data and shows that indeed the lateral spread in cases E1A and E2H is at least twice as large as in cases C1A and C2H. It also provides strong evidence, when coupled with the reduced transverse penetration, that the axis-switching phenomenon observed in other elliptical injection studies is preserved here.^{76,77}

To further address the axis-switching issue, the ratio of the lateral spread to the transverse penetration appears for each injection case in Fig. 5.33. The solid horizontal line shown on the plot indicates where this ratio equals unity (i.e., that the lateral spread is equal to the transverse penetration). The two cases using the circular nozzle begin just above this line with values of

$(z/d_{\text{eff}})/(y/d_{\text{eff}}) < 1.20$. Beyond this position, the transverse penetration increases more than the lateral spread causing the ratio to decrease to levels below unity by the farthest downstream measurement plane (i.e., $x/d_{\text{eff}} = 10$). Recall that the helium jet (high compressibility) contracts more slowly in the lateral direction than the air jet (low compressibility) resulting in the significantly larger value of $(z/d_{\text{eff}})/(y/d_{\text{eff}})$ for case C2H by $x/d_{\text{eff}} = 10$. The elliptical nozzle, on the other hand, demonstrates values well above unity in the region upstream of $x/d_{\text{eff}} = 8$. Again, due to the slower contraction of the helium case (case E2H) compared to the air case, the value of $(z/d_{\text{eff}})/(y/d_{\text{eff}})$ for case E1A is significantly smaller than for case E2H by ten effective diameters downstream. Also note the inconsistent behavior of case E2H at $x/d_{\text{eff}} = 0$ (compared to case E1A) resulting from the overshoot in the exit static pressure of the helium jet (and concomitantly deeper transverse penetration). From these data, it seems quite clear that an axis-switching phenomenon is occurring in the elliptical injector flowfield.

The areas enclosed by the 90% contours discussed above give further indications regarding the contraction phenomenon present in these four injection cases. Figure 5.34 presents the results of calculating the enclosed areas (A_{90}) normalized by the injector exit area at each streamwise position. The data in the plot clearly follow two separate trends. Both air injection cases indicate increasing areas up to approximately $x/d_{\text{eff}} = 4$. After this position, the enclosed areas decrease monotonically. The trend for helium injection is quite different in that the area ratio data continue increasing beyond $x/d_{\text{eff}} = 4$, although case C2H experiences a decline beyond $x/d_{\text{eff}} = 8$ due to the lateral and transverse contraction shown in Figs. 5.30-5.32. The increases beyond $x/d_{\text{eff}} = 4$ for the helium cases are more gradual than the sharp change occurring between $x/d_{\text{eff}} = 0$ and 4. As discussed above, the area enclosed by the 90% contour becomes smaller as the number of scattering particles (i.e., the amount of freestream fluid) in the jet region increase. Thus, the sharp reduction in area observed for the air injection cases beyond $x/d_{\text{eff}} = 4$ suggests the presence of freestream fluid in the jet region. This is a strong indication of large-scale entrainment of freestream fluid. On the other hand, the fact that the helium contours do not experience the same decreasing trend in area within the present measurement domain suggests that freestream fluid (and

therefore scattering particles) is not as prominent within the jet region for these cases. The instantaneous images from the air injection cases (C1A and E1A) consistently showed a more broken structure downstream of $x/d_{eff} = 4$ and larger numbers of intermediate gray scales throughout the jet region than cases C2H and E2H using helium. Large-scale eddies also appeared more frequently in these cases than in their helium counterparts, where small-scale vortices seemed more common. Based on these observations and the trends produced from the analysis of the ensemble-averaged images and contours, the low compressibility air injection cases seem to result in better large-scale entrainment than the high compressibility helium injection cases. Further analysis of this phenomenon follows below as the intensity fluctuations are examined in detail.

5.3.1.3 Standard Deviation Results

Beyond the ensemble-averaged data, it is important to understand the fluctuations found in turbulent, compressible mixing flowfields. By examining the image standard deviation given by Eq. 5.4, more insight into the location, formation, and development of regions of fluctuating fluid can be gained. For example, the interface region between the jet and freestream fluids may be examined in more detail. The shear layer formed in this region can fluctuate intensely and is a prime contributor to the entrainment and mixing of freestream fluid. Additionally, the spatial lifetime of the undisturbed jet core can be identified in terms of streamwise position.

To quantitatively compare the standard deviation results from the four cases examined here, a normalization scheme was employed to provide consistent interpretations of the data. Each standard deviation image computed using Eq. 5.4 contained low intensity levels in regions of the flow characterized by small fluctuations (i.e., the freestream and jet core) and high intensity levels in regions characterized by large fluctuations. These intensity levels were reassigned so that small fluctuations have high intensities while large fluctuations have low intensities. Then, each image was normalized by an average fluctuation level from the freestream ($\bar{\sigma}_{\infty}$) such that

$$\sigma_{norm_{i,j}} = \left| 1 - \frac{\sigma_{i,j}}{\bar{\sigma}_{\infty}} \right|. \quad (5.10)$$

By reassigning intensity levels as described above, Eq. 5.10 could be meaningfully applied, resulting in processed images with intensity values ranging from essentially zero in the freestream and jet core regions to values near unity in the intensely fluctuating shear layers. Had the original convention been retained, the results of Eq. 5.10 would have been normalized improperly since the average freestream fluctuation would have been smaller than the mixing layer fluctuations. As with the ensemble-averaged images presented above, either 20 or 100 images were used to compute the normalized standard deviations shown (20 shots at $x/d_{eff} = 0$ and 8, 100 shots at $x/d_{eff} = 4$ and 10).

The normalized standard deviation images given in Fig. 5.35 are from the circular injection flowfield using air (case C1A). Each of the four images includes a scale that indicates the gray level corresponding to a certain value of σ_{norm} . At the first measurement station, several details are worth noting. First, the bow shock appears to fluctuate slightly. The ensemble of instantaneous shots from this location revealed that the bow shock reacted to the presence of the large-scale eddies that intermittently formed at the jet's upper edge, as noted in §5.3.1.1. As expected, when a large eddy protrudes at the upper edge of the jet, the bow shock position changes slightly due to the concomitant change in frontal area of the jet plume. Second, the shearing region around the periphery of the jet is observed. As suggested by the ensemble-averaged image from this position in Fig. 5.22a, thin regions of fluctuating fluid characterize the sides of the jet compared to the thicker regions along the upper edge. Thus, most of the freestream entrainment that occurs at this location does so due to the large-scale eddies evolving at the upper edge of the jet. Third, the jet core and the crossflow are black indicating essentially undisturbed fluid. Moving downstream to $x/d_{eff} = 4$, the development of the mixing region around the periphery of the jet can be examined in closer detail. Here, the region of fluctuating fluid grows substantially on both the sides and the top of the jet. Note the region between the two counter-rotating vortices near the bottom wall where significant fluctuations appear. Also note that the central cores of the two counter-rotating vortices remain relatively devoid of fluctuating fluid compared to the region surrounding them. Thus, some regions of "unmixed" fluid (in terms of the turbulent fluctuations) still exist within the jet core.

Continuing downstream, similar characteristics are observed, although the spatial extent of the fluctuating fluid continues to increase. By $x/d_{eff} = 10$, essentially no undisturbed core remains.

Figure 5.36 presents spanwise intensity traces taken from the standard deviation images of case C1A discussed above. These profiles give indications of the relative levels of fluctuations occurring across the span of the image at a given transverse position. All of the spanwise profiles presented in this section show a slight asymmetric character towards the negative z -direction. This phenomenon has been observed in several other experimental investigations of wall injection into supersonic streams where nonintrusive and probe-based instrumentation are used,^{32,61,62,73,98} and it is most likely the remains of some instability associated with the jet boundary layer. Despite this asymmetry, the profiles do reveal the desired information concerning the regions containing the majority of the fluctuations in these transverse injection flowfields. The trace at the upper left represents the intensity variation occurring at 1.3 effective diameters above the bottom wall at the streamwise centerline (i.e., $x/d_{eff} = 0$) of the injector. Two dominant peaks emerge at the spanwise edges of the jet fluid indicating the presence of the developing shear layers. These features provide the only evidence of intensely fluctuating fluid at the selected transverse position. By $x/d_{eff} = 4$, Fig. 5.36b, the levels of the fluctuations within these shear layers reduce somewhat as they widen. Also observed in this trace, taken at 1.8 effective diameters above the injector wall, is a region near the spanwise centerline of the jet where relatively strong fluctuations occur. This region corresponds to the void between the counter-rotating vortex pair where seeded fluid from the freestream enters the core of the jet. Downstream of this position, no distinct maxima appear, although remnants of these three features can be discerned. The trace in Fig. 5.36c at $x/d_{eff} = 8$, $y/d_{eff} = 1.8$ indicates a smoothing trend in that the prominent regions of high and low fluctuations observed in the upstream traces diffuse into one another. The trace from the final measurement station at $x/d_{eff} = 10$, $y/d_{eff} = 1.8$ demonstrates this effect even more clearly. Another noteworthy observation in this trace is that the fluctuation intensity level increases across the jet region from the previous station. This indicates that the effects of large-scale engulfment no longer dominate the mixing process; rather, small-scale turbulence takes over in the far-field of this injection scheme.

The curves shown in Fig. 5.37 present the distribution of fluctuating intensities obtained by cutting the flowfield created by injection of air through the circular nozzle (case C1A) in the transverse direction at the spanwise centerline of the jet (i.e., $z/d_{eff} = 0$). At the $x/d_{eff} = 0$ measurement location, shown in Fig. 5.37a, the undisturbed jet core quickly transitions into the highly fluctuating shear layer positioned directly above the injector exit. This large-scale mixing region is substantially thicker than the two shear layers at either side of the jet observed in Fig. 5.36a. Assuming that the thickness of this mixing layer serves as the local integral length scale of the flow, then the large-scale eddies formed within this layer are of the same order of magnitude in size. Since there is a significant peripheral variation in the shear layer thickness (and therefore the integral length scale) at the jet/freestream interface, it follows that the eddies at the upper edge of the jet are larger than those at the sides of the jet and therefore contribute more strongly to the near-field mixing by entraining larger quantities of freestream fluid. Another feature in this intensity trace is the fluctuating bow shock positioned near $y/d_{eff} = 4.5$. The region between the shear layer and the shock contains fluid with no appreciable fluctuations. Moving downstream to $x/d_{eff} = 4$, several features again become apparent. First, the fluctuations near the injector wall increase significantly due to the presence of the unsteady wake region behind the jet. A thin depression in the trace shown in Fig. 5.37b indicates the remaining core fluid at this location. Recall that two such depressions emerged in the corresponding spanwise trace (Fig. 5.36b) and were identified as the centers of the counter-rotating vortex pair. The fluctuation intensities rise again above the filament of core fluid at the upper shear layer. At this location, the mixing layer appears quite thick as it spans more than two effective diameters. Beyond this streamwise position (i.e., $x/d_{eff} = 4$), the transverse intensity traces are essentially the same shape. The fluctuating intensity traces smooth out across the jet region and the general level of the standard deviation increases slightly.

Normalized standard deviation images from case C2H appear in Fig. 5.38. The image computed at the streamwise jet centerline, $x/d_{eff} = 0$, contains several features common to the corresponding image from case C1A, including the slight fluctuation in the bow shock position and the essentially unfluctuating nature of the freestream and jet core. In contrast, however, the

fluctuations in the position of the bow shock are not as large and the peripheral mixing region seems thinner. The spanwise extent of this region also appears reduced compared to that shown in Fig. 5.35a. Proceeding downstream to $x/d_{eff} = 4$, the region of highest fluctuations around the periphery of the jet again appears thinner than its counterpart in case C1A. This observation is consistent with the results presented above which suggest that the helium injection flowfield gives rise to smaller and less frequent large-scale protrusions into the crossflow than air injection due to its larger convective Mach number. This image also suggests that the jet core occupies more area in the central region of the jet as compared to case C1A. Figures 5.38c and 5.38d appear qualitatively similar to the one from $x/d_{eff} = 4$ although the prominence of the jet core decays with increasing streamwise distance. The images from these last two planes suggest that the region of fluctuations occupies more total area than in case C1A.

Spanwise profiles of normalized standard deviation taken from Fig. 5.38 are presented in Fig. 5.39. The upper two traces are quite similar to the profiles presented above for case C1A. However, the shear layer region located at the left edge of the jet in Fig. 5.39a is roughly 50% thinner than the corresponding feature from Fig. 5.36a. The spanwise separation between the two peaks is slightly smaller than the earlier trace as well. A three-lobed trace indicating the edge shear layers and the central entrainment region emerges at $x/d_{eff} = 4$. The features in this plot have very similar dimensions as those in Fig. 5.36b, although the core regions (intensity valleys between the two mixing layers) are somewhat wider as suggested by the standard deviation image from this streamwise position, Fig. 5.38b. As the image plane moves downstream in this case, the distinct three-lobed profile persists. Some diffusion effects appear by $x/d_{eff} = 10$, although far less compared to the trace in Fig. 5.36d for case C1A. This trend seems to indicate that the large-scale eddies forming in the helium injection flowfield do not provide the same entrainment characteristics as those formed in the case using air injection. This is most likely an effect of the increased compressibility associated with the helium injection flowfield.

Examining the transverse traces from $z/d_{eff} = 0$ for case C2H shown in Fig. 5.40 provides more evidence supporting this idea. First, the trace from the streamwise centerline (i.e., $x/d_{eff} = 0$)

contains a shear layer at the upper edge of the jet that is approximately 20% thinner than the one from case C1A shown in Fig. 5.37a. This observation suggests that the fluctuations present in the helium injection case do not extend as far into the jet region compared to those observed in air injection. Figure 5.40b shows the trace from $x/d_{eff} = 4$. Here, the emergence of fluctuations from the unsteady wake region found below about $y/d_{eff} = 0.8$ appear. In a similar manner to the plot presented in Fig. 5.37b, a gradual decay occurs toward the core region within the jet (which is broader here than in case C1A) followed by an increase in the average level of fluctuations in the upper edge shear layer. At this streamwise location, however, the mixing layer above the core of the jet is even smaller compared to case C1A than was found at $x/d_{eff} = 0$. The two downstream positions display the gradual disappearance of the core region and a general increase in the level of the fluctuations. However, by $x/d_{eff} = 10$, a discernible region of relatively low fluctuations remains in the helium flowfield. In comparison, the trace from the corresponding air injection flowfield (Fig. 5.37d) provides no evidence of this phenomenon, suggesting that small-scale turbulence (i.e., diffusion) develops faster in the air injection flowfield.

Figure 5.41 shows the normalized standard deviation images computed from the ensemble of instantaneous images of case E1A. Bow shock oscillation remains a feature in the images from $x/d_{eff} = 0$. More evident in Fig. 5.41a, however, is the shear layer region around the jet core. This region of relatively high fluctuations appears very similar to that observed in the circular injection flowfield with air as the injectant shown in Fig. 5.35a. Some suppression occurs in the transverse direction, although the lateral extent of this zone appears slightly larger. By four effective diameters downstream of the jet centerline, similar features persist. This image further suggests that the region of fluctuations above the jet suffers some transverse suppression compared to the case of circular injection of air. However, compared to case C1A, the lateral extent of the fluctuating region appears larger. The distance between the undisturbed cores of the counter-rotating vortices is clearly larger here than in the circular case. Fluctuations in the wake region, where freestream fluid is entrained into the central core of the jet, are again observed. Intermediate

gray scales move into the vortex cores by $x/d_{eff} = 8$; indications of these cores essentially disappear by the final imaging location.

Spanwise profiles taken from these images appear in Fig. 5.42. In the trace presented in Fig. 5.42a at $x/d_{eff} = 0$ and $y/d_{eff} = 1.3$, the two mixing layers positioned at the sides of the elliptical jet are clearly observed. These fluctuation zones are as thick or thicker than the corresponding mixing layers found in Fig. 5.36 for case C1A. An interesting feature in this trace is that the separation distance between the fluctuation maxima is essentially identical to the observed separation found in the circular injection case, even though the spanwise dimension of the elliptical nozzle is only about half that of the circular nozzle. This provides yet another piece of evidence for the axis-switching phenomenon characteristic of elliptical nozzles. By four effective diameters downstream, the three-lobed profile emerges with the mixing layers at the spanwise edges of the jet moving outward (peak-to-peak spread of about $4.0d_{eff}$ compared to $3.2d_{eff}$ in case C1A). The central entrainment region in this case is substantially larger than in case C1A as a result of the larger void created between the counter-rotating pair. Similar to the previous two cases, the effects of diffusion become more apparent as the image plane moves downstream of $x/d_{eff} = 4$. Remnants of the three-lobed profile remain in the two traces shown in Figs. 5.42c and 5.42d. However, the smoothing trend indicative of high and low fluctuation levels diffusing into one another is very prominent. The fluctuation intensity level increases across the jet region indicating that the effects of small-scale turbulence become more important to the mixing process in the far-field than the large-scale vortex structure of the jet/freestream interaction.

Figure 5.43 presents transverse profiles taken from the spanwise centerline (i.e., $z/d_{eff} = 0$) of the elliptical nozzle fueled by air. The mixing layer formed at the upper edge of the jet in case E1A is somewhat thinner and lower in elevation than the one created by circular injection of air. Also, the region of bow shock fluctuations occurs at a lower elevation, consistent with previous observations. Again, the upper edge shear layer is slightly wider than those formed at the sides of the jet. However, the peripheral thickness variation is not nearly as profound in this case. Growth of the mixing layer occurs as indicated in the trace taken from four effective diameters downstream.

Also present in this trace is a uniform level of fluctuations below the small core region located at approximately $y/d_{\text{eff}} = 2.4$. Traces from farther downstream indicate similar observations as those discussed in the previous two cases in that the core region of the jet disappears, and is replaced by a roughly uniform fluctuation level across the entire jet region by $x/d_{\text{eff}} = 10$. The small peak centered around $y/d_{\text{eff}} = 4.0$ in Fig. 5.43d indicates that the upper edge mixing layer continues to have some identity.

Examining the normalized standard deviation images from case E2H shown in Fig. 5.44 reveals several features similar to those observed in the previous images. For example, the bow shock fluctuations in Fig. 5.44a appear about as intense as in case E1A using air; however, the fluctuations occur over a larger spatial range. This is explained by the results from the instantaneous images that indicate less frequent large-scale protrusions in the helium injection flowfield. Some of these eddies are appreciably larger (see Fig. 5.18), leading to sharper adjustments in the position of the bow shock. In addition, the peripheral mixing region appears somewhat thinner at the spanwise edges in this case than in case E1A, whereas the upper edge mixing layer seems to be thicker and deeper into the freestream. The former observation is consistent with the results of the two circular cases while the latter two conflict. Deeper penetration of the mixing layer is not too surprising since this case operated at a somewhat higher value of J . However, the data to this point indicate that the helium injection cases result in poorer development of large-scale eddies than the air injection cases in the region near the injector exit. The occasional presence of large-scale structures extending farther into the freestream than average would result in a wider shear layer than more frequently occurring eddies falling near the average. As mentioned above, the instantaneous images provide evidence for this very occurrence. The region containing the highest fluctuations in the image at $x/d_{\text{eff}} = 4$ is very similar to its corresponding image from case E1A in terms of spanwise and transverse extent. However, the undisturbed vortex cores occupy more area in case E2H where helium is the injectant. This observation compares well with case C2H where a larger jet core region appeared relative to case C1A. At the downstream

stations, the region containing fluctuating fluid widens further as in case C2H. Again, essentially no distinct jet core appears downstream of $x/d_{eff} = 8$.

Figure 5.45 presents the spanwise data traces from the normalized standard deviation images computed for case E2H. The trace at the upper left confirms the observations from the $x/d_{eff} = 0$ centerline image that the shear layers positioned at the edges of the jet are somewhat thinner than in the air injection case E1A. As mentioned in §5.1, the shear layers developing in the helium injection flowfield are characterized by higher convective Mach numbers than in the air injection cases (see Table 5.1). Several past studies of the growth characteristics of compressible mixing layers show that as compressibility effects increase, shear layer growth rates decrease for given values of the density and velocity ratios.^{1,2} These effects correlate well with the convective Mach number defined in Eq. 2.6 and likely manifest themselves in the near-field development of the transverse jet flowfield. Broadening of the region between the two counter-rotating vortices begins to appear in the trace from four effective diameters downstream of the injector centerline. Beyond this location, the traces demonstrate characteristics similar to the previous plots in that some discernible remnants of the three-lobed profile remain with diffusive effects becoming more important than the large-scale entrainment processes.

Transverse intensity profiles at $z/d_{eff} = 0$ from case E2H appear in Fig. 5.46. The trace obtained from the first image plane shows a thicker mixing layer at the upper edge of the jet than in case E1A. It also indicates that the bow shock positions itself higher off the bottom wall. The previous observations that indicate the flowfield imaged in this particular ensemble had a slightly larger J than the others offers an explanation of these phenomena. The upper edge mixing layer thickens somewhat by $x/d_{eff} = 4$. Comparing this trace to the one from Fig. 5.43b for case E1A indicates that the core region in the helium injection flowfield remains relatively coherent for a longer spatial extent. Only a small region between approximately $y/d_{eff} = 2.2$ and 2.6 remains in the air injection case while a broad region between roughly 1.8 and 2.8 effective diameters exists in case E2H. Thus, the mixing layer in case E1A appears significantly thicker suggesting a more dominant large-scale presence. Although somewhat indistinct, both of the final two traces from

case E2H show indications of the decaying influence of the helium core with increasing fluctuation levels occurring more slowly than in the previous case.

An arbitrary intensity contour (here $\sigma_{\text{norm}} = 0.30$) was selected in the normalized data that gave an accurate representation of the region containing fluctuating fluid. This region can be thought of as an active mixing zone. It in no way attempts to quantify the amount of freestream fluid being entrained into the shear layer. Within this contour, however, either large- or small-scale mixing of the two fluids occurs as inferred from the presence of turbulent fluctuations. Large-scale mixing involves the large eddies actively entraining fluid from the crossflow, thereby initiating the turbulent energy cascade and giving the two fluids the potential to become molecularly mixed. Small-scale mixing, on the other hand, involves the two fluids diffusing into one another at scales smaller than the discernible pixel resolution. Thus, the contours obtained from this analysis lead to concepts regarding the “mixing potential” of a particular injection scheme since they essentially enclose the entire mixing region.

Figure 5.47 presents the contours obtained from the images shown in Fig. 5.35 (case C1A). At $x/d_{\text{eff}} = 0$, the contour outlines the peripheral mixing region around the jet core. Obviously, the width of this region above the jet is significantly larger than at the sides due to the larger turbulent eddies residing there. As the image plane moves downstream, the region of fluctuations grows dramatically. Figure 5.47b shows the contour obtained at $x/d_{\text{eff}} = 4$. Here, the fluctuating fluid extends into the crossflow by roughly 5.3 effective diameters vertically and 4.8 effective diameters laterally. Also apparent in this contour are the centers of the counter-rotating vortices where only small fluctuation levels occur. Evidence of the wake region develops directly below the jet cores at this location. By $x/d_{\text{eff}} = 8$, the cores of the jet disappear. The extent of the fluctuating region reduces somewhat in the lateral direction, and the fluctuations in the wake region lessen as well. Finally, Fig. 5.47d shows the last measurement station at $x/d_{\text{eff}} = 10$ where the contour fills the entire vertical dimension of the plot.

Contours derived from the images in Fig. 5.38 for case C2H are shown in Fig. 5.48. The first two mixing zones shown confirm the observations discussed above in that the contours from

$x/d_{\text{eff}} = 0$ and 4 are thinner both at the spanwise and upper edges of the jet as compared to case C1A. Figure 5.48b also confirms that the unfluctuating jet cores for this helium injection case occupy a larger area than in case C1A. In fact, the cores within the counter-rotating vortices persist until approximately $x/d_{\text{eff}} = 8$. No evidence of the vortex cores remains by the final measurement station, where the fluctuation region again fills the entire vertical dimension of the plot. The final two contours presented in this case appear fuller in the spanwise direction than the corresponding contours from case C1A.

Applying the 30% definition to the normalized standard deviation images in Fig. 5.41 for case E1A produces the contours shown in Fig. 5.49. As observed in Fig. 5.41, the regions of fluctuation are wider than those from case C1A. This is expected since the instantaneous and ensemble-averaged data consistently provide evidence of the axis-switching phenomenon where spreading in the minor-axis plane becomes greater than spreading in the major-axis plane. The contours also confirm the observations from Fig. 5.41 that the transverse extent of the large-scale mixing zone is smaller in the elliptical case than for the circular case. Again, this result is not surprising since the elliptical jets were found to penetrate slightly less than the circular jets on average. The cores of the jet in case E1A appear to remain coherent for a longer spatial period than in case C1A. Here, evidence for some core fluid is present as far downstream as $x/d_{\text{eff}} = 8$, although what little jet fluid remains is highly fractured.

Finally, contours computed from the images in Fig. 5.44 for case E2H appear in Fig. 5.50. These contours essentially combine the results of cases C2H and E1A. The jet core is more prominent in the helium injection flowfield, and contours from elliptical injection are substantially wider than those from circular injection although they suffer from slightly reduced transverse extent.

To quantify the mixing potential of the four cases studied here, further analysis of the 30% contours was undertaken. Large-scale eddies that form in the shear layer entrain freestream fluid and enhance the volume of fluid within the mixing zone along with both the interfacial surface area and perimeter between the two streams. The mixing zone cross-sectional area (A_G) and perimeter

(P) computed from the contours permit a geometric analysis involving a shape parameter (S), defined by

$$S = \frac{P}{2\pi r_o} \text{ where } r_o = \sqrt{\frac{A_\sigma}{\pi}}. \quad (5.11)$$

This shape parameter has been used in a recent investigation of parallel injection behind an extended strut in a supersonic stream with good success.¹⁰¹ It attempts to describe the relationship between the perimeter and area of a given contour by comparing them to a perfectly circular contour of radius r_o . If the contour of interest were a perfect circle, the value of S produced would be unity. The circular geometry also leads to a minimum value of the shape parameter defined above. Thus, contours that yield shape parameters greater than unity are considered to have greater large-scale mixing potential than those having values of S near unity by virtue of increased mixing area and the presence of large-scale structures that enhance the surface area and perimeter of the mixing zone. Small-scale mixing does occur inside these contours along with large-scale entrainment. However, as small-scale effects increase, the fluctuations diffuse and become more uniform causing the contours to become more circular and the values of S to tend toward unity.

The contours presented above permit calculations of their enclosed area and their perimeters leading to values of the area ratio and shape parameter. Plots of these quantities appear in Figs. 5.51 and 5.52, respectively. Some very discernible trends appear in these data. First, Fig. 5.51 shows the area ratio R_σ resulting from the computations. This ratio is defined as the area enclosed within the standard deviation contour, A_σ , divided by the area within the 90% contour computed from the ensemble-averaged images, A_{90} . Thus, values of R_σ near unity indicate that the mixing zone area is of the same size as the area enclosed by the penetration contour at a given streamwise position. When this ratio takes values greater than unity, the result is that the mixing zone has grown beyond the bounds of the penetration contour. The curves in Fig. 5.51 show all four cases with approximately the same value of R_σ at $x/d_{eff} = 0$, though the elliptical cases both have slightly larger values than the circular cases. Downstream of the streamwise centerline (i.e., $x/d_{eff} = 0$),

two separate trends develop. Cases C1A and E1A show increasing trends to values of approximately $R_G = 1.5$ by four effective diameters downstream while the two helium injection cases reach values near $R_G = 1.2$. Beyond this streamwise plane, the two sets of curves depart from each other more dramatically with air injection cases continually falling above the helium injection cases. Eventually, by the final measurement location (i.e., $x/d_{eff} = 10$), the area ratios from cases C1A and E1A reach a level of roughly $R_G = 3.0$ while the other two cases finish between $R_G = 1.7$ and 2.0 . Thus, when compared to the penetration contours taken from the ensemble-averaged images, the mixing zones for the air injection cases are substantially larger than those for the helium injection cases. This observation provides further indications that the low compressibility cases (C1A and E1A) provide substantially better entrainment characteristics than cases C2H and E2H where compressibility levels are significantly larger.

Figure 5.52 illustrates the shape parameter data for each case. All four curves have similar characteristics in that a sharp decay is experienced in the far-field (between $x/d_{eff} = 8$ and 10). The plateau region occurs at or above a value of approximately $S = 3.0$ in the near-field region. This suggests that the near-field contours are highly convoluted when compared to a perfect circle. The sharp decay indicates that the contours tend to become more circular in the far-field mixing region. Given enough streamwise distance to mix, the shape parameters would most likely decay to a value of $S = 1.13$. This is the shape parameter of the 131.0 mm x 152.4 mm test section (i.e., the test section perimeter is 566.8 mm, while the cross-sectional area 19,974 mm² leading to an effective radius of $r_0 = 79.7$ mm). Thus, large-scale entrainment appears more prominent in the near-field regions of these injection flowfields. Glawe, et al.¹⁰¹ indicate that the combination of a large shape parameter and a large mixing zone area is desired for favorable large-scale mixing characteristics. On the basis of this observation and the data presented in Figs. 5.51 and 5.52, the air injection flowfields, characterized by relatively low levels of compressibility, appear to result in better large-scale mixing characteristics over the range of study than the helium cases since they produce larger area ratios while the shape parameters are approximately the same for air and helium. Thus, this analysis suggests that injection cases characterized by relatively high convective

Mach numbers remain relatively unmixed, while cases giving rise to mixing layers with lower levels of compressibility result in better mixing potential for $x/d_{eff} \leq 10$. This observation is consistent with the previous instantaneous and ensemble-averaged results.

5.3.2 Single-Shot Side View Images

Imaging the jet/freestream interaction from the side yields a more conventional look at the flow such as that illustrated in Fig. 1.1. Here, the camera is oriented directly 90° off the beam propagation direction resulting in improved signal levels ($S/N \approx 40-50$) compared to the end views presented earlier. The pixel resolutions in these visualizations were approximately $(\Delta x, \Delta y, \Delta z) = (87.6 \mu\text{m}, 87.6 \mu\text{m}, 200 \mu\text{m})$. Each side view image displayed in this section covers roughly 5.6 effective diameters (35.6 mm) in the streamwise direction and 5.3 effective diameters (33.7 mm) in the transverse direction. Ensembles of temporally uncorrelated images were acquired from two adjacent streamwise imaging planes (100 images each) positioned at the spanwise centerline of the jet (i.e., $z/d_{eff} = 0$) so that a wide field of view could be examined. A small gap (0.4 effective diameters = 2.5 mm) between the planes resulted; therefore, all the images from the downstream position presented in this section are separated from the upstream images by an amount consistent with this physical gap. The flow direction in all the images is from left to right. Due to the size of the test section, neither laser sheet position was influenced by reflections of the three-dimensional bow shock emanating from the top or side walls. Again, the gray scale palette highlights the features in the jet fluid by showing pure seeded fluid (freestream) as black and pure unseeded fluid (injectant) as white.

Instantaneous images provide a great deal of information regarding the flowfield structure and the characteristics of the jet, with particular emphasis on the large-scale eddies that form at the interface between the jet and freestream fluids. Ensemble-averaged images computed with Eq. 5.3 reveal near-field transverse jet penetration and yield some information regarding the mixing layer behavior at the upper edge of the jet. Finally, analyses of standard deviations computed using Eq. 5.4 provide substantial information concerning the fluctuations in this turbulent, three-dimensional

flowfield. These images reveal further details about the behavior of the wake and upper edge mixing layer, as well as the spatial extent of the jet core fluid found at the spanwise centerline of the jet. Additionally, two-dimensional spatial correlations of the intensity fluctuations were computed at various positions within the images. These results provide quantitative measures of the large-scale structure size, shape, and orientation within the upper edge mixing layer.

5.3.2.1 Instantaneous Images

Figure 5.53 shows select instantaneous images of the flowfield created by injection of air through the circular nozzle (case C1A). Four pairs of images appear in the figure; several observations can be quickly made from them. First, the upstream image in each pair illustrates the formation of the bow and separation shocks ahead of the jet exit. Some small fluctuations in the bow shock's position are visible, consistent with the information produced in the various end view images presented in §5.3.1.1. Intermittent large-scale eddies influence the position of the bow shock near the injector wall. Secondly, the jet/freestream interface demands attention due to the fact that it is inundated with vortex structures that form rapidly as the jet fluid enters the freestream. As the jet bends downstream due to the momentum of the crossflow, these eddies grow, interact with each other, and apparently entrain large quantities of freestream fluid. Discernible braiding regions form between pairs of large structures. These regions highlight the role of large-scale eddies in the engulfment process, where the large, well-pronounced structures strain the interface between them and then wrap freestream fluid into their cores. Such interfacial strain leads to locally steep concentration gradients and molecular diffusion across the interface. As other investigations of transverse injection into low speed and supersonic crossflows have suggested,^{37,40,49,68-71} the predominant roll-up direction of the eddies in these images is into the freestream fluid (i.e., counter-clockwise). This implies that the jet fluid tangent to the interface moves with a higher velocity than the adjacent freestream fluid. The large-scale vortex motions appear highly diffused in the downstream portions of the flowfield. The first pair of images in Fig. 5.53 illustrates this observation clearly where the structure located at $x/d_{eff} = 8$ seems highly

broken and filled with gray levels indicative of intermediately mixed fluid. Comparing this eddy to the one positioned at $x/d_{eff} = 3$ in the same pair of images reveals that the jet fluid not only mixes with crossflow as it travels downstream, but the inclination angle of the eddies with respect to the freestream also rotates, becoming steeper.

Downstream of approximately $x/d_{eff} = 5$, the jet core region in case C1A rapidly breaks up resulting in the increased gray areas shown in Fig. 5.53, which are indicative of fluid mixed to some intermediate level. The sharp intensity gradients between regions of jet and freestream fluid have weakened and some evidence of vortex structures in the wake region appears. As shown in Fig. 2.5, these eddies reach from the bottom wall up to the lower edge of the jet. The first, third, and fourth image pairs shown in Fig. 5.53 illustrate these vertical structures rather clearly, though they are not nearly as prominent as in the low speed case of Fric and Roshko.⁵³ It is inconclusive at this point whether or not an ordered system of wake vortices similar to that documented in incompressible injection studies⁵³ is established here. A final observation concerning these images involves the local velocities as inferred from the roll-up direction of the structures. As noted above, the large eddies at the interface predominantly roll into the freestream. However, the third pair of images in Fig. 5.53 shows a structure, formed near the point where the core breaks up ($x/d_{eff} \approx 6$), that has a reversed, clockwise direction. This particular vortex structure rolls toward the jet fluid indicating a local reversal of the high and low velocity streams. That is, in some instances near and beyond the point where the core breaks up, the jet fluid interacts with freestream fluid having a higher velocity.

Circular injection using helium results in significant differences in structure size and shape compared to the air injection case just described. Recall from the data in Table 5.1 that helium injection, under the present conditions, leads to the formation of an upper edge mixing layer which is substantially more compressible than the one formed in air injection. The instantaneous images shown in Fig. 5.54 provide evidence of this effect. The structures in case C2H are much flatter and more amorphous than those found in air injection. No images of the helium injection flowfield contained any of the large, well-defined rollers present in case C1A. Also, the braiding regions are

not nearly as well-pronounced suggesting that less freestream engulfment occurs in case C2H as compared to case C1A. These regions appear as “finger-like” intrusions of freestream into the jet fluid. Small-scale eddies appear more common along the interface as they ride with the larger motions that predominantly roll-up into the freestream fluid. Compared to case C1A, the eddies in case C2H appear to diffuse more slowly in the downstream regions of the interaction. The same observation resulted when examining the images from the end view of this case (Figs. 5.10-5.13). White regions, indicating relatively pure jet fluid, persist even at the farthest downstream location (i.e., $x/d_{eff} = 10$) in Fig. 5.54. Structures present between the wall and the jet again suggest that some vertically oriented wake vortices emerge in this flowfield. These are clearest in the first, third, and fourth image pairs of Fig. 5.54. Also noteworthy are the features in several images that indicate the presence of eddy shocklets. The shadowgraph photos of case C2H (Fig 5.2) also showed these relatively strong waves.

As mentioned earlier in this chapter (§5.1), the helium injection case C2H is characterized by a significantly larger convective Mach number than the air injection case C1A. Thus, based on the results from two-dimensional shear layers,^{89,90} one would expect the helium injection case to have structures that are flatter and more poorly defined than those from air injection. Examination of the instantaneous side view images provides exactly this observation. This issue will be examined in more detail in the discussion section following the presentation of the remaining data.

Examination of the instantaneous side view images from case E1A (Fig. 5.55) reveals features similar to those found in case C1A. Well-defined large-scale eddies form at the interface between the jet and freestream fluids. These structures grow as they convect downstream presumably by some vortex pairing mechanism where the upstream vortices catch up with the downstream eddies as they decelerate. Again, the vortices roll into the freestream fluid, suggesting that the injectant fluid moves faster tangent to the interface than the freestream fluid. The wide braid regions created between any two consecutive structures appear to promote freestream entrainment and enhancement of local small-scale diffusion across the highly strained interface. The jet rapidly breaks up downstream of approximately $x/d_{eff} = 5$ resulting in intermediate gray

scales that indicate intermediately mixed fluid. The large-scale vortex motions again appear highly diffused in the downstream portions of the flowfield in a similar fashion to case C1A (Fig. 5.53) as the sharp gradients between regions of jet and freestream fluid weaken. Some evidence of vortex structures in the wake region appears in the second and fourth pairs of images shown in Fig. 5.55. In addition to the structural development of the interface, these images provide indications of the weaker bow shock formed in the elliptical injection flowfield along with the smaller region beneath the separation shock upstream of the injector nozzle. The upstream image in the third pair presented in Fig. 5.55 shows the separation shock extending above the bottom wall by about $1.4d_{eff}$. In contrast, the separation shock in case C1A consistently stretches more than two effective diameters above the injector wall as observed in Fig. 5.53. A final observation from the images of case E1A is the slightly reduced transverse penetration afforded by the elliptical injector. The end view data also indicated this trend; more quantitative descriptions of the transverse jet penetration from analyzing the ensemble-averaged images appear in the following section.

Figure 5.56 presents select instantaneous images from the flowfield created in case E2H by injecting helium through the elliptical nozzle. As was observed in case C2H, the structures at the interface in this case appear rather flat and amorphous compared to those found in air injection. Thin filaments of freestream fluid intrude into the jet region between these large eddies. Compared to the significant braid regions between large structures in the air case (case E1A), the “finger-like” features in this case seem to entrain far less freestream fluid into the jet region where small-scale mixing can begin. The eddies seem to diffuse as they convect downstream, though not to the degree that was observed in the air injection case shown in Fig. 5.55. Relatively sharp gradients between the freestream and jet fluids remain present even at the farthest downstream position (i.e., $x/d_{eff} = 9.6$). Evidence of wake structures is less common here than in other instantaneous side view images, although the third and fourth pairs in Fig. 5.56 contain some indications that these vortices are present. Finally, the bow shock located upstream of the jet exit is again weaker than was found in circular injection, and the intersection of the separation shock with the bow shock

appears to occur at a lower transverse elevation above the bottom wall. Both of these observations agree with earlier results from the shadowgraph photos shown in §5.2 and the end view images presented in §5.3.1.

5.3.2.2 Ensemble-Averaged Results

Figure 5.57 shows the images obtained from applying Eq. 5.3 to the ensembles of data from case C1A. These images present actual averaged intensity levels within the jet/crossflow interaction normalized by the average freestream intensity downstream of the bow shock. The bow shock wave standing ahead of the jet fluid is clearly revealed. The region containing jet fluid becomes difficult to determine by eye beyond the jet exit as the fluid mixes with the freestream. However, intensity profiles taken at various streamwise positions provide a much clearer look at the mixing layer behavior found at the upper edge of the jet. These profiles also illustrate the deficit region in the center of the jet that gradually diminishes as freestream fluid enters the core. Figure 5.58 presents transverse intensity profiles taken from numerous streamwise positions in the averaged images of case C1A. This plot includes profiles of normalized mean intensity taken from nine streamwise planes between $x/d_{eff} = 0$ and 8. Dotted lines in the plot indicate the locations where the normalized intensities reach values of unity as shown by the scale included on the plot's upper axis. The two profiles taken from $x/d_{eff} = 0$ and 1 illustrate the bow shock at the location where sharp jumps in the normalized intensity occur. Each of the nine profiles shows the development of the mixing layer at the upper edge of the jet. Normalized intensity levels gradually decrease from near unity in the freestream to well below unity in the jet region. By roughly three effective diameters downstream, the intensity levels in the wake region near the injector wall begin to rise toward freestream values providing strong indications of freestream fluid being entrained into the wake. Downstream of this location, the normalized intensity levels within the central region of the jet gradually increase as freestream fluid is entrained into the jet core.

The normalized ensemble-averaged images from case C2H appear in Fig. 5.59. The bow shock is again very prominent and the jet appears to diffuse more slowly than in the air case. This

observation is inferred from the slight intensity gradient between the jet and freestream fluids that remains by the downstream portions of the field of view. To clarify the jet's behavior, normalized intensity profiles extracted from the images appear in Fig. 5.60. As observed in Fig. 5.58 for case C1A, the bow shock position is revealed in the first two profiles of Fig. 5.60 at $x/d_{\text{eff}} = 0$ and 1. The most obvious features in the profiles of case C2H are the very predominant jet region and the gentle growth of the wake region close to the injector wall. Figure 5.60 shows that the jet region is characterized by much smaller normalized intensity values for a longer streamwise spatial extent than what were observed for case C1A in Fig. 5.58. The profiles for case C2H show similar behavior near the freestream in that \bar{I}/\bar{I}_{∞} drops from unity to much lower values within the jet region. However, the decay of the normalized intensity values into the jet core is much more pronounced. Also, the increase of the normalized intensity values found in the wake region is more gentle than in Fig. 5.58 for case C1A. Together, these two observations indicate that the helium jet core remains more coherent over a longer streamwise distance than the air jet core. Thus, the entrainment effects afforded by the large-scale eddies formed within the peripherally oriented mixing layer are less effective in the helium injection case (high compressibility) than in case C1A (low compressibility). This conclusion lends credence to the inferences from the instantaneous images shown in Figs. 5.53 and 5.54, where the eddies that form in case C1A appeared to provide more entrainment than the large, amorphous structures formed in the mixing layer of case C2H. This is also consistent with the results obtained from the end view imaging experiments where the helium injection flowfields were found to provide lower mixing potential than the air injection cases. Thus, increased convective Mach number (i.e., higher compressibility) appears to be detrimental to the interfacial structural development that leads to entrainment of freestream fluid into the jet.

Ensemble-averaged images of the flowfield created by air injection through the elliptical nozzle (case E1A) appear in Fig. 5.61. Rapid turning of the jet fluid can be seen in the upstream image along with the shallow bow shock characteristic of the elliptical injection flowfields. The downstream image shows increased gray levels indicative of mixing between the two streams.

Beyond that, the contrast between the jet and freestream fluids becomes too small to visually distinguish between the two regions. Normalized intensity profiles presented in Fig. 5.62 illustrate the jet's behavior more clearly. The two profiles at $x/d_{\text{eff}} = 0$ and 1 illustrate the bow shock by the intensity jump at roughly four and five effective diameters above the bottom wall. From these two profiles it is apparent that the shock is weaker in case E1A than in either circular injection case since the shock's position is closer to the injector wall. The jet region appears prominently in the profiles near the injector ($x/d_{\text{eff}} \leq 3$). Beyond this location, the rapid growth of the wake region near the bottom wall coupled with the effects of entrainment from the eddies in the upper edge mixing layer account for the dramatic increase in normalized intensity values within the core region of the jet. These profiles have very similar characteristics compared to the normalized intensities shown in Fig. 5.58 for case C1A where the wake and upper edge mixing layer appear to promote mixing in the jet at the spanwise centerline (i.e., $z/d_{\text{eff}} = 0$) of the interaction. However, the transverse extent of the jet region is somewhat smaller and the normalized intensities contained within it are slightly higher in case E1A as compared to case C1A. This suggests that, at the spanwise centerline, the elliptical injection flowfield mixes slightly better than the circular injection flowfield by $x/d_{\text{eff}} = 8$.

Ensemble-averaged images from case E2H are shown in Fig. 5.63. As was the case in Fig. 5.59, where the ensemble-averaged images from case C2H were presented, specific information regarding the behavior of the helium jet cannot be obtained from visual inspection of these images. The weaker bow shock clearly appears in the upstream image, and, in general, the helium jet seems to require a longer streamwise extent to diffuse to the intermediate gray levels present in the air injection flowfield (case E1A). To better understand the jet's behavior, several normalized intensity profiles presented in Fig. 5.64 permit closer examination of the development of the mixing layer at the upper edge and the diffusive effects that take over in the downstream regions. As in Fig. 5.60 for case C2H, the profiles in Fig. 5.64 show the jet region remaining rather wide at positions upstream of $x/d_{\text{eff}} = 5$. However, downstream of this location, the elliptical injection case appears to produce somewhat better mixing as the jet region in Fig. 5.64

contains higher normalized intensity levels than in case C2H. Also, by $x/d_{\text{eff}} = 8$, the jet region in case E2H has become significantly smaller in transverse extent than in case C2H. As mentioned above, these observations suggest that the elliptical nozzle leads to better mixing between the injectant and freestream fluids than the circular nozzle, at least at the spanwise centerline of the jet/crossflow interaction.

The results of analyzing the averaged side view images for jet penetration appear in Fig. 5.65. The intensity of the jet boundary presented corresponds to 90% of the average freestream intensity behind the bow shock (i.e., outer edge of the jet). As explained in §5.3.1.2, this 90% definition provides a boundary between essentially pure freestream fluid and mixed fluid at some intermediate mixture fraction. Regions falling outside this contour contain either pure freestream fluid (values near 100%) or jet fluid mixed with the seeded freestream to a signal level above the 90% threshold, while fluid within this contour can be either pure injectant (values near 0%) or injectant mixed with the seeded freestream to a level that brings the signal below the 90% threshold. Each of the plots in Figs. 5.65a and 5.65b compares the performance of an individual injector configuration, where circular and elliptical injection results appear in Figs. 5.65a and 5.65b, respectively. Figure 5.65c directly compares the performance of the circular and elliptical injector geometries. Keffer and Baines²² found that the penetration profile data obtained from a low speed jet in crossflow for several values of the jet-to-freestream momentum flux ratio collapsed to a single curve in the near-injector region when the coordinate axes were scaled by J^{-1} . Results of a recent study examining helium injection into a supersonic crossflow at various jet-to-freestream momentum flux ratios confirmed these results for the high speed case in the region near the injector orifice.⁴⁰ The data in Figs. 5.65 reflect the same axis scaling convention.

The transverse penetration data from cases C1A and C2H, shown in Fig. 5.65a, collapse very well in the near-field region when the inverse J scaling is used. In this plot, circular symbols show the average upper boundary in case C1A while square symbols indicate the average upper boundary in case C2H. A power law curve fit applied to all the experimental data presented in the plot resulted in the following correlation:

$$\frac{y}{d_{eff} \cdot J} = 1.20 \left(\frac{x + a}{d_{eff} \cdot J} \right)^{0.344} \quad (5.12)$$

This expression fits the experimental data with a correlation coefficient of approximately 98%. Clearly, this equation can only be applied in the near-field region since it predicts the transverse penetration tending toward infinite levels as the streamwise position moves far downstream.

Examining the experimental results obtained from the cases using the elliptical nozzle shown in Fig. 5.65b yields similar conclusions regarding the collapse of the air and helium injection data when the inverse J scaling is applied to the coordinate axes. This injector geometry, however, leads to smaller transverse penetration levels in the injector near-field. The power law correlation obtained for these injection cases is

$$\frac{y}{d_{eff} \cdot J} = 1.00 \left(\frac{x + a}{d_{eff} \cdot J} \right)^{0.344}, \quad (5.13)$$

where the correlation coefficient is roughly 97%. Note that both correlations shown in Eqs. 5.12 and 5.13 predict the same dependence on the streamwise distance from the upstream edge of the injector nozzle. This is also the exact form of the correlation found in a previous study undertaken in the same facility using a different diagnostic technique,⁴⁰ indicating that the 90% intensity definition used to define the injectant boundary produces consistent predictions of near-field transverse penetration. In that study,⁴⁰ the origin of the streamwise coordinate was the upstream edge of the injector orifice rather than the centerline used here (see Fig. 1.2). Thus, the expressions given in Eqs. 5.12 and 5.13 incorporate a shift of the streamwise coordinate to the upstream edge of the injector. Figure 5.65c is a plot showing both correlations. From this figure, it appears clear that the jets from the elliptical injector suffer significant reductions in transverse penetration compared to the circular cases. This is most likely a manifestation of the asymmetric instability created around the elliptical orifice that leads to axis-switching. As shown earlier in the analysis of the ensemble-averaged end view images (§5.3.1.2), the elliptical jet spreads more in the spanwise direction than the circular jet. Taken together, these observations of better lateral spread

with suppressed transverse penetration provide rather conclusive evidence that the axis-switching phenomenon is occurring in the two elliptical injection cases studied in this investigation. It is also worth noting that the transverse penetration is insensitive to the injectant molecular weight (air has greater than seven times the molecular weight of helium) making the jet-to-freestream momentum flux ratio (J) the most important parameter describing the penetration of a transverse jet into the crossflow.

5.3.2.3 Standard Deviation Results

Standard deviation statistics are important tools that aid in understanding the fluctuations found in turbulent, compressible mixing flowfields. Their utility was demonstrated in the end view analysis presented in §5.3.1.3. In a similar way, the intensity standard deviations from the side view images provide more insight into the location, formation, and development of regions of fluctuating fluid. The interfacial region between the jet and freestream fluids may be examined in more detail. The shear layer formed in this region can fluctuate intensely and has been shown in the material above to be a prime contributor to the entrainment of freestream fluid. The spatial extent of the undisturbed jet core at the spanwise centerline can be identified in terms of streamwise position, and the fluctuations within the wake region downstream of the injector can also be examined. In all of the results that follow, the visualization plane is the spanwise centerline (i.e., $z/d_{\text{eff}} = 0$) of the jet/crossflow interaction. The images and profiles presented are created using the normalized standard deviation results from the application of Eqs. 5.4 and 5.10 to the ensembles of instantaneous images. Recall that the normalization is accomplished by taking the absolute value of unity minus the quotient of the actual standard deviation and the average freestream standard deviation behind the bow shock.

The upstream and downstream standard deviation images from air injection through the circular nozzle (case C1A) appear in Fig. 5.66. As with the ensemble-averaged images presented above, 100 instantaneous images were used to compute the standard deviation results shown. Regions that appear black in the images have normalized standard deviations of essentially zero

while lighter regions contain intensity fluctuations. The left image in Fig. 5.66 illustrates the slight fluctuation in the bow shock position. As in the end view image from $x/d_{eff} = 0$ (Fig. 5.35a), the intermittent large-scale eddies formed at the upper edge of the jet boundary were found to influence the shock's position. More intense fluctuations of the bow shock position localize themselves near the mixing layer where the large-scale eddies form, as indicated by the relatively light region just above the jet shear layer. Farther out in the freestream, the shock fluctuations appear to diminish in intensity. The most prominent feature observed in this image is the mixing layer that develops from the upstream edge of the injector orifice. This mixing region grows very rapidly as the jet bends due to the oncoming freestream flow. Other features visible in the left image include the freestream and jet core regions which contain relatively low intensity fluctuation levels. The jet core viewed at the spanwise jet centerline (i.e., $z/d_{eff} = 0$) exists until approximately $x/d_{eff} = 6$, where the fluctuations of the mixing layer above and wake below appear to coalesce. This observation is essentially consistent with the findings in the end view images that showed the jet core becoming indistinct somewhere between four and eight effective diameters downstream. Beyond this position, the entire jet region contains fluctuating fluid and the core cannot be distinguished.

Transverse intensity profiles were used in the ensemble-averaged images to examine the behavior of the mixing layer, wake, and jet core. These profiles proved useful in that they allowed direct comparisons of the normalized intensity levels found within the four cases studied in this investigation. Similar profiles taken from the normalized standard deviation images allow closer inspection of these features in terms of the relative levels of fluctuations present and the gradual transition from large-scale mixing to small-scale diffusion effects. Figure 5.67 illustrates several of these profiles obtained from the images computed for case C1A (shown in Fig. 5.66). The plot includes intensity profiles from nine streamwise planes between $x/d_{eff} = 0$ and 8. Dotted lines in the plot indicate locations where the normalized standard deviations reach values of unity as indicated by the scale shown on the plot's upper axis. Also included in the plot is a dashed line that represents the penetration correlation given above in Eq. 5.12. Consistent with the ensemble-

averaged results shown in Fig. 5.58, the two profiles positioned at $x/d_{eff} = 0$ and 1 demonstrate the effects of the bow shock. The regions directly above and below this feature are essentially undisturbed as the normalized fluctuation levels found there fall to zero. Mixing layer fluctuations appear in both of these profiles as indicated by the two local peaks in the normalized intensity centered near transverse positions of $y/d_{eff} = 2.2$ and 2.9, respectively. Downstream of $x/d_{eff} = 1$, the bow shock influence no longer appears in the profiles leaving only the fluctuating shear layer, the jet core, and the growing wake region near the bottom wall. The presence of the core region decays gradually as the mixing layer and wake begin to coalesce. Downstream of about $x/d_{eff} = 6$, the distinct influence of the jet core disappears leaving only a slight depression in the profiles that are otherwise dominated by the mixing layer and wake. It should also be noted that the normalized fluctuation levels within the upper edge shear layer decrease with streamwise position downstream of approximately five effective diameters from the injector centerline. However, the mixing layer continues to display growth up to the final position shown at $x/d_{eff} = 8$. Interestingly, the peak values of normalized standard deviation generally fall well below the average penetration boundary of the jet. This indicates that the regions of high fluctuations in the upper shear layer occur closer to the jet core and therefore freestream fluid is entrained far into the jet region.

The two normalized standard deviation images computed for case C2H appear in Fig. 5.68. Three main features demonstrate appreciable fluctuations in these images: the bow shock, the upper edge mixing layer, and the wake region developing near the injector wall. The images from case C2H contain several noticeable differences when compared to the results shown in Fig. 5.66 for case C1A. First, the fluctuation of the bow shock in the helium injection case appears less intense than in Fig. 5.66, as suggested by its darker color. As noted in the instantaneous visualizations from these two cases, the air injection flowfield (low compressibility) fostered the development of periodic large-scale structures in the upper edge mixing layer that were long and well-defined compared to those in case C2H. Also, the braid regions that formed between two consecutive eddies in case C1A were rather wide compared to the narrow braiding regions formed between the flat structures found in the helium injection case (high compressibility). Thus, the

bow shock in case C1A had more oscillatory disturbances acting on it than in case C2H, leading to the observed differences in shock fluctuation levels. Secondly, the upper edge mixing layer developing in case C2H appears somewhat thinner in Fig. 5.68 than the corresponding feature in Fig. 5.66. For example, in Fig. 5.68, the mixing layer appears to extend from roughly $y/d_{\text{eff}} = 2.5$ to $y/d_{\text{eff}} = 4.6$ at a streamwise position of $x/d_{\text{eff}} = 3.2$. In Fig. 5.66, a similar examination shows that the mixing layer exists between approximately $y/d_{\text{eff}} = 2.3$ to $y/d_{\text{eff}} = 4.9$. This comparison indicates that the shear layer formed at the upper edge of the helium injector is nearly 20% thinner at this streamwise position than the same feature observed in case C1A. Because of its apparently slower growth, the upper edge shear layer in case C2H remains more distinct in the downstream regions of the image (see Fig. 5.68 at $x/d_{\text{eff}} = 6$ to 9) than in Fig. 5.66 for case C1A. The wake region that develops downstream of the injector orifice in case C2H, however, seems to grow in a manner similar to what appears in Fig. 5.66. As a result, the jet core region remains preserved for a longer streamwise distance in case C2H. That is, the fluctuations in the wake and shear layer do not coalesce as far upstream in the helium injection flowfield as they do in case C1A.

Normalized intensity profiles from case C2H shown in Fig. 5.69 provide clearer evidence of these observations. Bow shock fluctuation intensities found in the profiles at $x/d_{\text{eff}} = 0$ and 1 are slightly lower than those observed in Fig. 5.67 from case C1A. Also, the widths of the upper edge mixing layer indicated in these two profiles are significantly narrower than in Fig. 5.67. Moving downstream, the development of both the wake region and the upper edge shear layer are clearly shown. The low intensity region between these two features indicates the persistent core of the jet. As the profiles in Fig. 5.69 illustrate, the core remains relatively distinct as far downstream as $x/d_{\text{eff}} = 8$. This profile shows the peak-to-peak distance between the fluctuation intensities in the mixing layer and the wake to be about 2.8 effective diameters, while the same distance in the downstream profile of Fig. 5.67 for case C1A is about 1.8 effective diameters. In addition to the wider region in case C2H, the normalized intensities found within this region are appreciably lower than in case C1A indicative of slower turbulent diffusion into the jet core. This effect is primarily

due to the slower growth of the upper edge shear layer in the helium injection case. Also, the peak normalized intensity values within the mixing layer of case C2H occur at higher transverse positions relative to the mean jet penetration curve than shown in Fig. 5.67. This phenomenon contributes to the persistence of the jet core since the strongest turbulent fluctuations in the upper shear layer remain well above the central portion of the jet region for the helium injection case. This was also observed in the end view results shown in Figs. 5.37 and 5.40 from cases C1A and C2H, respectively. Thus, in the high convective Mach number case (C2H), the entrainment characteristics of the large-scale eddies appear significantly suppressed as compared to those of the low convective Mach number case (C1A).

Figure 5.70 displays the two normalized standard deviation images computed for case E1A. The relatively bright region found within the jet core of the upstream image results from intermittent near-wall reflections. This case was examined at a different time than the rest of the side view experiments such that slight differences in the spanwise position of the laser sheet within the test section may have existed. The alignment of the laser sheet is prone to such slight positional errors due to its thickness ($\sim 200 \mu\text{m}$). Had it been in exactly the same spanwise location as in the other experiments, the effect observed in this image would not be present. Nonetheless, both images highlight the development of the fluctuations within the mixing layer and the wake along with the slight changes in bow shock position. Rapid mixing layer growth appears at the interface between the jet and freestream fluids. The jet core seems to disappear between 4.2 and 5.4 effective diameters downstream of the injector centerline, consistent with the end view standard deviation images from this case (Fig. 5.41) that showed the jet core at the spanwise centerline (i.e., $z/d_{\text{eff}} = 0$) to be completely indistinguishable between $x/d_{\text{eff}} = 4$ and 8. Beyond this location, the entire jet region contains intermediate gray levels indicative of fluctuating fluid. Transverse intensity profiles permit closer examination of the various features illustrated in these images.

Profiles of normalized fluctuation intensity from case E1A are presented in Fig. 5.71. Normalized fluctuation levels in the freestream are consistently zero, and the fluctuations in the bow shock's position occur only in the two profiles at $x/d_{\text{eff}} = 0$ and 1 in the figure. The

abnormally high normalized fluctuation levels that occur directly below the mixing layer result from the slight laser sheet positional errors associated with this particular case. Aside from these features, the profiles illustrate the development of the upper edge mixing layer and the gradual growth of the wake region. Fluctuation levels within the jet region rapidly increase as the mixing layer and wake coalesce just downstream of $x/d_{eff} = 4$. Farther downstream, the profiles show only a single peak occurring within the mixing layer. These profiles are very different from those found in case C1A shown in Fig. 5.67 where the bimodal nature caused by peaks in both the shear layer and the wake persisted even by eight effective diameters downstream of the jet exit. This suggests that, at least on the spanwise centerline of the jet/crossflow interaction, the elliptical nozzle leads to more rapid diffusion of the fluctuating regions into the jet core. The mixing layer revealed in Fig. 5.71 is also substantially thinner than observed in the results of case C1A shown in Fig. 5.67. End view standard deviation results from these two cases demonstrated similar trends (see Figs. 5.37 and 5.43). As in case C1A, the locations where peak values in the normalized standard deviation profiles occur are generally well below the average jet penetration contour of Eq. 5.12. This suggests that, in air injection, the large-scale eddies formed within the upper edge mixing layer provide deeper entrainment of freestream fluid into the jet region.

The two images displaying the normalized standard deviations computed for case E2H appear in Fig. 5.72. As observed in all the other side view images of this statistical quantity, the images of case E2H illustrate the fluctuations in the bow shock position along with the turbulent fluctuations characteristic of the upper edge mixing layer and the wake region close to the injector wall. Mixing layer growth seems slower in this case as compared to case E1A shown in Fig. 5.70. The development of the wake region, however, appears very similar to the other elliptical injection flowfield. Comparing the gray levels found in the downstream regions of the right hand image suggests that the fluctuation levels in the mixing layer remain larger than those found in the wake.

Figure 5.73 presents the profiles of normalized standard deviation computed from case E2H using Eq. 5.10. These curves reveal some interesting differences between the two elliptical

injection flowfields. First, the fluctuations in the upper edge mixing layer in case E2H demonstrate a gradual reduction with streamwise position although the location of the peak value remains at higher transverse positions relative to the mean jet penetration contour than in case E1A. Thus, helium injection cases (high compressibility) appear to suffer from a shallower extent of freestream entrainment into the jet region than the low compressibility air injection cases, resulting in a more prominent jet core. Also, as observed in the images presented in Fig. 5.72, the mixing layer appears significantly thinner and more distinct than the corresponding feature in case E1A. Both elliptical injection cases demonstrate the disappearance of the jet core at roughly the same streamwise location (i.e., near $x/d_{eff} = 5$). However, the depression in the central region of the profiles from $x/d_{eff} = 6$ to 8 in case E2H suggests slower diffusion of the fluctuations into the jet core than the profiles from case E1A (Fig. 5.71). That is, the diffusion of wake and mixing layer fluctuations into the jet core occurs more rapidly for case E1A, resulting in relatively uniform normalized standard deviation profiles downstream of $x/d_{eff} = 6$. The profiles shown in Fig. 5.73 for case E2H strongly resemble those obtained in the end view standard deviation images computed for this flowfield (Fig. 5.46).

5.3.2.4 Spatial Correlation Results

Structures with a wide variety of sizes and orientations appear in the ensembles of instantaneous side view images. To this point, the mixing layer thickness, as inferred from the standard deviation results, has provided a comparative measure of the large-scale structure size in the different cases examined. Another result that provides information about the behavior of the large eddies formed in the upper edge mixing layer is the two-dimensional spatial correlation field. This statistical property has been used by other authors to examine the development of large-scale structures in a variety of flowfields.¹³⁶⁻¹³⁹ The form used in this investigation is represented as

$$C(\Delta x, \Delta y) = \frac{1}{N} \sum_{n=1}^N I'(x, y) \cdot I'(x + \Delta x, y + \Delta y), \quad (5.14)$$

where the point (x, y) is the reference location about which the features are correlated. The correlations are computed using the intensity fluctuations and the two lag parameters, Δx and Δy . For the present calculations, the correlations are computed over a domain that is 256 pixels wide by 256 pixels high corresponding to a box that is just over 3.5 effective diameters (22.2 mm) on a side. Each pixel location is used as a reference location in the calculation to avoid subjectivity. The center of the computational domain is placed at one location in each instantaneous upstream and downstream image obtained from the four cases studied in this investigation. For the upstream images, the center of the domain corresponds to a location on the theoretical near-field penetration curve (either Eq. 5.12 or Eq. 5.13 depending on the injector geometry). In the downstream images, the center of the domain is placed roughly in the center of the upper edge mixing layer at a given streamwise position. Finally, the results from the instantaneous images are averaged together over the entire ensemble producing an ensemble-averaged correlation map of the given spatial region. Note that the two-dimensional spatial correlation used in this way sheds no light on a structure's three-dimensionality. However, over a large ensemble of images, the use of the spatial correlation in the side view plane positioned at the spanwise centerline of the injector does provide measures of the average geometric features of the large-scale eddies that can be used for comparison between the four cases studied here.

The correlation fields presented in Figs. 5.74-5.85 show contour lines that are in even increments of 0.125 about the central peak that was normalized to unity. Instantaneous spatial correlation results are shown along with the actual regions taken from the individual images in Figs. 5.74-5.81. Note that the instantaneous image/correlation pairs displayed here are taken from the instantaneous side view images shown in Figs. 5.53-5.56. Figures 5.74-5.81 provide evidence of the significant structural variation that occurs within a given ensemble. To quantify the geometric parameters of the large-scale eddies on average, the 50% contour lines in the ensemble-averaged correlation maps are used. Analyses of these ensemble-averaged contours, shown in Figs. 5.82-5.85, reveal that the structures are elliptical in shape with their major axes being inclined somewhat to the freestream direction. These elliptical contours produce geometric

properties of the large-scale structures, including major and minor axis size ($2a$ and $2b$), elliptical eccentricity (ϵ), and angular orientation with respect to the freestream direction (α). The expression used to compute the eccentricity appears in §3.2.3 as Eq. 3.3. All of this information obtained from the ensemble-averaged results appears in tabulated form in Table 5.3. Also present in the table are the center coordinates of the computational boxes.

Instantaneous spatial correlation results from the side view images of case C1A appear in Figs. 5.74 and 5.75. These images and their respective contours illustrate the variety of structures that form in the mixing layer at the upper edge of the jet. The results from the upstream images in Fig. 5.74 show that the structures indeed appear elliptical in shape. The first image shows two complete eddies in the domain. The correlation field from this particular image reveals the dominant peak at the center of the domain and islands on either side of it containing secondary peaks that represent the separation between the pair of structures in the image. The other three image/correlation map pairs in Fig. 5.74 demonstrate variations in structure size and angular orientation with respect to the freestream. Correlation fields from the downstream image plane shown in Fig. 5.75 present additional results. Here, some structures appear highly elongated and flat (see the third correlation map) while others are more inclined to the freestream flow direction (see the second correlation map) than in Fig. 5.74. Generally, the images indicate that the structures have become less organized by the downstream position, and the correlations confirm this in that the 50% contours are somewhat smaller than those found in the upstream maps of Fig. 5.74.

Results computed from the upstream and downstream instantaneous images of case C2H appear in Figs. 5.76 and 5.77, respectively. In Fig. 5.76, the structures revealed in the correlation maps appear somewhat larger than those from the upstream results of case C1A. Several of these contours suggest flatter shapes, though the central regions of the contours look more circular than in Fig. 5.74. Also note the islands observed in the fourth correlation map that indicate the secondary peak associated with the other eddies in the corresponding instantaneous image. Again, the distance between the primary and secondary peaks indicates the spacing between the centers of

the structures. The downstream results shown in Fig. 5.77 suggest that, in general, the structures have rotated somewhat becoming more inclined to the oncoming freestream flow and have increased in size. The ensemble-averaged results will address these observations further.

The correlation fields computed from instantaneous images of case E1A are shown in Figs. 5.78 and 5.79 for the upstream and downstream image positions, respectively. Similar features are found in the correlation fields of Fig. 5.78 compared to the others from the upstream region, though the structure inclination angle appears slightly lower than those found in circular injection. The existence of a secondary peak found in the second map indicates the presence of the two eddies appearing in the imaged domain. Rotation of the structures is suggested by the results shown in Fig. 5.79 from the downstream images. Also, the correlation contours suggest that the eddies in these results are somewhat smaller than those in Fig. 5.78 and they also appear more circular. As in case C1A, the structures from the images of this case appear to quickly become less organized as they travel downstream; the spatial correlation results confirm this observation by suggesting smaller contours of high correlation in the downstream regions of the flowfield.

The final instantaneous results presented are those in Figs. 5.80 and 5.81 from case E2H. In the upstream results shown in Fig. 5.80, the correlation contours appear more skewed to the freestream than in case E1A (Fig. 5.78). As with the circular injection case using helium (case C2H), the eddies in case E2H appear relatively flat and elongated compared to those formed in the air injection case. In contrast though, the correlation contours suggest that the vortices in case E2H are smaller than those in case E1A. Indications of secondary peaks within the correlation fields appear most obviously in the fourth map. Figure 5.81 shows the correlation fields and image regions found in case E2H as the image plane moves downstream. The correlation contours in this figure suggest rotation of the structures to steeper inclination angles. They also indicate that the structures grow somewhat as they convect downstream.

The ensemble-averaged correlation fields for case C1A are presented in Fig. 5.82. Here the upstream and downstream contour maps appear. Recall that the contour levels shown vary in increments of 0.125 from 0.125 to unity. The 50% contour from Fig. 5.82a yields a normalized

major axis of $2a/d_{\text{eff}} = 0.44$ (see Table 5.3). The eccentricity of the elliptical structure is $\epsilon = 0.75$ where a circular contour has an eccentricity of zero, and the inclination angle above the freestream flow direction (i.e., horizontal) is about $\alpha = 24^\circ$. Moving downstream, the structure's inclination angle increases, as observed in the instantaneous results, to about $\alpha = 45^\circ$. The normalized major axis becomes shorter ($2a/d_{\text{eff}} = 0.33$) and the 50% contour becomes more circular with an eccentricity of $\epsilon = 0.65$. Thus, the structure loses some of its coherency and rotates significantly into the freestream as it convects downstream due to the mixing between the injectant and crossflow.

Ensemble-averaged results from case C2H (Fig. 5.83) are somewhat different. The 50% contour in Fig. 5.83a indicates that the major axis is 0.43 effective diameters long and the structure's eccentricity is about $\epsilon = 0.67$. These values suggest that the average eddy in the helium case at this streamwise position is slightly smaller than in case C1A (by about 2%) while it takes a slightly more circular shape. It is also more inclined to the freestream flow with an inclination angle of about $\alpha = 29^\circ$. Figure 5.83b shows an increase in normalized structure size to approximately $2a/d_{\text{eff}} = 0.54$. The average structure in the downstream position has an eccentricity of about $\epsilon = 0.73$ and an inclination angle of nearly $\alpha = 64^\circ$. Thus, in the high compressibility helium injection case, the large-scale structures rotate more as they move downstream compared to case C1A, and they grow in size. Throughout the results presented to this point, helium injection consistently provides evidence of slower diffusion and break-up of the large-scale eddies as they move downstream than does air injection. The results of the present correlation analysis substantiate this observation further by showing growth of the average eddy in case C2H as it convects downstream, while the average eddy in case C1A shrinks. Apparently, increasing compressibility diminishes the entrainment effectiveness of the large-scale eddies that form at the jet/freestream interface leading to slower large-scale break-up.

The ensemble-averaged correlation fields computed for the case of elliptical injection of air (case E1A) appear in Fig. 5.84. From the upstream position, the average structure is found to have a major axis of $2a/d_{\text{eff}} = 0.50$ and an eccentricity of $\epsilon = 0.69$. Also, the structure inclines

itself at approximately $\alpha = 14^\circ$ above the freestream flow direction. Due to the imaged field of view and the correlation box size requirements, the streamwise position of the correlation domain in case E1A is farther upstream than in case C1A (see Table 5.3). Therefore, direct comparisons between the upstream cases cannot be made. However, the downstream results are obtained at positions identical to those in case C1A. Here, the resulting contour map appears in Fig. 5.84b. Results from the 50% contour indicate an average structure inclination of roughly $\alpha = 39^\circ$ along with a normalized major axis of $2a/d_{\text{eff}} = 0.20$ and an eccentricity of $\epsilon = 0.60$. Thus, compared to the upstream results of Fig. 5.84a, the downstream structure has again rotated into the freestream, become more circular, and contracted. Compared to case C1A, the downstream results show that the structure from case E1A is smaller (by about 40%), more circular, and inclined at a shallower angle to the freestream.

Finally, the results of analyzing the ensemble-averaged correlation fields for case E2H (Fig. 5.85) show similar trends to those already discussed. First, in the upstream position, the average eddy has an inclination angle of about $\alpha = 32^\circ$ along with a major axis and eccentricity of $2a/d_{\text{eff}} = 0.18$ and $\epsilon = 0.63$, respectively. Thus, compared to case E1A, the high compressibility helium injection case leads to smaller, more circular eddies oriented at steeper inclination angles. Circular injection of helium (case C2H) also produced steeper inclination angles and smaller, more circular structures than case C1A. Moving downstream, the 50% contour in Fig. 5.85b indicates structural growth to a major axis of about 0.24 effective diameters. The elliptical eccentricity increases from the upstream position to approximately $\epsilon = 0.74$ while angular inclination increases to roughly $\alpha = 59^\circ$. Thus, in comparison to the upstream position in case E2H, the structures become larger, more inclined to the freestream, and more elliptical as they convect downstream. These are the exact same trends as observed for the two spatial locations from case C2H. Thus, the spatial correlation results presented above indicate that the large-scale structures formed in air injection flowfields are somewhat larger in the near-field and become less coherent as they convect downstream (indicated by the shrinking major axis). They also appear to become more circular in shape and rotate into the oncoming freestream, becoming more inclined to the horizontal direction.

Helium injection, on the other hand, produces eddies that grow and become more elliptical as they travel downstream. These eddies also tend to rotate into the approaching freestream fluid, becoming more inclined to the horizontal direction as they convect downstream. Comparing the two injector geometries indicates that the eddies formed in the jets issuing from the elliptical injector are typically smaller than those in the jets formed using the circular injector.

5.3.3 Bow Shock/Jet Boundary Interaction Images

The side view images presented in §5.3.2 provided clear visualizations of the large-scale vortices formed in the mixing layer that develops at the interface between the freestream and injectant fluids. These eddies were found to intermittently influence the position of the bow shock generated upstream of the injector orifice due to the blockage created by the jet itself. Side view images also showed the region enclosed by the separation shock ahead of the injector nozzle where the bow shock interacts with the turbulent boundary layer resulting in the creation of an adverse pressure gradient and incipient boundary layer separation (see Fig. 1.1). This region has been shown to produce locally high wall static pressures in both experiments^{7,16,140} and numerical predictions.^{11-15,108} Also, in their numerical investigation of a reacting two-dimensional transverse jet of hydrogen in a supersonic air stream, Takahashi and Hayashi¹⁴¹ found that the static temperatures occurring within this zone were significantly higher than in any other region of their computational domain. The potential for significant erosion of the injector wall exists due to this local high temperature zone. Though always present in flowfields created by transverse injection into a supersonic crossflow, reductions in the size of the region beneath the separation shock should diminish the effects of this local hot-spot.

The side view images presented above indicated that the elliptical nozzle geometry produced an area below the separation shock upstream of the injector exit that was smaller in terms of its transverse and streamwise extent than the circular nozzle geometry, although the total extent of this region was not observed. The elliptical nozzle also resulted in a weaker bow shock than the circular nozzle implying that smaller total pressure losses are likely to exist across the elliptical

injection flowfield. By examining a smaller field of view positioned just upstream of the injector exit, these two phenomena, along with the interaction of the large-scale eddies with the bow shock, may be studied in more detail. The following sections present the results of this effort where instantaneous, ensemble-averaged, and standard deviation images illustrate the various features present in this region of the flowfield. In these images, the signal-to-noise ratios were typically $S/N \approx 40-50$ as the camera was placed 90° off the direction of laser sheet propagation. Pixel resolutions for these images were approximately $(\Delta x, \Delta y, \Delta z) = (47.0 \mu\text{m}, 47.0 \mu\text{m}, 200 \mu\text{m})$. Each side view image displayed in this section covers roughly 4.3 effective diameters (27.2 mm) in the streamwise direction and 2.8 effective diameters (18.0 mm) in the transverse direction. The freestream flow direction is from left to right while the injectant flow enters the field of view from the lower edge of the picture. Gray levels in these images were assigned using a convention opposite to the images presented previously so that the jet fluid appears dark while seeded freestream fluid appears light. Ensembles of 50 images were acquired for cases C1A and E1A, with the laser sheet positioned at the spanwise centerline of the jet (i.e., $z/d_{\text{eff}} = 0$). Since the characteristics of the separation shock formed ahead of the injector were found to be more dependent on injector geometry than injectant gas, the helium cases were not studied in these experiments.

5.3.3.1 Instantaneous Images

The instantaneous images from cases C1A and E1A appear in Figs. 5.86 and 5.87, respectively. Six images are presented from each case. The visualizations of case C1A shown in Fig. 5.86 are rather striking in appearance. The region of interest appears more clearly in these images as compared to the instantaneous shots displayed in §5.3.2 where a smaller magnification was used. Many images in the ensemble capture the upper edge of the approaching boundary layer. For example, all of the images except the second shot presented in Fig. 5.86 show some boundary layer fluid as it enters the region beneath the separation shock wave. Several other features can be easily observed in these images including the bow shock standoff distance (i.e., the

distance upstream of the injector leading edge where the bow shock intersects the lower edge of the image), the streamwise and transverse dimensions associated with the upstream separation shock wave, and the large-scale vortices that develop as the jet enters the crossflow behind the shock/boundary layer interaction.

The behavior of the bow shock below the point of intersection with the separation shock appears strongly influenced by the intermittent large-scale eddies that form immediately after the jet fluid enters the crossflow. The six images shown in Fig. 5.86 illustrate the range of behavior clearly. Some instantaneous visualizations reveal the bow shock in this region to be essentially perpendicular to the wall. In these instances (see the first, fourth, and sixth images), large eddies do not appear very near the wall. In contrast, the fifth image of Fig. 5.86 contains a turbulent structure centered at roughly one effective diameter above the wall. In response to the presence of this eddy, the bow shock curves sharply upstream increasing its distance from the injector centerline. This upstream curvature is then followed by a region where the bow shock bends back downstream. Several images from the ensemble show characteristics similar to these as the large-scale eddies disturb the bow shock's behavior below the point of intersection with the separation shock. Another interesting occurrence is shown in the third image of the figure where the bow shock apparently lifts off the wall allowing boundary layer fluid and injectant fluid to mix subsonically upstream of the injector exit. This periodic lifting of the shock wave, caused when the approaching boundary layer is relatively thick and the sonic line occurs at a higher elevation off the bottom wall, probably exacerbates the hot-spot phenomenon associated with reacting transverse injection flowfields since fuel is allowed to propagate farther upstream. Despite the dynamic nature of the bow shock's behavior below the intersection with the separation shock, a standoff distance of approximately $0.5d_{eff}$ consistently occurs. In the region above the point where the separation shock and bow shock intersect, fluctuations in the bow shock's position continue to occur although they do not result in the dramatic curvature changes noted in the region of nearly normal shock behavior close to the injector wall. In all the images obtained from case C1A, the bow shock was found to intersect the top edge of the image between $-0.50 \leq x/d_{eff} \leq 0$.

The region found between the bow and separation shocks is an important feature in transverse injection flowfields in relation to its flame-holding capability in combustions situations. As noted above, this region has been found to contain the highest temperatures in the flowfield created by a hydrogen jet injected into air.¹⁴¹ At the spanwise centerline of the jet/crossflow interaction, two points describe the extent of the separation shock. The first is the point upstream of the injector where the separation shock intersects the bottom edge of the image. The second point is the intersection of the bow and separation shocks that defines the highest transverse elevation of this wave. In the ensemble of images collected for case C1A, the position of the first point was found to fall between $-3.0 \leq x/d_{\text{eff}} \leq -2.25$. Examining these images shows that the transverse location of the second point varies from about 1.6 to 2.8 effective diameters above the bottom wall.

In addition to these features, the images of Fig. 5.86 provide clear visualizations of the large-scale eddies that develop in the earliest stages of the flowfield created by transverse injection of air through a circular nozzle. A wide range of structures appear in the images presented, several of which are reminiscent of the two-dimensional rollers observed in low convective Mach number mixing layers.^{89,142,143} All of these shots illustrate the highly dynamic interface that occurs near the injector orifice. Large- and small-scale eddies are revealed in each image along with the braiding regions between consecutive eddies. Some structures resembling mushroom-shaped protrusions appear (see the sixth image in Fig. 5.86). In general, the eddies roll into the freestream fluid as expected since the underexpanded air accelerates rapidly out of the nozzle leading to much higher injectant fluid velocities compared to the local freestream fluid velocity near the exit. Some instances of oppositely oriented vorticity appear (as in the downstream half of the large eddy in the sixth image), though the predominant vortex wrap-up direction indicates vorticity in the + z-direction (i.e., out of the page). Intermediate gray scales found throughout the jet/freestream interface suggest that a significant amount of mixing between the two fluids occurs very near the orifice. Coupled with the large excursions of jet fluid and the relatively wide braiding regions that allow both freestream engulfment by the large eddies and diffusion across the highly strained

interface, these observations suggest that the large-scale vortices play vital roles in the near-field mixing in this flowfield. However, the bow shock near the injector wall appears quite strong and the area beneath the separation shock upstream of the jet is very pronounced, such that the near-field mixing may come at the high cost of significant total pressure losses and potentially detrimental hot-spots in a combustor flowfield.

Figure 5.87 shows the instantaneous images obtained from case E1A. All of the images presented in Fig. 5.87 show the upper edge of the approaching crossflow boundary layer as it enters the region beneath the separation shock just upstream of the jet orifice. As in the results from the circular case examined above, several other features can be easily observed in the images of case E1A, including the bow shock standoff distance, the streamwise and transverse extent of the separation shock, and the large-scale vortices that develop at the jet/freestream interface.

Large-scale eddies formed near the injector wall appear to influence the behavior of the bow shock below the point of intersection with the separation shock in case E1A, though not to the degree that was observed in the images from case C1A presented in Fig. 5.86. The images shown in Fig. 5.87 give some evidence of the curvature changes induced by the presence of eddies (see the second and fifth images). Also, the sixth image presented shows the shock lifting phenomenon that appeared in case C1A (Fig. 5.86). The bow shock standoff distance (i.e., the bow shock's intersection with the lower edge of the image) is approximately $0.25d_{eff}$ upstream of the jet centerline. This is about 50% closer to the injector leading edge than was observed for case C1A. This is explained by the asymmetric vortex development associated with the elliptical geometry that leads to more rapid spreading in the minor-axis direction than in the major-axis direction. Apparently, the jet fluid expands more in the spanwise direction than in the streamwise direction at the exit plane of the elliptical nozzle. This allows the shock to stand closer to the jet exit in the elliptical injector flowfield and still accomplish the necessary pressure correction.

In the region above the point of intersection of the bow and separation shocks, some small fluctuations in the bow shock's position occur. These fluctuations are similar to those for case C1A in that no dramatic curvature changes appear. However, the images shown in Fig. 5.87

indicate a substantially weaker bow shock in the elliptical injection flowfield than in case C1A as inferred by its slope. This observation was also made from both the end and side view images presented in §5.3.1 and §5.3.2. The ensemble of images obtained here for case E1A indicates that the bow shock intersects the upper edge of the image at streamwise positions between $-0.25 \leq x/d_{\text{eff}} \leq 0$. Therefore, in addition to being weaker than the wave in case C1A, the bow shock formed in the elliptical injection flowfield appears to fluctuate over a smaller spatial range.

As in case C1A, the ensemble of images from case E1A allows the extent of the separation shock upstream of the injector to be defined. The upstream extent, found where the separation shock intersects the bottom of the image, falls between $-2.75 \leq x/d_{\text{eff}} \leq -1.75$, while the point of intersection of the bow and separation shocks is between 1.1 and 2.1 effective diameters above the bottom wall. These values are significantly lower than those obtained from case C1A indicating that the area beneath the separation shock associated with the elliptical injector is smaller than in circular injection at the spanwise centerline of the jet/crossflow interaction.

Structural activity at the interface between the jet and freestream fluids appears very dynamic in the images shown in Fig. 5.87. Large-scale eddies rapidly develop and grow as the injectant fluid bends toward the downstream direction. These eddies appear smaller and more periodically spaced than in the images of case C1A presented in Fig. 5.86. Clear visualizations of the tightly wound eddies are shown in several of the six images from case E1A. For example, the first image shows a large structure centered at about two effective diameters above the bottom wall. This structure demonstrates the entraining ability of these vortices as unseeded injectant fluid wraps the bright freestream fluid around and into its core. Small-scale eddies are very common throughout the images both within the braiding regions between pairs of large structures and around the periphery of the individual large-scale vortices. Close examination of the third image in Fig. 5.87 shows the birth of a small eddy at an elevation of roughly 0.9 effective diameters above the bottom wall. As in Fig. 5.86 from case C1A, the predominant direction of vortex roll-up is into the freestream fluid such that the vorticity of the eddies at the spanwise centerline of the jet is oriented out of the page (i.e., in the + z-direction). Finally, the intermediate gray levels found

within the interfacial region indicate significant near-field mixing as in case C1A. Thus, as in the circular injection flowfield, large-scale vortices appear to be key components in the near-field mixing that occurs in case E1A, since they actively entrain freestream fluid into the jet and strain the interface leading to molecular diffusion. However, the weaker bow shock and smaller area beneath the separation shock upstream of the elliptical injector would make this geometry a better alternative to transverse injection through a circular nozzle if the mixing characteristics are equivalent. More quantitative information regarding such issues is presented in the results of the probe-based measurements given in a later section.

5.3.3.2 Ensemble-Averaged and Standard Deviation Results

Applying Eq. 5.3 to the image ensembles obtained for the bow shock/jet boundary interaction studies of cases C1A and E1A yields the two images shown in Figs. 5.88 and 5.89, respectively. The gray scale palette for these two images is the same as that for the instantaneous images of Figs. 5.86 and 5.87 where seeded freestream appears light and unseeded injectant appears dark. These images are rather vague in terms of their ability to produce specific information about the region below the separation shock upstream of the jet due to the small intensity gradient between the approaching freestream fluid and the fluid within this region. However, they do illustrate the average characteristics of the bow shock, including its standoff distance and its intersection with the upper edge of the image. These images also reveal the intensity decay through the upper edge mixing layer in each case, which is indicative of the mixing that occurs between the jet and freestream fluids.

Figure 5.88 shows the average bow shock standoff distance to be approximately $0.5d_{eff}$ upstream of the nozzle leading edge in the flowfield of case C1A. It also indicates that the shock intersects the upper edge of the image at roughly $x/d_{eff} = -0.25$. The corresponding locations found in Fig. 5.89 for case E1A are $x/d_{eff} \approx -0.25$ for the standoff distance and $x/d_{eff} = 0$ for the intersection of the bow shock with the upper edge of the image. These observations are consistent with the ranges of shock motion obtained from the ensemble of instantaneous shots discussed in

§5.3.3.1. Thus, as expected from the previous results, the bow shock in the elliptical injection flowfield is appreciably weaker than the one created by injection through a circular nozzle.

Transverse mean intensity profiles taken from the streamwise centerline of each injector (i.e., $x/d_{\text{eff}} = 0$) appear in Fig. 5.90. These profiles provide a better comparison of the two jets than afforded by visual analysis of the images shown in Figs. 5.88 and 5.89. Because of the limited vertical field of view, the region of freestream fluid available for normalization occurs directly behind the bow shock and therefore suffers from higher than normal signal levels due to the increased particle number density. For this reason, only raw intensity levels are presented in the profiles. In Fig. 5.90, circular symbols indicate the circular injector geometry (case C1A) while squares represent the intensity values from the elliptical geometry (case E1A). Each profile illustrates the behavior of the upper edge mixing layer. The profiles clearly indicate that the shear layer in the circular injection flowfield is slightly thicker by this streamwise position than the one in the elliptical injection flowfield. This was observed in the material presented in §5.3.2.2 also. Apparently, the eddies that form at the spanwise centerline of the upper edge mixing layer in case E1A are smaller than those formed in case C1A.

Images showing the standard deviation results of cases C1A and E1A appear in Figs. 5.91 and 5.92, respectively. As in previous standard deviation images, regions appearing dark indicate fluid with relatively small fluctuations while light regions highlight the areas containing fluctuating fluid. These images show the near-field mixing layer development along with the bow shock oscillation and slight indications of the separation shock. Direct comparison of the two images reveals that the mixing layer in the circular injection case (Fig. 5.91) does appear to be wider than the corresponding feature in case E1A shown in Fig 5.92. The position of the bow shock fluctuates about a relatively wide spatial region in case C1A compared to the elliptical injection case as observed in the ensembles of instantaneous images. These observations suggest further that the large-scale eddies formed in the elliptical injection flowfield are smaller than those from case C1A in the very near-field of the jet/crossflow interaction. Finally, the regions beneath the separation shocks ahead of the injectors are quite different in size, although the actual extents of these regions

are difficult to discern in the images shown in Figs. 5.91 and 5.92. The fluctuations in the separation shock position are not very intense in either flowfield. Also, as observed in the instantaneous images, the density gradients across the separation waves are not nearly as strong as across the bow waves, making them fainter, and the turbulent boundary layer fluid present in several shots clouds the images somewhat.

Intensity profiles taken from the streamwise centerline (i.e., $x/d_{\text{eff}} = 0$) of each standard deviation image are presented in Fig. 5.93. These profiles provide a more quantitative look at the mixing layer formed between the jet and freestream fluids. As with the profiles of Fig. 5.90, these contain raw intensity values rather than normalized standard deviations due to the lack of a large undisturbed freestream region behind the bow shock. Immediately apparent from the plot is that the upper edge shear layer formed in the circular injection case is markedly wider than in case E1A. This provides strong evidence that the large-scale eddies formed in the elliptical injector flowfield are smaller than those that develop in the circular case at the spanwise centerline of the interaction. Another noteworthy observation in this plot is that the peak intensity fluctuations in the two shear layers occur at roughly the same transverse position. Also, the peak standard deviation in case C1A is slightly higher than in the elliptical flowfield at this particular streamwise position, indicating that the flowfield created in case C1A fluctuates more severely than in case E1A.

5.3.4 Double-Pulsed Side View Images

The side view images presented in §5.3.2 and §5.3.3 provide convincing evidence for the existence of large-scale eddies in the mixing layer that forms at the interface between the freestream and injectant fluids. These eddies appear to significantly influence the entrainment and mixing characteristics in the near-field region of the jet/freestream interaction. The spatial correlation results presented in §5.3.2.4 indicated some substantial differences between the eddies that form in the four cases studied in this investigation. The convective Mach numbers that arise for the two injectant gases used seem to have a significant effect on the size, shape, and angular orientation of the structures, while the injector geometry affects these features to a lesser extent. Temporally

correlated image pairs should provide more information regarding the development of the large-scale vortices within the upper edge mixing layers of the four cases examined here, including the convection velocities and convection angles of these dominant near-field structures.

To obtain these results, the optical and electronic arrangements shown in Figs. 4.8-4.10 were used to capture two images of the same region within the flowfield at fixed temporal separations. Pixel dimensions in the images were roughly $(\Delta x, \Delta y, \Delta z) = (66.8 \mu\text{m}, 66.8 \mu\text{m}, 200 \mu\text{m})$. Each side view image displayed in this section covers roughly 5.2 effective diameters (33.0 mm) in the streamwise direction and 4.0 effective diameters (25.4 mm) in the transverse direction. The freestream flow direction is from left to right while the injectant flow enters the field of view from the lower edge of the picture. Gray levels in these images were assigned using the same convention as in the images presented in §5.3.3 so that the jet fluid appears dark while seeded freestream fluid appears light. Ensembles of 20 image pairs were acquired for all four cases (C1A, C2H, E1A, and E2H) with the laser sheets positioned at the spanwise centerline of the jet (i.e., $z/d_{\text{eff}} = 0$). Temporal separations were set at 2 μs in cases C1A and E1A, and 1.0 μs and 1.2 μs in cases C2H and E2H, respectively.

The two cameras used in this experimental arrangement produced images with significantly different signal-to-noise ratios making mathematical manipulation of the data using a cross-correlation technique entirely inconclusive. Thus, these images were analyzed manually such that individual structures were tracked from one shot to the next and their positions in the streamwise and transverse directions (i.e., x_1, y_1, x_2 , and y_2 from images #1 and #2, respectively) were determined. In this tracking procedure, the position of the center of a particular feature was identified in each image. Once known, these positions yield the structure's displacement between images from

$$\Delta r = \sqrt{(x_2 - x_1)^2 + (y_2 - y_1)^2}, \quad (5.15)$$

and, for a known laser sheet time separation Δt , the convection velocity of the large-scale eddy is determined using

$$U_c = \frac{\Delta r}{\Delta t}. \quad (5.16)$$

Note that Eqs. 5.15 and 5.16 assume that the eddy moves only in the plane of the laser sheet for a given temporal separation. The convection angle ϕ associated with this velocity magnitude may be computed from the following trigonometric relation.

$$\phi = \arctan\left(\frac{y_2 - y_1}{x_2 - x_1}\right) \quad (5.17)$$

Figure 5.94 provides a schematic that illustrates these quantities and the general method for obtaining them from the images. Analyzing the images in this way produces some subjectivity concerning the pixel location of a given structure in the two images. It is estimated that the error involved in measuring the structural displacements in the two coordinate directions was ± 1 pixel. This leads to potential errors in the reported values of U_c and ϕ . All of the results presented below that were computed from the images are qualified with error bars that represent this measurement uncertainty. The sections that follow present instantaneous image pairs obtained from the four injection cases and then the results of the convection velocity analysis.

5.3.4.1 Instantaneous Image Pairs

Select instantaneous image pairs from the four cases studied here appear in Figs. 5.95-5.98. A grid has been superimposed on the individual images so that structural movement from the first image to the second image is more easily identified. The problems associated with the two different cameras are readily apparent in all of the image pairs presented. The right hand images exhibit relatively poor definition in the very near-field of the injector exit, though structures in the downstream portion of these images are clearer. Figure 5.95 shows an image pair from case C1A, where a time delay of $2 \mu\text{s}$ was used. Three structures present in the first image are visible in the second image. These are located near $x/d_{\text{eff}} = 1.75, 2.5$, and 3.0 in the first image. Notice how, even after only $2 \mu\text{s}$, the structure positioned near $x/d_{\text{eff}} = 3.0$ has moved downstream and rotated somewhat. The interfacial structure in the images of case C2H, shown in Fig. 5.96, is somewhat

clearer than that of case C1A. In this case, a time delay of $1\ \mu\text{s}$ was used. The smaller eddies that dominate the interface are all easily tracked from one image to the next allowing several convection velocity measurements to be made from one image pair.

Image pairs obtained from the elliptical nozzle appear in Figs. 5.97 and 5.98. The first figure shows two images from case E1A with a laser sheet time delay of $2\ \mu\text{s}$. These images have three well-defined large-scale eddies positioned at the jet interface. Again, distinct movement of the structures can be observed so that the temporal displacement can be easily computed. Finally, images from case E2H appear in Fig. 5.98. Here, a time delay of $1.2\ \mu\text{s}$ was used and the resulting images again clearly show both interfacial structure and displacement.

5.3.4.2 Large-Scale Convection Velocity Measurements

The ensembles of image pairs have been analyzed using the methodology and expressions discussed above and shown in Fig. 5.94. This procedure results in measurements of large-scale convection velocity (U_c) and structure convection angle (ϕ) for approximately 30 instantaneous eddies in each case. It should be emphasized that these measurements are instantaneous in nature (i.e., not ensemble-averaged); thus, scatter in the data is expected although general trends may be observed. Both of these quantities are functions of the streamwise and transverse positions of the individual structure; however, the results that follow are only plotted against the streamwise coordinate. This gives some indication of the behavior of the interfacial eddies as the jet is turned downstream. Again recall that these results assume that the large-scale eddies only move in the plane of the laser sheets (i.e., $z/d_{\text{eff}} = 0$) for the given time interval.

Figures 5.99 and 5.100 present the results of analyzing the image pairs of case C1A. Large-scale convection velocities appear in Fig. 5.99. This plot contains two velocity reference lines that indicate the crossflow air velocity ($u_\infty = 516\ \text{m/s}$) and the velocity of the air jet at its exit ($u_{e,j} = 317\ \text{m/s}$). Also note that error bars are included on all of the measured values of U_c . In this case, the ± 1 pixel uncertainty in the structure's position translates into a measurement uncertainty of $\pm 47\ \text{m/s}$. Initially, near $x/d_{\text{eff}} = 0$, the eddies that form at the jet/freestream interface convect

with velocities that are larger than the exit velocity of the jet. This phenomenon results from the fact that the jet is underexpanded and, as it expands out of the nozzle, the velocity of the jet fluid increases. As the jet turns toward the downstream direction, the convection velocities of the structures generally increase toward the freestream velocity. Several eddies, however, move with velocities close to the jet exit velocity downstream of $x/d_{\text{eff}} = 1$. Results of applying Eq. 5.17 to the eddy position measurements are presented in Fig. 5.100. In this plot, the crossflow direction is represented using a solid line at $\phi = 0^\circ$. The circles that indicate the actual measured convection angles are bounded by horizontal error bars above and below that correspond to the ± 1 pixel accuracy of the measurements. As the air jet exits the circular nozzle, the structural convection angle is relatively high as evidenced by the values plotted near $x/d_{\text{eff}} = 0$. This is expected since the jet's momentum is originally perpendicular to the flow direction of the approaching freestream. With increasing streamwise position, the eddies begin to move at shallower angles to the crossflow direction. By the farthest downstream measurement station, however, the structure convection angles generally remain greater than zero suggesting that the transverse penetration of the jet fluid is still increasing. This is consistent with the ensemble-averaged end view results of §5.3.1.2 and the ensemble-averaged single-shot side view results presented in §5.3.2.2 that indicated transverse penetration increasing until roughly eight effective diameters downstream of the injector exit.

Circular injection of helium (case C2H) results in significantly different trends regarding the convection velocities of the large-scale vortices. Figure 5.101 presents the convection velocity measurements from within this flowfield. Note the two reference lines on the plot that are the crossflow air velocity ($u_\infty = 515$ m/s) and the jet exit velocity ($u_{e,j} = 882$ m/s). In this case, the jet exit velocity is larger than the approaching freestream velocity as opposed to case C1A where the opposite was true. The error bars in this plot are twice as wide (± 95 m/s) as in Fig. 5.99 since the temporal separation of the laser sheet is only $1.0 \mu\text{s}$. Clearly, as the helium jet exits the circular nozzle, the large-scale eddies formed in the upper edge shear layer move markedly faster than the jet exit velocity. Comparing the performance of the two injectant gases in the very near-field of the jet/crossflow interaction ($x/d_{\text{eff}} \leq 2$) shows that the eddies in case C2H move roughly three times

faster than those from case C1A. This observation provides further evidence of the effects of the large value of convective Mach number ($M_c \approx 1.9$) for this case. The data in Fig. 5.101 suggest a local maximum in U_c occurring near $x/d_{eff} = 1.0$, downstream of which the convection velocity rapidly relaxes toward the freestream velocity. The plot of structure convection angles in Fig. 5.102 for case C2H closely resembles Fig. 5.100 for case C1A in that the data show relatively large angles as the jet enters the freestream fluid, and these angles rapidly decrease in the streamwise direction becoming more parallel to the crossflow.

Figures 5.103 and 5.104 illustrate the results obtained from analyzing the image pairs from case E1A. The convection velocity data presented in Fig. 5.103 show the eddies rapidly reaching the crossflow velocity. Compared to Fig. 5.99 for case C1A, the near-field results in Fig. 5.103 suggest a quicker acceleration up to the freestream velocity. However, as the flow develops farther downstream, the two cases behave very similarly in that each produces large-scale convection velocity magnitudes that hover around the velocity of the freestream. Examining the structure convection angles presented in Fig. 5.104 shows that the large-scale eddies move more shallowly with respect to the freestream fluid in the near-injector region than in case C1A (see Fig. 5.100). This observation provides additional support for the reduced transverse penetration characteristic of the elliptical injector as found in the analysis of the ensemble-averaged end view images (§5.3.1.2) and the ensemble-averaged side view images (§5.3.2.2). The angles plotted in Fig. 5.104 decay as expected toward the freestream flow direction ($\phi = 0^\circ$) with increasing streamwise distance from the injector exit. It is suspected that the axis-switching phenomenon present in the elliptical injector flowfield causes the observed differences in the behavior of U_c and ϕ in the near-field regions of cases C1A and E1A. This phenomenon, caused by the asymmetric distribution of momentum thickness around the elliptical nozzle exit,⁷⁴ results in faster spreading in the minor axis plane than in the major axis plane (see the results shown in Fig. 5.33). Another potential contributor to the observed differences in behavior of the convection velocity and convection angle results for the circular and elliptical injectors is the weaker bow shock present in the elliptical injector flowfield. The bow shock strength directly affects the velocity distribution of the freestream fluid behind it.

In addition, this fluid is one of the streams involved in the formation of the mixing layer at the upper edge of the jet fluid. Since the convection characteristics of the large-scale eddies that form within the mixing layer are highly sensitive to the velocities of either stream involved in its development,^{144,145} the differences in shock strength could result in the observed differences in U_c and ϕ between circular and elliptical injection.

Results from case E2H appear in Figs. 5.105 and 5.106. The very near-field of this injection case contains eddies that convect with velocities between the jet exit velocity and the freestream velocity as in case E1A. As the eddies move downstream, their convection velocities begin to taper off toward the freestream velocity, though several of the instantaneous structures analyzed have measured values of U_c both higher and lower than u_∞ . The near-field behavior in this case is substantially different from that observed in case C2H (Fig. 5.101) where the shear layer vortices moved much faster than the jet exit velocity. This difference is again thought to be caused by the axis-switching phenomenon associated with the elliptical nozzle geometry. Apparently, the momentum thickness asymmetry that leads to axis-switching also affects the development of the vortices in the mixing layer that forms at the jet/freestream interface. It is also possible that the weaker bow shock formed in the elliptical injection flowfield plays a role in the significantly different near-field convection velocity characteristics of the large-scale eddies. The structure convection angles presented in Fig. 5.106 appear very similar to those from case E1A that were shown in Fig. 5.104. The near-injector region contains relatively shallow convection angles compared to case C2H while the angles gradually tend toward the freestream flow direction as expected. The non-zero angles found by four effective diameters downstream of the injector exit are consistent with the other double-pulsed data and with the results of both the ensemble-averaged end view and single-shot side view images that indicate increasing transverse penetration at this streamwise position.

5.4 Pitot and Concentration Probe Measurements

Probe-based measurement techniques permit the collection of important information regarding the time-averaged pressure losses and mixing characteristics present in transverse injection flowfields. Results from these measurements appear in this section for circular and elliptical injection of helium (cases C2H and E2H). Pitot probe measurements from two streamwise planes ($x/d_{\text{eff}} = 4$ and 10) are discussed first followed by helium mole and mass fraction results obtained using the concentration probe and reduction procedure described in §4.4.2 and §4.4.3. Data were obtained from each probe at discrete points in the two measurement planes. In the upstream plane, 441 locations were sampled at increments of 0.4 effective diameters from $z/d_{\text{eff}} = -4$ to 4 and $y/d_{\text{eff}} = 0.25$ to 8.25 . The downstream plane was sampled more sparsely at increments of 0.8 effective diameters over the same spatial area. Figure 5.107 shows the discrete measurement locations. At each streamwise measurement location, 1000 samples of data were obtained from each traversing probe along with 1000 samples of data yielding time-averaged measurements of the operating parameters $p_{0,\infty}$, $p_{e,j}$, $T_{0,\infty}$, and $T_{0,j}$. Two-dimensional arrays of these values permit the generation of contour plots using software running on a Power Macintosh computer. The pitot pressure measurements provide comparisons between the two injection geometries in terms of total pressure loss. Concentration measurements produce information regarding the time-averaged mixing characteristics of the two injection flowfields. Together, these measurements give excellent quantitative information regarding two critical performance characteristics associated with injection of fuel into a supersonic stream.

5.4.1 Pitot Probe Results

Figure 5.108 presents the pitot probe results from both streamwise planes for circular injection using helium (case C2H). Each plot in this figure shows contours of normalized pitot pressure, $\Pi_{2,\infty}$, defined as

$$\Pi_{2,\infty} = \frac{p_{0,2}}{p_{0,\infty}}. \quad (5.18)$$

In this expression, the total pressure measured by the probe ($p_{o,2}$, the stagnation pressure behind the normal shock that stands upstream of the probe) is normalized by the freestream total pressure measured in the settling chamber, $p_{o,\infty}$. Both contour plots presented appear very symmetrical about the spanwise centerline of the flow (i.e., $z/d_{\text{eff}} = 0$); recall from Fig. 5.107 that the measurements spanned the entire region and were not merely “mirrored” about the jet centerline. Contours in the upper portion of the plot in Fig. 5.108a indicate the presence of the bow shock formed upstream of the injector. The normalized pitot pressure increases from levels near 0.73 in the region above the upper 0.80 contour to a peak of approximately 0.88 between the two 0.80 contour lines. For the freestream Mach number of 1.98, the normalized pitot pressure would theoretically have a value of 0.73 in an undisturbed region of the flow. This ratio is easily computed using the normal shock relation given by

$$\frac{p_{o,2}}{p_{o,1}} = \left[\frac{\frac{\gamma+1}{2} M_1^2}{1 + \frac{\gamma-1}{2} M_1^2} \right]^{\frac{\gamma}{\gamma-1}} \left[\frac{2\gamma M_1^2 - (\gamma-1)}{\gamma+1} \right]^{\frac{1}{1-\gamma}} \quad (5.19)$$

where $p_{o,2}/p_{o,1}$ is the total pressure ratio across a normal shock at a Mach number of M_1 . Thus, the region above the upper 0.80 contour contains essentially undisturbed freestream fluid. Clearly, the lowest measured pitot pressures occur in the vicinity of the helium jet. The central region of the jet has levels of $\Pi_{2,\infty}$ below 0.20 with a minimum value of approximately $\Pi_{2,\infty} = 0.14$. Contours near the center of the jet have shapes suggesting the presence of the counter-rotating vortex pair that forms in the jet fluid, and the total pressure ratio increases quickly into the surrounding freestream fluid that has passed through the bow shock. Results from the downstream plane (i.e., $x/d_{\text{eff}} = 10$) appear in Fig. 5.108b. Here, the normalized pitot pressures within the jet region have increased somewhat with the minimum value of roughly $\Pi_{2,\infty} = 0.30$. Compared to the upstream plot of Fig. 5.108a, all of the contours have moved outward toward the freestream by this streamwise position.

The results obtained from the elliptical injection flowfield using helium (case E2H) are presented in Fig. 5.109. In the upstream contour plot (Fig. 5.109a), the bow shock is again present in the upper region of the measurements and the normalized pitot pressures in the central jet region of this case are higher than in case C2H. The minimum value found in Fig. 5.109a is approximately $\Pi_{2,\infty} = 0.20$ compared to 0.14 from Fig. 5.108a for circular injection of helium. This represents an increase of over 40% and provides quantitative evidence that the pressure losses associated with the elliptical injection flowfield are smaller near the core of the jet than in circular injection. Other notable differences between the results from the two injector geometries are the spanwise and transverse extents of the various contours. For instance, the 50% contour in Fig. 5.108a from case C2H extends from about $-1.75 \leq z/d_{\text{eff}} \leq 1.75$. It also extends upward to nearly 2.75 effective diameters. The same contour line in the elliptical injection flowfield is slightly wider (from $-1.90 \leq z/d_{\text{eff}} \leq 1.90$) and shallower (up to $y/d_{\text{eff}} \approx 2.6$). Thus, relatively low total pressure regions extend farther out in the spanwise direction while relatively high total pressures exist above the jet in the near-field region of case E2H. Results from the downstream plane, shown in Fig. 5.109b, indicate that the normalized pitot pressure levels increase from those obtained upstream. Here, the minimum value of $\Pi_{2,\infty}$ within the central jet region is found to be roughly 0.32. However, the 50% contour in this plot is again wider than the corresponding one in Fig. 5.108b for circular injection by about 7%. The transverse extent of the 50% contour in Fig. 5.109b is essentially equal to that of the same contour in Fig. 5.108b. Apparently, the elliptical injector causes a stronger disturbance to the freestream in the spanwise direction than the circular injector does due to its enhanced lateral spreading. This is another piece of evidence supporting the axis-switching phenomenon that was first observed in the images presented earlier. Aside from the wider character of the profiles in Fig. 5.109b, the data from circular and elliptical injection at $x/d_{\text{eff}} = 10$ are very similar.

To better compare the performance characteristics of the two nozzles, the ratio of the measured pressure distributions from the two injectors is examined. Equation 5.20 is used to generate contours of the pitot pressure ratio Π_{ce} .

$$\Pi_{ce} = \frac{(\Pi_{2,\infty})_c}{(\Pi_{2,\infty})_e} = \frac{(p_{o,2}/p_{o,\infty})_c}{(p_{o,2}/p_{o,\infty})_e} \quad (5.20)$$

Regions in the measurement domain having values of Π_{ce} greater than unity indicate locations where the pitot pressure in the circular injection flowfield is higher than in the elliptical injection flowfield, while regions having values of Π_{ce} less than unity imply relatively high pitot pressures in case E2H. Contours of this ratio appear in Fig. 5.110 for both streamwise measurement planes. In these plots, contours of Π_{ce} less than unity appear as dashed lines while contours of Π_{ce} greater than unity are indicated with solid lines. Examination of the upstream results in Fig. 5.110a reveals some interesting observations. Total pressures in the central jet region are substantially lower in the circular injection flowfield than in case E2H. The contours from this region of the flow ($-1 \leq z/d_{eff} \leq 1$ and $0.25 \leq y/d_{eff} \leq 2.25$) distinctly show the two cores of the circular jet. Inside these contour lines, minimum values of Π_{ce} approximately equal to 0.50 appear. These elevated pitot pressures in the core of the elliptical jet may suggest a weaker Mach disk (i.e., that the elliptical jet accelerates to smaller Mach numbers within the barrel shock region). Two smaller regions located outside the central jet take values of Π_{ce} greater than unity. These zones essentially correspond to the regions just above and outside the helium cores of the elliptical injection flowfield. In these regions, the normalized pitot pressures in case C2H are higher than those from case E2H by between 10-50%. Again, the existence of these regions may be related to the behavior of the Mach disks generated in these two injection flowfields. Finally, relatively high values of Π_{ce} also occur near the injector wall due to the rapid lateral spread and suppressed transverse penetration of the elliptical jet.

Differences between the two measured pitot pressure fields are much smaller in magnitude at the downstream measurement plane. Figure 5.110b shows the results of applying Eq. 5.20 to the normalized circular and elliptical pitot pressure data at $x/d_{eff} = 10$. Here, the central region of the elliptical jet continues to show higher total pressure levels than the circular jet. Note that the minimum value of Π_{ce} is about 0.86 compared to roughly 0.50 in the upstream plane. Two wide bands formed beneath the central jet region contain values of Π_{ce} greater than unity. The maximum

level within these bands is about $\Pi_{ce} = 1.16$. From examinations of the pressure ratio contours presented above, it seems that the elliptical injector provides slightly better performance, in terms of higher pitot pressure, than the circular injector in the near-field of the jet/crossflow interaction. By ten effective diameters downstream, however, the two pressure fields have become nearly equivalent with some slight differences arising due to the enhanced lateral spread associated with case E2H.

An area-averaged total pressure provides another method for comparing the performance of these two injection cases. Fuller, et al.⁹⁸ used probes to measure pitot pressure, injectant concentration, cone-static pressure, and total temperature in their study of oblique injection into supersonic crossflows. These data were combined using various gas dynamic relations to yield the density, velocity, and total pressure fields (among others). Then, a total pressure parameter, defined as

$$p_{tp} = \frac{\int_A \rho u p_o dA}{\int_A \rho_\infty u_\infty p_{o,\infty} dA + \rho_j u_j p_{o,j} A_j}, \quad (5.21)$$

was used to quantify the total pressure loss. Application of Eq. 5.21 in this investigation is impossible because the local density, velocity, and total pressure fields are not known (see numerator of Eq. 5.21). However, this fact does not preclude the use of a global parameter that provides a comparison of the two injection cases. Three such parameters were defined using the pitot pressure data that were available; these definitions are listed in Eqs. 5.22-5.24.

$$\overline{p_{o_a}} = \frac{1}{A} \int_A \Pi_{2,\infty} dA \quad (5.22)$$

$$\overline{p_{o_b}} = \frac{1}{p_{o,2,\infty} \cdot A} \int_A p_{o,2} dA \quad (5.23)$$

$$\overline{p_{o_c}} = \frac{1}{A_j} \int_{A_j} \Pi_{2,\infty} dA \quad (5.24)$$

The first area-averaged total pressure, $\overline{p_{o_a}}$, is computed using the entire measurement domain. This can lead to significantly biased results when the region of measurement within the jet is small compared to that in the freestream. The second parameter, $\overline{p_{o_b}}$, uses a theoretical value of the pitot pressure from the freestream (i.e., the results of applying Eq. 5.19 to the undisturbed freestream flow) to provide the normalization and both numerator and denominator are integrated over the entire measurement area. Finally, the third total pressure parameter, $\overline{p_{o_c}}$, relies on a predetermined area enclosing the jet region such as the area A_{90} computed from the ensemble-averaged end view images discussed in §5.3.1.2. Applying each of these expressions to the pitot pressure data obtained from the two measurement planes in each injection case results in the values presented in Table 5.4. From these results, it is easily seen that there are at most very small differences between the various area-averaged total pressure data computed for the circular and elliptical injection cases (C2H and E2H) at $x/d_{eff} = 4$ and 10. Equations 5.22 ($\overline{p_{o_a}}$) and 5.23 ($\overline{p_{o_b}}$) predict that the elliptical jet has slightly higher values of these total pressure quantities in the near-field region than the circular jet, while downstream, no differences are observed. Equation 5.24 results in equal values of $\overline{p_{o_c}}$ for circular and elliptical injection at both measurement stations. Thus, at most, the elliptical injector provides slightly better (~1%) performance than the circular injector at $x/d_{eff} = 4$.

5.4.2 Concentration Probe Results

The concentration probe provides measurements of the helium mole and mass fractions within the jet/crossflow interaction at the same two streamwise planes as the pitot probe measurements (i.e., $x/d_{eff} = 4$ and 10). Anemometer response voltage, sampling pressure, and sampling temperature provide the input data for calculation of the helium molar concentration using the calibration curves shown in Fig. 4.18. The data reduction code also computes the helium mass fraction from a two-species mass balance as

$$y_{He} = \frac{x_{He}\mathcal{M}_{He}}{x_{He}\mathcal{M}_{He} + (1 - x_{He})\mathcal{M}_{Air}} \quad (5.25)$$

where \mathcal{M}_{He} and \mathcal{M}_{Air} are species molecular weights and x_{He} and y_{He} are helium mole and mass fractions, respectively. Contours of these mixture fractions yield information concerning the time-averaged distribution of helium across the mixing zone.

Figure 5.111 presents helium mole fraction contours from both streamwise planes for case C2H. Contour levels marked on the curves appear in the key at the right side of each plot. Also included in this key is the maximum mole fraction encountered in the particular array of data. A slight asymmetry appears in the upstream contour plot from this case (Fig. 5.111a). This is consistent with the results from the end view imaging experiments where a slight asymmetric nature existed in all of the statistical results presented. Despite this observation, the contours are generally very symmetric about the spanwise centerline of the flowfield. Examining the 10% mole fraction contour for its extent into the freestream reveals very comparable values to those obtained from the ensemble-averaged end view images. The probe data indicate a lateral spread of approximately 4.5 effective diameters and a transverse penetration of about 4.4 effective diameters. Recall that the results of §5.3.1.2 showed corresponding values of $z/d_{\text{eff}} = 4.6$ and $y/d_{\text{eff}} = 4.4$ obtained from the 90% penetration contour (see Figs. 5.30 and 5.31). Further, the kidney-shaped region in the center of the jet indicates the presence of the counter-rotating vortex pair. The centers of these vortices contain the peak helium concentration levels in the plot; values of 98% and 91% helium in air are found within the cores positioned at $z/d_{\text{eff}} = -0.75$ and 0.75 , respectively. The downstream location (Fig. 5.111b) shows essentially no increase in the transverse penetration and only marginal increases in the lateral spread of the 10% contour. However, appreciable mixing between the freestream and injectant has occurred as indicated by both the reduced maximum mole fraction (here $x_{\text{He, max}} = 0.71$) and the reduced mole fraction levels throughout the mixing region. It should also be noted that these contours exhibit an even higher degree of spanwise symmetry than those from the upstream position.

Results from the elliptical injection flowfield (case E2H) presented in Fig. 5.112 show several differences compared to the mole fractions measured in case C2H. In the upstream contour plot (Fig. 5.112a), the mixing region appears shallower and wider than in Fig. 5.111a. The 10%

contour indicates a lateral spread of approximately $z/d_{\text{eff}} = 5$ and a transverse penetration of about $y/d_{\text{eff}} = 3.8$. As with the results presented above from case C2H, these values compare very closely to those obtained from the ensemble-averaged end view images shown in Figs. 5.30 and 5.31. Mixing appears to occur slightly faster in the elliptical flowfield in the region between the two counter-rotating vortices that form within the jet fluid. Here, the 70% contour elevates into the relatively wide void region at the center of the jet. The maximum injectant mole fraction found within the jet region of Fig. 5.112a is about 98%. This is the same level observed in the flowfield created by injecting helium through the circular nozzle. The downstream results of Fig. 5.112b indicate that the elliptical jet remains wider than the circular jet. These contours also indicate an increase in transverse penetration of the elliptical jet as compared to those from the upstream location. Both of these observations are consistent with the imaging results presented earlier (see Figs. 5.30 and 5.31). The 50% contour in this plot encloses a smaller area (by about 13%) than the same contour in Fig. 5.111b for case C2H and the maximum injectant mole fraction is again about $x_{\text{He, max}} = 0.71$. Apparently, the wider spacing of the counter-rotating vortices in the elliptical injection flowfield allows more freestream entrainment and faster mixing between the injectant and crossflow fluids in the central region of the jet than in circular injection. However, the region between the jet core and the injector wall contains higher mole fractions in the downstream plot from case E2H. The reduced transverse penetration in the elliptical injection flowfield likely inhibits crossflow fluid from entering the near-wall region.

Figure 5.113 presents the results of using Eq. 5.25 to compute the helium mass fractions from the mole fraction data of case C2H. As with the mole fraction contours, the contour levels marked on the curves appear in the key at the right side of each plot. Also included in this key is the maximum mass fraction encountered in the particular array of data. Qualitatively, the contours in Fig. 5.113 show the same features as the mole fraction contours presented in Fig. 5.111. Evidence of the counter-rotating vortices are apparent and the mass fraction levels within their cores are higher than anywhere else in the jet region. The maximum mass fraction found in the upstream measurement plane (i.e., $x/d_{\text{eff}} = 4$) is about $y_{\text{He, max}} = 0.86$ and corresponds to the

central core located to the right of the spanwise centerline. As the measurement plane moves downstream to $x/d_{eff} = 10$, the measured helium mass fractions decrease dramatically (Fig. 5.113b). By this location, the maximum injectant mass fraction within the jet core region is about $y_{He, max} = 0.25$.

Mass fraction results obtained from the elliptical injection case are again significantly different from those of case C2H, as was the case with the mole fraction data. Figure 5.114 presents the contour plots from the upstream and downstream locations where the same mass fraction levels as in the circular case are shown. Globally, the plot in Fig. 5.114a is very similar to both the ensemble-averaged end view images and the time-averaged mole fraction results presented earlier. The jet region is wider and shallower than in the circular injection case. The two counter-rotating vortices are very dominant and appear to be more coherent than those from case C2H. That is, the contours are tightly spaced around the central cores that contain the maximum mass fractions in this plot, indicating stronger concentration gradients in the radial direction out toward the jet boundary. However, faster mixing is suggested in the void region between the two cores as freestream fluid wraps upward. In Fig. 5.114a, two 32% contours appear, rather than the one shown in Fig. 5.113a from case C2H that envelops both cores and the entire central region of the jet. The maximum mass fraction computed at this streamwise plane is about $y_{He, max} = 0.87$. Figure 5.114b shows the results from the downstream measurement plane (i.e., $x/d_{eff} = 10$). Here, the maximum injectant mass fraction has decayed to the same level as was found in case C2H (i.e., $y_{He, max} = 0.25$). The contours again suggest faster mixing between the freestream and injectant fluids in the central region of the jet compared to Fig. 5.113b from case C2H. Evidence of this is contour number 4 (14% mass fraction) that encloses a smaller area of high values of y_{He} . As was noted in the mole fraction results presented above, mixing in the region between the jet core and the injector wall appears relatively slow in case E2H as suggested by the relatively high mass fractions found in comparison to Fig. 5.113b. This is likely caused by the reduced transverse penetration of the elliptical jet.

The concentration results presented suggest that the two injector geometries provide slightly different mixing characteristics. In order to quantify these differences further, area-averaged mole and mass fractions are computed from the arrays of concentration data using

$$\overline{x_{He}} = \frac{1}{A_j} \int_{A_j} x_{He} dA \quad (5.26)$$

and

$$\overline{y_{He}} = \frac{1}{A_j} \int_{A_j} y_{He} dA \quad (5.27)$$

where the area of integration is defined as that inside the 10% mole fraction contour. This corresponds to the area enclosed by the end view penetration contours defined in §5.3.1.2. Table 5.5 presents the results of these calculations for both injection cases at each streamwise measurement plane. These tabulated values of the area-averaged concentrations indicate that indeed the two injector geometries lead to slightly different mixing characteristics. At the upstream measurement station (i.e., $x/d_{eff} = 4$), the area-averaged mole fraction from case E2H is about 6% lower than that from case C2H, suggesting that the elliptical nozzle produces slightly better mixing performance in the injector near-field. Similar results are observed for the area-averaged mass fractions from the two cases at this streamwise location although the difference is only about 8%. By ten effective diameters downstream, the two area-averaged mole fractions from cases C2H and E2H have reached the same level of roughly $\overline{x_{He}} = 0.26$. The area-averaged mass fractions at $x/d_{eff} = 10$ are also identical with values of $\overline{y_{He}} = 0.06$.

This concludes the presentation of the various results gathered in this investigation of transverse injection into a supersonic crossflow. The discussion section that follows attempts to bring all of the various observations and results together to produce specific conclusions regarding the global injection flowfield characteristics and the role of the large-scale turbulent structures in the mixing between the injectant and crossflow fluids.

5.5 Discussion

This section presents a summary of the various results from this investigation as they apply to four categories: the shock structure present in the injection flowfields, the transverse penetration and lateral spread of the jet fluid, the large-scale structures formed within the jet fluid and at the jet/freestream interface, and the entrainment and mixing that occur between the injectant and freestream fluids. Each topic draws on the applicable results from the three diagnostic techniques used in these experiments including shadowgraph photos, Rayleigh/Mie scattering images, and probe-based measurements. The material presented in the following sections also appears in tabulated form in Table 5.6.

5.5.1 Shock Structure

As illustrated in Figs. 1.1 and 1.2, the shock structure created by transverse injection of an underexpanded gas into a supersonic crossflow is quite involved. In the present investigation, instantaneous shadowgraph photos and two-dimensional Rayleigh/Mie scattering images capture the various shock waves generated in the flow while the pitot probe measurements provide information about their effects on the flow in terms of total pressure loss.

The bow and separation shock waves were observed in all four cases. Both the shadowgraphs and the Rayleigh/Mie images provide evidence suggesting that the bow shocks created in the elliptical injector flowfields are weaker than those generated in the circular injection cases. Shadowgraphs and side view images show that the region of normal shock behavior near the injector wall at the spanwise centerline of the flow extends farther from the wall in the transverse direction in the circular cases. Both techniques indicate that the region beneath the separation shock formed upstream of the injectors is larger in circular injection cases. Results of the side view images of the bow shock/jet boundary interaction show that this feature extends farther upstream in circular injection by approximately 17% and farther up in the transverse direction by about 38%. End view images from the plane at the streamwise centerline of the injector (i.e., $x/d_{\text{eff}} = 0$) clearly illustrate the cross-sectional shape of the bow shock and its

interaction with the separation shock as the two features wrap around the injector. Once again, these results indicate that the circular injection cases produce stronger bow shocks than the elliptical cases as inferred from their respective transverse extents. In addition to the average bow shock location, slight fluctuations in its position are observed. These positional variations arise due to the intermittent effects associated with the formation and passage of large-scale vortices within the jet/freestream mixing layer. The side view images of the bow shock/jet boundary interaction indicate that the normal shock region near the wall is very susceptible to such effects, but that the mixing layer behavior has less influence on the bow shock at higher transverse positions. Finally, both Rayleigh/Mie images and shadowgraph photos show curved shock waves propagating into the freestream behind the bow shock. These waves, thought to be shocklets emanating from the large-scale eddies formed in the mixing layer, are often strong enough to impart changes in the slope of the bow shock at their point of intersection. They are also more prevalent in injection cases using helium (high compressibility), where the large-scale eddies move supersonically with respect to the freestream fluid and appear to be more bulky and amorphous.

The shock structure within the jet fluid, including the barrel shock and Mach disk, appears only in the shadowgraph photos of the air injection cases. These features are hidden in the helium injection cases due to the spatial integration effects associated with this line-of-sight technique and the large density gradients that occur at the outer edges of the helium jet. No jet shocks are found in the Rayleigh/Mie images since both the helium and air streams are dry and therefore devoid of any scattering media. Shadowgraphs indicate slight differences between the jet shock structure occurring in circular and elliptical injection cases. Apparently, the elongated major axis of the elliptical nozzle results in a barrel shock that orients itself with a steeper angle to the freestream than the same feature in circular injection.

The pitot probe measurements show some interesting differences between the jets issuing from the two injector geometries in the near-field of the jet/freestream interaction. Elliptical injection, by virtue of an apparently weaker Mach disk, results in about 40% higher pitot pressures in the core region of the jet than does circular injection. However, injection through the circular

nozzle yields regions of relatively high pitot pressure just outside this central core. Measurements from farther downstream show the two pitot pressure fields becoming nearly identical with only small variations remaining. Computed values of an area-averaged pitot pressure indicate that the elliptical injection scheme has roughly 1% higher pitot pressure than the circular injection case at the upstream station (i.e., $x/d_{\text{eff}} = 4$), while the two configurations result in essentially equal values farther downstream.

5.5.2 Transverse Penetration and Lateral Spread

Ensemble-averaged end and side view images permit examination of the physical characteristics of the injectant stream in terms of its lateral spread and transverse penetration into the crossflow. Time-averaged mole fraction data obtained from the concentration probe also provide this information at the two streamwise measurement planes investigated in the two helium injection cases. Such information addresses the crucial issue of gaseous fuel dispersal into the freestream in supersonic combustor applications. In a fundamental sense, the lateral spread of a particular injection geometry will also affect the characteristics of the bow shock formed ahead of the injector due to the frontal area of the injectant plume. The lateral spread also influences the freestream flow around the injector plume, the mixing between the injectant and air streams, and, potentially, the vortex development both within the jet fluid and at the jet/freestream interface. In a more practical sense, lateral spreading affects the placement of injector nozzles in a multiple-injector combustor design. Conceivably, interference between two or more jets may prove either beneficial or detrimental to the mixing and pressure loss characteristics of a given design.

The results obtained from analyzing the ensemble-averaged end view images for lateral spread, defined as the maximum width of the 90% normalized intensity contour, show very little effect of injectant gas (i.e., compressibility) in the injector near-field. Injector geometry has much more influence at the value of jet-to-freestream momentum flux ratio used in this investigation. Farther downstream, the lateral spreading trends appear sensitive to the injectant gas due to the different structural characteristics that develop in the helium and air injection flowfields.

Nevertheless, the effects of injector geometry remain most prominent. It was found that the elliptical nozzle produces jets that spread laterally into the crossflow much more than jets issuing from the circular nozzle. When scaled by the physical spanwise dimension of the injector, the elliptical jets show spreading levels that are greater than twice the levels associated with the circular jets. In terms of the effective diameter, the elliptical jet plumes remain up to 25% wider than the circular jet plumes. The probe-based concentration studies also allow investigation of the lateral spread of the jet. Defined in these measurements as the maximum width of the 10% injectant mole fraction contours, the absolute lateral spreading results compare well with those obtained from the imaging experiments.

Transverse penetration data obtained from the images indicate that the jet issuing from the circular nozzle extends approximately 20% deeper into the freestream than the jet from the elliptical nozzle. Both jets experience increasing penetration until about eight effective diameters downstream of the jet exit. Power law correlations were developed from the side view images. These profiles demonstrate that the near-field penetration data from either nozzle collapse well when the inverse of the jet-to-freestream momentum flux ratio is used to scale the coordinate axes. Thus, injectant molecular weight appears to have a relatively insignificant effect on the transverse penetration of sonic jets injected into supersonic crossflows as long as the jet-to-freestream momentum flux ratio is held constant. Also, the forms of the correlations that result from the side view data compare very well to the results of other studies that use alternate methods to determine the upper edge of the jet (see the comparisons in Fig. 2.1 and Table 2.2). Again, transverse penetration results obtained from the 10% mole fraction contours of the probe measurements compare quite well with the imaging results.

Combining the observed trends in lateral spread and transverse penetration associated with elliptical and circular injection leads to the conclusion that an axis-switching phenomenon, similar to that found in elliptical injection into quiescent and co-flowing environments,⁷⁴⁻⁷⁷ is retained in the transverse injection flowfield. When compared directly, the ratio of lateral spread to transverse penetration shows the axis-switch very clearly. In fact, at the streamwise centerline of the nozzle

(i.e., $x/d_{\text{eff}} = 0$), this ratio is roughly 40% larger in the elliptical injection cases than in the circular injection cases.

5.5.3 Large-Scale Structures

In flowfields created by transverse injection into a supersonic stream, large-scale vortex motions have been frequently observed using instantaneous imaging techniques.^{37,40,68-71} In the present investigation, both shadowgraphs and instantaneous Rayleigh/Mie scattering images provide convincing evidence demonstrating the existence of large-scale vortex motions within the jet fluid. Additionally, the results of applying conventional statistical analyses to the ensembles of instantaneous images reveal more detailed information regarding the behavior of these vortices in terms of their sizes, shapes, and convection characteristics.

Two dominant classes of vortices, namely, the counter-rotating vortex pair and the shear layer eddies, are found to be present in this flowfield while some indications of a wake vortex system are also found. Instantaneous end view images consistently show the emergence of the counter-rotating vortex pair as the jet lifts from the bottom wall of the test section. These vortices rapidly develop a void between them that fills with freestream fluid drawn in from the wake region beneath the jet plume. The counter-rotating structures that form in the air injection cases rapidly become inundated with pockets of freestream fluid while helium injection leads to structures that retain their identities for longer spatial extents. It is therefore thought that compressibility plays an important role in the organizational character of the large-scale vortices that form in transverse injection flowfields. Apparently, the high convective Mach numbers associated with the mixing layers formed in the helium injection flowfields act to delay the break-up of the largest structures. Injector geometry also affects the formation and behavior of the counter-rotating vortex pair. The axis-switch phenomenon that results in more rapid lateral spreading and suppressed transverse penetration in the elliptical injection cases also causes the centers of the counter-rotating vortex pair to move outward, creating a wider void between them than was found in the injection cases using the circular nozzle. This observation has significant implications where entrainment and mixing are

concerned; further discussion of these issues appears in the following section. End view images also illustrate the eddies that form around the periphery of the jet. Compressibility appears to affect these eddies also, as small-scale motions are more prominent in the helium injection cases (high compressibility) than in air injection cases (low compressibility). This leads to the regions of high fluctuation in the helium injection cases being markedly narrower than the corresponding regions in the air injection cases.

Instantaneous side view images obtained from the spanwise centerline of the jet/freestream interaction clearly show the vortices that develop in the upper edge mixing layer. Those eddies observed in the air injection cases (low compressibility) appear long and well-defined. The braid regions that form between two consecutive structures are also well-defined, extending rather deeply into the jet fluid. Spatial correlation results indicate a loss of organization of the structures as they convect downstream by showing smaller structure sizes with increasing streamwise position. The correlation results further indicate that the eddies rotate to orientations more inclined to the freestream fluid and become increasingly circular as they travel downstream. Large-scale eddy sizes also appear influenced by the geometry of the injector, where elliptical injection produces smaller structure sizes than circular injection (when compared at the same streamwise position). It is thought that this observation results from the axis-switch present in the injection cases using the elliptic nozzle.

Convection velocity measurements show that the large-scale eddies formed in the low compressibility cases (air jets) travel faster than the jet exit velocity in the near-field region, but slower than the freestream velocity. These measurements also indicate that the injector geometry influences the convection characteristics of the structures in the near-field since elliptical injection produces interfacial eddies that move slightly faster and more shallowly in the near-field than those generated by circular injection. Additionally, the large structures that form in the interfacial mixing layer generally roll into the freestream fluid (i.e., they predominantly have vorticity oriented in the $+z$ -direction). This implies that the injectant fluid moves with a higher velocity tangent to the interface than the freestream fluid. However, near the location where the core of the jet

disintegrates, eddies are formed that occasionally experience an opposite roll-up direction. At this position, the freestream fluid above the eddy moves faster than the injectant fluid below the eddy. Thus, the streamwise extent of the high speed injectant core fluid affects the character of the eddies that form adjacent to it.

In the helium injection cases (high compressibility), the large-scale eddies appear rather amorphous in comparison to the air injection results, and the braid regions are stringy with thin filaments of freestream entering the jet fluid. The structures continue to roll-up into the freestream fluid indicative of vorticity in the $+z$ -direction. Correlation results show significantly different trends regarding the organizational and behavioral characteristics of these amorphous eddies compared to those vortices formed in the low compressibility air injection cases. For example, these structures become larger as they propagate downstream. Additionally, the orientations of the eddies become more inclined to the freestream flow direction (same as air injection results) and they become more elliptical (opposite to air injection results) with increasing streamwise distance from the injector exit. Thus, increased levels of compressibility give rise to large-scale eddies that remain more coherent and more elliptical in shape as they convect downstream. Injector geometry also influences the sizes of the large-scale eddies formed in the upper edge mixing layer of the helium injection flowfield. Elliptical injection again leads to smaller structure sizes, in general, than circular injection. Convection velocity measurements show that the large-scale eddies formed in the high compressibility cases travel much faster in the near-field region than their low compressibility counterparts while they decelerate toward the freestream velocity in the far-field. These measurements also indicate that the injector geometry influences the convection characteristics of the structures in the near-field. Elliptical injection, apparently as a result of the axis-switching phenomenon, produces interfacial eddies that move slower and more shallowly in the near-field than those generated by the circular injector.

Another class of vortices that forms periodically in the transverse injection flowfields studied in this investigation are the wake vortices. These vertically oriented structures, which are only intermittently observed in the side view images, form in the wake region between the injectant

fluid and the injector wall. They do not appear highly organized; however, the instantaneous side view images do not provide the optimum perspective for investigating their behavior. Planar images showing the top view would shed more light on the structural characteristics of these vortices.

5.5.4 Entrainment and Mixing Issues

Finally, the important issues of entrainment and mixing are discussed in the material to follow. The planar images obtained in this investigation produce a wealth of information that leads to quantitative comparisons of the entrainment characteristics associated with transverse injection into a supersonic crossflow. However, due to the combination of the relatively poor spatial resolution of the images (i.e., the smallest resolvable scales are much larger than either the Kolmogorov or Batchelor scales) and the nonpassive nature of the combined seeding technique used, molecular mixing information cannot be inferred from the Rayleigh/Mie scattering results. However, the probe-based concentration measurements reveal, at least on a time-averaged basis, the injectant mole and mass fractions throughout the jet/crossflow interaction.

As noted above, the counter-rotating vortices open a void in the injectant fluid that fills with freestream fluid. Thus, these eddies are strong contributors to the freestream entrainment that occurs in the near-field of the transverse injection scheme. Penetration contours derived from the ensemble-averaged end views show this central entrainment region to be significantly wider in the elliptical injection cases than in circular injection. These contours also indicate that the level of compressibility affects the entrainment characteristics of a particular injection scheme. Recall that the helium and air plumes were found to experience variable rates of contraction whereby the area enclosed by the penetration contour decreased as the image plane moved downstream. The contours contract rapidly in the air injection (low compressibility) cases while this phenomenon was delayed in cases using helium. It was shown that this observation indicates that the low compressibility injection cases using air provide better entrainment characteristics than the high compressibility cases using helium. This result is further substantiated by examining the standard

deviation end view data. Through the use of a shape parameter and an analysis of the mixing zone contours obtained from the standard deviation images, the low compressibility cases were shown to provide more mixing potential by way of the large-scale fluctuations than the high compressibility cases. This is principally due to the increased mixing zone area in the cases using air as the injectant. Further analysis of the normalized fluctuation levels in these flowfields reveals that the mixing layers that develop in the high compressibility cases are thin compared to those found in air injection cases. Also, the fluctuations in the upper edge mixing layer appear to intrude deeper into the jet core and diffuse more rapidly for the low compressibility cases. Thus, the end view images indicate that high compressibility acts to suppress the entrainment characteristics of the mixing region by changing the behavior of the eddies that form in the upper edge mixing layer. Also, the elliptical injector geometry provides a larger central entrainment region where freestream fluid from the wake is drawn up into the jet core. This result is particularly important considering the findings of VanLerberghe,⁷⁰ who investigated transverse injection using PLIF of acetone. It was found in this study that the central entrainment region provided the best mixing characteristics in the transverse injection flowfield. Thus, enlargement of this region using passive (such as elliptical injection) or active methods could lead to better entrainment and mixing characteristics.

The side view images indicate that the eddies forming in the upper edge mixing layer also greatly influence the amount of freestream entrainment that occurs in these flowfields. These images indicate the significant effects of compressibility in this region. Instantaneous visualizations clearly show the lack of entrainment in the cases using helium (high compressibility) while air injection (low compressibility) appears to generate large vortices with distinct braid regions forming between consecutive eddies. Ensemble-averaged and standard deviation data also indicate this suppression of the entrainment characteristics of the high compressibility cases. The jet core region, on average, remains coherent over a longer spatial extent when helium is used as the injectant. The standard deviation results show that the maximum normalized fluctuations occurring in the upper edge mixing layer remain localized near the upper edge of the jet in helium injection cases while they intrude far into the jet core region in air injection cases. Thus, the

freestream entrainment provided by the shear layer eddies is more effective in the low compressibility cases.

As mentioned above, these results can only be extended to the entrainment of freestream fluid into the jet by the large-scale eddies present in the mixing regions of the flowfield. The large-scale eddies act in this capacity in two ways. First, they actively engulf fluid from the freestream into their cores. Secondly, they strain the interface between the two fluids and create more interfacial surface area across which diffusion may occur. However, the descriptions just presented cannot necessarily be extended to those involving the molecular mixedness of the two fluids since molecular mixing occurs at length scales that are irresolvable using the current imaging technique. Nevertheless, the fact that compressibility effects alter the characteristics of the large-scale eddies suggests that entrainment of freestream fluid occurs more slowly in transverse injection cases where the convective Mach number of the mixing layer is relatively high. Since entrainment of freestream fluid into the injectant fluid is an essential first step to the two becoming molecularly mixed, inhibiting the degree of entrainment logically leads to a poorer degree of molecular mixing. Thus, effective transverse injection schemes should strive to avoid highly compressible mixing regions as quantified by the convective Mach number.

Finally, the probe-based concentration results indicate that the elliptical injection scheme provides better time-averaged mixing characteristics in the central entrainment region than the circular injection scheme in the near-field. However, the concentration data very near the injector wall indicate poorer mixing for the jet issuing from the elliptical nozzle. This result likely follows from the reduced transverse penetration and enhanced lateral spread of the elliptical jet which does not allow as much freestream fluid into the lowest regions of the wake. Area-averaged results indicate that the elliptical injector provides better mixing than the circular injector by approximately 6% at the near-field measurement station (i.e., $x/d_{eff} = 4$) and by about 8% at the downstream measurement station (i.e., $x/d_{eff} = 10$).

6. CONCLUSIONS AND RECOMMENDATIONS

From a fundamental fluid mechanics point of view, transverse injection into a supersonic crossflow represents a complicated problem. The three-dimensional bow shock formed upstream of the injector due to the presence of the jet behaves like a normal shock near the injector wall and like a Mach wave far away from the injector wall at the spanwise centerline of the jet/freestream interaction. Also, a separation shock forms upstream of the injector nozzle as the boundary layer on the injector wall experiences an adverse pressure gradient and separates from the wall. This wave is also three-dimensional in nature and both it and the bow shock wrap around the injector. This behavior results in a substantially varying field of pressures, velocities, and densities into which the injectant gas flows. A horseshoe vortex system, generated due to the upstream separation regions, also wraps around the injector nozzle. In addition to the freestream flow, the behavior of the injectant gas is highly complicated. If underexpanded, the jet accelerates to supersonic velocities outside of the nozzle into the relatively low pressure of the freestream. In doing so, a system of shock waves forms within the jet fluid including a barrel shock and a Mach disk. Injectant fluid not contained within the barrel shock also accelerates to supersonic velocities in a peripheral shear layer. Then, due to the oncoming freestream flow, the jet bends rapidly downstream. Just downstream of the injector nozzle, another separated zone occurs. A highly intermittent wake region formed behind the jet exit may contain a system of vertically oriented vortices that interact with the lower edge of the jet boundary. Within the jet fluid, a pair of counter-rotating vortices develops due to the vorticity contained within the jet boundary layer. These vortices dominate the structure of the jet and provide vital sources for mixing the injectant and freestream fluids. Another vortex system develops within the mixing layer that forms between the two fluids around the periphery of the jet core. These eddies also appear to contribute strongly to the near-field mixing that occurs. A vortex system established in the wake region downstream of the injector may also play an important role in the transport of freestream fluid upward into the core of the jet and injectant fluid downward into the near-wall region.

A large body of work has contributed to the description just given for this difficult flowfield. However, at the initiation of this research, descriptions of the large-scale eddies formed at the jet/freestream interface and within the injectant fluid were not available. These eddies are thought to be significant contributors to the entrainment of freestream fluid into the jet, yet no information concerning the development of these vortex structures and their roles in the mixing process existed. Further, the effects of injectant gas and injector geometry on the near-field region were largely uncharacterized. Potential fuels for SCRAMJET engines include both relatively light (hydrogen) and heavy (hydrocarbon) gases. The mixing region formed between the fuel and oxidizer streams typically contains large-scale vortex structures that develop intermittently and act to strain the interface between the two fluids as well as to entrain fluid from one stream into the other. The characteristics of these eddies are strongly influenced by the constituent streams through one or more of several parameters, including the density ratio, velocity ratio, and convective Mach number. In the transverse injection flowfield studied here, these parameters are all quite difficult to define since the density and velocity fields (among others) are highly three-dimensional and vary as the peripheral mixing layer develops. Injector geometry can also have a significant impact on a given SCRAMJET design, especially when considering the dispersal of the fuel stream, the actual mixing afforded by the given configuration, and the total pressure losses incurred by the freestream.

With this information in mind, the primary objective of the present research was to gain a better understanding of the dominant features that govern the near-field mixing and structural characteristics in flowfields created by transverse injection into a supersonic stream. Two specific injector configurations were examined, and each injector was operated at one condition (governed by the jet-to-freestream momentum flux ratio) with two injectant gases. Rayleigh/Mie scattering from silicone dioxide particles seeded into the moist freestream allowed the collection of ensembles of digital images from several measurement planes in each case; end view planes were examined at four streamwise locations and the spanwise centerplane was investigated extensively. Analyses of the image ensembles produced mean and standard deviation statistics, lateral spreading and

transverse penetration characteristics, large-scale mixing information, two-dimensional spatial correlation fields, pertinent bow and separation shock features, and large-scale convection velocity measurements. Pitot and concentration probes were used at two end view planes in the two cases using helium as the injectant gas. Data from the probe-based measurement techniques provided quantitative comparisons of the total pressure losses and time-averaged mixing characteristics in transverse injection flowfields created using circular and elliptical injector nozzles.

6.1 Summary of Major Results and Conclusions

The important results and conclusions of this investigation are summarized below:

- Clear images of the flowfields created by transverse injection of air and helium through circular and elliptical nozzles into a supersonic crossflow were obtained. Instantaneous images distinctly reveal the freestream shock structure, the characteristic counter-rotating vortex pair, the large-scale turbulent structures formed at the jet/freestream interface, and the development of the wake region downstream of the injector exit.
- This represents the first investigation examining the effects of compressibility on the large-scale structure of the transverse injection flowfield. The two injectant gases used, namely air and helium, result in near-field mixing layers with dramatically different compressibility levels as quantified by the convective Mach number. Shadowgraph photos and instantaneous and statistically analyzed Rayleigh/Mie scattering images are used to examine the effects of compressibility on the injection flowfields.
- The experimental results of this investigation are the first reported for transverse injection through a small aspect ratio elliptical nozzle into a supersonic crossflow. This injector configuration has been shown to promote mixing in studies using quiescent and co-flowing environments.^{74,77,104} It was chosen based on the hypothesis that it may

provide passive mixing enhancement and smaller freestream total pressure losses in the near-field region compared to injection through a circular nozzle.

- The large-scale vortices that develop at the interface between the jet and freestream fluids generally roll into the freestream indicating that the injectant fluid below the mixing layer has larger velocities tangent to the shear layer than does the crossflow fluid directly above it. However, some eddies are formed in the region where the jet core begins to disintegrate for which the opposite roll-up direction is observed.
- Normalized standard deviation profiles from both the side and end view images indicate that the peak fluctuations occurring in the upper edge mixing layer intrude deeper into the jet core region in the low compressibility air injection cases than they do in the high compressibility helium injection cases. Thus, increased levels of compressibility act to localize the upper edge turbulent fluctuations to regions nearer the outer edge of the jet. This leads to poorer freestream entrainment and a more prominent jet core in the high compressibility cases.
- Normalized standard deviation results from the side and end view images show thinner mixing layers developing in the high compressibility cases. These results also show that the upper edge mixing layer is significantly thicker than those developing on the sides of the jet fluid irrespective of the injector geometry or compressibility level. This indicates that more freestream entrainment (resulting from the larger turbulent structures residing there) occurs at the upper edge of the jet than at the sides.
- Normalized standard deviation results suggest that, as the jet develops in the streamwise direction, the turbulent fluctuations located at the edges of the jet fluid diffuse into the unfluctuating core region more rapidly in the low compressibility cases.

- Analyses of the mixing zone contours derived from the end view standard deviation images using an area ratio (mixing zone area divided by penetration contour area) and a shape factor were undertaken. These results provide comparisons of the mixing potential of a given flowfield. The area ratio results indicate that the air injection cases (low compressibility) contained relatively larger mixing zones than their helium injection (high compressibility) counterparts. Results of the shape factor analysis provide evidence suggesting that the large-scale eddies which dominate the near-field become less influential downstream of $x/d_{eff} = 8$ for all cases studied, giving way to small-scale turbulence. Taken together, these results indicate that the mixing potential afforded by the low compressibility air injection cases is larger than that of the high compressibility helium injection cases.
- Two-dimensional spatial correlations computed from the ensembles of side view images provide information regarding the structure sizes and orientations of the large-scale eddies that form in the upper edge mixing layer. Instantaneous correlation maps indicate that a wide variety of eddy sizes and spacings develop in these injection flowfields. Ensemble-averaged correlation fields show that both compressibility and injector geometry affect the development of these large-scale vortices. In low compressibility cases (air injection), the eddies become less organized as they propagate downstream. These cases also lead to eddies that become more inclined to the freestream and more circular as they evolve. High compressibility cases (helium injection) contain structures that grow as they convect downstream becoming more coherent. These eddies are found to become more inclined to the freestream and more elliptical in shape as they move downstream. Injector geometry, on the other hand, predominantly affects the size of the average large-scale structure. The jets issuing from the elliptical nozzle contain eddies that are markedly smaller than those in the jet

issuing from the circular nozzle. This is thought to be a result of the axis-switching phenomenon present in the elliptical injection flowfield.

- Lateral spreading characteristics inferred from the ensemble-averaged end view images indicate that the jet issuing from the elliptical nozzle spreads roughly twice as far into the crossflow fluid as the jet created using the circular nozzle when the distance is scaled by the physical spanwise nozzle dimension.
- Compressibility effects manifest themselves in the rate of contraction of the average jet penetration contour. These contours, obtained from applying the 90% penetration definition to the ensemble-averaged end view images, indicate that the injectant plumes in the high compressibility cases (i.e., helium injection) contract slowly compared to those from the low compressibility cases (i.e., air injection). Since at a given streamwise location a larger penetration contour implies less freestream entrainment, the results suggest that the low compressibility cases provide substantially better entrainment characteristics than the high compressibility cases.
- When the streamwise and transverse positions are scaled using the jet-to-freestream momentum flux ratio (as suggested by Keffer and Baines²²), the transverse penetration data obtained from the ensemble-averaged side view images collapse very well in the near-field region. These results indicate that mixing layer compressibility does not strongly affect the transverse penetration of the jet fluid as it enters the freestream. Injector geometry, however, does play a role in the jet's ability to penetrate into the crossflow. Penetration correlations indicate that injection through the elliptical nozzle produces a jet with suppressed transverse extent (by 20%) compared to the jet issuing from the circular nozzle at the same jet-to-freestream momentum flux ratio. Also, the power law form of the penetration correlation found in this investigation produces

results that compare closely to those of other studies using different diagnostic techniques, lending credence to the present definition of the upper edge of the jet, at least in the injector near-field.

- The transverse penetration and lateral spreading characteristics of the elliptical injection flowfield indicate the presence of an axis-switching phenomenon resulting from the asymmetric momentum thickness distribution around the nozzle exit.
- The bow shock formed upstream of the injector exit is sensitive to the formation and passage of large-scale structures at the jet/freestream interface. The standard deviation results from both end and side views indicate that the bow shock position fluctuates slightly due to these vortices. Images of the bow shock/jet boundary interaction show that the bow shock is most sensitive in the region of nearly normal shock behavior closest to the injector wall. Here, large structures create significant changes in the frontal area of the jet plume necessitating positional responses by the shock wave.
- Injection using the elliptical nozzle results in a weaker bow shock compared to injection through the circular nozzle at the same jet-to-freestream momentum flux ratio. The region of normal shock behavior near the injector wall is smaller, and, at any given streamwise position, the bow shock does not extend as far above the injector wall.
- The elliptical injection scheme leads to a separation shock upstream of the injector exit that does not extend as far either in the streamwise or transverse direction as the separation wave formed ahead of the circular nozzle for a given jet-to-freestream momentum flux ratio. This suggests that the “hot-spot” phenomenon common in reacting transverse injection flowfields, where fuel travels into the separated region

upstream of the injector nozzle and is ignited, may be reduced by using an elliptical fuel injector.

- Large-scale convection velocity measurements obtained from temporally correlated image pairs show a strong dependence on both compressibility level and injector geometry. For a given injector geometry, the near-field convection velocities are larger for the high compressibility cases (helium injection) than for the low compressibility cases (air injection). In the far-field, the eddies tend to convect with velocities that are closer to the velocity of the freestream. Injector geometry principally affects the near-field behavior. Convection angles are shallower in elliptical injection than in circular injection, and the near-field convection velocities from the elliptical injection cases are skewed toward the freestream velocity. It is thought that the axis-switching phenomenon affects the development of the large-scale eddies in the near-field of the elliptical injector, resulting in the observed trends.
- Injection through the elliptical nozzle results in a maximum pitot pressure that is about 40% higher in the near-field of the injector exit (i.e., $x/d_{eff} = 4$) than injection through the circular nozzle. This is principally due to differences in bow shock and Mach disk behavior between the two cases. Area-averaged pitot pressures in the near-field region are only slightly higher (about 1%) in the elliptical injection flowfield, while farther downstream (i.e., $x/d_{eff} = 10$), the two geometries result in essentially equal area-averaged pitot pressures.
- Probe-based concentration results indicate that the elliptical injector produces slightly favorable mixing characteristics over the circular injector by roughly 6% at the upstream location (i.e., $x/d_{eff} = 4$) and 4% at the downstream location (i.e., $x/d_{eff} = 10$). This was observed to be largely an effect of the wider void created between the two counter-

rotating vortices in the elliptical injection flowfield. This wide void provides additional freestream entrainment leading to the better mixing performance. Decay rates of the maximum injectant mole and mass fractions are essentially identical over the domain of the present measurements.

- The probe-based concentration results yield transverse penetration and lateral spreading data that compare very closely to those obtained from the ensemble-averaged side and end view images.
- Indications of wake vortices are intermittently found in the instantaneous side view images of these transverse injection flowfields. These eddies appear as vertically-oriented structures that reach from the lower side of the jet plume down toward the injector wall. Because of the relatively good mixing that occurs below the jet centerline (as indicated by the current probe-based concentration measurements and the PLIF results of VanLerberghe⁷⁰), it seems reasonable to suppose that these wake vortices may play potentially important roles in the entrainment and mixing processes that occur in this region of the flow.

6.2 Recommendations for Future Work

To fully understand the flowfields created by transverse injection into supersonic crossflows, several other measurements are required. The following recommendations for further investigations should be of general interest to the research community.

- The wake vortex structure that forms in transverse injection flowfields may play a key role in the mixing that occurs between the injectant and crossflow fluids. These eddies were intermittently observed in the side view images collected in this investigation. However, plan view images obtained by positioning the laser sheet just above the

injector wall and viewing the flowfield from above provide a better method for more thorough studies of the wake region.

- Compressibility issues were observed to be extremely important when examining the structure of the large-scale vortices that form at the interface between the jet and freestream fluids. Since the range of potential fuels for SCRAMJET engines includes those with very low molecular weights (i.e., hydrogen) and those with relatively high molecular weights (i.e., hydrocarbons), further studies are required to investigate these effects in more detail. Examinations, either experimental or computational, of the effects of compressibility on the mixing of injectant and crossflow streams would prove very useful in terms of both fundamental knowledge of the mixing processes and practical knowledge concerning the advantages or deficiencies associated with particular fuels.
- Understanding the mean and fluctuating static pressure and temperature fields around the injectant plume would be of particular interest. As has been noted throughout this document, the flowfield created by single jet transverse injection into a supersonic crossflow is highly three-dimensional. Traditional probe-based measurements of cone-static pressure in this near-field region may prove of little use since the flow angles span the range from those parallel to the crossflow fluid to those perpendicular to the crossflow fluid. Additionally, the response time of the intrusive probes is generally not sufficiently short to obtain resolvable information regarding the turbulent fluctuations present. Nonintrusive methods for measuring the static pressure and temperature fields, such as Coherent Anti-stokes Raman Scattering (CARS) or degenerate four-wave mixing (DFWM) may prove very useful.

- Instantaneous, spatially- and temporally-resolved injectant concentration measurements are essential to complete understanding of the mixing processes taking place in the transverse injection flowfield. Two principal vortex mechanisms appear to drive the entrainment of freestream fluid into the jet region in the near-field. However, it is not clearly understood where the best mixing takes place in these flows. These concentration measurements would provide, on an instantaneous basis, fundamental information regarding the mixing that occurs. Insight as to efficient mixing enhancement techniques might also be drawn from such measurements.
- Planar measurements of the instantaneous velocity field using Particle Image Velocimetry (PIV) would prove very useful in studying the vorticity generated in these flowfields. Such information can also be used in several side and top view planes to instantaneously examine the entrainment characteristics (by seeding only one of the streams), the strain rates, and the velocity fluctuation levels.
- Laser Doppler velocimetry (LDV) applied to the near- and far-field regions of the flowfields created using the circular and elliptical injector geometries could also provide a wealth of information about these flowfields. Use of a three-component LDV system would allow measurements of all the turbulence properties found in these flows. Additionally, vorticity information would be obtained along with the distribution of turbulent kinetic energy found throughout the flow. Measurements of the entire turbulence field would also allow estimations of the production, dissipation, convection, and diffusion terms in the equation governing the transport of turbulent kinetic energy.
- Pressure-sensitive paint could be used to document the wall static pressure field around the two injector configurations used in this study. This technique has been applied to a

single circular injector before (Everett, et al.¹⁶), but comparisons between the circular and elliptical nozzles may yield further detail in regard to the axis-switching phenomenon present in the elliptical injection flowfield. This technique would also provide better insight into the structure of the wake region in the elliptical injection case.

- Refinements can be made to the imaging technique used in this investigation. Potentially, if the seed can be made truly passive in nature, more quantitative measurements of the injectant concentration could be made. The advantage that making instantaneous planar concentration measurements provides is the ability to construct probability density functions (PDFs) throughout the region of interest. These PDFs would then shed more light on the instantaneous mixing levels that occur throughout the flowfield. Refinement of this imaging technique would also provide a tool for fast acquisition of injectant concentration data, making parametric studies of candidate injection schemes less time-consuming.
- The double-pulsed imaging technique as used in this investigation can provide information regarding the temporal evolution of the large-scale structures occurring at the jet/freestream interface. Refinements to the hardware (e.g., the acquisition of a digital camera with comparable performance characteristics to the one presently on site) are required so that the collected image pairs may be analyzed using a cross-correlation technique. This would provide ensemble-averaged, rather than instantaneous, measurements of the large-scale convection velocities and convection angles.

TABLES

Table 2.1 Incompressible Transverse Injection Penetration Correlations and Conclusions

Author	Technique	J	Correlation/Conclusion
Abramovich ²⁵	Empirical and theoretical	-	Empirical: $\frac{y}{d} = J^{0.434} \left(\frac{x}{d} \right)^{0.333}$ Theoretical: $\frac{y}{d} = 8.314 \cdot \sqrt{J} \cdot \ln \left[1 + 0.1 \frac{x}{d} \left(1 + \sqrt{1 + \frac{20}{x/d}} \right) \right]$
Keffer and Baines ²²	Hot wire	4-100	Axes scaled by J^{-1} collapse near-field data
Pratte and Baines ²¹	Photos of smoke-filled jet	25-1225	$\frac{y}{d \cdot J^{0.5}} = a \left(\frac{x}{d \cdot J^{0.5}} \right)^{0.28} \begin{cases} y = y_{top}, a = 2.63 \\ y = y_{mid}, a = 2.05 \\ y = y_{bottom}, a = 1.35 \end{cases}$
Kamotani and Greber ²⁶	Hot wire, thermocouple	15.3, 59.6	Velocity CL: $\frac{y}{d} = 0.89 \cdot J^{0.47} \left(\frac{x}{d} \right)^{0.36}$ Temperature CL: $\frac{y}{d} = 0.73 \cdot J^{0.52} \left(\frac{\rho_j}{\rho_\infty} \right)^{0.11} \left(\frac{x}{d} \right)^{0.29}$
Chassaing, et al. ²⁷	Pressures, hot wire	5.6-40.3	Velocity CL: $\frac{y}{r} = (1.53 + 0.90 \cdot J^{0.50}) \left(\frac{x}{r} \right)^{0.385}$
Broadwell and Briedenthal ²⁸	Vortex model	-	$\frac{y}{d \cdot J^{0.5}} = C \left(\frac{x}{d \cdot J^{0.5}} \right)^{0.333}$ with C unspecified
Smith, et al. ²³	Acetone PLIF	36-196	Used results of Pratte and Baines; ²¹ demonstrated excellent comparison
Lozano, et al. ²⁴	Acetone PLIF	50.4-400	Used results of Pratte and Baines; ²¹ demonstrated excellent comparison

Table 2.2 Compressible Transverse Injection Penetration Correlations and Conclusions

Author	Technique	J	Correlation/Conclusion
Orth and Funk ²⁹	Schlieren, concentration	0.63-2.43	Used results of Abramovich; ²⁵ good agreement in near-field ($x/d \leq 8$)
Schetz, et al. ^{30,31}	Schlieren	1.27-8.20 12.5-25.7	p_{eb} taken as 80% of static pressure behind normal shock in freestream; barrel shock penetration increased with M_j but J not constant
Chrans and Collins ⁶	Schlieren	0.46-12.0	Verified scaling of Zukoski and Spaid; ³ verified role of jet-to-freestream momentum flux ratio ⁴
Torrence ^{32,33}	Concentration	0.51-3.08	Upper edge (~0% injectant concentration): $\frac{y}{d} = 1.68 \cdot \left(J \frac{M_\infty}{M_j} \cos^2 \theta \right)^{0.5} \left(\frac{x}{d} \right)^{0.087}$
Rogers ^{34,35}	Concentration	0.50-1.50	Upper edge (0.5% injectant concentration): $\frac{y}{d} = 3.87 \cdot J^{0.3} \left(\frac{x}{d} \right)^{0.143}$
Cohen, et al. ¹⁸	Schlieren	0.68-11.3	Top and middle of Mach disk: $\frac{y}{d} = \frac{k}{1 + \cos \theta} J^{0.5}; \quad \left\{ \begin{array}{l} y = y_{top}, k = 1.51 \\ y = y_{mid}, k = 1.05 \end{array} \right\}$
McDaniel and Graves ²⁰	Iodine PLIF, densitometer	0.35-1.02	Upper edge (1% injectant concentration): $\frac{y}{d} = J^{0.344} \ln \left[2.08 \cdot \left(\frac{x}{d} + 2.06 \right) \right]$
Rothstein ³⁶	OH PLIF	5.90-38.6	Upper edge: $\frac{y}{d} = 2.173 \cdot J^{0.276} \left(\frac{x}{d} \right)^{0.281}$ and from McDaniel and Graves: ²⁰ $\frac{y}{d} = J^{0.344} \ln \left[4.70 \cdot \left(\frac{x}{d} + 0.64 \right) \right]$
Hermanson and Winter ³⁷	Ethanol Mie Scattering	3.95-4.90	Used results of Cohen, et al. ¹⁸ for top of Mach disk; poor agreement for transverse injector
Papamoschou and Hubbard ³⁸	Schlieren	1.70-8.30	Used results of Pratte and Baines; ²¹ overpredicts jet edge from visual analysis of schlieren photos
Randolph, et al. ³⁹	Schlieren	1.83-2.91	Used results of Abramovich; ²⁵ good agreement in near-field ($x/d \leq 8$)
Gruber, et al. ⁴⁰	Water Mie Scattering	1.00-3.00	Upper edge (90% of mean freestream intensity) $\frac{y}{d_{eff} \cdot J} = 1.23 \cdot \left(\frac{x}{d_{eff} \cdot J} \right)^{0.344}$

Table 2.2 (continued)

Author	Technique	J	Correlation/Conclusion
Present Results	Silane/Water Rayleigh/Mie Scattering	2.90-2.93	<p>Upper edge (90% of mean freestream intensity) Helium and air injection through circular and elliptical nozzles</p> $\frac{y}{d_{eff} \cdot J} = 1.20 \cdot \left(\frac{x+a}{d_{eff} \cdot J} \right)^{0.344} \quad \text{Circular}$ $\frac{y}{d_{eff} \cdot J} = 1.00 \cdot \left(\frac{x+a}{d_{eff} \cdot J} \right)^{0.344} \quad \text{Elliptical}$

Table 3.1 Injector Geometries

Injector	a (mm)	b (mm)	d _{eff} (mm)	ε
Circular	3.18	3.18	6.35	0
Elliptical	6.25	1.63	6.35	0.97

Table 5.1 Experimental Conditions

Quantity	Cases Studied			
	C1A	C2H	E1A	E2H
Injector	Circular	Circular	Elliptical	Elliptical
Injectant Gas	Air	Helium	Air	Helium
$p_{0,\infty}$ (kPa)	317	317	317	317
$T_{0,\infty}$ (K)	302	300	302	300
p_∞ (kPa)	41.8	41.8	41.8	41.8
T_∞ (K)	169	168	169	168
u_∞ (m/s)	516	515	516	515
M_∞	1.98	1.98	1.98	1.98
ρ_∞ (kg/m ³)	0.860	0.866	0.860	0.866
μ_∞ (Pa-s)	1.15×10^{-5}	1.14×10^{-5}	1.15×10^{-5}	1.14×10^{-5}
$Re_\infty = (\rho_\infty \cdot U_\infty) / \mu_\infty$ (m ⁻¹)	3.87×10^7	3.91×10^7	3.87×10^7	3.91×10^7
$p_{0,j}$ (kPa)	902	832	902	832
$T_{0,j}$ (K)	300	300	300	300
$p_{e,j}$ (kPa)	476	405	476	405
$T_{e,j}$ (K)	250	225	250	225
$u_{e,j}$ (m/s)	317	882	317	882
$M_{e,j}$	1	1	1	1
$\rho_{e,j}$ (kg/m ³)	6.64	0.867	6.64	0.867
$\mu_{e,j}$ (Pa-s)	1.60×10^{-5}	1.62×10^{-5}	1.60×10^{-5}	1.62×10^{-5}
$Re_j = (\rho_{e,j} \cdot U_{e,j} \cdot d_j) / \mu_{e,j}$	8.36×10^5	3.00×10^5	8.36×10^5	3.00×10^5
γ_j	1.40	1.67	1.40	1.67
J	2.90	2.93	2.90	2.93
$Re = (\Delta U \cdot \delta_\omega) / \bar{v}$	150,000	428,000	-	-
M_{c1}, M_{c2}	0.66, 0.66	1.89, 1.94	-	-
λ_K (μ m)	0.58	0.23	-	-

Table 5.2 Interrogation Planes

Case	Diagnostic Technique	Interrogation Plane	Single-Shot Image Ensemble Size
C1A	Shadowgraph	Side View	-
	End View Rayleigh/Mie Scattering	$x/d_{\text{eff}} = 0, 4, 8, 10$	20, 100, 20, 100
	Side View Rayleigh/Mie Scattering	$z/d_{\text{eff}} = 0$	100
C2H	Shadowgraph	Side View	-
	End View Rayleigh/Mie Scattering	$x/d_{\text{eff}} = 0, 4, 8, 10$	20, 100, 20, 100
	Side View Rayleigh/Mie Scattering	$z/d_{\text{eff}} = 0$	100
	Probe-Based Measurements	$x/d_{\text{eff}} = 4, 10$	-
E1A	Shadowgraph	Side View	-
	End View Rayleigh/Mie Scattering	$x/d_{\text{eff}} = 0, 4, 8, 10$	20, 100, 20, 100
	Side View Rayleigh/Mie Scattering	$z/d_{\text{eff}} = 0$	100
E2H	Shadowgraph	Side View	-
	End View Rayleigh/Mie Scattering	$x/d_{\text{eff}} = 0, 4, 8, 10$	20, 100, 20, 100
	Side View Rayleigh/Mie Scattering	$z/d_{\text{eff}} = 0$	100
	Probe-Based Measurements	$x/d_{\text{eff}} = 4, 10$	-

Table 5.3 Ensemble-Averaged Two-Dimensional Spatial Correlation Results

Case	Center Position	$2a/d_{\text{eff}}$	$2b/d_{\text{eff}}$	ϵ	α
C1A	$x/d_{\text{eff}} = 1.8, y/d_{\text{eff}} = 2.9$	0.44	0.29	0.75	24°
	$x/d_{\text{eff}} = 7.0, y/d_{\text{eff}} = 3.5$	0.33	0.25	0.65	45°
C2H	$x/d_{\text{eff}} = 1.8, y/d_{\text{eff}} = 2.9$	0.43	0.32	0.67	29°
	$x/d_{\text{eff}} = 7.0, y/d_{\text{eff}} = 3.5$	0.54	0.37	0.73	64°
E1A	$x/d_{\text{eff}} = 1.4, y/d_{\text{eff}} = 2.2$	0.50	0.36	0.69	14°
	$x/d_{\text{eff}} = 7.0, y/d_{\text{eff}} = 3.5$	0.20	0.16	0.60	39°
E2H	$x/d_{\text{eff}} = 1.4, y/d_{\text{eff}} = 2.2$	0.18	0.14	0.63	32°
	$x/d_{\text{eff}} = 7.0, y/d_{\text{eff}} = 3.5$	0.24	0.16	0.74	59°

Table 5.4 Area-Averaged Total Pressure Values

Case	x/d_{eff}	$\overline{p_{o_a}}$	$\overline{p_{o_b}}$	$\overline{p_{o_c}}$
C2H	4	0.69	0.95	0.54
	10	0.63	0.86	0.56
E2H	4	0.70	0.96	0.54
	10	0.63	0.86	0.56

Table 5.5 Area-Averaged Concentration Values

Case	x/d_{eff}	$\overline{x_{\text{He}}}$	$\overline{y_{\text{He}}}$
C2H	4	0.34	0.12
	10	0.26	0.06
E2H	4	0.32	0.11
	10	0.26	0.06

Table 5.6 Contributions of Present Work

Topic	Technique/Methodology	Contributions	Significance
Shock Structure	Shadowgraph Rayleigh/Mie Scattering Pitot Probe	Weaker bow shock in elliptical injection flowfield	Potentially smaller pressure losses in elliptical injection flowfield
		Smaller area beneath separation shock at spanwise centerline in elliptical injection flowfield	Potentially smaller "hot-spot" upstream of injector orifice in elliptical injection case with combustion
		Large-scale eddies influence bow shock	Eddies affect near-wall bow shock leading to positional fluctuations
		Eddy shocklets more prominent in high compressibility injection cases	High compressibility injection produces eddies convecting supersonically with respect to freestream
		Shock structure within jet fluid observed for low compressibility injection cases	Jet shocks hidden by larger density gradients in high compressibility cases
		Steeper barrel shock in elliptical injection flowfield	Nozzle orifice influences expansion characteristics and shock structure in jet
		Higher pitot pressures in elliptical jet core at four effective diameters downstream	Nozzle orifice influences expansion characteristics and shock structure in jet
Transverse Penetration and Lateral Spread	Rayleigh/Mie Scattering Concentration Probe	Higher area-averaged pitot pressures in elliptical injection flowfield (by ~1%) at four diameters	Slightly smaller pressure losses in elliptical injection flowfield
		Elliptical injection results in better lateral spreading but suppressed transverse penetration compared to circular injection	Axis-switching phenomenon preserved in elliptical injection flowfield
		Probe-based data agree with imaging results	Imaging useful for rapid assessment
		Compressibility does not strongly affect near-field penetration and spreading characteristics	Jet-to-freestream momentum flux ratio and injector geometry are key parameters in near-field

Table 5.6 (continued)

Topic	Technique/Methodology	Contributions	Significance
Large-Scale Structures	Shadowgraph Rayleigh/Mie Scattering	Two dominant classes of vortices exist near injector exit: counter-rotating vortex pair and peripherally oriented shear layer eddies	Further evidence indicating the significant contributions of near-field vortices on overall flowfield
		Some evidence of wake vortex structures	Second study providing some evidence
		Injector geometry affects counter-rotating vortices (elliptical nozzle yields wider entrainment region) and shear layer eddies (circular nozzle yields larger vortices)	First quantification of geometric effects on development of large-scale structures in transverse injection flowfields
		Compressibility plays strong role in development and break-up characteristics of large-scale eddies: high compressibility injection results in amorphous shear layer eddies with thin braid regions compared to well-defined vortices with pronounced braid regions in low compressibility cases; faster large-scale eddy break-up in low compressibility cases	First quantification of compressibility effects on development of large-scale structures in transverse injection flowfields; important consideration when selecting fuels for SCRAMJETS in that convective Mach number has significant impact on large-scale structure of injection flowfields
Entrainment and Mixing Issues	Rayleigh/Mie Scattering Concentration Probe	Convection velocities of shear layer eddies dependent on both injector geometry and compressibility level	First study of convection velocities in transverse injection flowfield
		Low compressibility injection yields wider mixing regions, better mixing potential	Importance of instantaneous images for fluctuation analysis, not just average
		Poorer entrainment characteristics develop in high compressibility injection cases	Compressibility affects mixing characteristics of SCRAMJET fuels
		Peak fluctuations localized at outer edge of jet in high compressibility injection cases	Explains more rapid break-up of low compressibility jet plumes
		More rapid onset of diffusion in low compressibility injection cases	Large eddies break-up faster allowing rapid dominance of small-scales

FIGURES

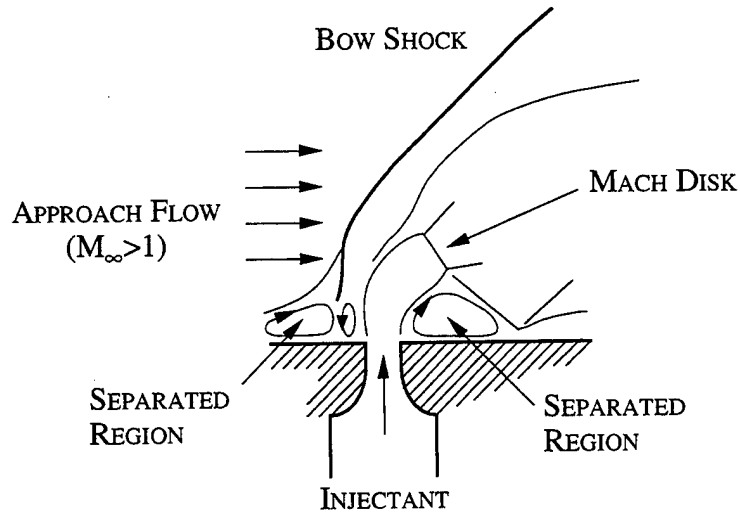


Figure 1.1 Transverse Injection Flowfield Schematic

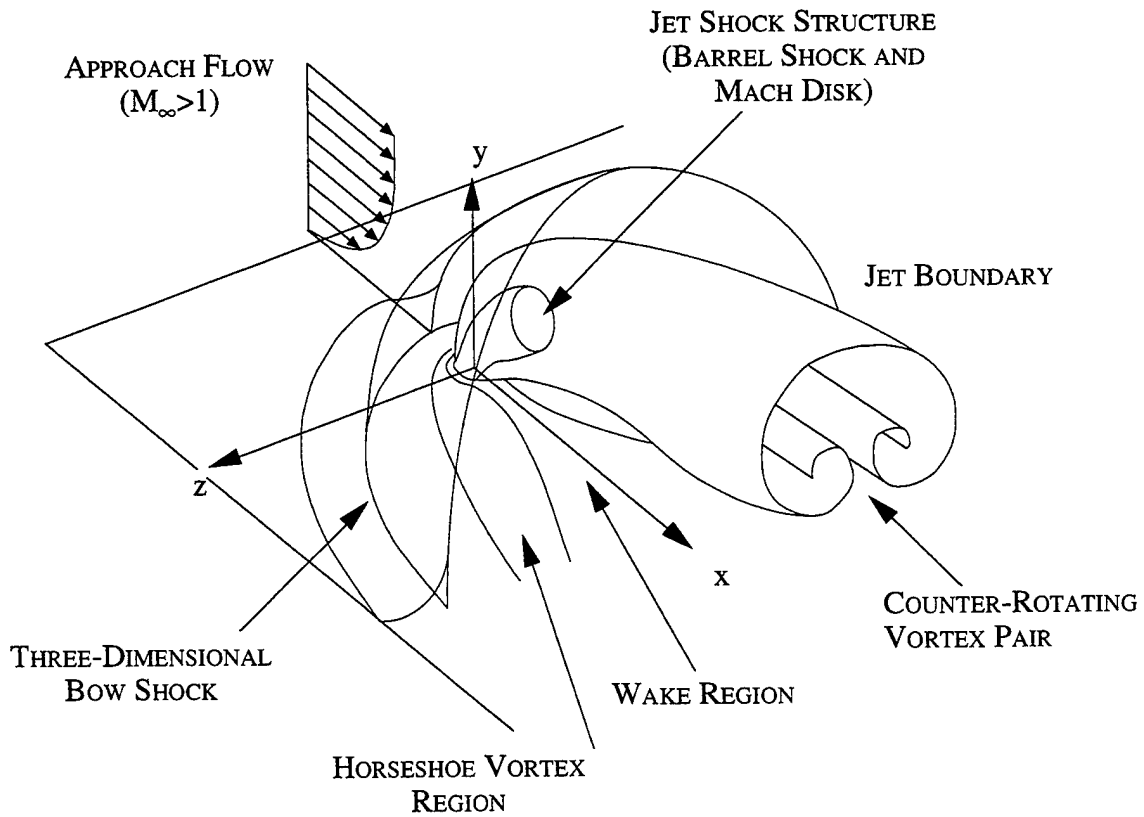


Figure 1.2 Perspective View of Transverse Injection Flowfield

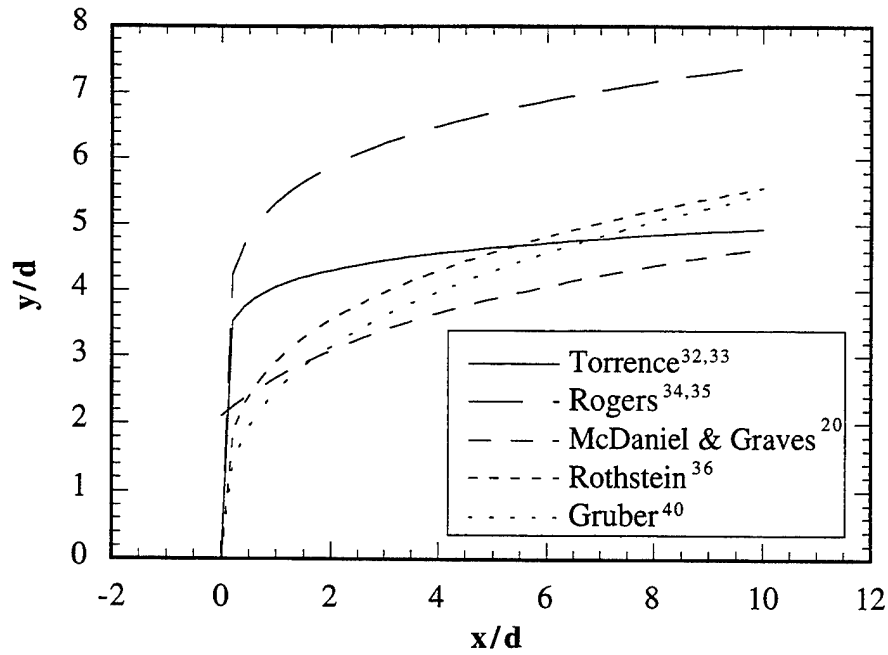


Figure 2.1 Comparison of Transverse Jet Penetration Correlations

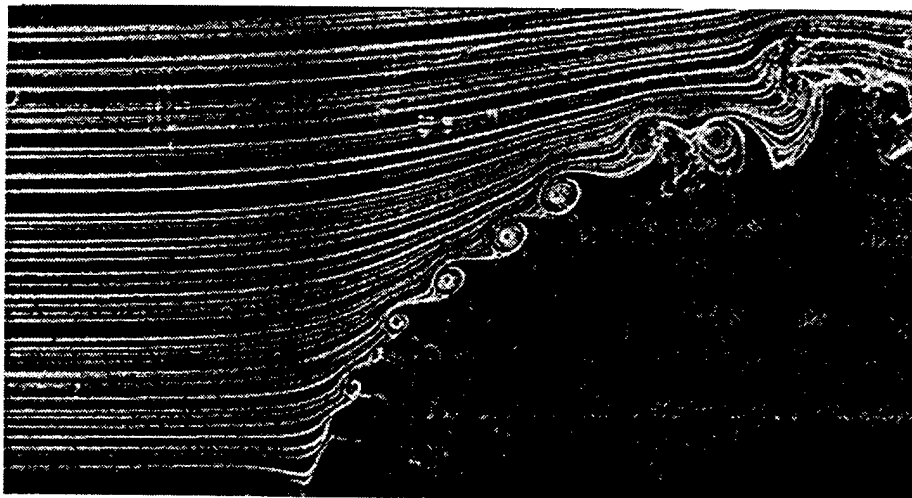


Figure 2.2 Smoke-Wire Visualization of Low Speed Jet in Crossflow Showing Shear Layer Vortices ($J = 4$) [from Fric and Roshko⁴⁹]

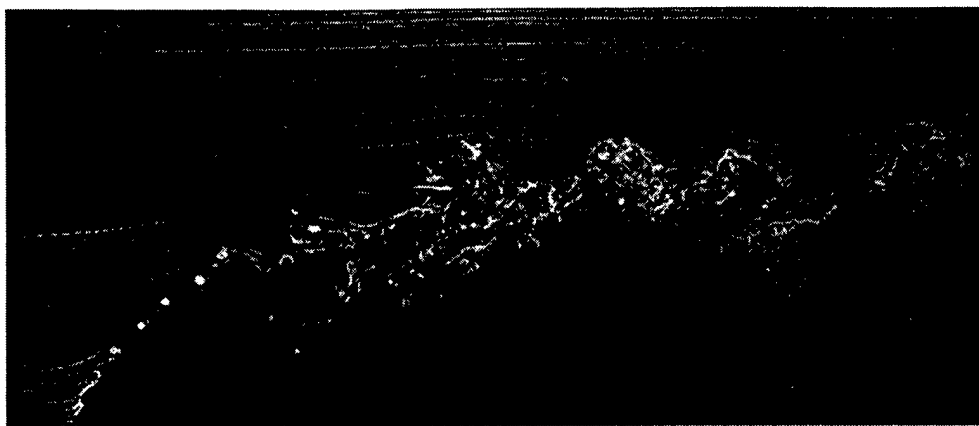


Figure 2.3 Smoke-Wire Visualization of Low Speed Jet in Crossflow-Wide View Showing Shear Layer Vortices ($J = 4$) [from Fric and Roshko⁵³]



Figure 2.4 Dye Injection Visualization of Low Speed Jet in Crossflow Showing Shear Layer Vortices ($J = 4.8$) [from Perry, et al.⁵²]

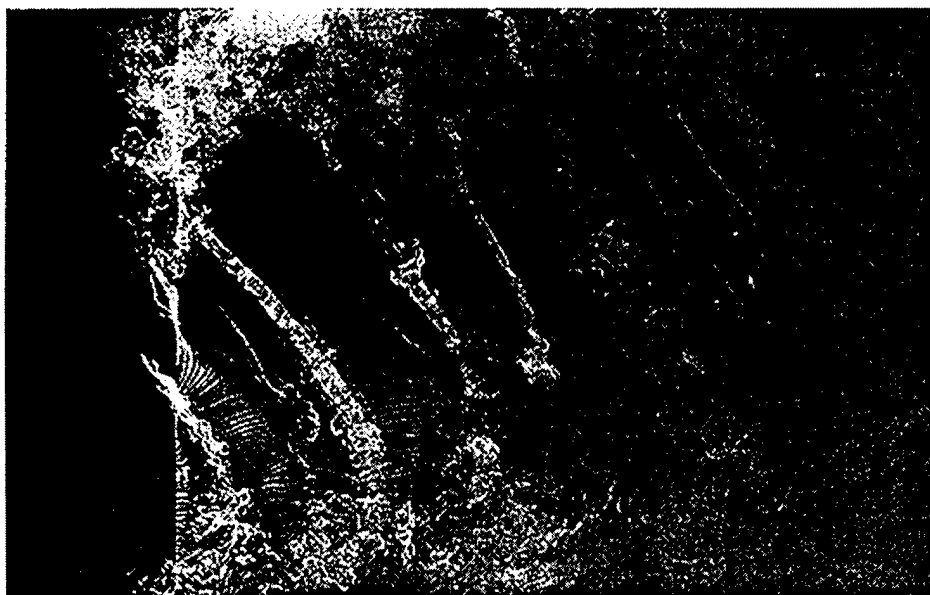


Figure 2.5 Smoke-Wire Visualization of Low Speed Jet in Crossflow Showing Wake Vortices ($J = 4.8$) [from Fric and Roshko⁵³]

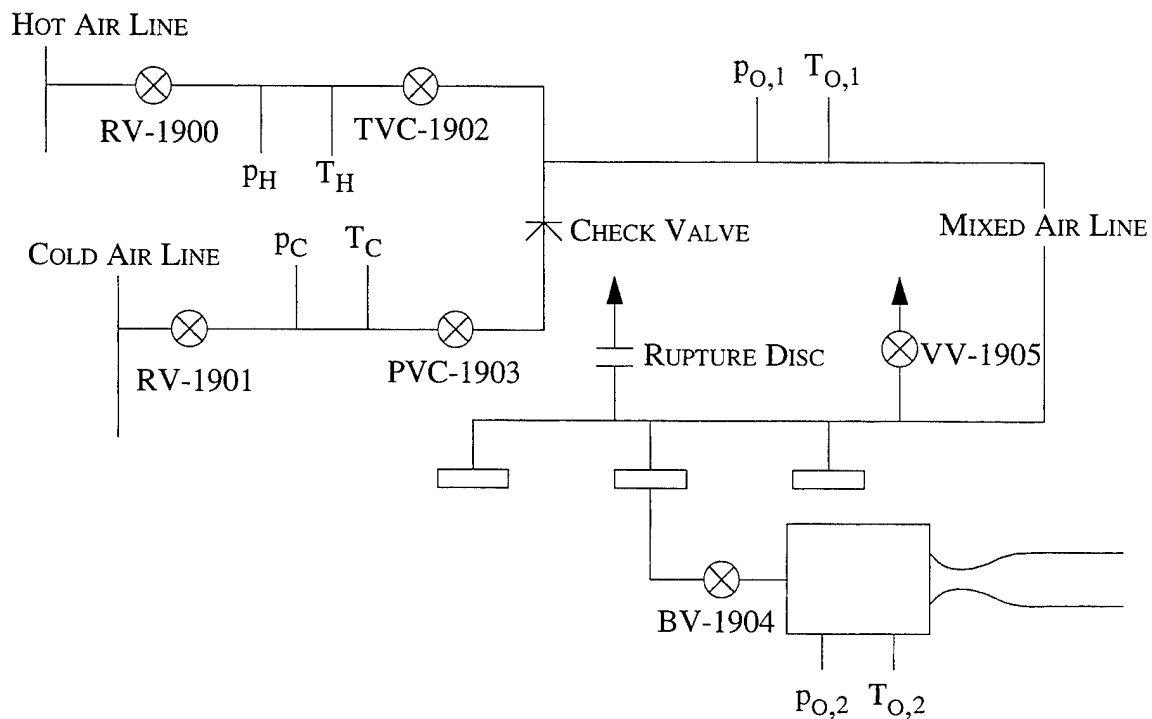


Figure 3.1 Air Supply System Schematic

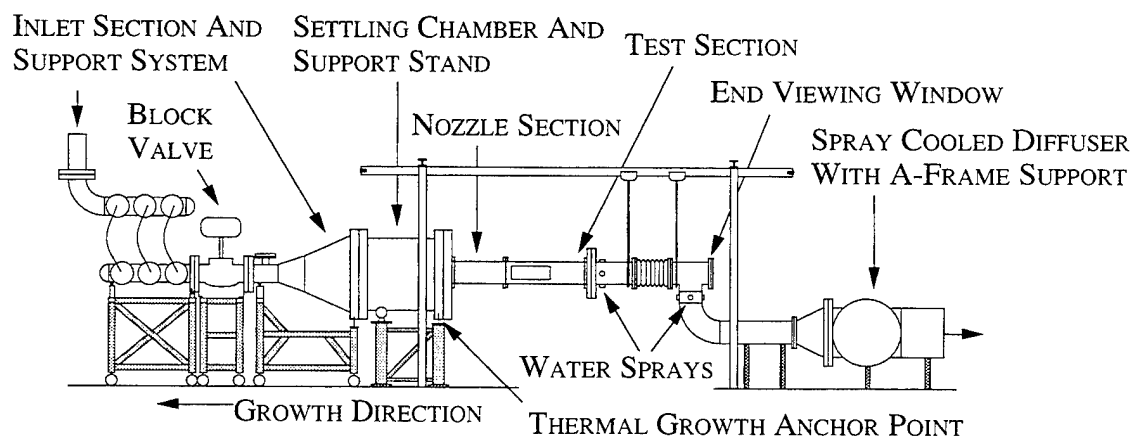


Figure 3.2 Schematic of Supersonic Combustion Tunnel

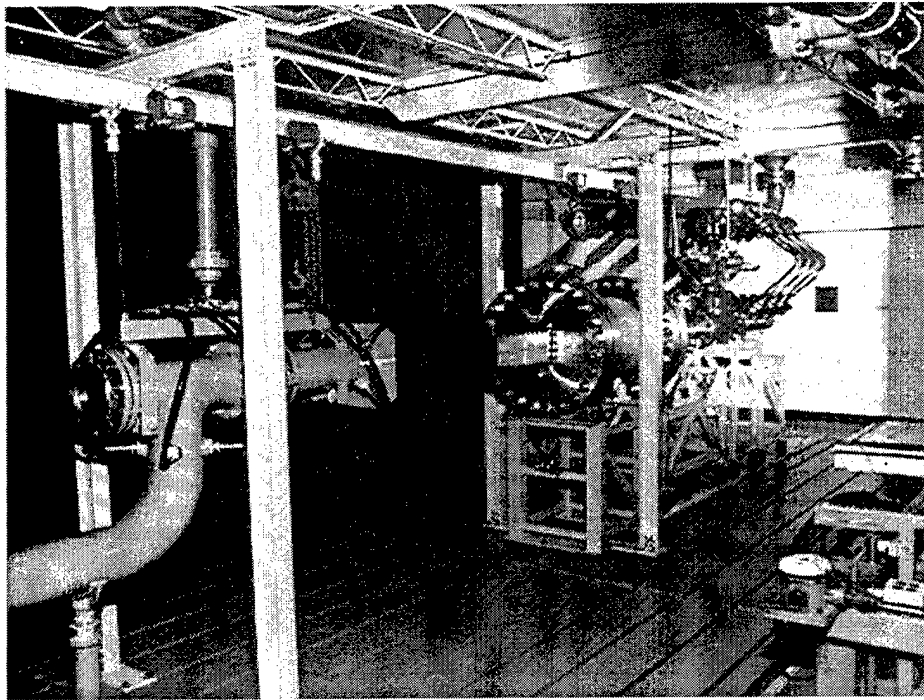


Figure 3.3 Photograph of Supersonic Combustion Tunnel

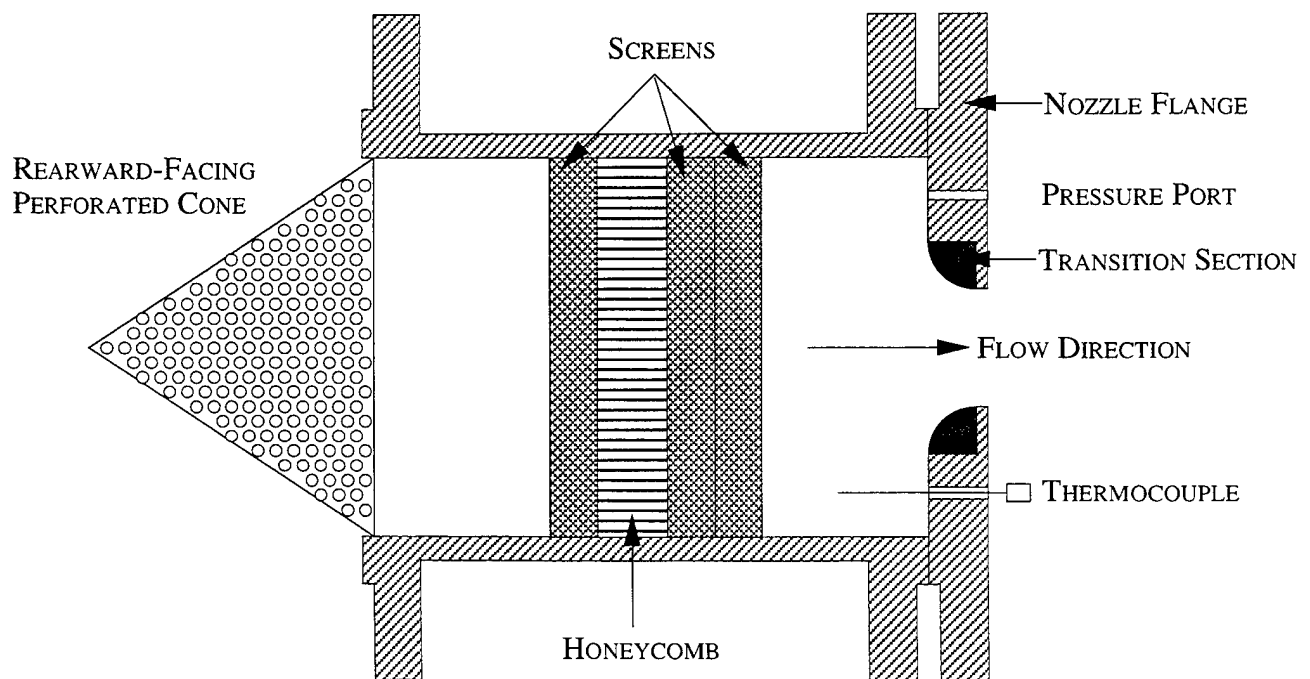


Figure 3.4 Schematic of Settling Chamber

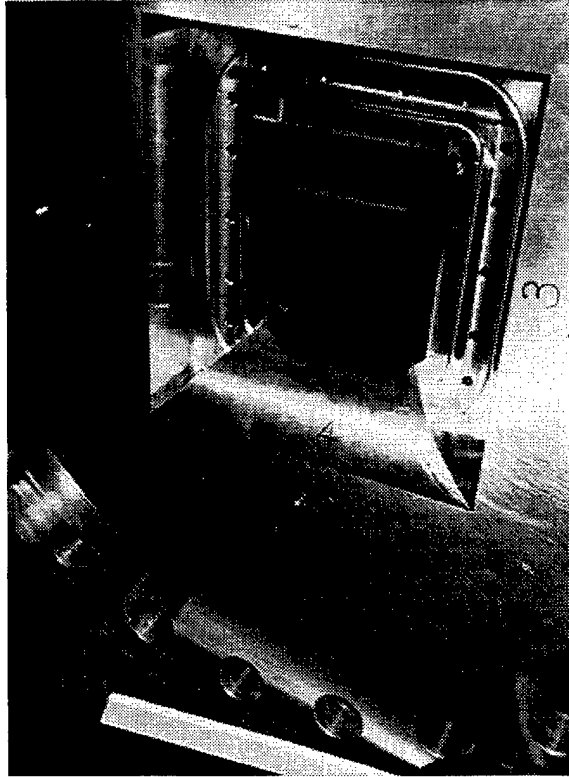


Figure 3.5 Photograph of Transition Section with One Piece Installed

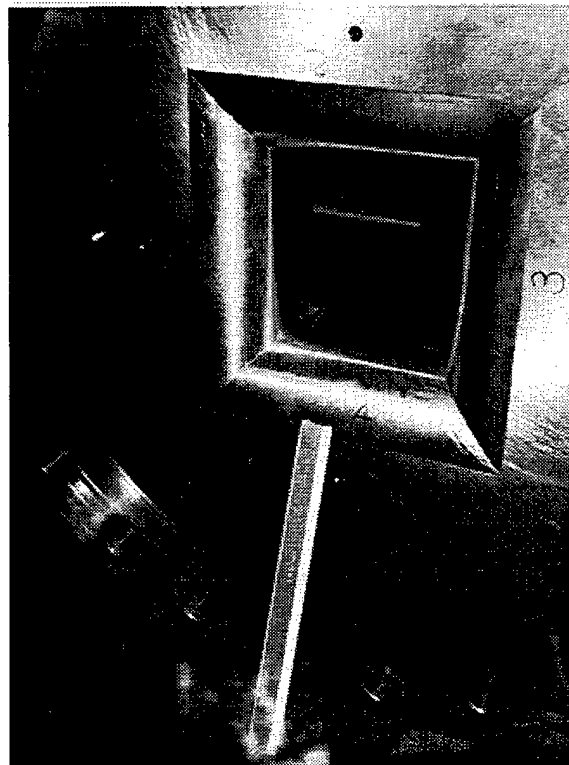


Figure 3.6 Photograph of Completed Transition Section

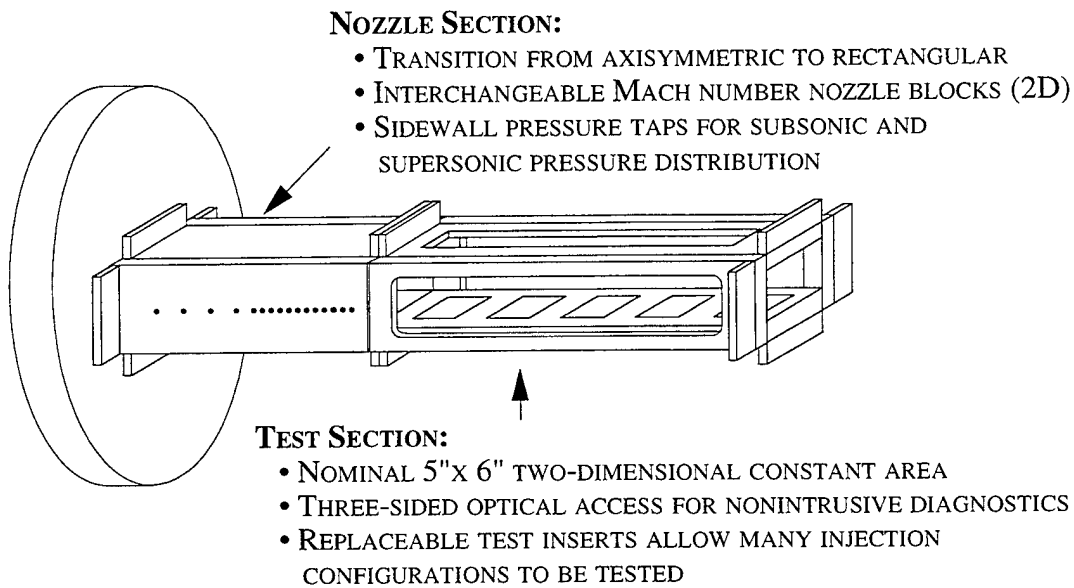


Figure 3.7 Nozzle Section/Test Section Schematic

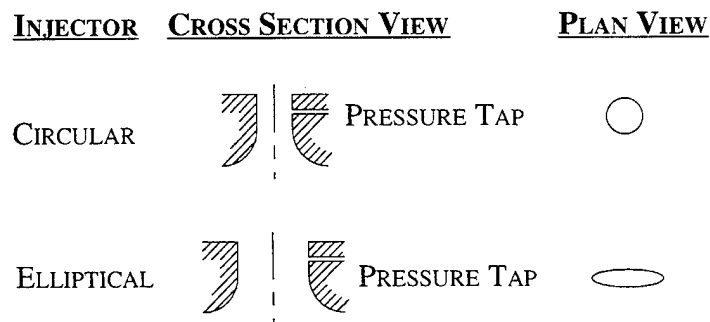


Figure 3.8 Illustration of Injector Configurations

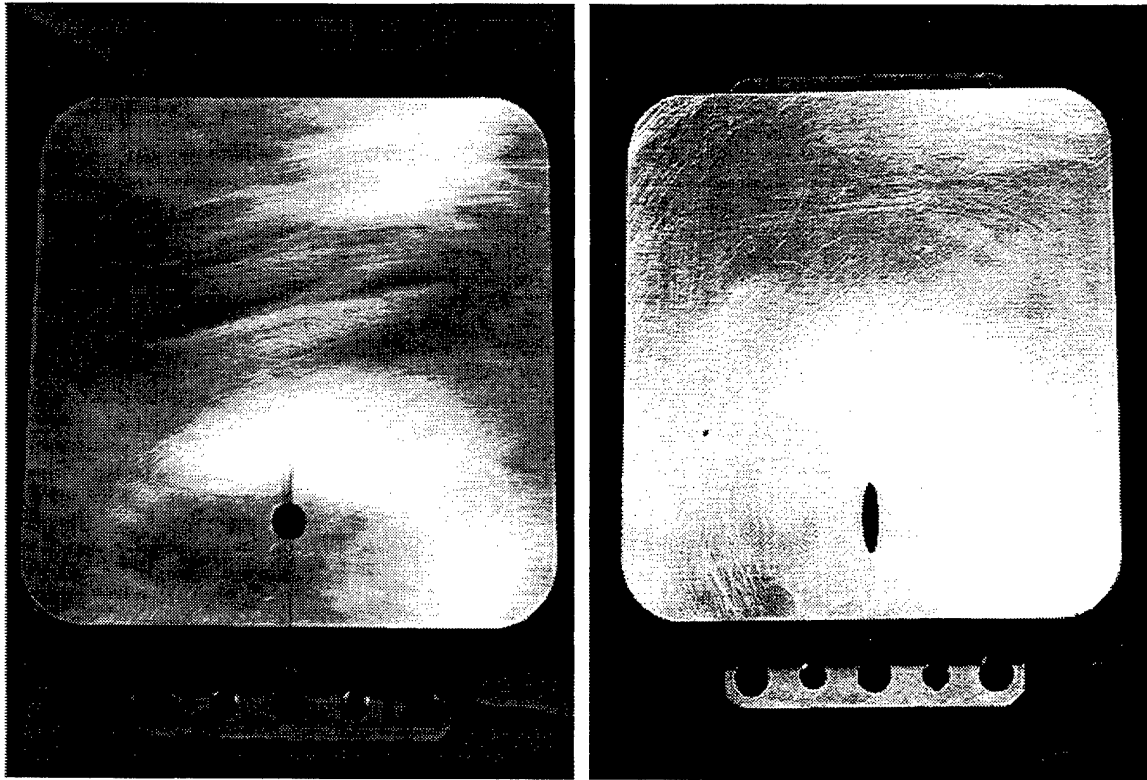


Figure 3.9 Photographs of Injectors

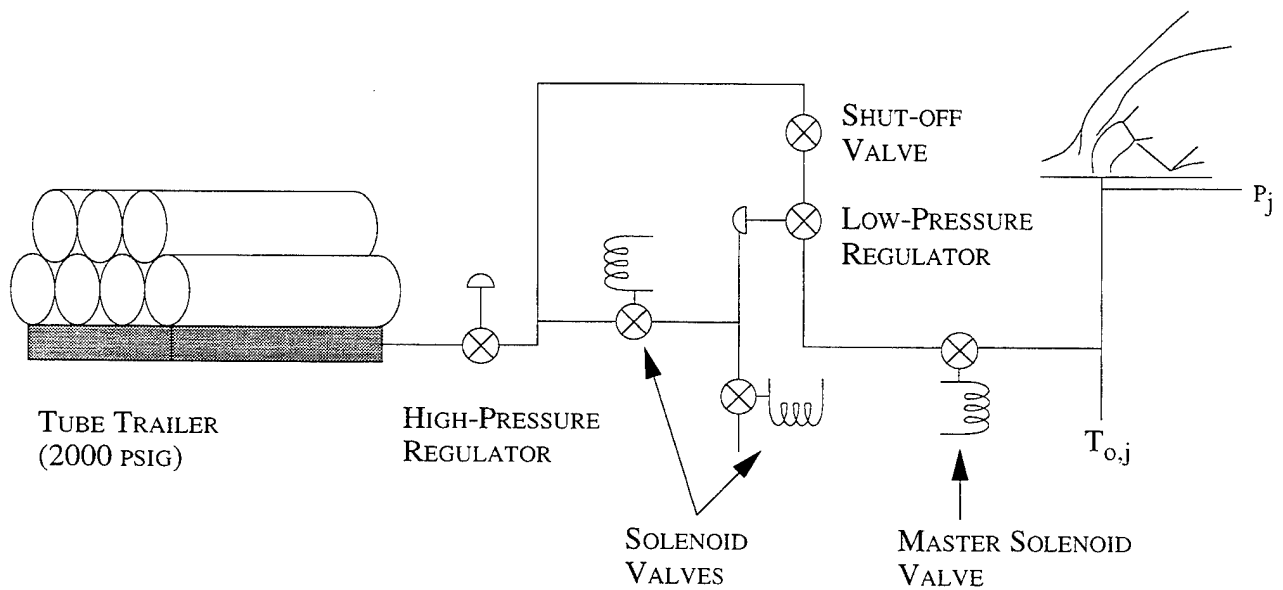


Figure 3.10 Jet Gas Supply Schematic

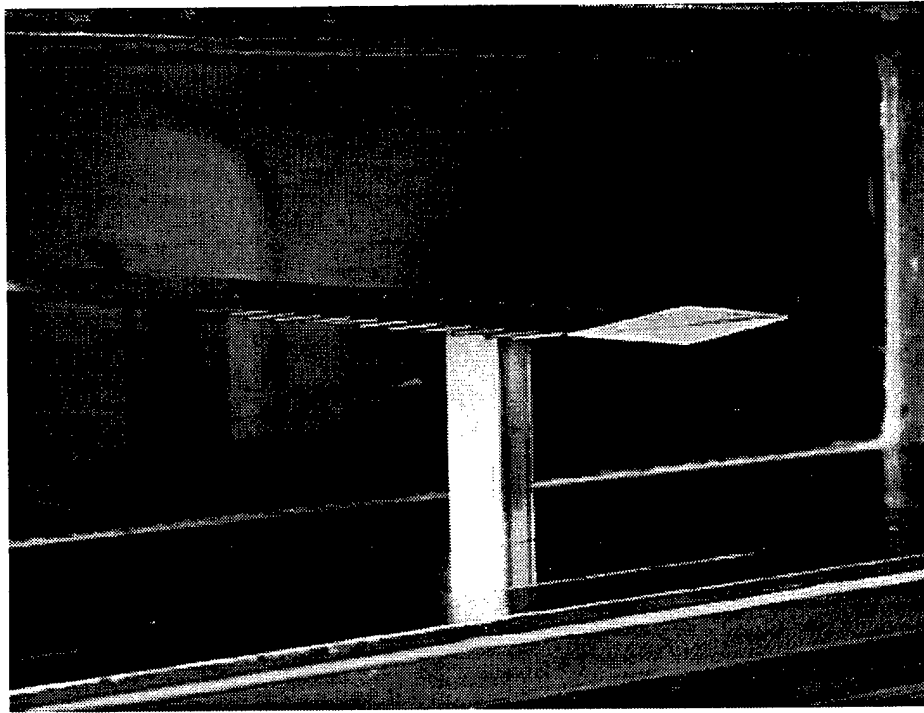


Figure 3.11 Photograph of Pitot Pressure Rake

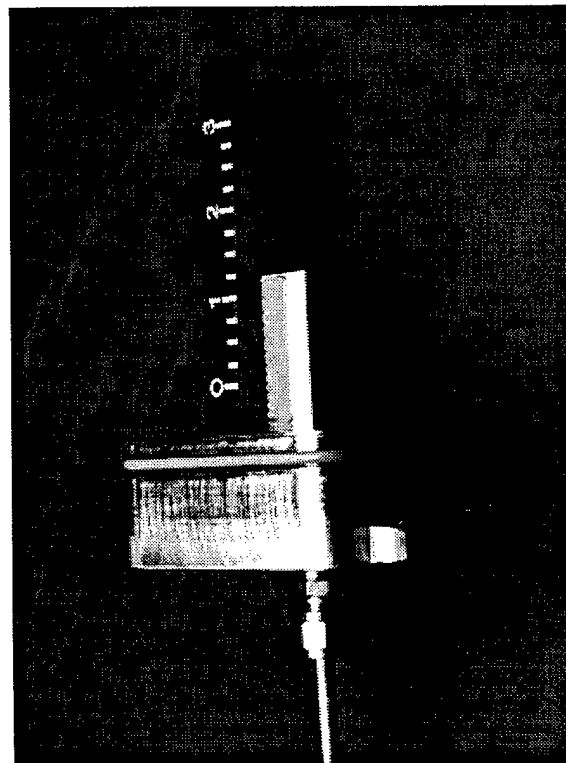


Figure 3.12 Photograph of Boundary Layer Rake

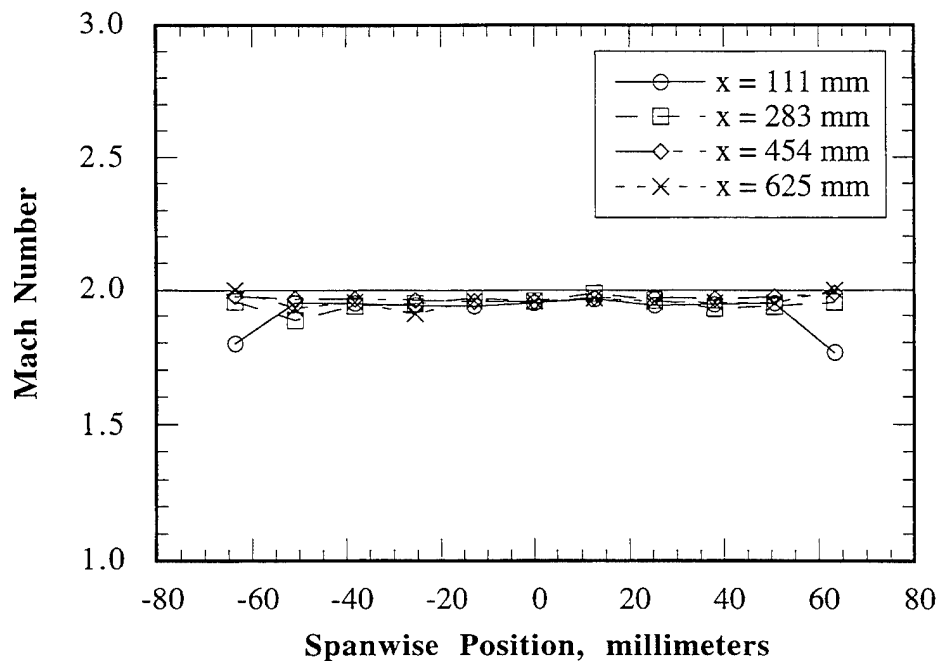


Figure 3.13 Streamwise and Spanwise Mach Number Distributions at Transverse Centerline

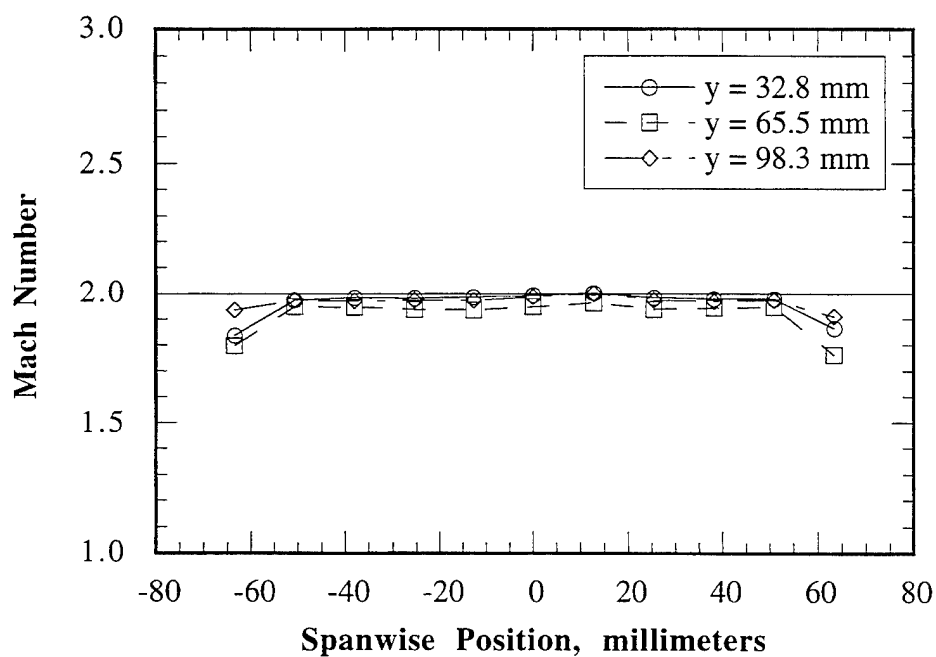


Figure 3.14 Transverse and Spanwise Mach Number Distributions at $x = 111$ mm

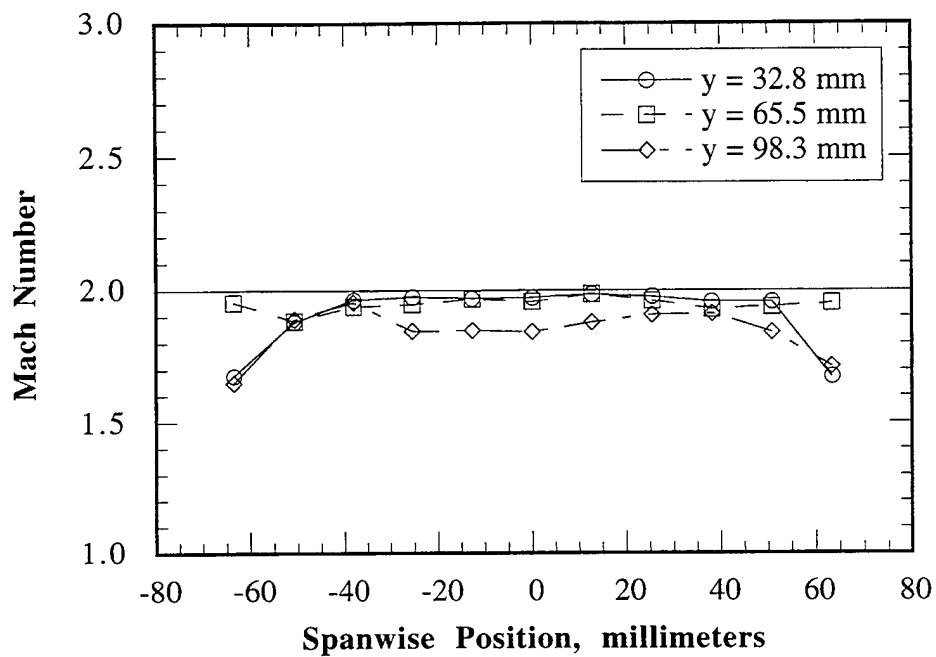


Figure 3.15 Transverse and Spanwise Mach Number Distributions at $x = 283$ mm

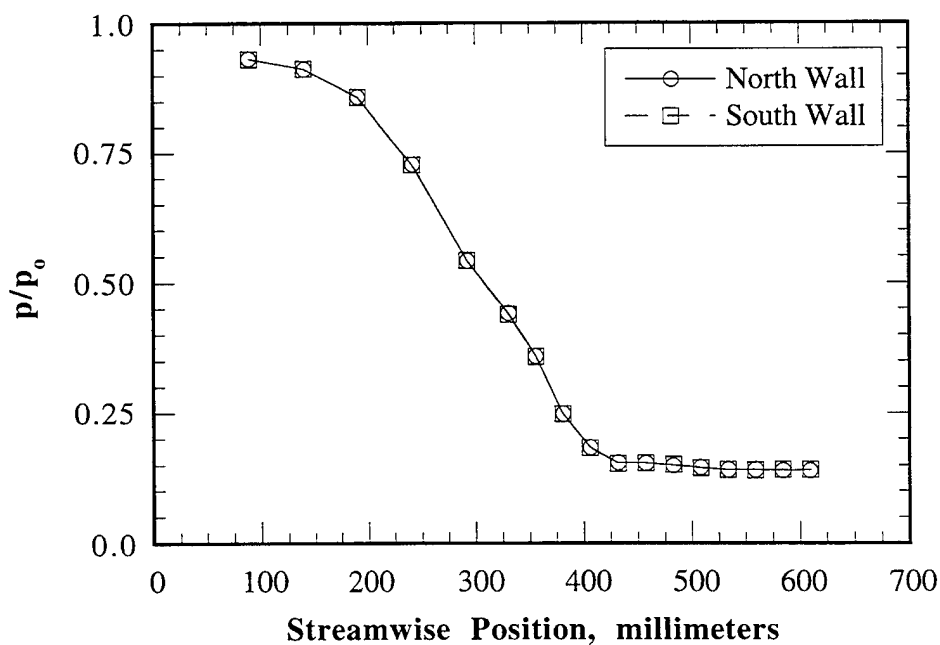


Figure 3.16 Pressure Ratio Profiles from Nozzle Sidewalls at $p_0 = 317$ kPa

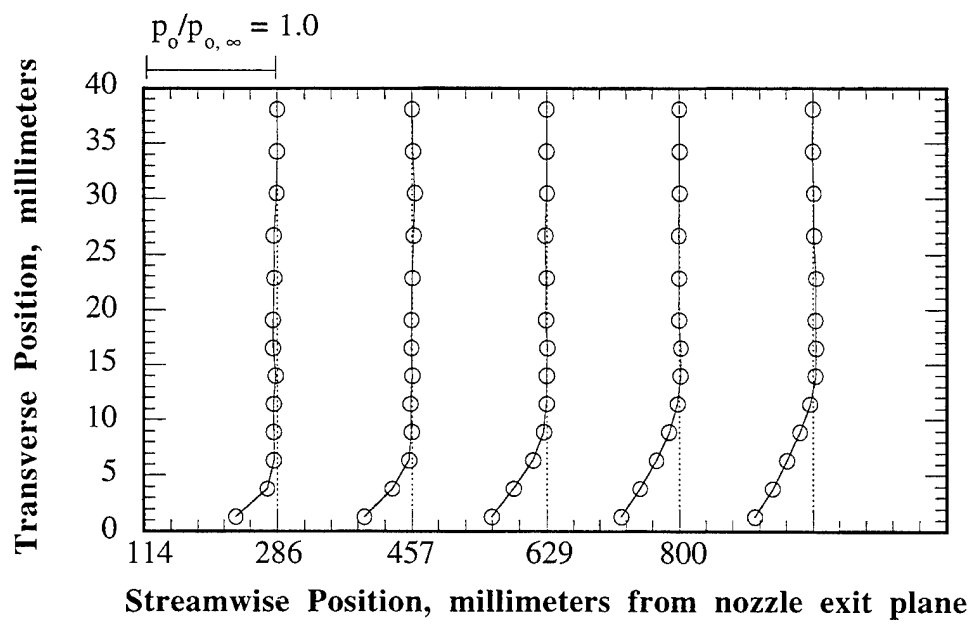


Figure 3.17 Contours of Rake Total Pressure Normalized by Freestream Total Pressure

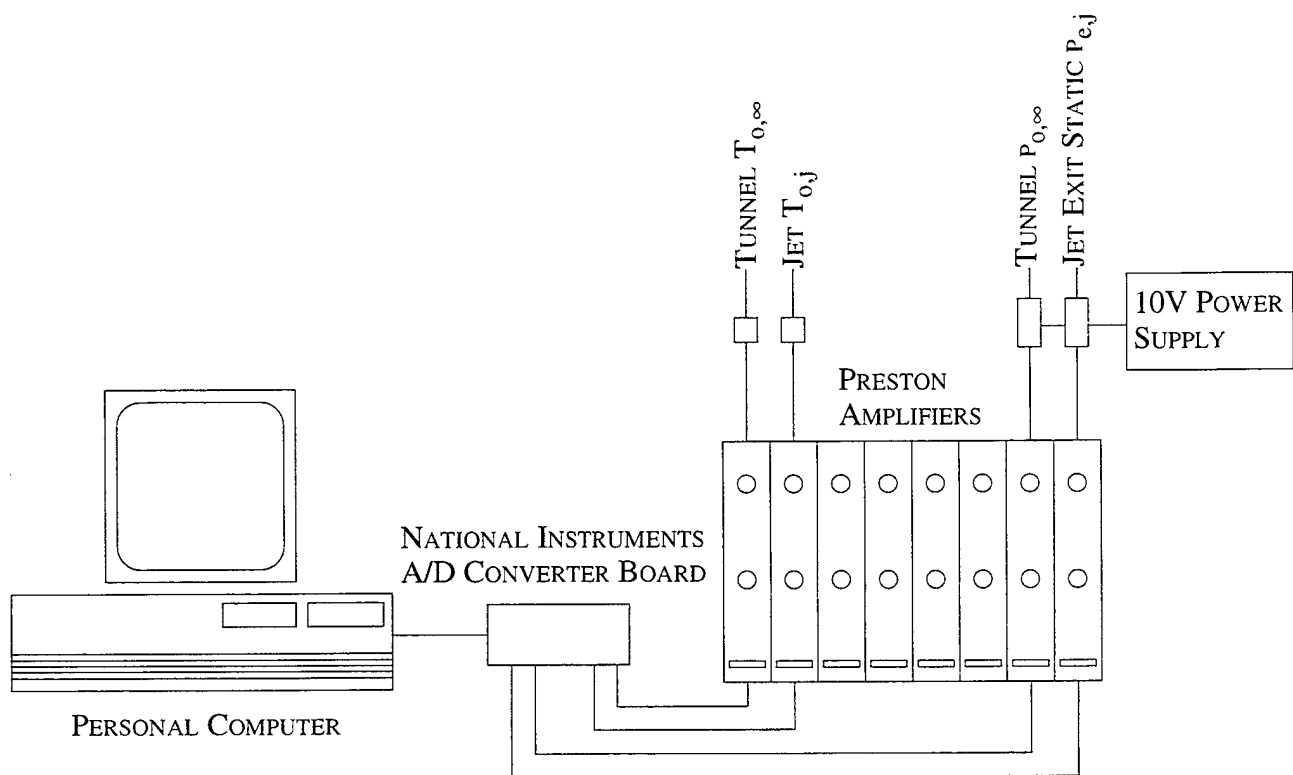


Figure 4.1 Schematic of General Data Acquisition System

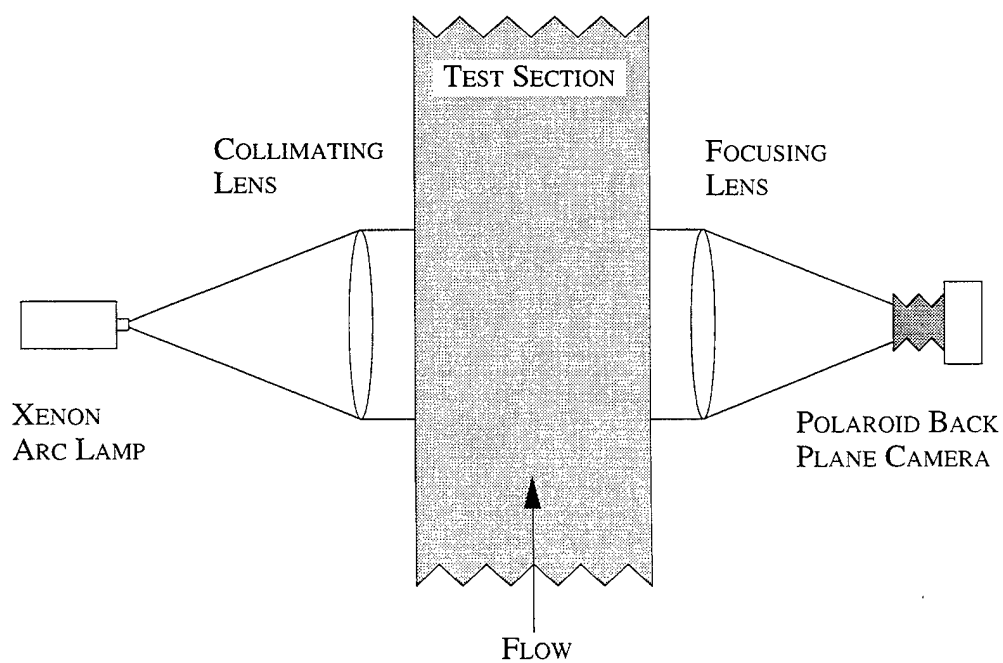


Figure 4.2 Schematic of Pulsed Shadowgraph System

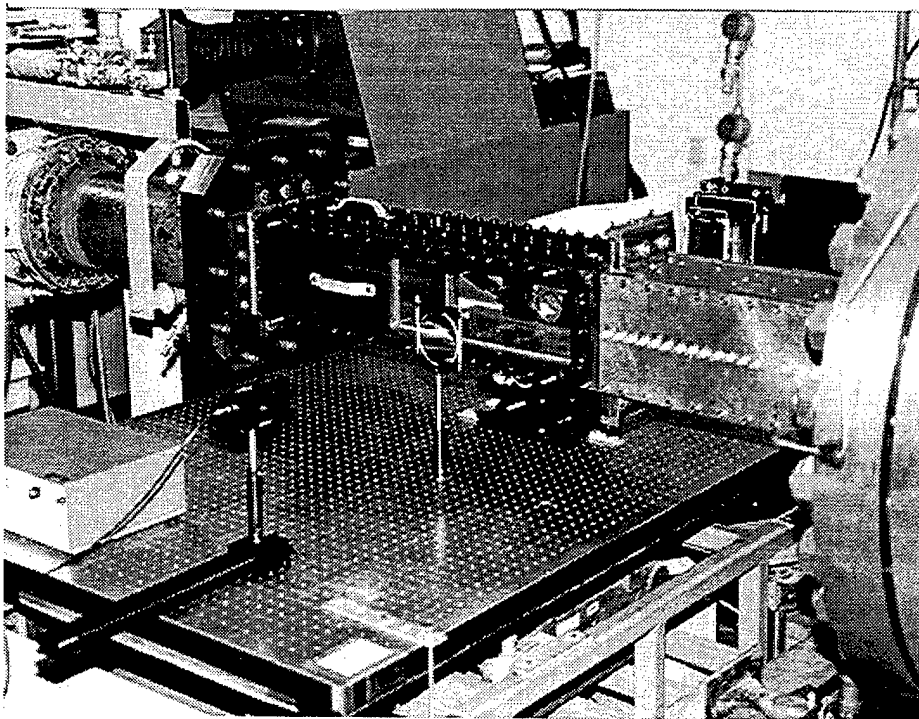


Figure 4.3 Photograph of Pulsed Shadowgraph System

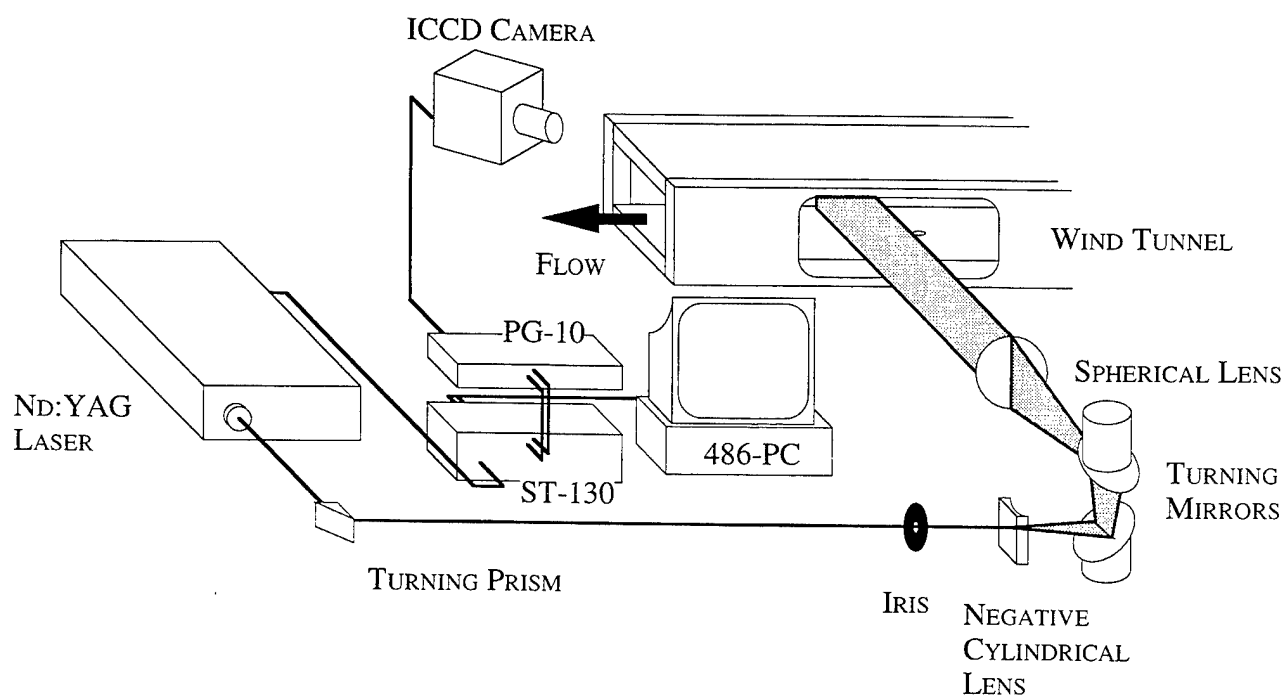


Figure 4.4 Schematic of End View Rayleigh/Mie Scattering Optical Arrangement

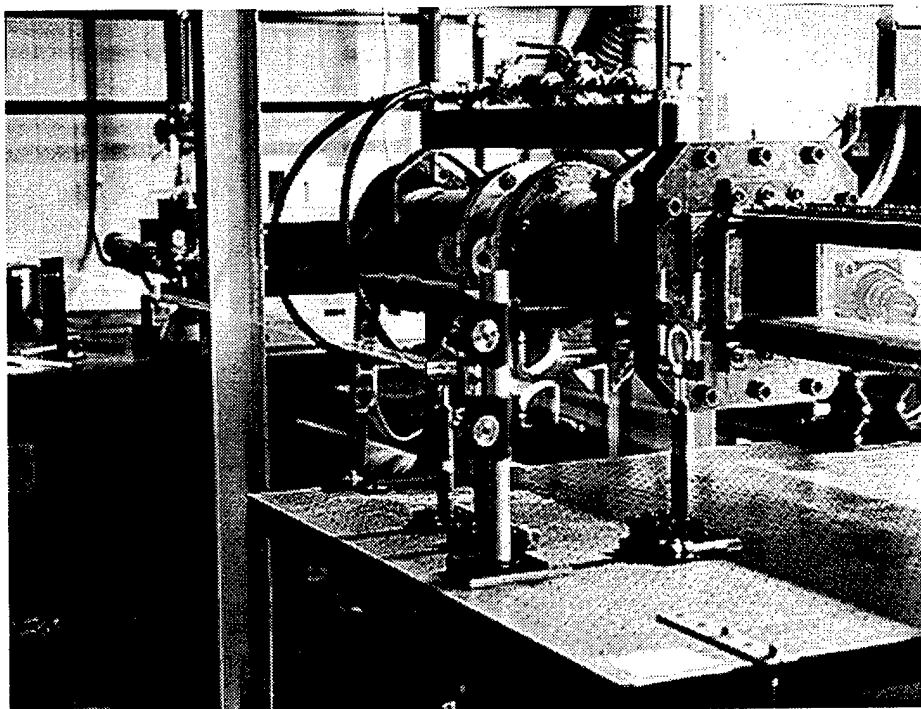


Figure 4.5 Photograph of End View Rayleigh/Mie Scattering Optical Arrangement

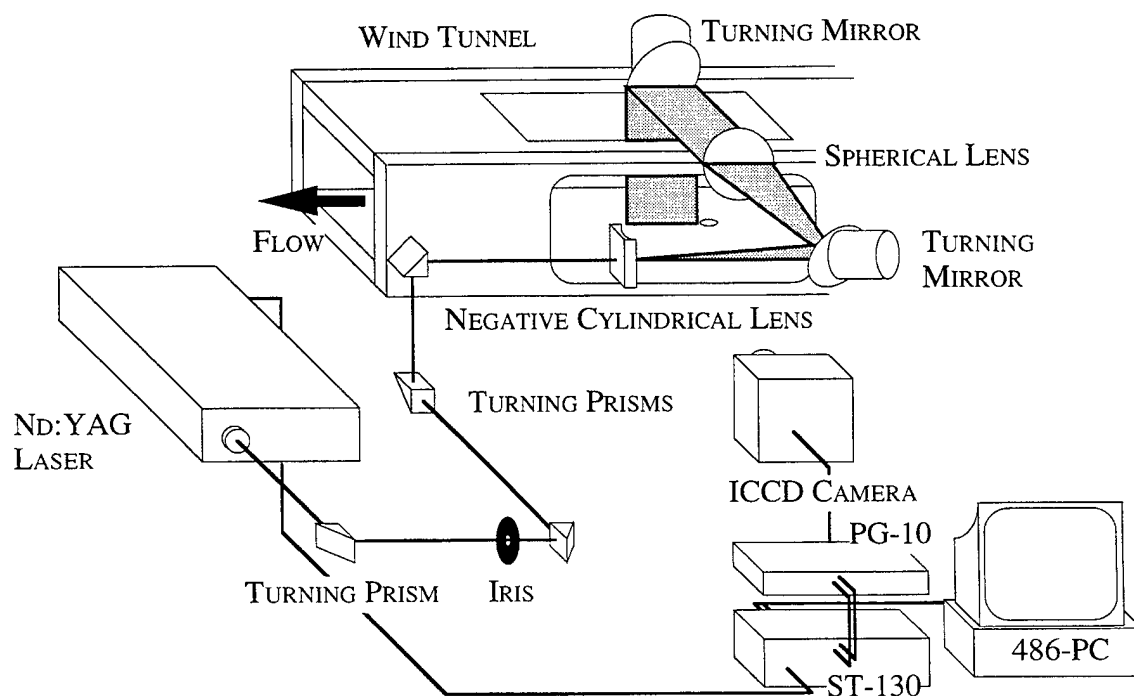


Figure 4.6 Schematic of Side View Rayleigh/Mie Scattering Optical Arrangement (Single Shot)

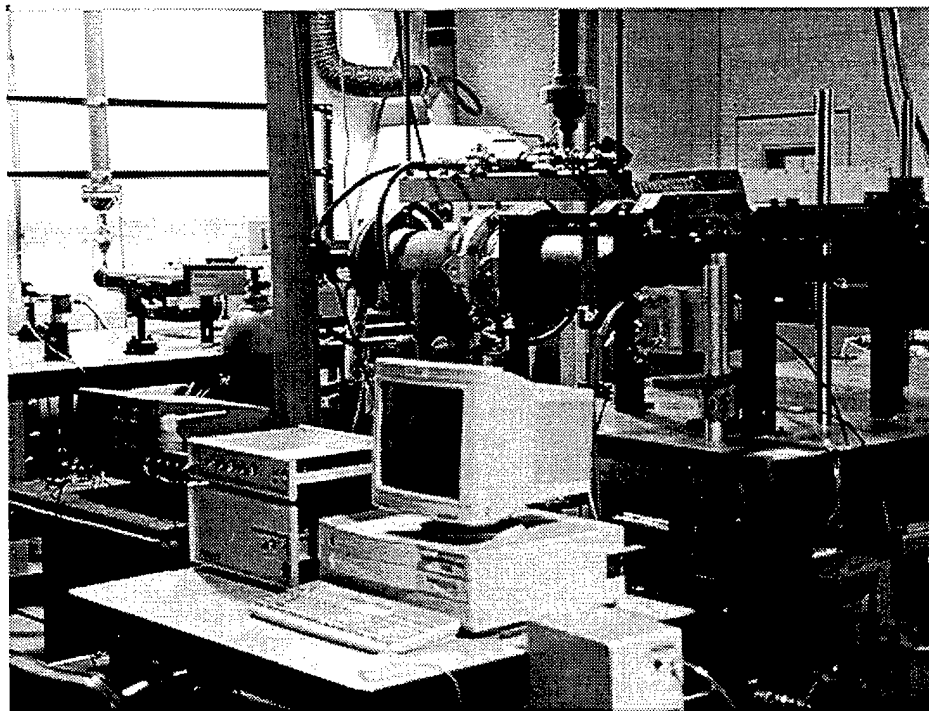


Figure 4.7 Photograph of Side View Rayleigh/Mie Scattering Optical Arrangement (Single Shot)

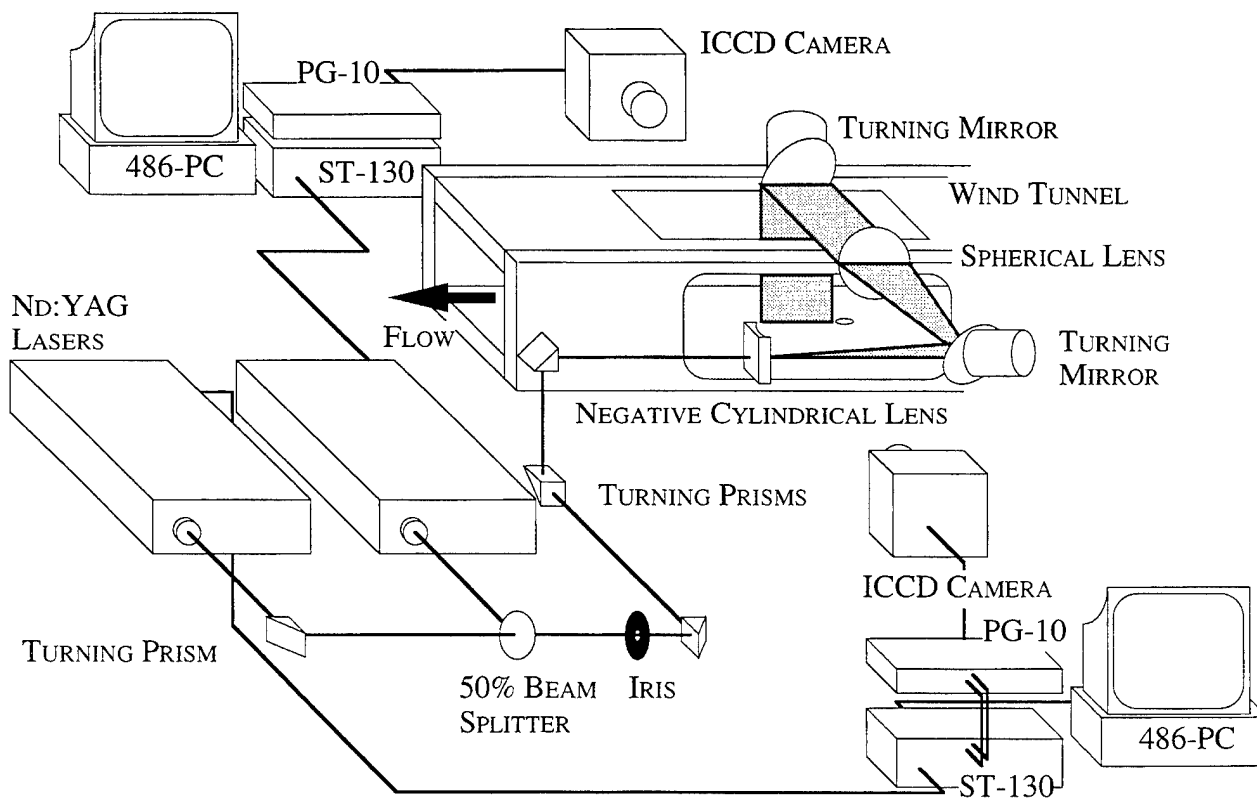


Figure 4.8 Schematic of Double Pulsed Rayleigh/Mie Scattering Optical Arrangement

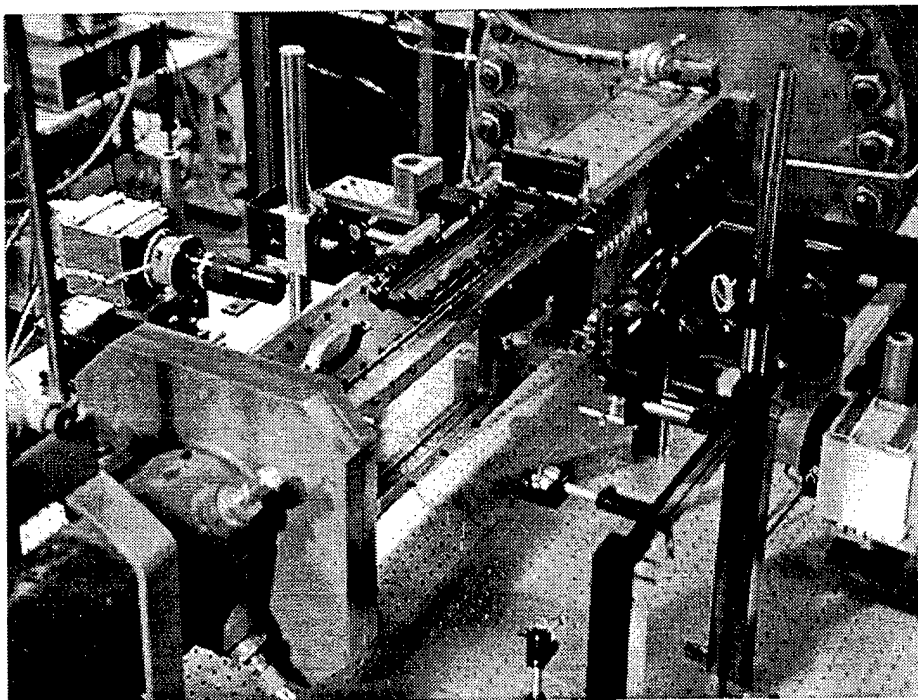


Figure 4.9 Photograph of Double Pulsed Rayleigh/Mie Scattering Optical Arrangement

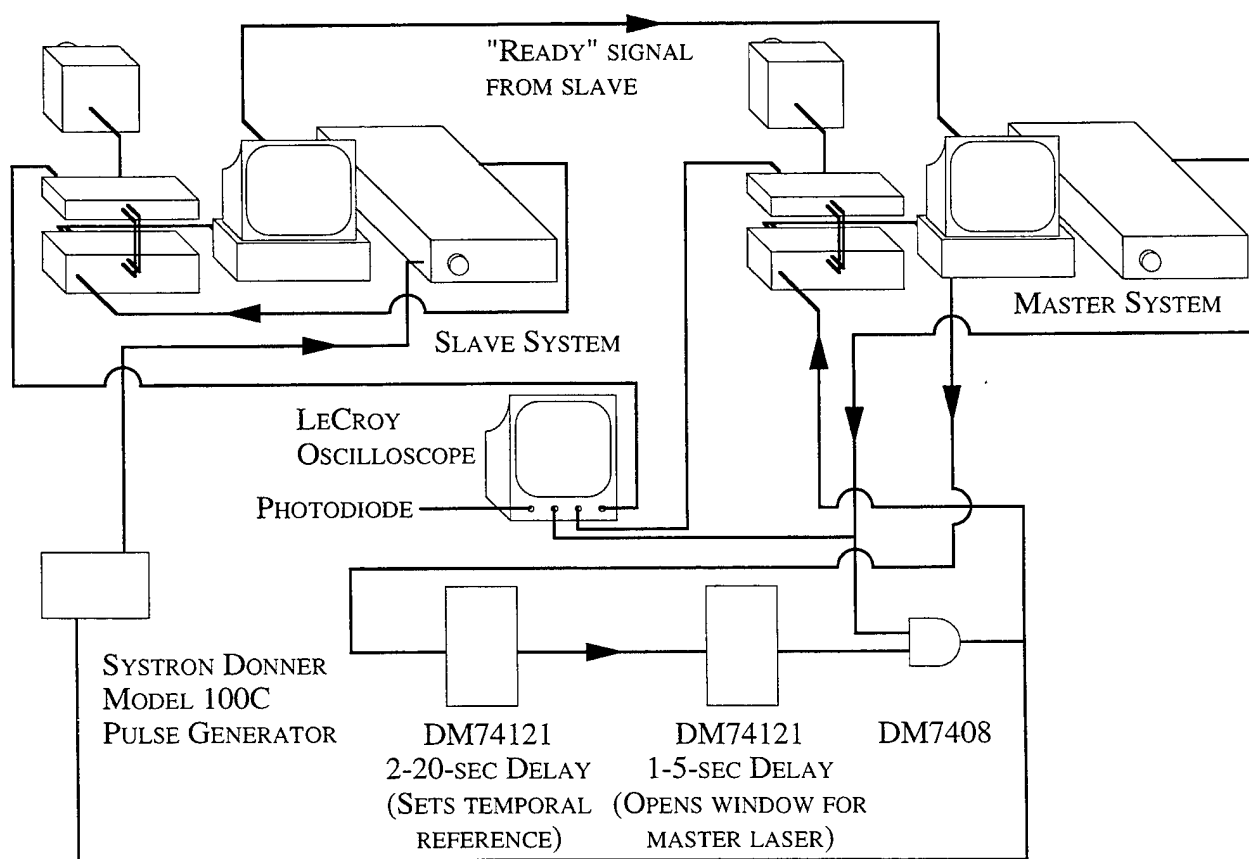


Figure 4.10 Delay System Electrical Schematic

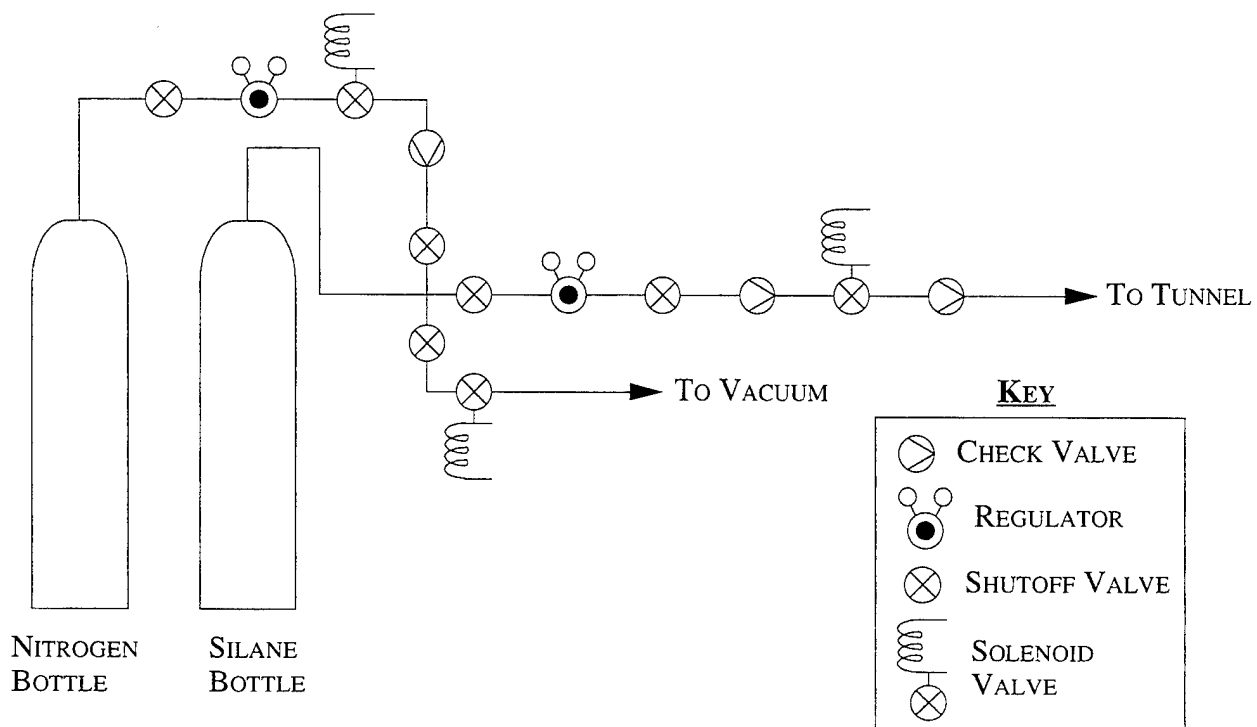


Figure 4.11 Silane Seeding System Schematic

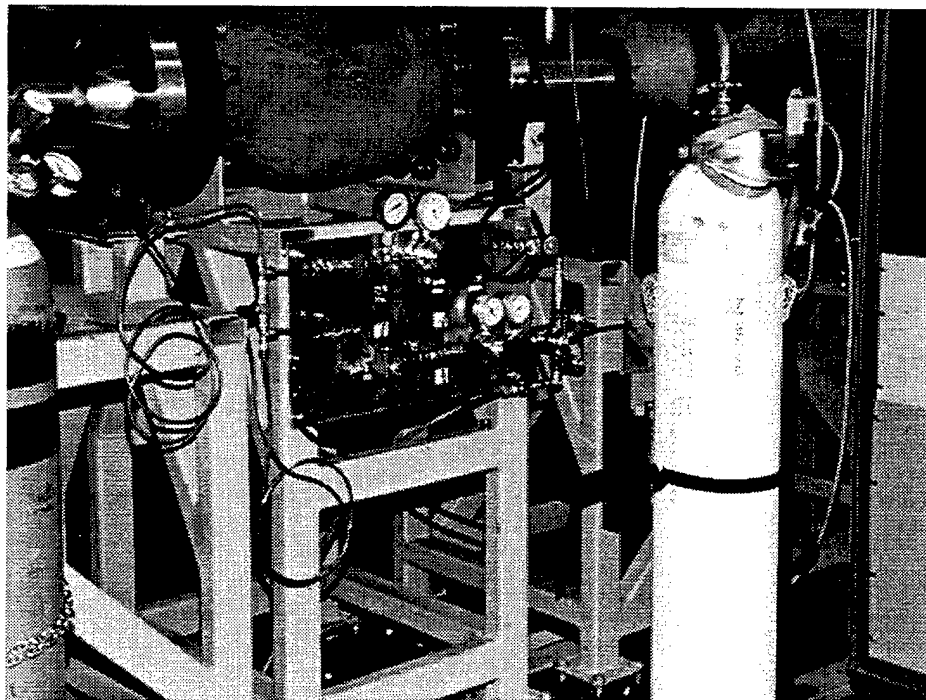


Figure 4.12 Photograph of Silane Seeding System

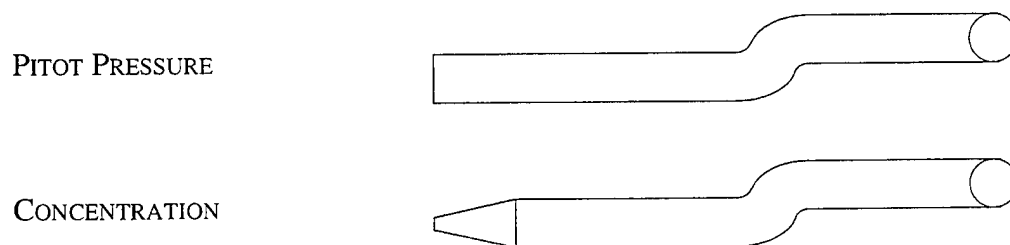


Figure 4.13 Illustration of Mean Flow Probe Designs (Side View)

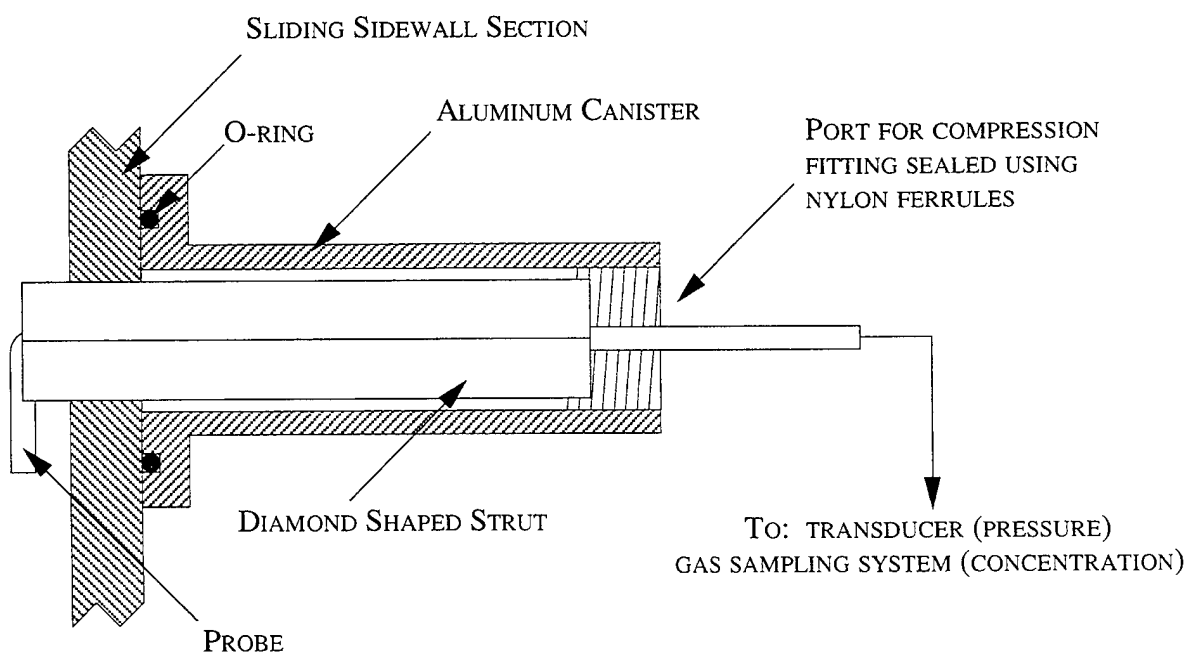


Figure 4.14 Schematic of Probe Installation

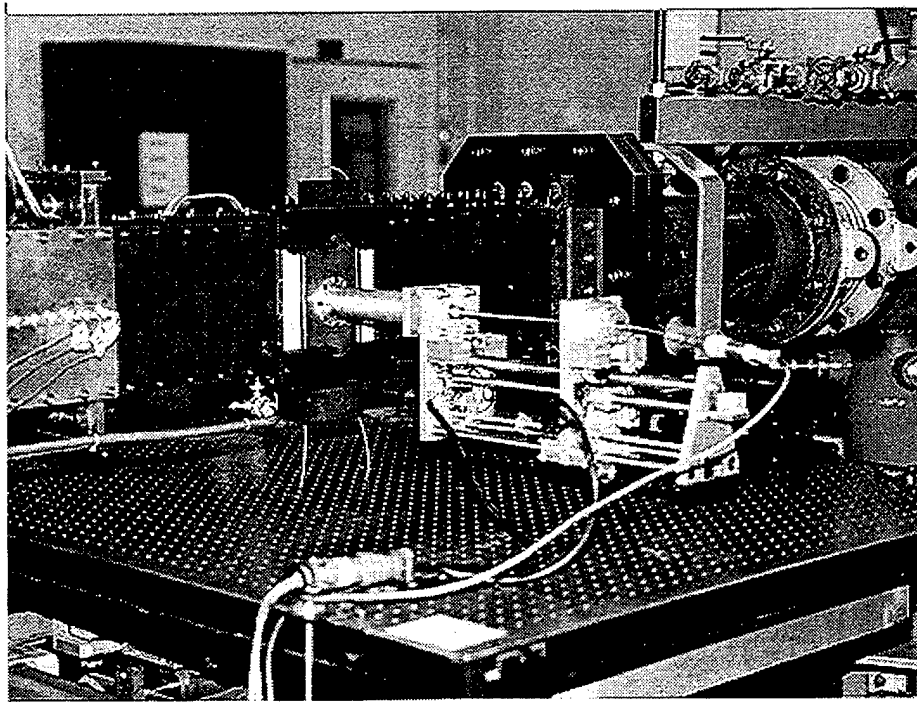


Figure 4.15 Photograph Showing Probe Drive Hardware

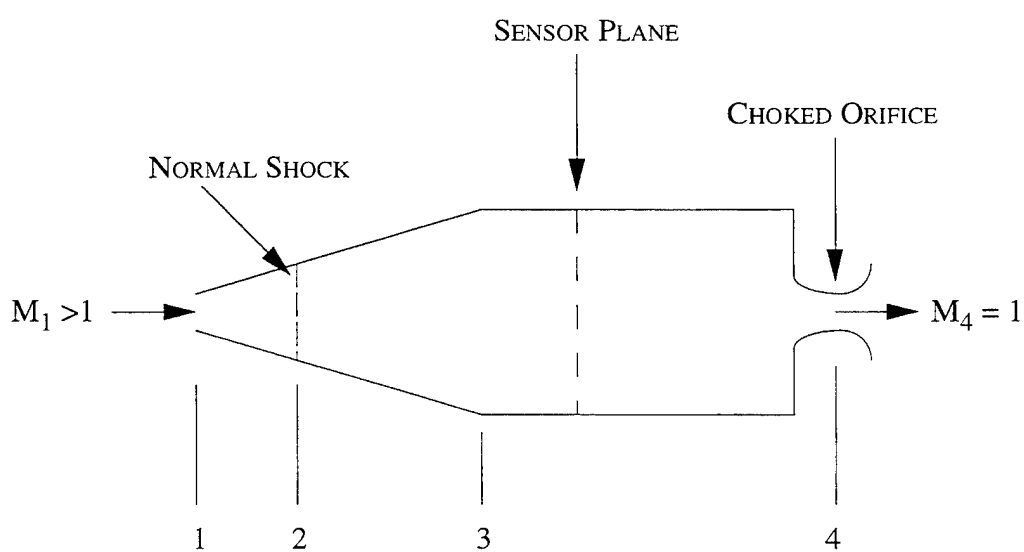


Figure 4.16 Model of Concentration Probe

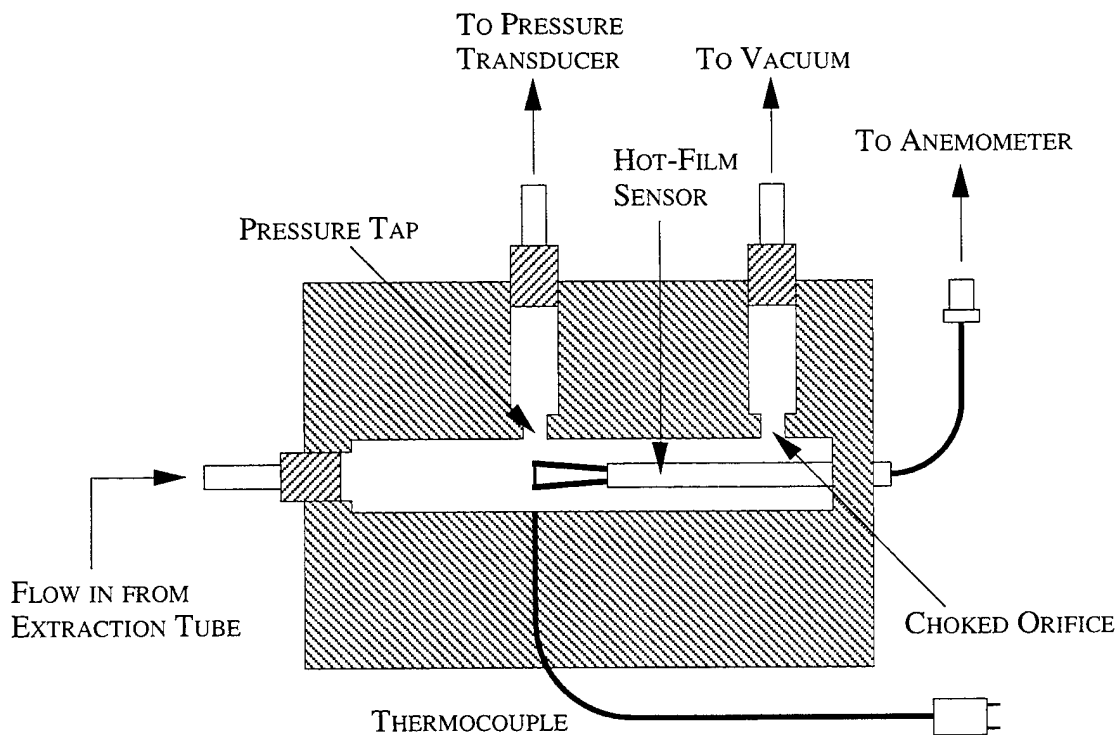


Figure 4.17 Schematic of Sampling Vessel

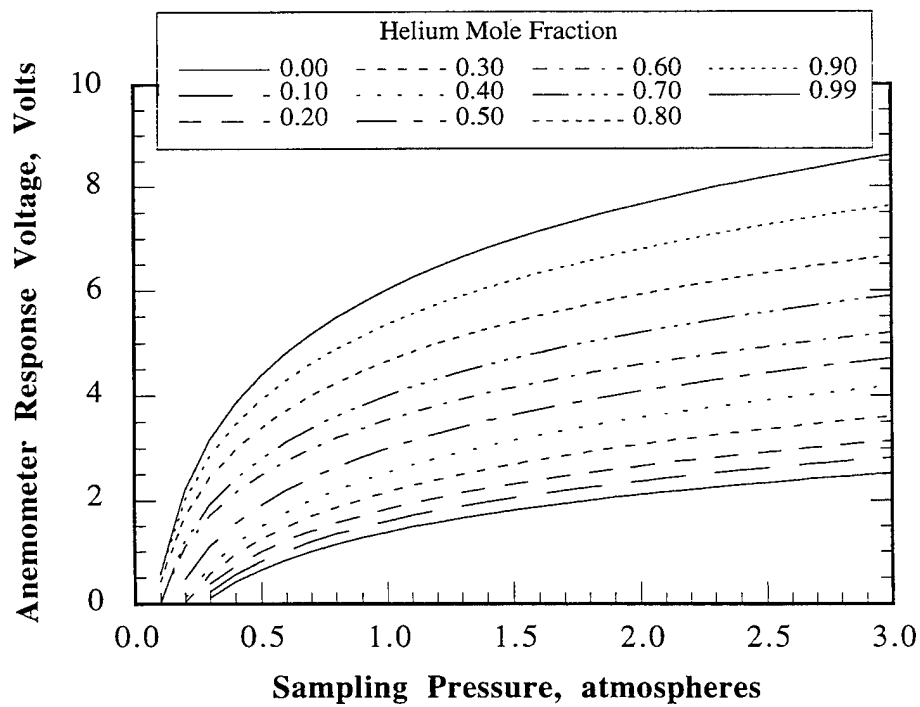


Figure 4.18 Concentration Probe Calibration Profiles

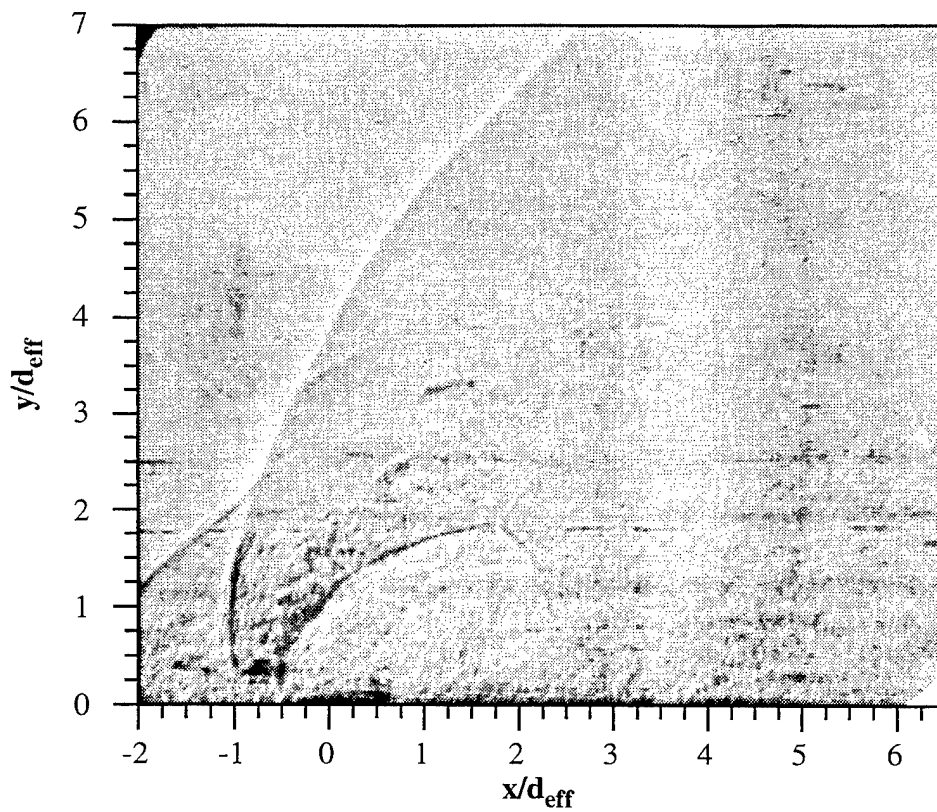


Figure 5.1 Shadowgraph of Circular Injection Using Air (Case C1A)

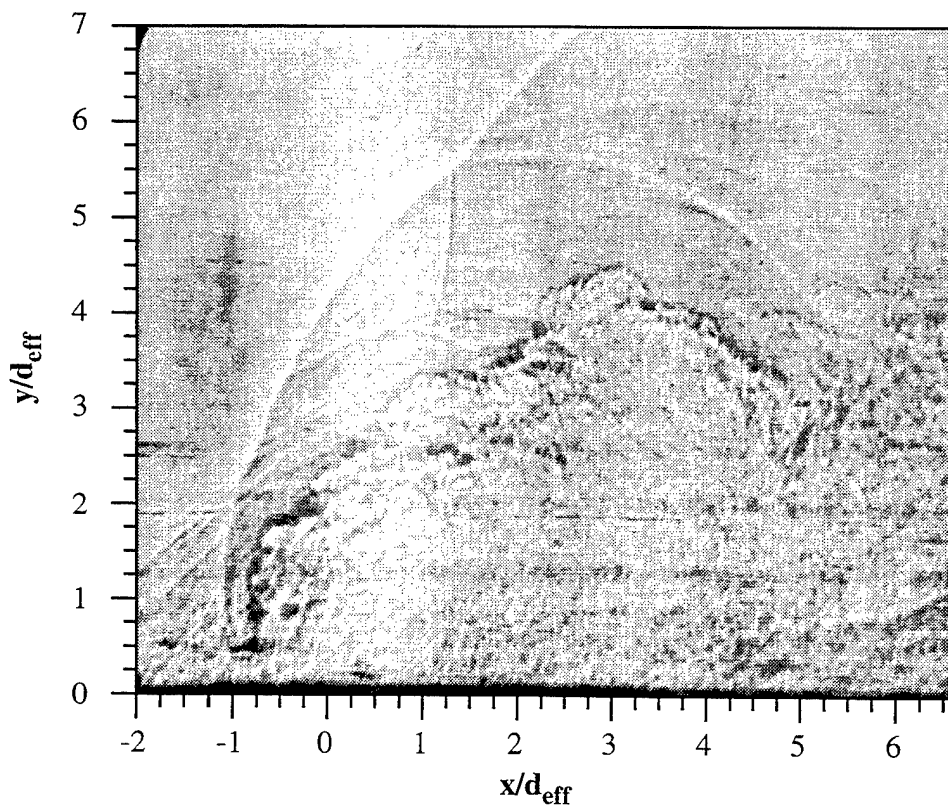


Figure 5.2 Shadowgraph of Circular Injection Using Helium (Case C2H)

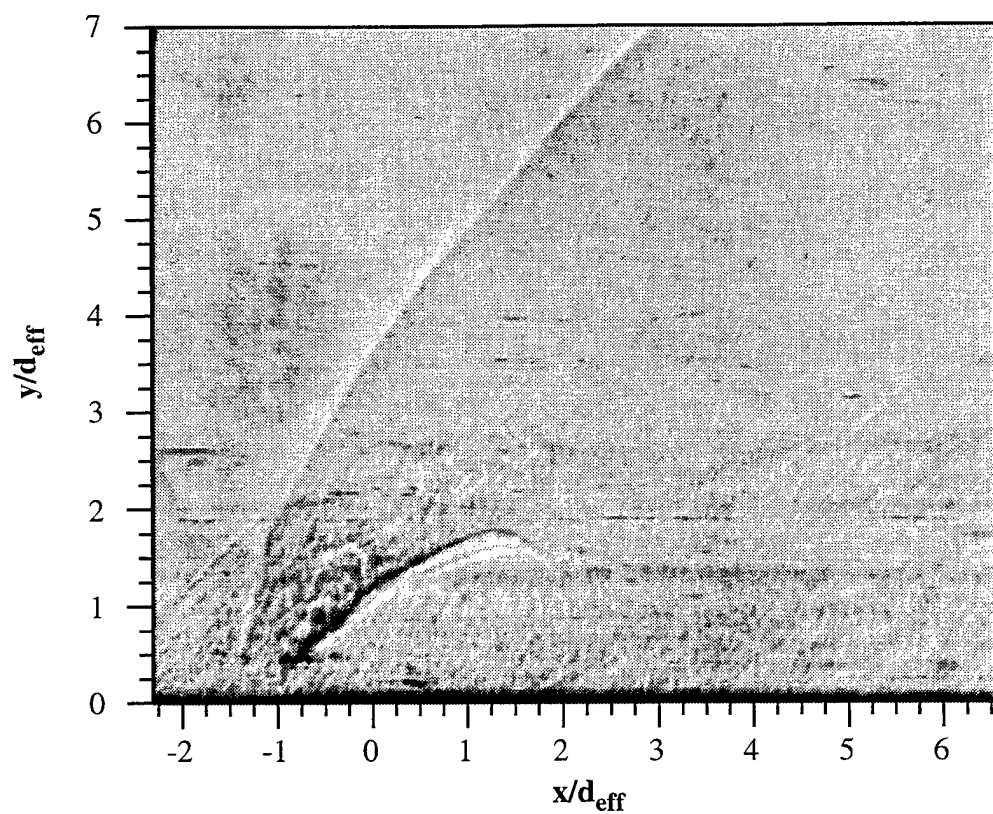


Figure 5.3 Shadowgraph of Elliptical Injection Using Air (Case E1A)

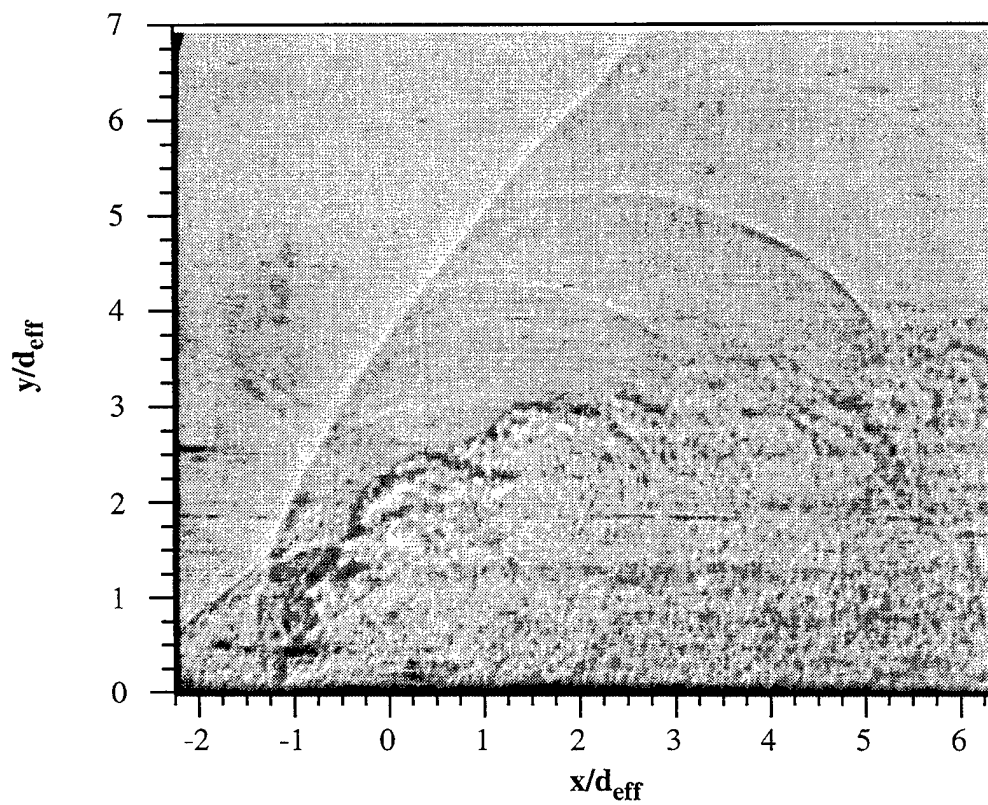
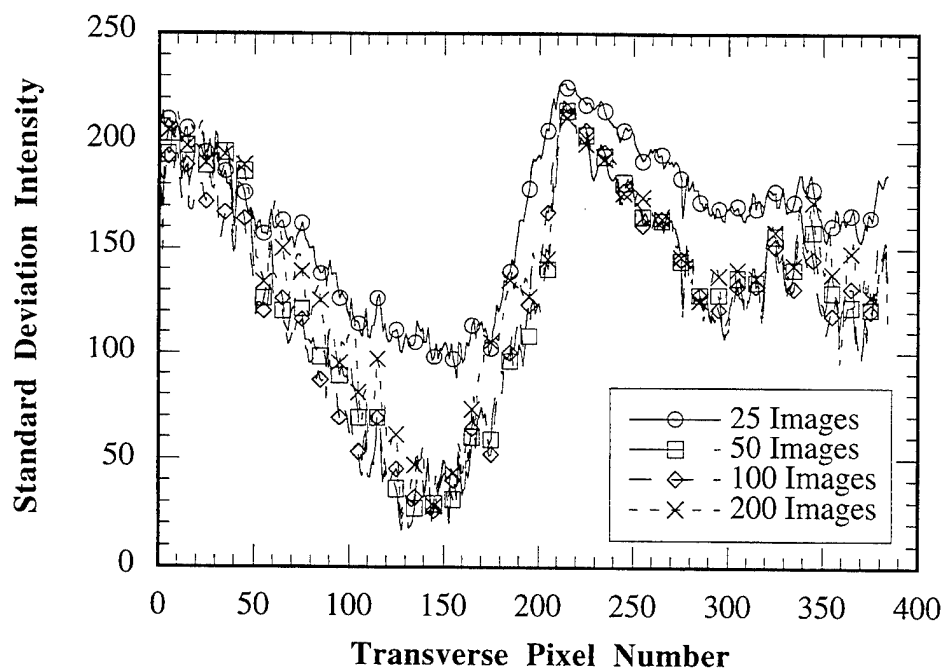
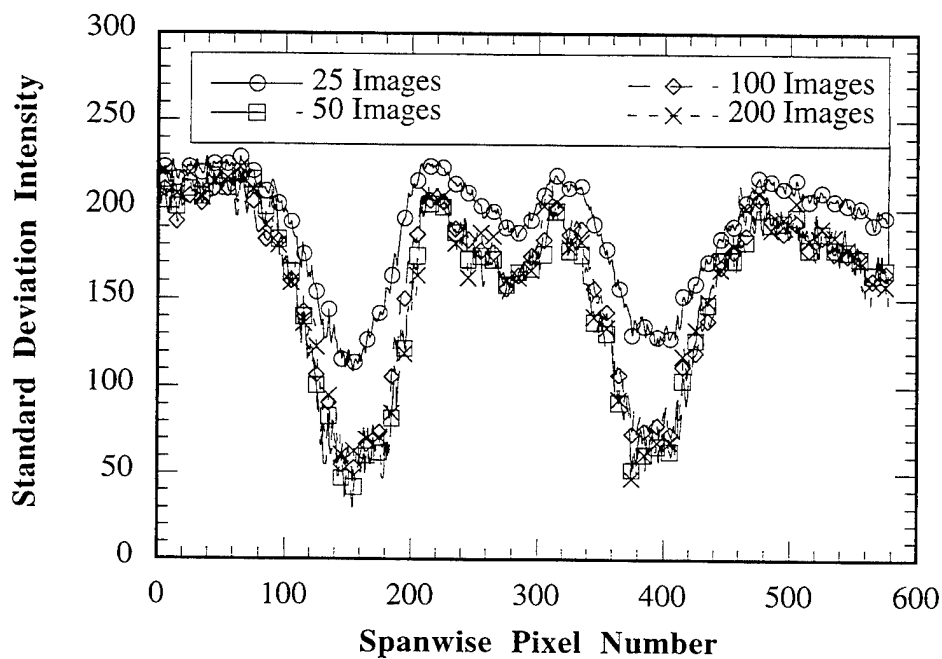


Figure 5.4 Shadowgraph of Elliptical Injection Using Helium (Case E2H)



a) Transverse Data Trace from $z/d_{\text{eff}} = 0$



b) Spanwise Data Trace from $y/d_{\text{eff}} = 1.8$

Figure 5.5 Standard Deviation Intensity Traces from Case C1A at $x/d_{\text{eff}} = 4$
a) Transverse Data Trace from $z/d_{\text{eff}} = 0$ and b) Spanwise Data Trace from $y/d_{\text{eff}} = 1.8$

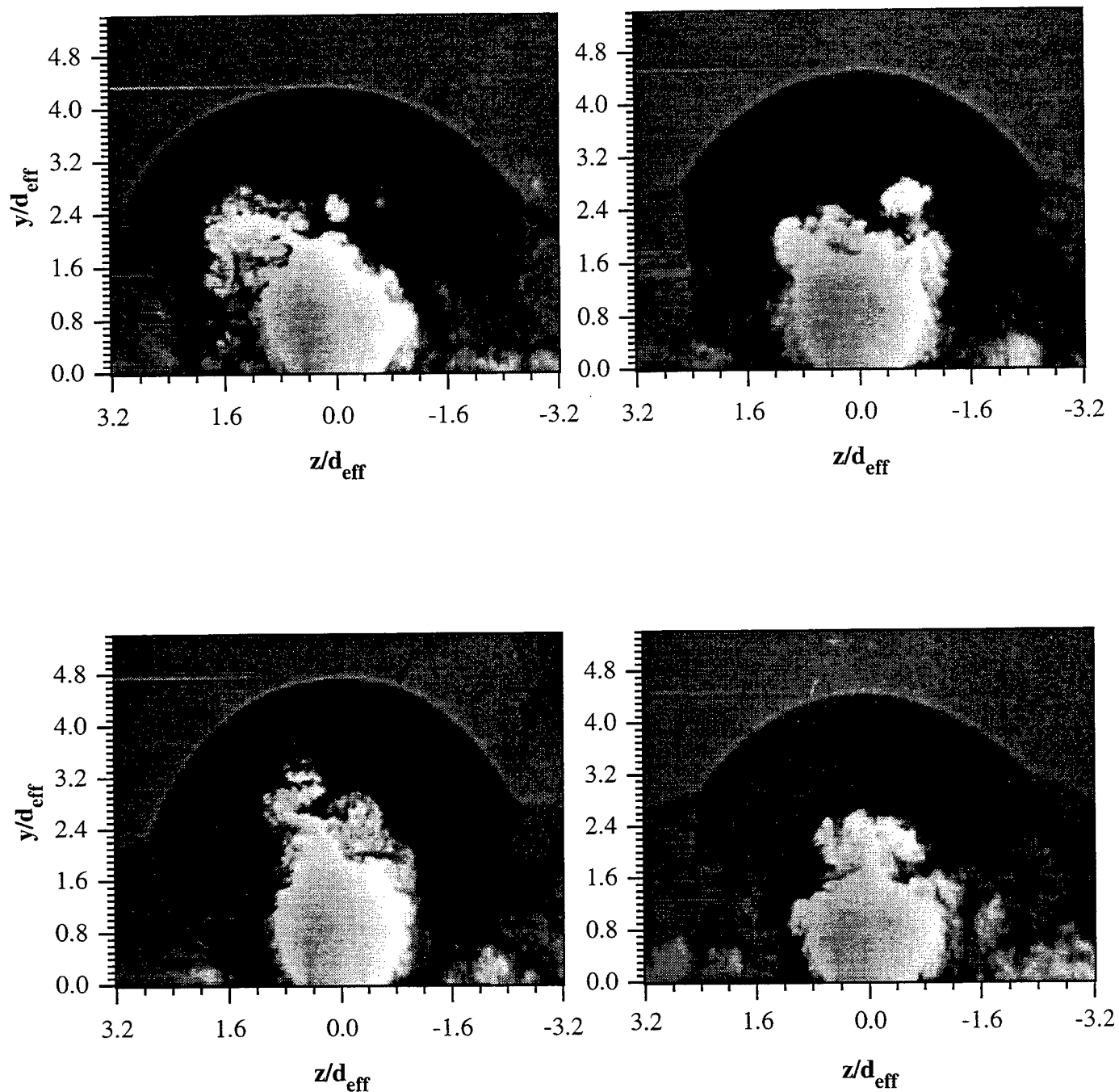


Figure 5.6 Instantaneous End View Images of Circular Injection Using Air
(Case C1A) at $x/d_{\text{eff}} = 0$

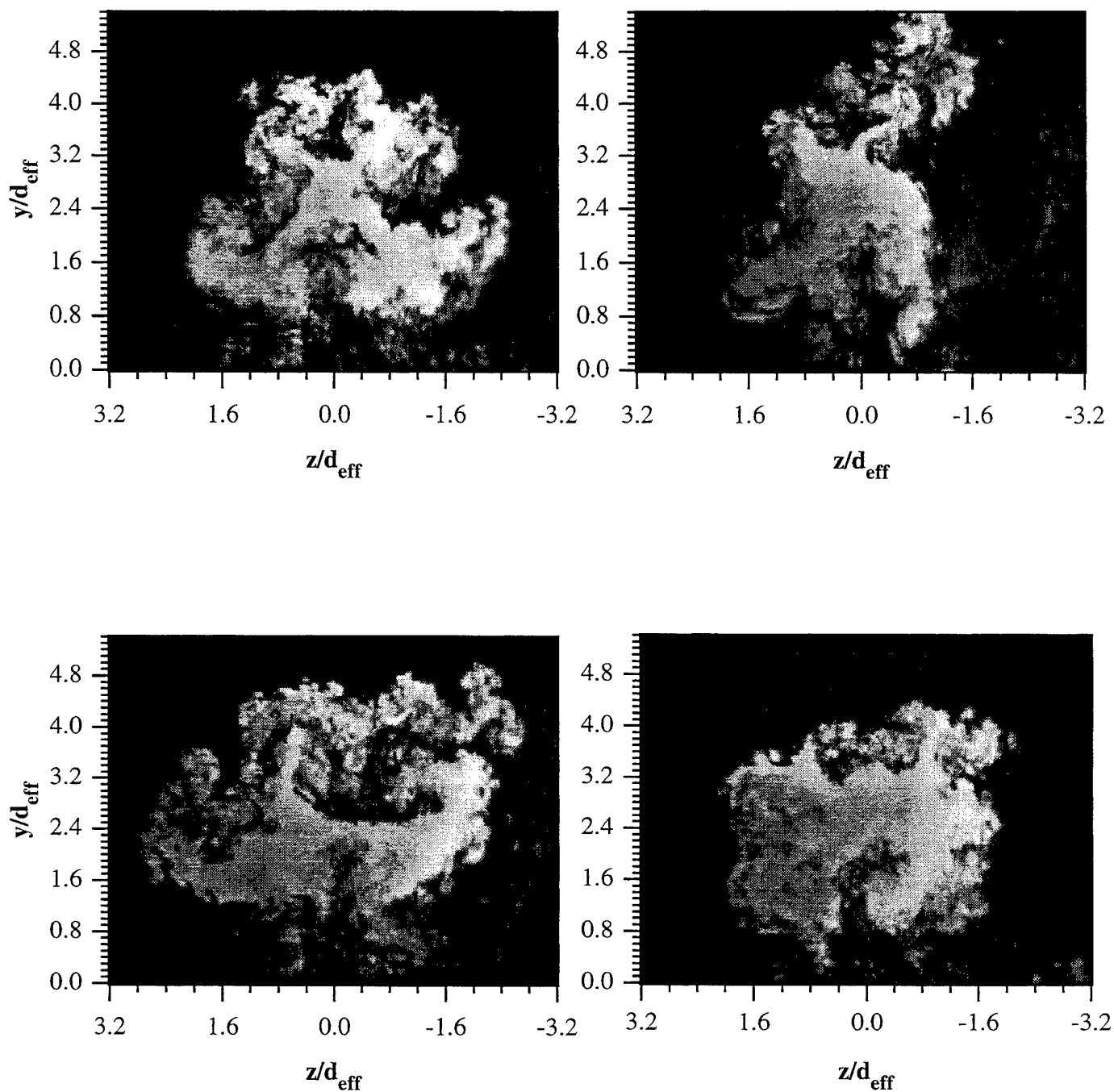


Figure 5.7 Instantaneous End View Images of Circular Injection Using Air
(Case C1A) at $x/d_{\text{eff}} = 4$

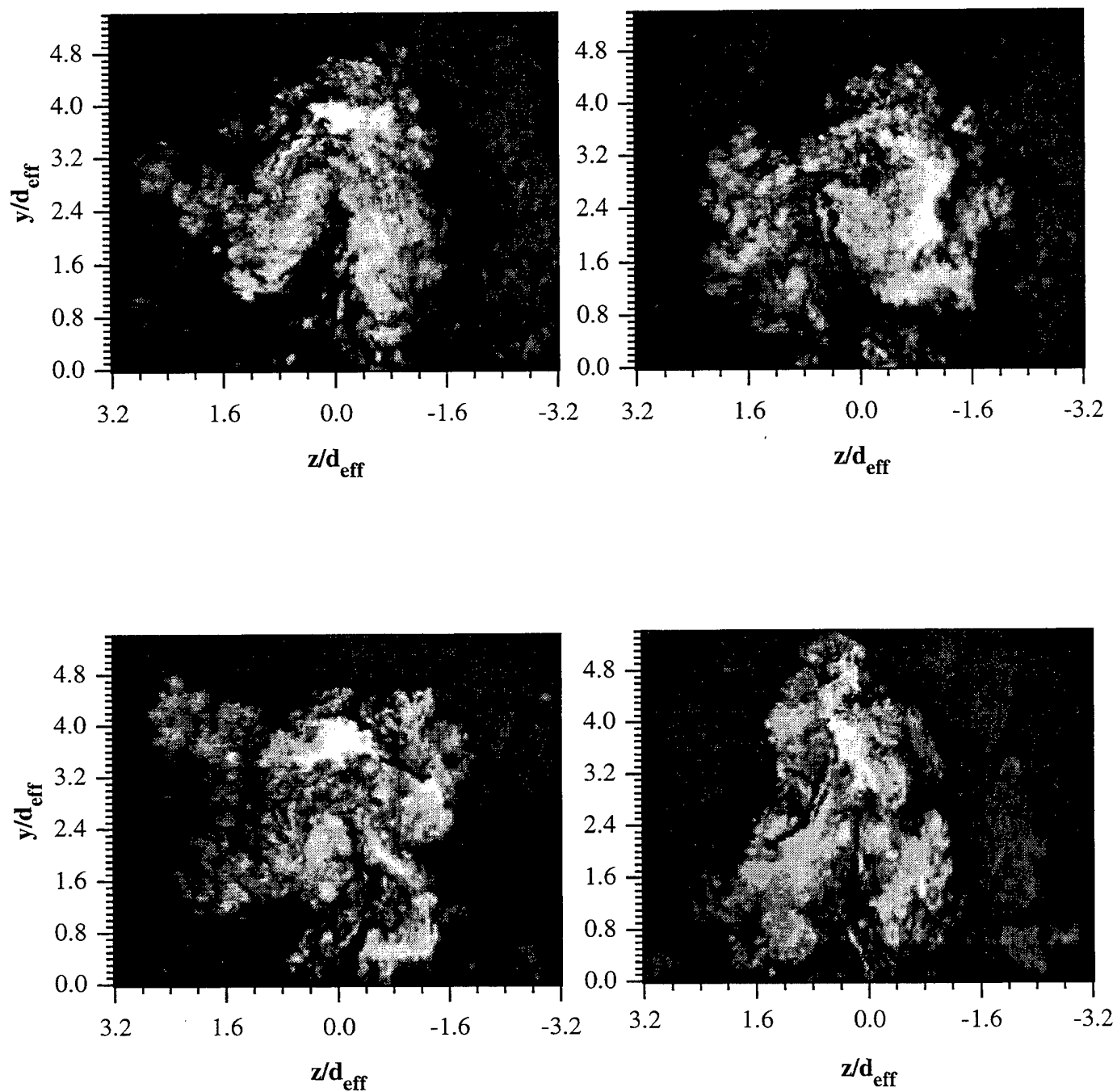


Figure 5.8 Instantaneous End View Images of Circular Injection Using Air
(Case C1A) at $x/d_{\text{eff}} = 8$

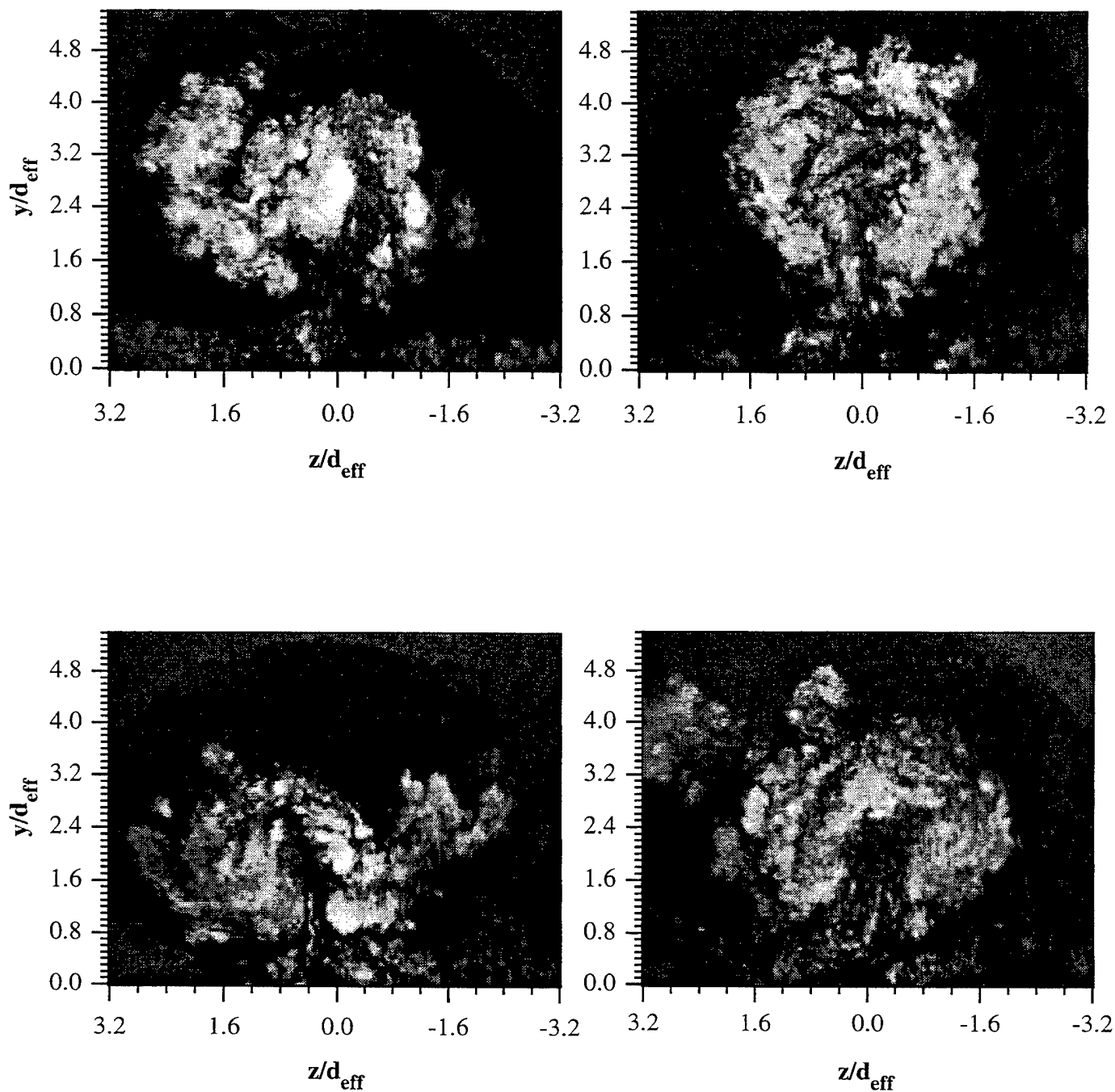


Figure 5.9 Instantaneous End View Images of Circular Injection Using Air
(Case C1A) at $x/d_{\text{eff}} = 10$

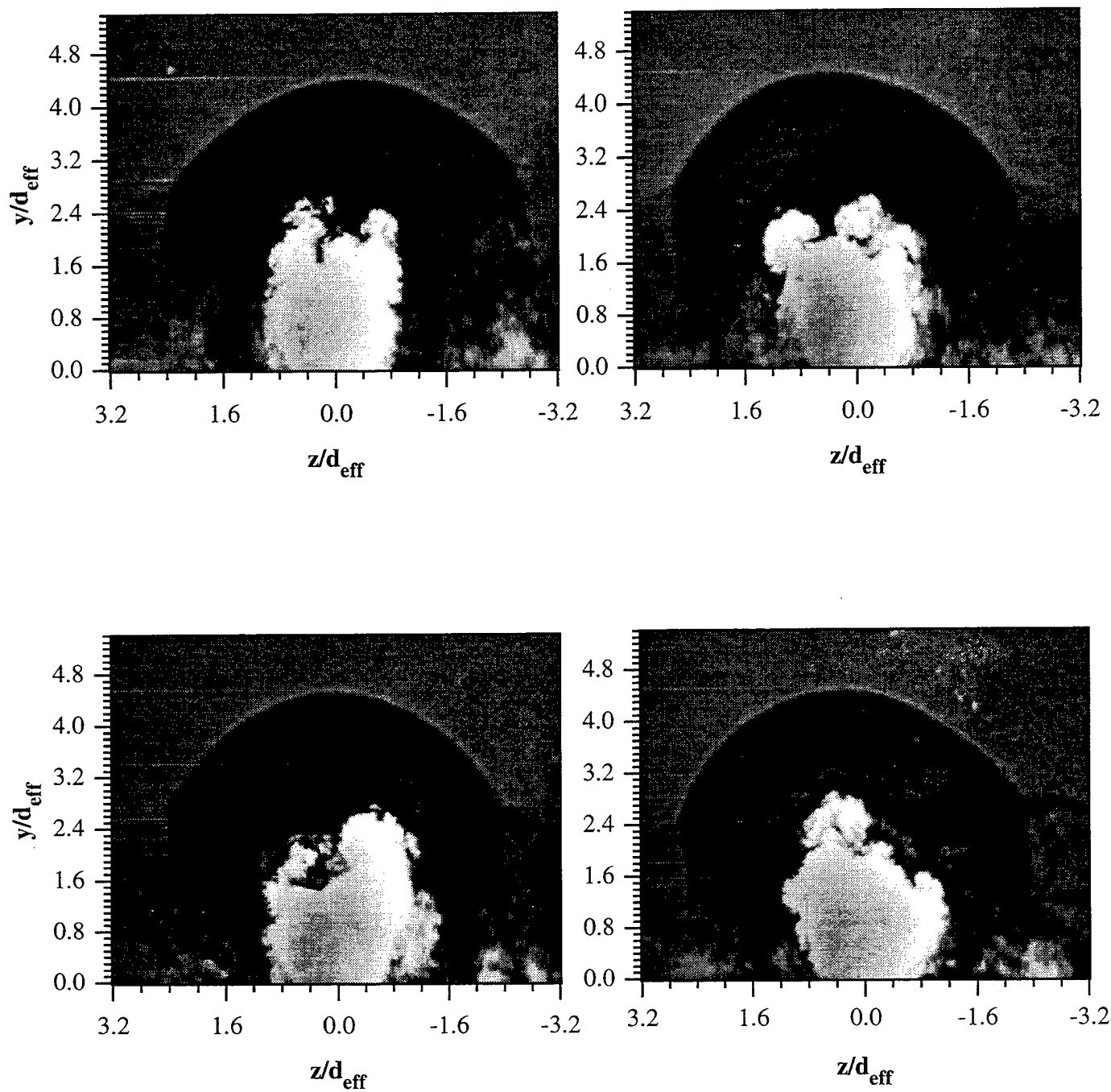


Figure 5.10 Instantaneous End View Images of Circular Injection Using Helium
(Case C2H) at $x/d_{\text{eff}} = 0$

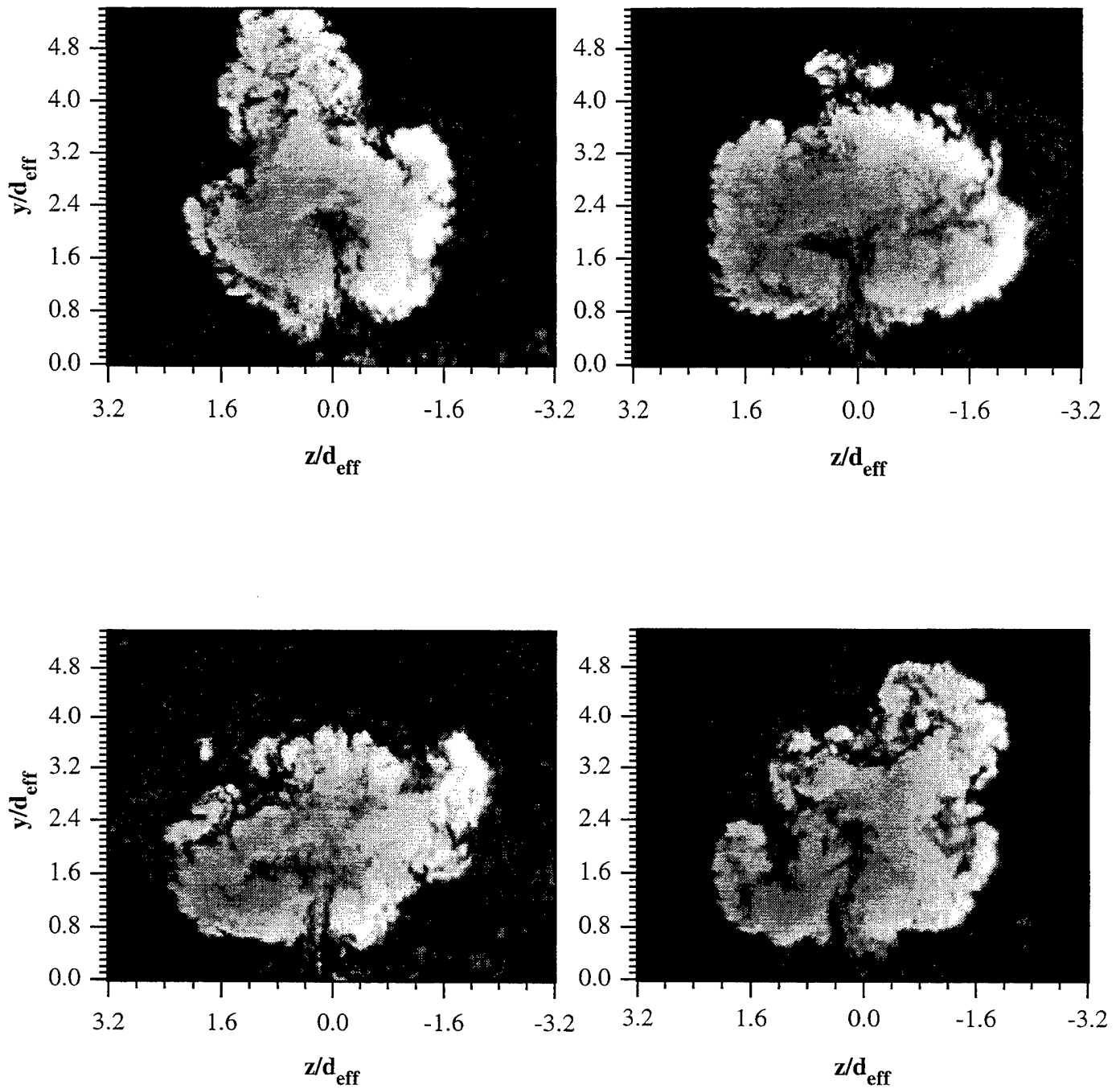


Figure 5.11 Instantaneous End View Images of Circular Injection Using Helium
(Case C2H) at $x/d_{\text{eff}} = 4$

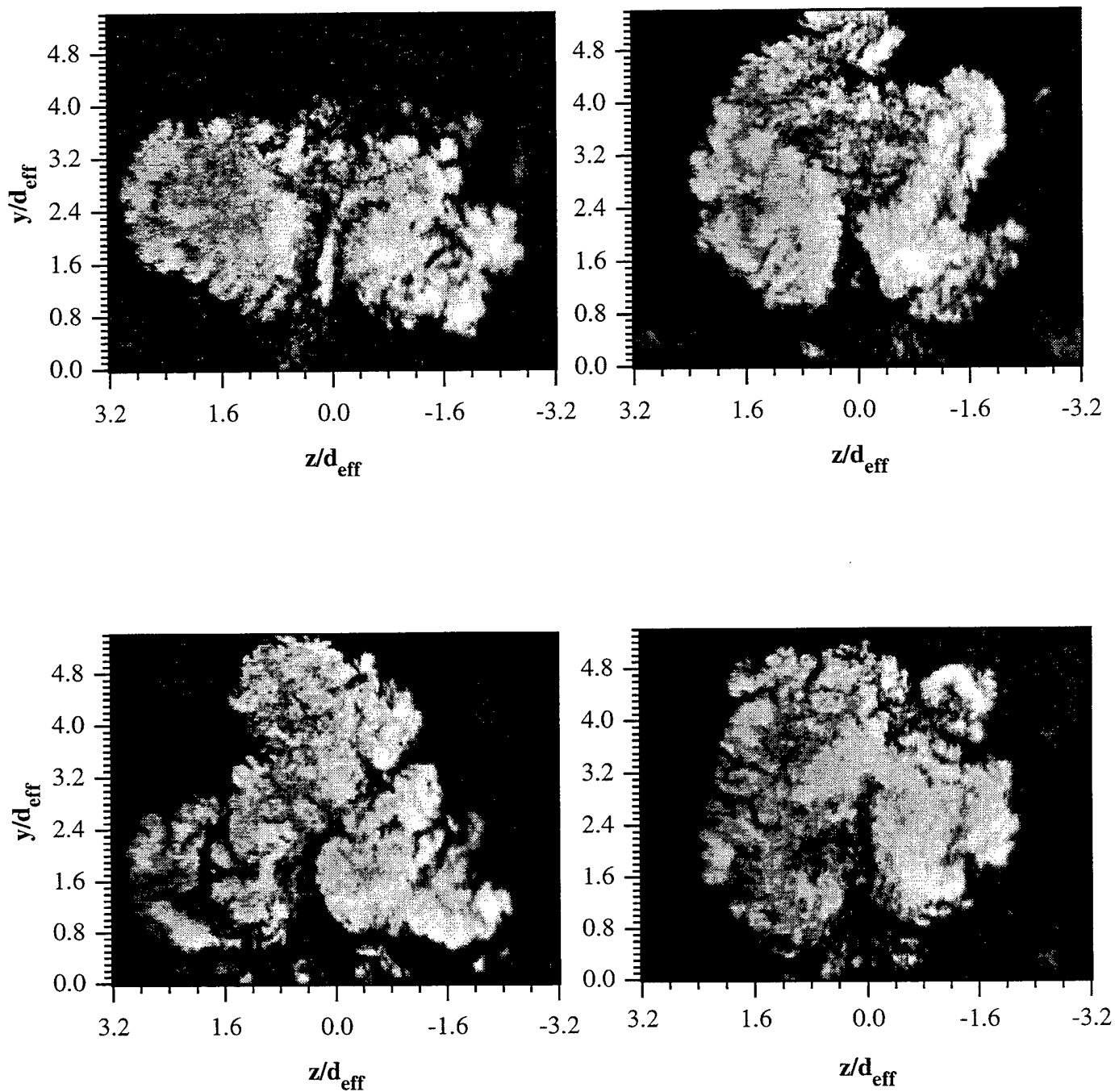


Figure 5.12 Instantaneous End View Images of Circular Injection Using Helium
(Case C2H) at $x/d_{\text{eff}} = 8$

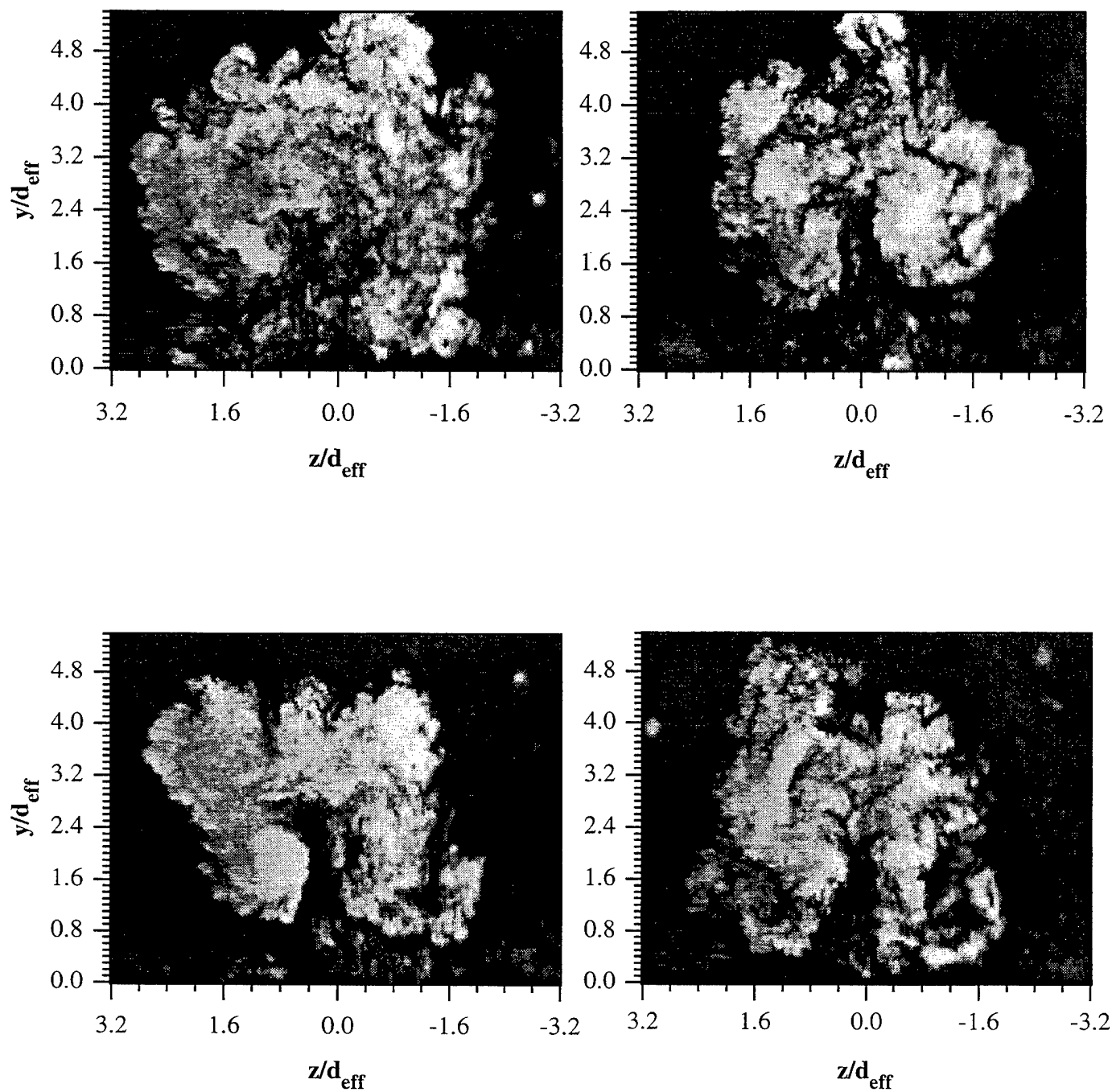


Figure 5.13 Instantaneous End View Images of Circular Injection Using Helium
(Case C2H) at $x/d_{\text{eff}} = 10$

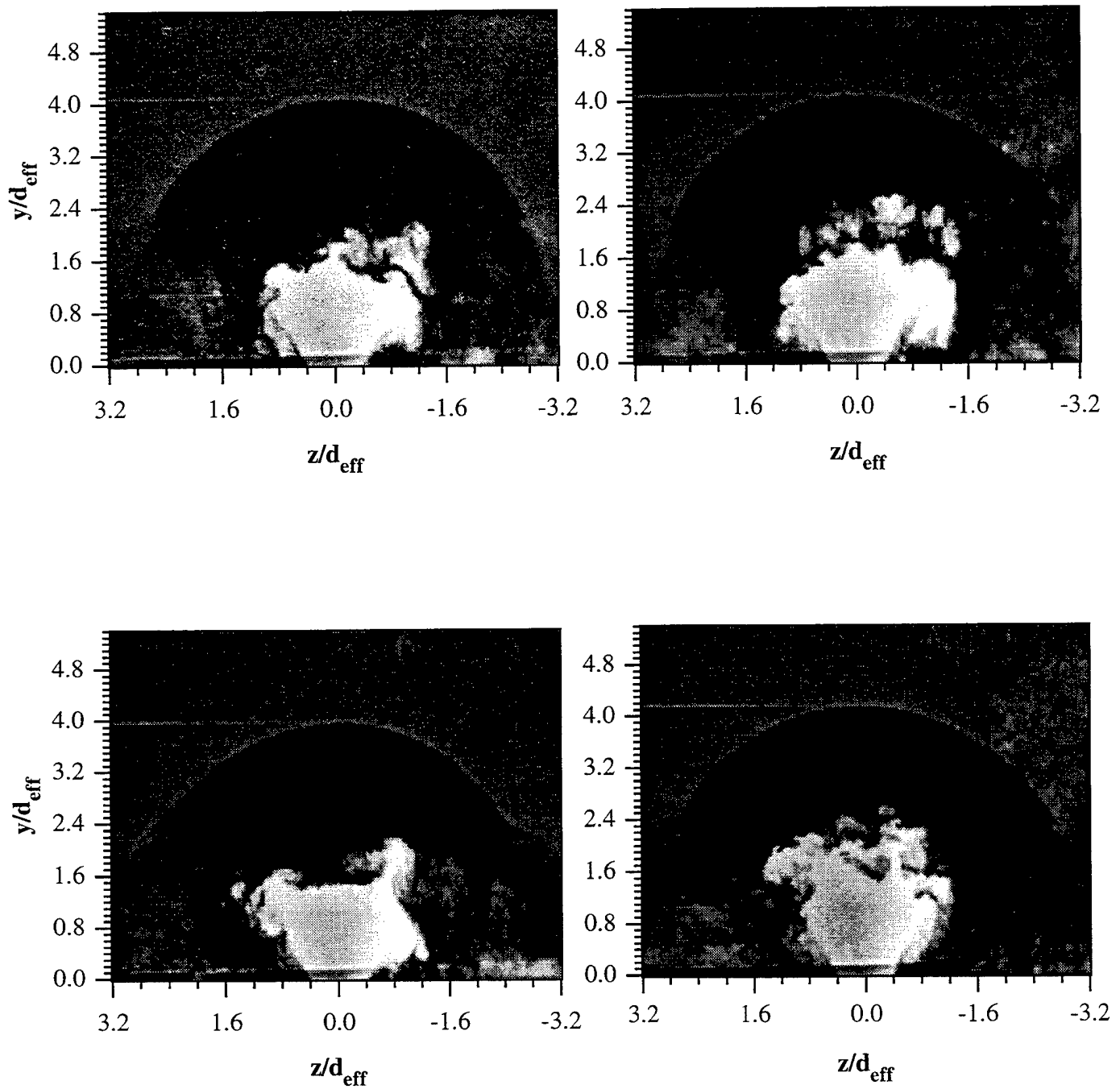


Figure 5.14 Instantaneous End View Images of Elliptical Injection Using Air
(Case E1A) at $x/d_{\text{eff}} = 0$

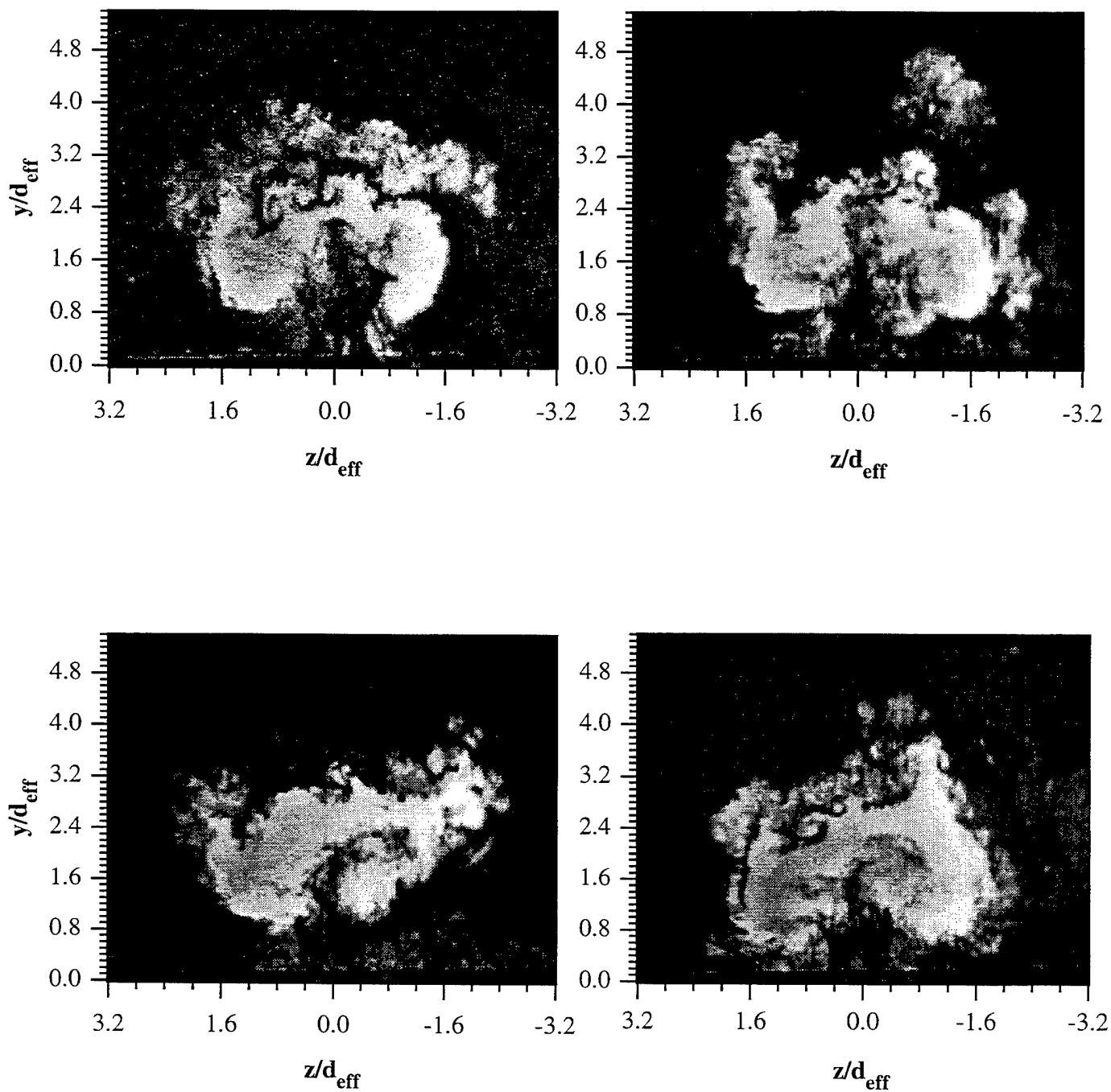


Figure 5.15 Instantaneous End View Images of Elliptical Injection Using Air
(Case E1A) at $x/d_{\text{eff}} = 4$

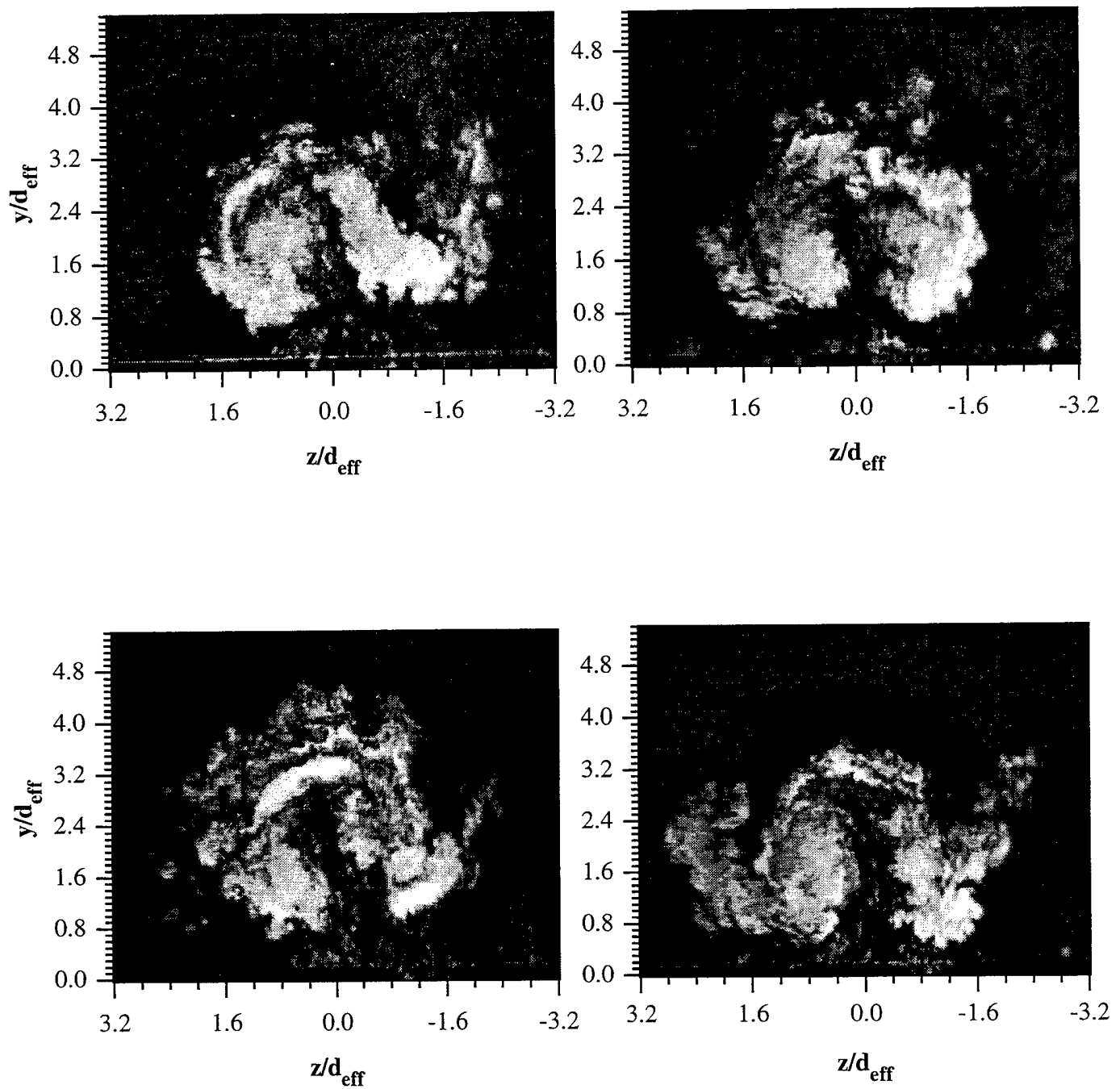


Figure 5.16 Instantaneous End View Images of Elliptical Injection Using Air
(Case E1A) at $x/d_{\text{eff}} = 8$

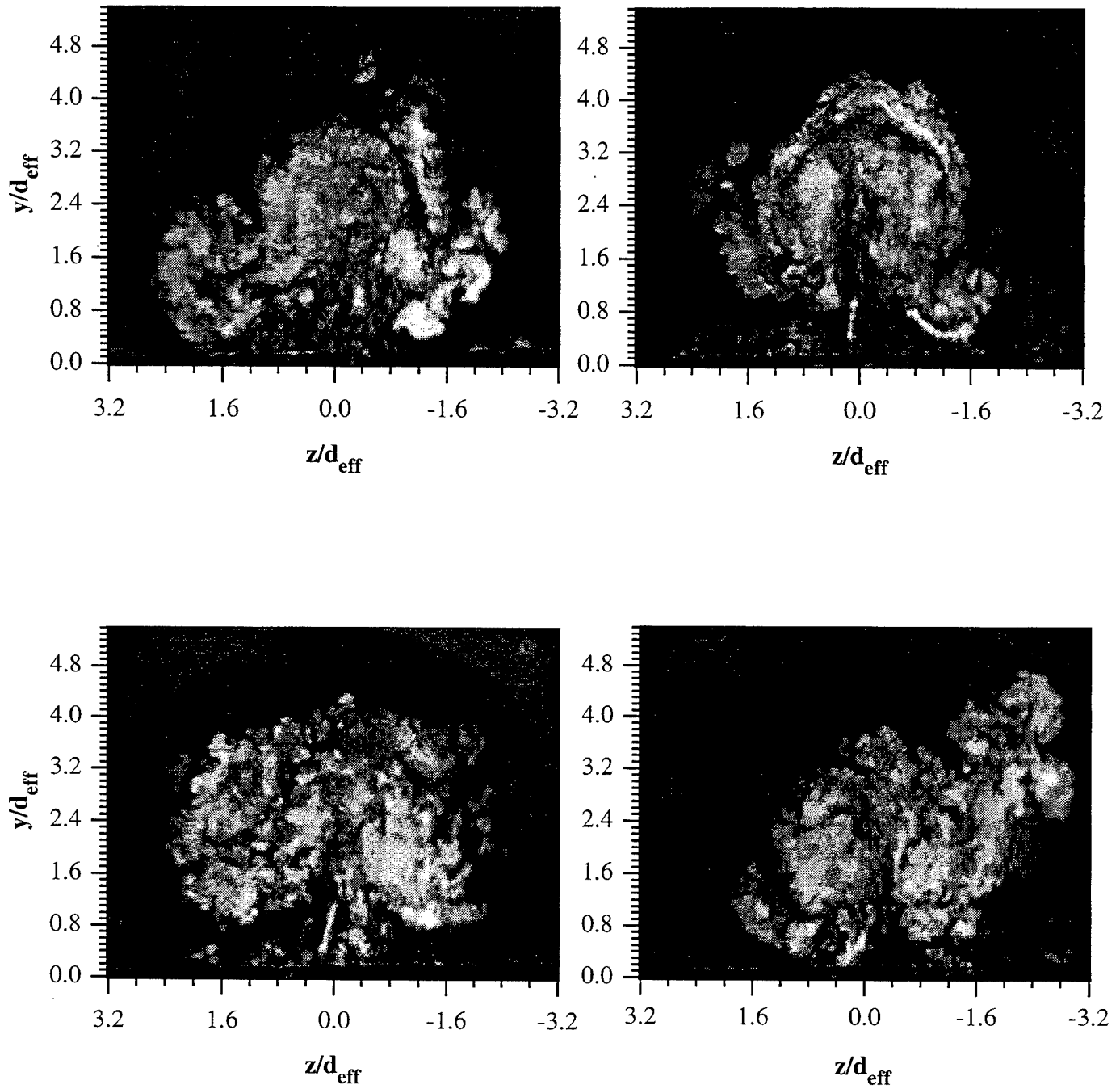


Figure 5.17 Instantaneous End View Images of Elliptical Injection Using Air
(Case E1A) at $x/d_{\text{eff}} = 10$

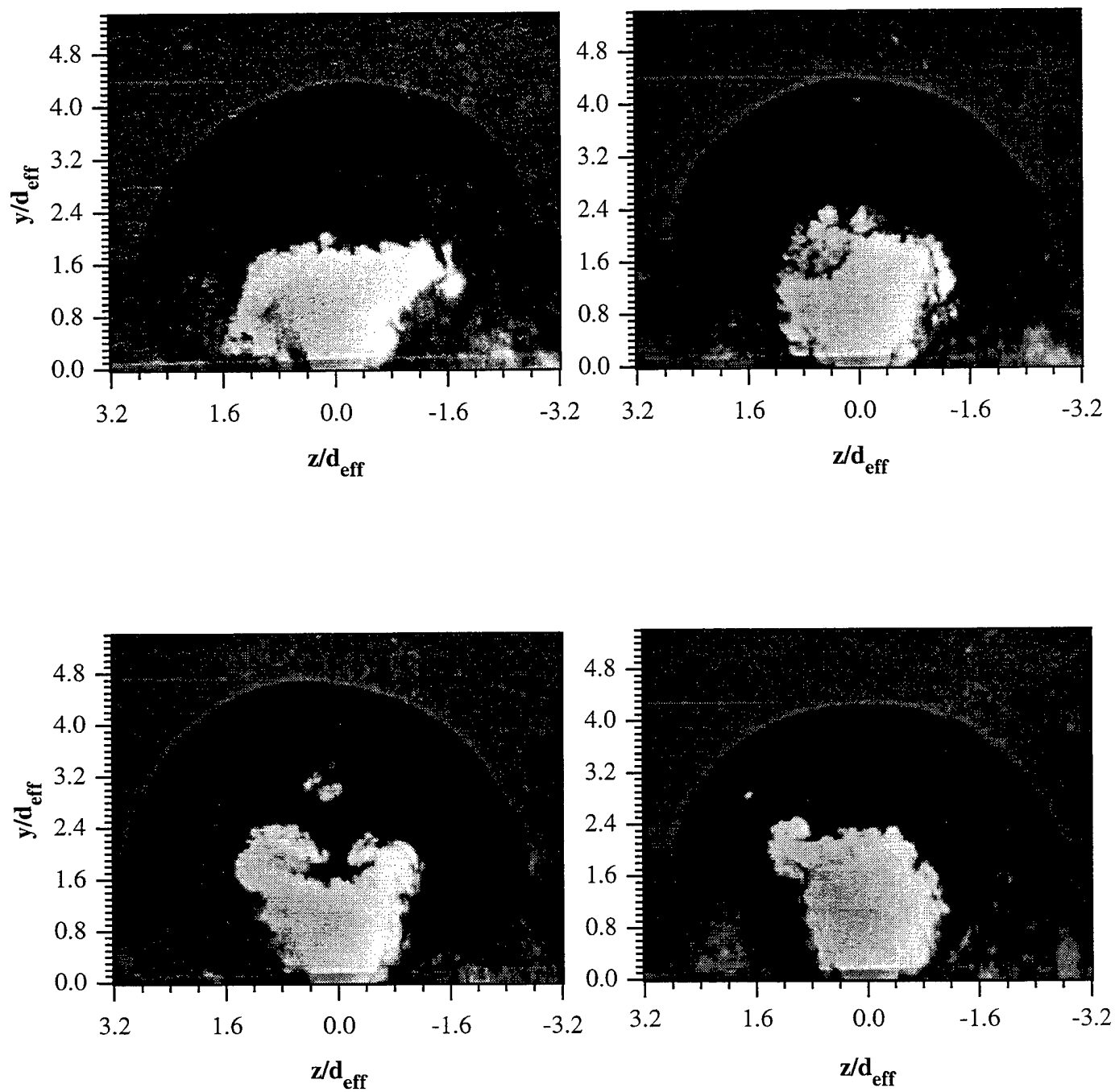


Figure 5.18 Instantaneous End View Images of Elliptical Injection Using Helium
(Case E2H) at $x/d_{\text{eff}} = 0$

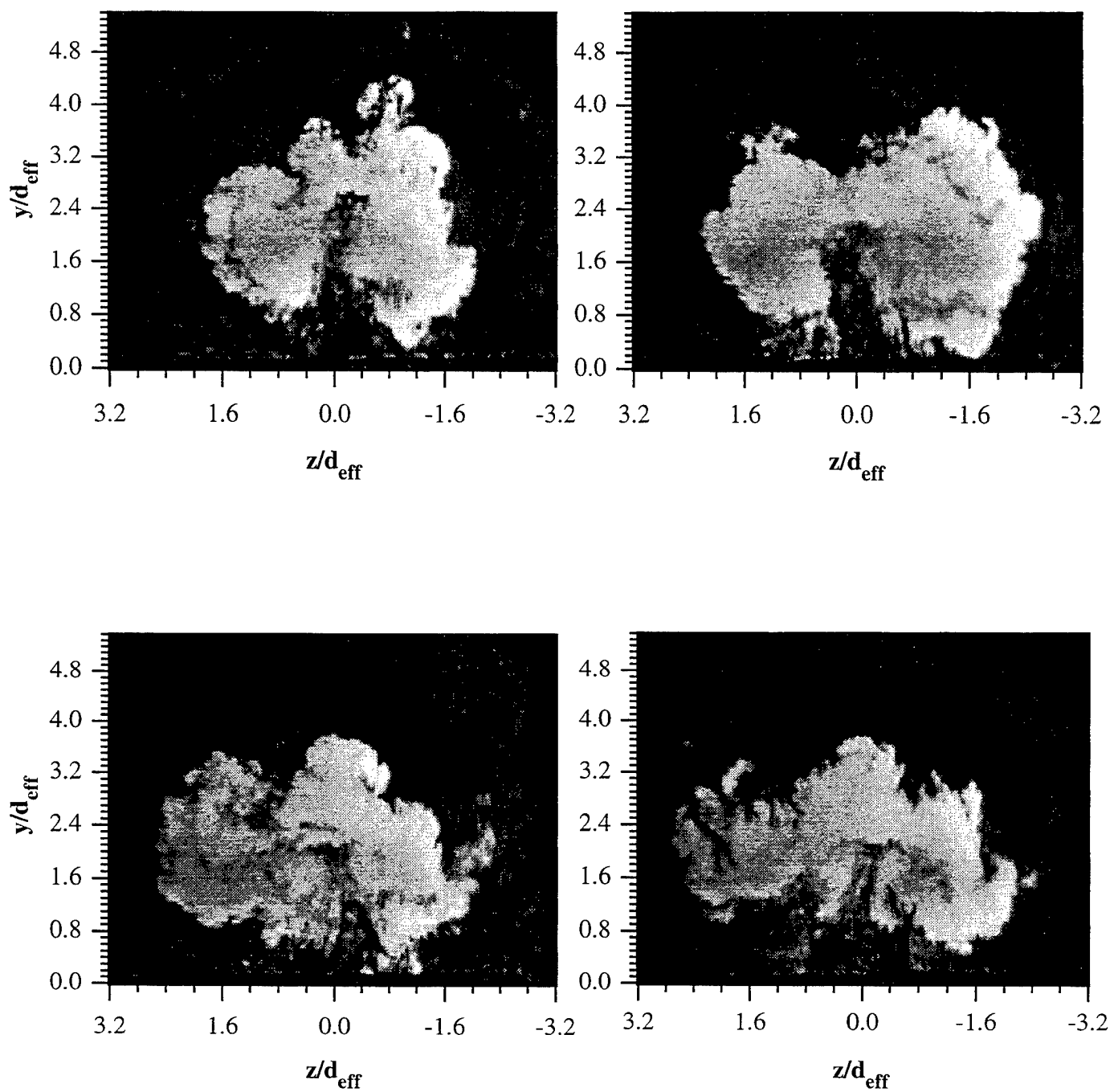


Figure 5.19 Instantaneous End View Images of Elliptical Injection Using Helium
(Case E2H) at $x/d_{\text{eff}} = 4$

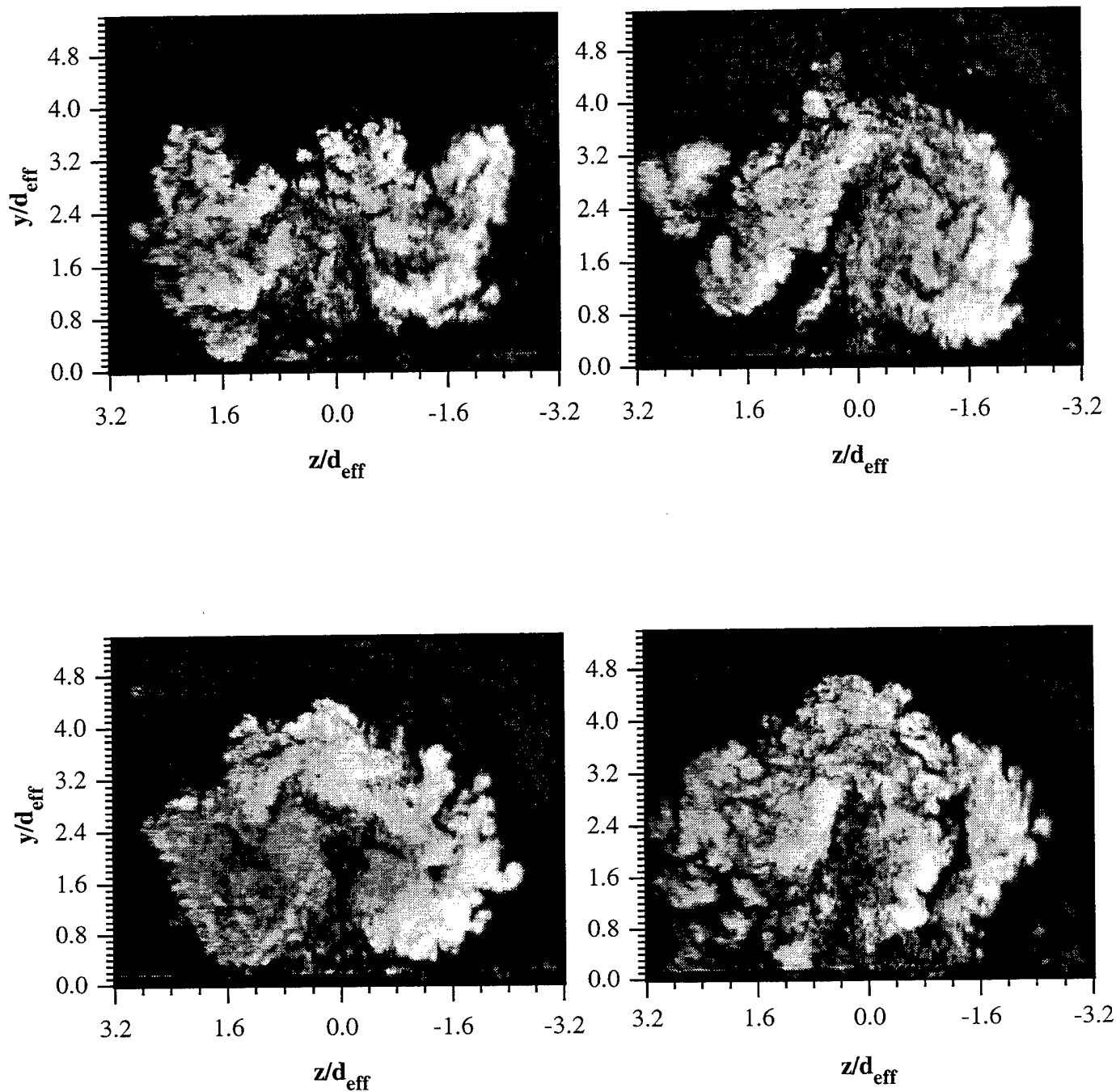


Figure 5.20 Instantaneous End View Images of Elliptical Injection Using Helium
(Case E2H) at $x/d_{\text{eff}} = 8$

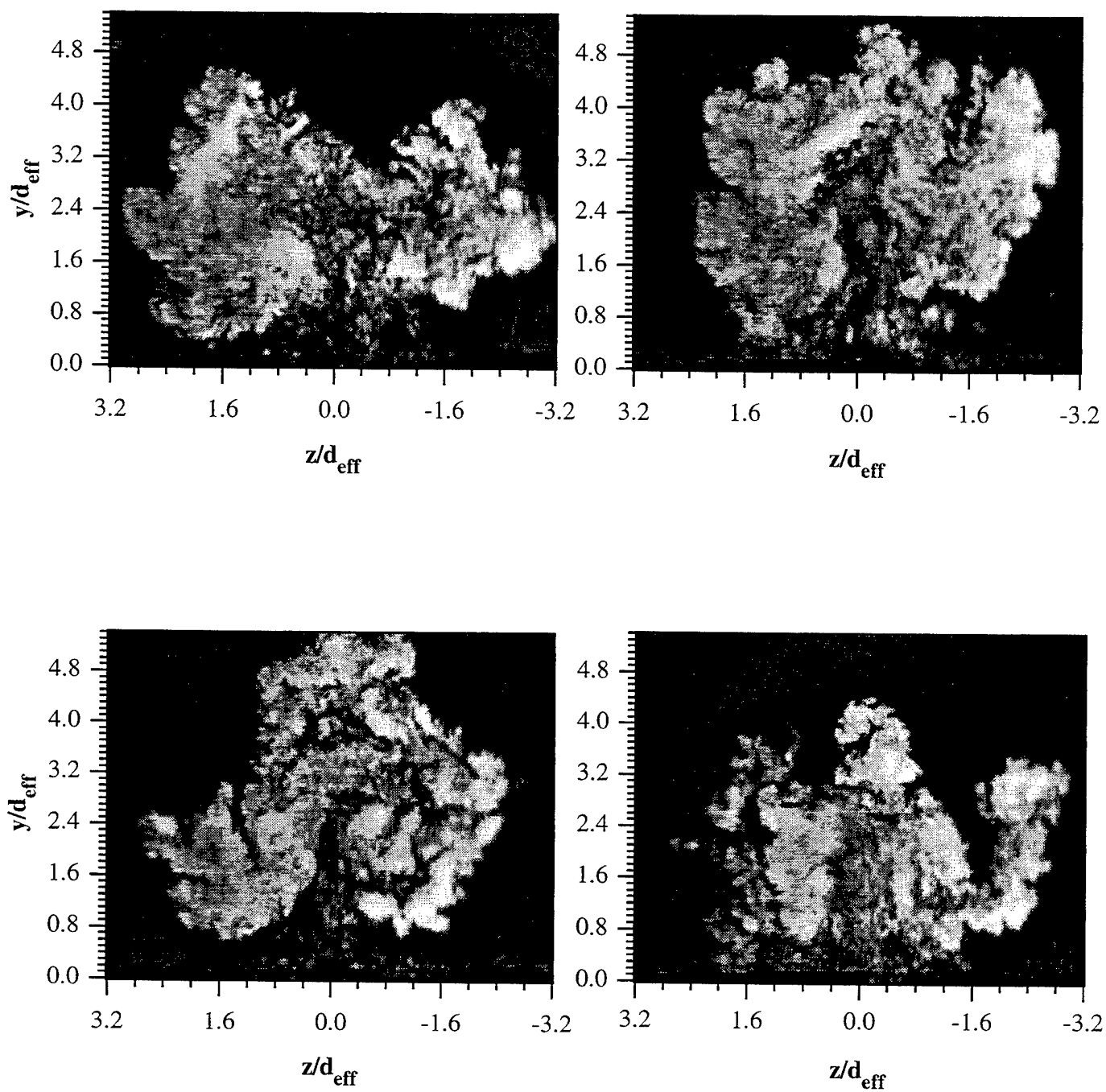


Figure 5.21 Instantaneous End View Images of Elliptical Injection Using Helium
(Case E2H) at $x/d_{\text{eff}} = 10$

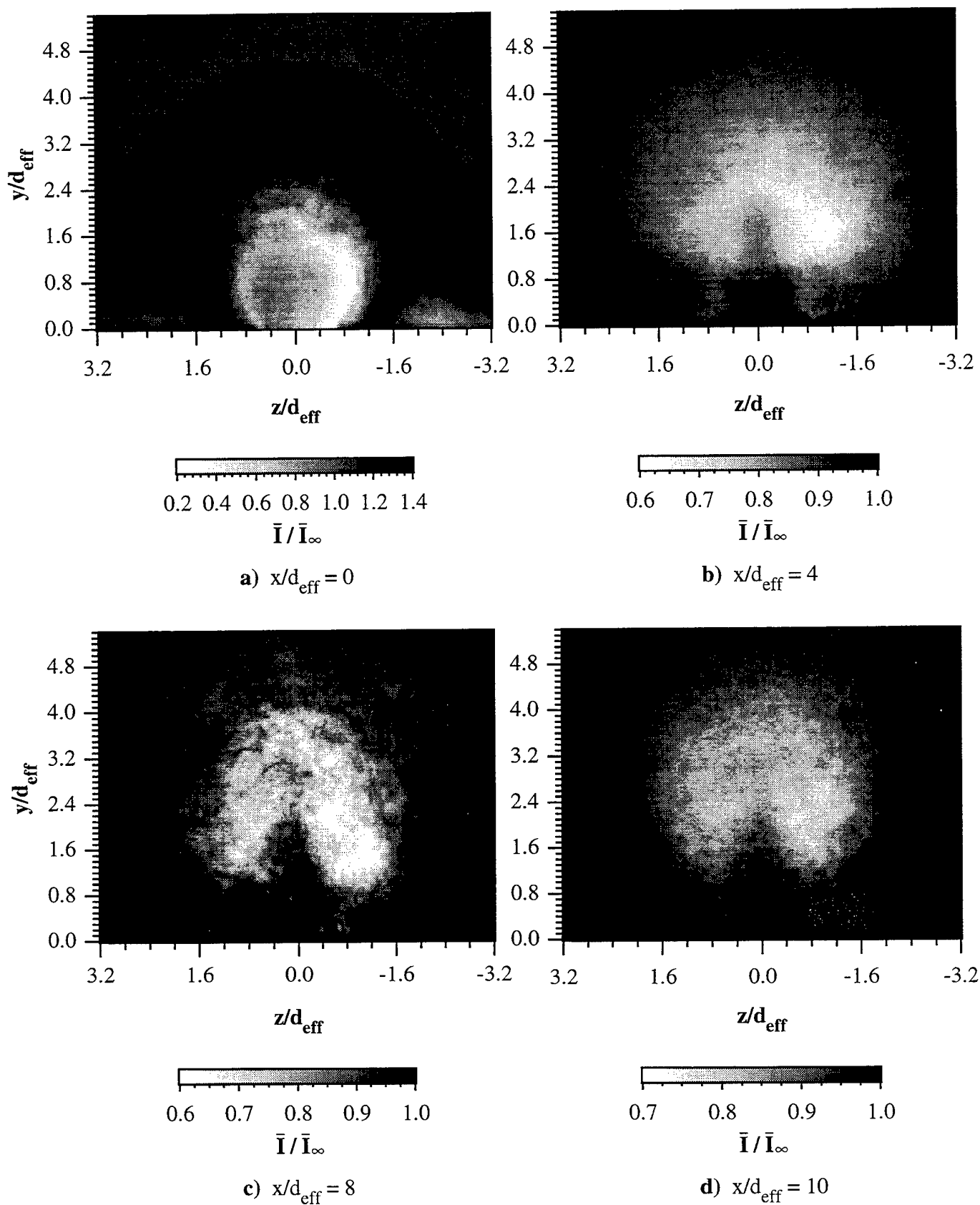


Figure 5.22 Normalized Ensemble-Averaged End View Images of Circular Injection Using Air (Case C1A) **a)** $x/d_{\text{eff}} = 0$, **b)** $x/d_{\text{eff}} = 4$, **c)** $x/d_{\text{eff}} = 8$, and **d)** $x/d_{\text{eff}} = 10$

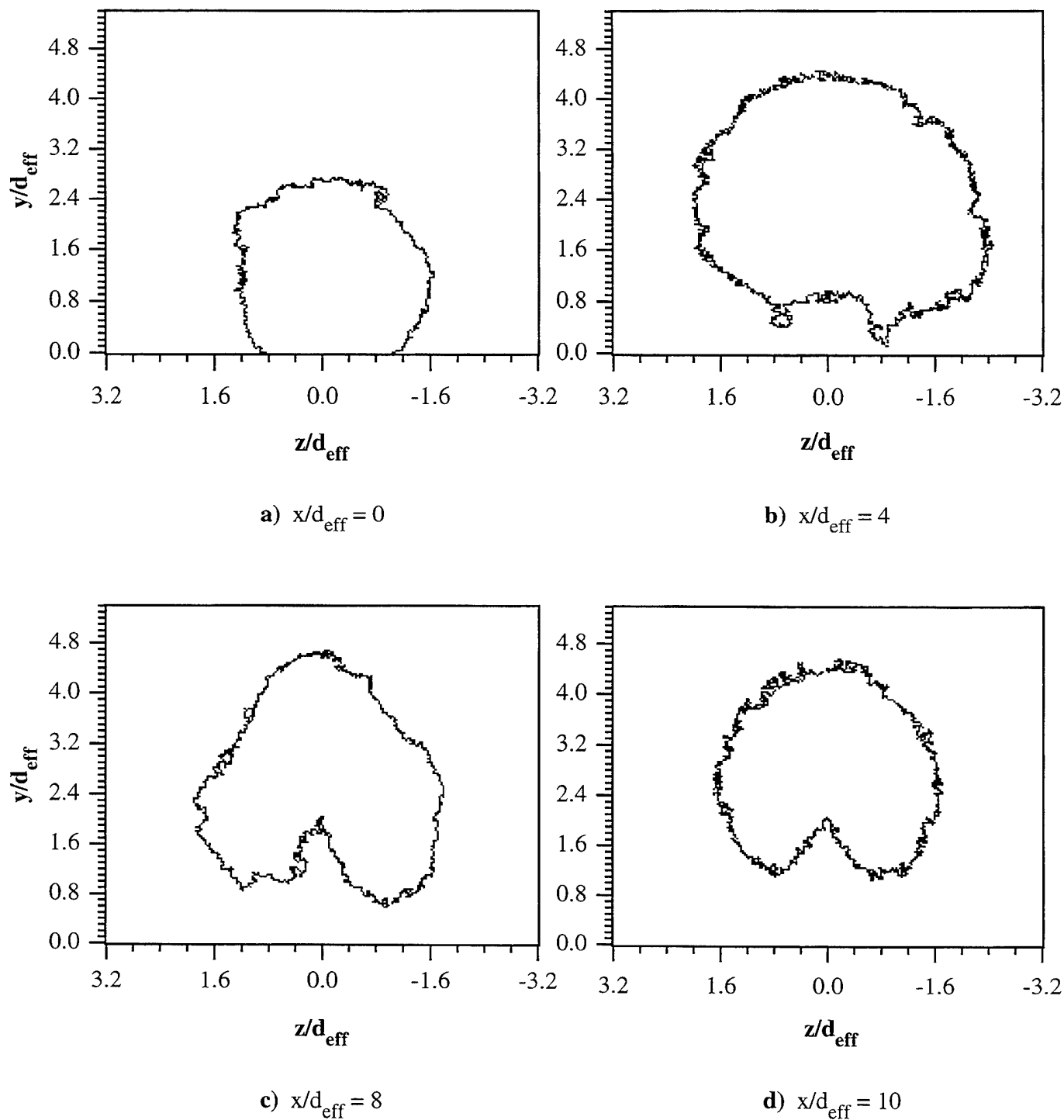


Figure 5.23 End View Penetration Contours for Case C1A a) $x/d_{\text{eff}} = 0$, b) $x/d_{\text{eff}} = 4$, c) $x/d_{\text{eff}} = 8$, and d) $x/d_{\text{eff}} = 10$

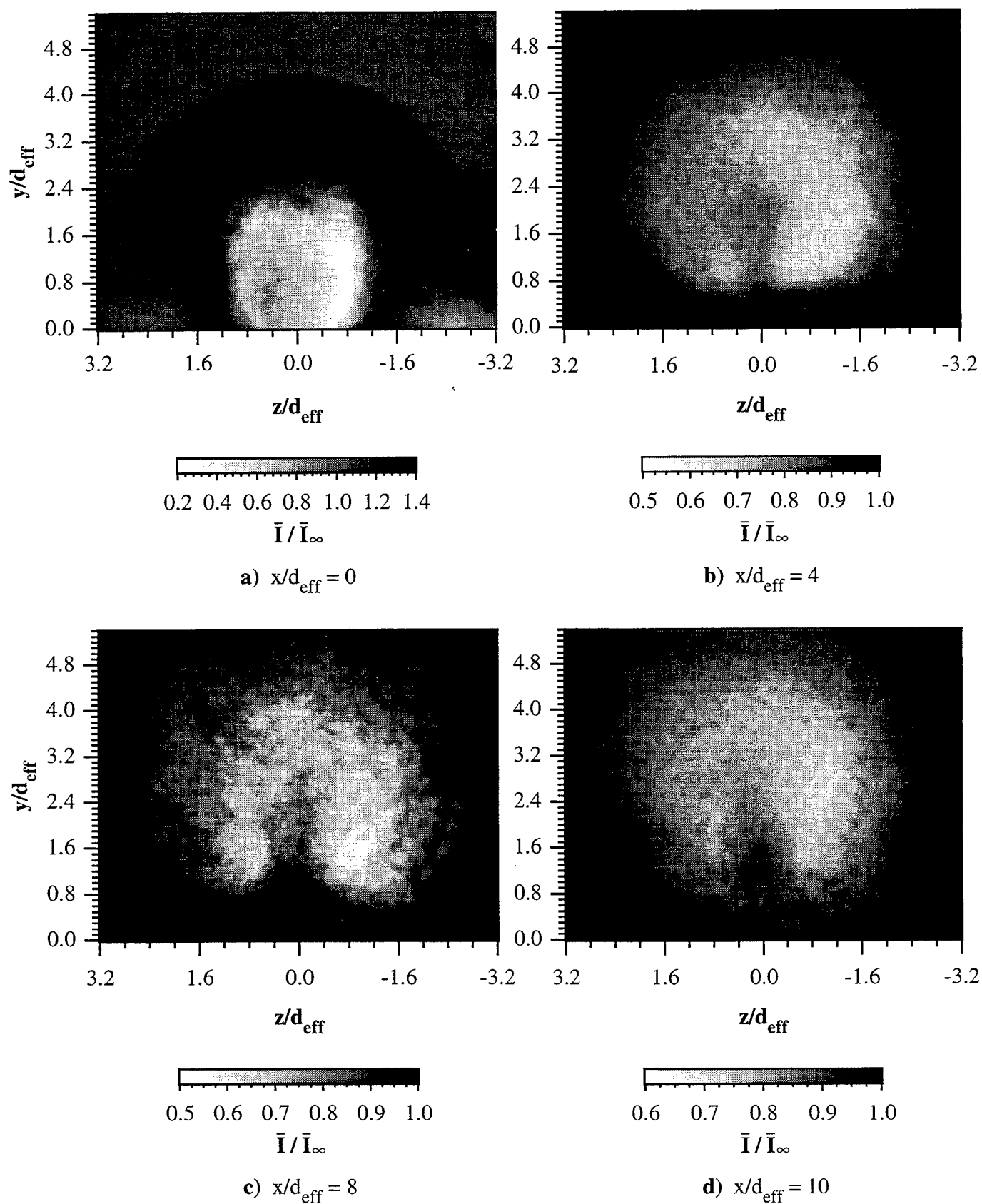


Figure 5.24 Normalized Ensemble-Averaged End View Images of Circular Injection Using Helium (Case C2H) **a)** $x/d_{\text{eff}} = 0$, **b)** $x/d_{\text{eff}} = 4$, **c)** $x/d_{\text{eff}} = 8$, and **d)** $x/d_{\text{eff}} = 10$

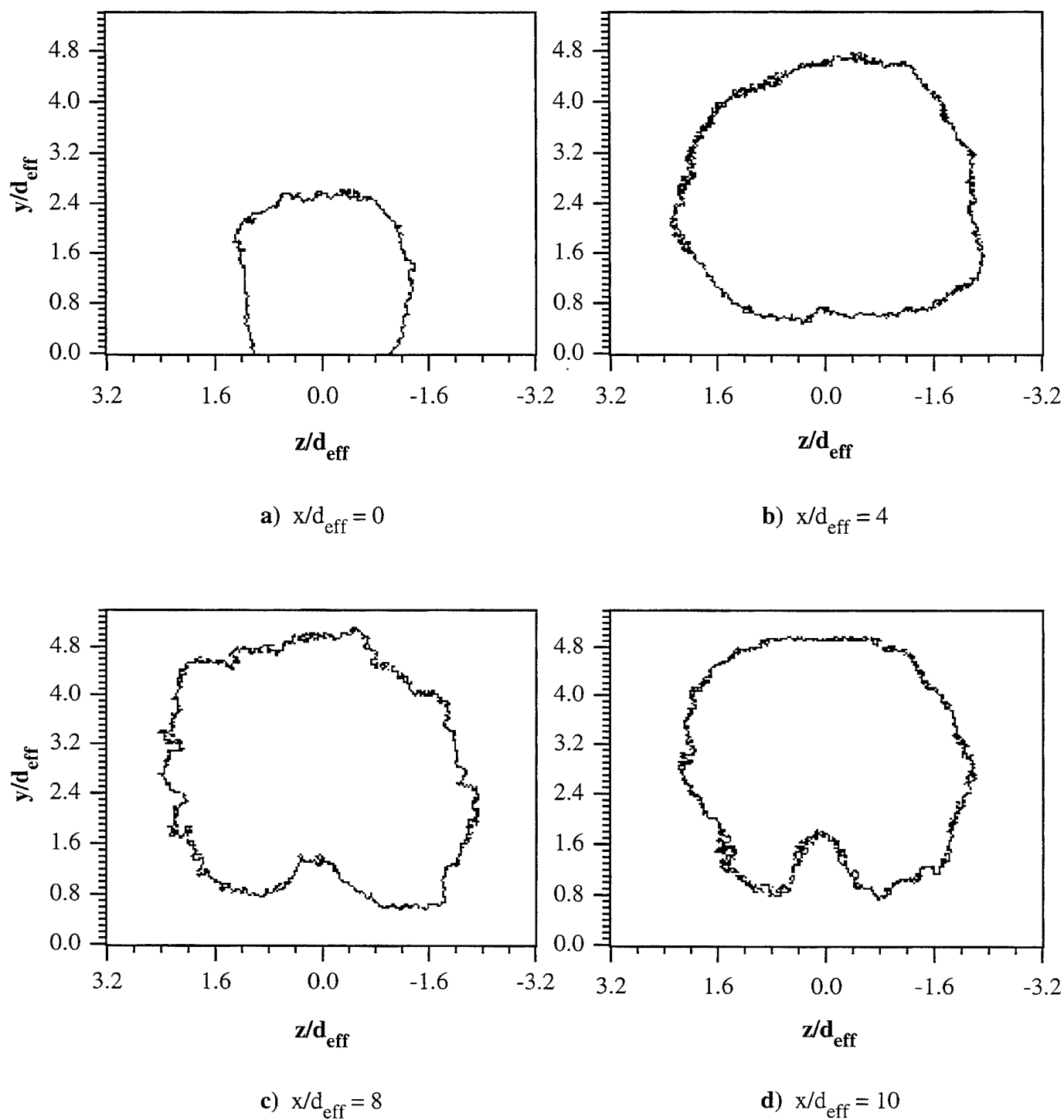


Figure 5.25 End View Penetration Contours for Case C2H a) $x/d_{\text{eff}} = 0$, b) $x/d_{\text{eff}} = 4$, c) $x/d_{\text{eff}} = 8$, and d) $x/d_{\text{eff}} = 10$

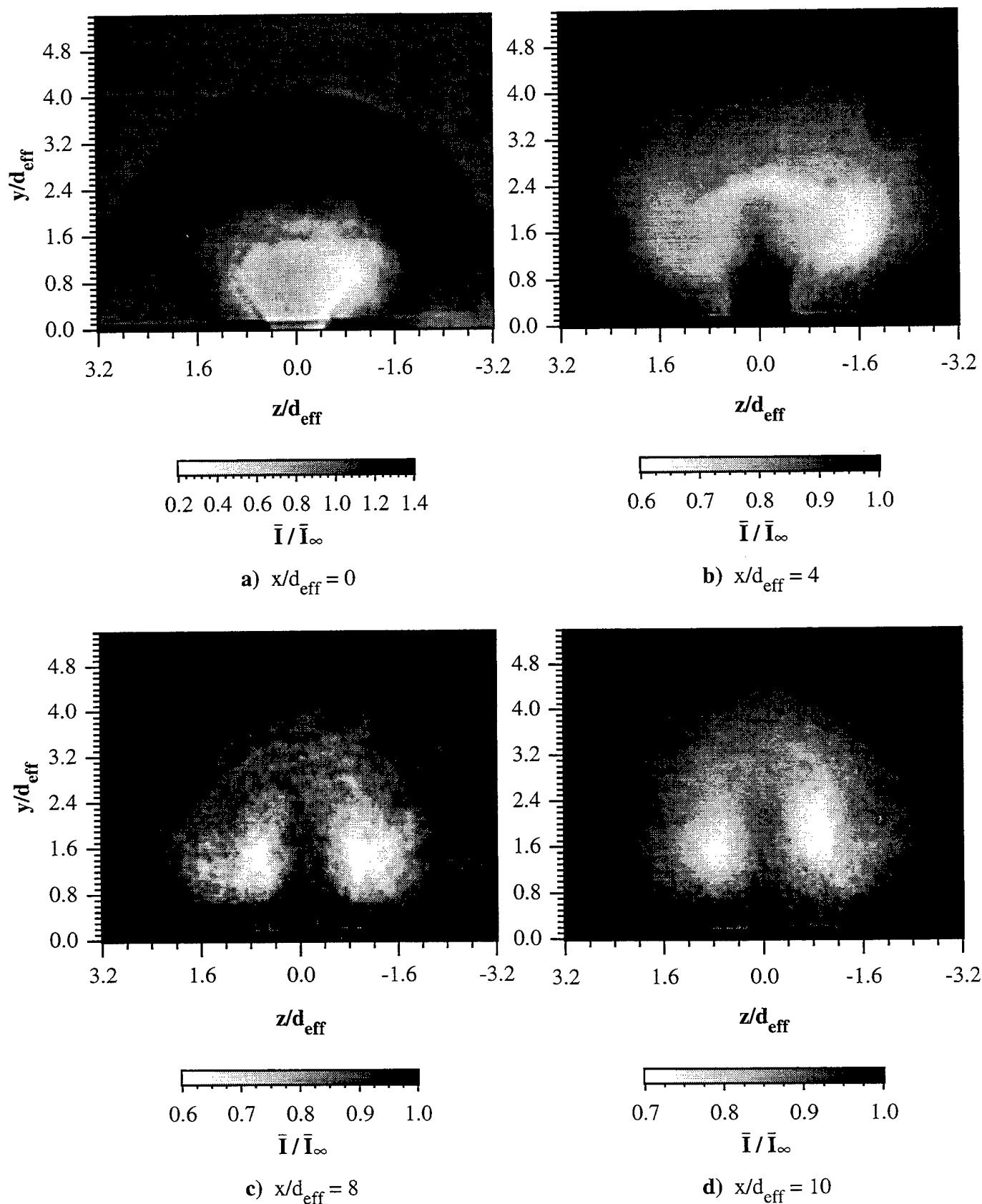


Figure 5.26. Normalized Ensemble-Averaged End View Images of Elliptical Injection Using Air (Case E1A) **a)** $x/d_{\text{eff}} = 0$, **b)** $x/d_{\text{eff}} = 4$, **c)** $x/d_{\text{eff}} = 8$, and **d)** $x/d_{\text{eff}} = 10$

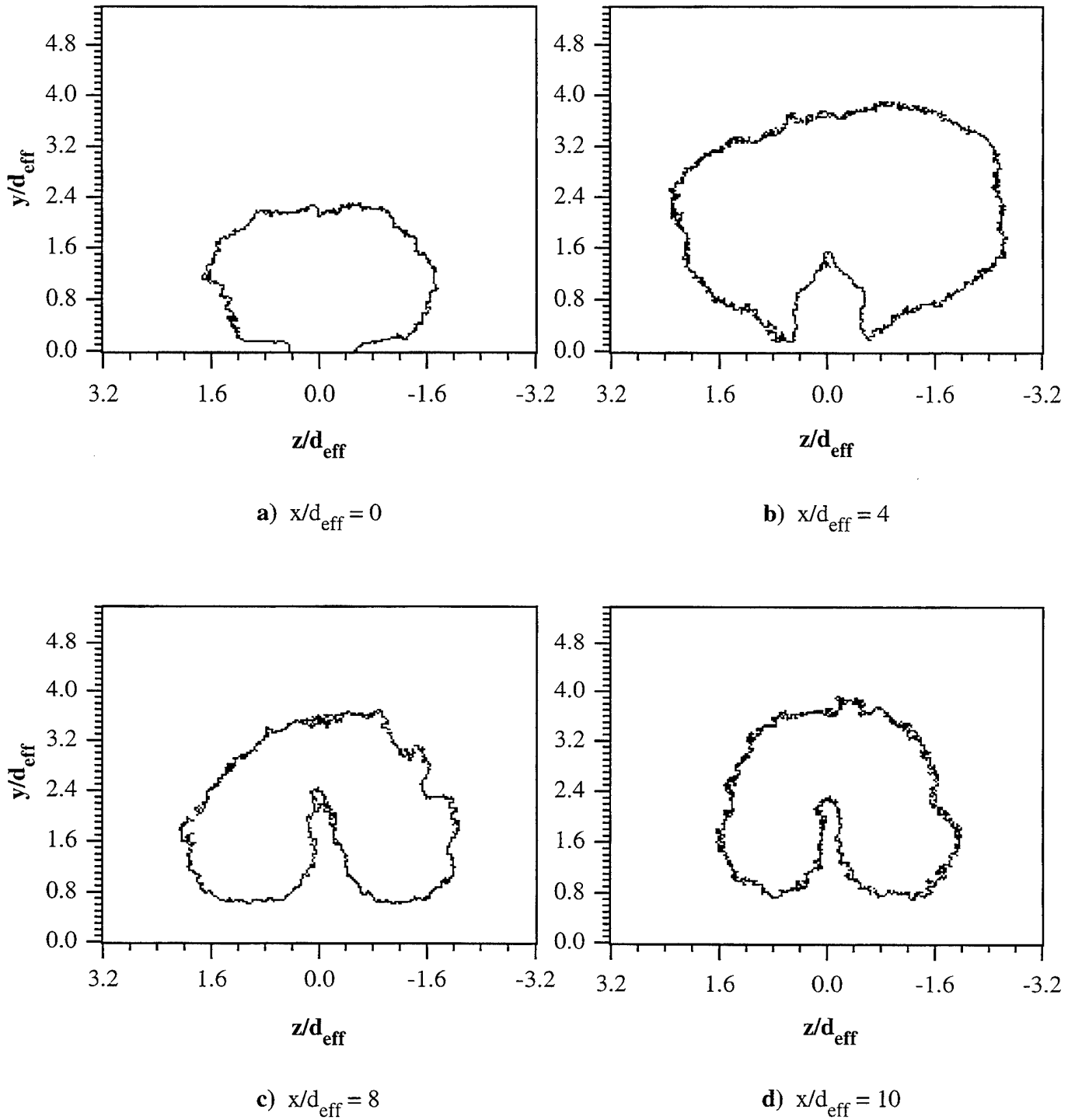


Figure 5.27 End View Penetration Contours for Case E1A a) $x/d_{\text{eff}} = 0$, b) $x/d_{\text{eff}} = 4$, c) $x/d_{\text{eff}} = 8$, and d) $x/d_{\text{eff}} = 10$

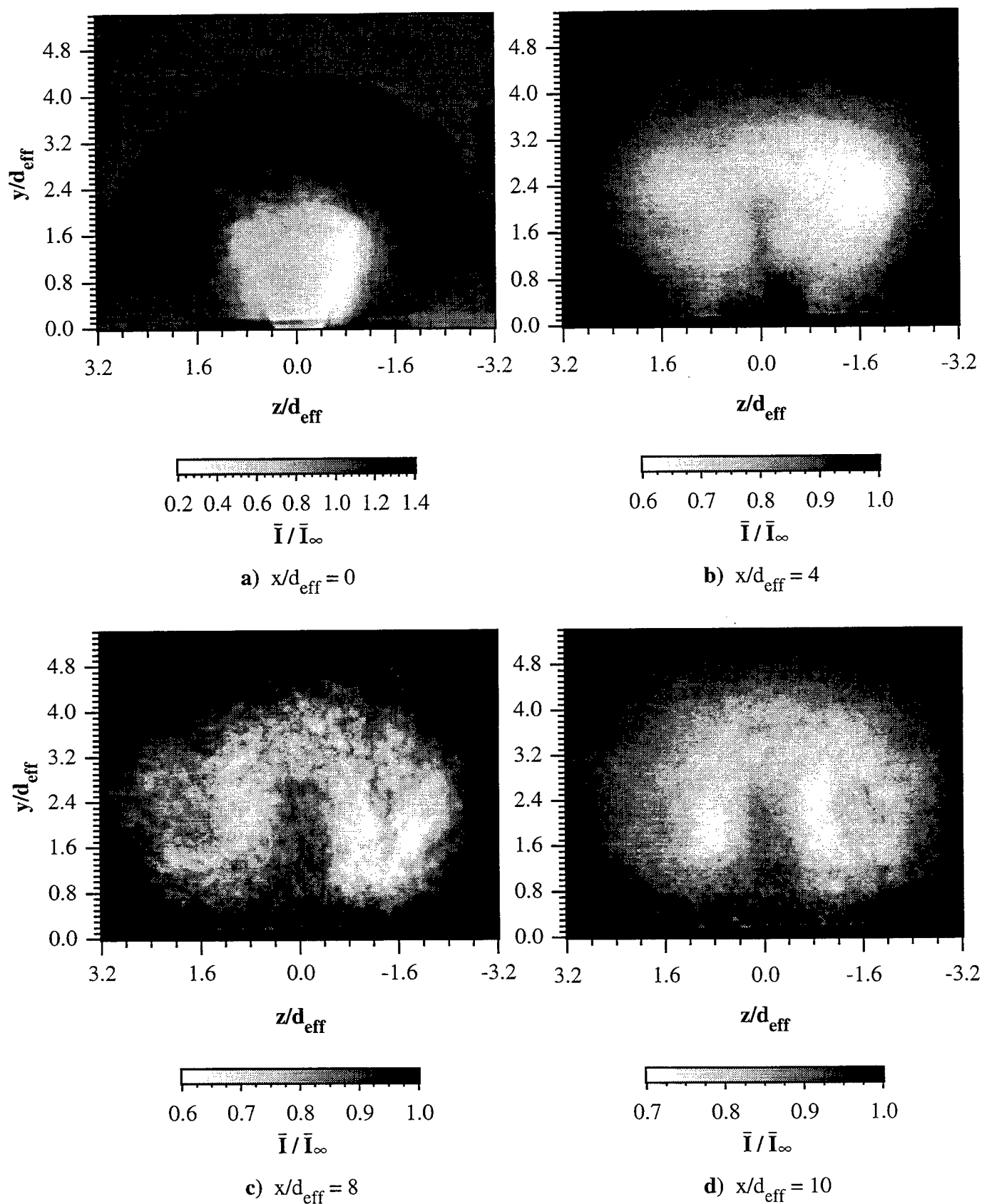


Figure 5.28 Normalized Ensemble-Averaged End View Images of Elliptical Injection Using Helium (Case E2H) **a)** $x/d_{\text{eff}} = 0$, **b)** $x/d_{\text{eff}} = 4$, **c)** $x/d_{\text{eff}} = 8$, and **d)** $x/d_{\text{eff}} = 10$

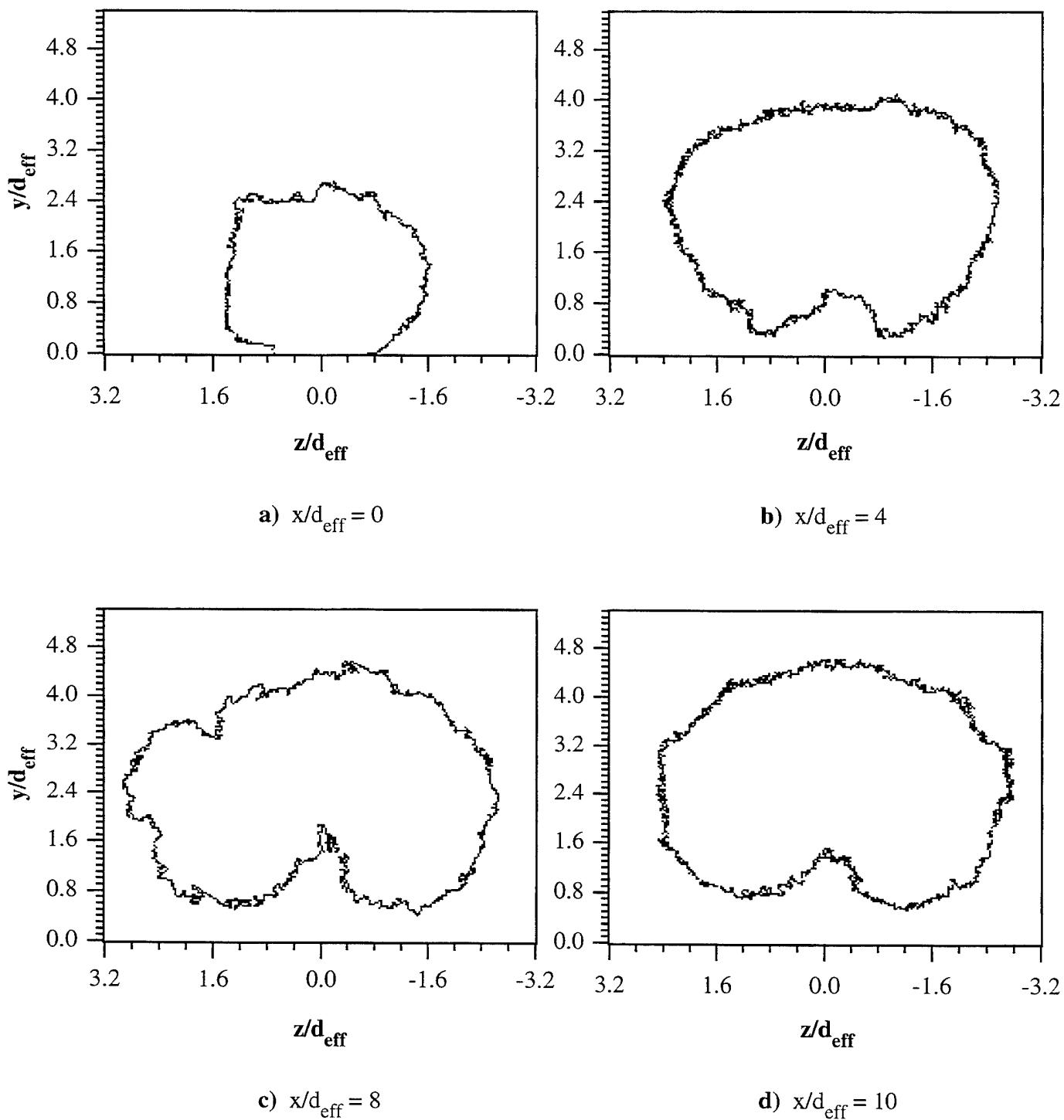


Figure 5.29 End View Penetration Contours for Case E2H **a)** $x/d_{\text{eff}} = 0$, **b)** $x/d_{\text{eff}} = 4$, **c)** $x/d_{\text{eff}} = 8$, and **d)** $x/d_{\text{eff}} = 10$

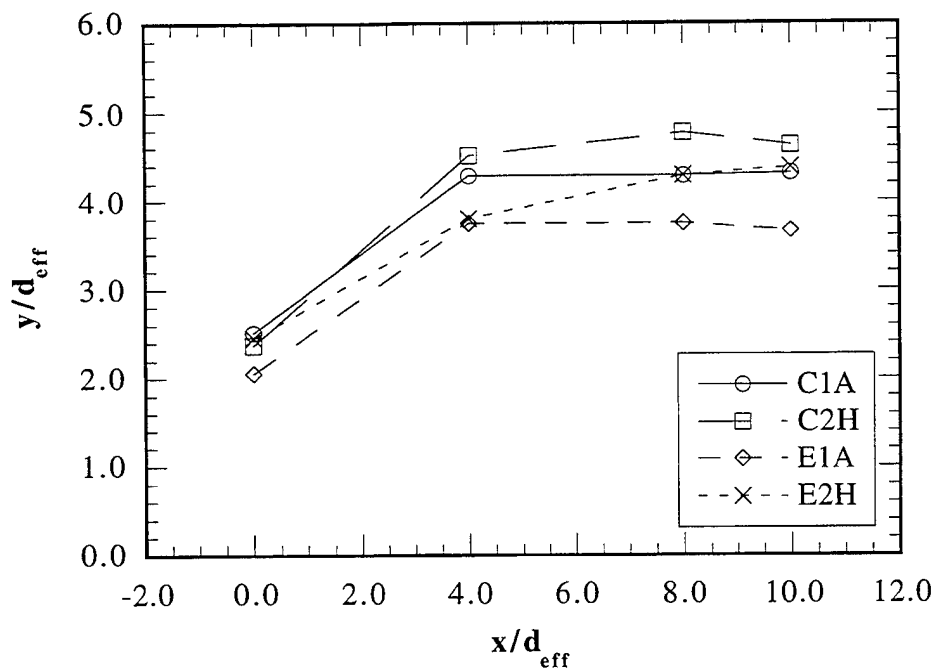


Figure 5.30 Transverse Penetration Profiles from Ensemble-Averaged End View Images

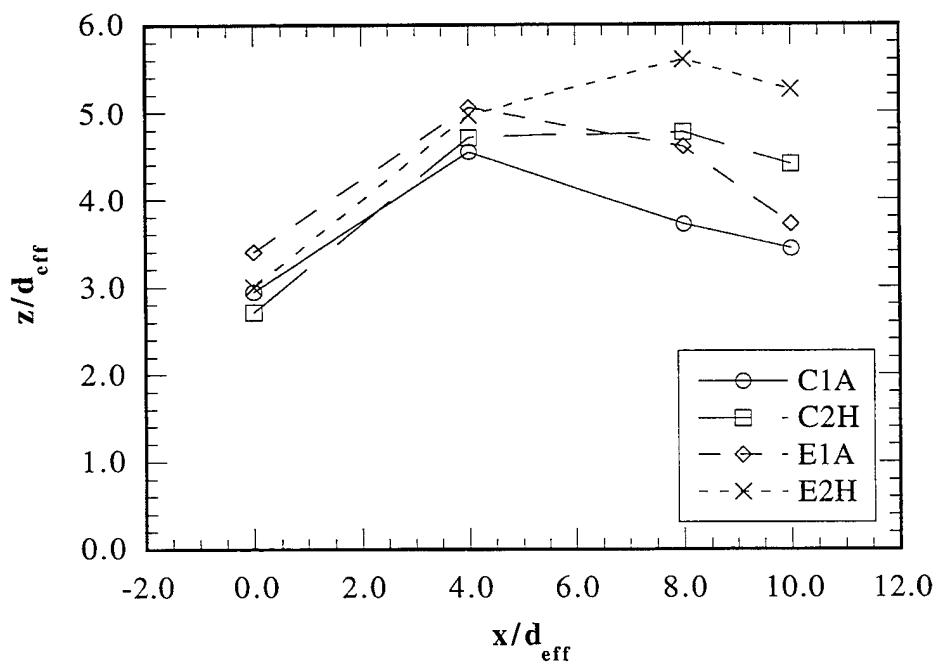


Figure 5.31 Lateral Spread Profiles from Ensemble-Averaged End View Images Using d_{eff} to Normalize the Spanwise Axis

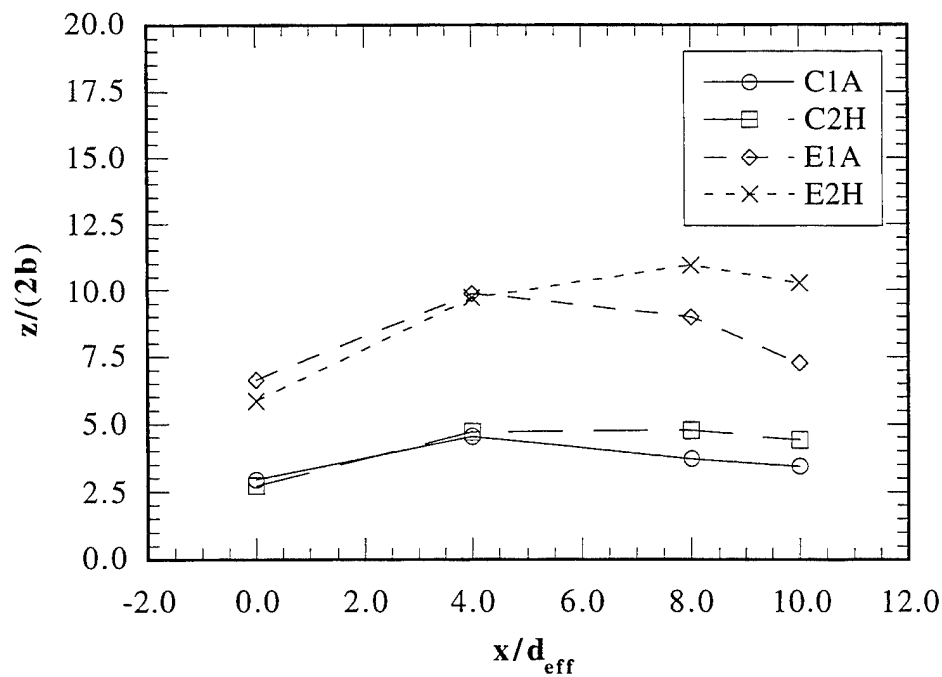


Figure 5.32 Lateral Spread Profiles from Ensemble-Averaged End View Images Using Physical Spanwise Nozzle Exit Dimension to Normalize the Spanwise Axis

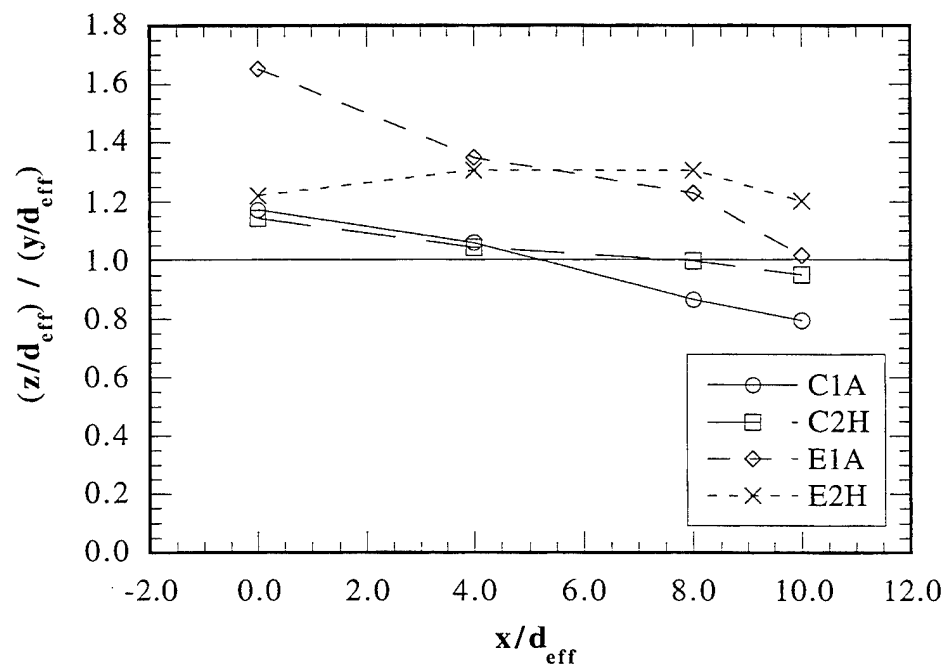


Figure 5.33 Relative Spreading in the Spanwise and Transverse Planes

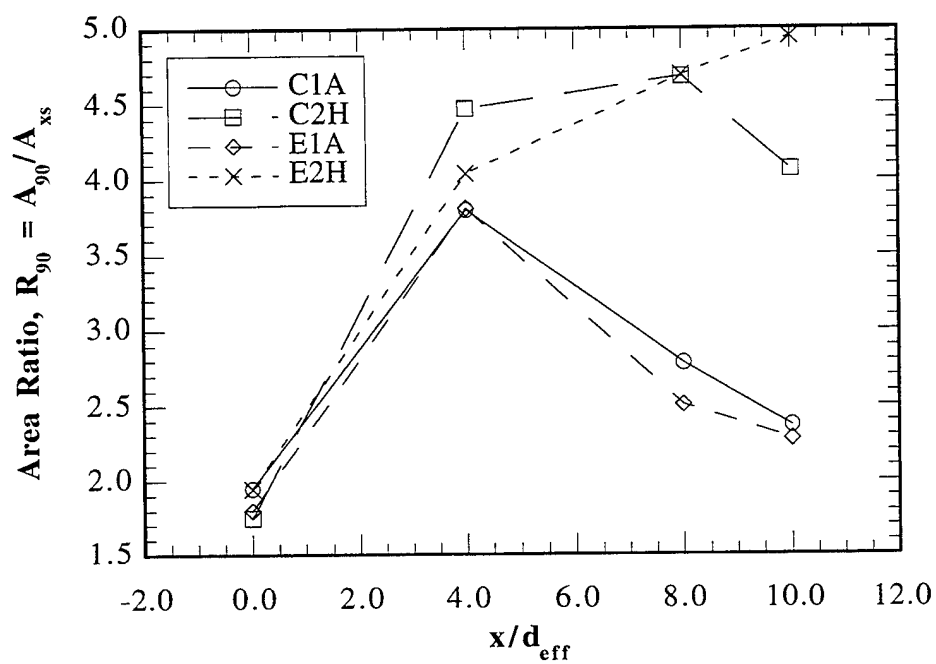


Figure 5.34 Area Ratios Determined Using Areas Enclosed Inside 90% Contours from Ensemble-Averaged End View Images

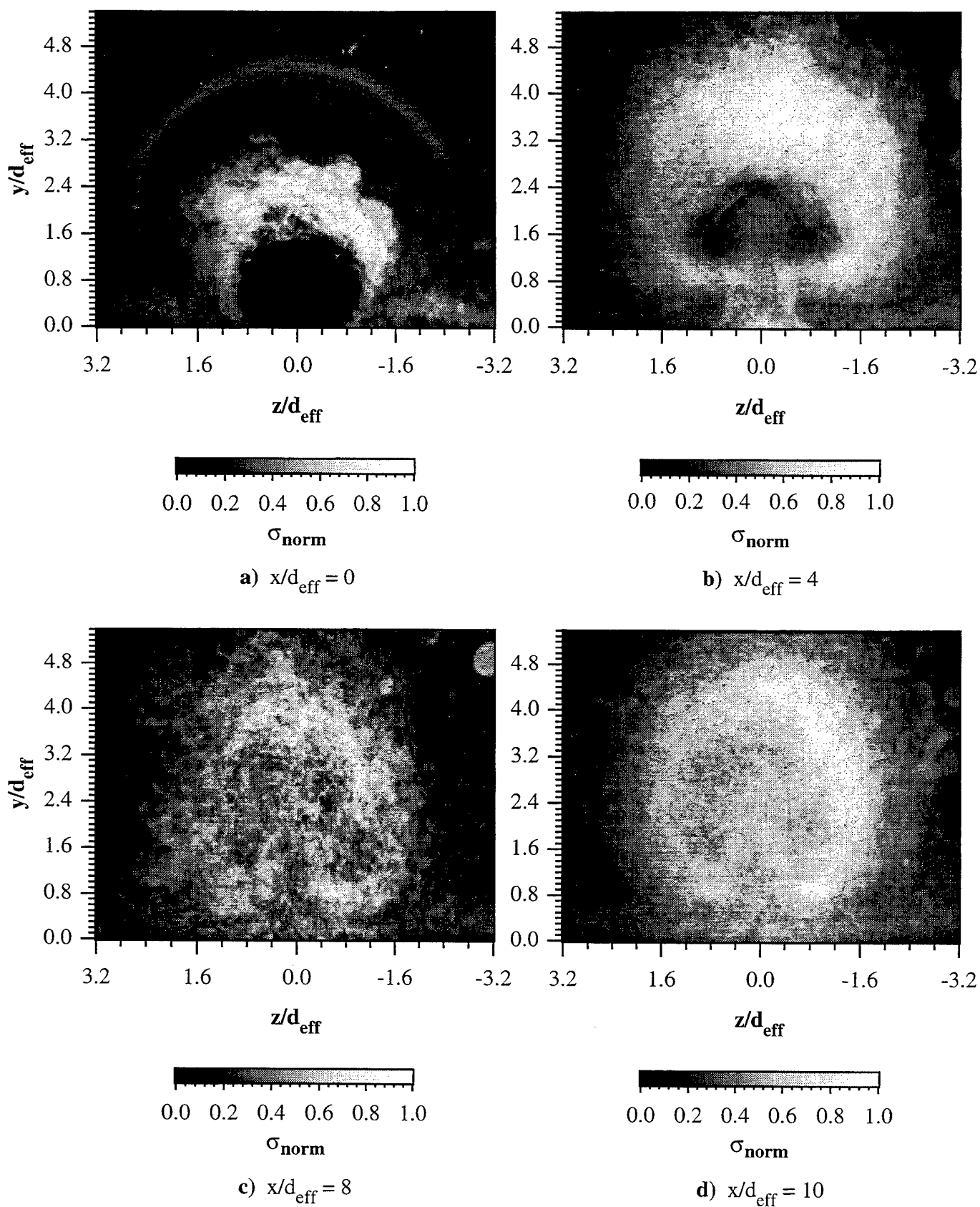


Figure 5.35 Normalized Standard Deviation End View Images of Circular Injection Using Air (Case C1A) **a)** $x/d_{\text{eff}} = 0$, **b)** $x/d_{\text{eff}} = 4$, **c)** $x/d_{\text{eff}} = 8$, and **d)** $x/d_{\text{eff}} = 10$

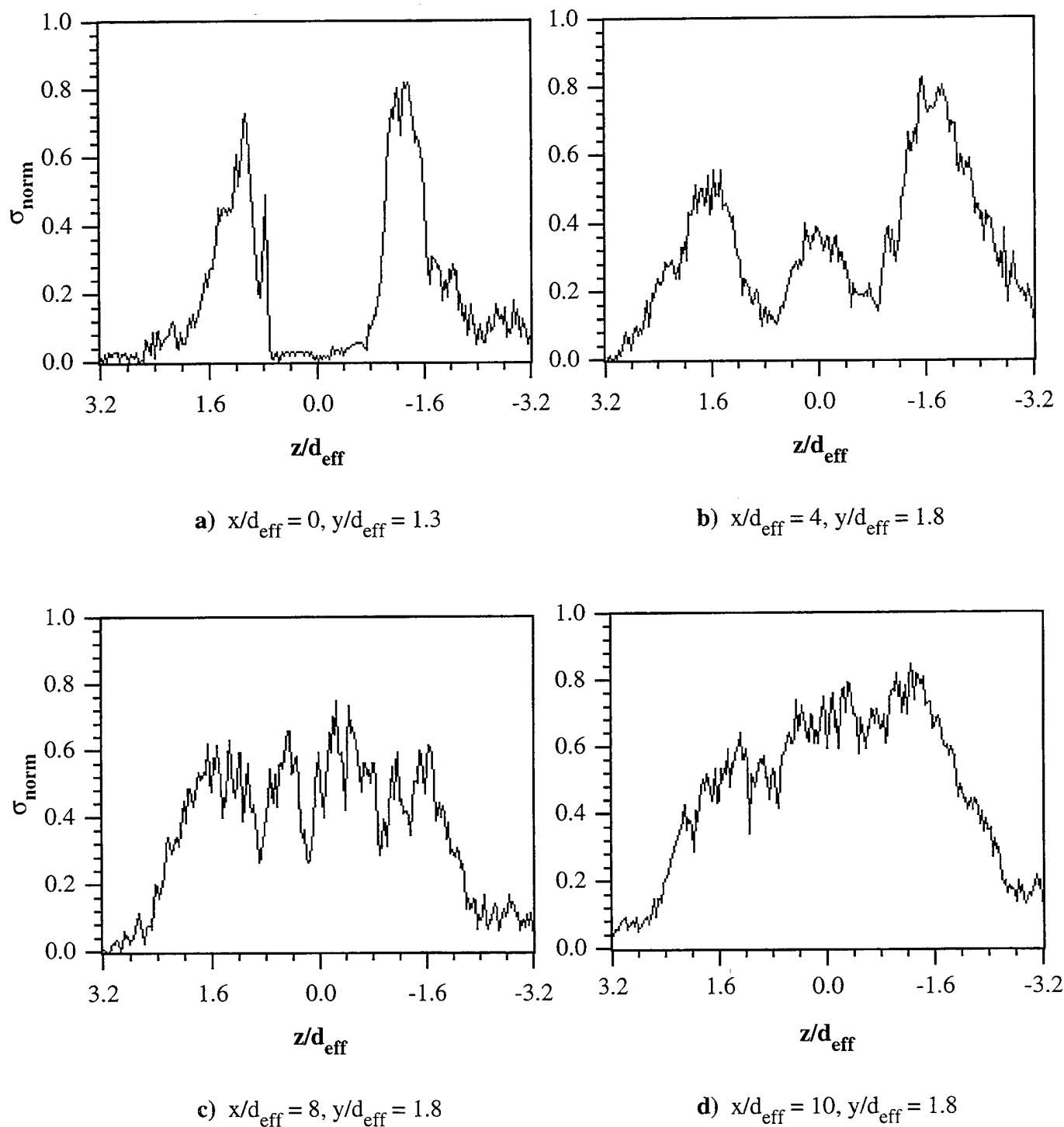
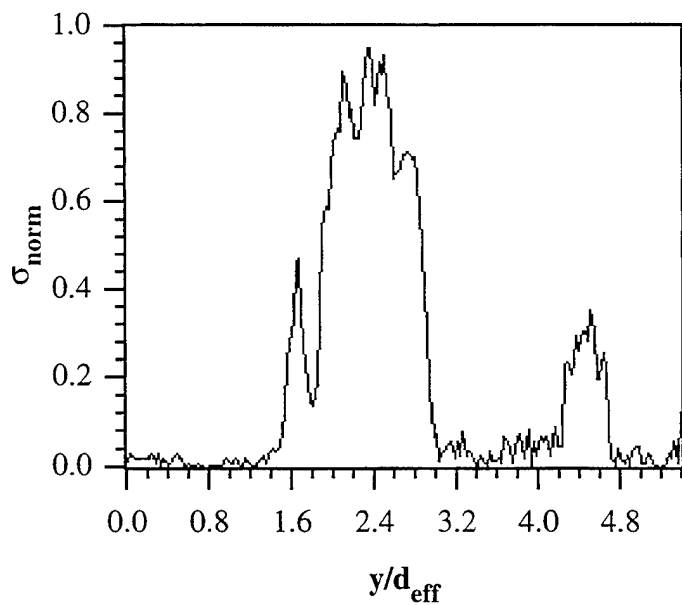
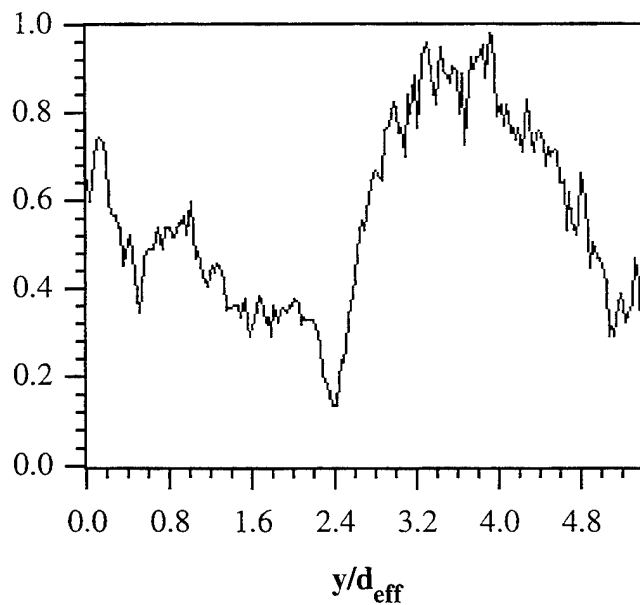


Figure 5.36 Spanwise Profiles of Normalized Standard Deviation for Case C1A

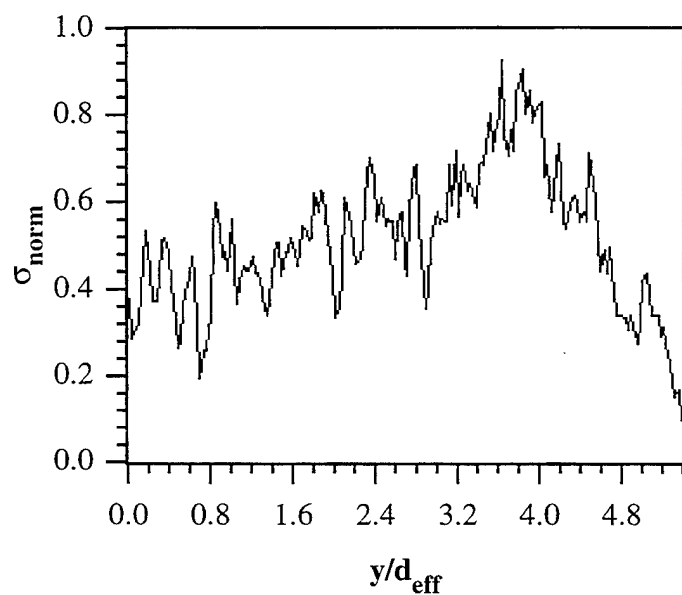
a) $x/d_{\text{eff}} = 0, y/d_{\text{eff}} = 1.3$, **b)** $x/d_{\text{eff}} = 4, y/d_{\text{eff}} = 1.8$, **c)** $x/d_{\text{eff}} = 8, y/d_{\text{eff}} = 1.8$, and
d) $x/d_{\text{eff}} = 10, y/d_{\text{eff}} = 1.8$



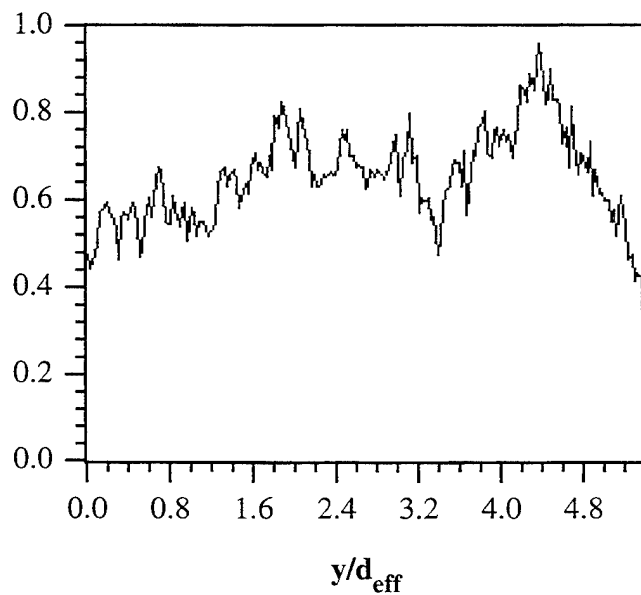
a) $x/d_{\text{eff}} = 0, z/d_{\text{eff}} = 0$



b) $x/d_{\text{eff}} = 4, z/d_{\text{eff}} = 0$



c) $x/d_{\text{eff}} = 8, z/d_{\text{eff}} = 0$



d) $x/d_{\text{eff}} = 10, z/d_{\text{eff}} = 0$

Figure 5.37 Transverse Profiles of Normalized Standard Deviation for Case C1A

a) $x/d_{\text{eff}} = 0, z/d_{\text{eff}} = 0$, b) $x/d_{\text{eff}} = 4, z/d_{\text{eff}} = 0$, c) $x/d_{\text{eff}} = 8, z/d_{\text{eff}} = 0$, and
d) $x/d_{\text{eff}} = 10, z/d_{\text{eff}} = 0$

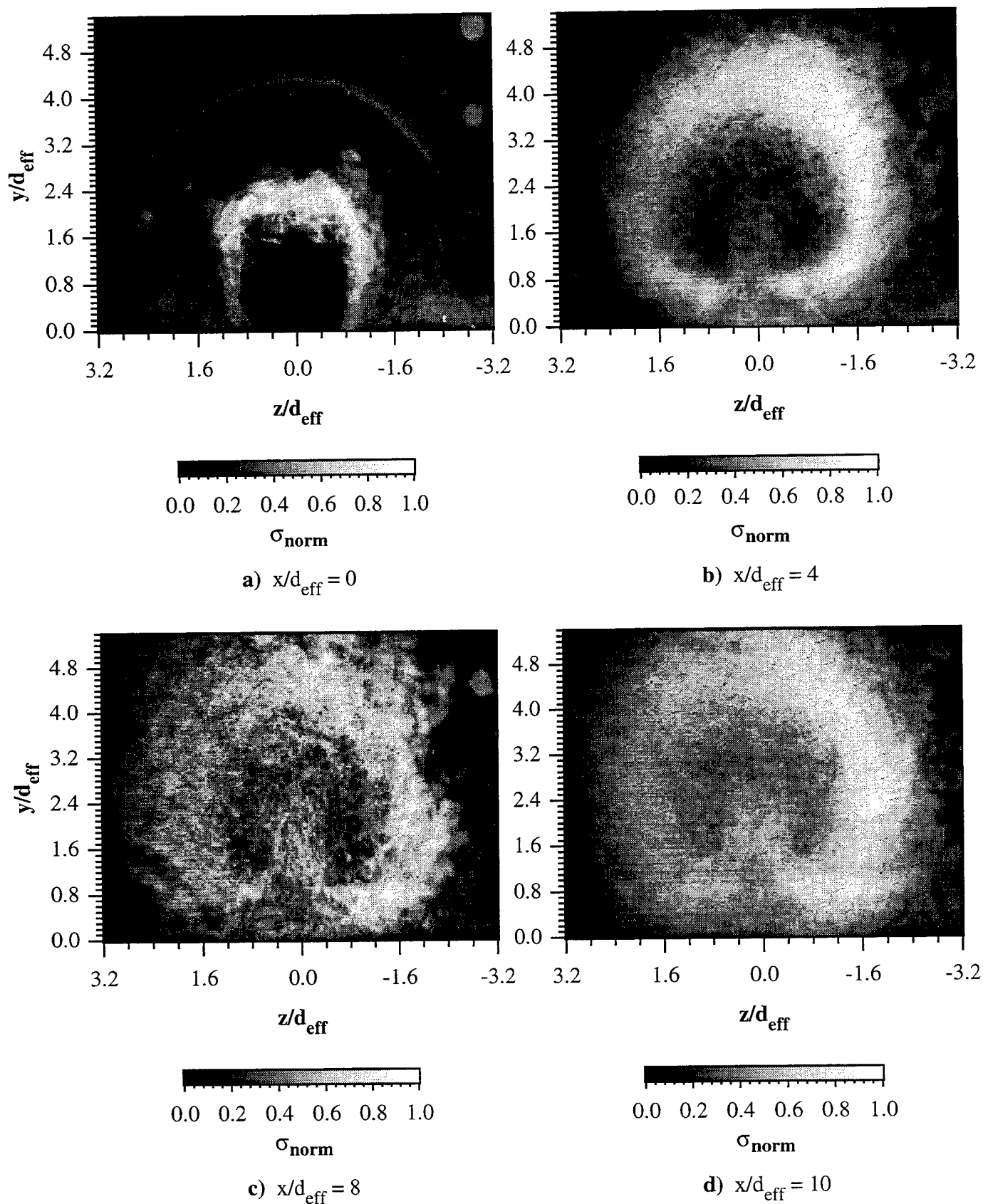
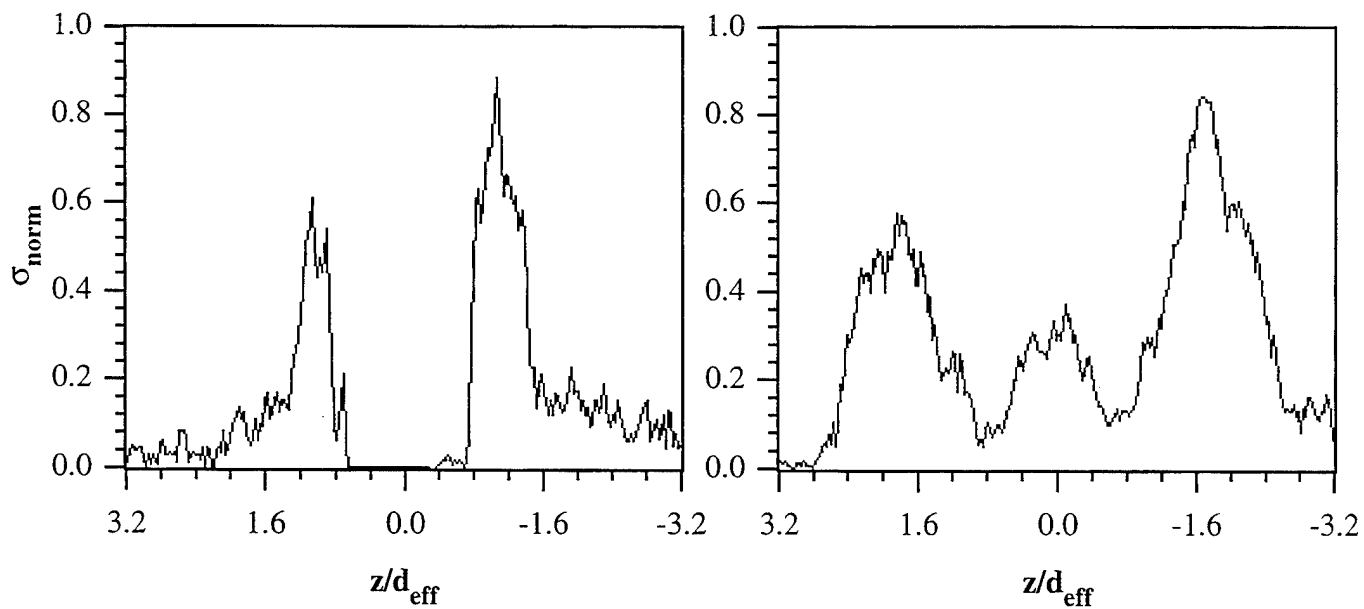
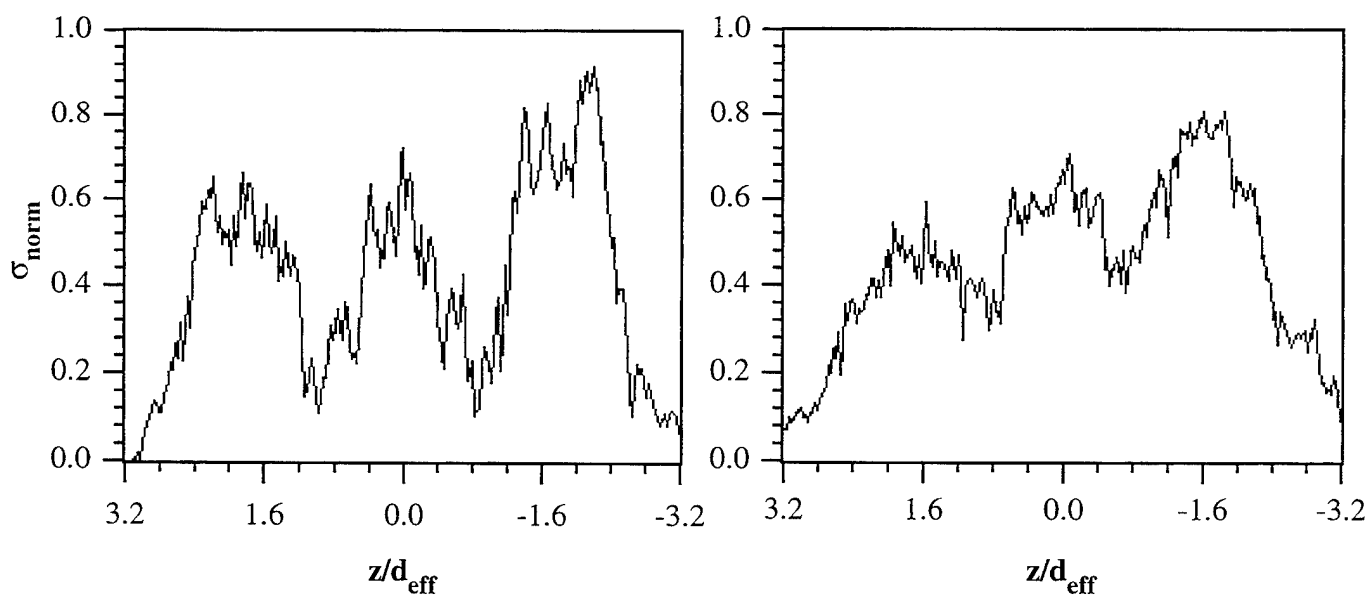


Figure 5.38 Normalized Standard Deviation End View Images of Circular Injection Using Helium (Case C2H) a) $x/d_{\text{eff}} = 0$, b) $x/d_{\text{eff}} = 4$, c) $x/d_{\text{eff}} = 8$, and d) $x/d_{\text{eff}} = 10$



a) $x/d_{\text{eff}} = 0, y/d_{\text{eff}} = 1.3$

b) $x/d_{\text{eff}} = 4, y/d_{\text{eff}} = 1.8$

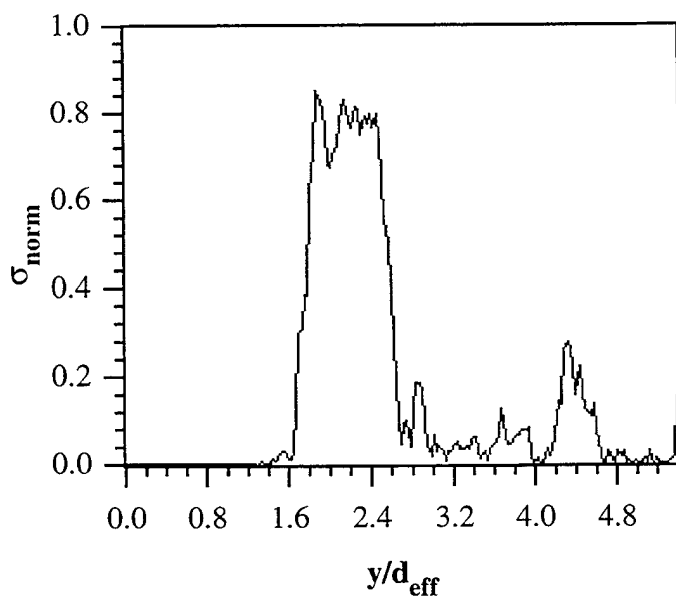


c) $x/d_{\text{eff}} = 8, y/d_{\text{eff}} = 1.8$

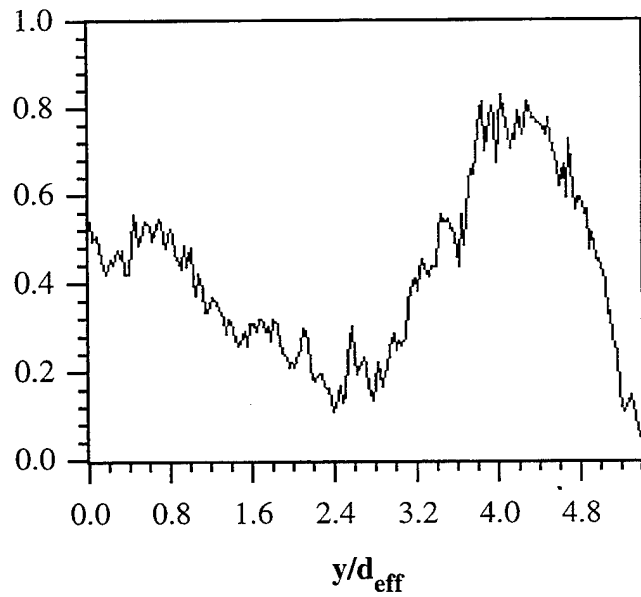
d) $x/d_{\text{eff}} = 10, y/d_{\text{eff}} = 1.8$

Figure 5.39 Spanwise Profiles of Normalized Standard Deviation for Case C2H

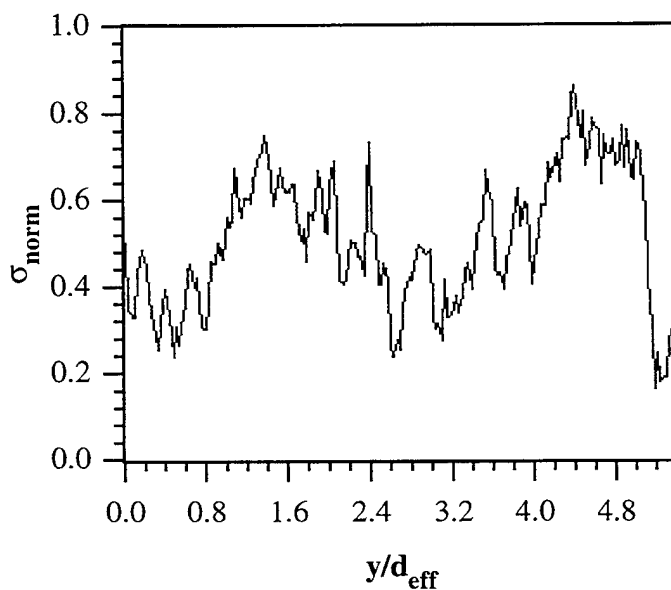
a) $x/d_{\text{eff}} = 0, y/d_{\text{eff}} = 1.3$, b) $x/d_{\text{eff}} = 4, y/d_{\text{eff}} = 1.8$, c) $x/d_{\text{eff}} = 8, y/d_{\text{eff}} = 1.8$, and
d) $x/d_{\text{eff}} = 10, y/d_{\text{eff}} = 1.8$



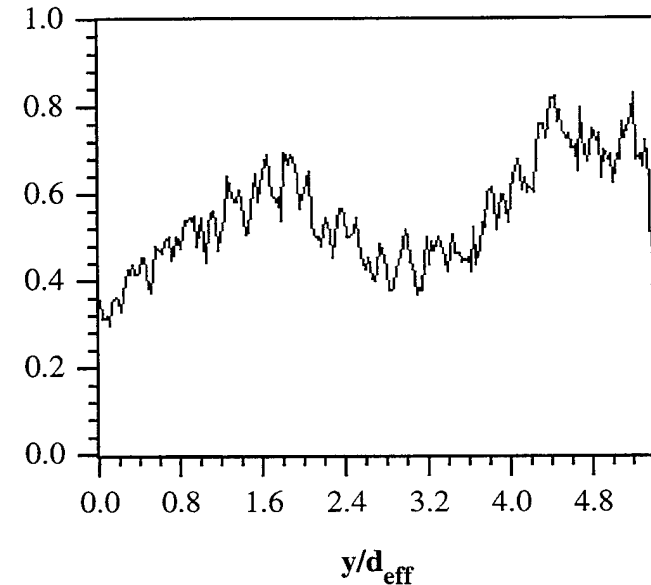
a) $x/d_{\text{eff}} = 0, z/d_{\text{eff}} = 0$



b) $x/d_{\text{eff}} = 4, z/d_{\text{eff}} = 0$



c) $x/d_{\text{eff}} = 8, z/d_{\text{eff}} = 0$



d) $x/d_{\text{eff}} = 10, z/d_{\text{eff}} = 0$

Figure 5.40 Transverse Profiles of Normalized Standard Deviation for Case C2H

a) $x/d_{\text{eff}} = 0, z/d_{\text{eff}} = 0$, b) $x/d_{\text{eff}} = 4, z/d_{\text{eff}} = 0$, c) $x/d_{\text{eff}} = 8, z/d_{\text{eff}} = 0$, and
d) $x/d_{\text{eff}} = 10, z/d_{\text{eff}} = 0$

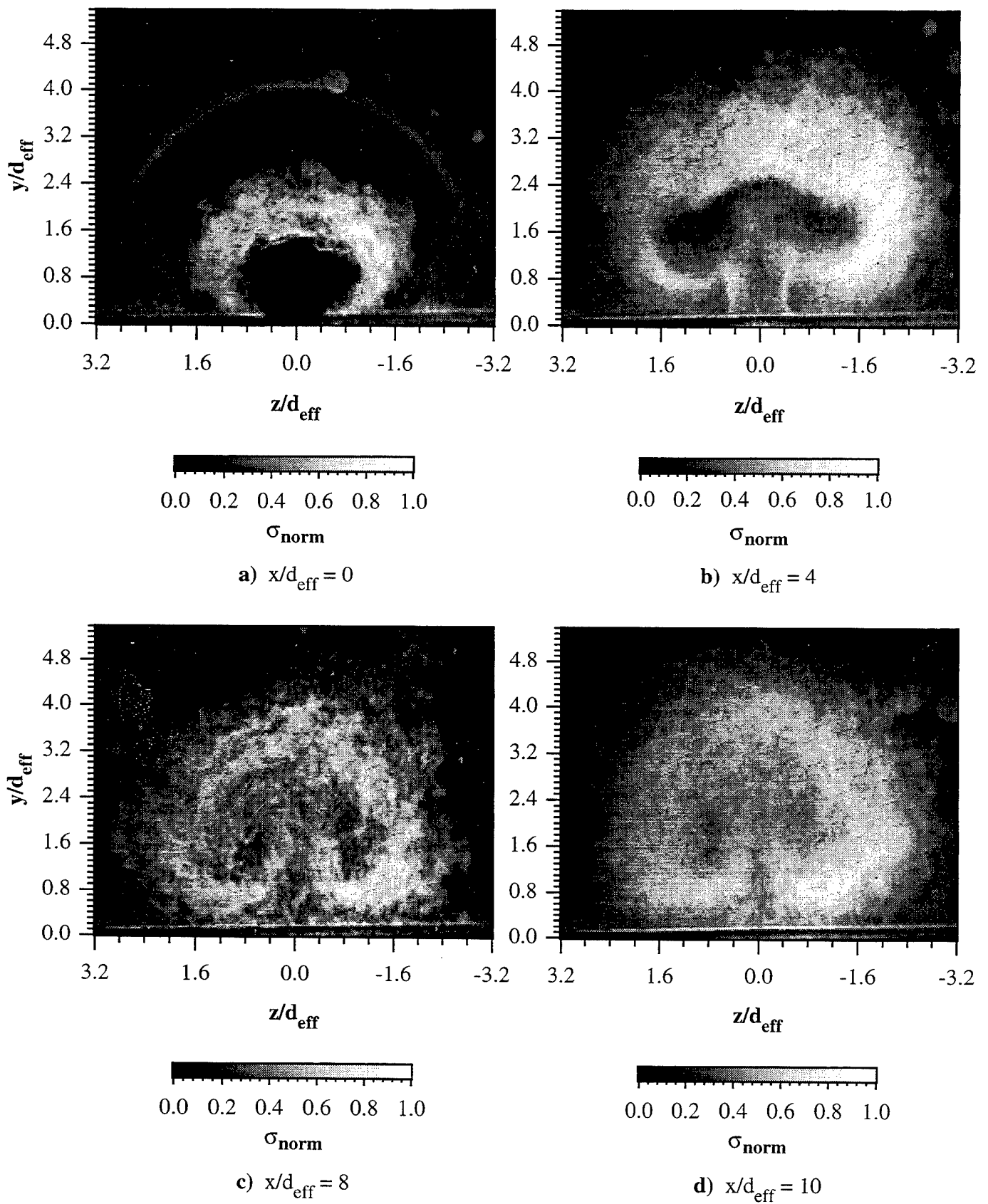


Figure 5.41 Normalized Standard Deviation End View Images of Elliptical Injection Using Air (Case E1A) a) $x/d_{\text{eff}} = 0$, b) $x/d_{\text{eff}} = 4$, c) $x/d_{\text{eff}} = 8$, and d) $x/d_{\text{eff}} = 10$

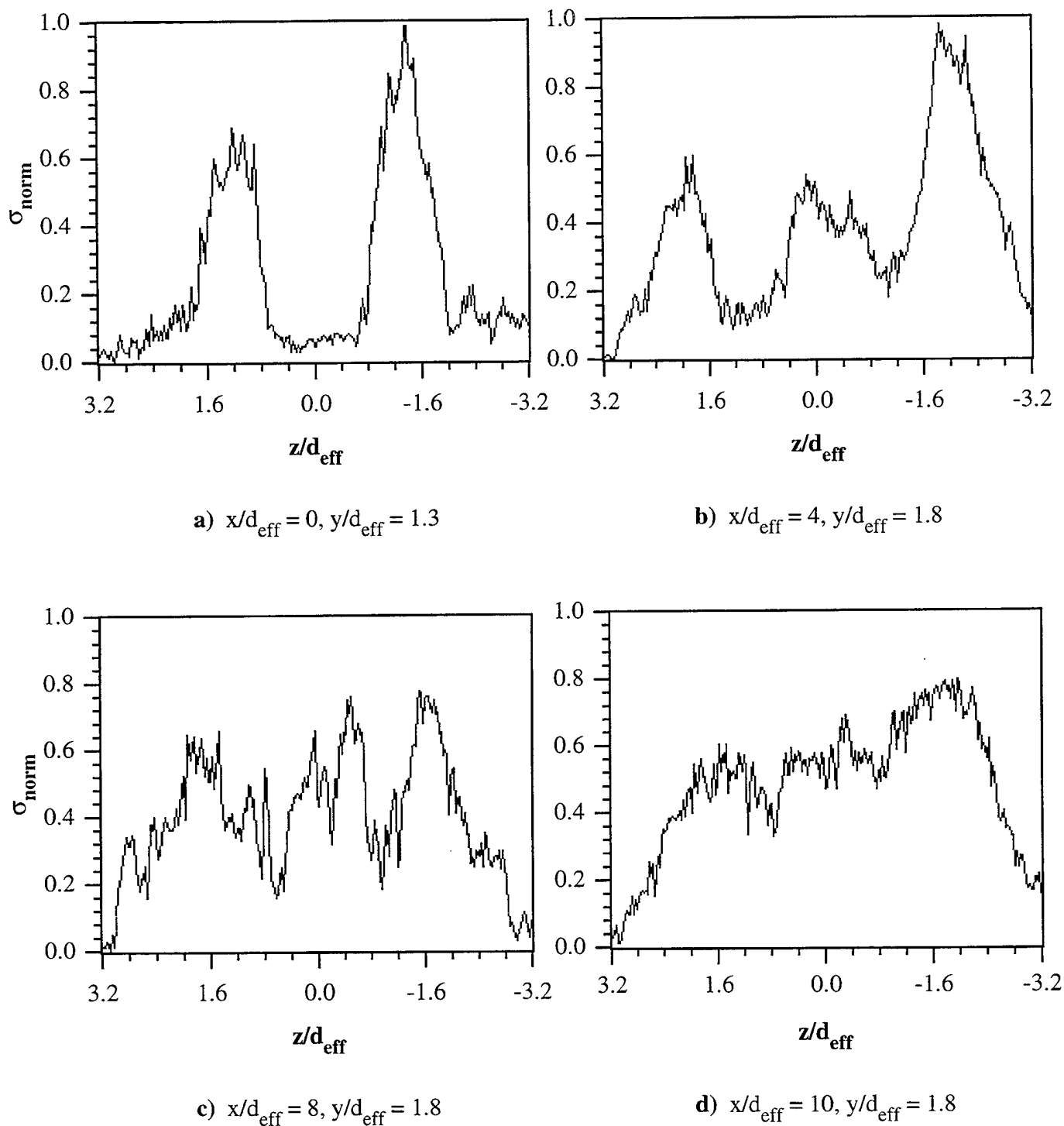


Figure 5.42 Spanwise Profiles of Normalized Standard Deviation for Case E1A

a) $x/d_{\text{eff}} = 0, y/d_{\text{eff}} = 1.3$, b) $x/d_{\text{eff}} = 4, y/d_{\text{eff}} = 1.8$, c) $x/d_{\text{eff}} = 8, y/d_{\text{eff}} = 1.8$, and
d) $x/d_{\text{eff}} = 10, y/d_{\text{eff}} = 1.8$

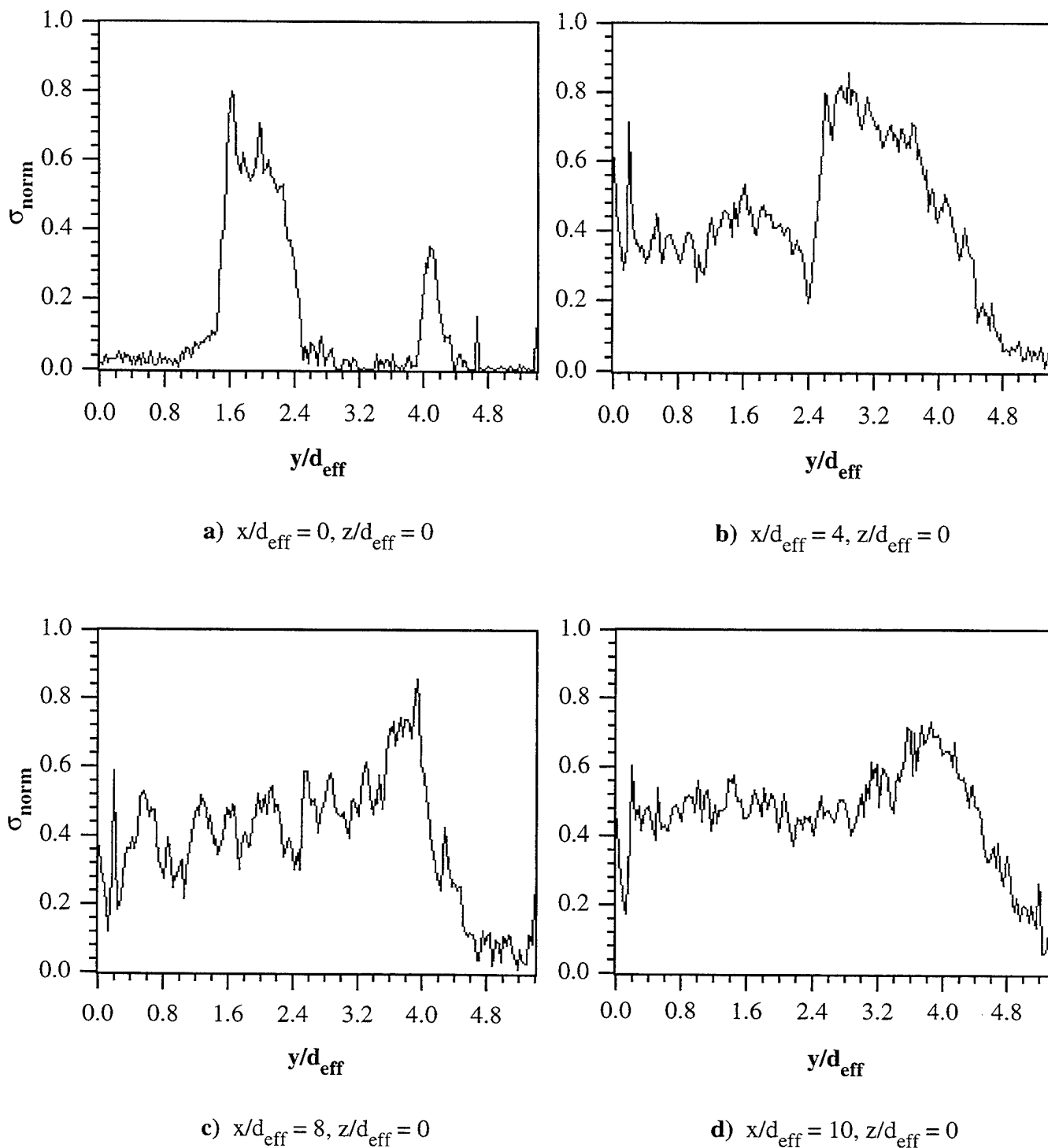


Figure 5.43 Transverse Profiles of Normalized Standard Deviation for Case E1A

a) $x/d_{\text{eff}} = 0, z/d_{\text{eff}} = 0$, **b)** $x/d_{\text{eff}} = 4, z/d_{\text{eff}} = 0$, **c)** $x/d_{\text{eff}} = 8, z/d_{\text{eff}} = 0$, and
d) $x/d_{\text{eff}} = 10, z/d_{\text{eff}} = 0$

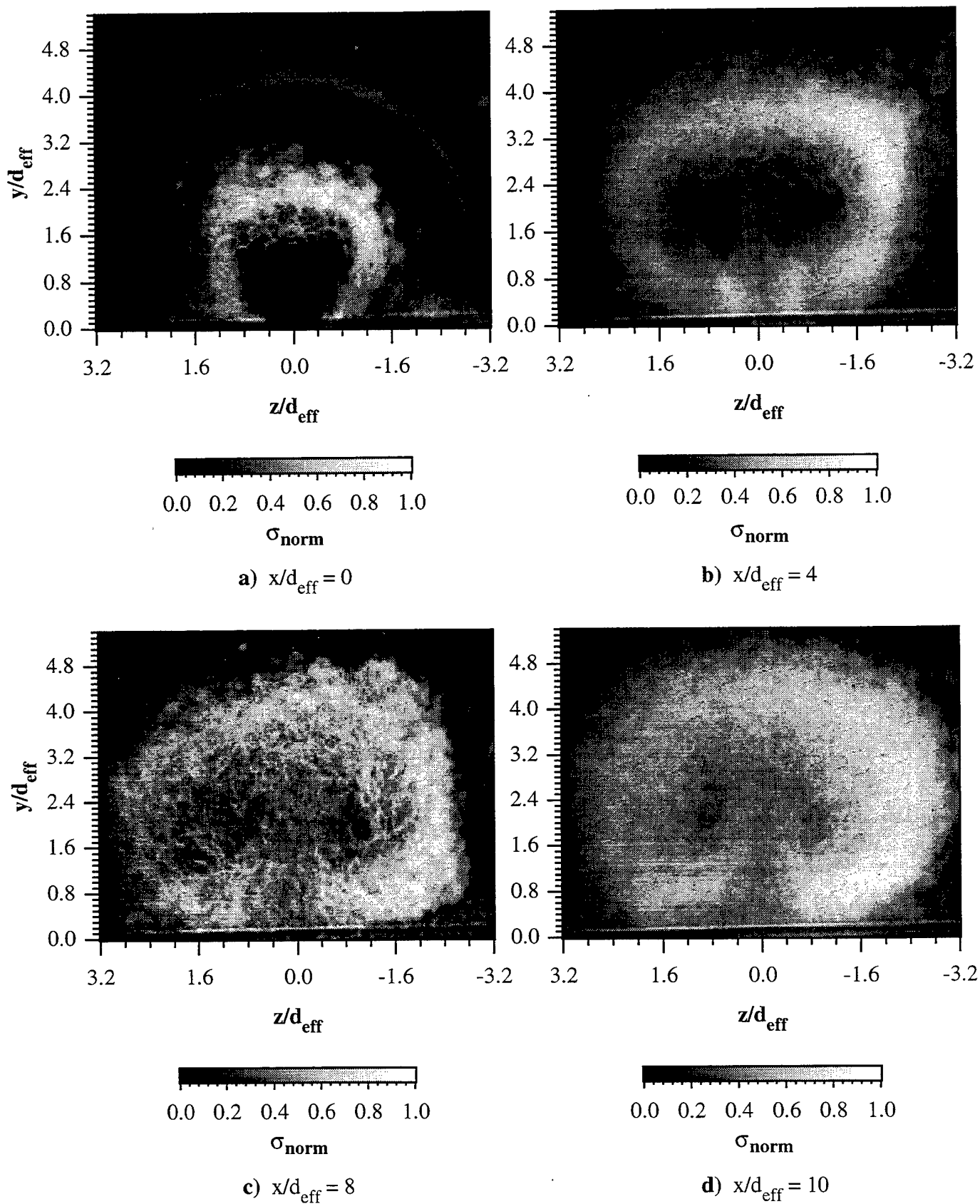
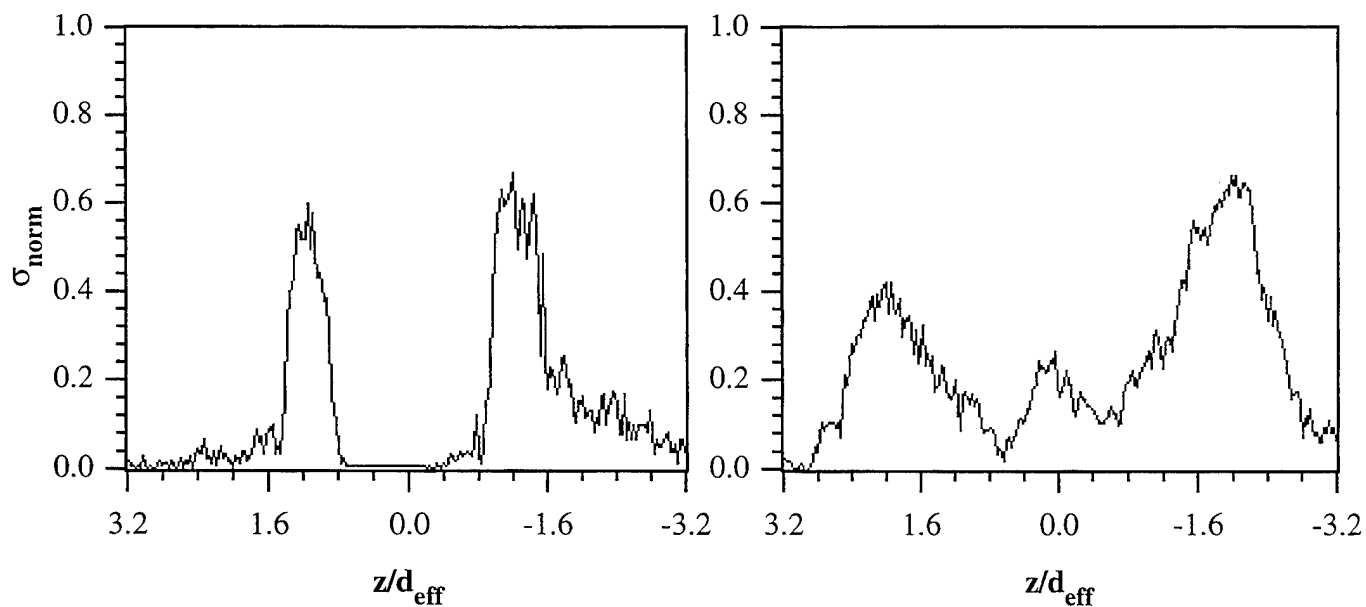
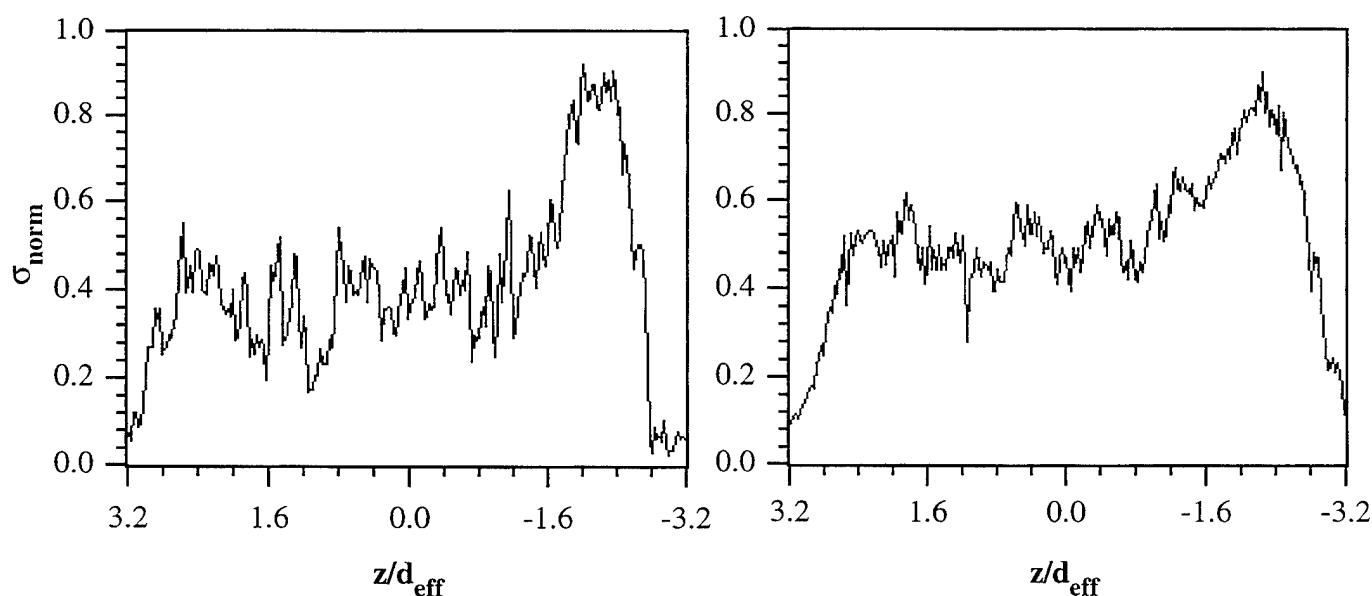


Figure 5.44 Normalized Standard Deviation End View Images of Elliptical Injection Using Helium (Case E2H) a) $x/d_{\text{eff}} = 0$, b) $x/d_{\text{eff}} = 4$, c) $x/d_{\text{eff}} = 8$, and d) $x/d_{\text{eff}} = 10$



a) $x/d_{\text{eff}} = 0, y/d_{\text{eff}} = 1.3$

b) $x/d_{\text{eff}} = 4, y/d_{\text{eff}} = 1.8$

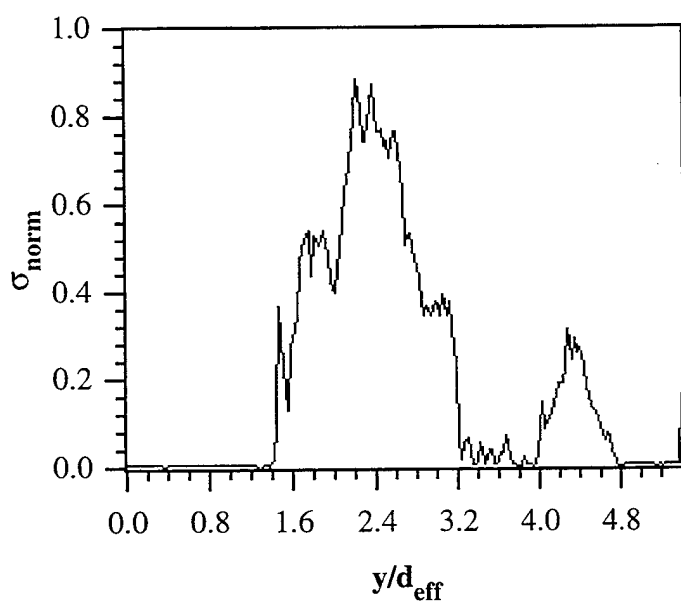


c) $x/d_{\text{eff}} = 8, y/d_{\text{eff}} = 1.8$

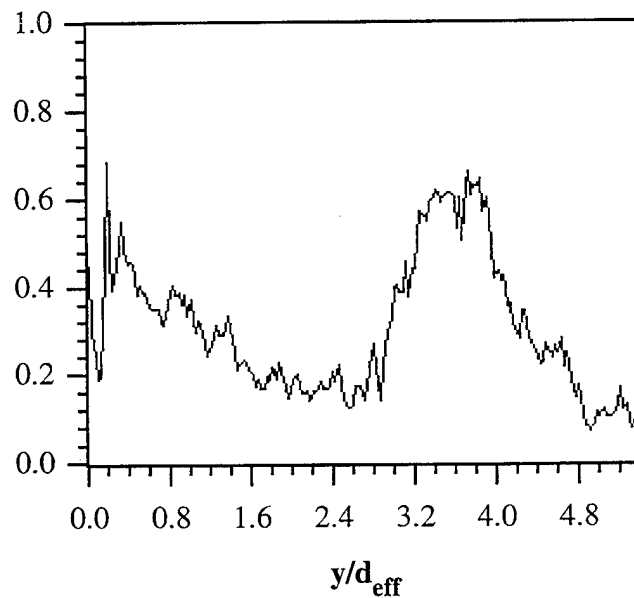
d) $x/d_{\text{eff}} = 10, y/d_{\text{eff}} = 1.8$

Figure 5.45 Spanwise Profiles of Normalized Standard Deviation for Case E2H

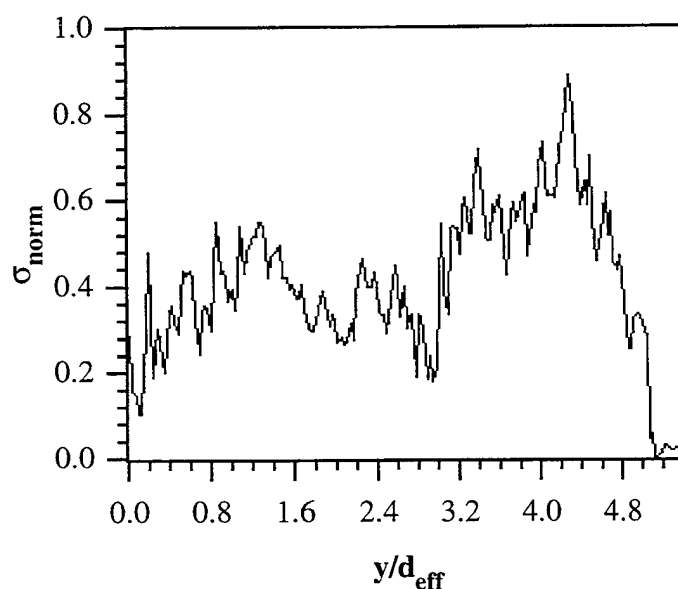
a) $x/d_{\text{eff}} = 0, y/d_{\text{eff}} = 1.3$, **b)** $x/d_{\text{eff}} = 4, y/d_{\text{eff}} = 1.8$, **c)** $x/d_{\text{eff}} = 8, y/d_{\text{eff}} = 1.8$, and
d) $x/d_{\text{eff}} = 10, y/d_{\text{eff}} = 1.8$



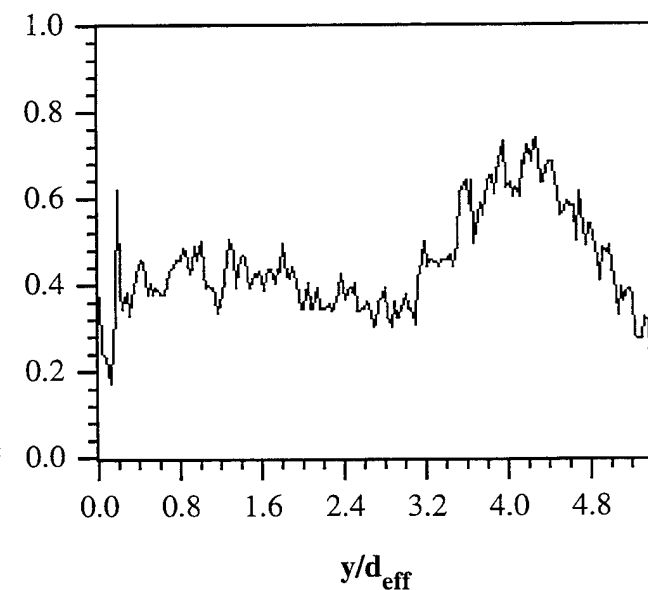
a) $x/d_{\text{eff}} = 0, z/d_{\text{eff}} = 0$



b) $x/d_{\text{eff}} = 4, z/d_{\text{eff}} = 0$



c) $x/d_{\text{eff}} = 8, z/d_{\text{eff}} = 0$



d) $x/d_{\text{eff}} = 10, z/d_{\text{eff}} = 0$

Figure 5.46 Transverse Profiles of Normalized Standard Deviation for Case E2H

a) $x/d_{\text{eff}} = 0, z/d_{\text{eff}} = 0$, b) $x/d_{\text{eff}} = 4, z/d_{\text{eff}} = 0$, c) $x/d_{\text{eff}} = 8, z/d_{\text{eff}} = 0$, and
d) $x/d_{\text{eff}} = 10, z/d_{\text{eff}} = 0$

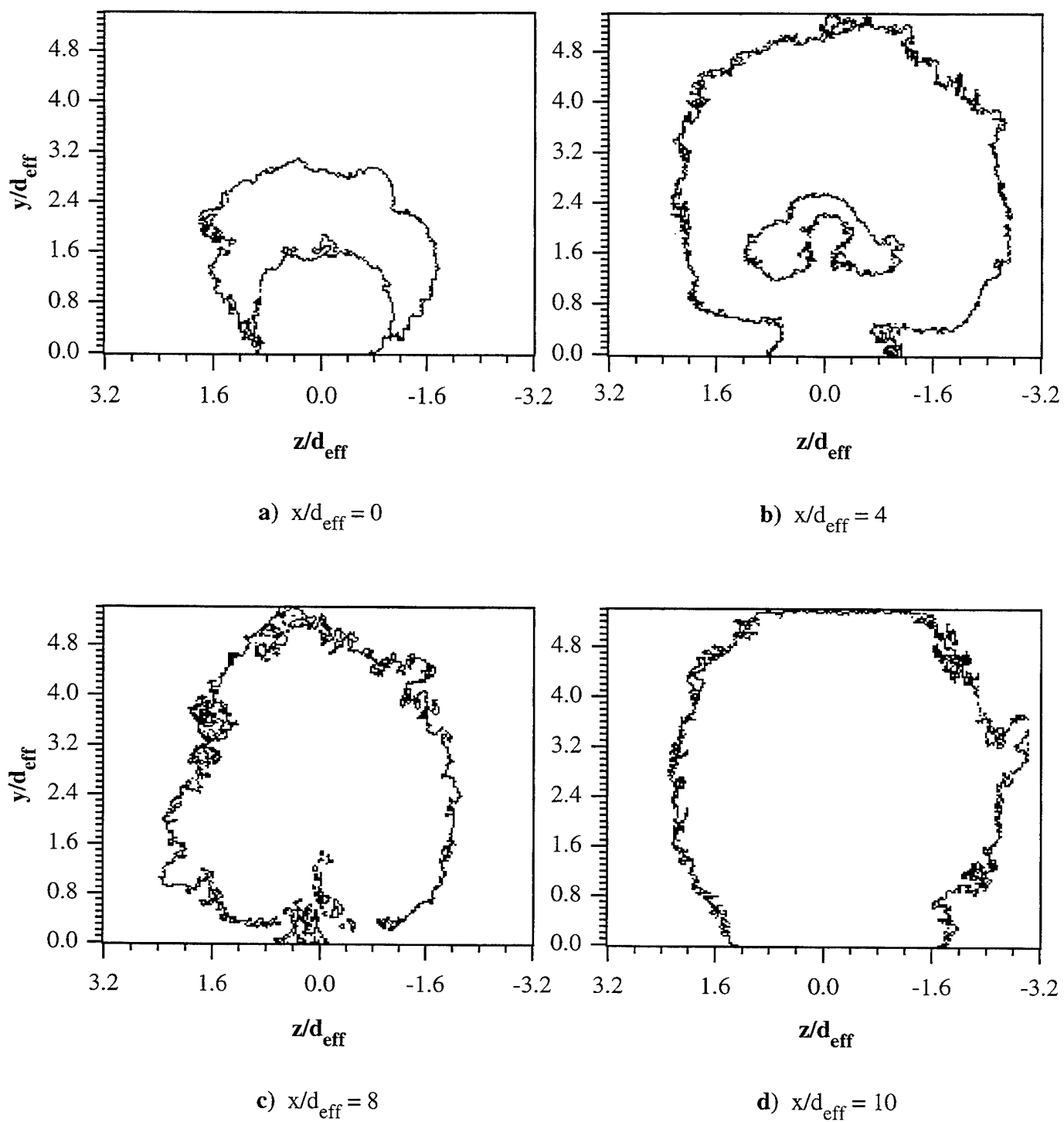


Figure 5.47 End View Mixing Zone Contours for Case C1A **a)** $x/d_{\text{eff}} = 0$, **b)** $x/d_{\text{eff}} = 4$, **c)** $x/d_{\text{eff}} = 8$, and **d)** $x/d_{\text{eff}} = 10$

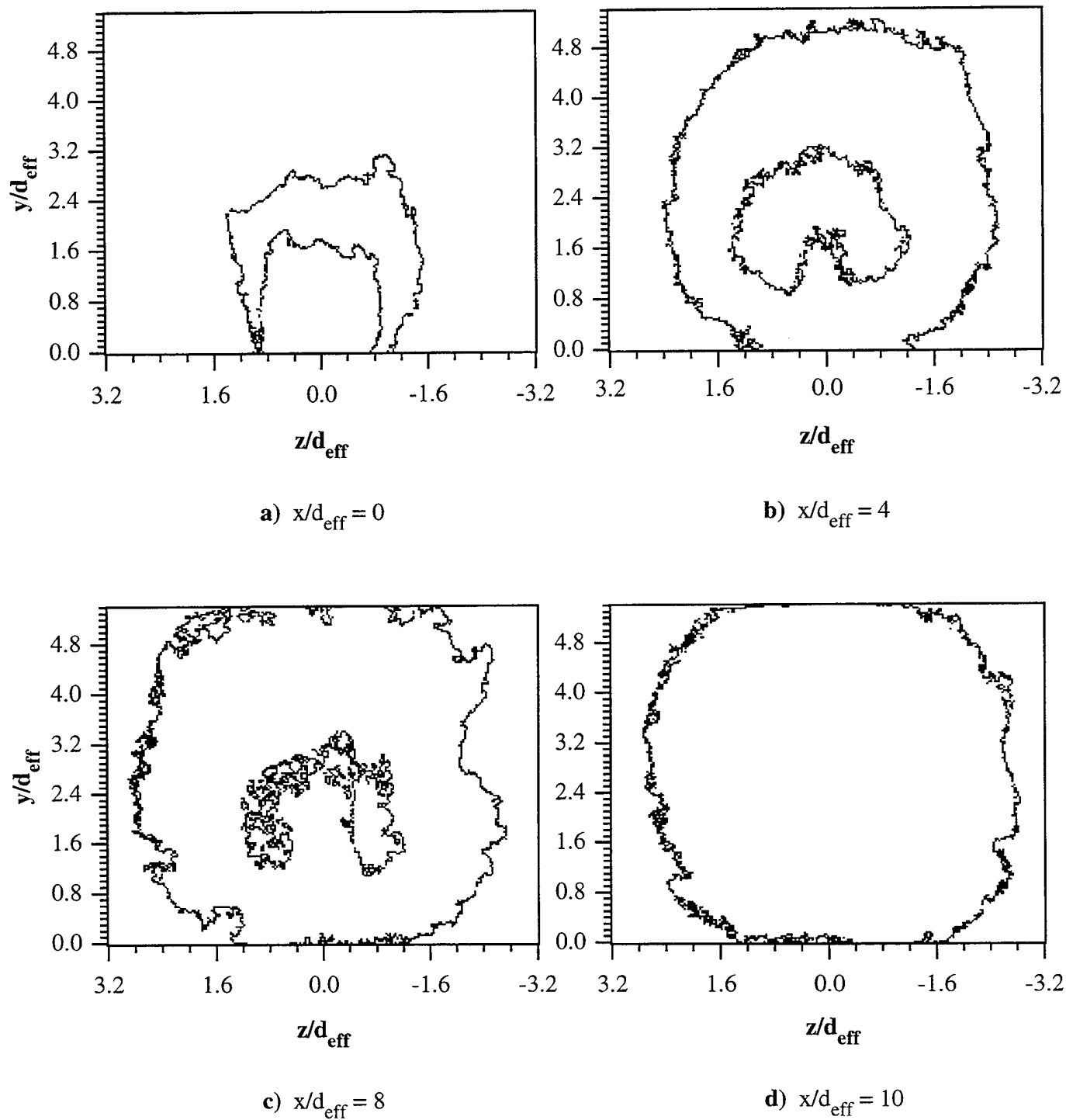


Figure 5.48 End View Mixing Zone Contours for Case C2H **a)** $x/d_{\text{eff}} = 0$, **b)** $x/d_{\text{eff}} = 4$, **c)** $x/d_{\text{eff}} = 8$, and **d)** $x/d_{\text{eff}} = 10$

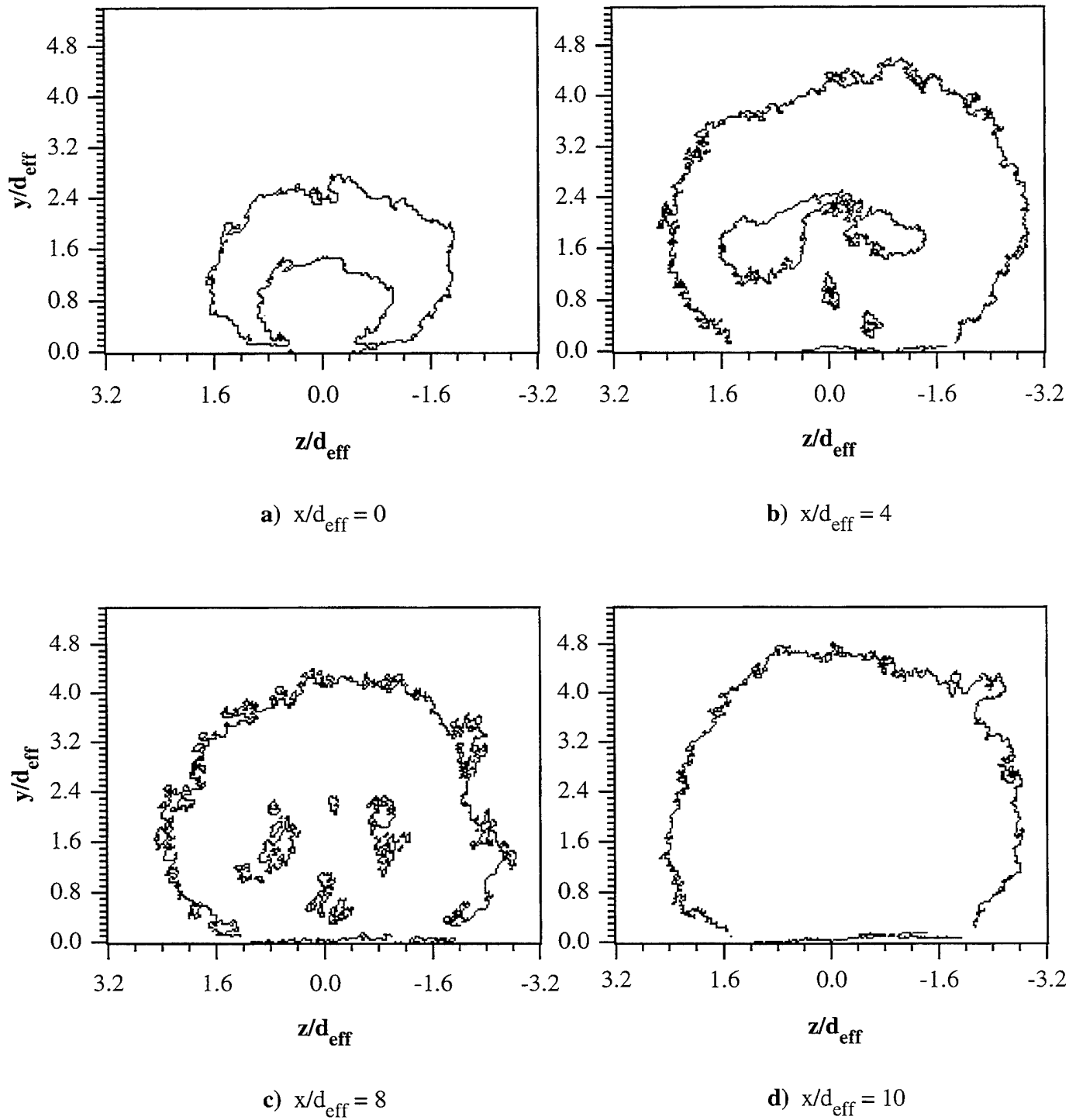


Figure 5.49 End View Mixing Zone Contours for Case E1A **a)** $x/d_{\text{eff}} = 0$, **b)** $x/d_{\text{eff}} = 4$, **c)** $x/d_{\text{eff}} = 8$, and **d)** $x/d_{\text{eff}} = 10$

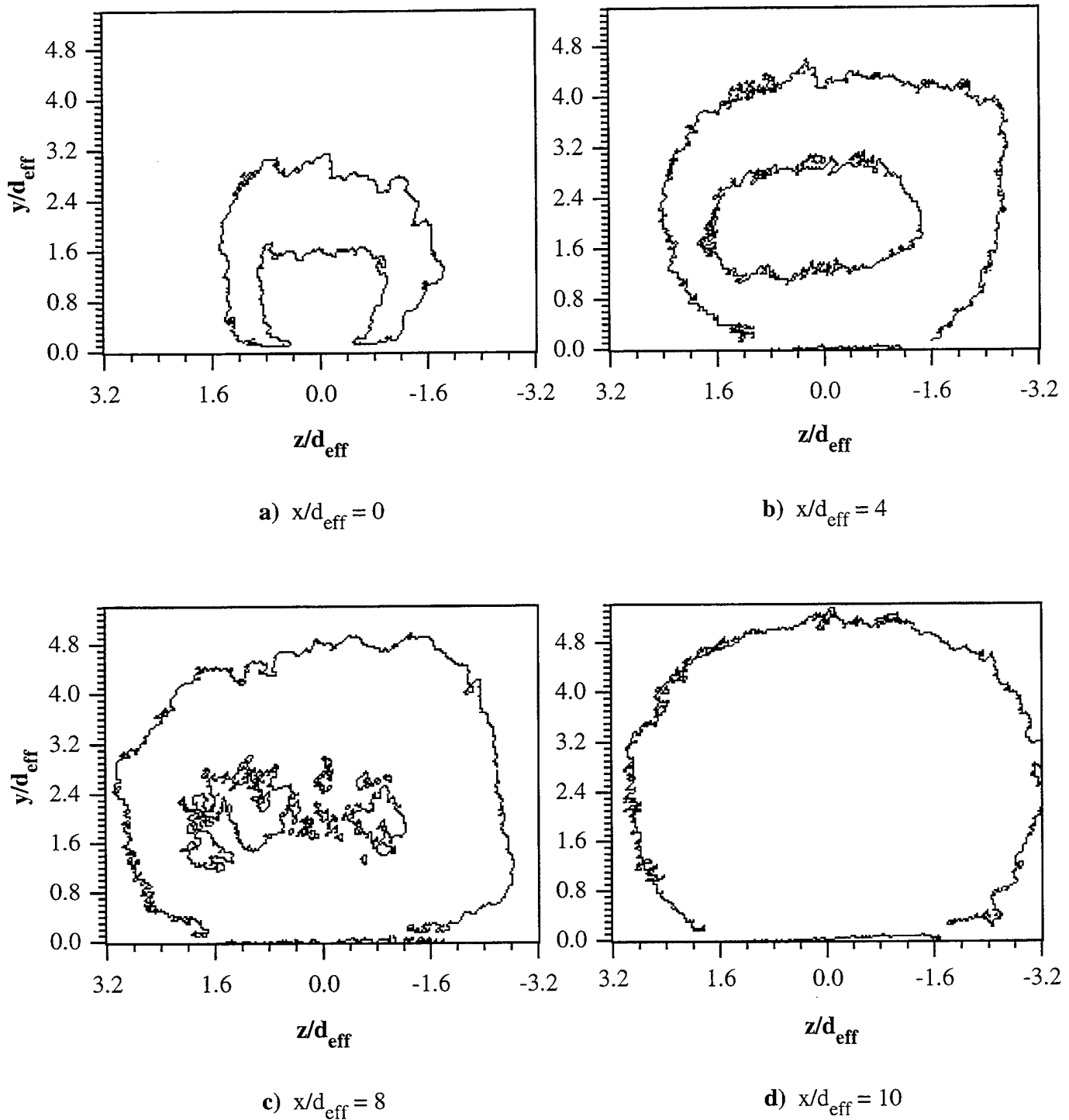


Figure 5.50 End View Mixing Zone Contours for Case E2H a) $x/d_{\text{eff}} = 0$, b) $x/d_{\text{eff}} = 4$, c) $x/d_{\text{eff}} = 8$, and d) $x/d_{\text{eff}} = 10$

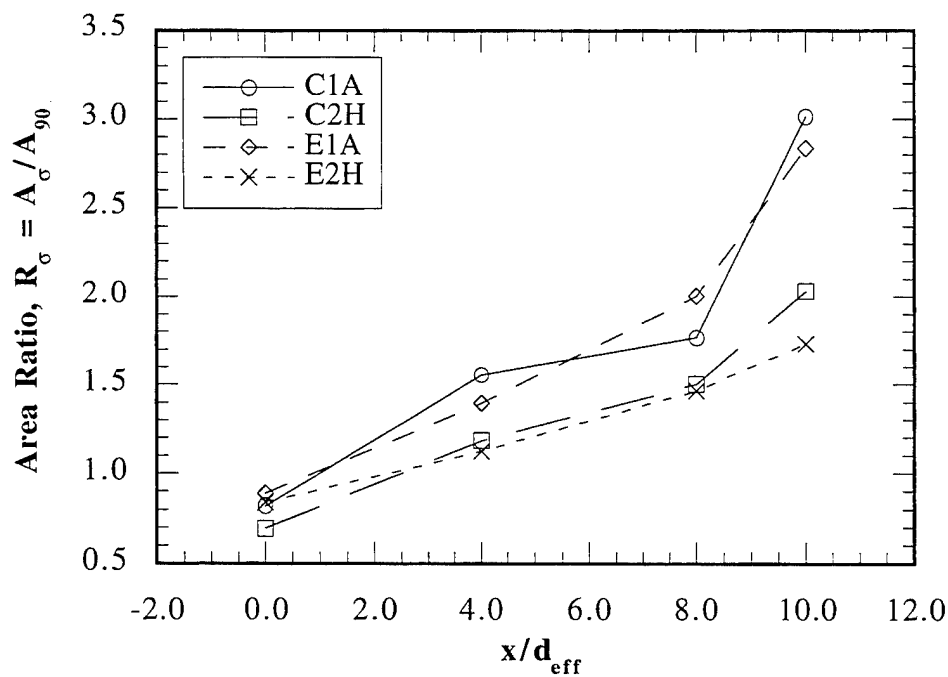


Figure 5.51 Area Ratios Determined from End View Standard Deviation Contours

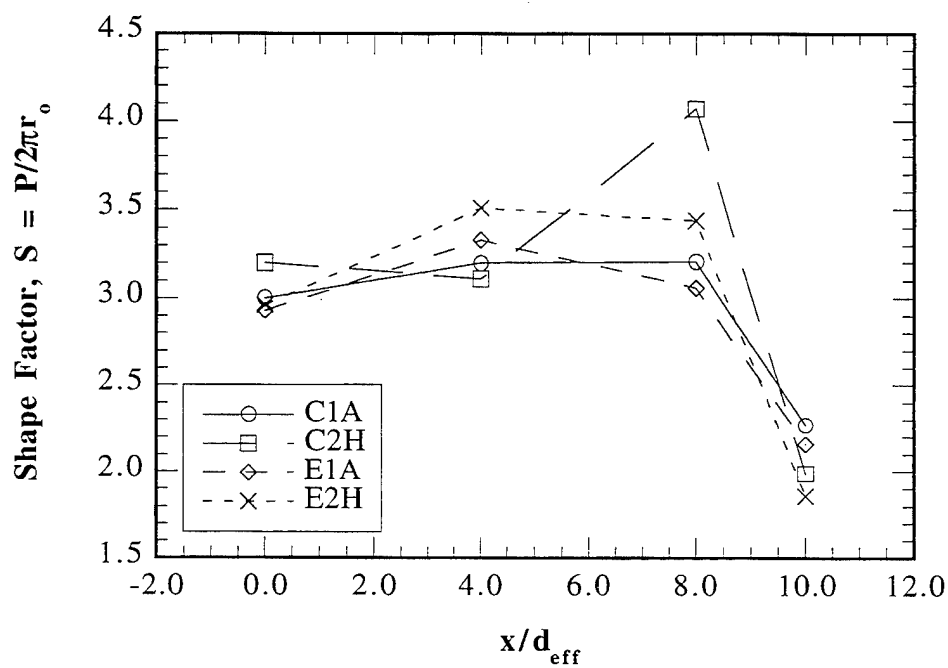


Figure 5.52 Shape Factors Determined from End View Standard Deviation Contours

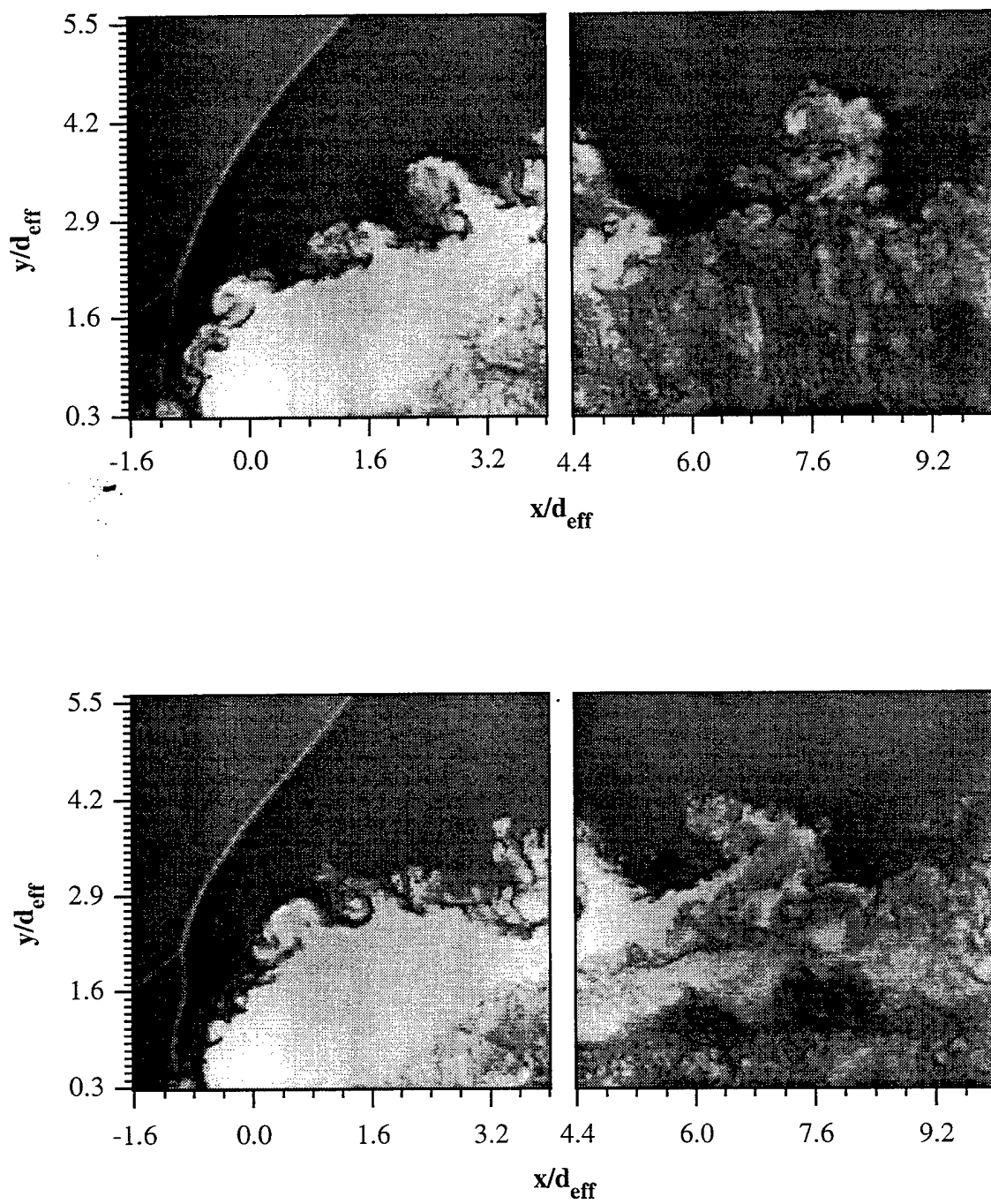


Figure 5.53 Instantaneous Side View Images of Circular Injection Using Air (Case C1A)

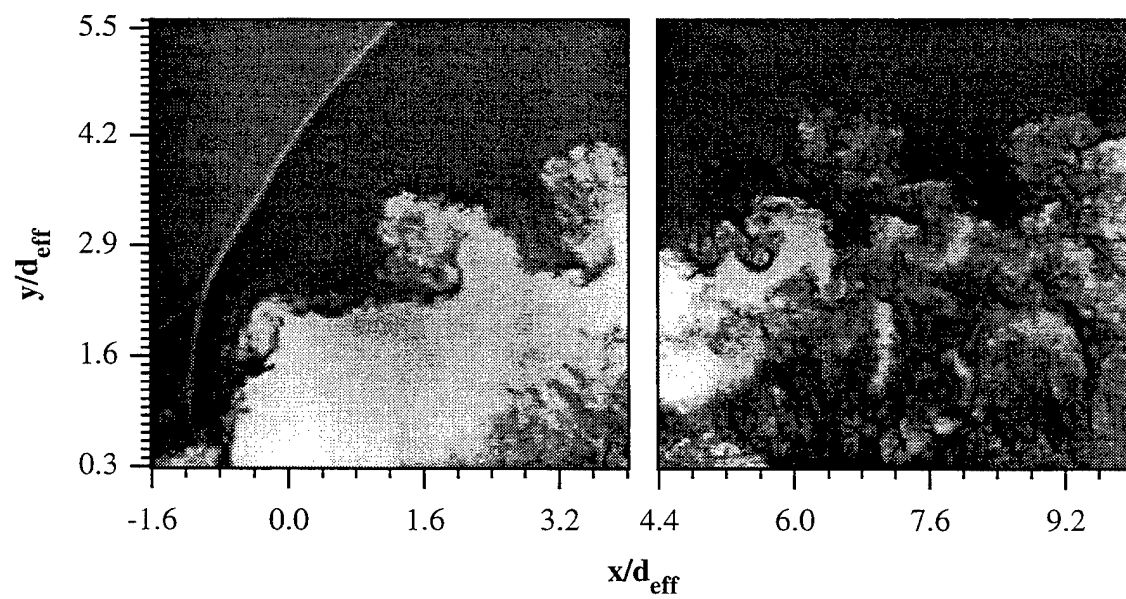
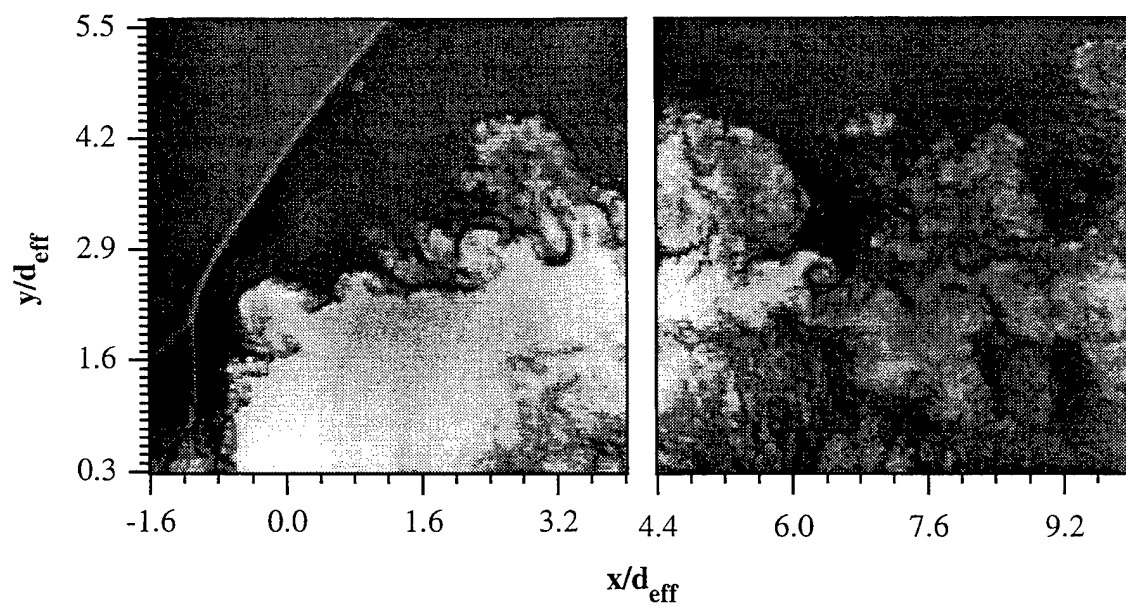


Figure 5.53 (continued)

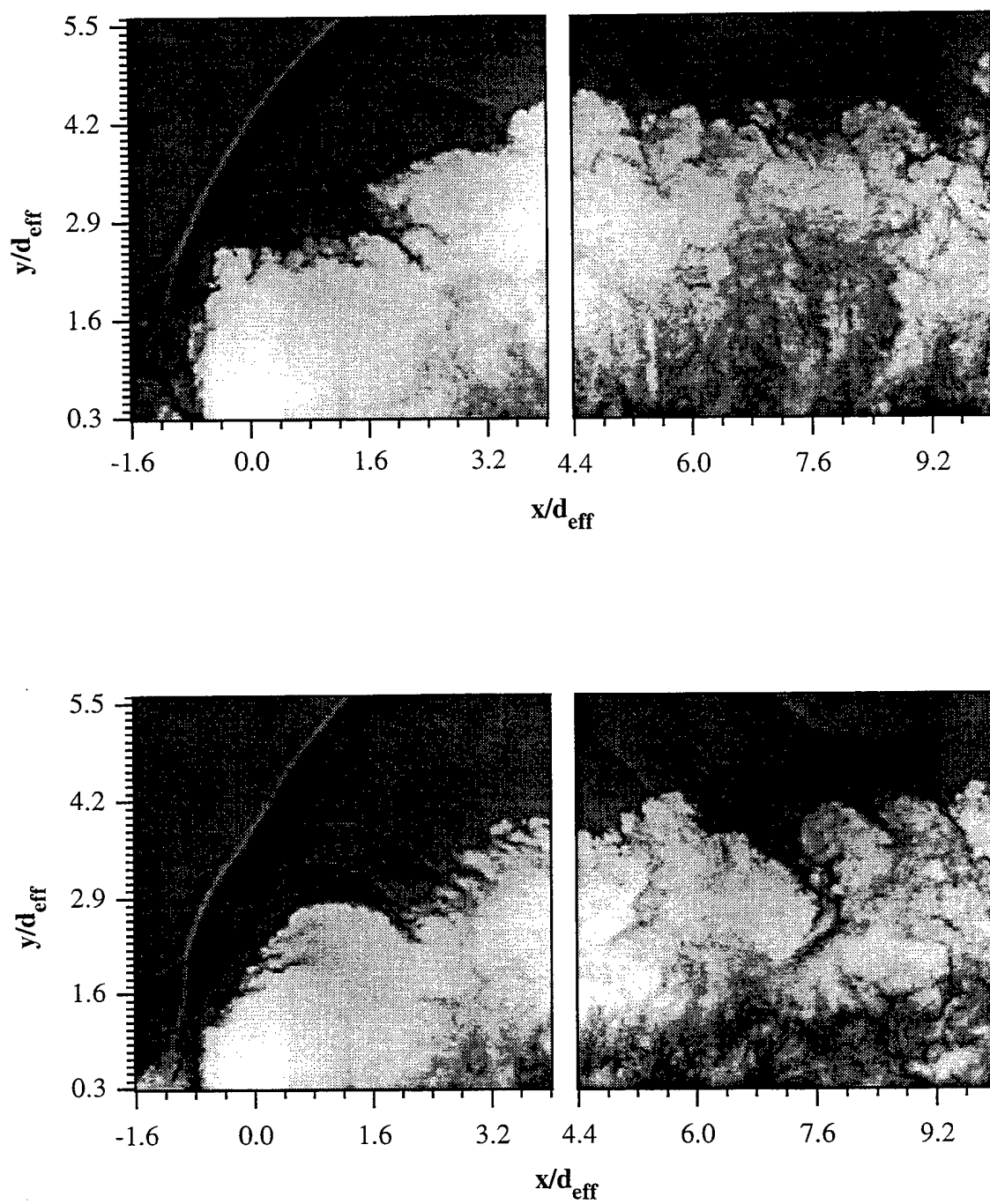


Figure 5.54 Instantaneous Side View Images of Circular Injection Using Helium (Case C2H)

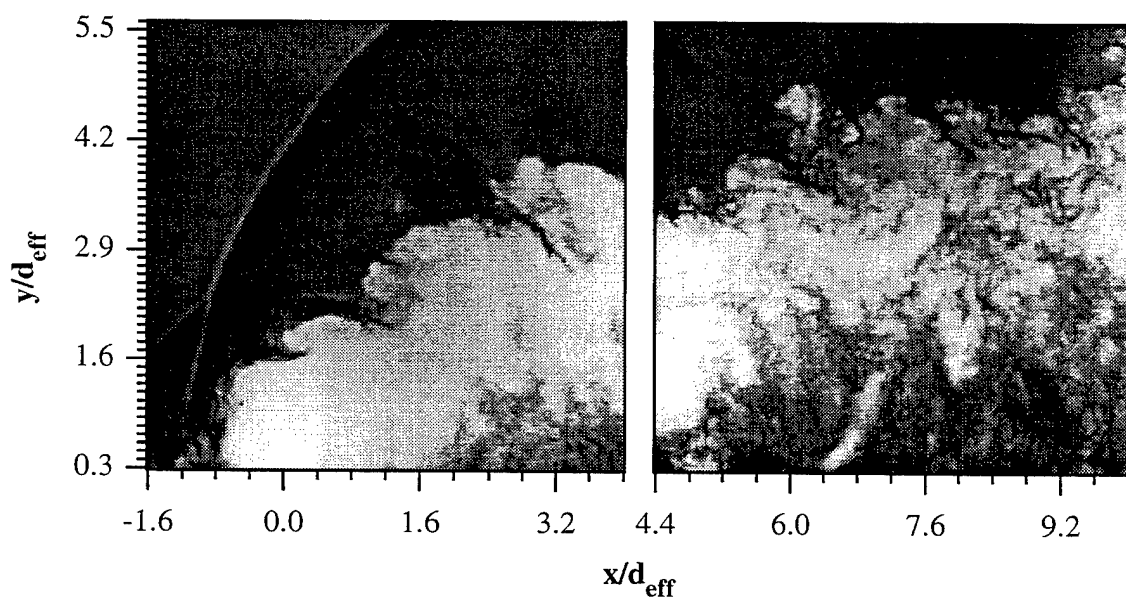
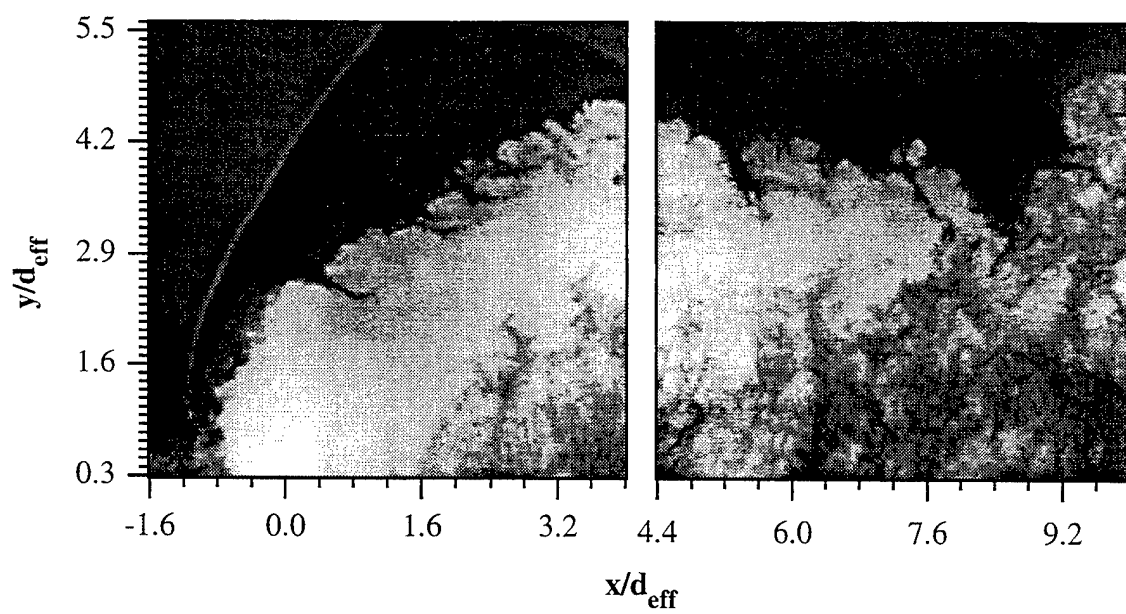


Figure 5.54 (continued)

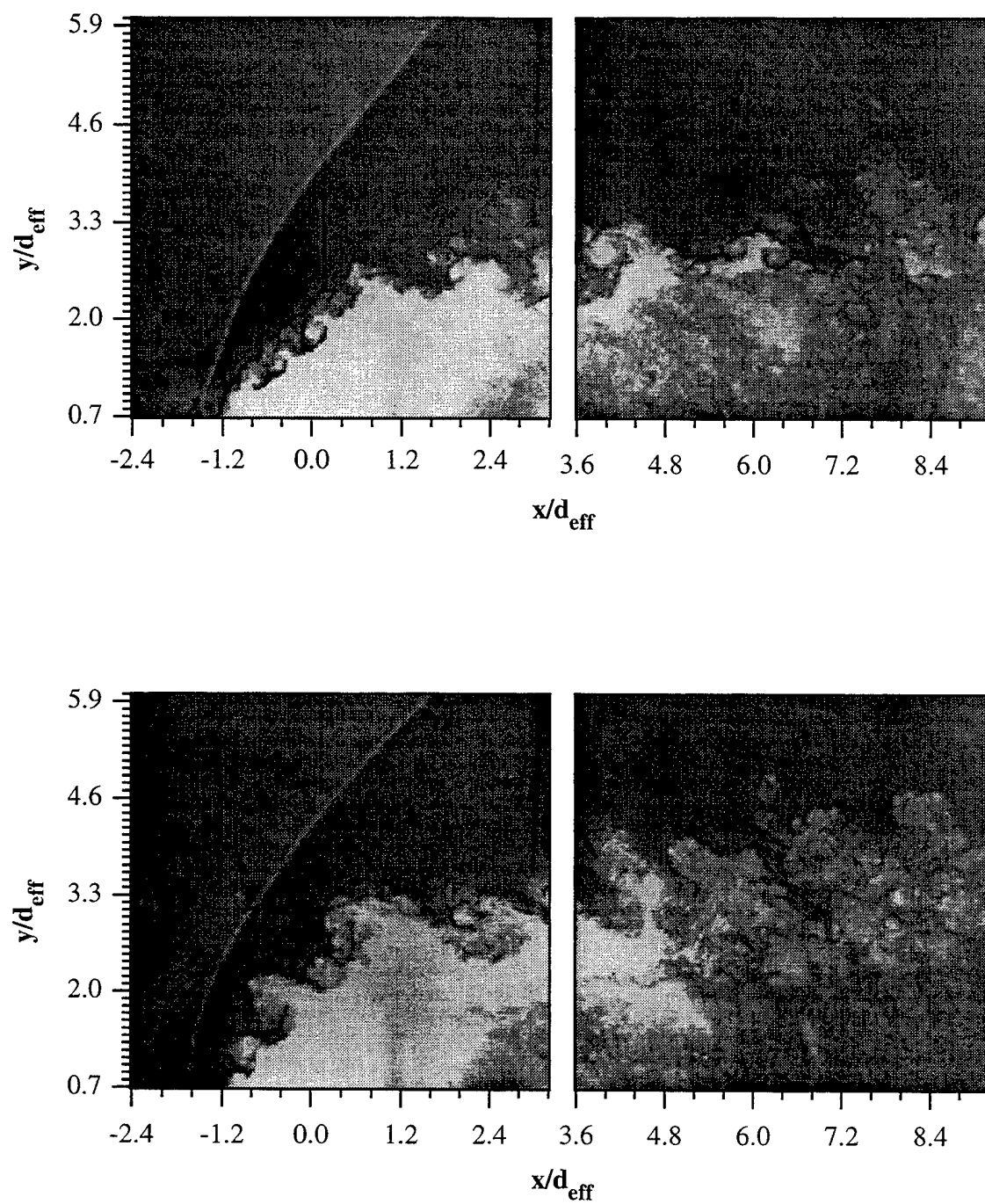


Figure 5.55 Instantaneous Side View Images of Elliptical Injection Using Air (Case E1A)

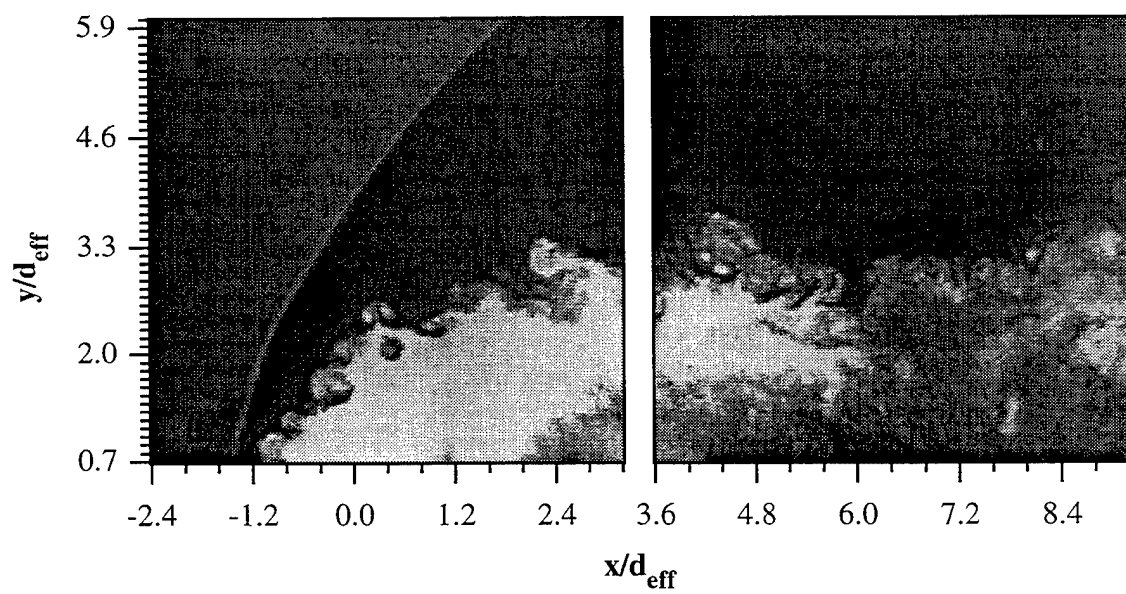
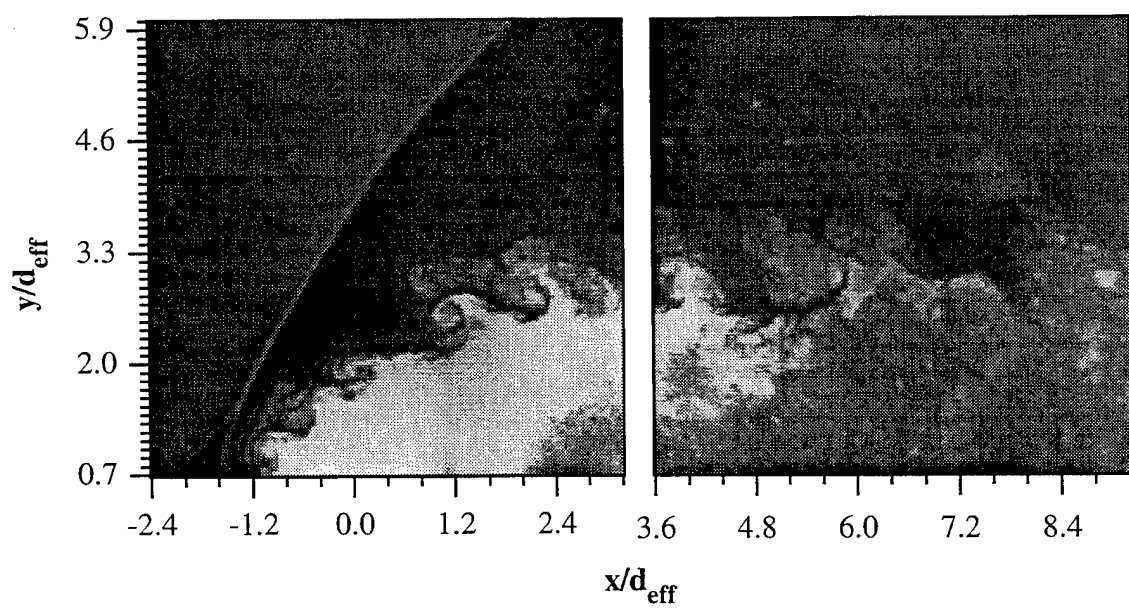


Figure 5.55 (continued)

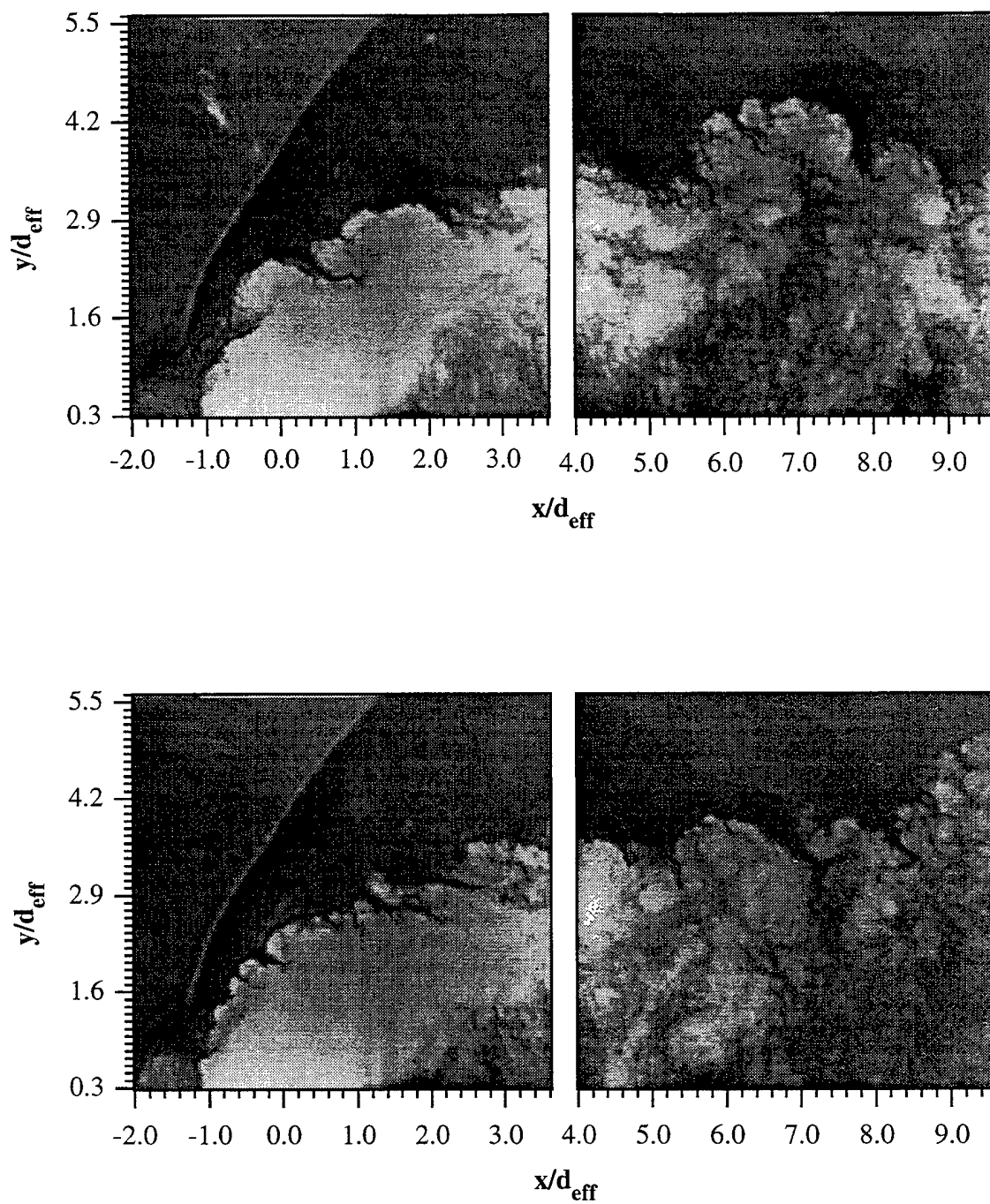


Figure 5.56 Instantaneous Side View Images of Elliptical Injection Using Helium (Case E2H)

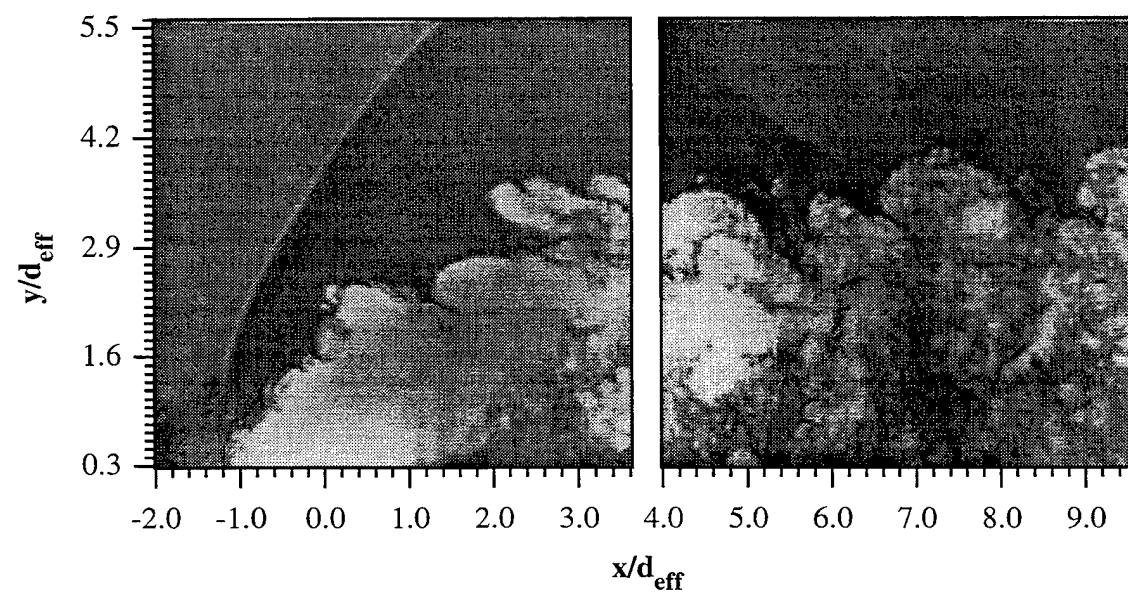
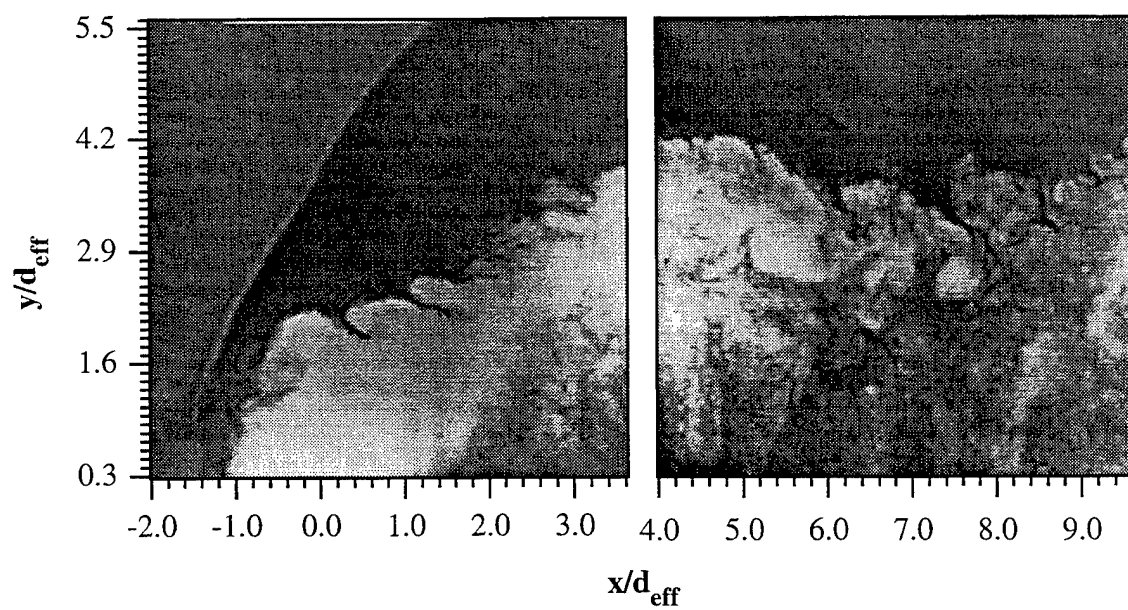


Figure 5.56 (continued)

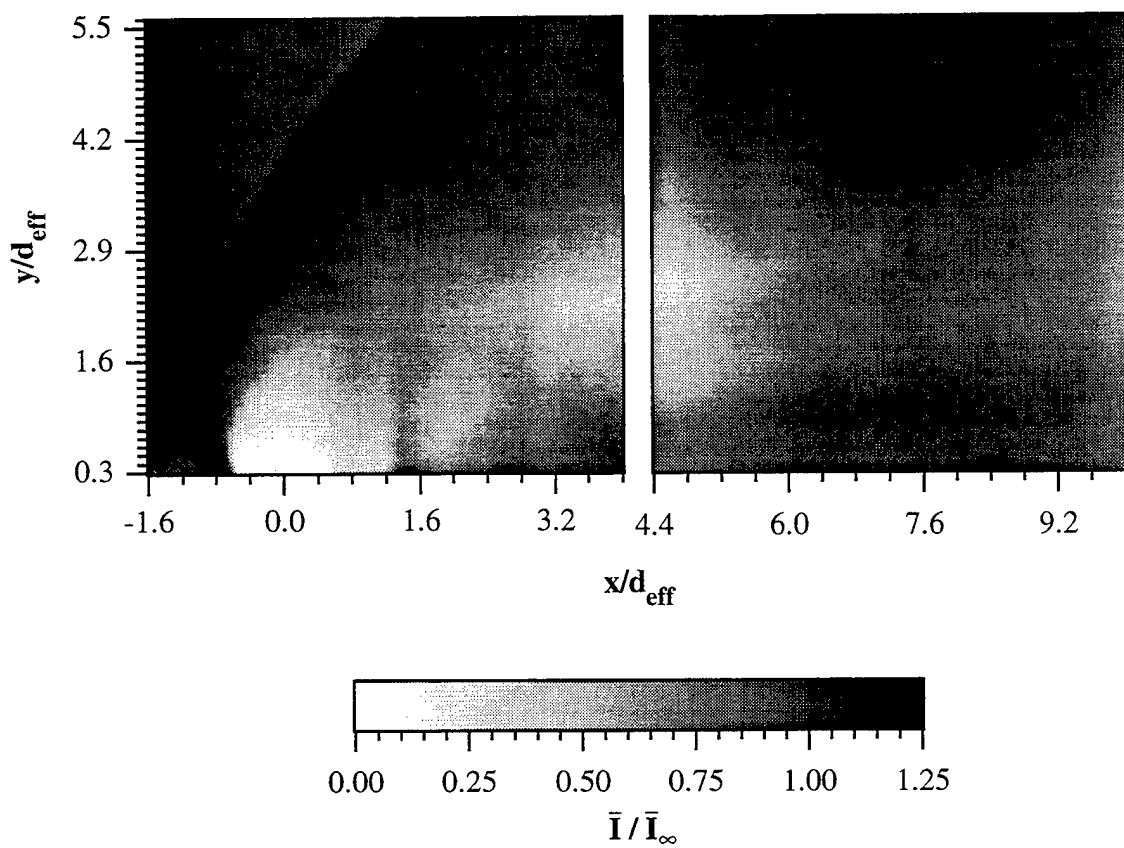


Figure 5.57 Normalized Ensemble-Averaged Side View Images of Circular Injection Using Air (Case C1A)

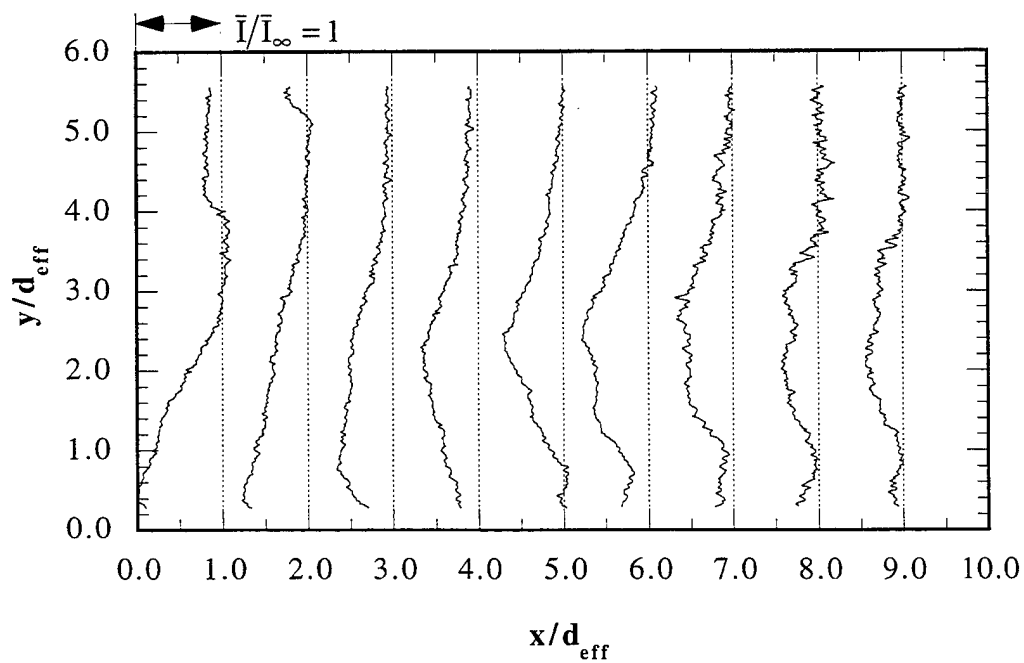


Figure 5.58 Transverse Profiles of Normalized Mean Intensity for Case C1A

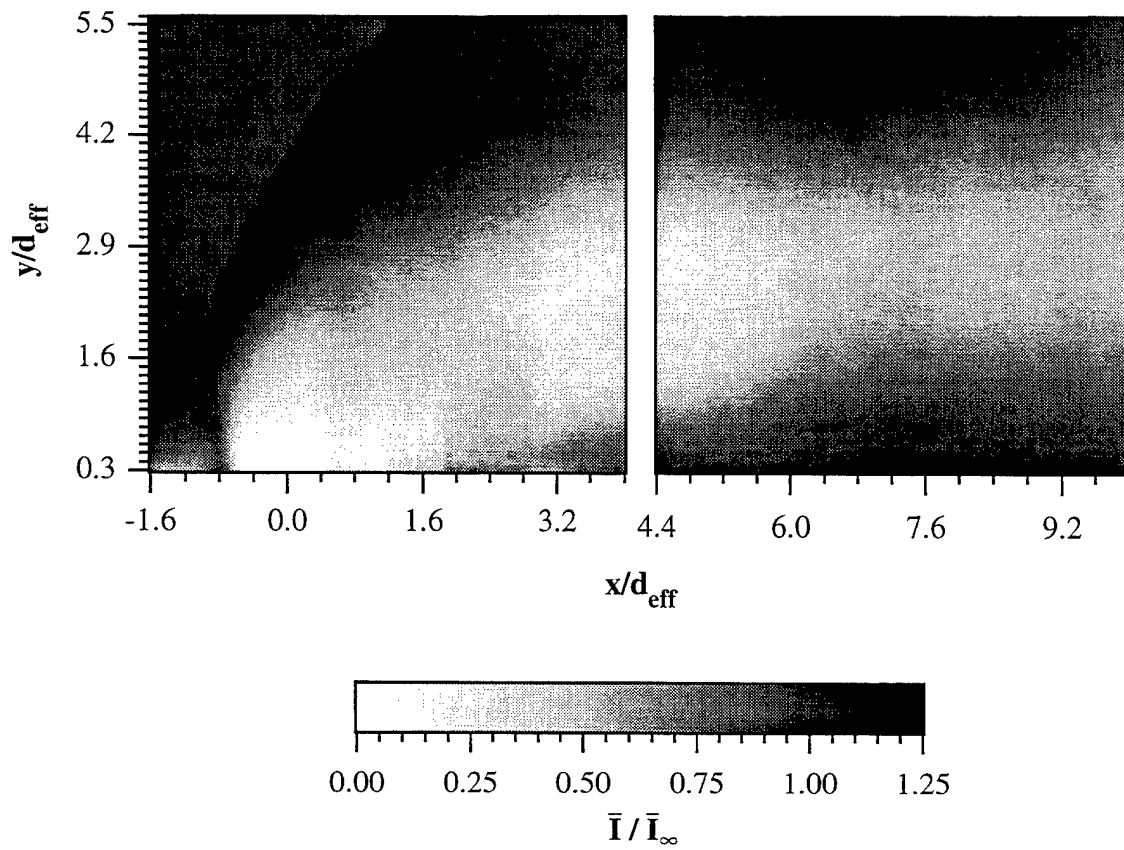


Figure 5.59 Normalized Ensemble-Averaged Side View Images of Circular Injection Using Helium (Case C2H)

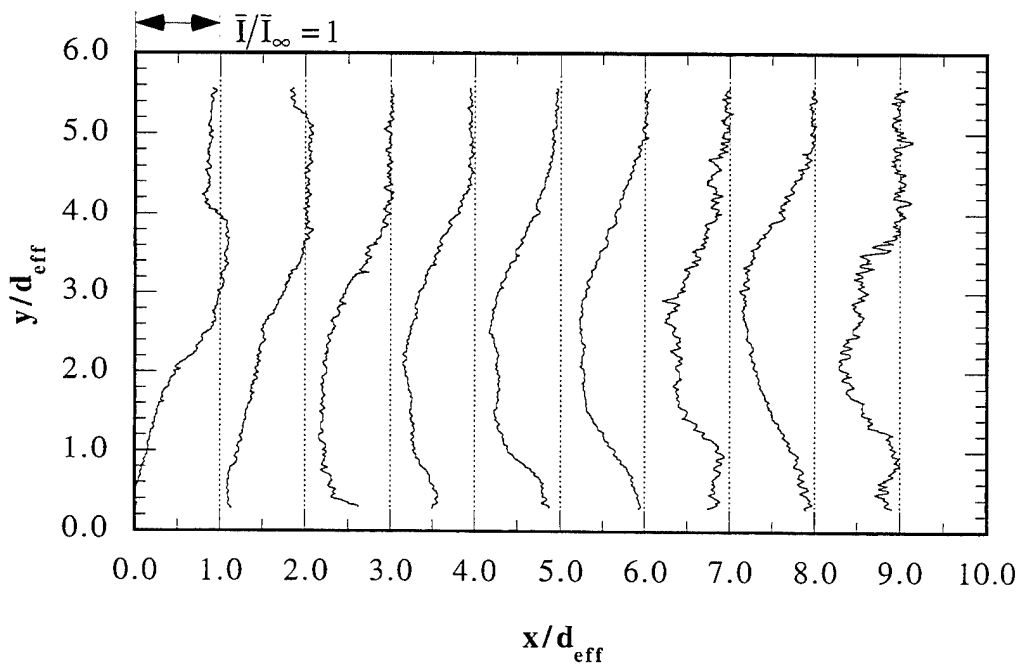


Figure 5.60 Transverse Profiles of Normalized Mean Intensity for Case C2H

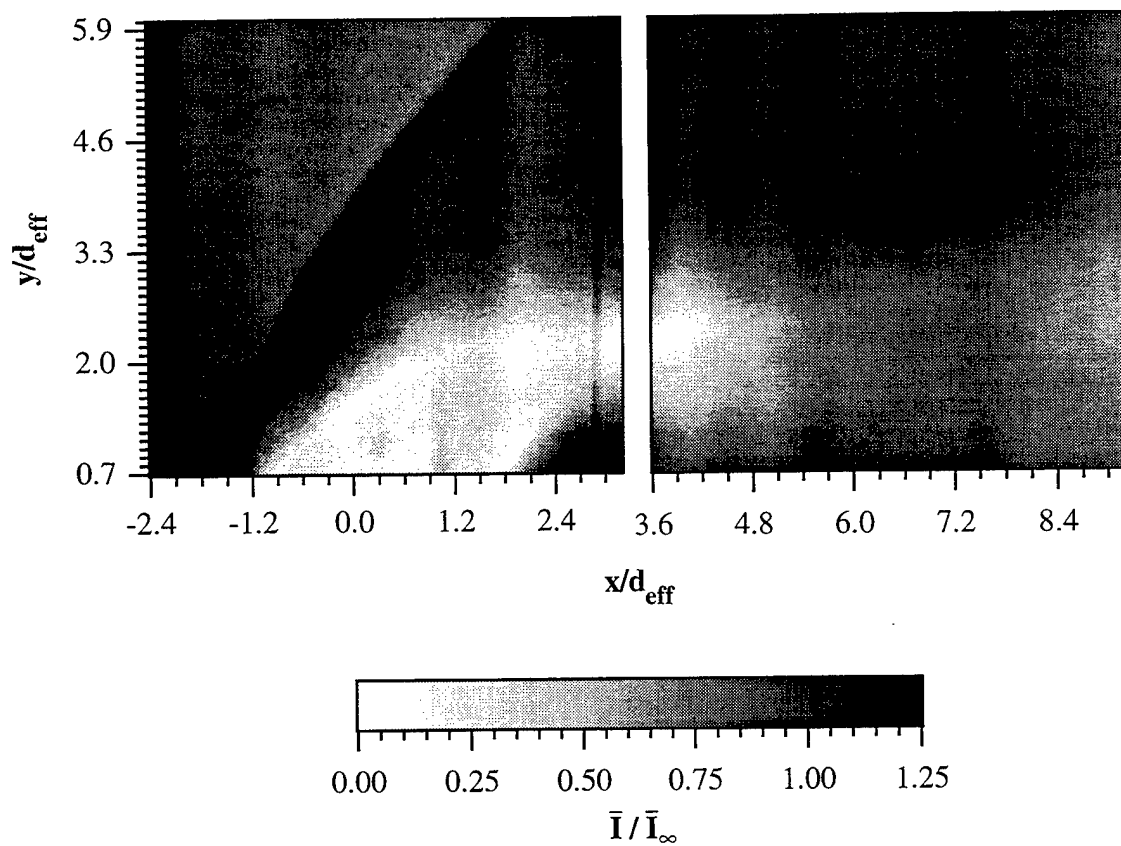


Figure 5.61 Normalized Ensemble-Averaged Side View Images of Elliptical Injection Using Air (Case E1A)

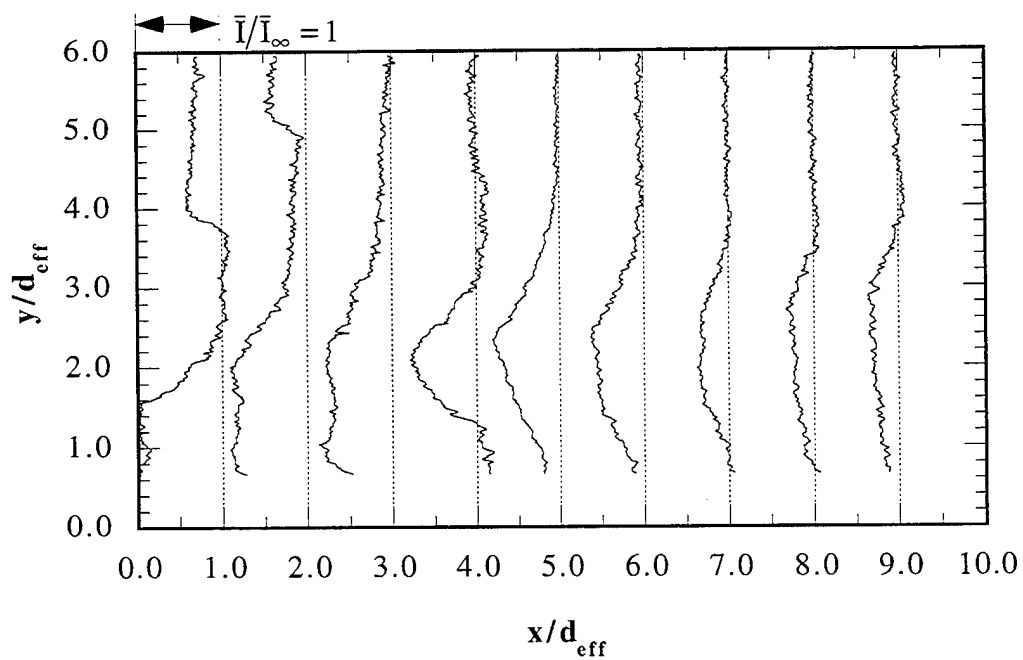


Figure 5.62 Transverse Profiles of Normalized Mean Intensity for Case E1A

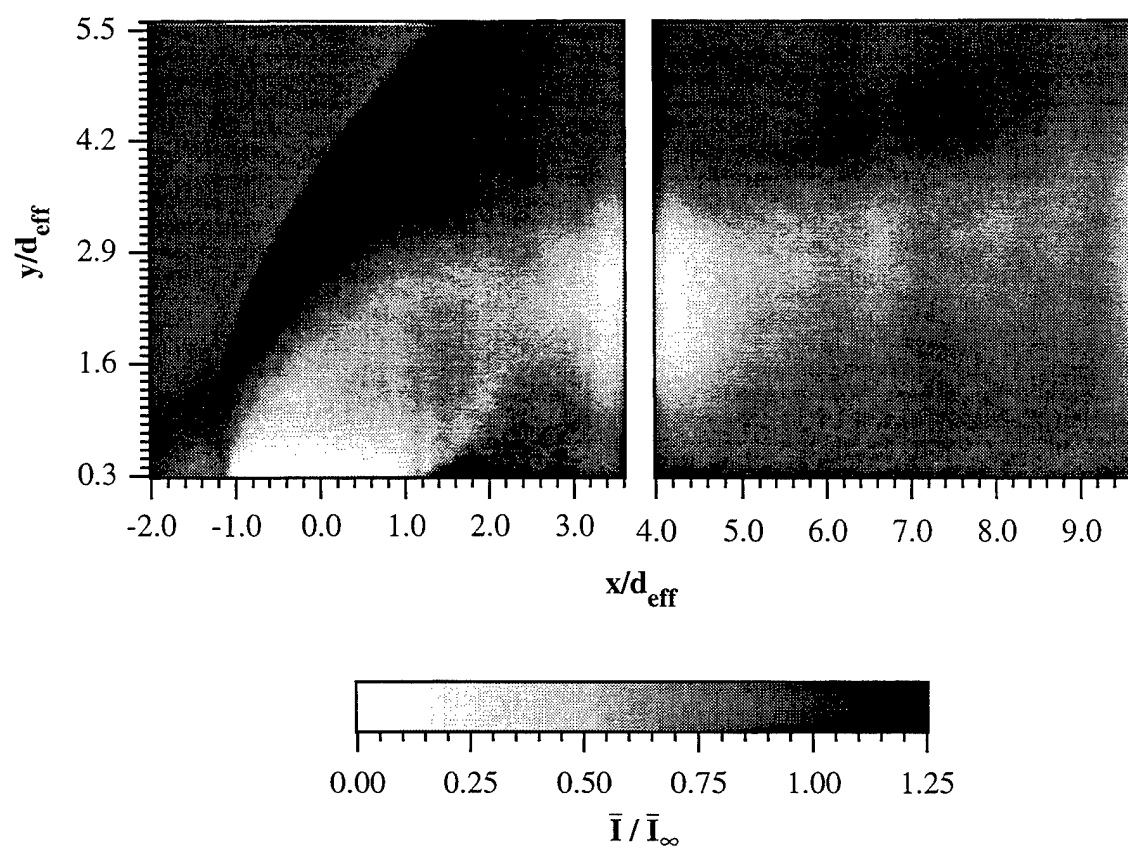


Figure 5.63 Normalized Ensemble-Averaged Side View Images of Elliptical Injection Using Helium (Case E2H)

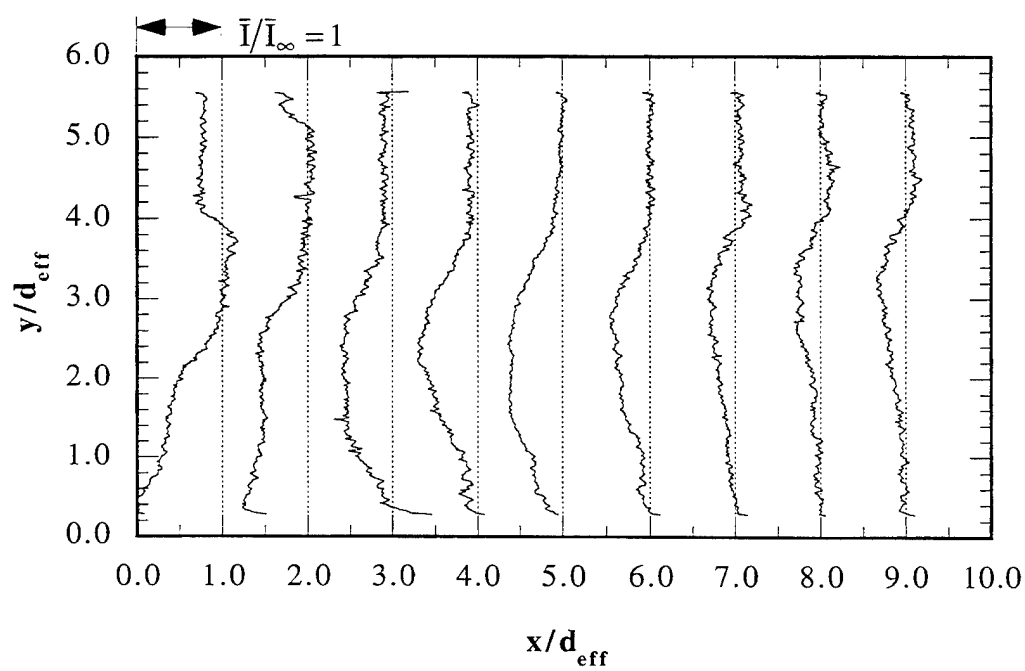
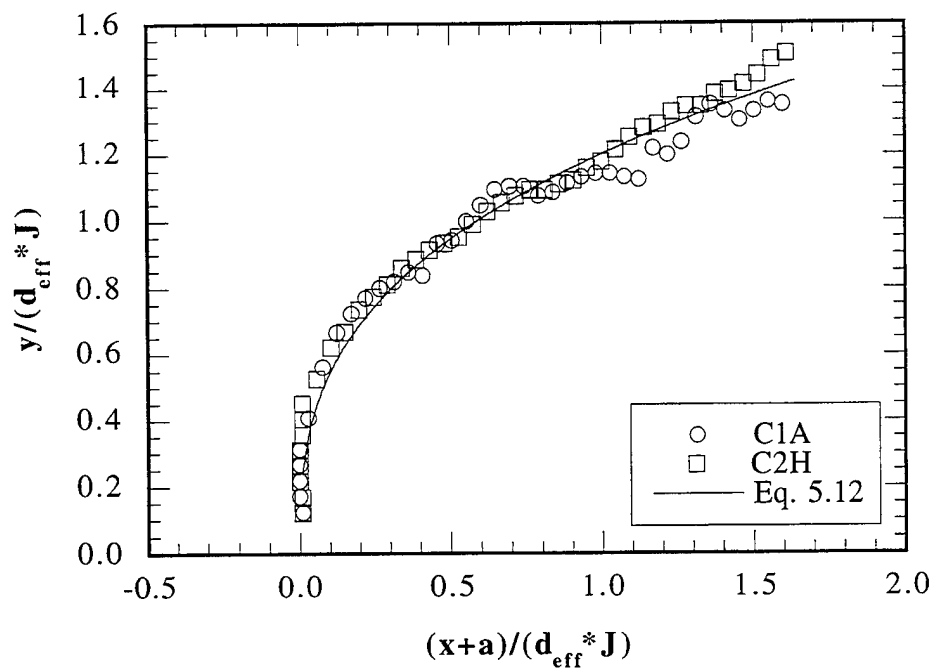
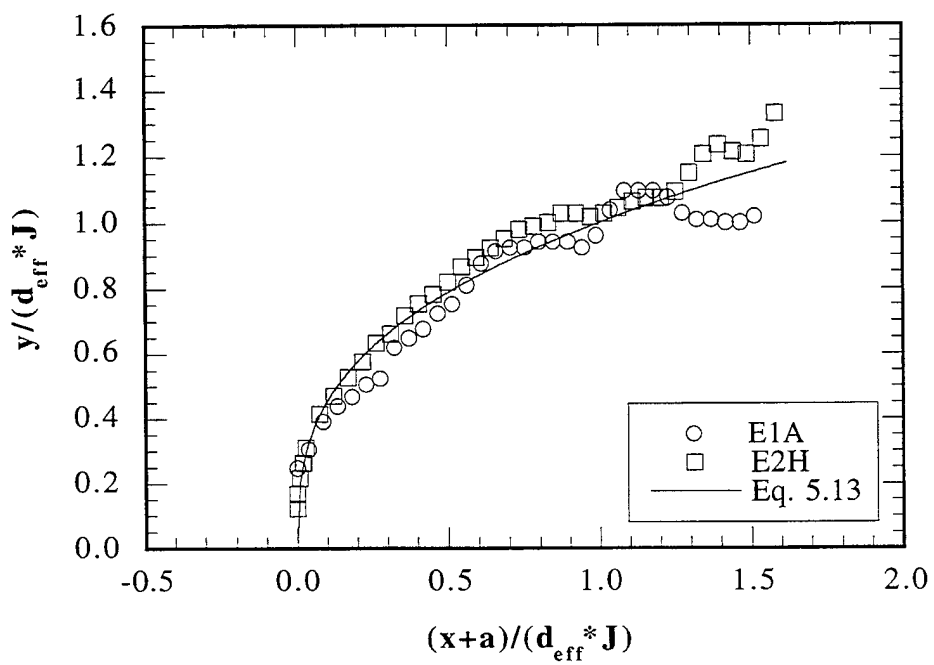


Figure 5.64 Transverse Profiles of Normalized Mean Intensity for Case E2H

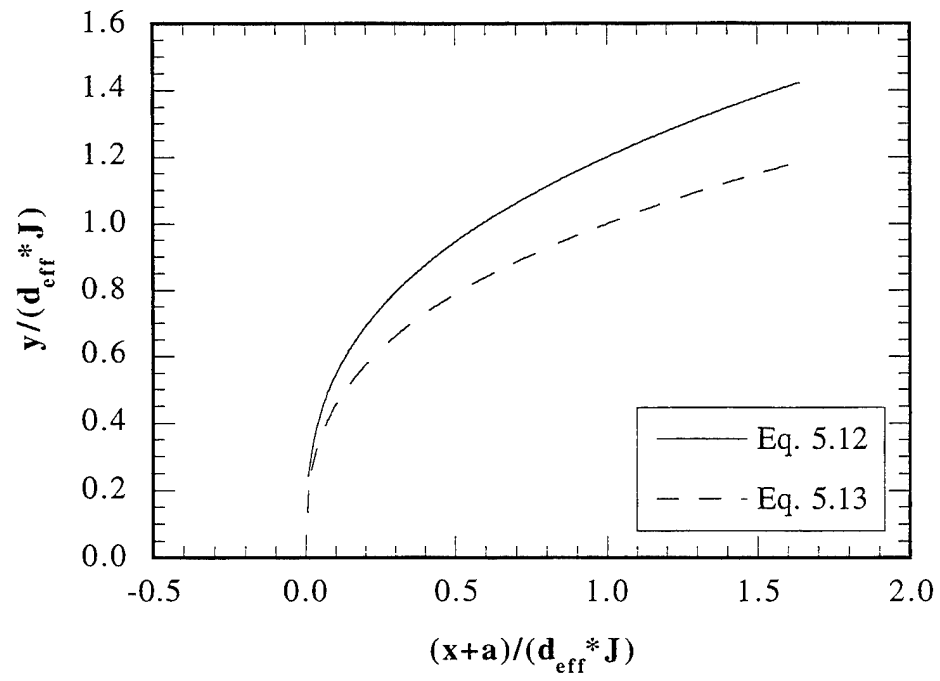


a) Circular Injection



b) Elliptical Injection

Figure 5.65 Transverse Penetration Profiles from Ensemble-Averaged Side View Images
a) Circular Injection, b) Elliptical Injection, and c) Circular and Elliptical Injection Correlations



c) Circular and Elliptical Injection Correlations

Figure 5.65 (continued)

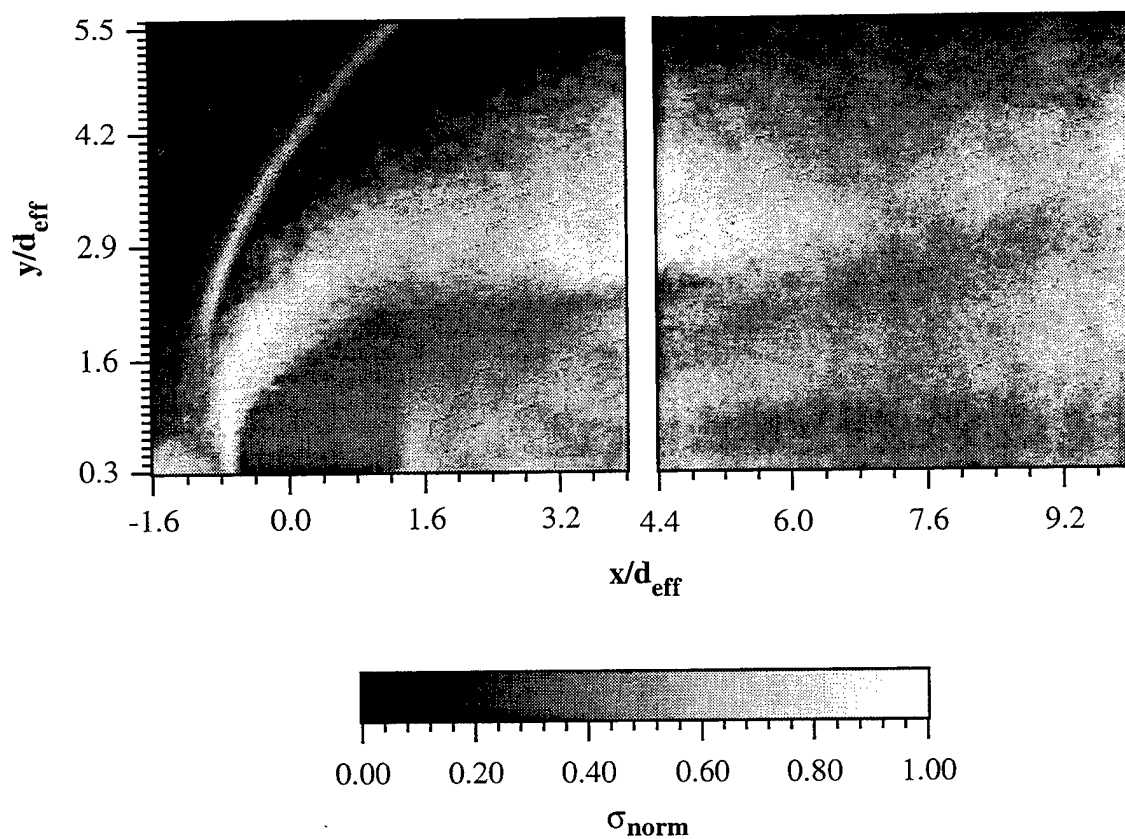


Figure 5.66 Normalized Standard Deviation Side View Images of Circular Injection Using Air (Case C1A)

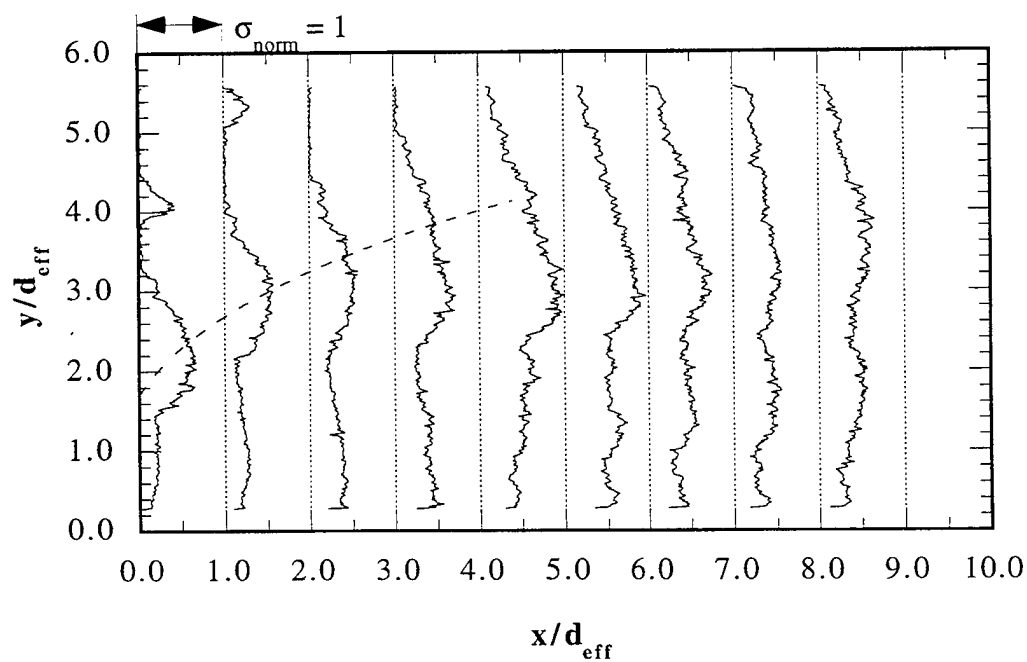


Figure 5.67 Transverse Profiles of Normalized Standard Deviation for Case C1A

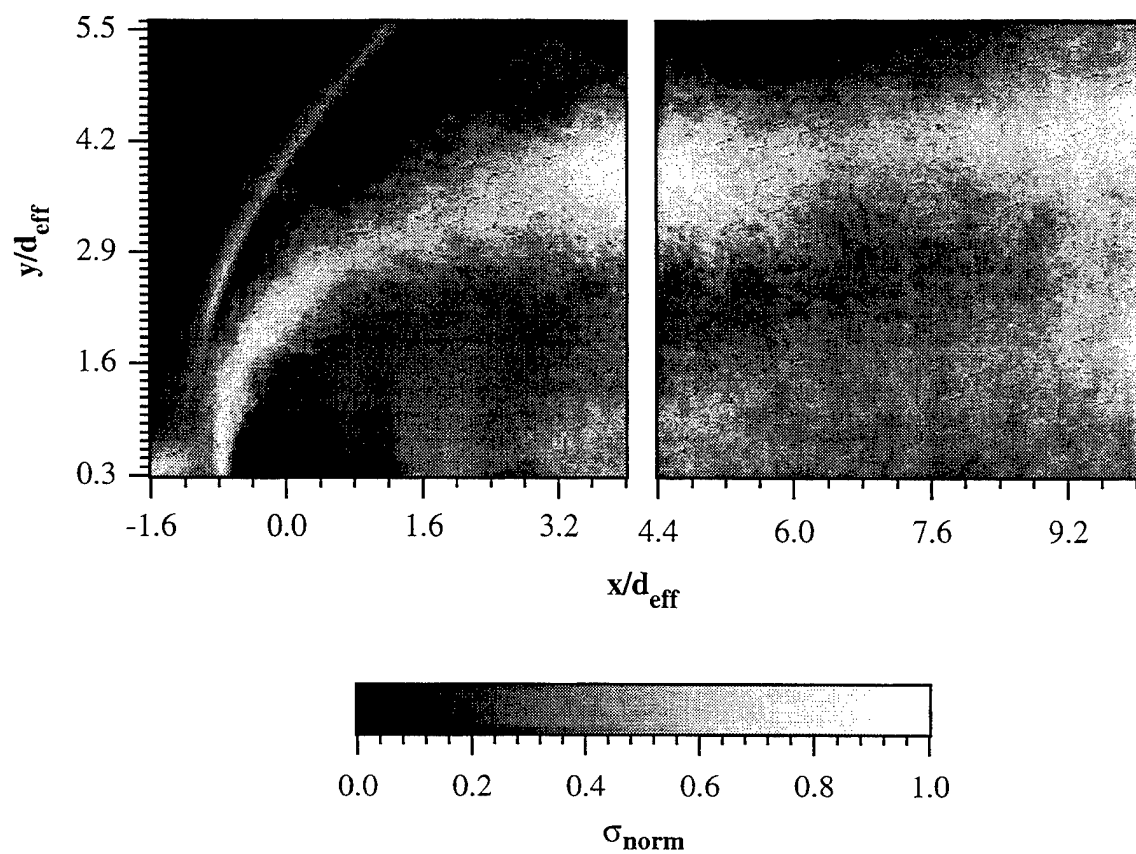


Figure 5.68 Normalized Standard Deviation Side View Images of Circular Injection Using Helium (Case C2H)

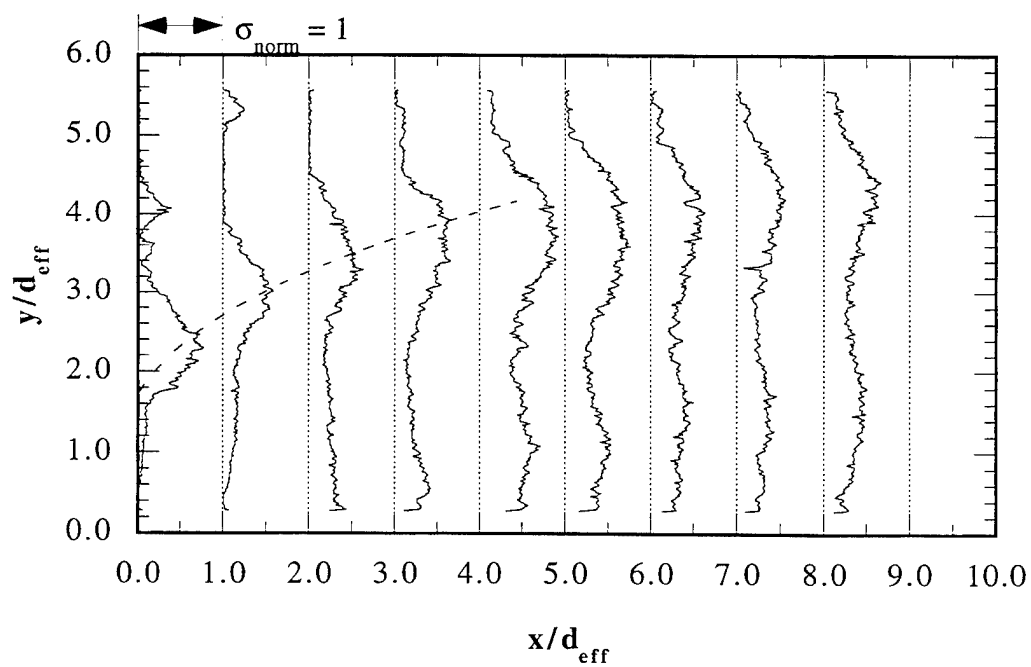


Figure 5.69 Transverse Profiles of Normalized Standard Deviation for Case C2H

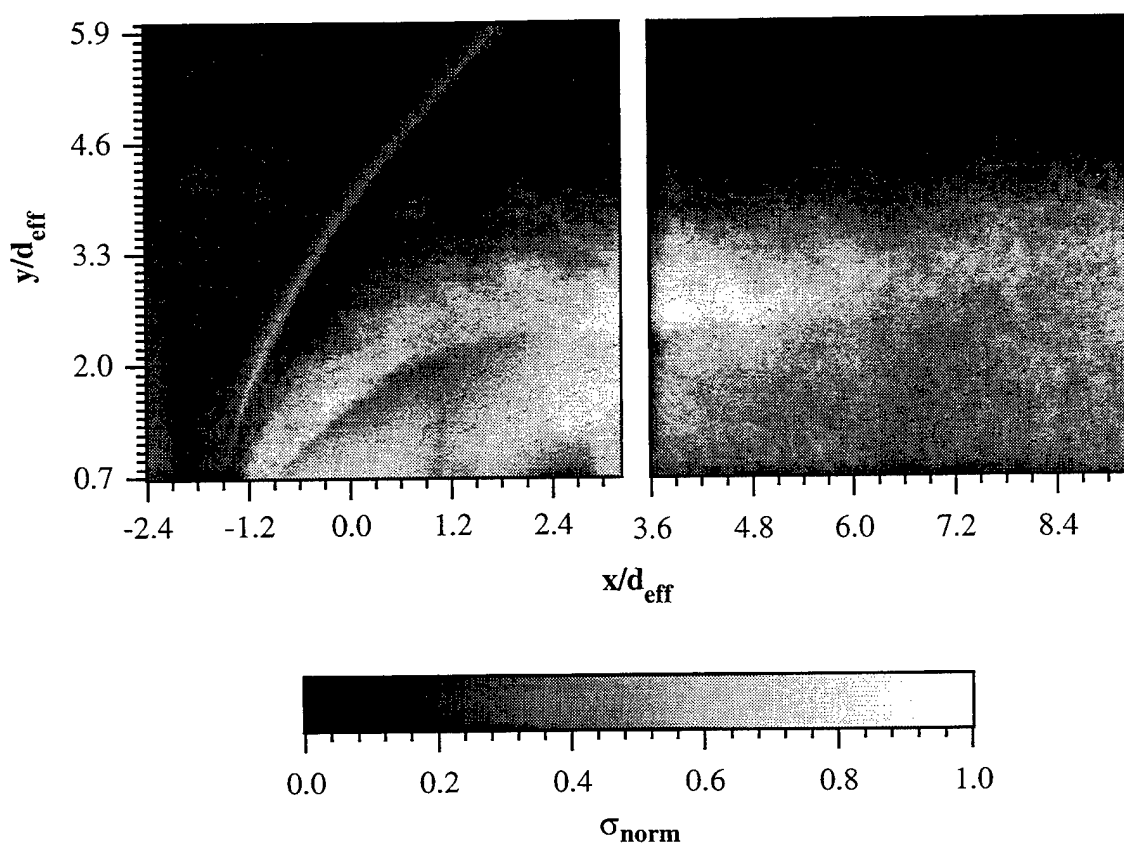


Figure 5.70 Normalized Standard Deviation Side View Images of Elliptical Injection Using Air (Case E1A)

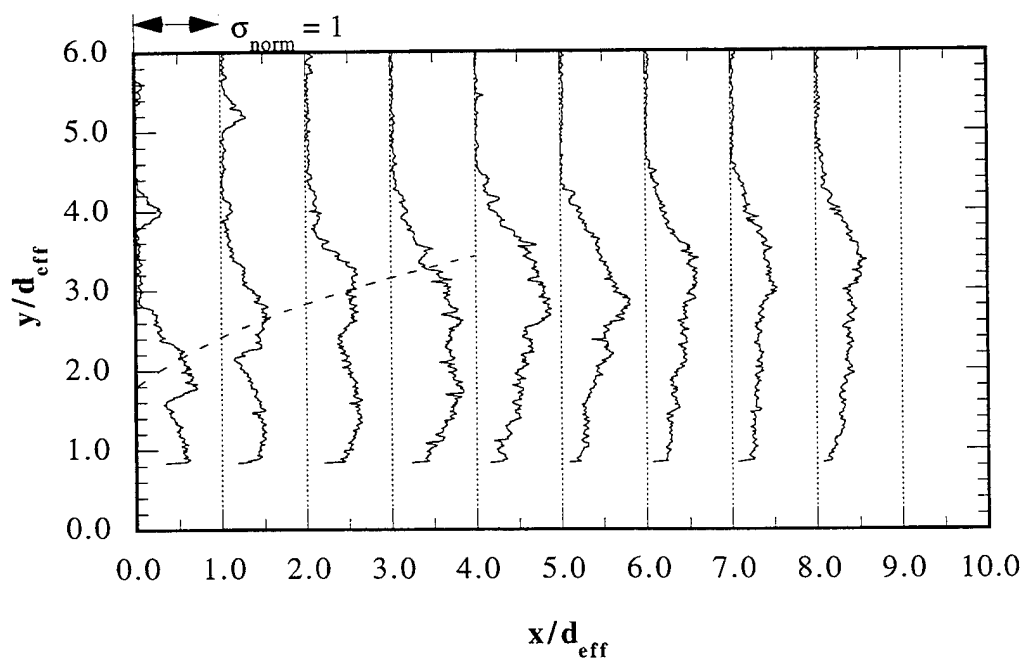


Figure 5.71 Transverse Profiles of Normalized Standard Deviation for Case E1A

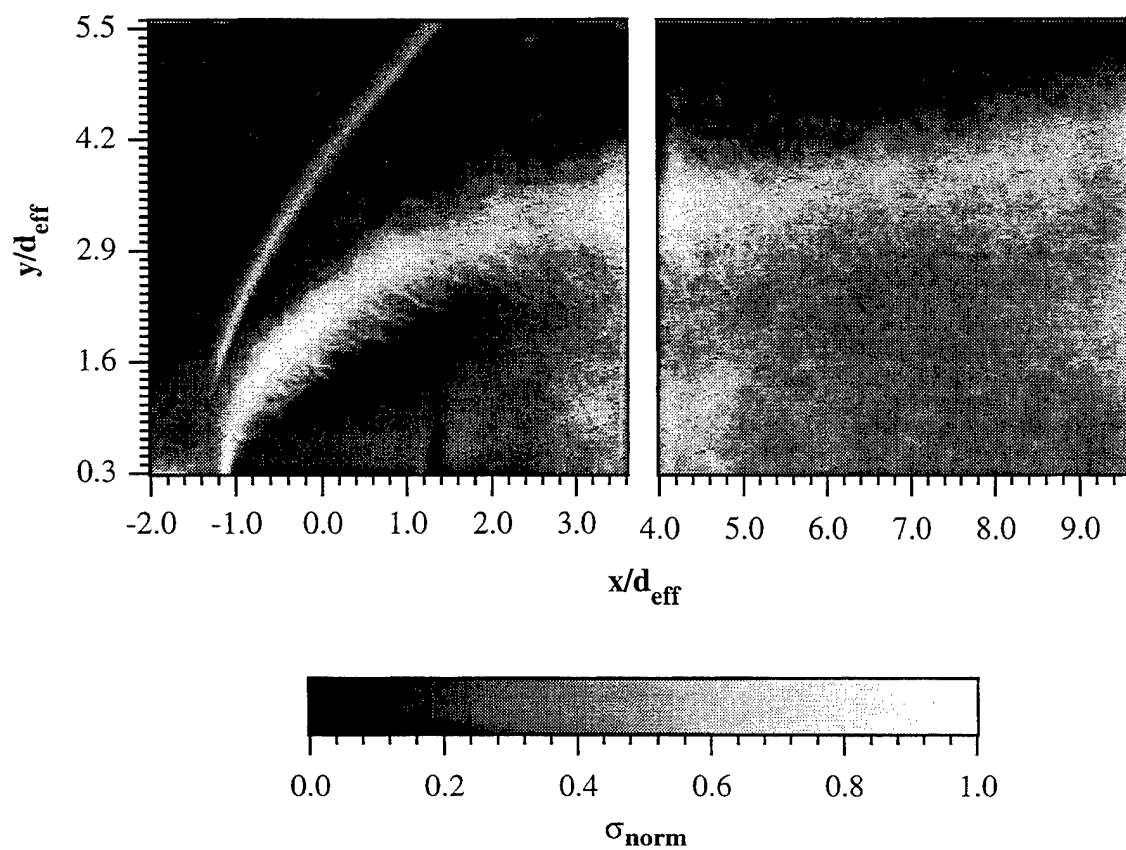


Figure 5.72 Normalized Standard Deviation Side View Images of Elliptical Injection Using Helium (Case E2H)

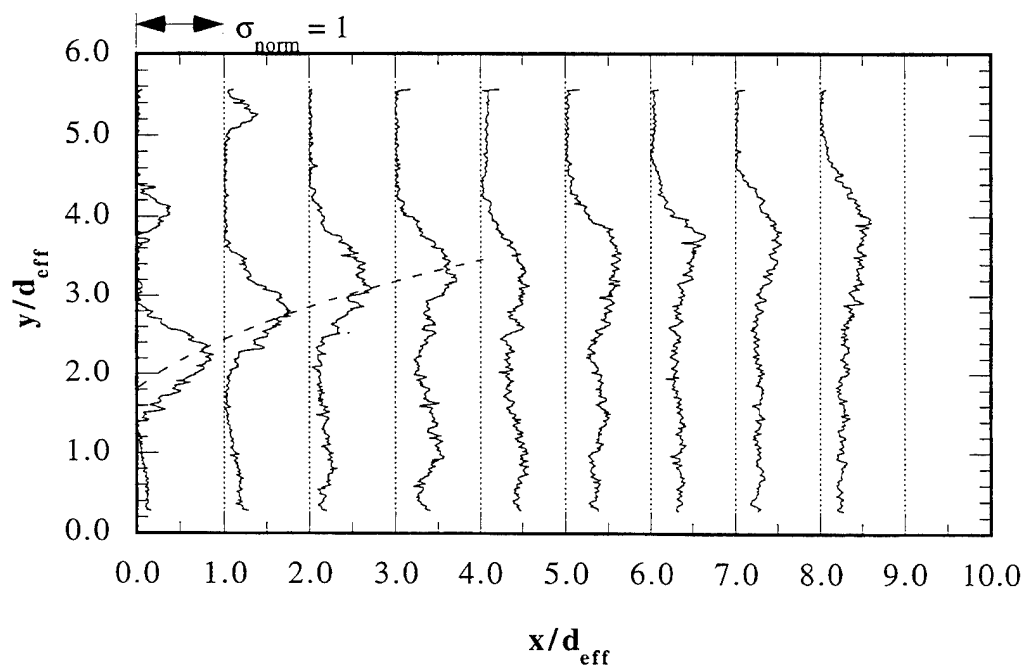


Figure 5.73 Transverse Profiles of Normalized Standard Deviation for Case E2H

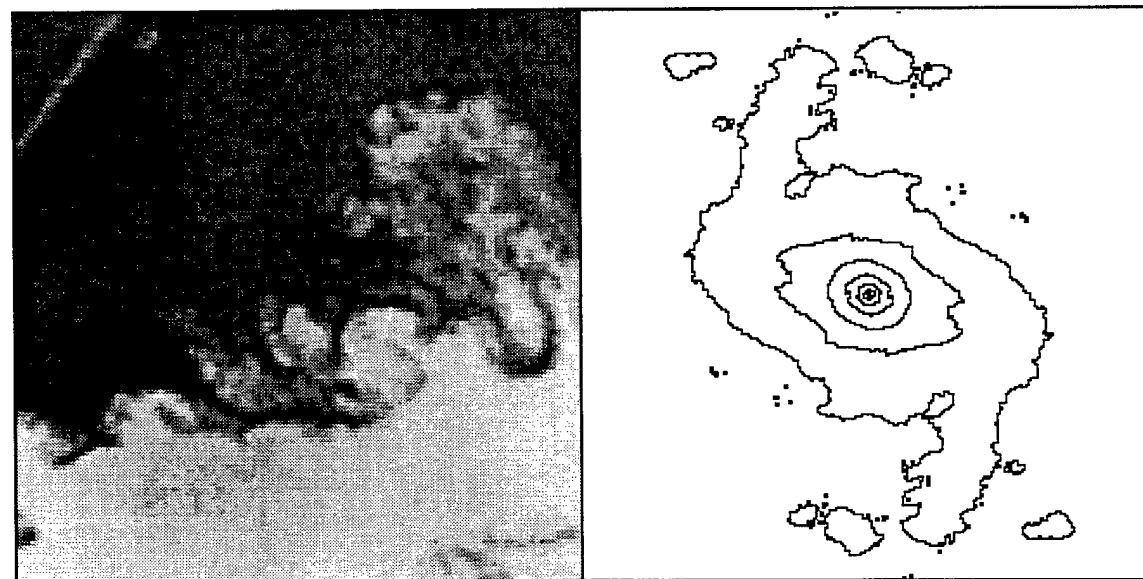
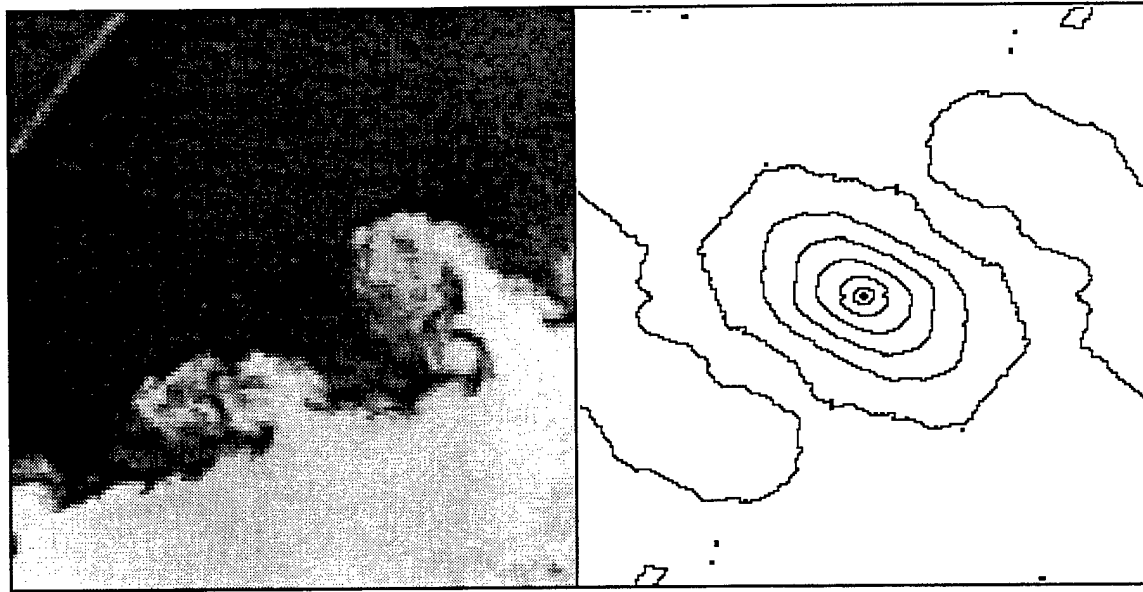


Figure 5.74 Two-Dimensional Spatial Correlation Fields from Upstream Instantaneous Side View Images of Circular Injection Using Air (Case C1A)

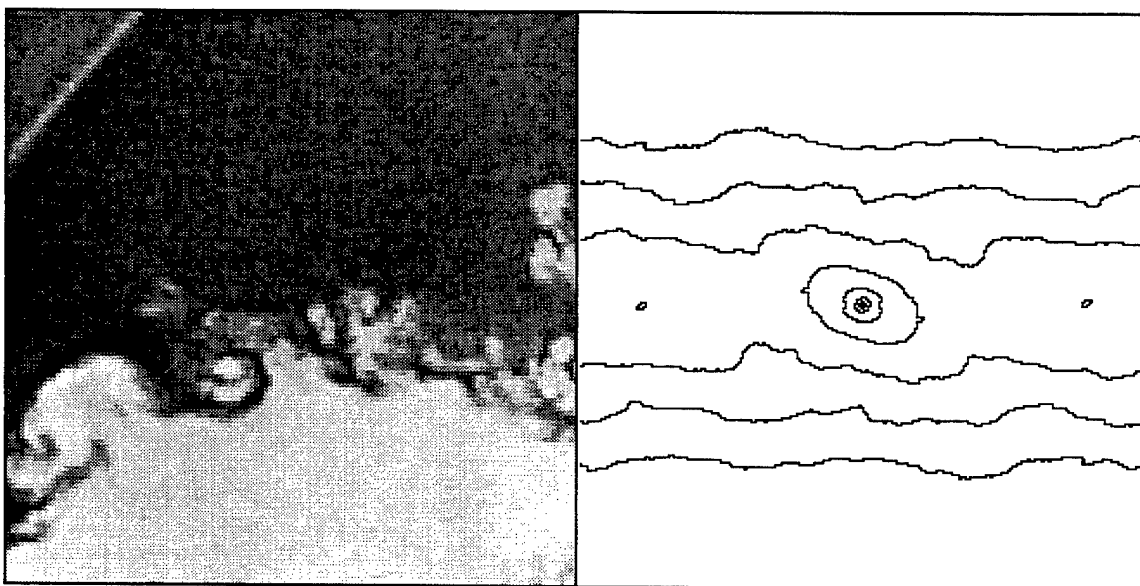
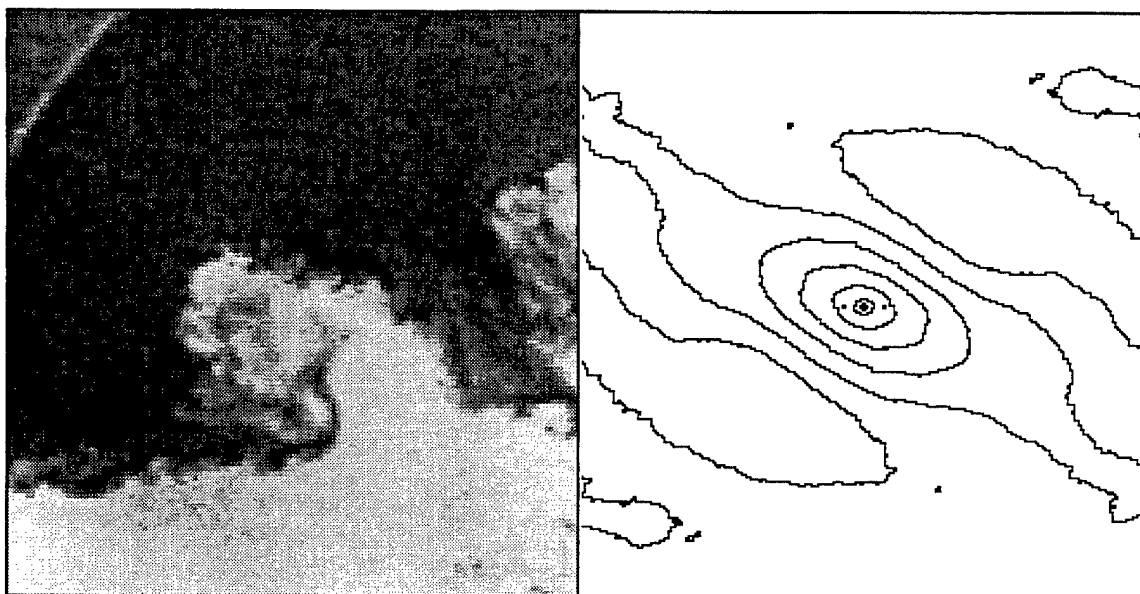


Figure 5.74 (continued)

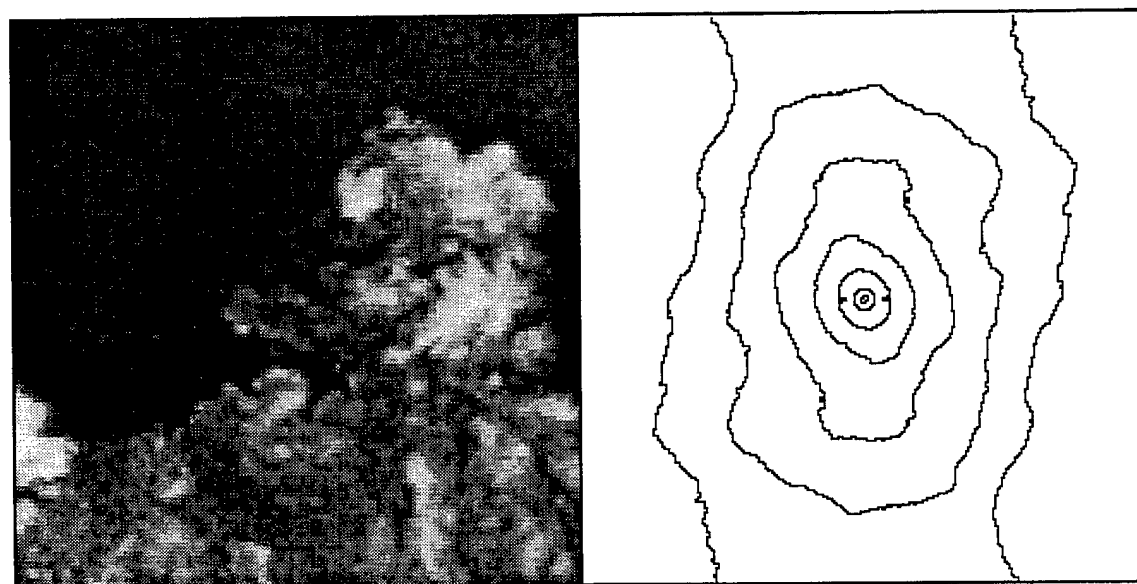
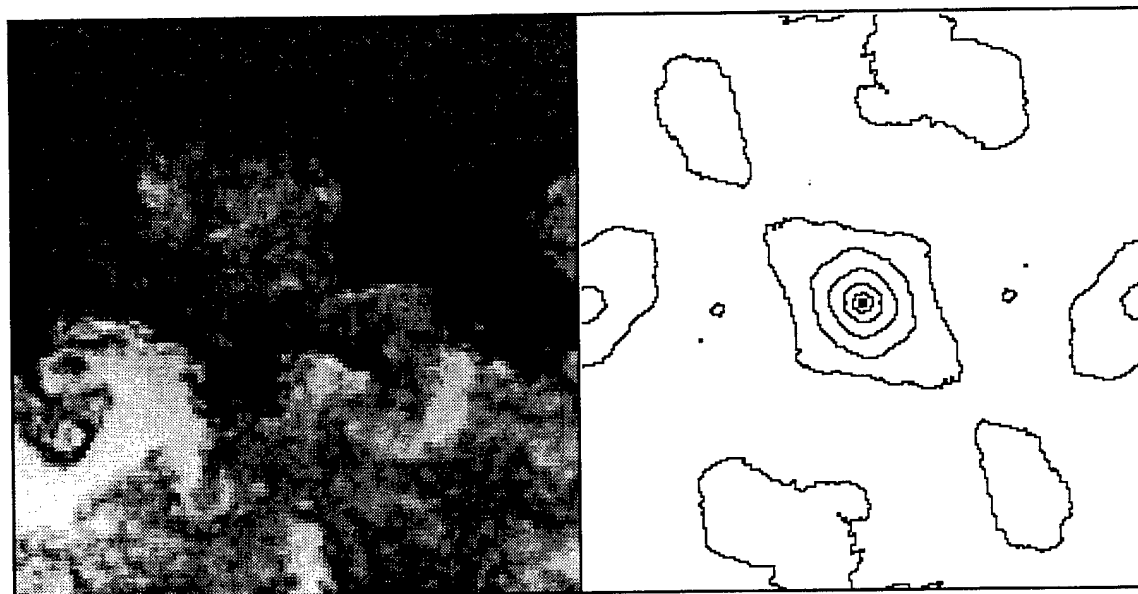


Figure 5.75 Two-Dimensional Spatial Correlation Fields from Downstream Instantaneous Side View Images of Circular Injection Using Air (Case C1A)

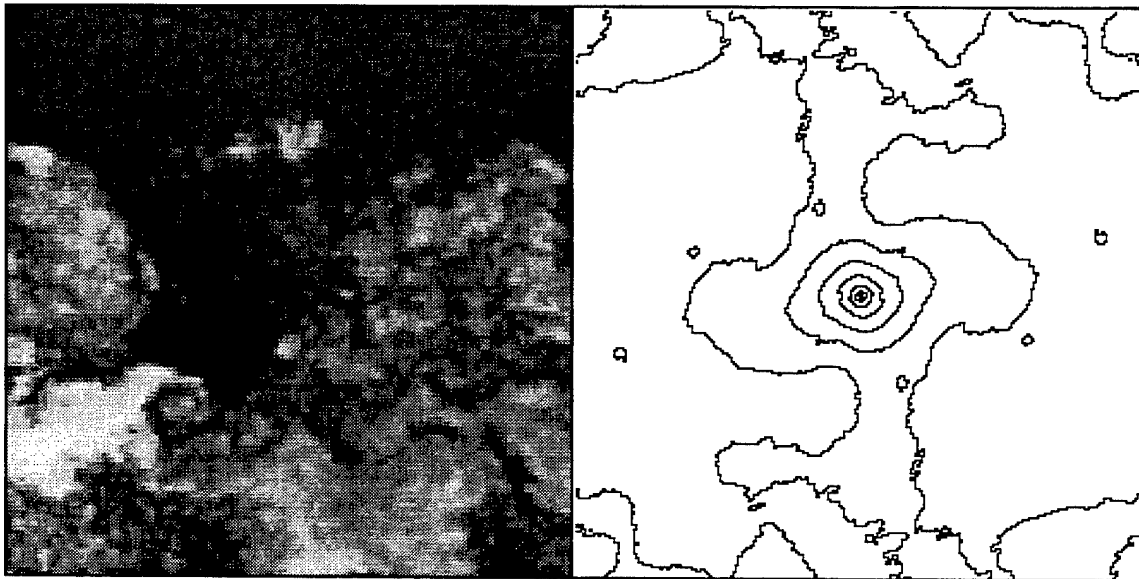
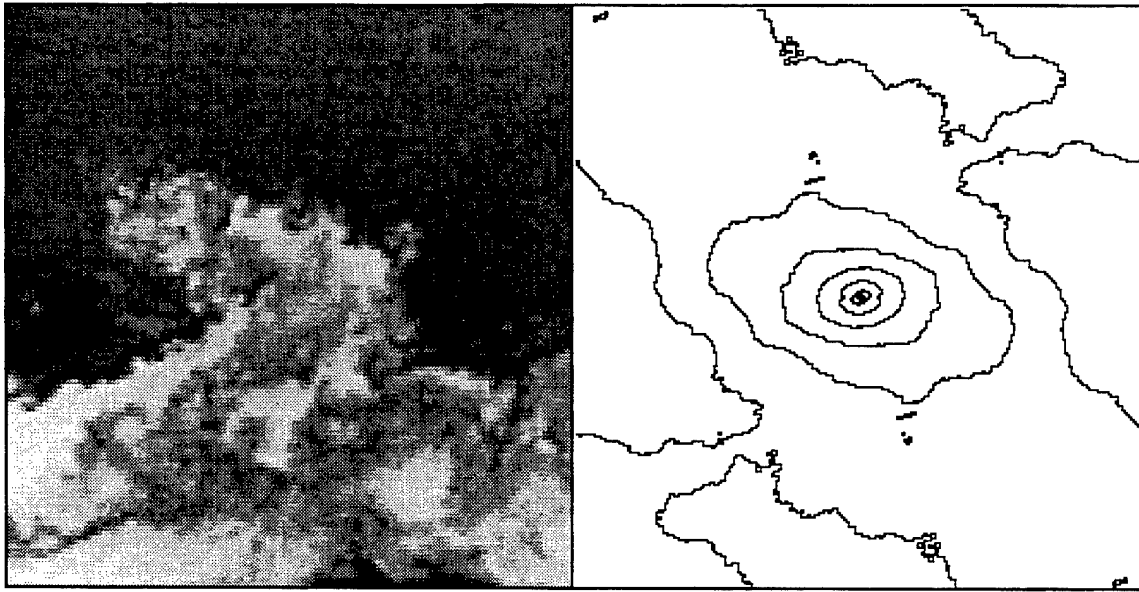


Figure 5.75 (continued)

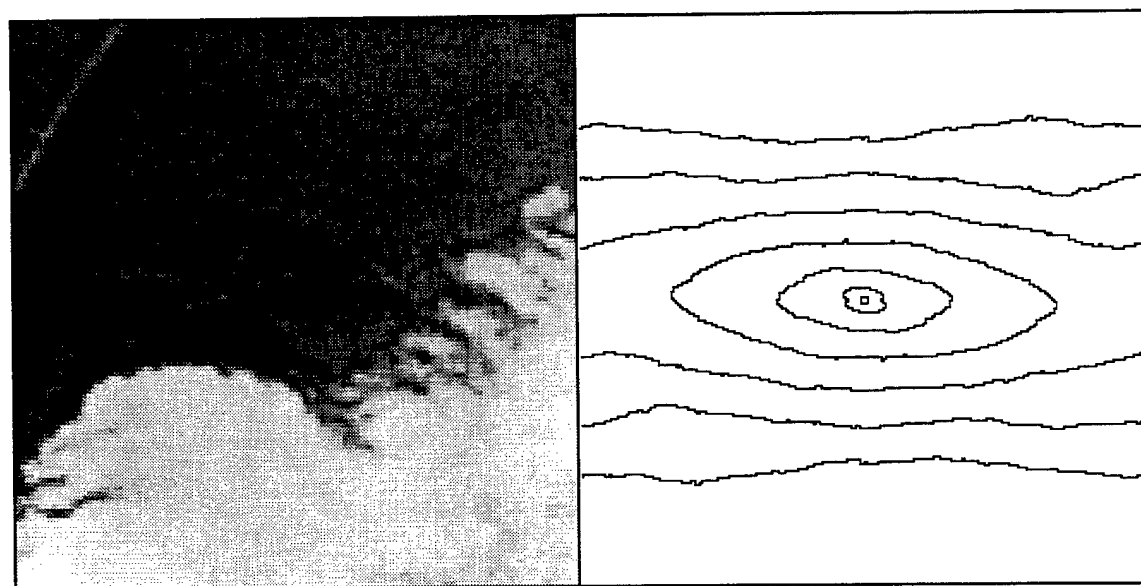
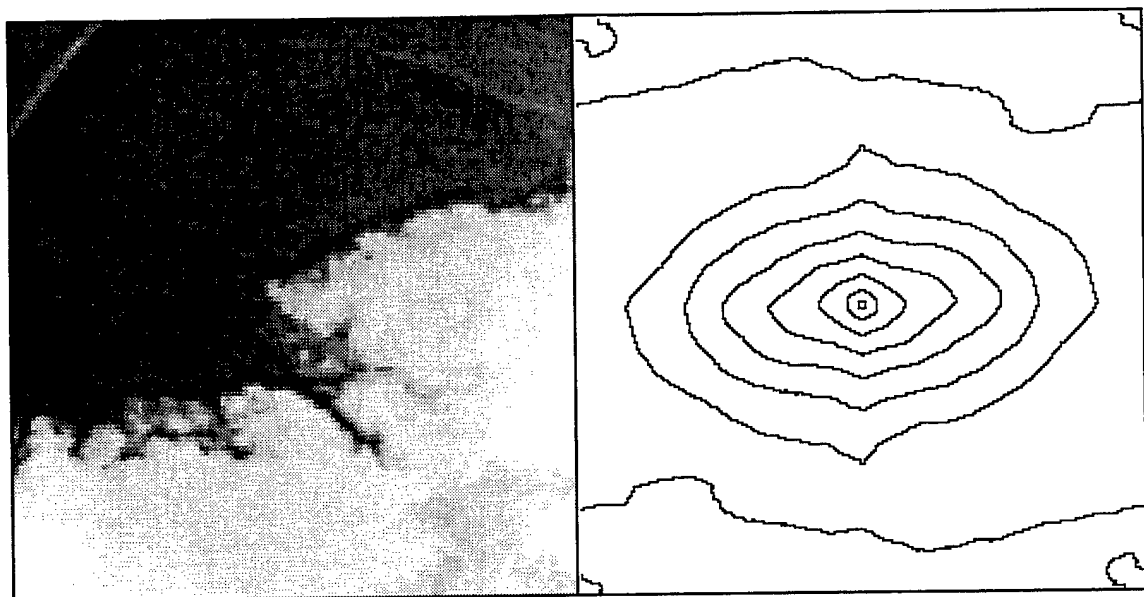


Figure 5.76 Two-Dimensional Spatial Correlation Fields from Upstream Instantaneous Side View Images of Circular Injection Using Helium (Case C2H)

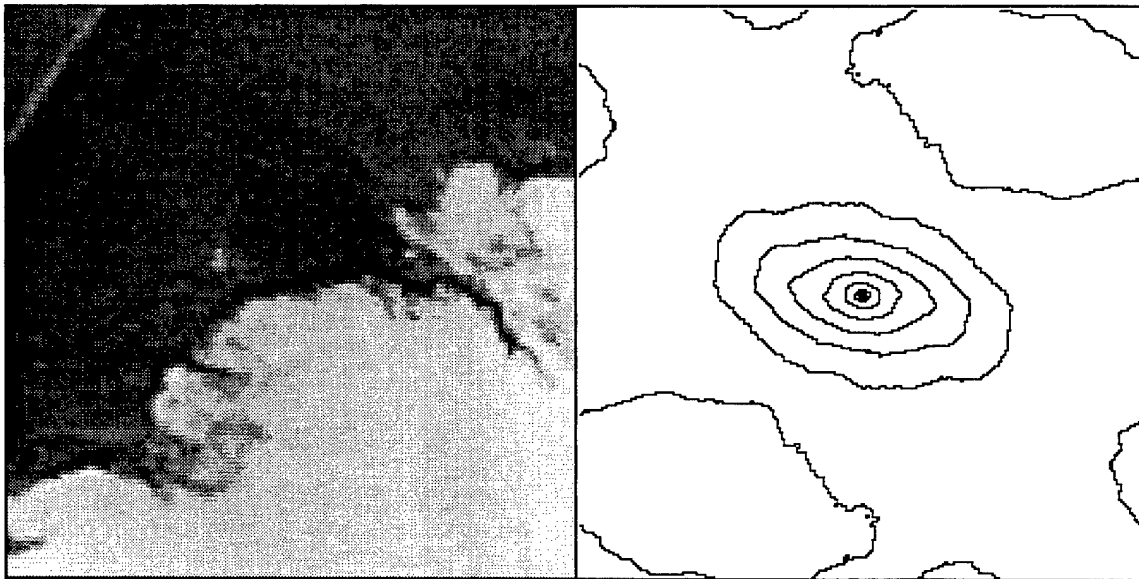
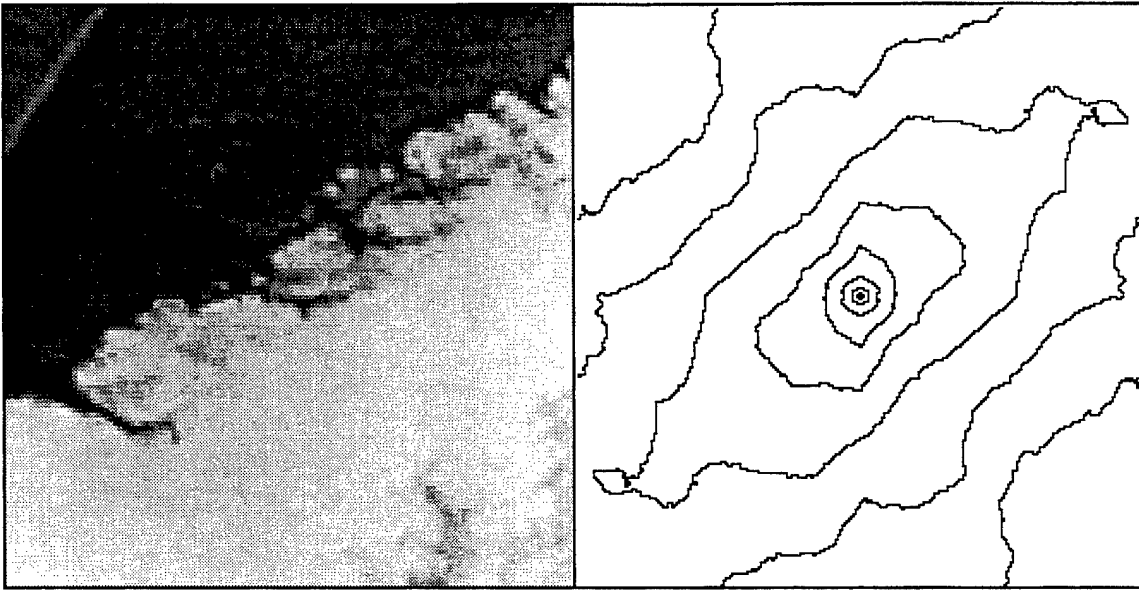


Figure 5.76 (continued)

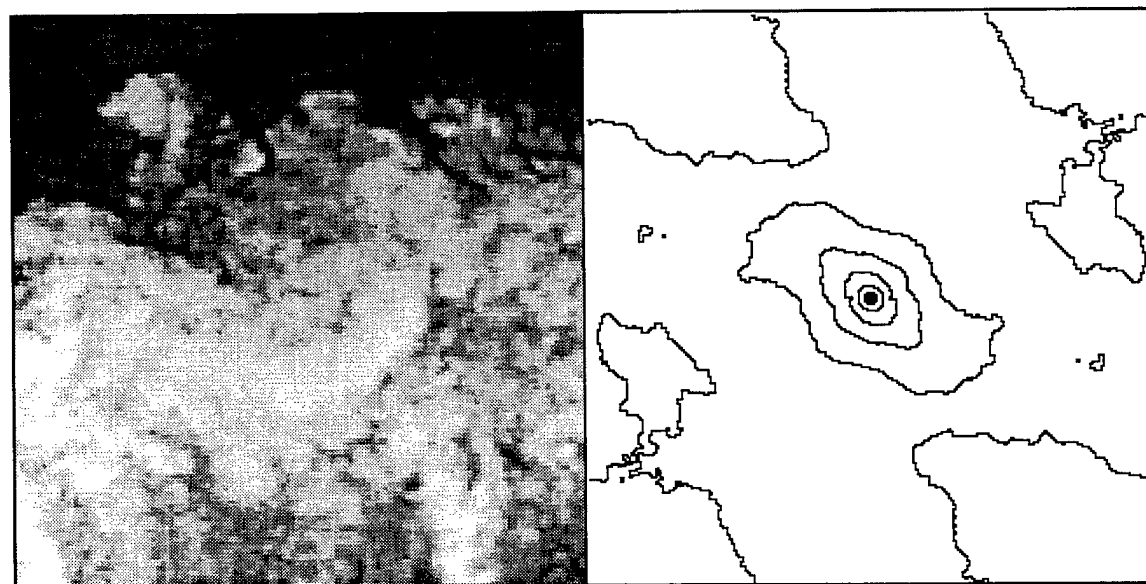
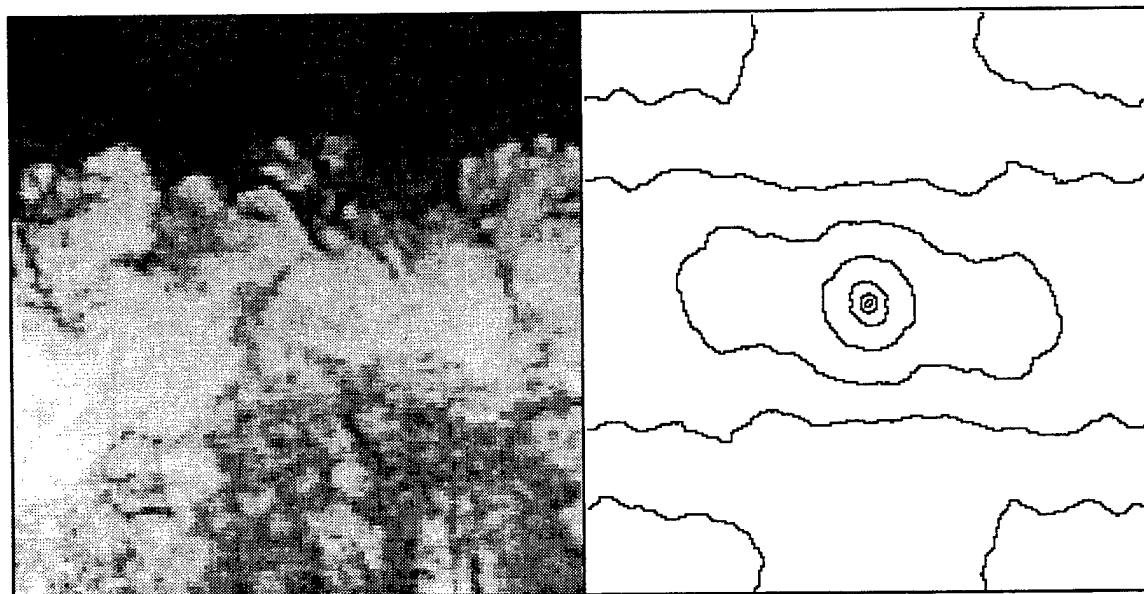


Figure 5.77 Two-Dimensional Spatial Correlation Fields from Downstream Instantaneous Side View Images of Circular Injection Using Helium (Case C2H)

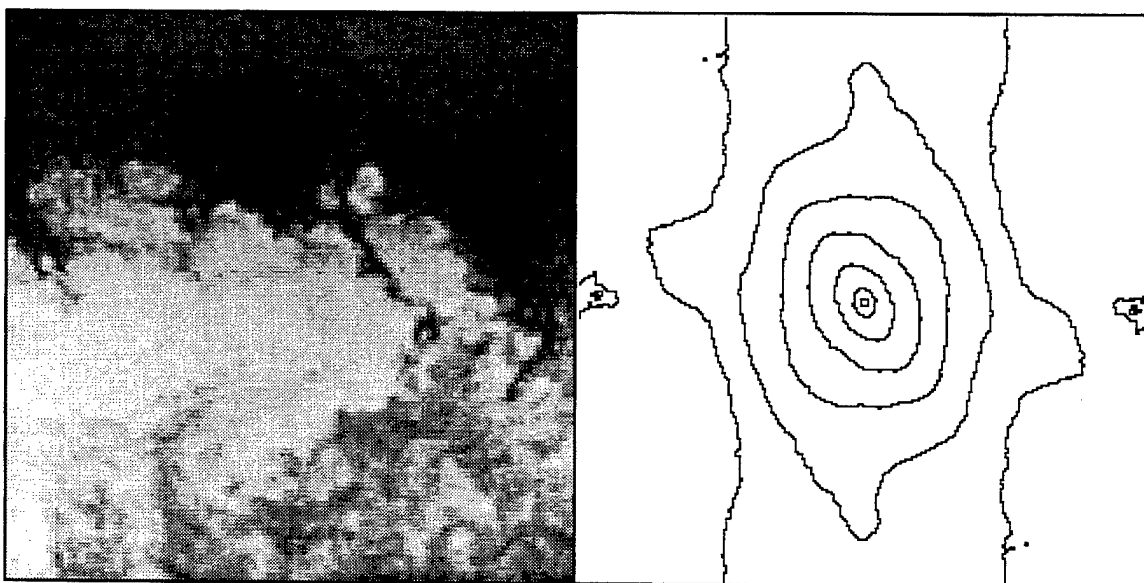
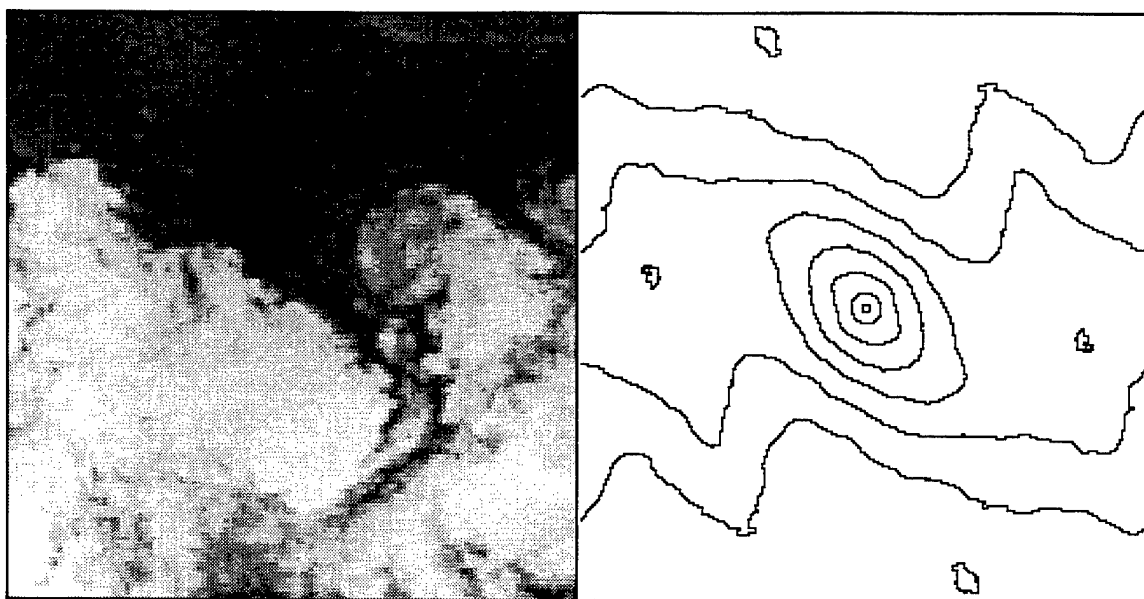


Figure 5.77 (continued)

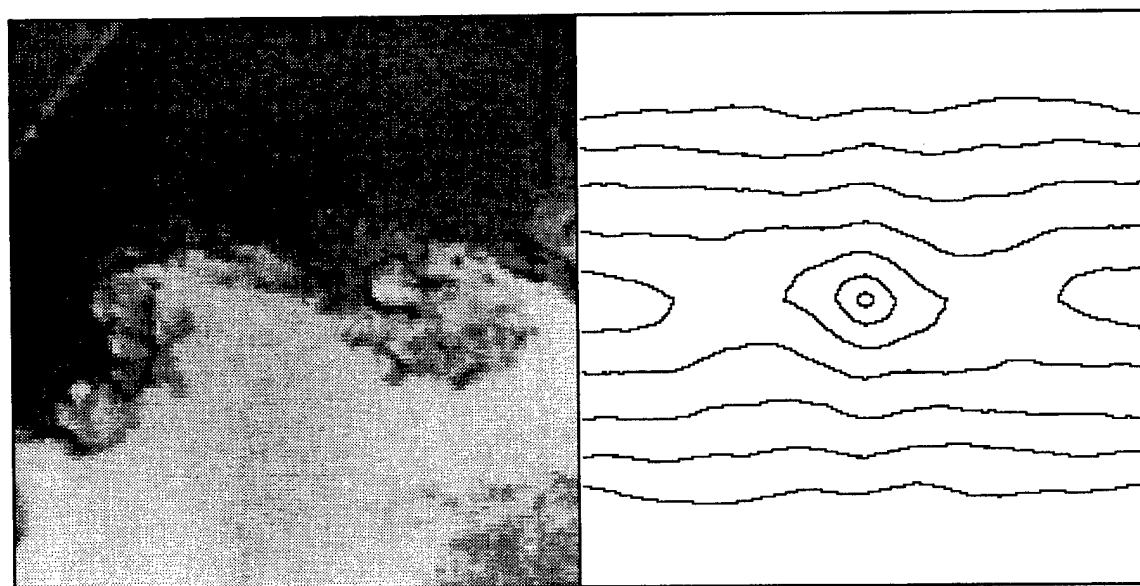
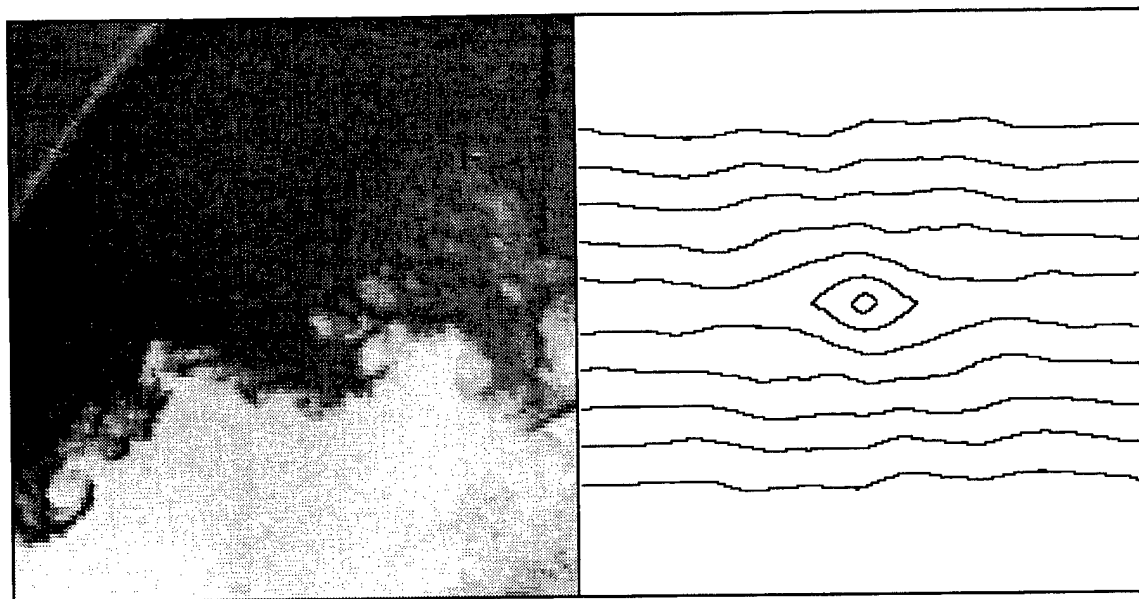


Figure 5.78 Two-Dimensional Spatial Correlation Fields from Upstream Instantaneous Side View Images of Elliptical Injection Using Air (Case E1A)

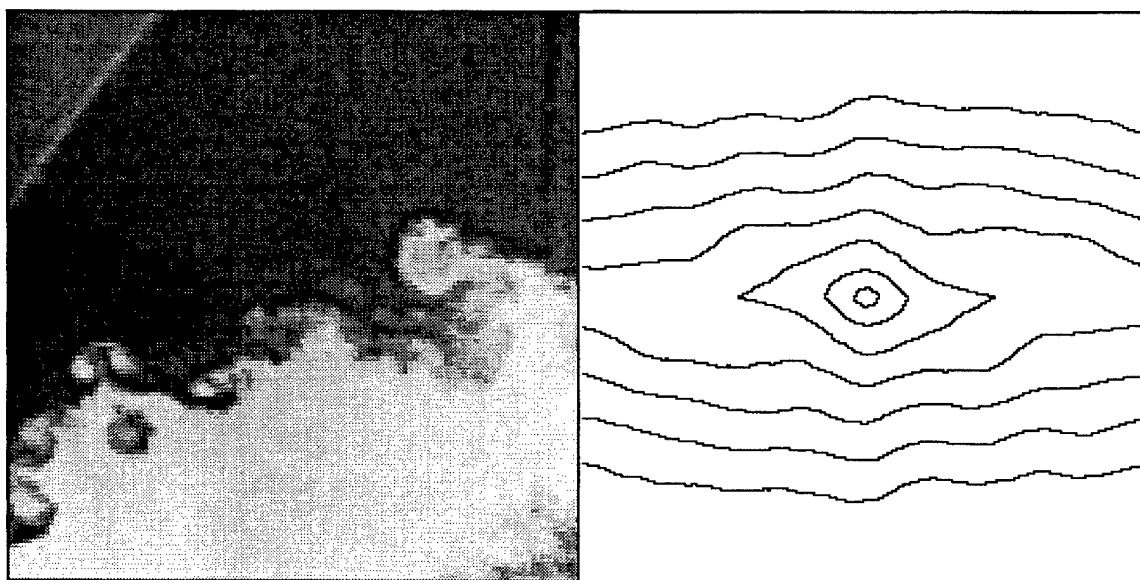
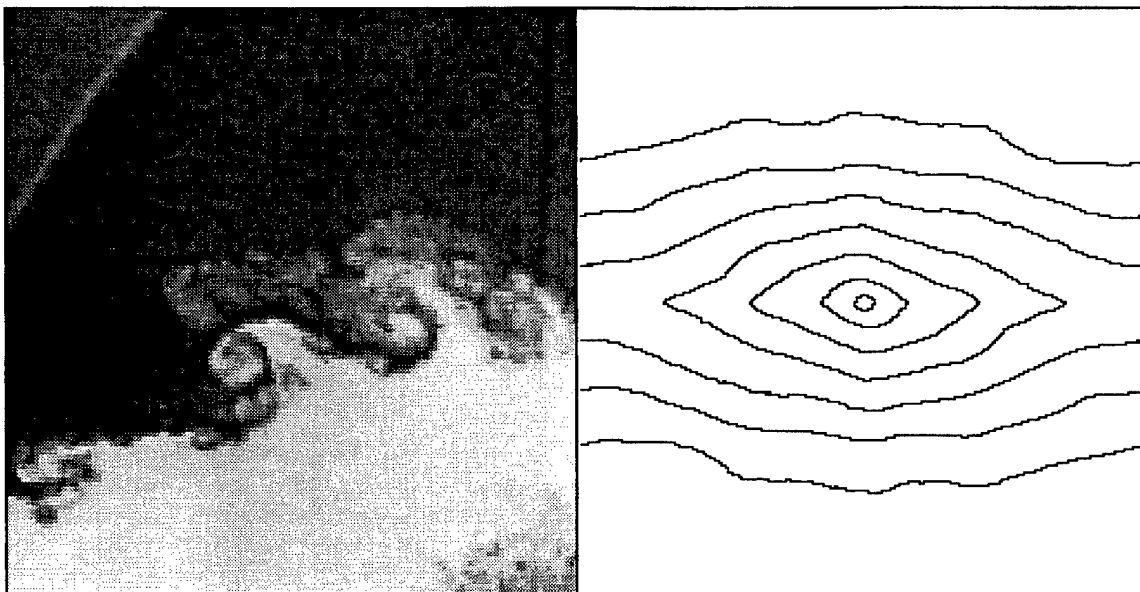


Figure 5.78 (continued)

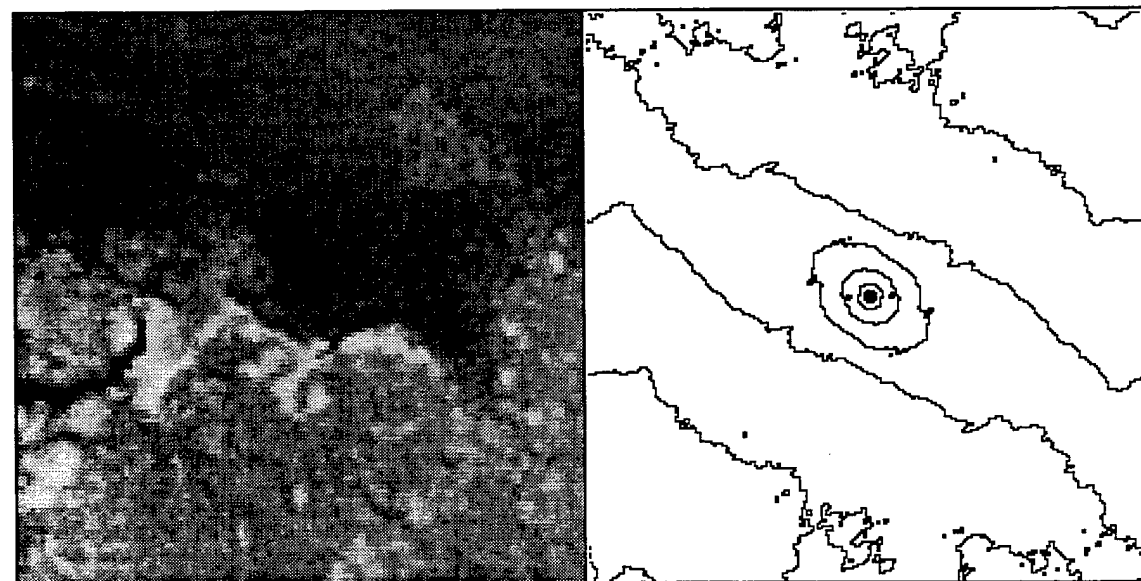
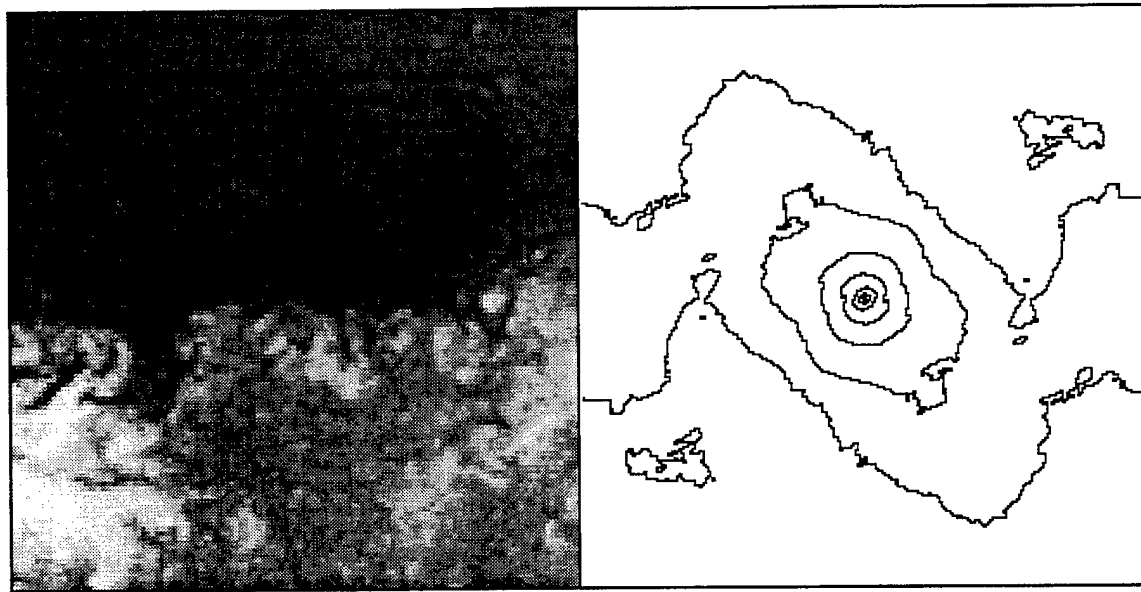


Figure 5.79 Two-Dimensional Spatial Correlation Fields from Downstream Instantaneous Side View Images of Elliptical Injection Using Air (Case E1A)

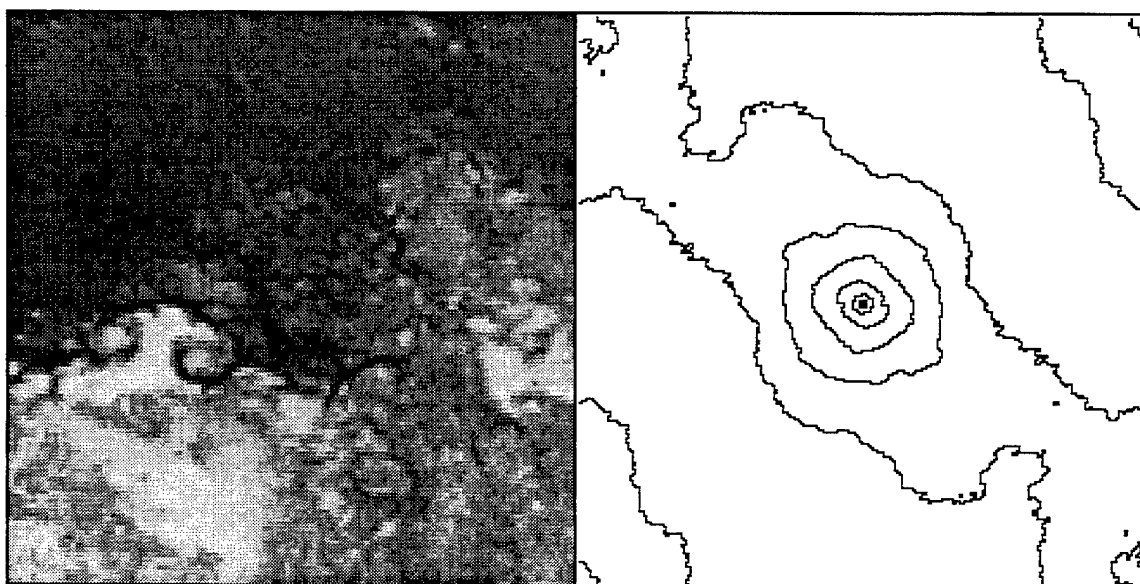
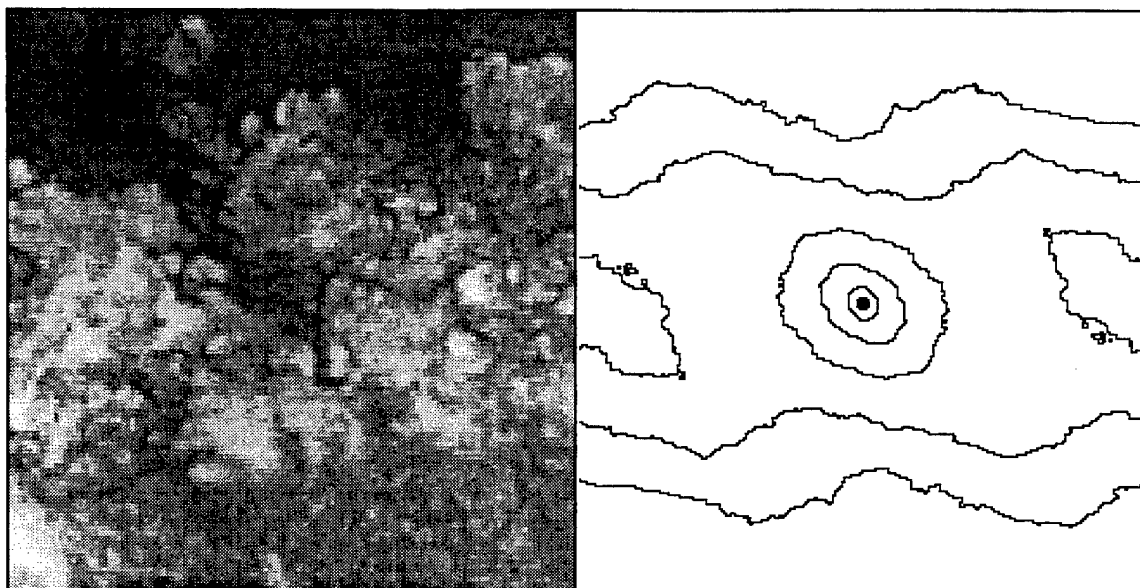


Figure 5.79 (continued)

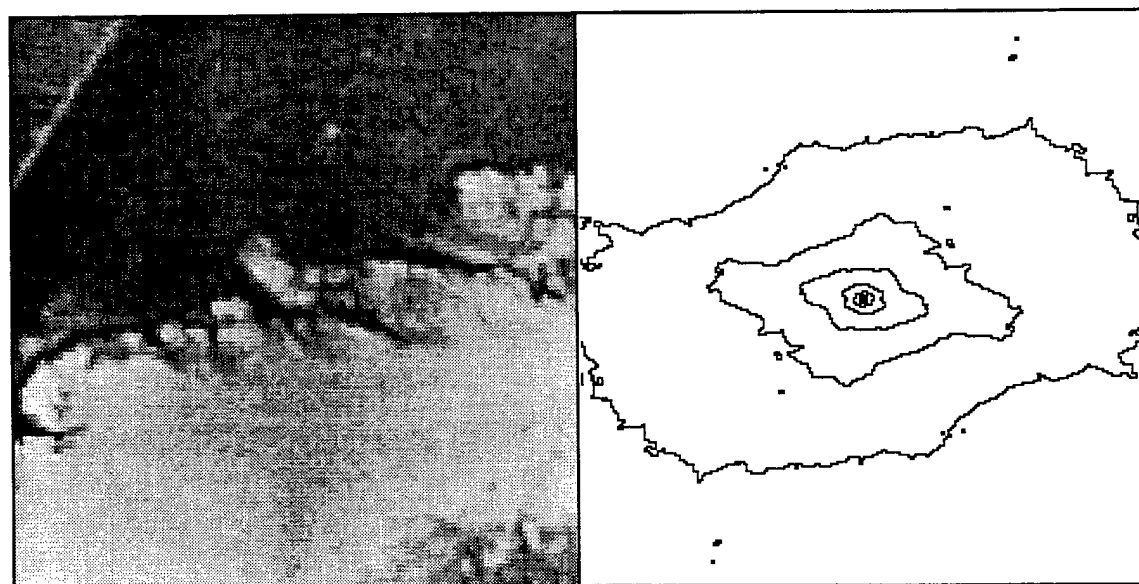
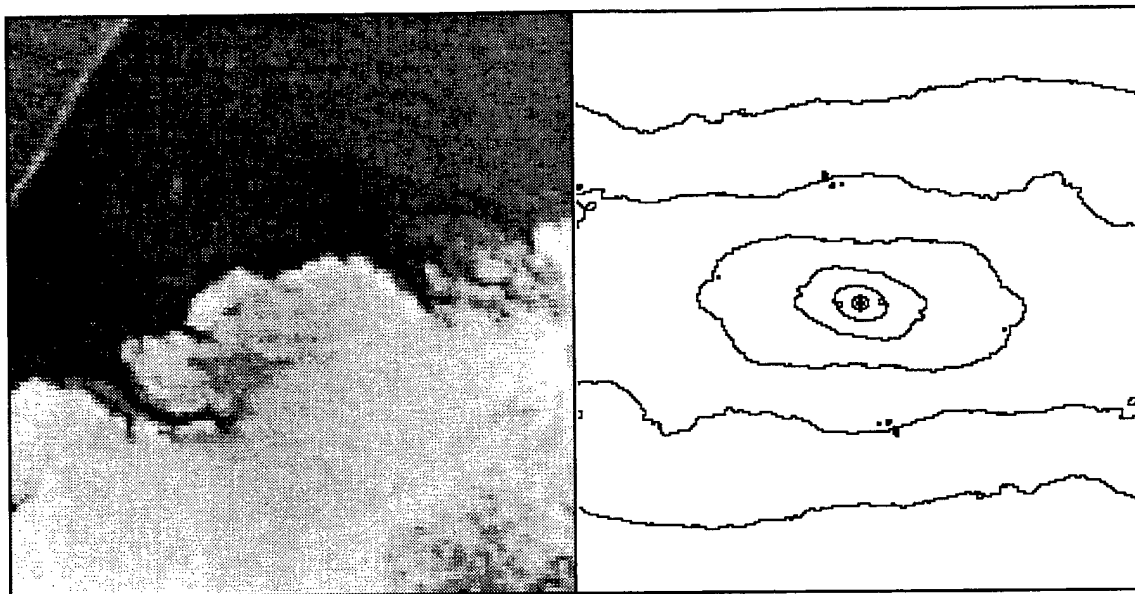


Figure 5.80 Two-Dimensional Spatial Correlation Fields from Upstream Instantaneous Side View Images of Elliptical Injection Using Helium (Case E2H)

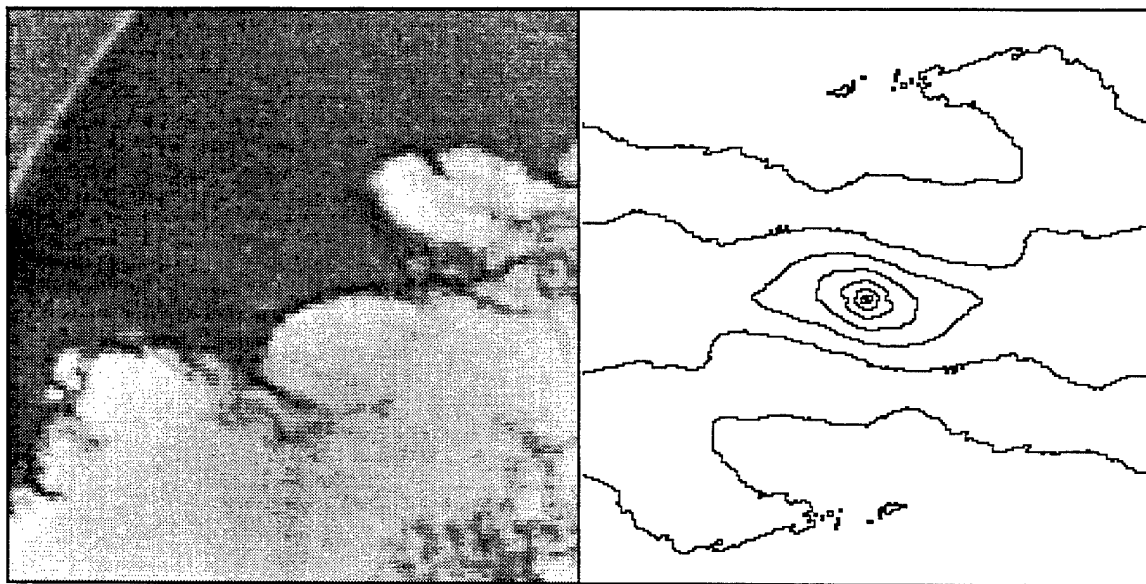
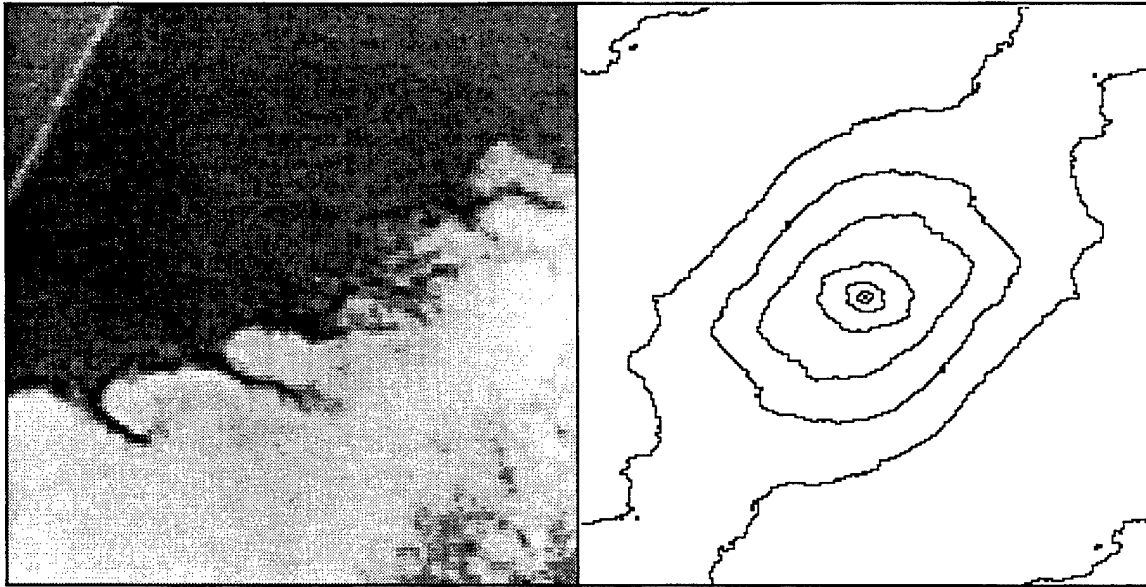


Figure 5.80 (continued)

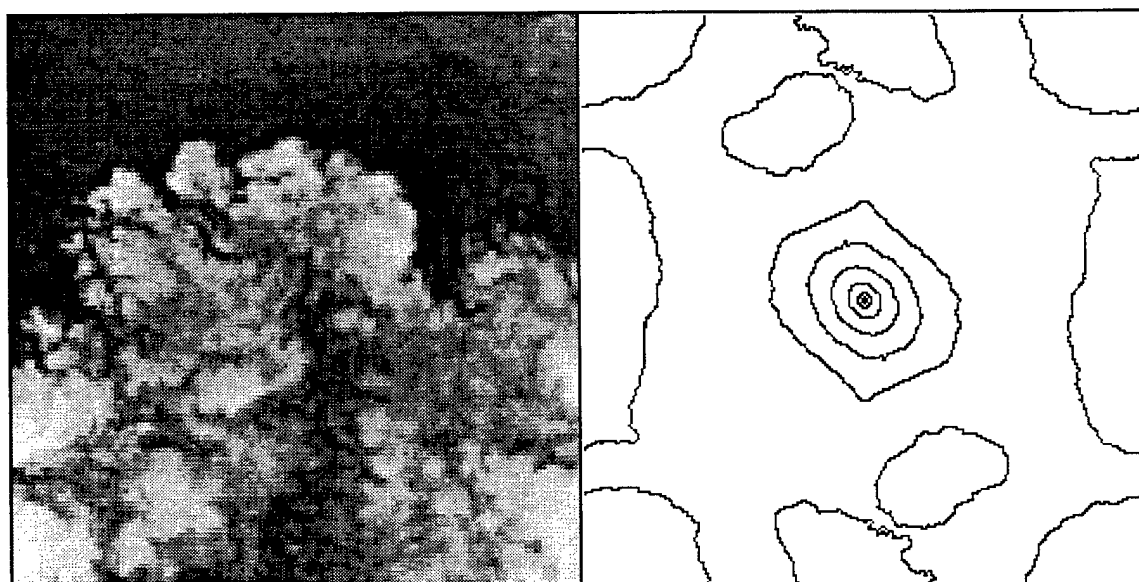
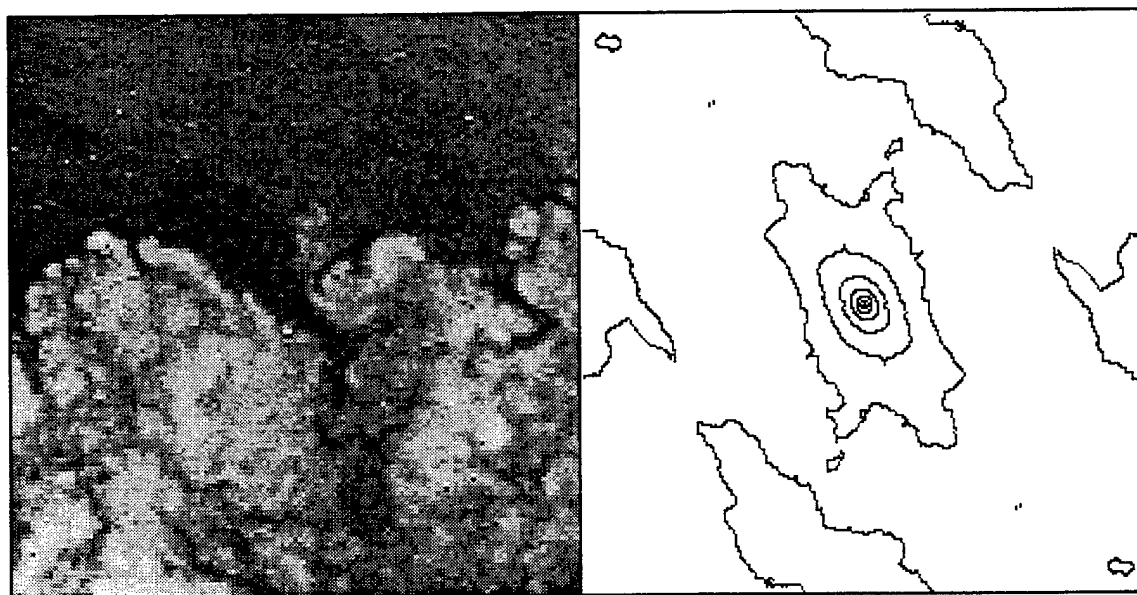


Figure 5.81 Two-Dimensional Spatial Correlation Fields from Downstream Instantaneous Side View Images of Elliptical Injection Using Helium (Case E2H)

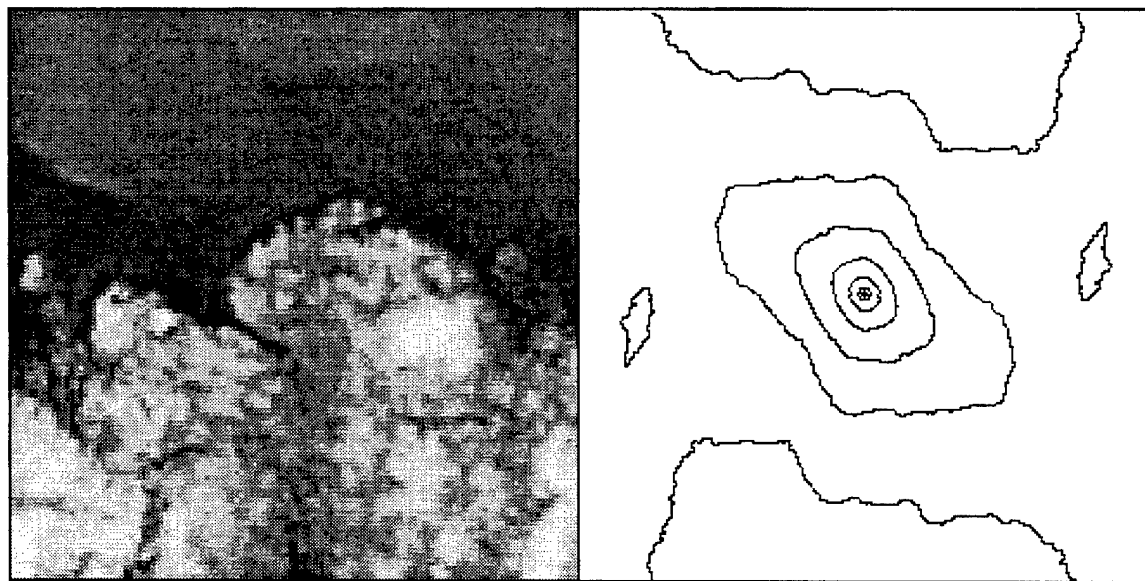
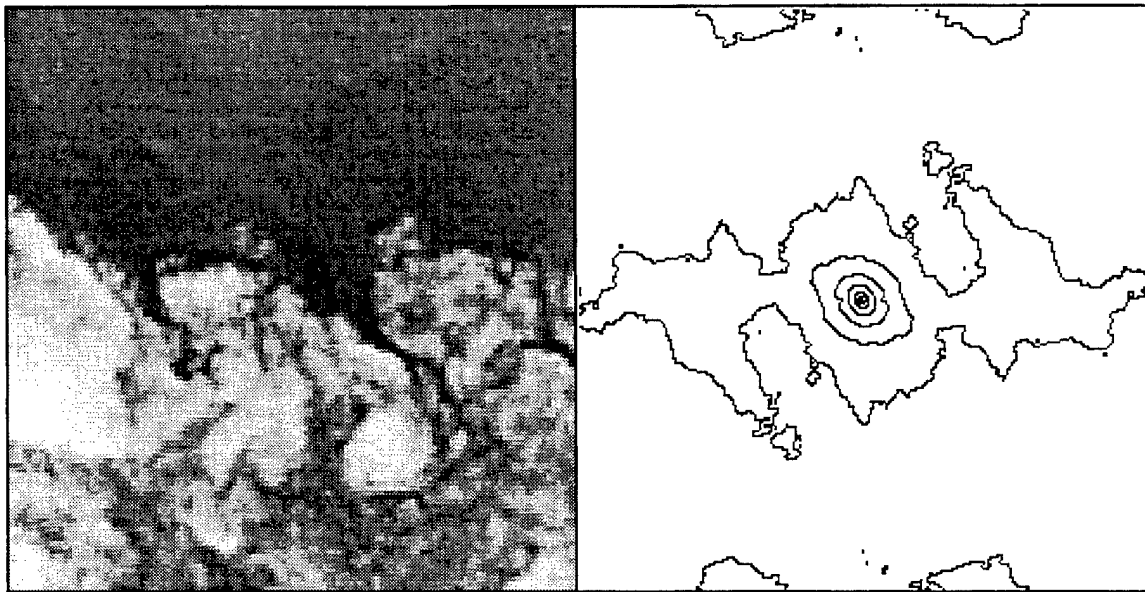
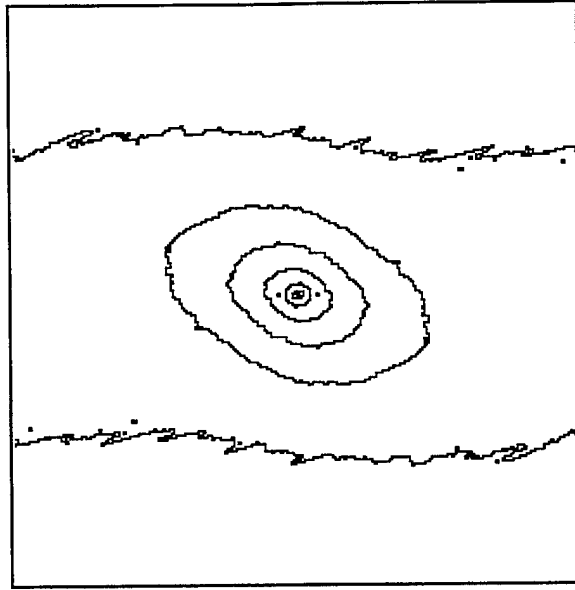
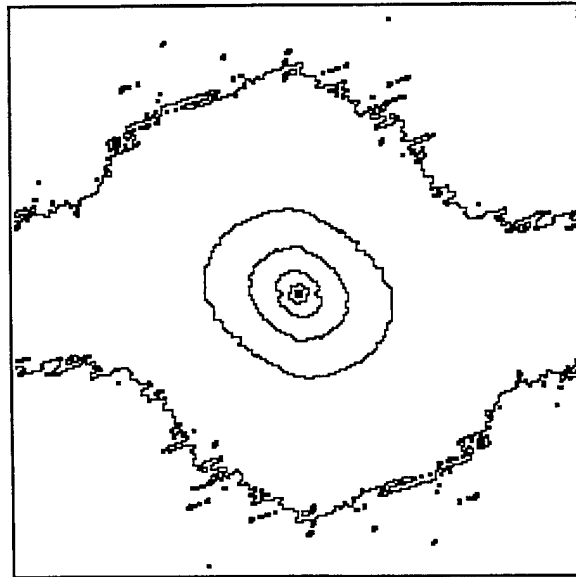


Figure 5.81 (continued)

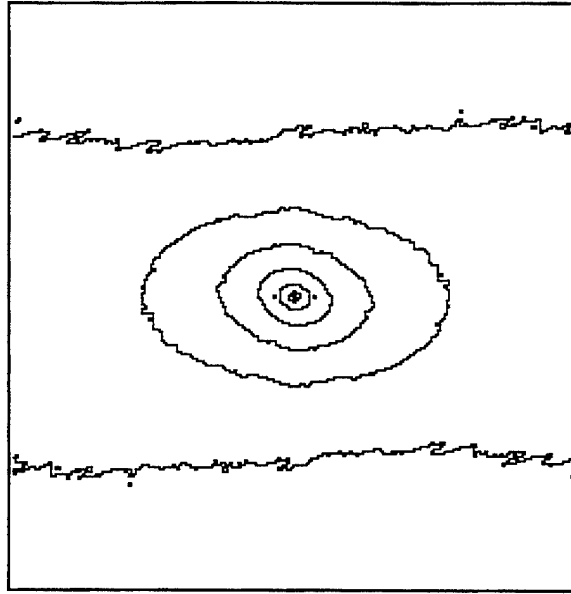


a) Upstream Image

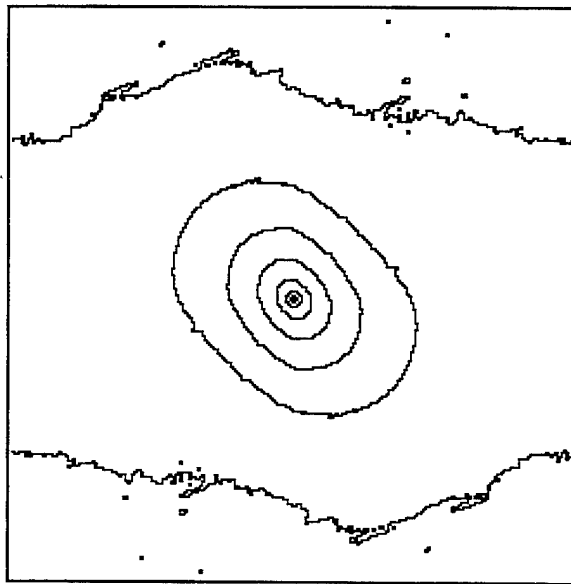


b) Downstream Image

Figure 5.82 Ensemble-Averaged Two-Dimensional Spatial Correlation Fields from Side View Images of Circular Injection Using Air (Case C1A) **a)** Upstream Image and **b)** Downstream Image

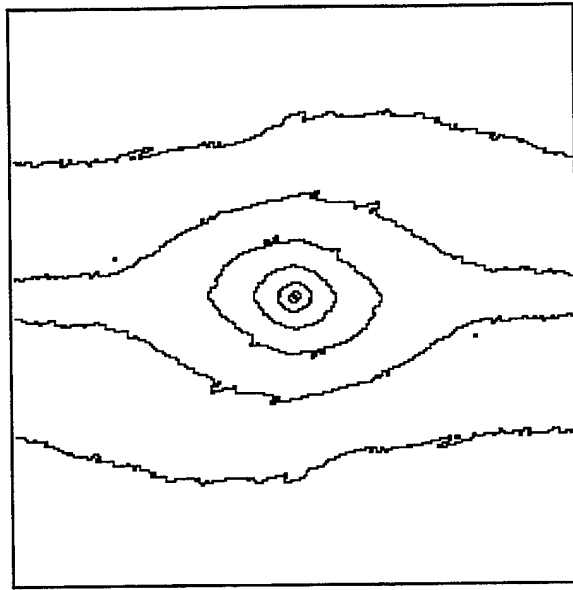


a) Upstream Image

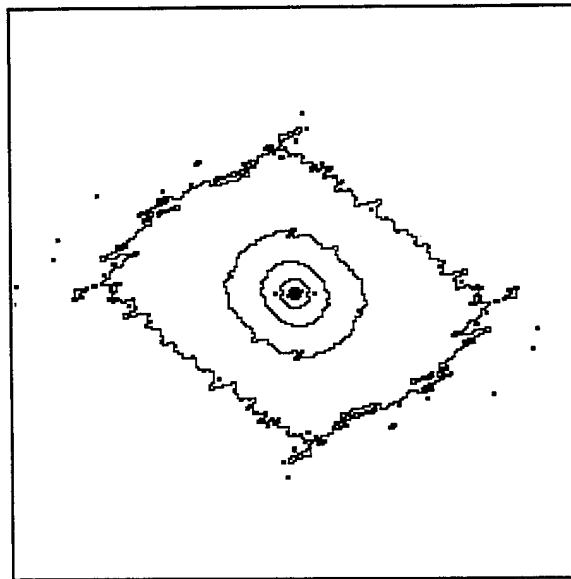


b) Downstream Image

Figure 5.83 Ensemble-Averaged Two-Dimensional Spatial Correlation Fields from Side View Images of Circular Injection Using Helium (Case C2H) **a)** Upstream Image and **b)** Downstream Image

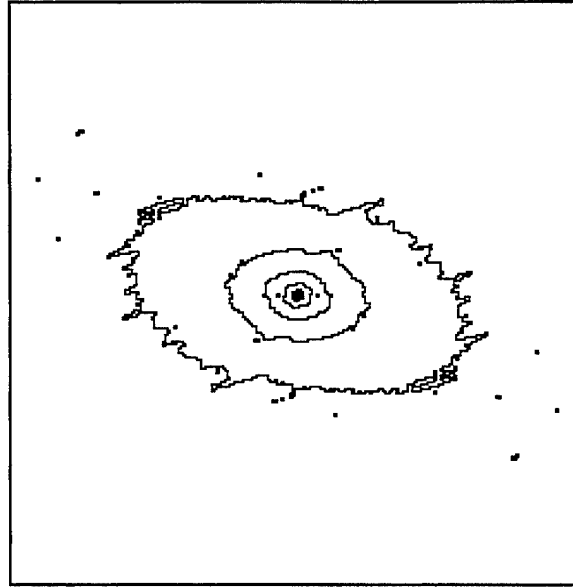


a) Upstream Image

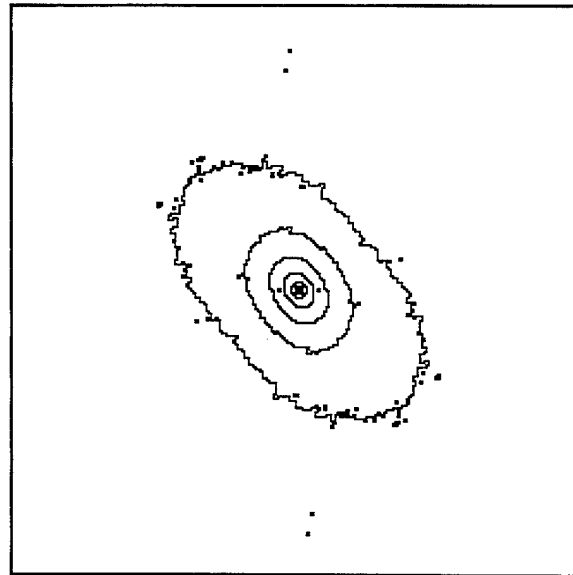


b) Downstream Image

Figure 5.84 Ensemble-Averaged Two-Dimensional Spatial Correlation Fields from Side View Images of Elliptical Injection Using Air (Case E1A) **a)** Upstream Image and **b)** Downstream Image



a) Upstream Image



b) Downstream Image

Figure 5.85 Ensemble-Averaged Two-Dimensional Spatial Correlation Fields from Side View Images of Elliptical Injection Using Helium (Case E1H) **a)** Upstream Image and **b)** Downstream Image

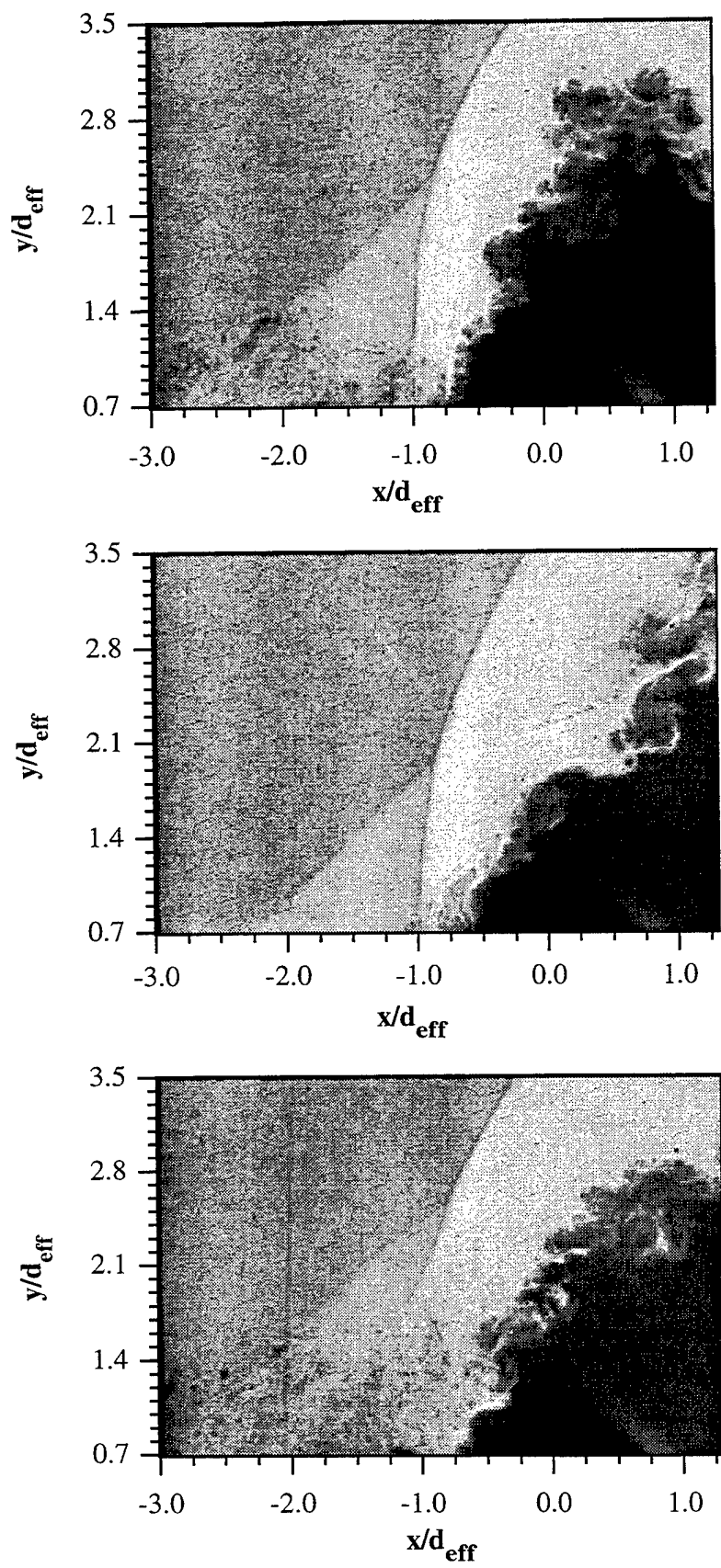


Figure 5.86 Instantaneous Images of Bow Shock/Jet Boundary Interaction Upstream of Circular Injector Using Air (Case C1A)

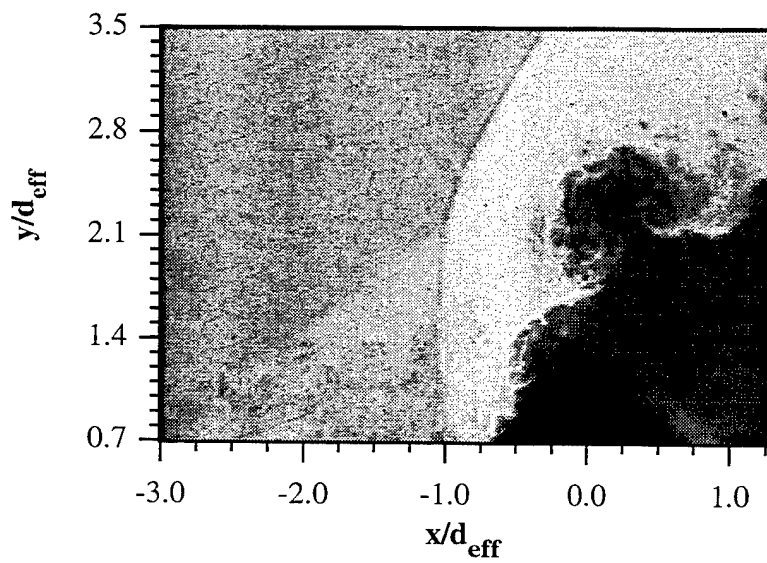
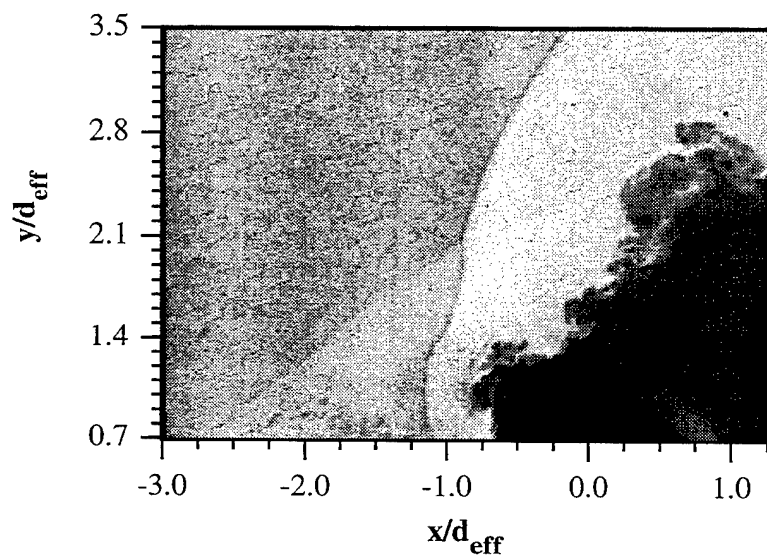
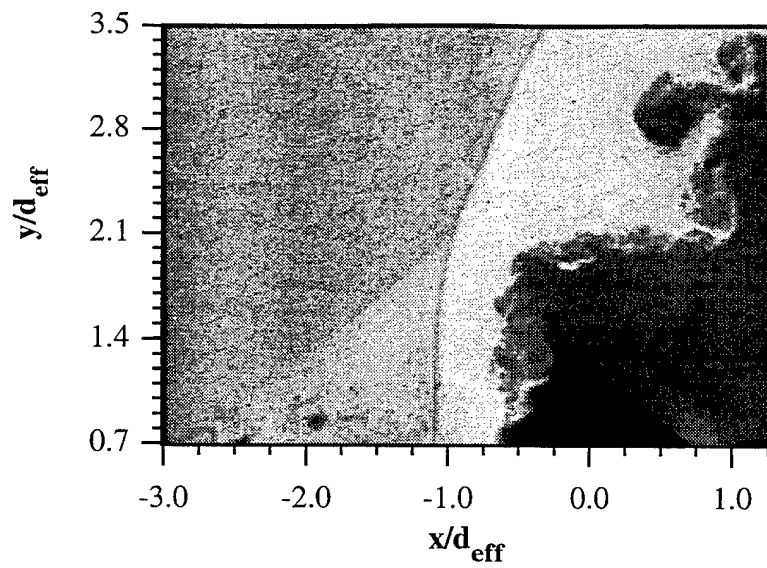


Figure 5.86 (continued)

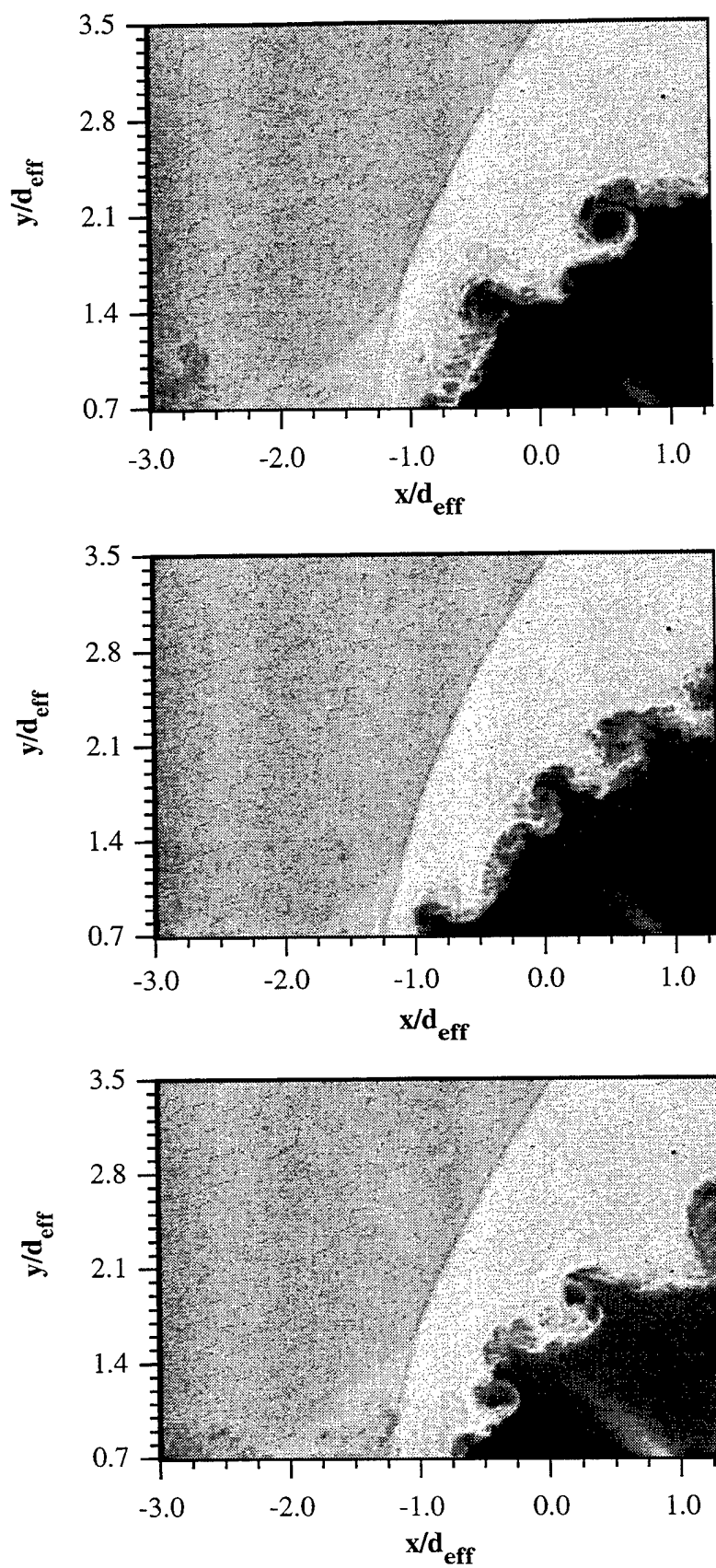


Figure 5.87 Instantaneous Images of Bow Shock/Jet Boundary Interaction Upstream of Elliptical Injector Using Air (Case E1A)

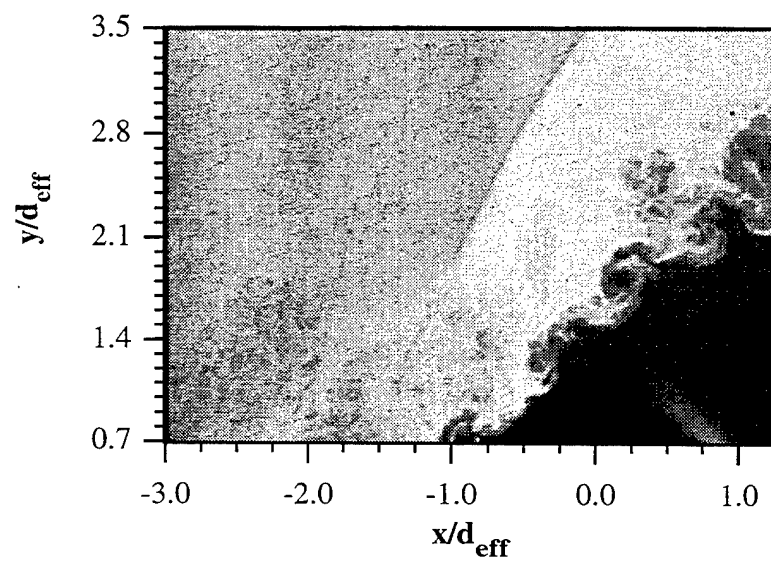
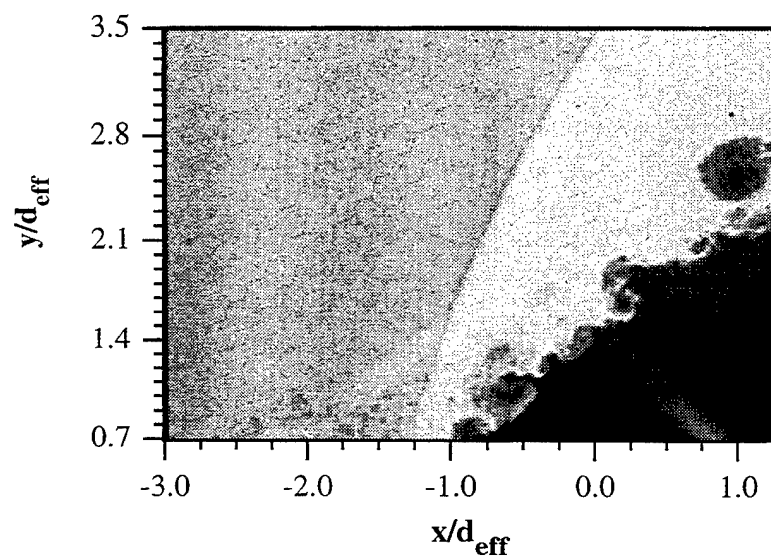
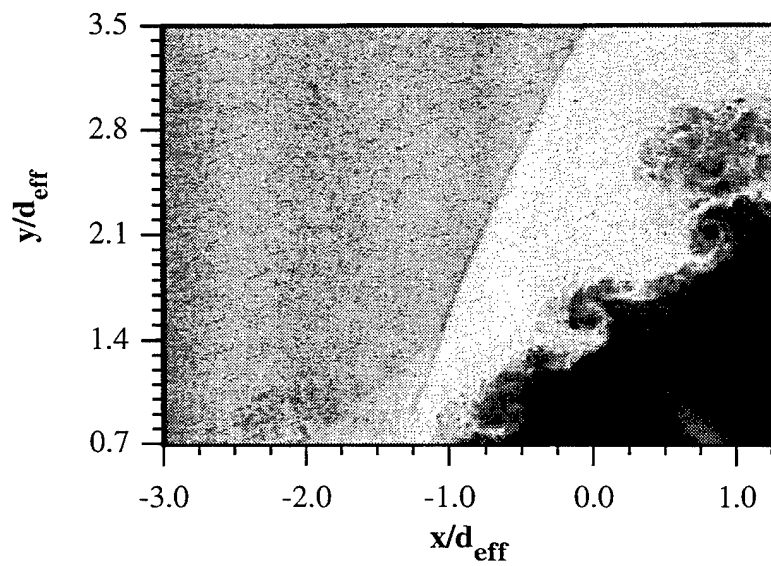


Figure 5.87 (continued)

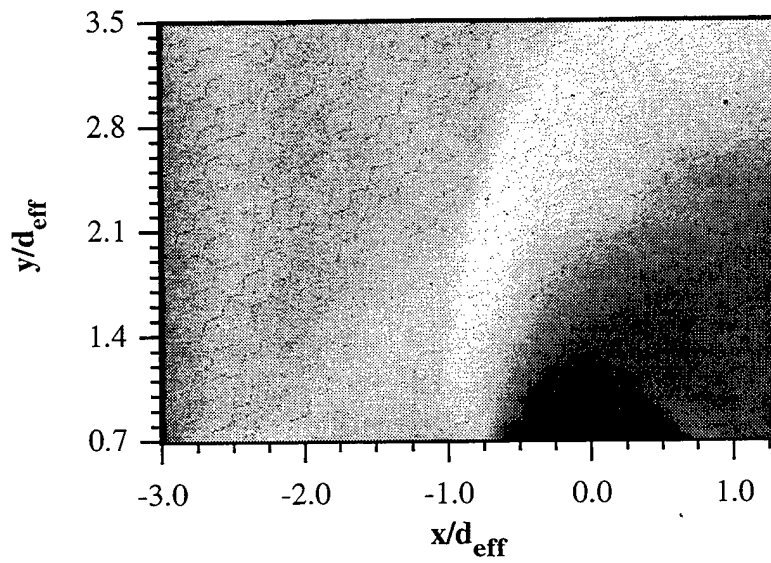


Figure 5.88 Ensemble-Averaged Image of Bow Shock/Jet Boundary Interaction Upstream of Circular Injector Using Air (Case C1A)

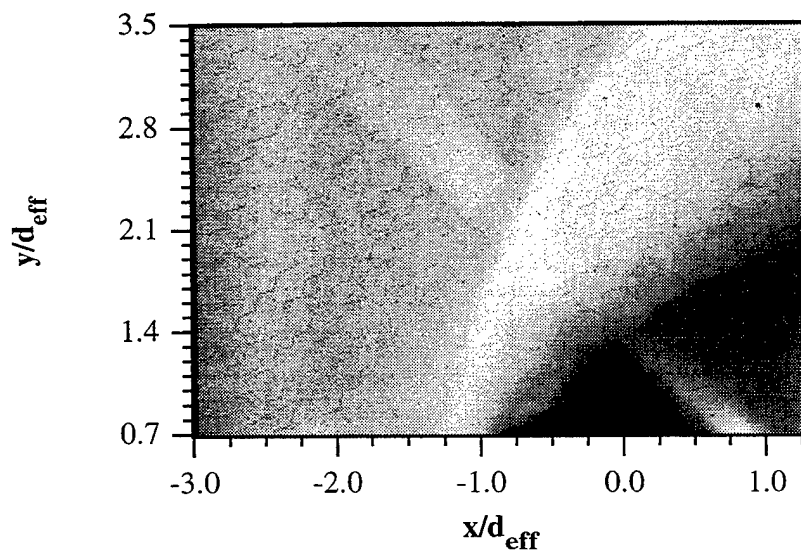


Figure 5.89 Ensemble-Averaged Image of Bow Shock/Jet Boundary Interaction Upstream of Elliptical Injector Using Air (Case E1A)

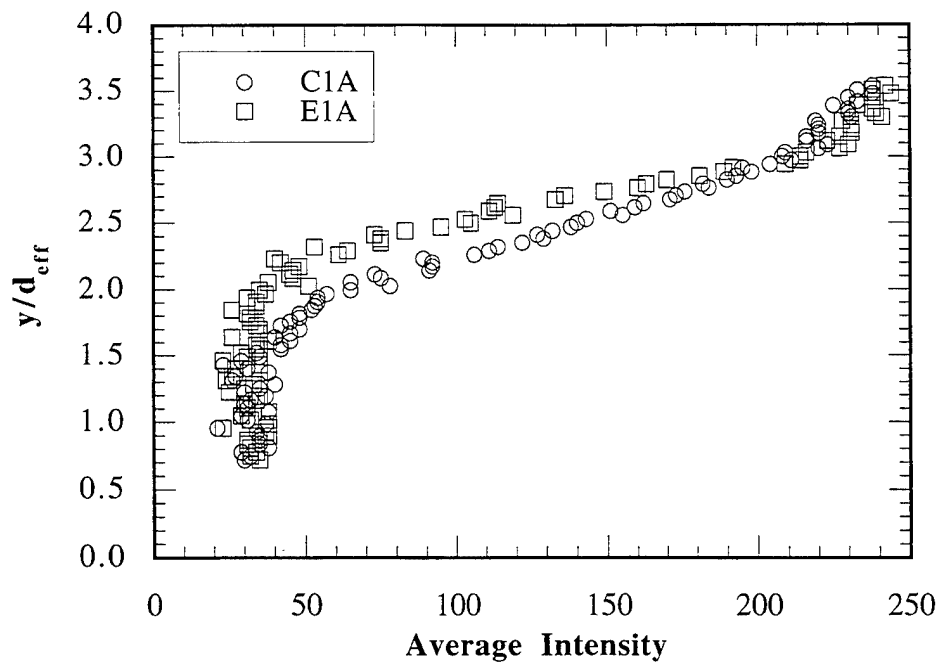


Figure 5.90 Intensity Profiles from Ensemble-Averaged Bow Shock/Jet Boundary Interaction Images of Cases C1A and E1A at $x/d_{\text{eff}} = 0$

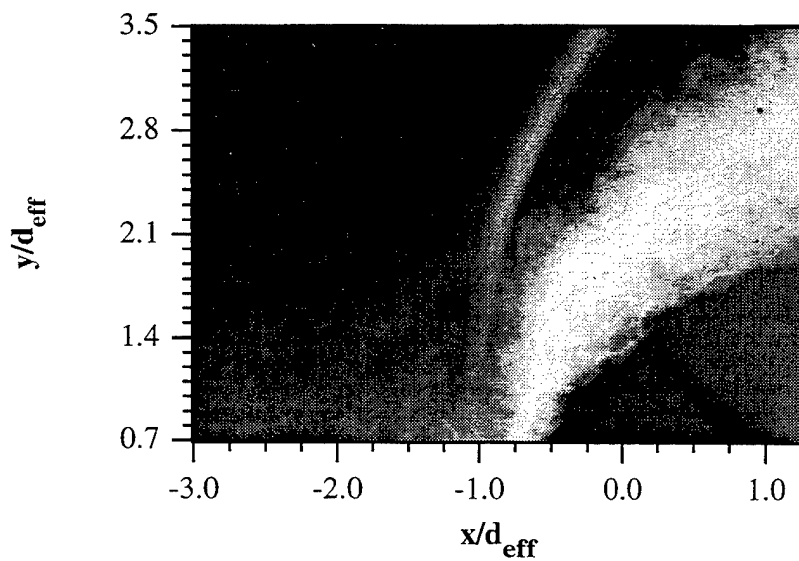


Figure 5.91 Standard Deviation Image of Bow Shock/Jet Boundary Interaction Upstream of Circular Injector Using Air (Case C1A)

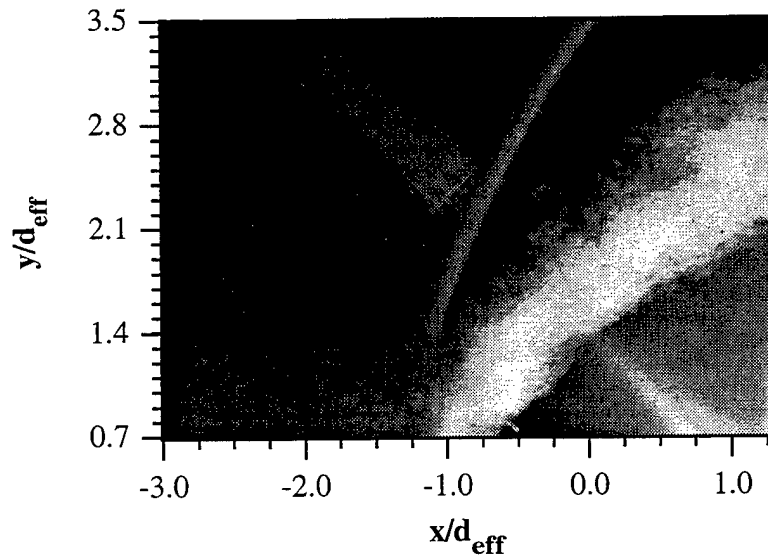


Figure 5.92 Standard Deviation Image of Bow Shock/Jet Boundary Interaction Upstream of Elliptical Injector Using Air (Case E1A)

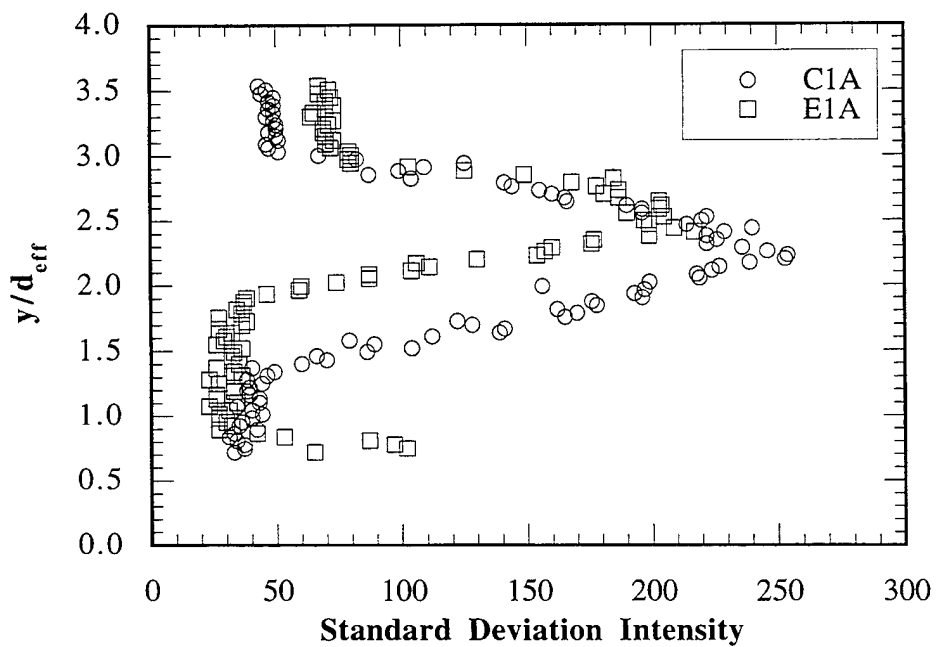


Figure 5.93 Intensity Profiles from Standard Deviation Bow Shock/Jet Boundary Interaction Images of Cases C1A and E1A at $x/d_{\text{eff}} = 0$

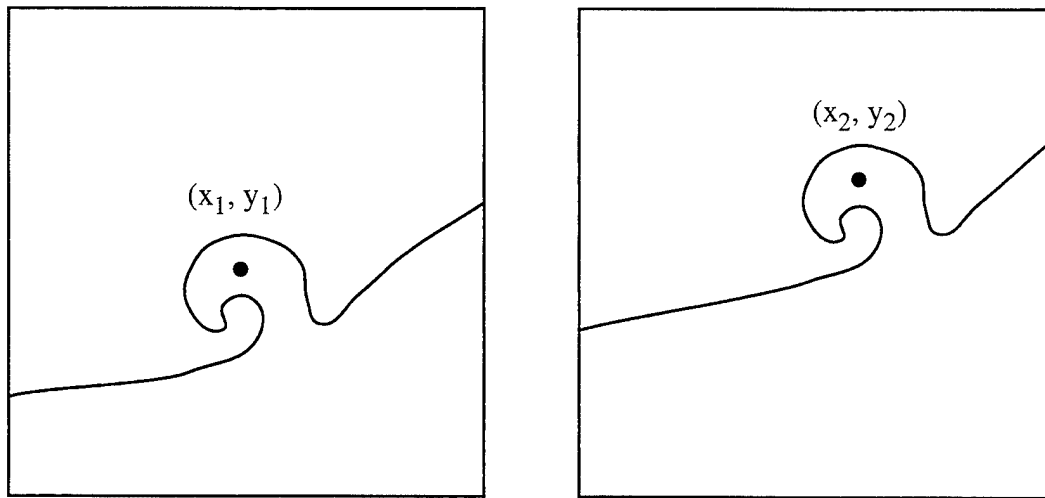
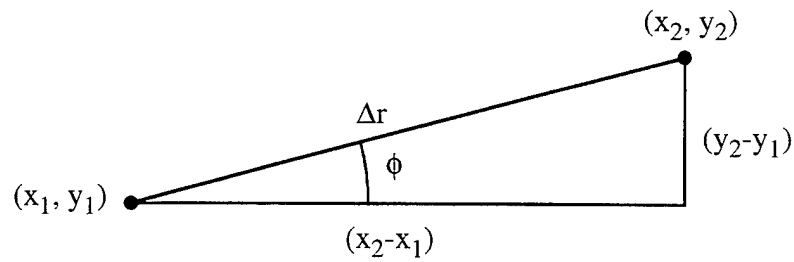


Image #1

Image #2



$$U_c = \frac{\Delta r}{\Delta t} = \frac{\sqrt{(x_2 - x_1)^2 + (y_2 - y_1)^2}}{\Delta t}$$

$$\phi = \arctan[(y_2 - y_1)/(x_2 - x_1)]$$

Figure 5.94 Large-Scale Convection Velocity and Structure Convection Angle Determination

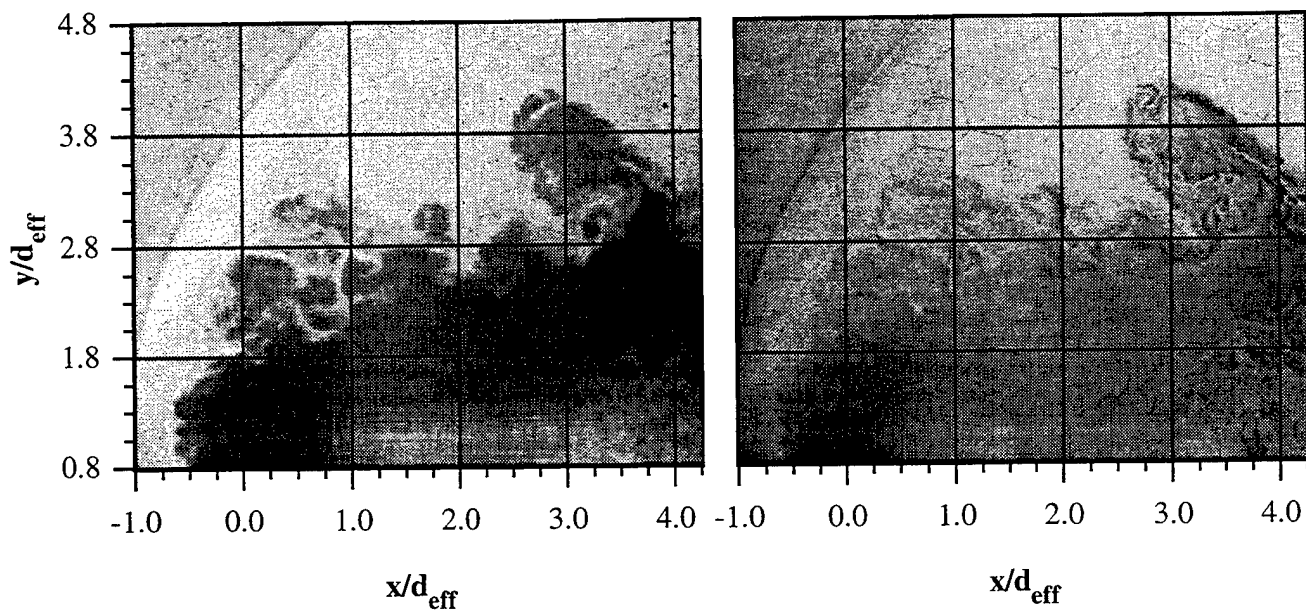


Figure 5.95 Instantaneous Double-Pulsed Image Pair from Circular Injection Using Air (Case C1A) with Laser Pulse Delay of $\Delta t = 2 \mu s$

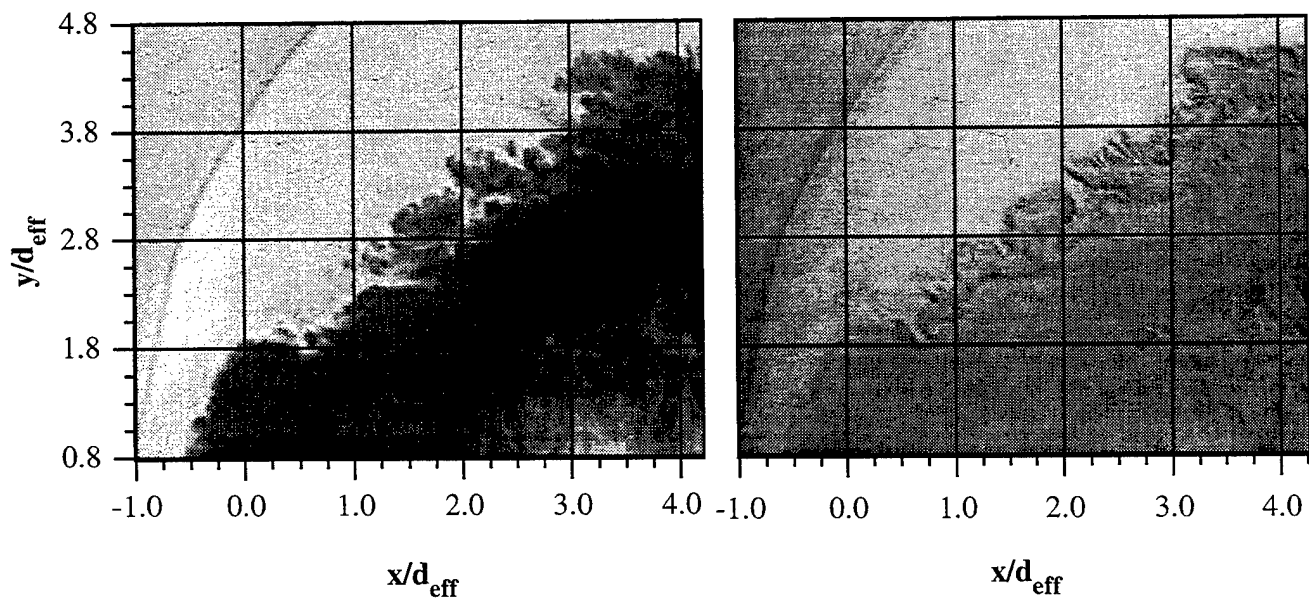


Figure 5.96 Instantaneous Double-Pulsed Image Pair from Circular Injection Using Helium (Case C2H) with Laser Pulse Delay of $\Delta t = 1 \mu s$

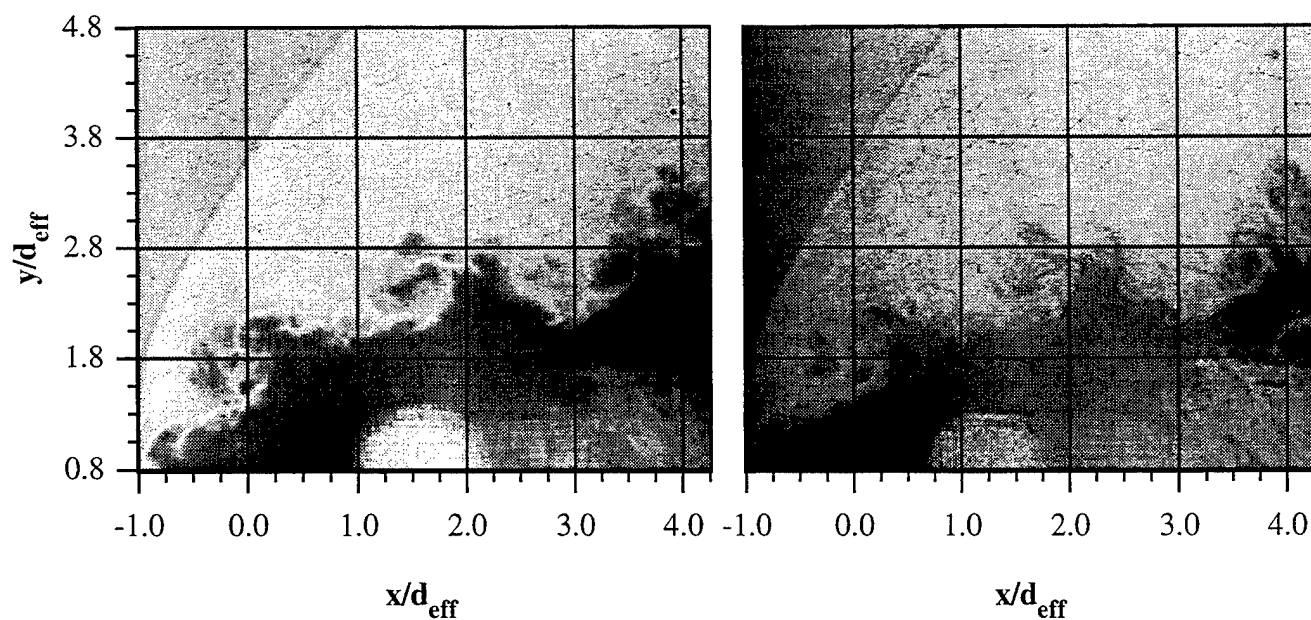


Figure 5.97 Instantaneous Double-Pulsed Image Pair from Elliptical Injection Using Air
(Case E1A) with Laser Pulse Delay of $\Delta t = 2 \mu s$

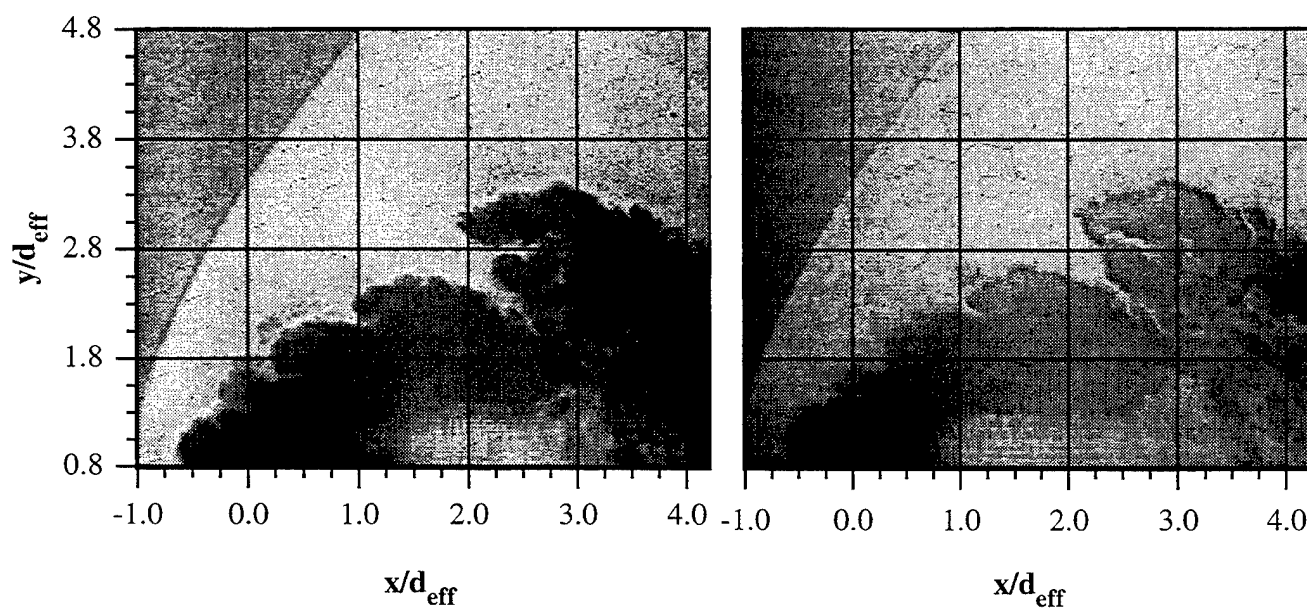


Figure 5.98 Instantaneous Double-Pulsed Image Pair from Elliptical Injection Using Helium
(Case E2H) with Laser Pulse Delay of $\Delta t = 1.2 \mu s$

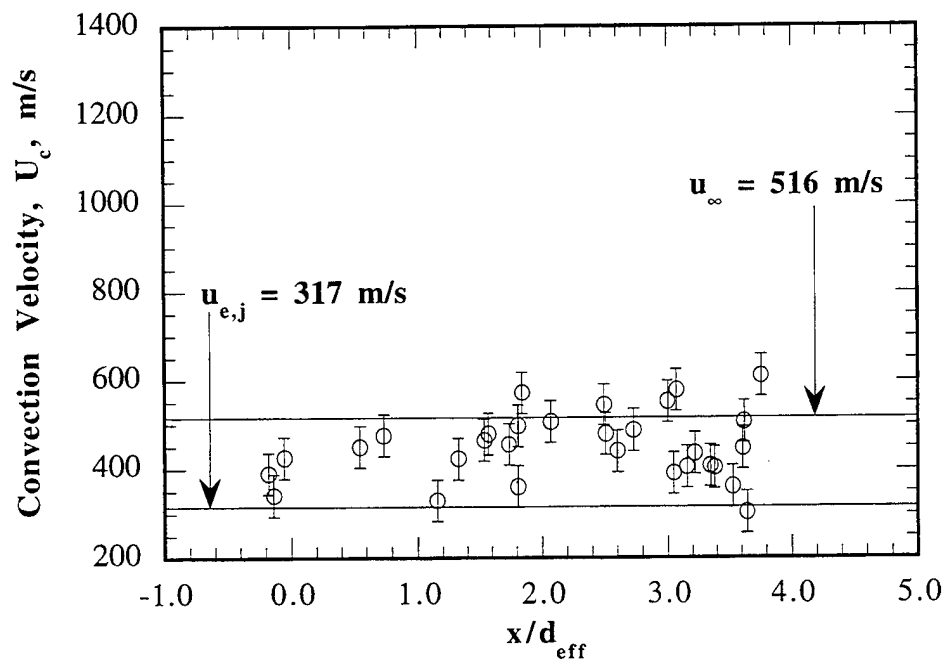


Figure 5.99 Large-Scale Convection Velocity as a Function of Streamwise Position for Circular Injection Using Air (Case C1A)

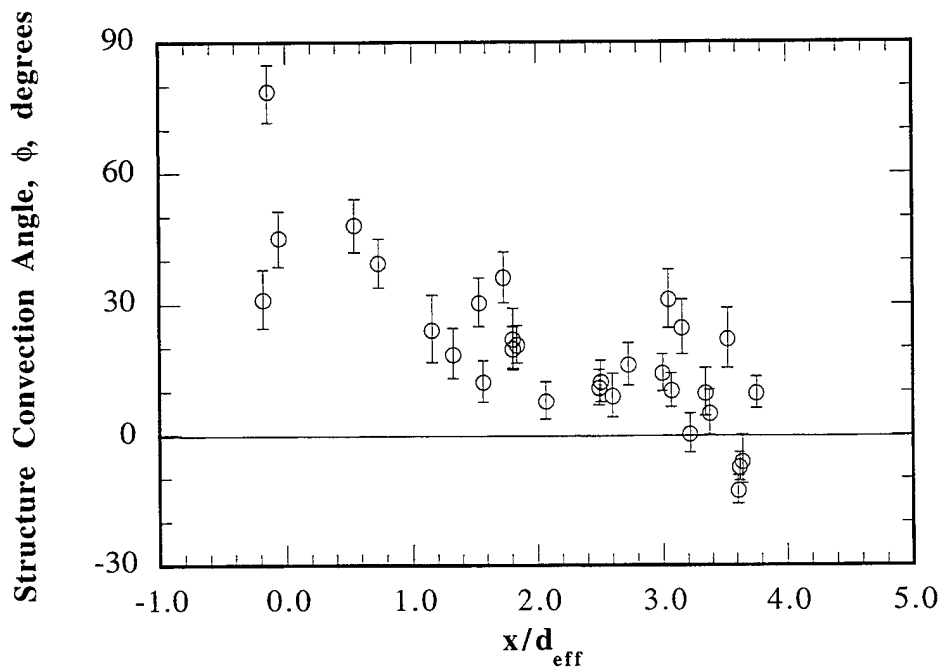


Figure 5.100 Structure Convection Angle as a Function of Streamwise Position for Circular Injection Using Air (Case C1A)

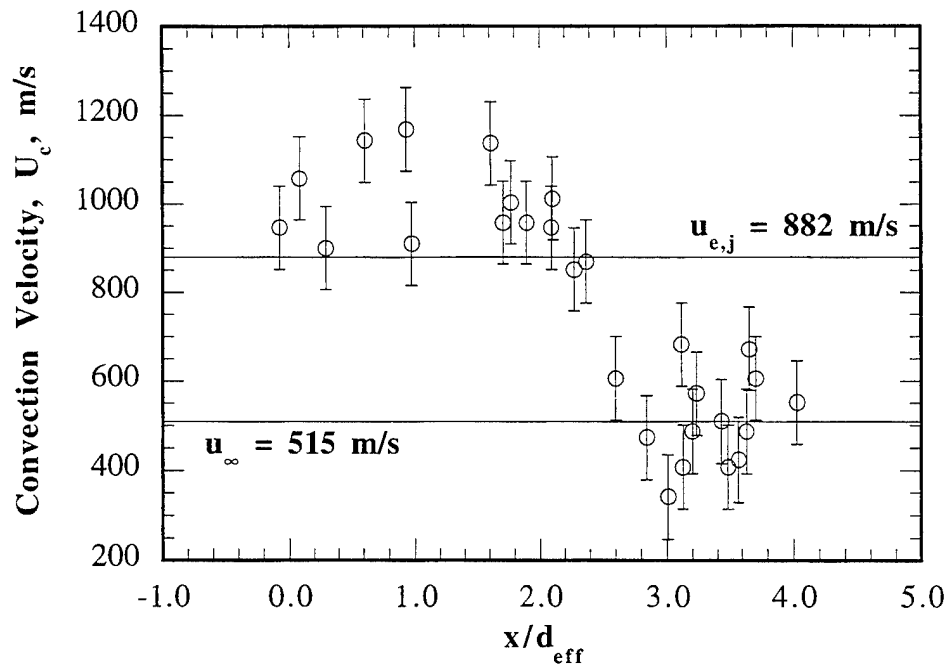


Figure 5.101 Large-Scale Convection Velocity as a Function of Streamwise Position for Circular Injection Using Helium (Case C2H)

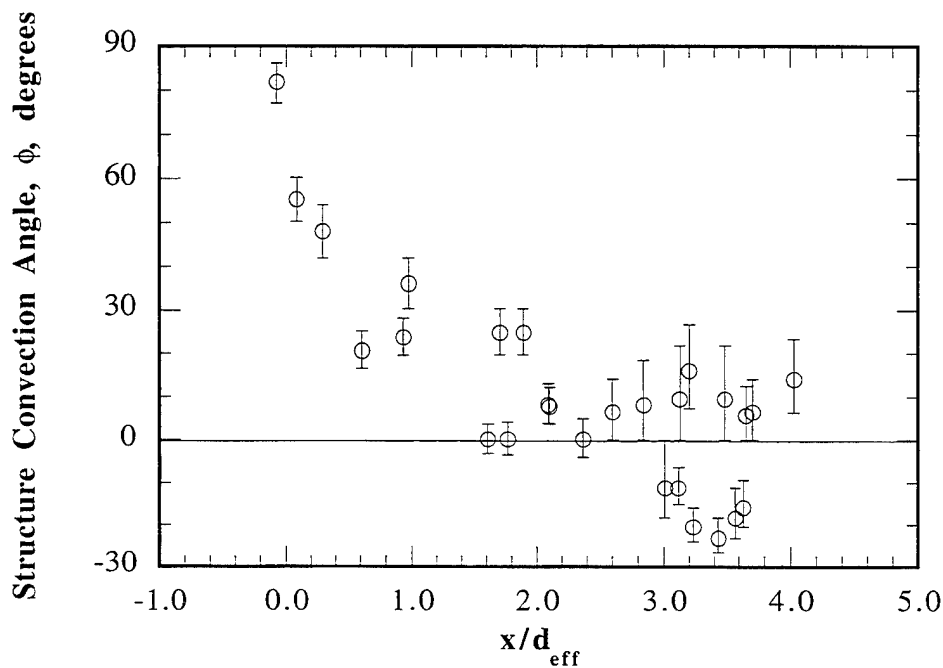


Figure 5.102 Structure Convection Angle as a Function of Streamwise Position for Circular Injection Using Helium (Case C2H)

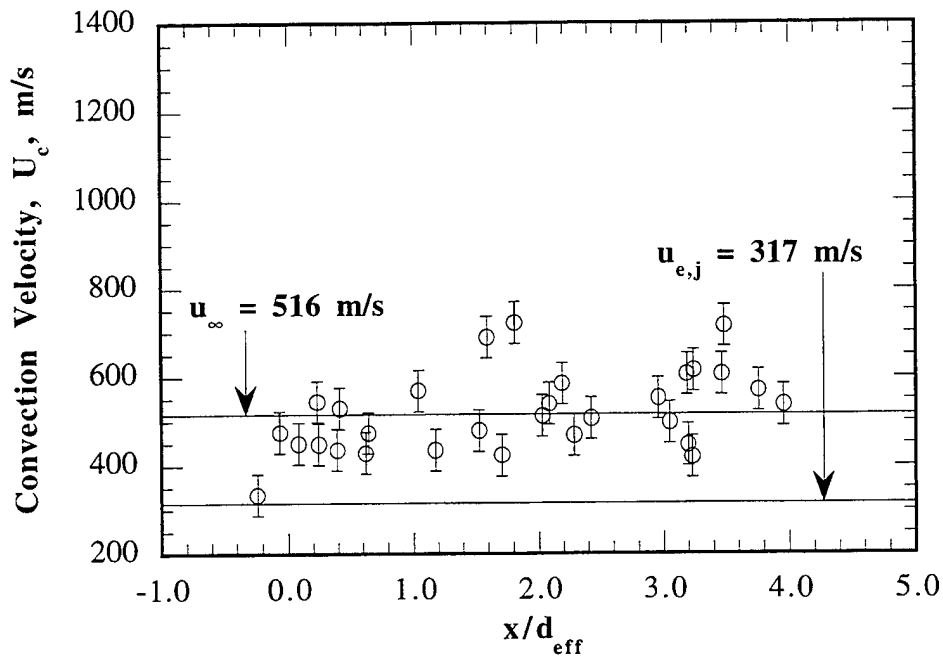


Figure 5.103 Large-Scale Convection Velocity as a Function of Streamwise Position for Elliptical Injection Using Air (Case E1A)

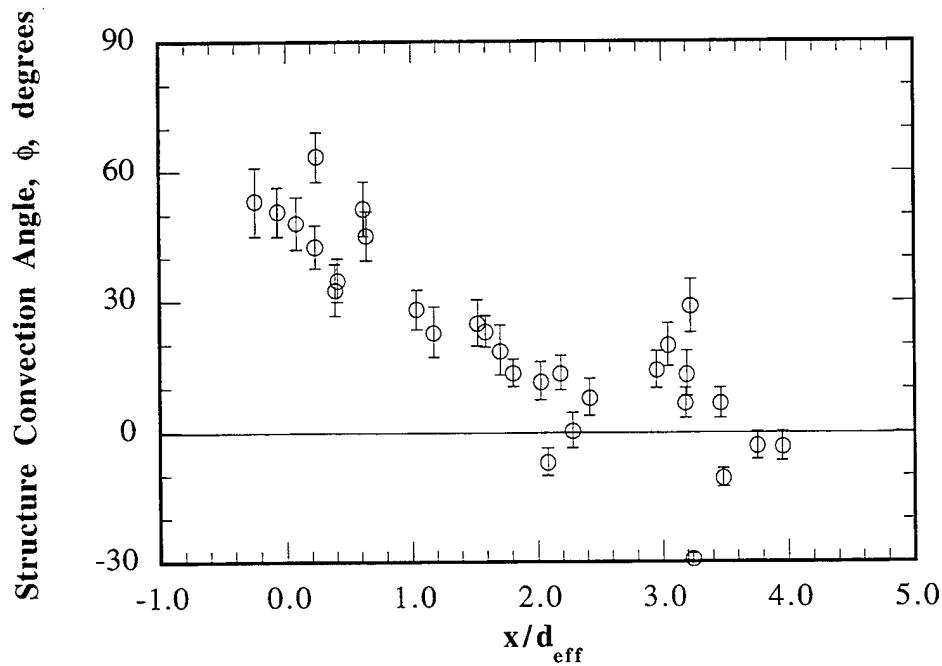


Figure 5.104 Structure Convection Angle as a Function of Streamwise Position for Elliptical Injection Using Air (Case E1A)

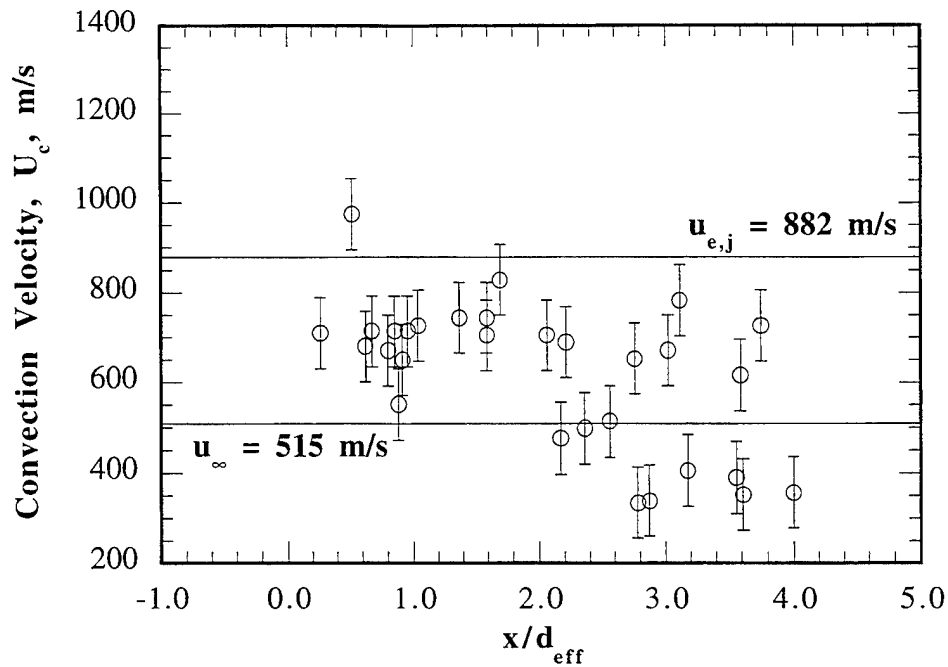


Figure 5.105 Large-Scale Convection Velocity as a Function of Streamwise Position for Elliptical Injection Using Helium (Case E2H)

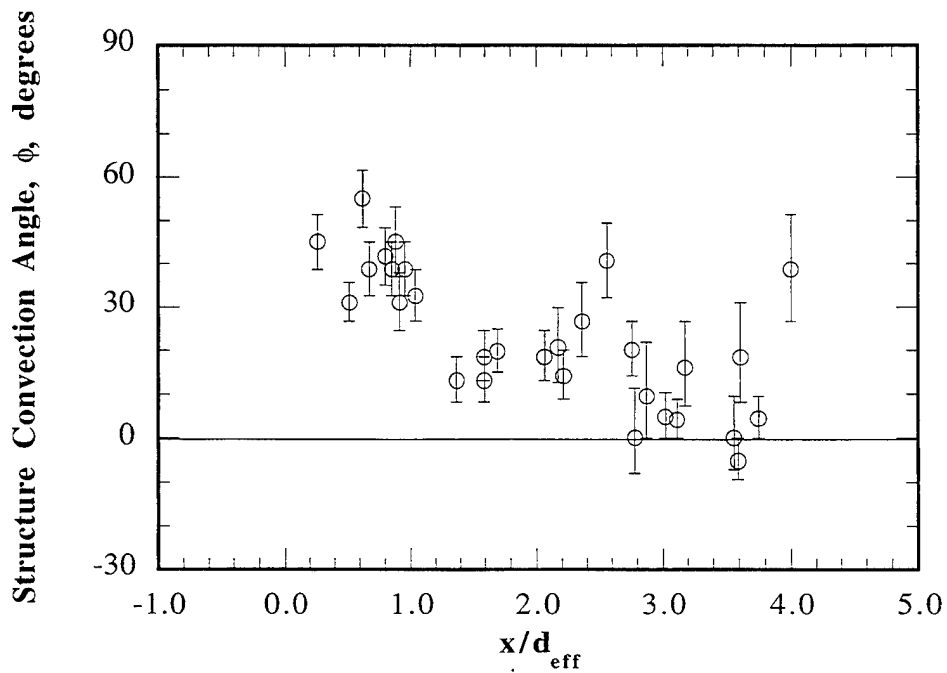


Figure 5.106 Structure Convection Angle as a Function of Streamwise Position for Elliptical Injection Using Helium (Case E2H)

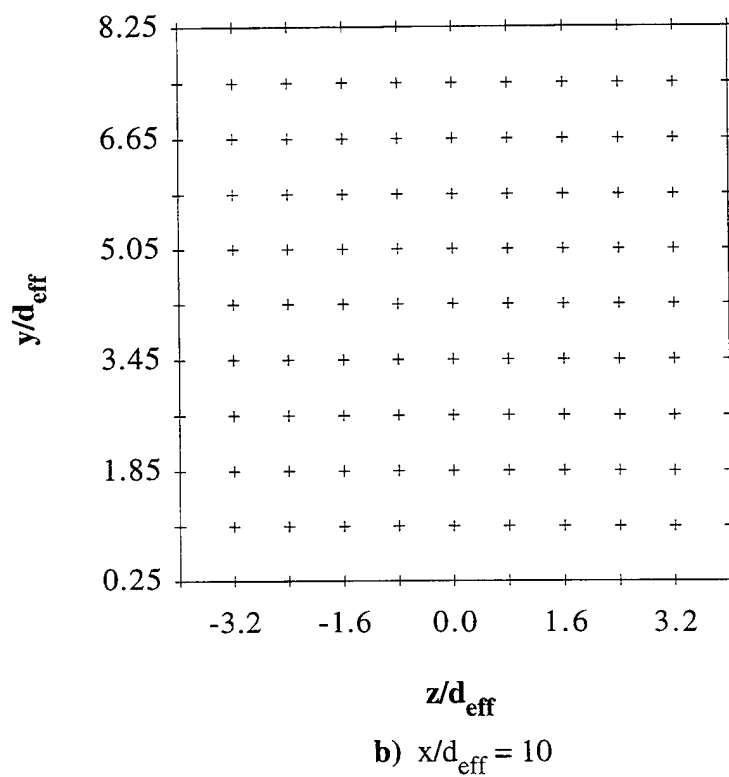
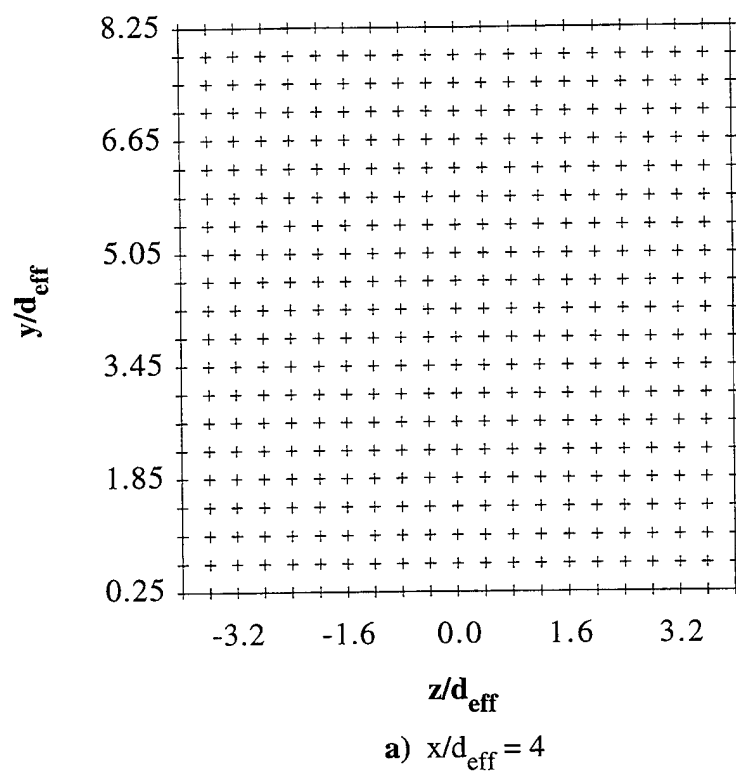


Figure 5.107 Measurement Locations for Probe-Based Studies a) $x/d_{\text{eff}} = 4$ and b) $x/d_{\text{eff}} = 10$

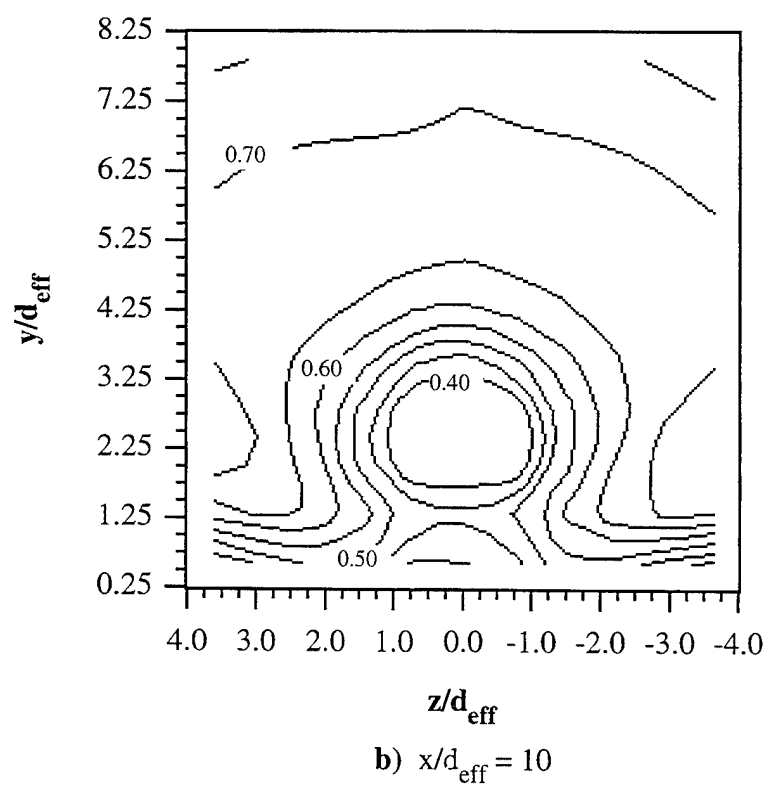
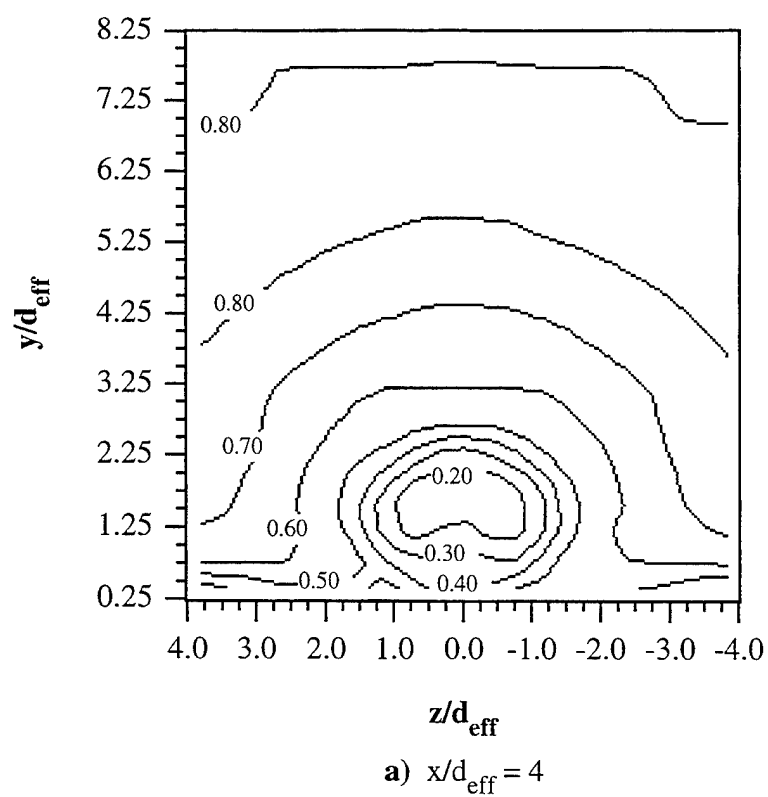


Figure 5.108 Contours of Normalized Pitot Pressure ($\Pi_{2,\infty}$) from Circular Injection Using Helium (Case C2H) a) $x/d_{\text{eff}} = 4$ and b) $x/d_{\text{eff}} = 10$

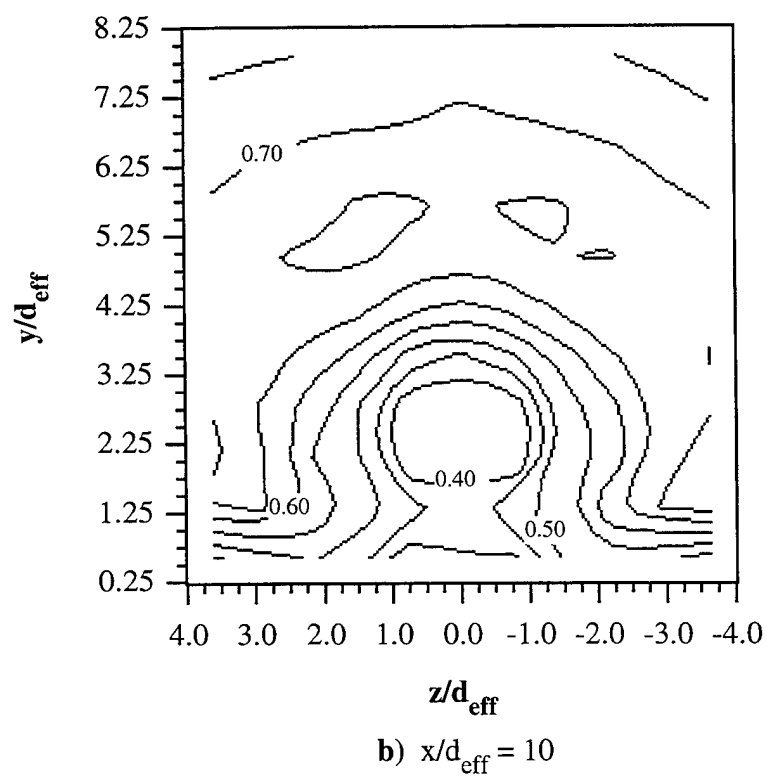
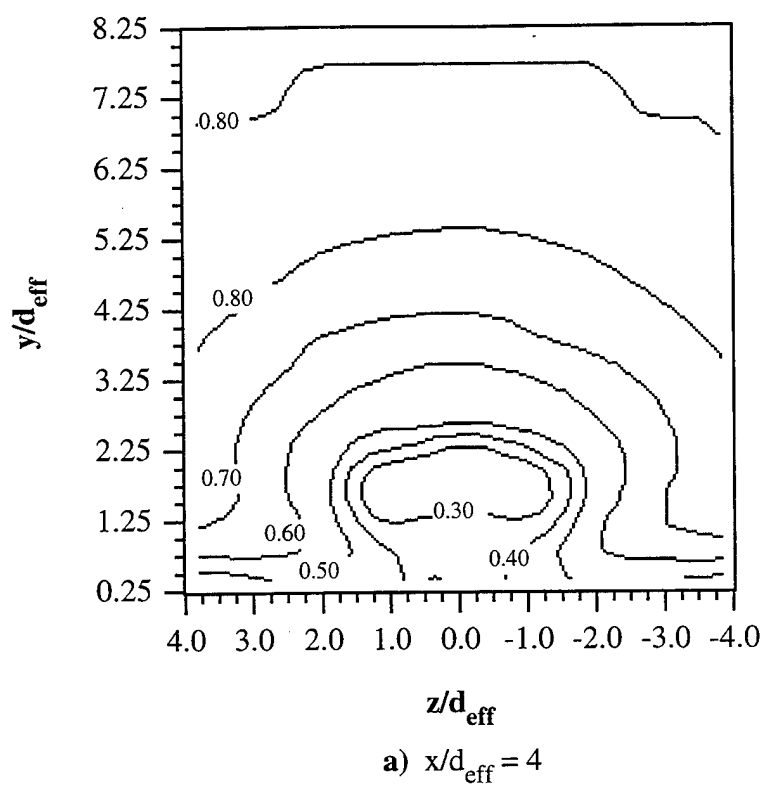


Figure 5.109 Contours of Normalized Pitot Pressure ($\Pi_{2,\infty}$) from Elliptical Injection Using Helium (Case E2H) a) $x/d_{\text{eff}} = 4$ and b) $x/d_{\text{eff}} = 10$

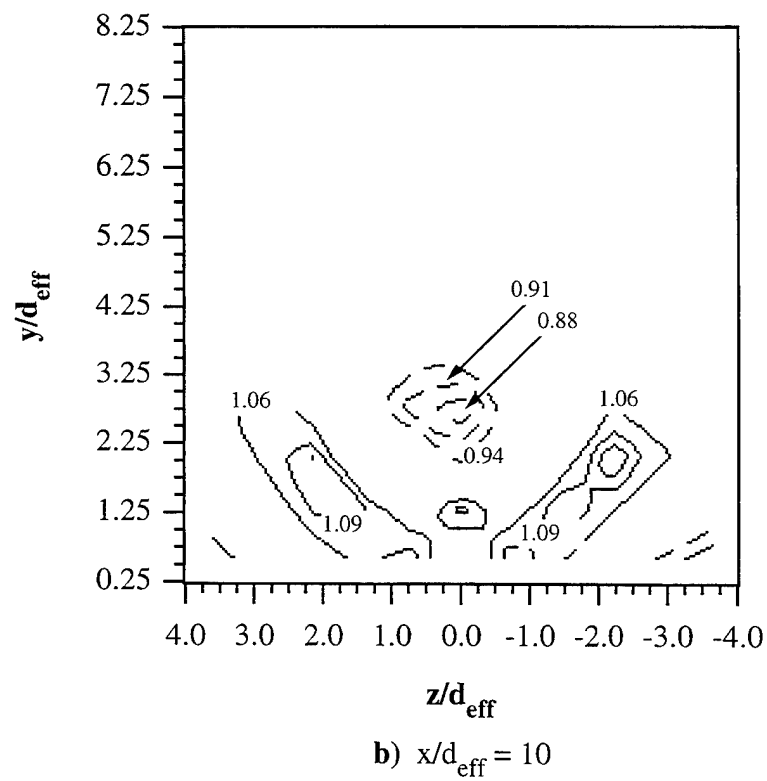
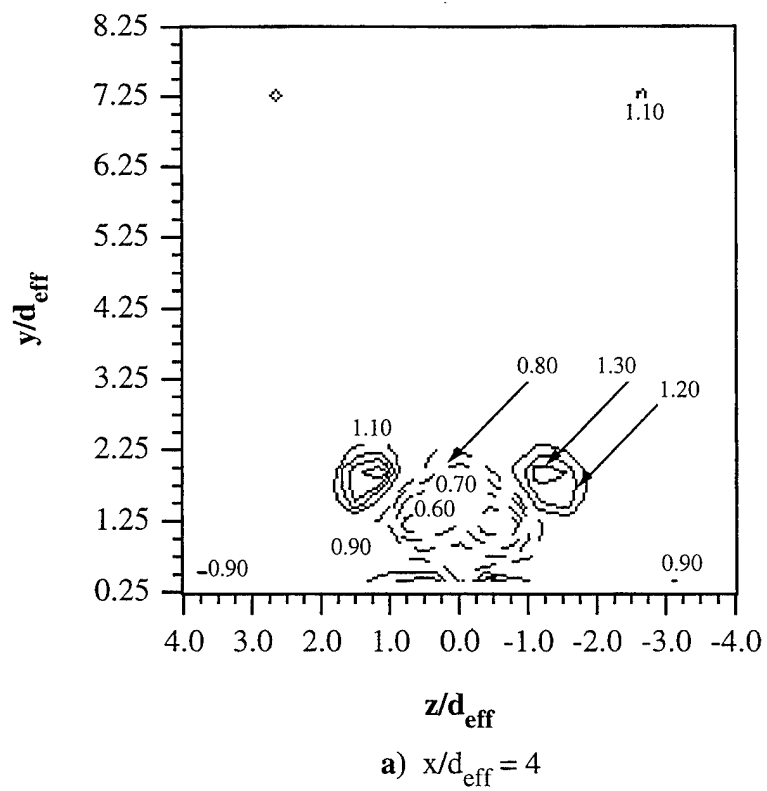


Figure 5.110 Contour Plots Showing Measured Pitot Pressure Ratio Π_{ce}
 a) $x/d_{eff} = 4$ and b) $x/d_{eff} = 10$

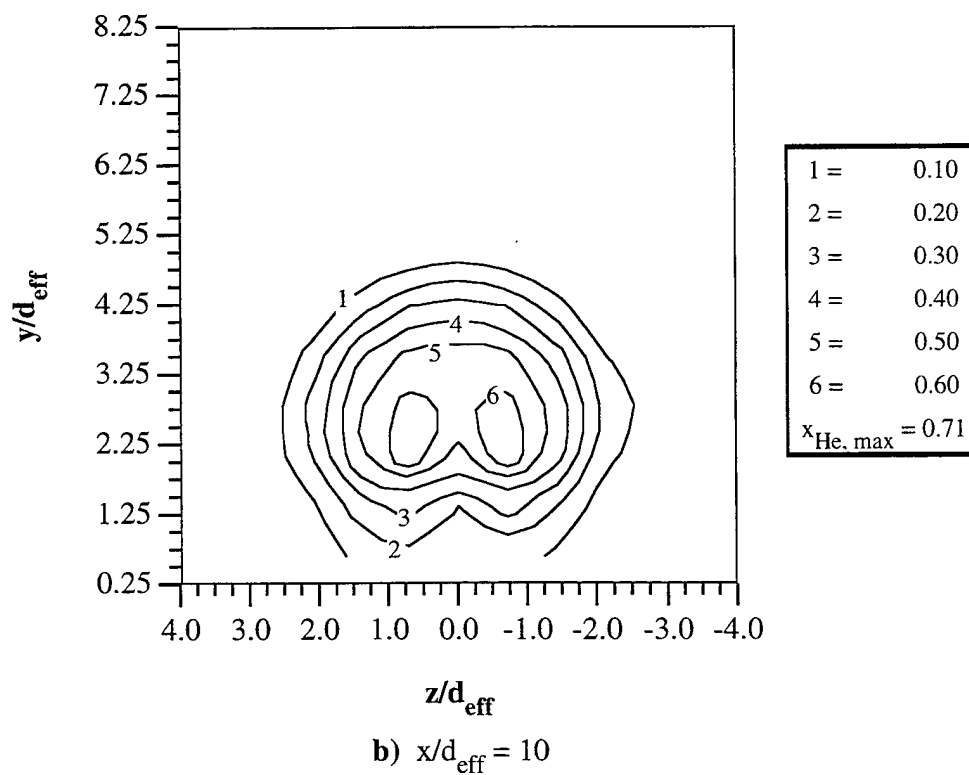
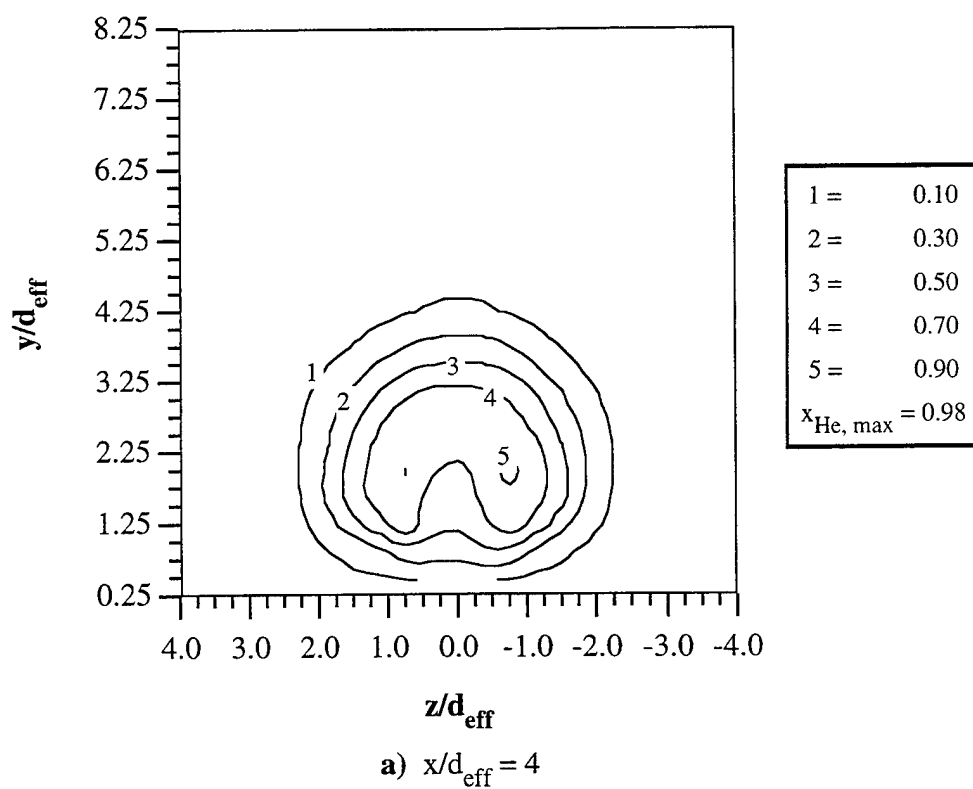


Figure 5.111 Helium Mole Fraction Contours from Circular Injection Using Helium
(Case C2H) a) $x/d_{\text{eff}} = 4$ and b) $x/d_{\text{eff}} = 10$

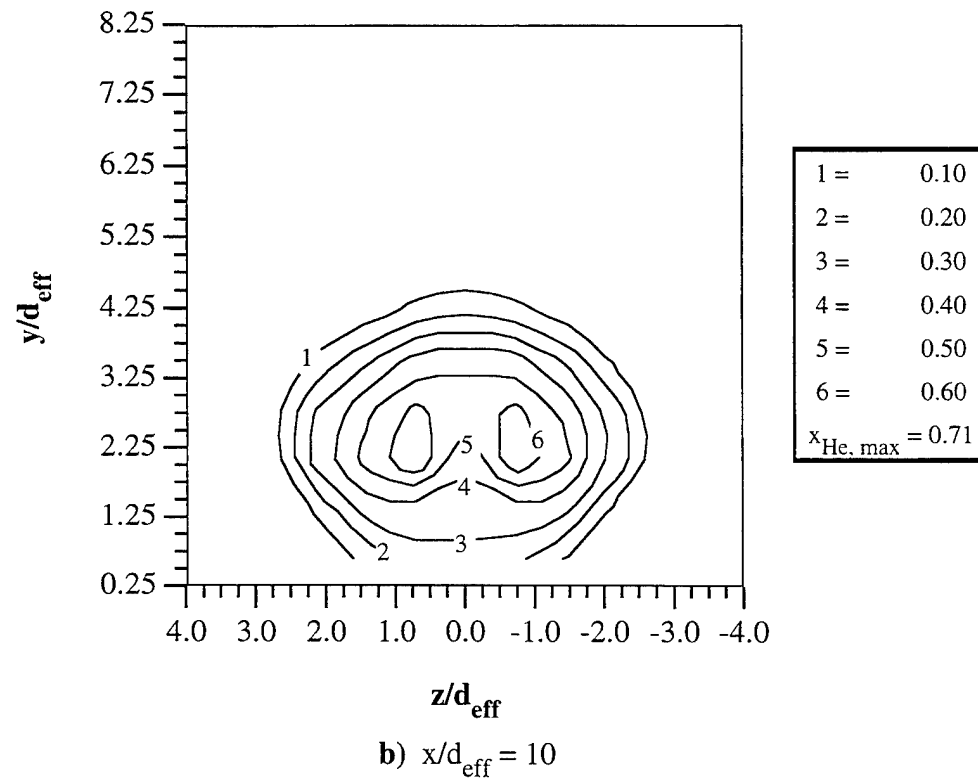
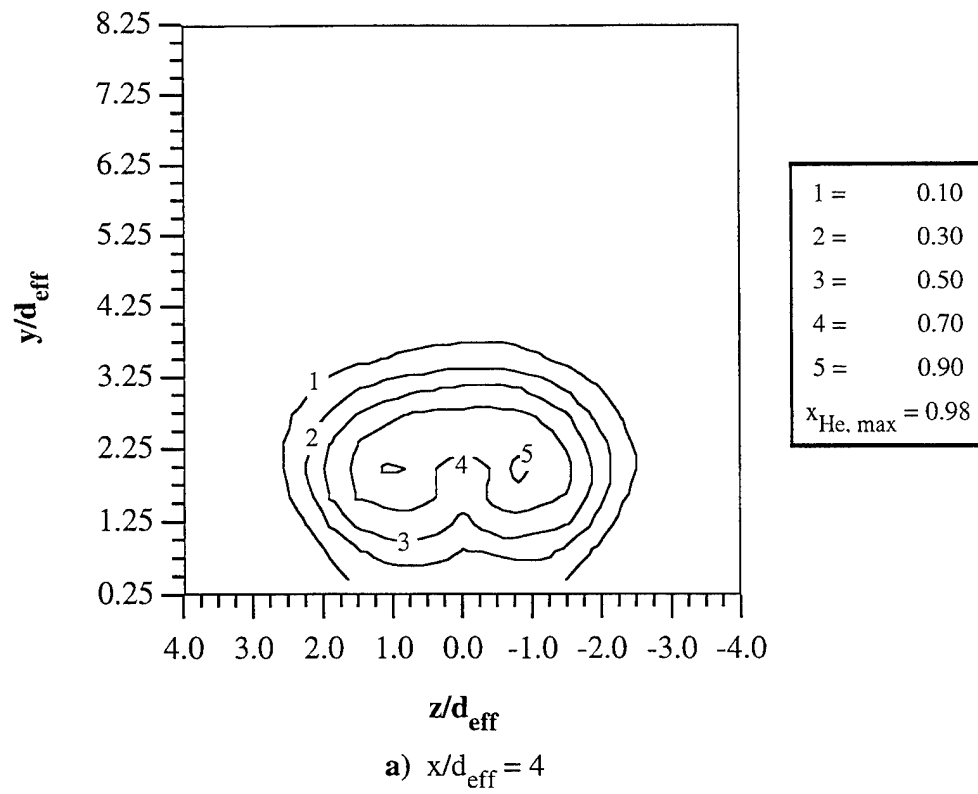


Figure 5.112 Helium Mole Fraction Contours from Elliptical Injection Using Helium (Case E2H) **a)** $x/d_{\text{eff}} = 4$ and **b)** $x/d_{\text{eff}} = 10$

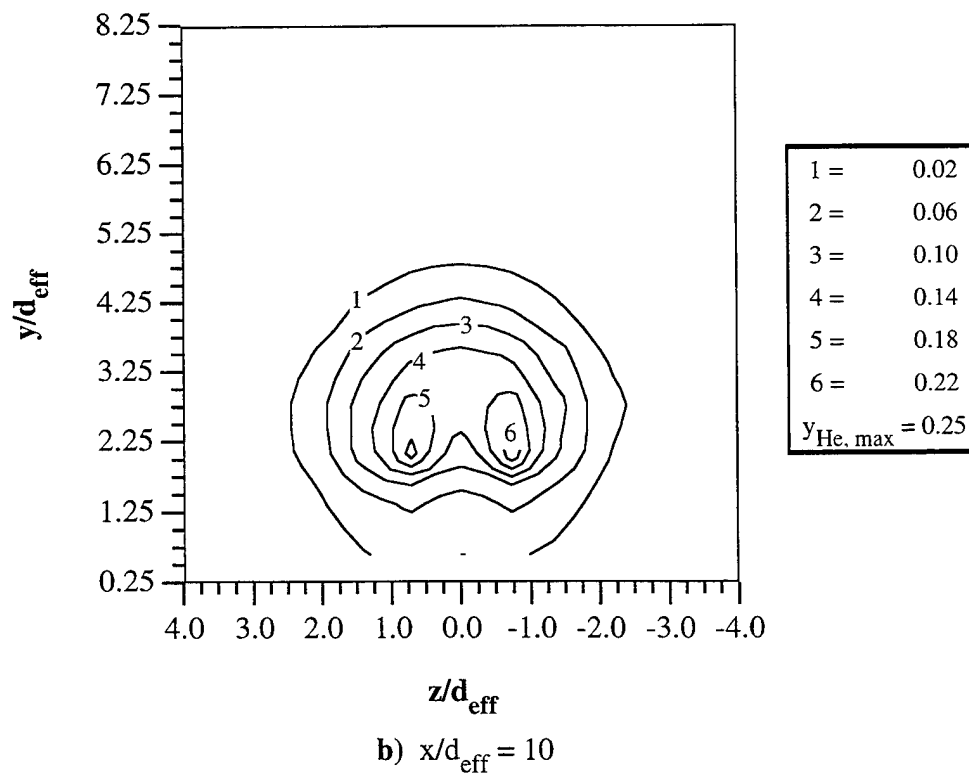
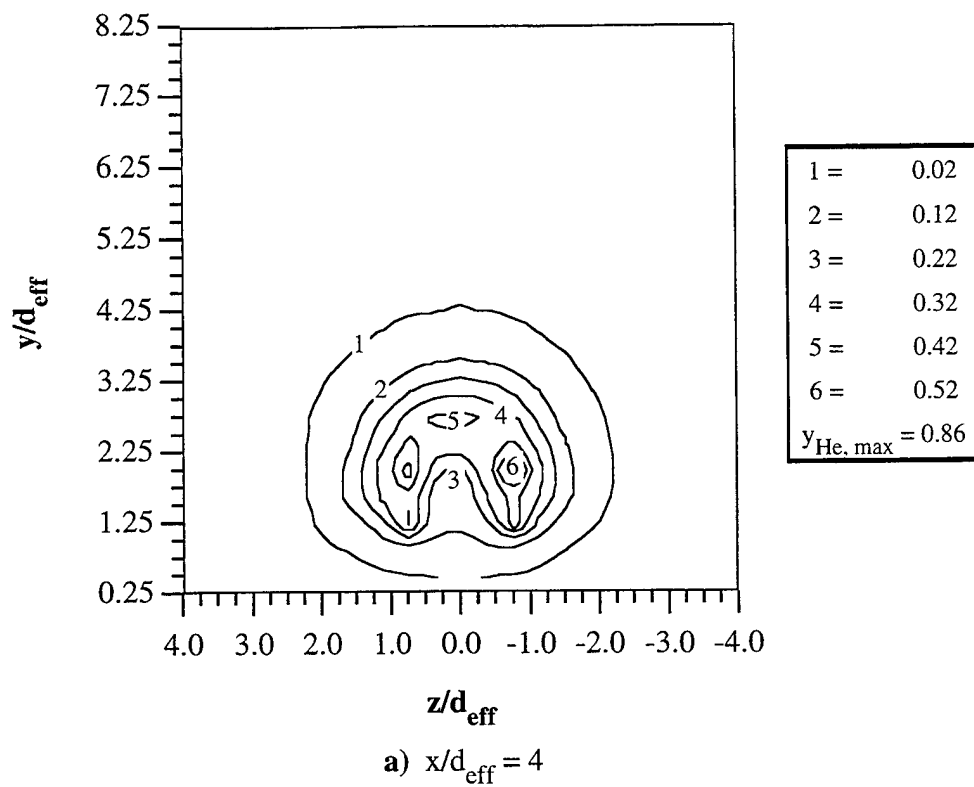


Figure 5.113 Helium Mass Fraction Contours from Circular Injection Using Helium
(Case C2H) a) $x/d_{\text{eff}} = 4$ and b) $x/d_{\text{eff}} = 10$

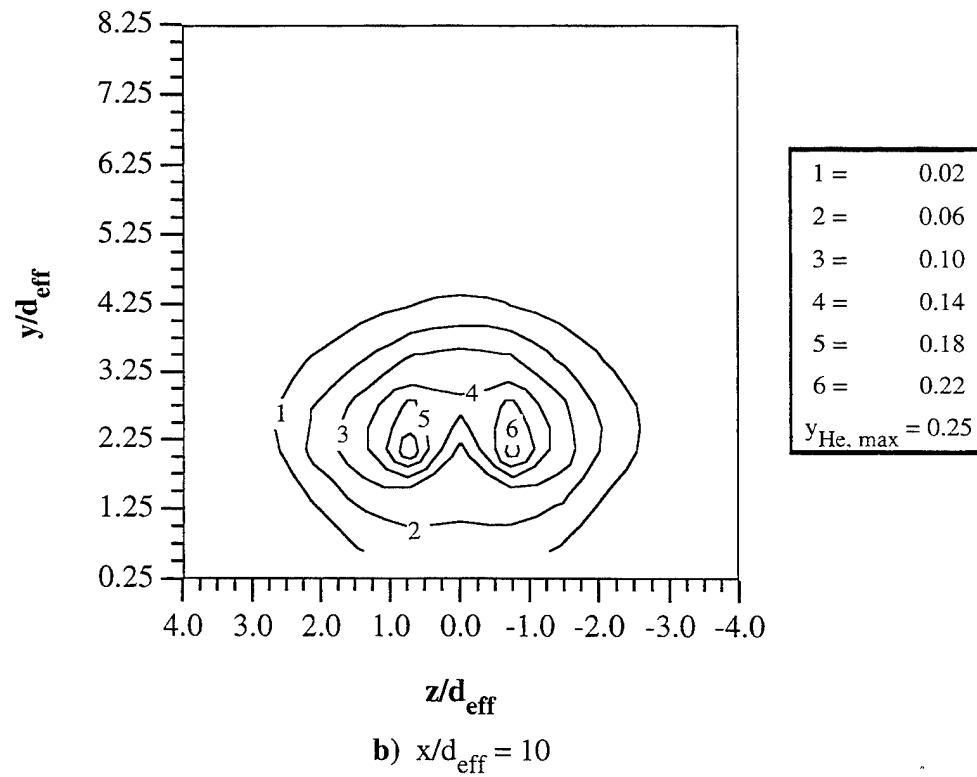
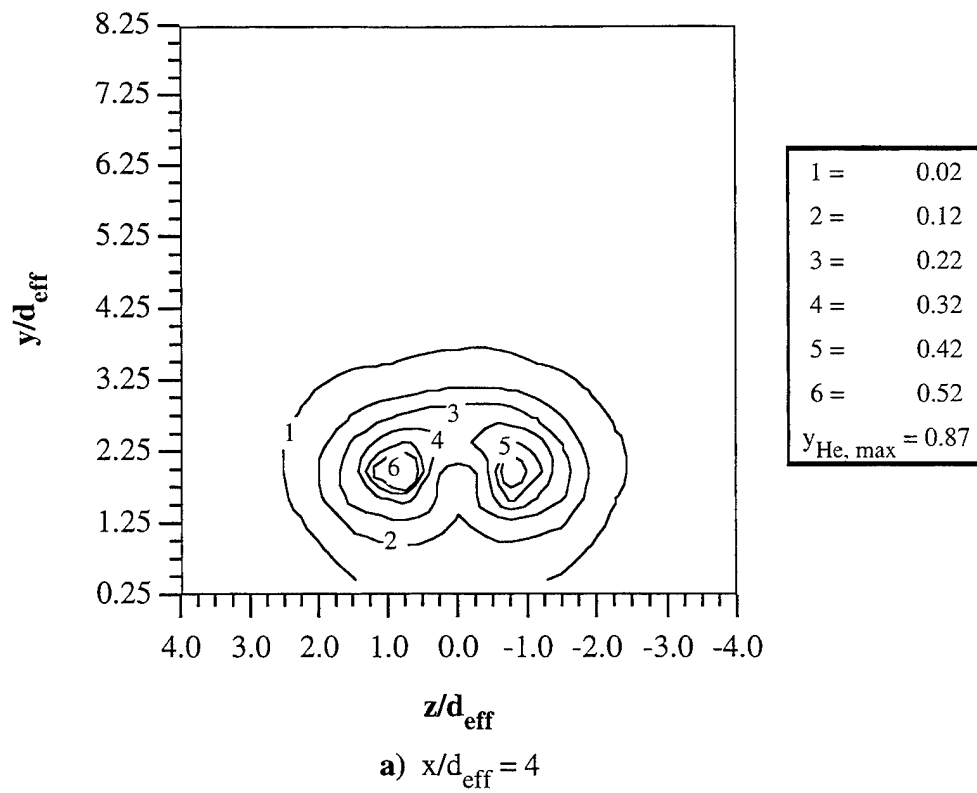


Figure 5.114 Helium Mass Fraction Contours from Elliptical Injection Using Helium
(Case E2H) **a)** $x/d_{\text{eff}} = 4$ and **b)** $x/d_{\text{eff}} = 10$

APPENDIX: ESTIMATION OF COMPRESSIBILITY LEVELS

Compressibility is an important issue to address in this study, as this property has been shown to affect the growth,^{1,2} turbulence structure,^{89,90} and stability^{91,92} of turbulent shear layers. In the classic constant pressure shear layer formed between two planar, constant velocity freestreams, compressibility effects are best correlated using the convective Mach number as defined in Eq. 2.6. In these flows, the two uniform freestreams (assumed to be ideal gases) allow relatively easy calculation of the convective Mach number through knowledge of the freestream composition, stagnation conditions, and Mach numbers. In the present transverse injection flowfield, however, several fluid dynamic features serve to complicate this determination. Unlike the simple two-dimensional shear layer, this injection flowfield is highly three-dimensional. The bow shock standing upstream of the injector exit alters the properties of the crossflow fluid so that uniform conditions around the mixing layer no longer exist. Injectant fluid expands as it enters the test section and accelerates rapidly within the barrel shock region to unknown supersonic velocities. Across the Mach disk, on the other hand, the injectant fluid rapidly decelerates. The pressure, temperature, and density fields also vary around the mixing layer in the near-field region. The combination of accelerating and/or decelerating constituent fluids and variable thermodynamic properties makes the convective Mach number rather difficult to predict and, presumably, not constant as the mixing layer develops. In addition, the field quantities are largely unknown throughout the jet/crossflow interaction. The analysis that follows is an attempt to quantify the mixing layer compressibility at a single characteristic point in the flowfield generated by injection through a circular nozzle into a supersonic crossflow.

Figure A.1 presents an idealized schematic at the spanwise centerline of the injection flowfield in question. The point labeled A in the figure is the location at which the convective Mach number is to be found. As shown in the drawing, the two constituent streams that form the mixing layer containing point A have velocities denoted U_1 (the injectant fluid) and U_2 (the freestream fluid). The eddies in the mixing layer at point A are assumed to convect with a velocity

U_c at an angle parallel to the two constituent streams. The inherent difficulties associated with the calculation of M_c at point A are that neither U_1 nor U_2 is known explicitly in the present flowfield. As noted above, the injectant fluid accelerates from the nozzle exit conditions and the freestream fluid is strongly decelerated by the bow shock standing ahead of the jet. Thus, additional assumptions are required that allow determination of the properties of the freestream fluid above and injectant fluid below point A.

For the injectant fluid, knowledge of the Mach number just upstream of the Mach disk is required. In his study of circular injection of air into a supersonic crossflow, Santiago⁷² experimentally measured the Mach number just upstream of the Mach disk as $M_1 = 2.66$. Unfortunately, these measurements were performed in a flowfield with $J = 1.7$, $M_\infty = 1.6$, $p_{o,j} = 476$ kPa, and $p_{o,\infty} = 241$ kPa. These conditions are significantly different from those of the present investigation. It is highly unlikely that the freestream and jet conditions used in the present study will produce a maximum Mach number equal to that measured by Santiago.⁷² However, knowing the value of M_1 permits the use of the relation for static pressure change across a normal shock given by

$$p_2 = \left(\frac{2\gamma_j M_1^2 - (\gamma_j - 1)}{\gamma_j + 1} \right) p_1, \quad (1)$$

and the isentropic pressure relation given by

$$p_1 = \frac{p_{o,j}}{\left(1 + \frac{\gamma_j - 1}{2} M_1^2 \right)^{\frac{\gamma_j}{\gamma_j - 1}}} \quad (2)$$

to determine the pressure downstream of the Mach disk. Combining these equations produces

$$p_2 = \left(\frac{2\gamma_j M_1^2 - (\gamma_j - 1)}{\gamma_j + 1} \right) \cdot \frac{p_{o,j}}{\left(1 + \frac{\gamma_j - 1}{2} M_1^2 \right)^{\frac{\gamma_j}{\gamma_j - 1}}} \quad (3)$$

and, for known freestream conditions (i.e., $p_{0,\infty}$ and M_∞), the pressure ratio p_2/p_∞ may be found using

$$\frac{p_2}{p_\infty} = \left(\frac{2\gamma_j M_1^2 - (\gamma_j - 1)}{\gamma_j + 1} \right) \cdot \frac{\left(1 + \frac{\gamma_\infty - 1}{2} M_\infty^2 \right)^{\frac{\gamma_\infty}{\gamma_\infty - 1}}}{\left(1 + \frac{\gamma_j - 1}{2} M_1^2 \right)^{\frac{\gamma_j}{\gamma_j - 1}}} \cdot \frac{p_{0,j}}{p_{0,\infty}} \quad (4)$$

For an air jet ($\gamma_j = 1.4$) with a maximum Mach number of $M_1 = 2.66$ and a stagnation pressure of $p_{0,j} = 476$ kPa, the static pressure behind the Mach disk of Santiago⁷² is computed from Eq. 3 to be $p_2 = 176$ kPa. Using Eq. 4 with the appropriate freestream parameters (i.e., $M_\infty = 1.6$ and $p_{0,\infty} = 241$ kPa) yields a value of the pressure ratio of $p_2/p_\infty = 3.1$. Again, since the freestream and injectant conditions of the present investigation are significantly different than those of Santiago,⁷² there is no reason to expect that this ratio of p_2/p_∞ should hold in the present cases. It should be clear, though, that prescribing a value for this pressure ratio combined with known injectant and freestream stagnation conditions and the freestream Mach number leads to the calculation of the Mach number upstream of the Mach disk by using Eq. 4. Knowing the value of M_1 then permits calculation of the pertinent flow properties of the injectant fluid using the isentropic relations. Thus, given the injectant and freestream stagnation conditions and the freestream Mach number, the properties of the injectant fluid below point A are fully prescribed by assuming a value for the pressure ratio, p_2/p_∞ . For the present calculations, a range of pressure ratios from $2 \leq p_2/p_\infty \leq 4$ was used to determine the sensitivity of p_2/p_∞ on the convective Mach number calculations.

For the freestream fluid above point A, the oblique shock relations may be used to determine the flow turning angle and fluid dynamic properties downstream of the bow shock at a prescribed shock angle. Thus, the shock angle (θ) was allowed to vary between 90° (i.e., normal shock behavior) and the Mach angle, given by

$$\theta_M = \arcsin\left(\frac{1}{M_\infty}\right) \quad (5)$$

The question of which shock angle yields the appropriate freestream velocity remains. The results of the double-pulsed imaging experiments guide this choice since they yield the inclination angle with which the large-scale structures convect (ϕ). It was assumed earlier that the upper and lower freestream velocities are parallel to the large-scale convection velocity; thus the bow shock angle that results in a turning angle equal to ϕ was used to determine the properties of the freestream fluid above point A.

Now that both constituent stream velocities have been determined and all the relevant properties of these streams are known, the large-scale convection velocity must be calculated in order to determine the convective Mach number using Eq. 2.6. In the convective frame of reference shown in Fig. A.2, there is a saddle point between two consecutive structures. This point is a stagnation point for both freestreams so that the total pressures of the streams at this point must be equal. Assuming that the static pressures of the streams are equal and that the flow is steady, the following expression must then hold:

$$\left[1 + \frac{\gamma_1 - 1}{2} \left(\frac{U_1 - U_c}{a_1}\right)^2\right]^{\frac{\gamma_1}{\gamma_1 - 1}} = \left[1 + \frac{\gamma_2 - 1}{2} \left(\frac{U_c - U_2}{a_2}\right)^2\right]^{\frac{\gamma_2}{\gamma_2 - 1}} \quad (6)$$

The terms in parentheses are the convective Mach numbers with respect to either freestream. Using Eq. 6 to compute the value of U_c permits solving Eq. 2.6 for either convective Mach number at point A shown in Fig. A.1. The following outline presents a summary of the assumptions and steps used in this model.

Injectant side of the mixing layer, Stream 1:

- (1) Assume that the desired conditions are associated with the maximum Mach number in the barrel shock region.

- (2) Assume that the injectant expands isentropically from known stagnation conditions to the maximum Mach number condition.
- (3) Assume that the Mach disk is a normal shock.
- (4) Compute the maximum Mach number (M_1) by solving Eq. 4 using a prescribed pressure ratio p_2/p_∞ .
- (5) Compute the fluid dynamic properties upstream of the Mach disk (yields p_1, T_1, ρ_1, U_1).

Freestream side of the mixing layer, Stream 2:

- (1) Compute conditions downstream of the bow shock for the range of shock angles between the Mach angle (found using Eq. 5) and 90° .
- (2) Use the streamwise position of point A to determine the structure convection angle from the double-pulsed images.
- (3) Assume that the freestream fluid velocity is parallel to the structure convection direction.
- (4) Choose the freestream conditions based on the bow shock turning angle being equal to the large-scale convection angle (yields p_2, T_2, ρ_2, U_2).

Convective Mach number calculation:

- (1) Assume a common stagnation point between two large-scale eddies in the convective frame of reference.
- (2) Solve Eq. 6 for U_c .
- (3) Compute convective Mach numbers $M_{c,1}$ and $M_{c,2}$ using Eq. 2.6.

Results obtained using this procedure and a range of pressure ratios from $p_2/p_\infty = 2.0$ to 4.0 are presented in Figs. A.3-A.6. The point of interest, A, was chosen at roughly $x/d_{eff} = 1.5$. Figure A.3 contains the variation in the maximum Mach number upstream of the Mach disk for injection of air and helium through the circular nozzle (cases C1A and C2H). This plot indicates, as expected, a moderate dependence on the selected pressure ratios. Values of M_1 computed at the

high pressure ratios are between 75-80% of the values computed at the low pressure ratio. However, the convective Mach number data shown in Figs. A.4 and A.5 indicate a comparatively weak dependence on the assumed pressure ratio. For example, in case C1A, the value of $M_{c,1}$ changes by only about 15% over the range of pressure ratios. The variation in the values for case C2H is slightly larger at about 17%. Despite the variation over the selected range of pressures, the clear observation from Figs. A.4 and A.5 is that *an extreme difference exists in the levels of compressibility associated with the two mixing layers in the air and helium injection flowfields*. The convective Mach number of the mixing layer formed in the helium injection case is roughly three times that of the air/air mixing layer at the selected point A (see Fig. A.1). Thus, the structural and stability characteristics associated with the two shear layers are expected to be quite different. Indeed, from the shadowgraph photos and Rayleigh/Mie scattering images presented in Chapter 5, these two flows appear strongly influenced by compressibility effects. The eddies that form in the helium injection cases (high compressibility) are flatter and more amorphous than those visualized in the low compressibility air injection cases.

In an attempt to determine the accuracy of the above analysis, the computed convection velocities were compared to the experimental results from the double-pulsed images obtained at point A ($x/d_{eff} = 1.5$). The convection velocity error, defined as

$$\text{Convective Velocity Error} = \frac{|U_{c,experimental} - U_{c,analytical}|}{U_{c,analytical}} \cdot 100 \quad (7)$$

was computed for each of these two cases and is presented in Fig. A.6. Reasonable agreement in each case appears, as the experimental values (instantaneous results) and computed values generally yield errors of between 10-20%. This comparison provides a good check for the assumptions and indicates that the model performs rather well for the given conditions. Note that the reported values in Table 5.1 are taken from the results of using a pressure ratio $p_2/p_\infty = 3.0$.

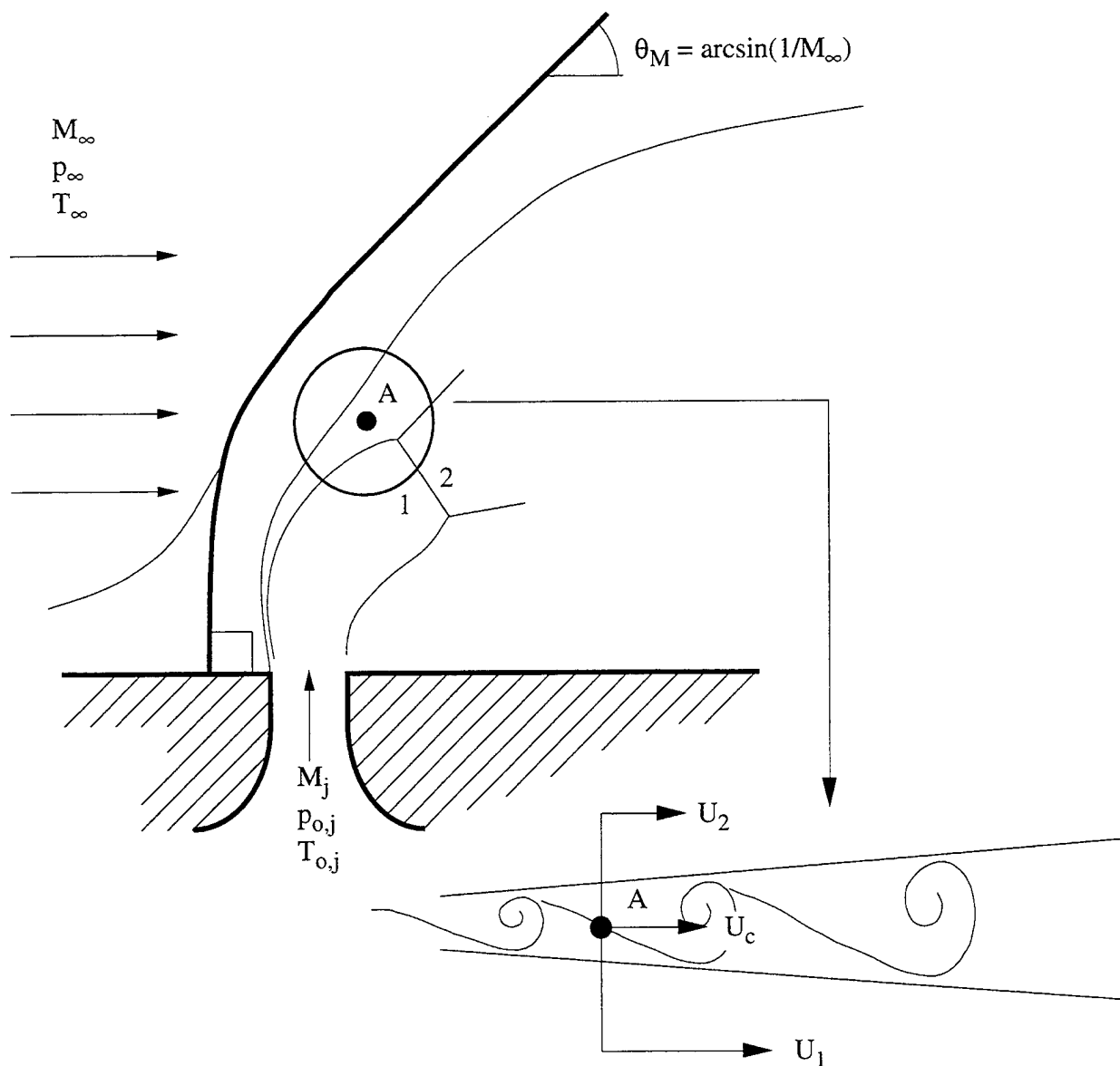


Figure A.1 Schematic of Region of Interest for Convective Mach Number Calculation

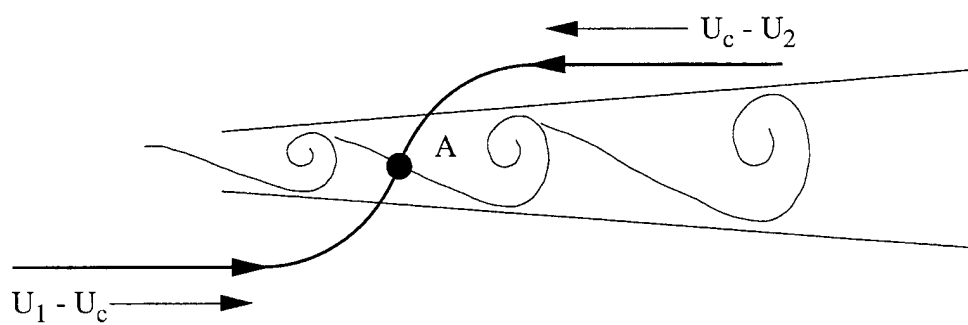


Figure A.2 Schematic of Mixing Layer in Convective Frame of Reference

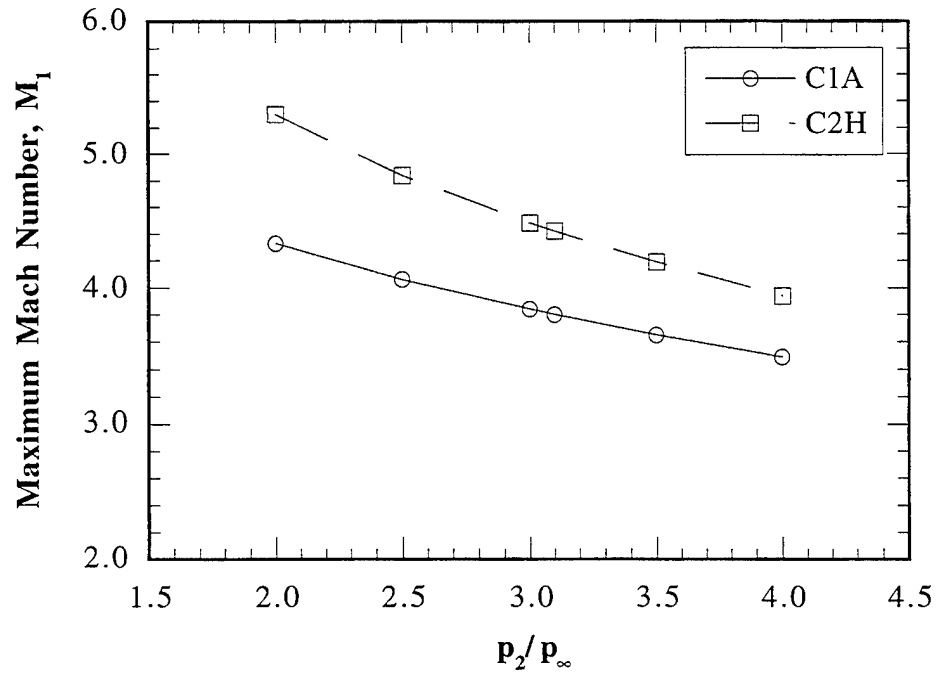


Figure A.3 Maximum Mach Number Dependence on Pressure Ratio p_2/p_∞

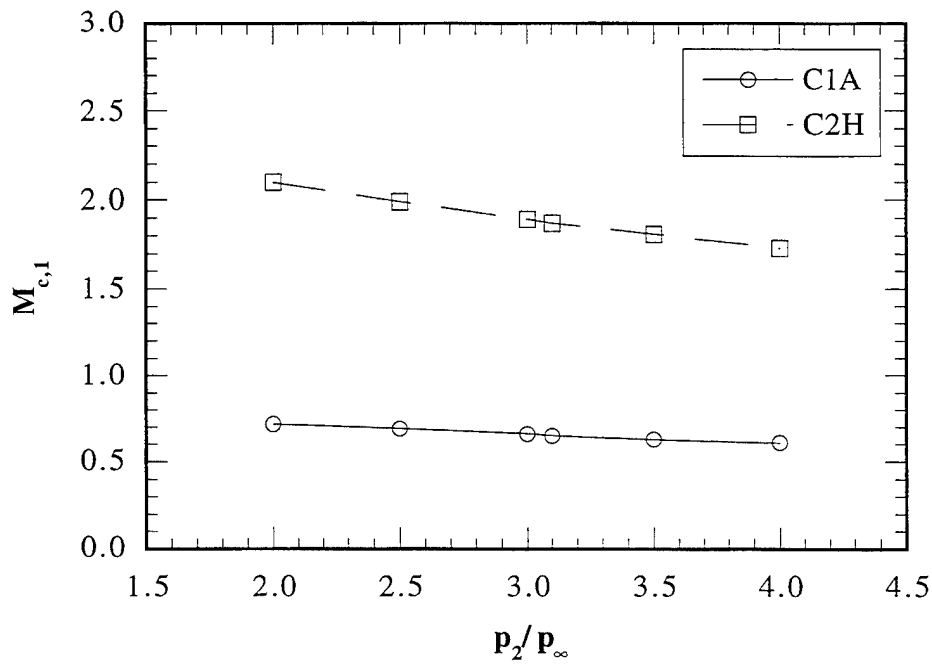


Figure A.4 Dependence of Convective Mach Number with Respect to Injectant Stream on Pressure Ratio p_2/p_∞

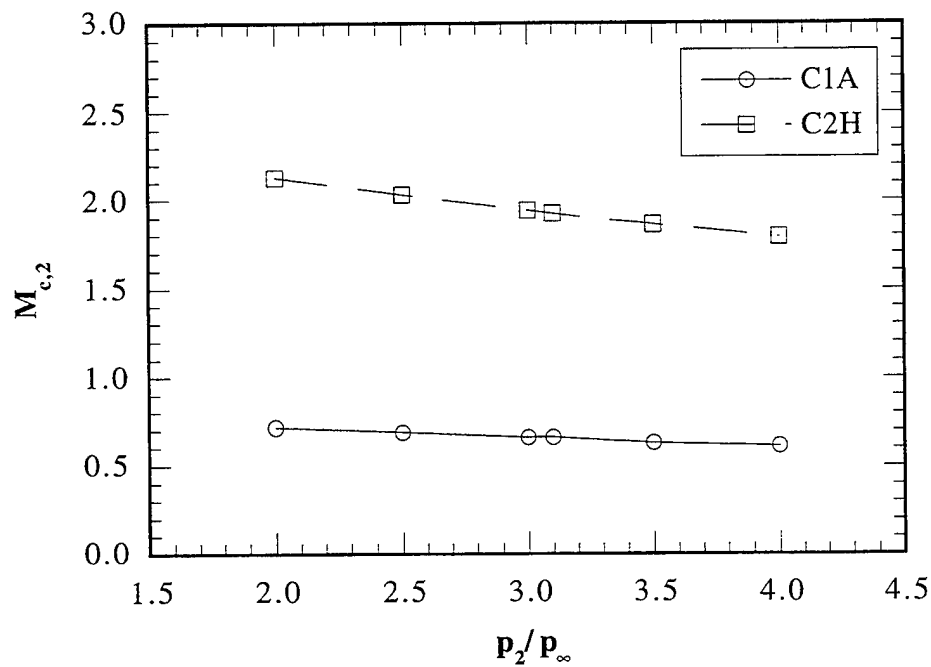


Figure A.5 Dependence of Convective Mach Number with Respect to Freestream on Pressure Ratio p_2/p_∞

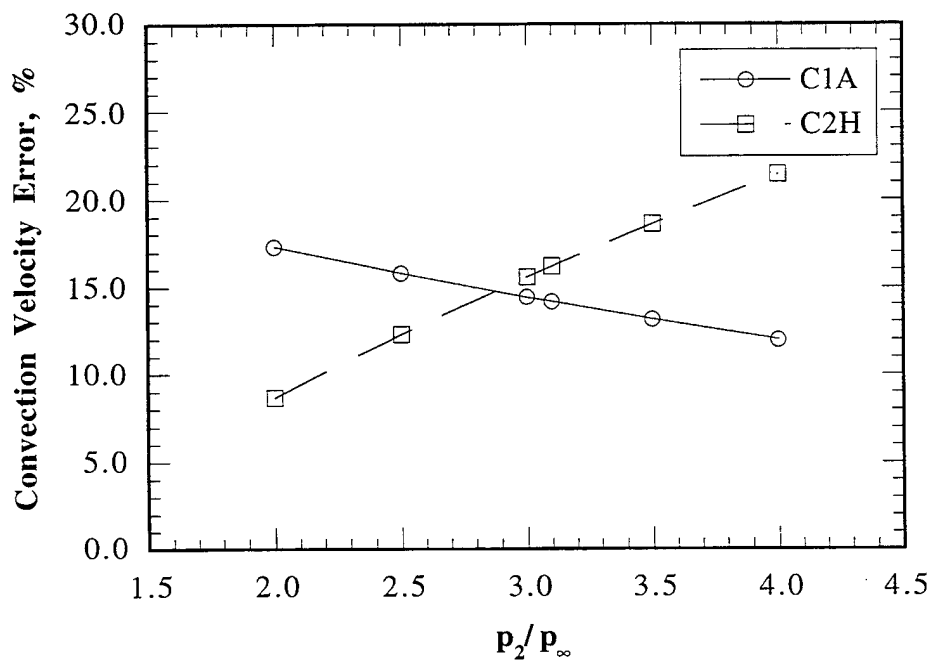


Figure A.6 Dependence of Convection Velocity Error on Pressure Ratio p_2/p_∞

REFERENCES

- ¹Papamoschou, D., and Roshko, A., "The Compressible Turbulent Shear Layer: An Experimental Study," *Journal of Fluid Mechanics*, Vol. 197, 1988, pp. 453-477.
- ²Goebel, S.G., and Dutton, J.C., "Experimental Study of Compressible Turbulent Mixing Layers," *AIAA Journal*, Vol. 29, No. 4, 1991, pp. 538-546.
- ³Zukoski, E.E., and Spaid, F.W., "Secondary Injection of Gases into a Supersonic Flow," *AIAA Journal*, Vol. 2, No. 10, 1964, pp. 1689-1696.
- ⁴Schetz, J.A., and Billig, F.S., "Penetration of Gaseous Jets Injected into a Supersonic Stream," *Journal of Spacecraft and Rockets*, Vol. 3, No. 11, 1966, pp. 1658-1665.
- ⁵Adamson, T.C., and Nicholls, J.A., "On the Structure of Jets from Highly Underexpanded Nozzles into Still Air," *Journal of the Aero/Space Sciences*, Vol. 26, 1959, pp. 16-24.
- ⁶Chrans, L.J., and Collins, D.J., "Stagnation Temperature and Molecular Weight Effects in Jet Interaction," *AIAA Journal*, Vol. 8, No. 2, 1970, pp. 287-293.
- ⁷Aso, S., Tannou, M., Maekawa, S., Okuyama, S., Ando, Y., Yamane, Y., and Fukuda, M., "A Study on Mixing Phenomena in Three-Dimensional Supersonic Flow with Circular Injection," AIAA Paper 94-0707, January 1994.
- ⁸Powerie, H.E.G., Ball, G.J., and East, R.A., "Comparison of the Interactions of Two and Three Dimensional Transverse Jets with a Hypersonic Free Stream," *AGARD Computational and Experimental Assessment of Jets in Cross Flow*, Winchester, 1993, pp. 20.1-20.8.
- ⁹Shang, J.S., McMaster, D.L., Scaggs, N., and Buck, M., "Interaction of Jet in Hypersonic Cross Stream," *AIAA Journal*, Vol. 27, No. 3, 1989, pp. 323-329.
- ¹⁰Spaid, F.W., and Zukoski, E.E., "A Study of the Interaction of Gaseous Jets from Transverse Slots with Supersonic External Flows," *AIAA Journal*, Vol. 6, No. 2, 1968, pp. 205-212.
- ¹¹Clark, S.W., and Chan, S.C., "Numerical Investigation of a Transverse Jet for Supersonic Aerodynamic Control," AIAA Paper 92-0639, January 1992.
- ¹²Fujimori, T., Kawai, M., Ikeda, H., Ando, Y., Ohmori, Y., Aso, S., and Fukuda, M., "Numerical Predictions of Two and Three Dimensional Sonic Gas Transverse Injections into Supersonic Crossflow," AIAA Paper 91-0415, January 1991.
- ¹³Gerlinger, P., Algermissen, J., and Brüggemann, D., "Simulation of Turbulent Slot Injection of Different Gases into a Supersonic Airstream," AIAA Paper 94-2247, June 1994.
- ¹⁴McDonough, J., and Catton, I., "Calculation of a Lateral Jet in a Hypersonic Cross-Flow," AIAA Paper 89-2549, July 1989.

- ¹⁵Rizzetta, D., "Numerical Studies of Slot Injection into a Turbulent Supersonic Stream," AIAA Paper 92-0827, January 1992.
- ¹⁶Everett, D.E., Dutton, J.C., and Morris, M.J., "Pressure-Sensitive Paint Measurements of the Pressure Field About a Sonic Jet Injected Transversely into a Mach 1.6 Freestream," AIAA Paper 95-0524, January 1995.
- ¹⁷Billig, F.S., Orth, R.C., and Lasky, M., "A Unified Analysis of Gaseous Jet Penetration," *AIAA Journal*, Vol. 9, No. 6, 1971, pp. 1048-1058.
- ¹⁸Cohen, L.S., Coulter, L.J., and Egan, W.J., "Penetration and Mixing of Multiple Gas Jets Subjected to a Cross Flow," *AIAA Journal*, Vol. 9, No. 4, 1971, pp. 718-724.
- ¹⁹Heister, S.D., and Karagozian, A.R., "Gaseous Jet in Supersonic Crossflow," *AIAA Journal*, Vol. 28, No. 5, 1990, pp. 819-827.
- ²⁰McDaniel, J.C., and Graves, J., "Laser-Induced Fluorescence Visualization of Transverse Gaseous Injection in a Nonreacting Supersonic Combustor," *Journal of Propulsion and Power*, Vol. 4, No. 6, 1988, pp. 591-597.
- ²¹Pratte, B.D., and Baines, W.D., "Profiles of the Round Turbulent Jet in a Cross Flow," *Journal of the Hydraulics Division, Proceedings of the American Society of Civil Engineers*, Vol. 93, No. HY6, 1967, pp. 53-64.
- ²²Keffer, J.F., and Baines, W.D., "The Round Turbulent Jet in a Cross-Wind," *Journal of Fluid Mechanics*, Vol. 15, 1963, pp. 481-496.
- ²³Smith, S.H., Lozano, A., Mungal, M.G., and Hanson, R.K., "Scalar Mixing in the Subsonic Jet in Crossflow," *AGARD Computational and Experimental Assessment of Jets in Cross Flow*, Winchester, 1993, pp. 6.1-6.13.
- ²⁴Lozano, A., Smith, S.H., Mungal, M.G., and Hanson, R.K., "Concentration Measurements in a Transverse Jet by Planar Laser-Induced Fluorescence of Acetone," *AIAA Journal*, Vol. 32, No. 1, 1994, pp. 218-221.
- ²⁵Abramovich, G.N., *The Theory of Turbulent Jets*, Massachusetts Institute of Technology Press, Cambridge, 1963.
- ²⁶Kamotani, Y., and Greber, I., "Experiments on a Turbulent Jet in a Cross Flow," *AIAA Journal*, Vol. 10, No. 11, 1972, pp. 1425-1429.
- ²⁷Chassaing, P., George, J., Claria, A., and Sananes, F., "Physical Characteristics of Subsonic Jets in a Cross-Stream," *Journal of Fluid Mechanics*, Vol. 62, 1974, pp. 41-64.
- ²⁸Broadwell, J.E., and Briedenthal, R.E., "Structure and Mixing of a Transverse Jet in Incompressible Flow," *Journal of Fluid Mechanics*, Vol. 148, 1984, pp. 405-412.

- ²⁹Orth, R.C., and Funk, J.A., "An Experimental and Comparative Study of Jet Penetration in Supersonic Flow," *Journal of Spacecraft and Rockets*, Vol. 4, No. 9, 1967, pp. 1236-1242.
- ³⁰Schetz, J.A., Hawkins, P.F., and Lehman, H., "Structure of Highly Underexpanded Transverse Jets in a Supersonic Stream," *AIAA Journal*, Vol. 5, No. 5, 1967, pp. 882-884.
- ³¹Schetz, J.A., Weinraub, R.A., and Mahaffey, R.E., "Supersonic Transverse Injection into a Supersonic Stream," *AIAA Journal*, Vol. 6, No. 5, 1968, pp. 933-934.
- ³²Torrence, M.G., "Concentration Measurements of an Injected Gas in a Supersonic Stream," NASA, TN D-3860, 1967.
- ³³Torrence, M.G., "Effect of Injectant Molecular Weight on Mixing of a Normal Jet in a Mach 4 Airstream," NASA, TN D-6061, 1971.
- ³⁴Rogers, R.C., "A Study of the Mixing of Hydrogen Injected Normal to a Supersonic Airstream," NASA, TN D-6114, 1971.
- ³⁵Rogers, R.C., "Mixing of Hydrogen Injected from Multiple Injectors Normal to a Supersonic Airstream," NASA, TN D-6476, 1971.
- ³⁶Rothstein, A.D., "A Study of Normal Injection of Hydrogen into a Heated Supersonic Flow Using Planar Laser-Induced Fluorescence," Los Alamos National Laboratory, LA-12287-T, 1992.
- ³⁷Hermanson, J.C., and Winter, M., "Mie Scattering Imaging of a Transverse, Sonic Jet in Supersonic Flow," *AIAA Journal*, Vol. 31, No. 1, 1993, pp. 129-132.
- ³⁸Papamoschou, D., and Hubbard, D.G., "Visual Observations of Supersonic Transverse Jets," *Experiments in Fluids*, Vol. 14, 1993, pp. 468-476.
- ³⁹Randolph, H., Chew, L., and Johari, H., "Pulsed Jets in Supersonic Crossflow," AIAA Paper 94-0256, January 1994.
- ⁴⁰Gruber, M.R., Nejad, A.S., Chen, T.H., and Dutton, J.C., "Mixing and Penetration Studies of Sonic Jets in a Mach 2 Freestream," *Journal of Propulsion and Power*, Vol. 11, No. 2, 1995, pp. 315-323.
- ⁴¹Hersch, M., Povinelli, L.A., and Povinelli, F.P., "Optical Study of Sonic and Supersonic Jet Penetration from a Flat Plate into a Mach 2 Airstream," NASA, TN D-5717, 1970.
- ⁴²McClinton, C.R., "The Effect of Injection Angle on the Interaction Between Sonic Secondary Jets and a Supersonic Free Stream," NASA, TN D-6669, 1972.
- ⁴³Durando, N.A., "Vortices Induced in a Jet by a Subsonic Cross Flow," *AIAA Journal*, Vol. 9, No. 2, 1971, pp. 325-327.

- ⁴⁴McMahon, H.M., Hester, D.D., and Palfrey, J.G., "Vortex Shedding from a Turbulent Jet in a Cross-Wind," *Journal of Fluid Mechanics*, Vol. 48, 1971, pp. 73-80.
- ⁴⁵Fearn, R., and Weston, R.P., "Vorticity Associated with a Jet in a Cross Flow," *AIAA Journal*, Vol. 12, No. 12, 1974, pp. 1666-1671.
- ⁴⁶Andreopoulos, J., and Rodi, W., "Experimental Investigation of Jets in a Crossflow," *Journal of Fluid Mechanics*, Vol. 138, 1984, pp. 93-127.
- ⁴⁷Karagozian, A.R., "An Analytical Model for the Vorticity Associated with a Transverse Jet," *AIAA Journal*, Vol. 24, No. 3, 1986, pp. 429-436.
- ⁴⁸Karagozian, A.R., "The Flame Structure and Vorticity Generated by a Chemically Reacting Transverse Jet," *AIAA Journal*, Vol. 24, No. 9, 1986, pp. 1502-1507.
- ⁴⁹Fric, T.F., and Roshko, A., "Structure in the Near Field of the Transverse Jet," *Seventh International Symposium on Turbulent Shear Flows*, Stanford University, 1989, pp. 225-237.
- ⁵⁰Kelso, R.M., Delo, C., and Smits, A.J., "Unsteady Wake Structures in Transverse Jets," *AGARD Computational and Experimental Assessment of Jets in Cross Flow*, Winchester, 1993, pp. 4.1-4.8.
- ⁵¹Kelso, R.M., and Smits, A.J., "Horseshoe Vortex System Resulting from the Interaction Between a Laminar Boundary Layer and a Transverse Jet," *Physics of Fluids*, Vol. 7, No. 1, 1995, pp. 153-158.
- ⁵²Perry, A.E., Kelso, R.M., and Lim, T.T., "Topological Structure of a Jet in a Cross Flow," *AGARD Computational and Experimental Assessment of Jets in Cross Flow*, Winchester, 1993, pp. 12.1-12.8.
- ⁵³Fric, T.F., and Roshko, A., "Vortical Structure in the Wake of a Transverse Jet," *Journal of Fluid Mechanics*, Vol. 279, 1994, pp. 1-47.
- ⁵⁴Bier, K., Kappler, G., and Wilhelmi, H., "Experiments on the Combustion of Hydrogen and Methane Injected Transversely into a Supersonic Air Stream," *Thirteenth Symposium (International) on Combustion*, Pittsburgh, 1971, pp. 675-682.
- ⁵⁵McDaniel, J.C., "Flow Visualization Studies of Transverse Fuel Injection Patterns in a Nonreacting Mach 2 Combustor," *Fourth International Symposium on Flow Visualization*, Paris, 1986, pp. 747-752.
- ⁵⁶Hartfield, R.J., Hollo, S.D., and McDaniel, J.C., "Planar Measurements of Flow Field Parameters in a Nonreacting Supersonic Combustor Using Laser-Induced Iodine Fluorescence," *AIAA Paper 90-0162*, January 1990.
- ⁵⁷Davis, D., Hingst, W., and Porro, A., "Experimental Investigation of a Single Flush-Mounted Hypermixing Nozzle," *AIAA Paper 90-5240*, October 1990.

- ⁵⁸Hollo, S.D., Hartfield, R.J., and McDaniel, J.C., "Injectant Mole Fraction Measurements of Transverse Injection in Constant Area Supersonic Ducts," AIAA Paper 90-1632, June 1990.
- ⁵⁹Lee, M.P., McMillin, B.K., Palmer, J.L., and Hanson, R.K., "Planar Fluorescence Imaging of a Transverse Jet in a Supersonic Crossflow," *Journal of Propulsion and Power*, Vol. 8, No. 4, 1992, pp. 729-735.
- ⁶⁰Shirinzadeh, B., Hillard, M.E., Balla, R.J., Waitz, I.A., Anders, J.B., and Exton, R.J., "Planar Rayleigh Scattering Results in Helium-Air Mixing Experiments in a Mach 6 Wind Tunnel," *Applied Optics*, Vol. 31, No. 30, 1992, pp. 6529-6534.
- ⁶¹Hartfield, R.J., Hollo, S.D., and McDaniel, J.C., "Experimental Investigation of a Supersonic Swept Ramp Injector Using Laser-Induced Iodine Fluorescence," *Journal of Propulsion and Power*, Vol. 10, No. 1, 1994, pp. 129-135.
- ⁶²Hollo, S.D., McDaniel, J.C., and Hartfield, R.J., "Quantitative Investigation of Compressible Mixing: Staged Transverse Injection into Mach 2 Flow," *AIAA Journal*, Vol. 32, No. 3, 1994, pp. 528-534.
- ⁶³Uenishi, K., and Rogers, R.C., "Three Dimensional Computation of Mixing of Transverse Injector in a Ducted Supersonic Airstream," AIAA Paper 86-1423, June 1986.
- ⁶⁴Uenishi, K., Rogers, R.C., and Northam, G.B., "Three Dimensional Computations of Transverse Hydrogen Jet Combustion in a Supersonic Airstream," AIAA Paper 87-0089, January 1987.
- ⁶⁵Dormieux, M., Guillen, P., and Abgrall, R., "Numerical Simulation of Transverse Jet Flows by a Non Reactive Two Species Multidomain Euler Flow Solver," AIAA Paper 90-0126, January 1990.
- ⁶⁶Riggins, D.W., and McClinton, C.R., "Analysis of Losses in Supersonic Mixing and Reacting Flows," AIAA Paper 91-2266, June 1991.
- ⁶⁷Waitz, I.A., Marble, F.E., and Zukoski, E.E., "Investigation of a Contoured Wall Injector for Hypervelocity Mixing Augmentation," *AIAA Journal*, Vol. 31, No. 6, 1993, pp. 1014-1021.
- ⁶⁸McMillin, B.K., Palmer, J.L., Antonio, A.L., and Hanson, R.K., "Instantaneous Two-Line Temperature Imaging of a H_2/NO Jet in Supersonic Crossflow," AIAA Paper 92-3347, July 1992.
- ⁶⁹McMillin, B.K., Palmer, J.L., Seitzman, J.M., and Hanson, R.K., "Two-Line Instantaneous Temperature Imaging of NO in a SCRAMJET Model Flowfield," AIAA Paper 93-0044, January 1993.
- ⁷⁰VanLerberghe, W.M., "Large-Scale Structure and Mixing in a Sonic Transverse Jet Injected into a Supersonic Crossflow," Ph.D. Thesis, Department of Mechanical and Industrial Engineering, University of Illinois at Urbana Champaign, Urbana, IL, 1995.

- ⁷¹Gruber, M.R., Nejad, A.S., and Dutton, J.C., "Circular and Elliptical Transverse Injection into a Supersonic Crossflow--The Role of Large-Scale Structures," AIAA Paper 95-2150, June 1995.
- ⁷²Santiago, J.S., "An Experimental Study of the Velocity Field of a Transverse Jet Injected into a Supersonic Crossflow," Ph.D. Thesis, Department of Mechanical and Industrial Engineering, University of Illinois at Urbana Champaign, Urbana, IL, 1995.
- ⁷³Gaillard, R., Geffroy, P., Jacquin, L., and Losfeld, G., "Etude Expérimentale sur les Interactions Entre un Jet Supersonique Chauffé Transversal et un Écoulement Supersonique Externe," *AGARD Computational and Experimental Assessment of Jets in Cross Flow*, Winchester, 1993, pp. 39.1-39.12.
- ⁷⁴Schadow, K.C., Wilson, K.J., and Lee, M.J., "Enhancement of Mixing in Reacting Fuel-Rich Plumes Issued from Elliptical Nozzles," *Journal of Propulsion and Power*, Vol. 3, No. 2, 1987, pp. 145-149.
- ⁷⁵Ho, C., and Gutmark, E., "Vortex Induction and Mass Entrainment in a Small-Aspect-Ratio Elliptic Jet," *Journal of Fluid Mechanics*, Vol. 179, 1987, pp. 383-405.
- ⁷⁶Gutmark, E., Schadow, K.C., and Wilson, K.J., "Noncircular Jet Dynamics in Supersonic Combustion," AIAA Paper 87-1878, June 1987.
- ⁷⁷Schadow, K.C., Gutmark, E., Koshigoe, S., and Wilson, K.J., "Combustion-Related Shear-Flow Dynamics in Elliptic Supersonic Jets," *AIAA Journal*, Vol. 27, No. 10, 1989, pp. 1347-1353.
- ⁷⁸Gutmark, E., Schadow, K.C., and Bicker, C.J., "Mode Switching in Supersonic Circular Jets," *Physics of Fluids A*, Vol. 1, No. 5, 1989, pp. 868-873.
- ⁷⁹Glass, D.R., "Effects of Acoustic Feedback on the Spread and Decay of Supersonic Jets," *AIAA Journal*, Vol. 6, No. 10, 1968, pp. 1890-1897.
- ⁸⁰Batchelor, G.K., "Small-Scale Variation of Convected Quantities Like Temperature in Turbulent Fluid. Part I. General Discussion and the Case of Small Conductivity," *Journal of Fluid Mechanics*, Vol. 5, 1959, pp. 113-133.
- ⁸¹Fletcher, D.G., and McDaniel, J.C., "Laser-Induced Iodine Fluorescence Technique for Quantitative Measurement in a Nonreacting Supersonic Combustor," *AIAA Journal*, Vol. 27, No. 5, 1989, pp. 575-580.
- ⁸²Abbitt, J.D., Hartfield, R.J., and McDaniel, J.C., "Mole Fraction Imaging of Transverse Injection in a Ducted Supersonic Flow," AIAA Paper 89-2550, July 1989.
- ⁸³McDaniel, J.C., Fletcher, D., Hartfield, R., and Hollo, S., "Staged Transverse Injection into Mach 2 Flow Behind a Rearward Facing Step: A 3-D Compressible Test Case for Hypersonic Combustor Code Validation," AIAA Paper 91-5071, December 1991.

- ⁸⁴Abbitt, J.D., McDaniel, J.C., Krauss, R.H., Whitehurst, R.B., and Segal, C., "Experimental Investigation of a Supersonic Combustor Flowfield Employing Staged Transverse Injection Behind a Rearward Facing Step," AIAA Paper 92-0090, January 1992.
- ⁸⁵Segal, C., Haj-Hariri, H., and McDaniel, J.C., "A Numerical Investigation of Hydrogen Combustion in a Mach 2 Airflow," AIAA Paper 92-0341, January 1992.
- ⁸⁶Donohue, J.M., McDaniel, J.C., and Haj-Hariri, H., "Experimental and Numerical Study of Swept Ramp Injection into a Supersonic Flowfield," AIAA Paper 93-2445, June 1993.
- ⁸⁷Eklund, D.R., Fletcher, D.G., Hartfield, R.J., McDaniel, J.C., Northam, G.B., Dancey, C.L., and Wang, J.A., "Computational/Experimental Investigation of Staged Injection into a Mach 2 Flow," *AIAA Journal*, Vol. 32, No. 5, 1994, pp. 907-916.
- ⁸⁸Bogdanoff, D.W., "Compressibility Effects in Turbulent Shear Layers," *AIAA Journal*, Vol. 21, No. 6, 1983, pp. 926-927.
- ⁸⁹Clemens, N.T., and Mungal, M.G., "Two- and Three-Dimensional Effects in the Supersonic Mixing Layer," *AIAA Journal*, Vol. 30, No. 4, 1992, pp. 973-981.
- ⁹⁰Messersmith, N.L., and Dutton, J.C., "Measurements of Scalar Mixing in Compressible Free Shear Layers," *Sixth International Symposium on Laser Techniques and Applications in Fluid Mechanics*, Lisbon, 1992, pp. 415-432.
- ⁹¹Sandham, N.D., and Reynolds, W.C., "Compressible Mixing Layer: Linear Theory and Direct Simulation," *AIAA Journal*, Vol. 38, No. 4, 1990, pp. 618-624.
- ⁹²Leep, L.J., and Dutton, J.C., "Three-Dimensional Simulations of Compressible Mixing Layers: Visualizations and Statistical Analysis," University of Illinois at Urbana-Champaign, UILU-ENG-92-4006, 1992.
- ⁹³King, P.S., Thomas, R.H., Schetz, J.A., and Billig, F.S., "Combined Tangential-Normal Injection into a Supersonic Flow," AIAA Paper 89-0622, January 1989.
- ⁹⁴Mays, R.B., Thomas, R.H., and Schetz, J.A., "Low Angle Injection into a Supersonic Flow," AIAA Paper 89-2461, July 1989.
- ⁹⁵Schetz, J.A., Thomas, R.H., and Billig, F.S., "Mixing of Transverse Jets and Wall Jets in Supersonic Flow," *IUTAM Symposium on Separated Flows and Jets*, Novosibirsk, 1990, pp. 807-837.
- ⁹⁶Wood, C., and Schetz, J., "Effects of Unsteady Shock Impingement on High-Speed Gaseous Mixing," AIAA Paper 91-5091, December 1991.
- ⁹⁷Fuller, E.J., Thomas, R.H., and Schetz, J.A., "Effects of Yaw on Low Angle Injection into a Supersonic Flow," AIAA Paper 91-0014, January 1991.
- ⁹⁸Fuller, E.J., Mays, R.B., Thomas, R.H., and Schetz, J.A., "Mixing Studies of Helium in Air at High Supersonic Speeds," *AIAA Journal*, Vol. 30, No. 9, 1992, pp. 2234-2243.

- ⁹⁹Cox, S.K., Fuller, R.P., Schetz, J.A., and Walters, R.W., "Vortical Interactions Generated by an Injector Array to Enhance Mixing in Supersonic Flow," AIAA Paper 94-0708, January 1994.
- ¹⁰⁰Waitz, I.A., Marble, F.E., and Zukoski, E.E., "Vorticity Generation by Contoured Wall Injectors," AIAA Paper 92-3550, July 1992.
- ¹⁰¹Glawe, D.D., Samimy, M., Nejad, A.S., and Chen, T.H., "Effects of Nozzle Geometry on Parallel Injection from Base of an Extended Strut into a Supersonic Flow," AIAA Paper 95-0522, January 1995.
- ¹⁰²Pratt, D.T., "Mixing and Chemical Reaction in Continuous Combustion," *Progress in Energy and Combustion Science*, Vol. 1, 1975, pp. 73-86.
- ¹⁰³Konrad, J.H., "An Experimental Investigation of Mixing in Two-Dimensional Turbulent Shear Flows with Applications to Diffusion-Limited Chemical Reactions," California Institute of Technology, CIT-8-PU, 1976.
- ¹⁰⁴Schadow, K.C., Gutmark, E., Wilson, K.J., and Parr, D.M., "Mixing Characteristics of a Ducted Elliptical Jet," *Journal of Propulsion and Power*, Vol. 4, No. 4, 1988, pp. 328-333.
- ¹⁰⁵Riggins, D.W., and McClinton, C.R., "A Computational Investigation of Mixing and Reacting Flows in Supersonic Combustors," AIAA Paper 92-0626, January 1992.
- ¹⁰⁶Grasso, F., and Magi, V., "Simulation of Transverse Gas Injection in Turbulent Supersonic Air Flows," *AIAA Journal*, Vol. 33, No. 1, 1995, pp. 56-62.
- ¹⁰⁷Baldwin, B.S., and Lomax, H., "Thin Layer Approximation and Algebraic Model for Separated Turbulent Flows," AIAA Paper 78-257, January 1978.
- ¹⁰⁸Dhinakaran, R., and Bose, T.K., "Two-Dimensional Jet Interaction Flowfield Predictions with an Algebraic Turbulence Model," AIAA Paper 95-2242, June 1995.
- ¹⁰⁹Gruber, M.R., and Nejad, A.S., "Supersonic Combustion Research Laboratory: Volume 1-Design and Fabrication," Wright Laboratory, WL-TR-93-2052, 1993.
- ¹¹⁰Gruber, M.R., and Nejad, A.S., "Development of a Large-Scale Supersonic Combustion Research Facility," AIAA Paper 94-0544, January 1994.
- ¹¹¹Gruber, M.R., and Nejad, A.S., "New Supersonic Combustion Research Facility," *Journal of Propulsion and Power*, Vol. 11, No. 5, 1995, pp. 1080-1083.
- ¹¹²Carroll, B.F., Dutton, J.C., and Addy, A.L., "NOZCS2: A Computer Program for the Design of Continuous Slope Supersonic Nozzles," University of Illinois at Urbana-Champaign, UILU ENG 86-4007, 1986.

- ¹¹³Burke, A.F., "Turbulent Boundary Layers on Highly Cooled Surfaces at High Mach Numbers," AFASD TR 61-645, 1961.
- ¹¹⁴Fiore, A.W., Moore, D.G., Murray, D.H., and West, J.E., "Design and Calibration of the ARL Mach 3 High Reynolds Number Facility," ARL, TR 75-0012, 1975.
- ¹¹⁵van de Hulst, H.C., *Light Scattering by Small Particles*, Dover Publications, Inc., New York, 1981.
- ¹¹⁶Wickramasinghe, N.C., *Light Scattering Functions for Small Particles with Applications in Astronomy*, John Wiley & Sons, New York, 1973.
- ¹¹⁷Aref, H., and Jones, S.W., "Enhanced Separation of Diffusing Particles by Chaotic Advection," *Physics of Fluids A*, Vol. 1, No. 3, 1989, pp. 470-474.
- ¹¹⁸Broadwell, J.E., and Mungal, M.G., "Large-Scale Structures and Molecular Mixing," *Physics of Fluids A*, Vol. 3, No. 5, 1991, pp. 1193-1206.
- ¹¹⁹Samimy, M., and Lele, S.K., "Motion of Particles with Inertia in a Compressible Free Shear Layer," *Physics of Fluids A*, Vol. 3, No. 8, 1991, pp. 1915-1923.
- ¹²⁰Melling, A., "Seeding Gas Flows for Laser Anemometry," *AGARD Advanced Instrumentation for Aero Engine Components*, Philadelphia, 1986, pp. 8.1-8.11.
- ¹²¹Wegener, P.P., and Pouring, A.A., "Experiments on Condensation of Water Vapor by Homogeneous Nucleation in Nozzles," *Physics of Fluids*, Vol. 7, No. 3, 1964, pp. 352-361.
- ¹²²Stein, G.D., and Wegener, P.P., "Experiments on the Number of Particles Formed by Homogeneous Nucleation in the Vapor Phase," *Journal of Chemical Physics*, Vol. 46, 1967, pp. 3685-3686.
- ¹²³Wegener, P.P., and Parlange, J.Y., "Non-Equilibrium Nozzle Flow with Condensation," *AGARD Recent Advances in Aerothermochemistry*, Oslo, 1967, pp. 607-634.
- ¹²⁴Thomann, H., "Size of Ice Crystals Formed During Rapid Expansion of Humid Air," *Physics of Fluids*, Vol. 9, No. 5, 1966, pp. 896-902.
- ¹²⁵Craig, R.R., Nejad, A.S., Hahn, E.Y., and Schwartzkopf, K.G., "A General Approach for Obtaining Unbiased LDV Data in Highly Turbulent Non-Reacting and Reacting Flows," AIAA Paper 84-0366, January 1984.
- ¹²⁶Craig, R.R., Nejad, A.S., Hahn, E.Y., and Schwartzkopf, K.G., "Approach for Obtaining Unbiased Laser Doppler Velocimetry Data in Highly Turbulent Flows," *Journal of Propulsion and Power*, Vol. 2, No. 6, 1986, pp. 541-545.
- ¹²⁷Hartman, J.R., Famil-Ghiriha, J., Ring, M.A., and O'Neal, H.E., "Stoichiometry and Possible Mechanism of SiH₄-O₂ Explosions," *Combustion and Flame*, Vol. 68, 1987, pp. 43-56.

- ¹²⁸Rogers, R.C., Weidner, E.H., and Bittner, R.D., "Quantification of Scramjet Mixing in the Hypervelocity Flow of a Pulse Facility," AIAA Paper 94-2518, June 1994.
- ¹²⁹Eckbreth, A.C., *Laser Diagnostics for Combustion Temperature and Species*, Abacus Press, Cambridge, Massachusetts, 1990.
- ¹³⁰Rosenweig, R.E., Hottel, H.C., and Williams, G.C., "Smoke-Scattered Light Measurement of Turbulent Concentration Fluctuations," *Chemical Engineering Science*, Vol. 15, 1961, pp. 111-129.
- ¹³¹Thomas, R.H., and Schetz, J.A., "Distributions Across the Plume of Transverse and Slurry Jets in Supersonic Airflow," *AIAA Journal*, Vol. 23, No. 12, 1985, pp. 1892-1901.
- ¹³²Ninnemann, T.A., and Ng, W.F., "Concentration Probe for the Study of Mixing in Supersonic Shear Flows," *Experiments in Fluids*, Vol. 13, 1992, pp. 98-104.
- ¹³³Incropera, F.P., and DeWitt, D.P., *Fundamentals of Heat and Mass Transfer*, John Wiley & Sons, New York, 1990.
- ¹³⁴Long, M.B., *Multidimensional Imaging in Combusting Flows by Lorentz-Mie, Rayleigh and Raman Scattering*, in *Instrumentation for Flows with Combustion*, ed. A.M.K.P. Taylor, Academic Press, San Diego, 1993, pp. 467-508.
- ¹³⁵Goebel, S.G., and Dutton, J.C., "Velocity Measurements of Compressible, Turbulent Mixing Layers," AIAA Paper 90-0709, January 1990.
- ¹³⁶Miles, R., and Lempert, W., "Two-Dimensional Measurement of Density, Velocity, and Temperature in Turbulent High-Speed Air Flows by UV Rayleigh Scattering," *Applied Physics B*, Vol. 51, 1990, pp. 1-7.
- ¹³⁷Messersmith, N.L., Dutton, J.C., and Krier, H., "Mie Scattering Measurements of Scalar Probability Density Functions in Compressible Mixing Layers," AIAA Paper 91-1686, June 1991.
- ¹³⁸Arnette, S.A., Samimy, M., and Elliott, G.S., "The Effect of Expansion on Large Scale Structure Evolution in a Compressible Turbulent Boundary Layer," AIAA Paper 94-2228, June 1994.
- ¹³⁹Smith, K.M., and Dutton, J.C., "Large-Scale Structures in Supersonic Reattaching Shear Flows," AIAA Paper 95-2251, June 1995.
- ¹⁴⁰Aso, S., Okuyama, S., Kawai, M., and Ando, Y., "Experimental Study on Mixing Phenomena in Supersonic Flow with Slot Injection," AIAA Paper 91-0016, January 1991.
- ¹⁴¹Takahashi, M., and Hayashi, A.K., "Numerical Study on Mixing and Combustion of Injecting Hydrogen Jet in a Supersonic Air Flow," AIAA Paper 91-0574, January 1991.

- ¹⁴²Brown, G.L., and Rebollo, M.R., "A Small, Fast-Response Probe to Measure Composition of a Binary Gas Mixture," *AIAA Journal*, Vol. 10, No. 5, 1972, pp. 649-652.
- ¹⁴³Messersmith, N.L., Dutton, J.C., and Krier, H., "Experimental Investigation of Large Scale Structures in Compressible Mixing Layers," AIAA Paper 91-0244, January 1991.
- ¹⁴⁴Papamoschou, D., "Structure of the Compressible Turbulent Shear Layer," AIAA Paper 89-0126, January 1989.
- ¹⁴⁵Papamoschou, D., and Bunyajitradulya, A., "Double-Exposure PLIF Imaging of Compressible Shear Layers," AIAA Paper 95-0513, January 1995.